WILEY-VCH

Edited by
Visakh P.M. and Maria José Martínez Morlanes

Nanomaterials and Nanocomposites

Zero- to Three-Dimensional Materials and Their Composites

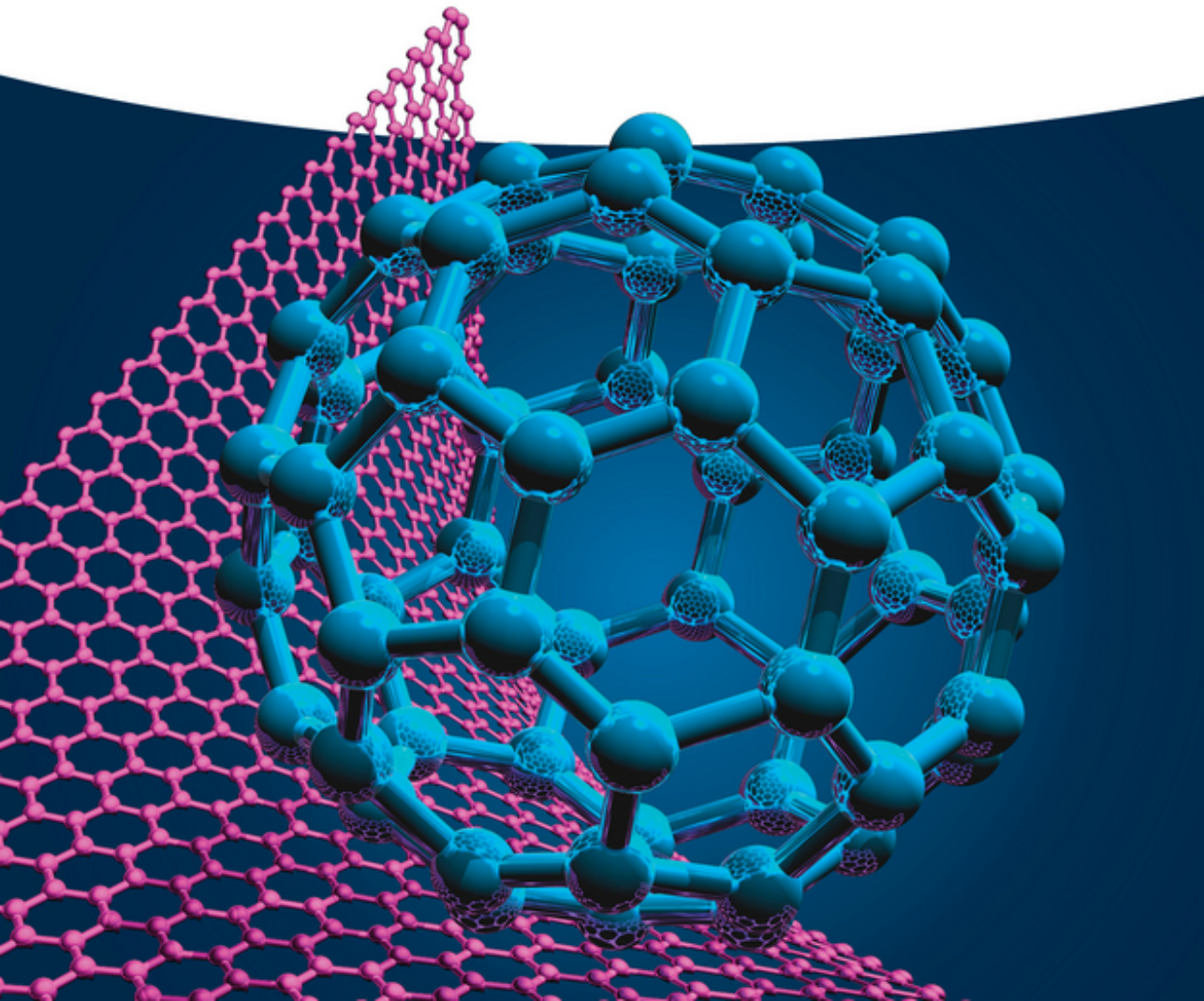

Edited by
Visakh P.M. and
Maria José Martínez Morlanes

Nanomaterials and Nanocomposites

Edited by Visakh P.M. and Maria José Martínez Morlanes

Nanomaterials and Nanocomposites

Zero- to Three-Dimensional Materials and Their Composites

WILEY-VCH
Verlag GmbH & Co. KGaA

Editors

Visakh P.M.
Tomsk Polytechnic University
Department of Ecology and Basic Safety
Lenin av. 30
634050 Tomsk
Russia

Dr. Mª José Martínez Morlanes
Department of Materials Science and Technology-EINA
Instituto de Investigación en Ingeniería de Aragón, I3A
Universidad de Zaragoza
E-50018 Zaragoza
Spain

Library of Congress Card No.: applied for

British Library Cataloguing-in-Publication Data
A catalogue record for this book is available from the British Library.

Bibliographic information published by the Deutsche Nationalbibliothek
The Deutsche Nationalbibliothek lists this publication in the Deutsche Nationalbibliografie; detailed bibliographic data are available on the Internet at <http://dnb.d-nb.de>.

Print ISBN: 978-3-527-33780-4
ePDF ISBN: 978-3-527-68374-1
ePub ISBN: 978-3-527-68376-5
Mobi ISBN: 978-3-527-68375-8
oBook ISBN: 978-3-527-68377-2

Typesetting SPi Global, Chennai, India
Printing and Binding

Printed on acid-free paper

Contents

List of Contributors

Abdullah M. Asiri
King Abdulaziz University
Center of Excellence for
Advanced Materials Research
(CEAMR)
Chemistry Department
P.O. Box 80203
Jeddah 21589
Saudi Arabia

Dipali R. Bagal-Kestwal
National Taiwan University
Institute of Food Science and
Technology
No. 1 Roosevelt Road
Section-4 Taipei
Taiwan
Republic of China

Been H. Chiang
National Taiwan University
Institute of Food Science and
Technology
No. 1 Roosevelt Road
Section-4 Taipei
Taiwan
Republic of China

Diana Elena Ciolacu
Romanian Academy
"Petru Poni" Institute of
Macromolecular Chemistry
Laboratory of Physical
Chemistry of Polymers
41A Grigore Ghica Voda Alley
700487 Iasi
Romania

Raluca Nicoleta Darie
Romanian Academy
"Petru Poni" Institute of
Macromolecular Chemistry
Laboratory of Physical
Chemistry of Polymers
41A Grigore Ghica Voda Alley
700487 Iasi
Romania

Sunita Devi
Maharani Kishori Jat Kanya
Mahavidyalaya
Department of Chemistry
Rohtak
Haryana 124001
India

Surender Duhan
D.C.R. University of Science and Technology
Nanomaterials Research Laboratory
Department of Materials Science and Nanotechnology
Murthal (Sonepat)
Haryana 131039
India

Hamid Garmabi
Amirkabir University of Technology
Department of Polymer Engineering and Color Technology
No. 28, 424 Hafez Ave.
Tehran
Iran

G. Gnana kumar
Madurai Kamaraj University
Department of Physical Chemistry
Alagar Kovil Main Road
Madurai
625021 Tamil Nadu
India

Dhorali Gnanasekaran
Dielectric Materials Division
Central Power Research Institute
Prof. Sir C.V. Raman Road
Bangalore 560080
India

Lida Hashemi
Tarbiat Modares University
Department of Chemistry
Faculty of Sciences
P.O. Box 14115-175
Jallal al ahmad street
Tehran
Islamic Republic of Iran

Rakesh M. Kestwal
National Taiwan University
Institute of Food Science and Technology
No. 1 Roosevelt Road
Section-4 Taipei
Taiwan
Republic of China

and

Product and Research Process Center
Food Industry Research and Development Institute (FIRDI)
No.331, Shih-Pin Road
Hsinchu 300
Taiwan
Republic of China

Anish Khan
King Abdulaziz University
Center of Excellence for Advanced Materials Research (CEAMR)
Chemistry Department
P.O. Box 80203
Jeddah 21589
Saudi Arabia

Ritu Malik
D.C.R. University of Science & Technology
Department of Physics
Murthal (Sonepat)
Haryana 131039
India

Ali Morsali
Tarbiat Modares University
Department of Chemistry
Faculty of Sciences
P.O. Box 14115-175
Jallal al ahmad street
Tehran
Islamic Republic of Iran

Aftab Aslam Parwaz Khan
King Abdulaziz University
Center of Excellence for
Advanced Materials Research
(CEAMR)
Chemistry Department
P.O. Box 80203
Jeddah 21589
Saudi Arabia

Sónia Simões
University of Porto
Center for Mechanical
Engineering (CEMUC)
Department of Metallurgical and
Materials Engineering
R. Dr. Roberto Frias
4200-465 Porto
Portugal

Vijay K. Tomer
D.C.R. University of Science and
Technology
Nanomaterials Research
Laboratory
Department of Materials Science
and Nanotechnology
Murthal (Sonepat)
Haryana 131039
India

Filomena Viana
University of Porto
Center for Mechanical
Engineering (CEMUC)
Department of Metallurgical and
Materials Engineering
R. Dr. Roberto Frias
4200-465 Porto
Portugal

Manuel F. Vieira
University of Porto
Center for Mechanical
Engineering (CEMUC)
Department of Metallurgical and
Materials Engineering
R. Dr. Roberto Frias
4200-465 Porto
Portugal

P. M. Visakh
Tomsk Polytechnic University
Department of Ecology and Basic
Safety
Lenin av. 30
634050 Tomsk
Russia

Yasser Zare
Amirkabir University of
Technology
Department of Polymer
Engineering and Color
Technology
No. 28, 424 Hafez Ave.
Tehran
Iran

1
Introduction for Nanomaterials and Nanocomposites: State of Art, New Challenges, and Opportunities

P. M. Visakh

1.1
Chemistry of Nanoscience and Technology

Science uses methodologies from synthetic chemistry and materials chemistry to obtain nanomaterials in specific sizes and shapes, with specific surface properties, defects, and self-assembly properties, designed to accomplish specific functions and uses [1]. *Nanoscale* is usually defined as being smaller than 1/10th of a micrometer in at least one dimension; this term is also used for materials smaller than 1 μm. An important aspect of nanomaterials is the vast increase in the surface area to volume ratio, which incorporates the possibilities of new quantum mechanical effects in such materials. Suspensions of nanoparticles are possible because the interaction of the particle surface with the solvent molecules is strong enough to overcome differences in density, which usually results from a material either sinking or floating in a liquid. Nanoparticles often have unexpected visual properties because they are small enough to confine their electrons and produce quantum effects. Nanostructured materials are classified as zero-dimensional, one-dimensional, two-dimensional, three-dimensional nanostructures. Nanomaterials are materials that are characterized by an ultrafine grain size (<50 nm) or by a dimensionality that is limited to 50 nm. Nanomaterials can be created with various modulation dimensionalities as defined by Richard W. Siegel: zero (atomic clusters, filaments, and cluster assemblies), one (multilayers), two (ultrafine-grained overlayers or buried layers), and three (nanophase materials consisting of equiaxed nanometer-sized grains). Recently, researchers are using a modified CVD technique for the fabrication of 0D Nanostructured materials (NSMs) [2, 3].

Palgrave and Parkin [4] used the aerosol-assisted CVD technique to fabricate the Au nanoparticles on a glass substrate. Toluene is used as a precursor to deposit gold nanoparticles onto glass. The sizes of Au nanoparticles are 100 nm. Boyd *et al.* [5] developed a new CVD process that can be used to selectively deposit materials of many different types. In this technique, they used the Plasmon resonance in nanoscale structures to create the local heating, which is crucial in order to initiate deposition when illuminated by a focused low-power laser [6]. Elihn *et al.* [7] synthesized the iron nanoparticles enclosed in carbon shells by

Nanomaterials and Nanocomposites: Zero- to Three-Dimensional Materials and Their Composites,
First Edition. Edited by Visakh P.M. and Maria José Martínez Morlanes.

laser-assisted chemical vapor decomposition (LCVD) of ferrocene ($Fe(C_5H_5)_2$) vapor in the presence of the Ar gas. One-dimensional nanomaterials have nanoscale sizes along two-dimensions and a rod-like or wire-like appearance. In such nanomaterials, quantum confinement and surface area-related nanoscale effects are more pronounced compared to 2D nanomaterials. Lyotropic liquid crystal (LLC) template-assisted synthesis is one of the most facile and most applied methods for the synthesis of 1D NSMs such as nanowires, nanorods, nanotubes, nanobelts, nanoribbons, and nanospindles [8–12]. Kijima *et al.* [12] fabricated the platinum, palladium, and silver nanotubes, with inner diameters of 3–4 nm and outer diameters of 6–7 nm, by the reduction of metal salts confined to lyotropic mixed Liquid Crystals (LCs) of two different sized surfactants.

Electrodeposition processes have a wide range of advantages such as low cost, low energy consumption, high growth rate at relatively low temperatures, being environmentally friendly, and having good control of the deposition thickness, shape, and size. Xia *et al.* [13] fabricated the MnO_2 nanotube and nanowire arrays via an electrochemical deposition technique using porous alumina templates. Tang *et al.* [14] prepared the Si nanowires on Si substrates by the hydrothermal deposition route under low temperature and pressure. The obtained Si nanowire consists of a polycrystalline Si core and an amorphous silica sheath. The diameter and length of Si nanowires were 170 nm and 10 lm, respectively. The essence of nanoscience and nanotechnology is the creation and use of molecules, molecular assemblies, materials, and devices in the range of 1–100 nm, and the exploitation of the unique properties and phenomena of matter at this dimensional scale.

1.2 Carbon Nanotubes and Their Nanocomposites

Carbon nanotubes CNTs consist of tubes formed by rolled sheets of graphene (one atomic layer of graphite). The tubes are arranged in a concentric manner to form single-walled carbon nanotubes (SWCNTs), double-walled carbon nanotubes (DWCNTs) and multi-walled carbon nanotubes (MWCNTs). CNTs are excellent candidates for use in various applications: as biological and chemical sensors, as probe tips for scanning probe microscopy, in nano-electromechanical systems (NEMS), and as reinforcement in nanocomposites [15, 16]. CNTs consist of rolled graphene sheets arranged in a concentric manner and are classified according to the number of walls. The length of the nanotubes is between a few hundred nanometers and a few micrometers. Due to their length they become entangled. In general, the SWCNTs are defect-free, whereas MWCNTs present defects. An individual graphene sheet has high strength (130 GPa) and high electrical and thermal conductivities [17, 18]. Due to these remarkable properties, it is expected that since the CNTs consist of rolled graphene sheets, they will also exhibit extraordinary properties. CNTs have generated a great deal of interest in recent years.

The application of CNTs as a reinforcement is very important in any kind of matrix, but is more widely used in polymer matrix composites. The conventional

polymer matrix composites have found application in a wide range of fields due to properties such as low density, reasonable strength, flexibility, and easy processability. However, the search for materials capable of improving the performance of advanced components has triggered the study and production of CNTs reinforced nanocomposites. CNTs/epoxy nanocomposites have been extensively investigated due to their industrial and technological applications. These nanocomposites are fabricated using melt mixing or solution mixing methods. Zhou *et al.* [19] demonstrated that it is possible to improve the strength and fracture toughness with the incorporation of 0.3 wt% CNTs in the epoxy matrix. Velasco-Santos *et al.* [20] studied the CNTs/PMMA (poly Methyl Methacrylate Monomer) nanocomposites and observed an increase in the storage modulus of 1135% for composites, with 1 wt% of CNTs dispersed using an *in situ* polymerization at 90 °C.

Ceramic matrices reinforced with CNTs can provide nanocomposites with super plastic deformability, high strength, improved fracture toughness, and higher electrical and thermal conductivities, while metallic matrices reinforced with CNTs are expected to produce nanocomposites of high strength and specific stiffness, which is a desirable coefficient of thermal expansion and good damping properties [21]. Yamamoto and Hashida [22] developed a new technique to obtain a more homogeneous dispersion of CNTs and improve the bonding to the alumina matrix. This treatment involved the use of a precursor method for the synthesis of an alumina matrix, MWCNTs modified by a covalent functionalization (by a concentrate H_2SO_4 and HNO_3 acid mixture), and the Spark Plasma Sintering (SPS) method. Nguyen *et al.* [23] showed that it is possible to produce ultrafine-grained MWCNT/Ni composites by the SPS method with 97% of density. The authors used modified CNTs by noncovalent functionalization to improve the cohesion between the CNT and Ni powders. The composites revealed a higher value of hardness in the CNT than the Ni. Kwon and Leparoux [24] obtained a higher strength for CNT/Al nanocomposites produced by mechanical ball milling followed by a direct powder hot extrusion process. The joining of the dispersion and mixture processes in a single step, by ultrasonication was effective in the formation of a uniform dispersion of CNTs through an Al matrix of the nanocomposites. CNTs are embedded in the grains of Al, which is essential for effective load transfer from the matrix to the reinforcement, and improves the mechanical properties of the nanocomposite.

1.3
Graphene- and Graphene Sheets-Based Nanocomposites

Graphene is extraordinarily strong (the strongest material ever known or tested), supernaturally light, and electrically super-conductive. It is 200 times stronger than steel, thinner than a sheet of paper, and more conductive than copper. Its flexibility and structure also make it the leading candidate as the primary component of next-generation, ultrahigh speed circuitry in everything from computers, to smart phones, to televisions. It is therefore of interest to a range of industries. Graphene CNTs can effectively stack transistors on top of one another

on microchips, allowing for exponentially more transistors on a chip without increasing the size. More transistors means more operations per second, which in turn means more processing power and faster processing speed. Graphene sheets are composed of carbon atoms linked in hexagonal shapes with each carbon atom covalently bonded to three other carbon atoms. Each sheet of graphene is only one atom thick, and each graphene sheet is considered a single molecule. Graphene's electron mobility is faster than any known material and researchers are developing methods to build transistors on graphene that would be much faster than the transistors currently built on silicon wafers. Another interesting application of graphene that is being developed takes advantage of the fact that the sheet is only as thick as a carbon atom. Researchers have found that they can use nanopores to quickly analyze the structure of DNA. In the 1960s, Boehm speculated that reducing exfoliated graphite oxide would yield monolayers in solution [25], although the term *graphene* was not coined until 1986 [26] and was formally accepted only in 1994 [27]. A number of early studies, as early as van Bommel in 1975, found monolayers of carbon in graphitic structures, formed on various carbide [28] and transition metal [29] surfaces, with SiC [30].

Many methods of removing the oxygen from the graphene oxide (GO) structure through chemical, [31] thermal, [32] electrochemical [33], or electromagnetic flash [34], as well as laser-scribe [35] techniques have been successful, but have generally resulted in inferior samples and are hence more precisely named reduced graphene oxide (rGO). Nethravathi and Rajamathi described that chemically modified graphene sheets are obtained through solvothermal reduction of colloidal dispersions of graphite oxide in various solvents. Reduction occurs at relatively low temperatures (120–200 °C). Reaction temperature, the self-generated pressure in the sealed reaction vessel, and the reducing power of the solvent influences the extent of reduction of graphite oxide sheets to modified graphene sheets.

Graphene nanocomposites at very low loading show substantial enhancements in their multifunctional aspects, compared to conventional composites and their materials. This not only makes the material lighter with simple processing, but also makes it stronger for various multifunctional applications [36]. Jang and Zhamu reviewed the processing of graphene nanoplatelets (GNPs) for fabrication of composite materials [37]. Mack *et al.* prepared nanocomposites of polyacrylonitrile (PAN) nanofibers strengthened by GNP, which they demonstrated to have improved mechanical qualities [38]. Das *et al.* [39] employed the nanoindentation technique to the graphene-reinforced nanocomposites fabricated by using polyvinyl alcohol (PVA) and poly Methyl Methacrylate Monomer (PMMM). The results showed significant improvement in crystallinity, elastic modulus, and hardness through the addition of only 0.06 wt% of graphene.

1.4 Nanocomposites of Polyhedral Oligomeric Silsesquioxane (POSS) and Their Applications

The most common representation of zero-dimensional nanomaterials is polyhedral oligomeric silsesquioxane POSS nanoparticles, POSS-based compounds

are thermally and chemically more stable than siloxanes. Of several structures of silsesquioxanes (random, ladder, and cage), cage structures contain eight silicon atoms placed at cube vertices. Cubic structural compounds are commonly represented based on the number of silicon atoms present in cubic structure. POSS is unique in the size (1.5 nm in core diameter) when compared to other nanofillers and can functionally tailor to incorporate a wide range of reactive groups [40]. POSS containing polymers received good attention during the last decade as a novel category of nanoscale-structured materials. Incorporation of bulky POSS particles into linear thermoplastic polymers can impart better organo-solubility because of the introduction of bulky POSS pendent group by decreasing the intermolecular forces between the polymer chains. Fina *et al.* [41] prepared the maleic anhydride-grafted polypropylene (PP-g-MA)/POSS hybrids by POSS grafting during a one-step reactive blending process. Polyamide 12/trisilanolphenyl–POSS composites were prepared via melt-compounding. The effect of POSS on crystalline structure and crystalline transition of PA 12 were studied and enhanced the tensile strength and thermal stability of PA 12 [42]. The POSS fractions in the nanocomposites were tailored by the PA–MI polymer maleimide contents and showed great influence on the thermal and mechanical properties of the polyamide–POSS nanocomposites [43]. Synthesis of liquid crystal POSS and specific problems connected with the nature of silsesquioxane cage, and special properties that their geometry imparts to their mesogenic behavior of liquid-crystal polyhedral silsesquioxane materials have been described [44]. POSS monomer (POSS-MA) was used as a novel dental restorative composites to replace commonly used dental base monomer 2,2′-bis-[4-(methacryloxypropoxy)-phenyl]-propane (Bis-GMA) [45]. Amino functionalized silsesquioxane provides curl retention for hair [46].

Polyfluorenes/POSS nanocrystal NC shows maximum luminescence intensity and quantum efficiency, which is almost twice as good as those of a Polytetrafluoroethylene (PFO EL) device, and is an excellent material for optoelectronic applications [47]. Castaldo *et al.* [48] presented polymeric NC sensors, based on a POSS by selecting a proper matrix such as poly[(propylmethacryl-heptaisobutyl-POSS)-*co*-(*n*-butylmethacrylate)] and a suitable choice of other external home-made fillers. Polyphenylsilsesquioxane is used as interlayer dielectrics and protective coatings films for semiconductor devices, liquid crystal display elements, magnetic recording media, and optical fiber coating.

Poly(aminopropyl silsesquioxane) and specific carbonyl compounds of silsesquioxane act as an antitumor agent. Silsesquioxane films, particularly OAPS/imide and OAPS/epoxide films, provide excellent O_2 barrier properties, and is an ideal candidate for packaging applications [49]. In Poly Vinyl Chloride (PVC), POSS behaves as a plasticizer like dioctyl phthalate (DOP) and could be used as a plasticizer [50]. Metal-containing POSS cages (gallium-containing cage silsesquioxanes and aluminosilsesquioxane) [51, 52] have been synthesized, for the use of silica-supported metal catalysts.

1.5 Zeolites and Composites

Zeolites are a series of crystalline microporous alumino silicates found on the earth's surface and in a number of environments, including soils, seafloor deposits, hydrothermal alteration products, altered volcanic deposits, sediments, and so on [53]. Zeolites find their application in sorbents, water purification, ion exchange beds, catalysts, optically active materials, polymerization science, separation technology, micro-electronics, photoelectrochemical applications in solar cells, thin-film sensors, and encapsulation of drugs and biomolecules for the targeted or controlled-release applications [54].

The significant advancements in zeolite synthesis were achieved by the utilization of organic components; specifically, the tremendous growth has been reported for the siliceous zeolites, and a number of new high-silica zeolites were successfully crystallized using organic cations with aluminosilicate gels at 100–200 °C. Koet al prepared the TiO_2/natural zeolite (TiO_2/NZ) composite from sol–gel derived nanotitania colloids and zeolite powder. Under vigorous magnetic stirring, natural zeolite was mixed with titania sol. The photophysical properties of zeolites are purely dependent upon the presence of cations in the zeolite framework and adsorbed water molecules over their surfaces [55]. Since the donor strength of guest molecules affects the absorption band of chromophores of strong electron acceptors, the optical property of chromophores can be effectively tuned by direct interaction with cations. The electrical properties of zeolites are associated with the composition and content variation of zeolite, pore size, and ion exchange capacity [56]. The movement of positive ions into the pore distribution along the zeolite varies the electrical conductivity. The location of charge balancing cations in zeolites exhibited excellent magnetic properties, owing to their unpaired electrons, influenced by the distribution of silicon and aluminum ions within the aluminosilicate framework [57].

The magnetic interaction of zeolite network depends upon the charged cations and the distance between the two charged species along the framework. Fuel cell is one of the most significant and outstanding electrochemical device in which the role of zeolites as catalysts and fillers in membranes is imperative. Zeolite serves as a better alternative to porous materials (employed in fuel cells), owing to its unique advantages including high electrical and thermal conductivity, high chemical and physical stability, extended surface area and porosity, low cost, and so on. The higher efficiency obtained is attributed to the lower methanol crossover as well as the excellent proton conductivity attained through the water up-taking ability of zeolites [58].

The lower methanol permeability obtained is attributed to the high diffusion resistance of the membrane achieved by the smaller pore size (0.3 A) and the inorganic nature of zeolites [59]. The improved performance of the anode was achieved by the higher surface area and porosity of zeolites for bacterial adhesion [60].

Boyas *et al.*, exploited the bifunctional Pt/zeolite (Pt-H-Y) as the catalyst in the hydrocracking of rapeseed oil. The time consumed by the Pt-H-Y catalyst for

cracking the rapeseed oil is 3 h, which is lower than that of other catalysts. Zeolite-based photocatalysts are promising material for the abatement of air and water pollution by using solar light, photoreduction of CO_2 by H_2O, photo-oxygenation of saturated hydrocarbons, photosplitting of water into hydrogen and oxygen, photogeneration of hydrogen peroxide, and other photo processes [61]. Fukahori *et al.*, synthesized the TiO_2/zeolite sheets through papermaking technique and the prepared material was exploited as the photocatalyst in the degradation of bisphenol A (BPA). The TiO_2/zeolite sheets exhibited a higher efficiency for BPA removal than that of bare TiO_2 sheets. The higher efficiency obtained is ascribed to the reversible adsorption, the free movement of BPA molecules on composite attained by the cage-like structure, and the pore connectivity of zeolites [62].

1.6 Mesoporous Materials and Their Nanocomposites

Zeolites, the first primitive porous materials, were first discovered in 1756 by the Swedish scientist Axel Fredrik Cronstedt. Zeolites have aluminosilicate frameworks, which were synthesized via nonsurfactant-assisted route employing a single molecule template and having small micropores inside it. Among the above-mentioned materials, mesoporous materials are of specific importance due to their high stability, surface areas, and large pore volumes, which make them the most suitable candidates to be used as adsorbents, ion-exchangers, catalysts, catalyst supports, and in many other related applications [63].

Mesoporous materials prepared using neutral surfactants as templates possess improved stability. In case of primary amine (with carbon tail lengths between C_8 and C_{18}) as templates, the pore size of the final mesoporous silicas can be tuned by changing the hydrophobic tail length of amines. Preparation of mesoporous molecular sieves with large framework wall thickness, small particle sizes, and complementary framework confined and textural mesoporosity. In addition, the S_oI_o approach allows for cost reduction by employing less expensive reagents and mild reaction conditions while providing for the effective and environmentally benign recovery and recyclability of the template. The basic interest in mesoporous silica stems from the presence of a well-ordered structure that provides high surface area and accessibility to molecular species through the channels. In addition, the possibility of synthesizing different types of mesostructures with multiple pore architecture further enhances their versatility for different applications. In 1998, regarding the preparation of large-pore ordered mesoporous silica with a 2D hexagonal structure, Zhao *et al.* used triblock copolymers as templates, which is very famously known as *SBA-15* [64].

In 1998, a new family of highly ordered mesoporous silica materials has been synthesized in an acid medium by the use of nonionic triblock copolymers ($EO_nPO_mEO_n$) with large polyethyleneoxide (PEO) and polypropyleneoxide (PPO) blocks. Different materials with a diversity of periodic arrangements have been prepared and denoted as SBA materials (the acronym for Santa Barbara Amorphous) [65].

Synthesis of mesoporous metal oxides with high surface area, crystalline frameworks, and well-connected uniform pores is particularly important to achieve improved application performances. Similar to that for silica-based mesoporous materials, the synthesis of mesoporous metal oxides is mainly accomplished through the soft-templating approach. Ordered mesoporous materials with different compositions from pure inorganic or pure organic frameworks to organic–inorganic hybrid frameworks have been widely reported in the past two decades. For example, mesoporous metal oxides and mixed oxides with semicrystalline frameworks, such as TiO_2, ZnO, WO_3, SnO_2, and Al_2O_3 are successfully prepared by a direct synthesis strategy using amphiphilic copolymer templates. For the synthesis of mesoporous metal oxides by this structure replication procedure, a precursor compound, typically a metal salt, is filled into the pores of the silica matrix. The precursor compound is then converted into the metal oxide by thermal decomposition, sometimes preceded by a pH-induced conversion into an intermediate phase (such as a hydroxide species). Mesoporous carbon has been used as a potential matrix for the immobilization of biomolecules [66]. The widespread applications of porous carbons are attributed to their remarkable physicochemical properties, including hydrophobicity of their surfaces, high corrosion resistance, good thermal stability, high surface area, large pore volume, good mechanical stability, easy handling, and low cost of manufacture. Introduction of organic moieties within the silicate framework increases the flexibility of mesoporous films and fibers and reduces the brittleness of monoliths. Organic/inorganic hybrid materials are important because they can be designed at a molecular level to perform many processes including catalysis, adsorption, separation, drug delivery, and sensing. Mesoporous silica has a large surface area and a lot of constrained space in the form of nanochannels. Polymers grown within the constrained space of periodic mesoporous silica may exhibit unusual mechanical, electronic, magnetic, and optical properties. The spatial control of the growth process is limited by the channel network of the silica host, which allows the fabrication of materials with designed shapes, particularly nanofibers, wires, and porous particles. Mesoporous silica/polymer nanocomposites are synthesized with extrusion polymerization and are found with special properties [67]. The reason is that the nanoreactor gives space constraints on polymer chains when they grow inside the nanochannels. For example, polyethylene made with this method had ultrahigh molecular weight, high melting temperature, and only extended chain crystals rather than folded chain crystals because of the space constraint which controlled the formation of crystals. Mesoporous silica/polymer nanocomposites can also be made through entrapping polymers in the nanochannels of mesoporous silica through the hydrogen bonding between the silanol groups on the silica surface and the groups in the polymer chain. Mesoporous materials thus provide improved delivery systems for biomolecules, which have local and sustained release over time, while simultaneously protecting the biopharmaceutical agent from degradation. These delivery systems maintain the concentration of drugs in the precise sites of the body within optimum range and under the toxicity threshold, improve the therapeutic efficacy, and reduce toxicity [68].

1.7
Bio-Based Nanomaterials and Their Bio-Nanocomposites

Bio-based nanocomposites are composite materials that are made of particles from renewable natural sources and are in the range of 1–100 nm in size. These bio-based nanomaterials such as building blocks, particles, fiber, and resin, are combined to engineer a new material with enhanced properties. These new immerging "nano–bio" materials comprise exotic, dynamic, and fascinating features that make them smart futuristic biodegradable material. Cellulose is the most abundant polymer available in nature, after which comes hemicelluloses followed by lignin. This motivates scientists to discover new possibilities for biological materials in the rapidly expanding field of nanotechnology. Lignin has many different applications, including its use as a composite material. Hemicellulose has already been used for food applications but there are possibilities for new polymer production. Likewise, many researchers have also prepared nanoparticles using other natural compounds such as chitosan, dextran, gelatin, alginate, albumin, and starch [69–74].

The cellulose nanocrystals (CNCs) are rod-like or whisker-shaped particles with transverse dimensions as small as 3–30 nm, providing a high surface to volume ratio, also called cellulose nanowhiskers (CNWs). These particles have also been named nanocrystalline cellulose, cellulose whiskers, cellulose nanowhiskers, and cellulose microcrystals. Nanocellulose composites offer new possibilities for unaccountable applications in day-to-day life. Unlike cellulose, nanostructured cellulose provides a large variety of options for Chemistry and engineering for many material applications. Fundamental domain structures with high intrinsic strength, high melting temperature, directional rigidity, and ease of chemical modification can provide high reinforcement and scaffolding in the formation of nanocomposites [75, 76].

Chitin $(C_8H_{13}O_5N)_n$ is one of the widely available natural polymers on earth and functions naturally as a structural polysaccharide similar to the cellulose in plants and collagen in animals. Chitin and Chitosan (CS) and their derivatives are highly eco-friendly and nontoxic and nonallergic. They also possess good biodegradability, bioactivity, biocompatibility, coating ability, and good miscibility. Because of their nonantigenic properties, they are highly compatible with animal as well as plant tissues. Chitin/chitosan has been studied as a natural cationic biopolymer because of its excellent biocompatibility, biodegradability, nontoxicity, antimicrobial capability, and stimulation of wound healing [77]. Both chitin and chitosan materials have found applications as components in different products and processes [78, 79].

The hydrophilic nature of starch is a major constraint that seriously limits the development of starch-based nanoparticles [80]. A good alternative to solve this problem is the grafting of hydrophobic side chains to the hydrophilic starch backbone [81]. Various synthetic methods for synthesis of starch nanoparticles such as high-pressure homogenization and miniemulsion cross-linking, precipitation/nanoprecipitation [82] emulsion [83, 84], and microemulsion [85] have

been explored by researchers. Ma *et al.* [86] have prepared starch nanoparticles by precipitating a starch solution within ethanol as the precipitant. Spherical or oval-shaped nanoparticles (diameters in the range of 10–20 nm) were prepared by the starch–butanol complex precipitation method [87].

Thus, starch bio-nanocomposites are of much academic as well as industrial interest. Most work has been oriented toward the use of new environmentally friendly polymers with starch nanocomposites such as natural rubber [88], water-borne polyurethane [89], waxy maize starch [90], cassava starch [91], pullulan [92], Poly Lactic Acid (PLA) [93], PVA [94], and soy protein isolate (SPI) [95].

1.8 Metal–Organic Frameworks (MOFs) and Their Composites

Metal–organic frameworks (MOFs) represent a class of crystalline and highly porous hybrid materials obtained by the assembly of metallic ions and organic ligands. MOFs exhibit interesting properties for gas separation, gas storage, and drug delivery and could also be used as sensors. Synthetic polymer–MOF composite membranes have been investigated using a polyimide (Matrimid) and a polysulfone polymer as the matrix. Composite membranes of MOF-5 and ZIF-8 (Zeolitic Imidazolate Framework) with Matrimid were prepared by the solution blending approach [96, 97]. Better quality composite membranes were formed by pretreatment of the MOF crystals with the silylating agent *N*-methyl-*N*-(trimethylsilyl)trifluoroacetamide. In a similar study, ZIF-8-polysulfone membranes were also obtained by the solution blending approach. The CO_2 diffusion properties of the composite membranes were studied, and the ZIF-8 crystals were shown to improve the transport of the gas through the membrane.

The monodisperse MOF–silica composites were tested as the High-Performance Liquid Chromatography (HPLC) stationary phase and showed good separation properties. In another report [98], silica and SiO_2/Al_2O_3 composite beads were used. Two methods were employed: formation under solvothermal conditions and immersion of the beads into preheated crystallization solutions. Recently opened new possibilities of applications are MOFs [99]. Yaghi and Li [100] were the first to describe the synthesis and properties of MOFs. In recent years, it has been shown that a large variety of 2D and 3D metal–organic networks with high porosity, unusual ion exchange, and adsorptive properties can be designed using intermolecular interactions and metal–ligand co-ordination [101].

The intercalation of graphene in MOF imparts new electrical properties such as photoelectric transport in the otherwise insulating MOF. The results point to the possibility of using functionalized graphene to synthesize a wide range of structural motifs in MOF with adjustable metrics and properties. Many research efforts have focused on these issues and the deposition of MOF on various supports such as alumina, silica, functionalized self-assembled monolayer (SAM), functionalized graphite, graphite oxide (GO), or amorphous carbon

have been recently reported as a way to produce MOF-based membranes or composites. The porosity of the hybrid materials is in the range of that of the MOF; however, a slight decrease is found (except for MGr5) due to the addition of low- or nonporous graphite.

The results indicate that the oxidation of graphite is important to build MOF/graphite hybrid materials with synergistic properties. The presence of functional groups on the substrate's surface enables the formation of bonds between the components and thus the composites can be formed. The results suggest that MOF/graphite hybrid materials represent a distorted physical mixture of MOF and graphite. Besides the chemical features of the graphite, the physical parameters, and especially the porosity and size of flakes, also seem to influence the formation of the hybrid materials. Most MOF materials still show relatively low CO_2 and CH_4 uptakes. To enhance CO_2 and CH_4 adsorption, it is imperative to develop new materials such as covalent organic frameworks (COFs) or to modify MOFs by using postsynthetic approaches.

One of the modification approaches is incorporation of CNTs into MOFs in order to achieve enhanced composite performance, because of the unusual mechanical and hydrophobicity properties of CNTs. Another approach is doping MOFs or COFs with electropositive metals. Recent studies indicate that the surface carboxylate functional groups of a substrate could act as nucleation sites to form MOFs by heterogeneous nucleation and crystal growth. MOFs have been evaluated as promising H_2 storage media as MOFs exhibit exceptionally high surface areas and tunable pore size. An additional advantage of MOFs is that preparation is economic as MOFs are synthesized by "one-pot" solvothermal methods under mild conditions. The large surface areas, low framework densities and high pore volumes of MOFs compared to other porous matrices have motivated a great deal of interest in these materials, which have significant potential for use in a variety of applications ranging from storage of gases to application in heterogeneous catalysis [102–104].

In particular, externally accessible nanosized cavities and channels allow for the incorporation of substrates inside the crystal to facilitate the heterogeneous catalytic action of these MOFs. In the past decade, MOFs have received much attention due to potentially useful properties. As a new type of functional materials, the exceptionally high crystallinity and designability of MOFs can also open the door for investigation of the mechanism as well as for the functional regulation of proton conductivity. In general, some specific physicochemical properties of MOFs are controlled and modified by the judicious selection of organic ligands and metal centers. In conclusion, micropore- and mesopore-integrated materials have been synthesized by using mesoporous silica and MOF. The composites were composed of nano-CuBTC (Copper Benzene 1,3,5 tricarboxylic acid) crystals and mesoporous silica, and the ratio of micropore/mesopore volume can be tuned by controlling the initial concentration of the reaction solution of CuBTC. Under synthesis in low-concentration solution of CuBTC, the obtained composites showed higher adsorption uptake than the estimated uptake of MOF–mesoporous silica mixture showing the retention nature of micro- and mesoporous materials and

formation of additional pore spaces that should be from the space between the nano-CuBTC crystals.

The MOFs are a class of the nanoporous materials. MOFs are most attractive for their high capacity for hydrogen absorption and storage, capture and separation of gases, and for applications in catalysis.

1.9 Modeling Methods for Modulus of Polymer/Carbon Nanotube (CNT) Nanocomposites

The CNT-reinforced nanocomposites are applied in a wide range of aerospace structures, automotive components, sporting goods, conducting plastics, electromagnetic interference shielding, optical barriers, biomaterial devices, and different sensors [105]. The mechanical properties of polymer nanocomposites depend on many parameters such as aspect ratio (α), alignment, waviness, dispersion, and agglomeration of nanoparticles as well as on the interaction between polymers and nanofillers [106–110].

The mechanical properties can be predicted by various computer modeling methods at large scales of length and time from molecular, microscale to macroscale, and their combination as multiscale techniques. Molecular modeling is a powerful instrument to study the atomic structure and interaction at the nanometer scale [111]. This approach assumes a noncontinuous organization of material wherein its discrete nature often limits the length and time scales. The commonly used techniques of molecular modeling for mechanical properties of polymer/CNT nanocomposites are molecular dynamics (MDs) and molecular mechanics (MMs) [112]. Molecular dynamics is the most widely used modeling technique that allows the accurate prediction of an interaction between constituent phases at the atomic size [113].

Griebel and Hamaekers [114] have shown an excellent agreement between MD results with rule of mixtures and extended rule of mixtures models for extremely long and short CNTs. The MD simulation of polystyrene (PS)/CNT nanocomposites exhibited that the ion beam deposition modification produces many cross-links between CNT and polymer chains which reinforce the nanocomposites [115]. The optimum condition for this sample was observed in high ion energy and compact structure. Using molecular mechanics simulation, Mokashi *et al.* [116] found that the length of CNTs and the configuration of polyethylene (PE) play an important role in the tensile properties of nanocomposites. The crystalline PE caused a moderate improvement by long CNT, while the short CNT caused a significant reduction in the modulus of amorphous PE resulted from a poor load transfer at the interface.

Huang *et al.* [117] considered the 3D end effects of SWCNT by introduction of a length factor. Their model can be applied for a CNT loading between 0 and 5 vol%, while the Finite element method (FEM) model is suitable for a CNT content about 5 vol% [118]. Song and Youn [119] also used the asymptotic expansion homogenization method to perform both localization and homogenization for a

heterogeneous system. They found a good agreement between the numerically and the analytically calculated elastic moduli.

The calculated modulus by M-T for PET/SWCNT (Poly ethylene teriphtalate) nanocomposites [120] has been higher than the experimental results. Ogasawara *et al.* [121] also studied the effect of 3D random orientation and entangled distribution of CNTs in polyimide/MWCNT nanocomposites, conducted based on the Eshelby–Mori–Tanaka theory. Coleman *et al.* [122] stated that the substantial increment of modulus in polymer/CNT nanocomposites is attributed to the formation of an ordered polymer layer around the CNT. The nucleation of this layer increases the crystallinity of polymer, which improves the stiffness of nanocomposites. Guzman de Villoria and Miravete [123] also introduced a new micromechanics model called the dilute suspension of clusters taking into account the influence of inhomogeneous dispersion of nanofillers in nanocomposites. The proposed model significantly improved the theoretical–experimental relationship for epoxy/clustered CNT nanocomposites.

Fisher *et al.* [124] studied the effect of the wavelength ratio of the CNT on the modulus assuming the minimal CNT waviness distribution ($0 < w < 1$) and the more moderate waviness ($0 < w < 1$). Bradshaw *et al.* [125] also predicted the effective modulus of nanocomposites containing aligned or randomly oriented CNT. Furthermore, Shao *et al.* [126] proposed a model to calculate the effect of CNT curvature and interfacial bonding on the effective modulus of nanocomposites. They found that the modulus is very sensitive to waviness and this sensitivity falls with the enhancement of waviness.

1.10
Nanocomposites Based on Cellulose, Hemicelluloses, and Lignin

Cellulose is considered to be the most ubiquitous and abundant biopolymer on the planet, which has been used for many centuries as a construction material, in the forest products, as natural textile fibers, as paper and boards, and so on. *Cellulose* is defined as a linear β-1,4-linked homopolymer of anhydroglucose or, more recently as a homopolymer of anhydrocellobiose [127]. The intramolecular hydrogen bonds are responsible for the stiffness of the chain and stabilize the twofold helix conformation of crystalline cellulose [128]. The intermolecular hydrogen bonding in cellulose is responsible for the sheet-like nature of native cellulose. The term *cellulose nanoparticles* generally refers to cellulosic particles having at least one dimension in the nanometer range [129]. On the basis of the cellulosic source and the processing conditions, cellulose nanoparticles (CNs) may be classified into three main subcategories, as nanofibrillated cellulose (NFC), CNCs, and bacterial nanocellulose (BNC).

Generally, the main extraction processes in the preparation of CNs are mechanical treatment and acid hydrolysis. Mechanical processes can be divided into high-pressure homogenization and refining [130], microfluidization [131], grinding [132], cryocrushing [133], and high-intensity ultrasonication [134].

In recent years, CNs-based nanocomposites have been extensively used in different areas such as food packaging materials, [135], optical, light-responsive composites and other electronic devices [136], as well as in advanced composites manufacturing [137], printing and paper industry, and pharmaceutical and medical applications [138]. As biomedical application, the CNs-based nanocomposites are used as scaffolds in artificial ligaments or tendon substitutes, due to their excellent cytocompatibility [139].

Hemicelluloses represent an important renewable resource of biopolymers, but their utilization for the achievement of new materials is rather limited. Moreover, the procurement of hemicelluloses in their pure form is still challenging. These constitute about 20–30% of the total mass of annual and perennial plants and have a heterogeneous composition of various sugar units classified as xylans (β-1,4-linked D-xylose units), mannans (β-1,4-linked D-mannose units), arabinans (α-1,5-linked L-arabinose units), and galactans (β-1,3-linked D-galactose units) [140]. Wide variations in hemicelluloses content and chemical structure can occur depending on the biomass type, that is, maize stems (28.0%), barley straw (34.9%), wheat straw (38.8%), and rye straw (36.9%) [141] or on the components of an individual plant, that is, stem, branches, roots, and bark [142].

Considerable interest has been directed to hemicelluloses-based biomaterials due to their nontoxicity, bio-based origin, bioactivity, biocompatibility, and oxygen barrier properties, which give them potential in numerous applications, such as drug delivery, tissue engineering, and food packaging. Among these research activities, hemicellulose-based films have received ever-increasing interest as oxygen barrier films, but suffer from low film-forming ability and mechanical performance. An effective and simple method to produce hemicelluloses-based nanocomposite film of high quality was proposed by Peng *et al.* [143] who incorporated cellulose nanofibers (CNFs) into xylan (XH) films in the presence of plasticizers. The sugar composition (relative weight percent) by the sugar analysis is: 89.38% xylose, 5.75% arabinose, 1.87% glucose, 0.66% galactose, 1.78% glucuronic acid, and 0.55% galacturonic acid.

The freeze–thaw technique was used by Guan *et al.* [144] to prepare a novel hybrid hydrogel from hemicelluloses extracted from bamboo (*Phyllostachys pubescens*) holocellulose, PVA, and chitin nanowhiskers. Lignin, the main aromatic component of vegetable biomass, presents a special interest both due to its vast reserves, which are still less valorized, as well as due to its active role in the complex process of organic material formation and conversion in biosphere.

Several studies revealed that similar functional groups are found in all types of lignin [145]. Thus, softwood lignin contains guaiacyl propane units that include a methoxy group bonded to the third carbon atom of the aromatic ring, while hardwood lignin has guaiacyl propane units and syringyl propane units.

The main advantage of the hydroxymethylated lignin is its high content of hydroxyl groups, which allows for its use as a phenol substitute in phenol formaldehyde resin synthesis [146], composites, biocides systems, and bioremediation [147].

Nevárez *et al.* [148] prepared biopolymer nanocomposite films by vapor-induced phase separation at controlled temperatures (35–55 °C) and relative humidity, RH (10–70%) using lignin as a filler and cellulose triacetate (CTA) as a polymer matrix. Lin *et al.* [149] showed that enzyme-hydrolyzed lignin content affected the structure and properties of the PANI–lignin (Polyanilene) nanocomposites.

References

1. Ozin, G.A. and Cademartiri, L. (2009) *Nanochemistry: What Is Next?*, Small 2009, vol. 5 (11), Wiley-VCH Verlag, Weinheim, pp. 1240–1244.
2. Zhang, Z., Wei, B.Q., and Ajayan, P.M. (2001) *Appl. Phys. Lett.*, **79**, 4207.
3. Seipenbusch, M. and Binder, A. (2009) *J. Phys. Chem. C*, **113**, 20606.
4. Palgrave, R.G. and Parkin, I.P. (2006) *J. Am. Chem. Soc.*, **128**, 1587.
5. Boyd, D.A., Greengard, L., Brongersma, M., El-Naggar, M.Y., and Goodwin, D.G. (2006) *Nano Lett.*, **6**, 2592.
6. Jäger, C., Huisken, F., Mutschke, H., Henning, T., Poppitz, W., and Voicu, I. (2007) *Carbon*, **45**, 2981.
7. Elihn, K., Landström, L., Alm, O., Boman, M., and Heszler, P. (2007) *J. Appl. Phys.*, **101**, 034311.
8. Huang, L.M., Wang, H.T., Wang, Z.B., Mitra, A., Bozhilov, K.N., and Yan, Y.S. (2002) *Adv. Mater.*, **14**, 61.
9. Huang, L.M., Wang, H.T., Wang, Z.B., Mitra, A.P., Zhao, D., and Yan, Y.S. (2002) *Chem. Mater.*, **14**, 876.
10. Kijima, T., Ikeda, T., Yada, M., and Machida, M. (2002) *Langmuir*, **18**, 6453.
11. Murali, S., Xu, T., Marshall, B.D., Kayatin, M.J., Pizarro, K., Radhakrishnan, V.K. *et al.* (2010) *Langmuir*, **26**, 11176.
12. Kijima, T., Yoshimur, T., Uota, M., Ikeda, T., Fujikawa, D., Mouri, S. *et al.* (2004) *Angew. Chem. Int. Ed.*, **43**, 228.
13. Xia, H., Feng, J., Wang, H., Lai, M.O., and Lu, L. (2010) *J. Power Sources*, **195**, 4410.
14. Tang, Y.H., Pei, L.Z., Lin, L.W., and Li, X.X. (2009) *J. Appl. Phys.*, **105**, 044301.
15. Philip Wong, H.-S. and Akinwande, D. (2011) *Carbon Nanotube and Graphene Device Physics*, Cambridge University Press, USA.
16. Philip Wong, H.-S. and Akinwande, D. (2011) *Carbon Nanotube and Graphene Device Physics*, Cambridge University Press.
17. Meyyappan, M. (ed) (2005) *Carbon Nanotubes: Science and Application*, CRC Press, LLC.
18. Lee, C., Wei, X.D., Kysar, J.W., and Hone, J. (2008) *Science*, **321** (5887), 385–388.
19. Zhou, Y., Pervin, F., Lewis, L., and Jeelani, S. (2008) *Mater. Sci. Eng., A*, **475** (1-2), 157–165.
20. Velasco-Santos, C., Martínez-Hernández, A.L., Fisher, F., Ruoff, R., and Castaño, V.M. (2003) *J. Phys. D: Appl. Phys.*, **36** (12), 1423–1428.
21. Tjong, S.C. (2009) *Carbon Nanotube Reinforced Composites Metal and Ceramic Matrices*, WILEY-VCH Verlag GmbH & Co. KGaA, Weinheim.
22. Yamamoto, G. and Hashida, T. (2012) in *Carbon Nanotube Reinforced Alumina Composite Materials, Composites and their Properties* (ed N. Hu), InTech, Rijeka, pp. 483–502.
23. Nguyen, J., Holland, T.B., Wen, H., Fraga, M., Mukherjee, A., and Lavernia, E. (2014) *J. Mater. Sci.*, **49** (5), 2070–2077.
24. Kwon, H. and Leparoux, M. (2012) *Nanotechnology*, **23** (41), 415701 (10pp).
25. Boehm, V.H.P., Clauss, A., Fischer, G.O., and Hofmann, U. (1962) *Z. Naturforsch.*, **17**, 150.
26. Boehm, H.P., Setton, R., and Stumpp, E. (1986) *Carbon*, **24**, 241.
27. Boehm, H.P., Setton, R., and Stumpp, E. (1994) *Pure Appl. Chem.*, **66**, 1893.

28. Stefan, P.M., Shek, M.L., Lindau, I., Spicer, W.E., Johansson, L.I., Herman, F., Kasowski, R.V., and Brogen, G. (1984) *Phys. Rev. B*, **29**, 5423.
29. Oshima, C., Bannai, E., Tanaka, T., and Kawai, S. (1977) *Jpn. J. Appl. Phys.*, **16**, 965.
30. Van Bommel, A.J., Crombeen, J.E., and Van Tooren, A. (1975) *Surf. Sci.*, **48**, 463.
31. Park, S., An, J., Jung, I., Piner, R.D., An, S.J. *et al.* (2009) *Nano Lett.*, **9**, 1593.
32. Rafiee, M.A., Rafiee, J., Wang, Z., Song, H., Yu, Z.-Z. *et al.* (2009) *ACS Nano*, **3**, 3884.
33. Shao, Y., Wang, J., Engelhard, M., Wang, C., and Lin, Y. (2010) *J. Mater. Chem.*, **20**, 743.
34. Cote, L.J., Cruz-Silva, R., and Huang, J. (2009) *J. Am. Chem. Soc.*, **131**, 11027.
35. Strong, V., Dubin, S., El-Kady, M.F., Lech, A., Wang, Y. *et al.* (2012) *ACS Nano*, **6**, 1395.
36. Winey, K.I. and Vaia, R.A. (2007) *MRS Bull.*, **32**, 314.
37. Jang, B.Z. and Zhamu, A. (2008) *J. Mater. Sci.*, **43**, 5092.
38. Mack, J.J., Viculis, L.M., Ali, A. *et al.* (2005) *Adv. Mater.*, **17**, 77.
39. Das, B., Eswar Prasad, K., Ramamurty, U., and Rao, C.N.R. (2009) *Nanotechnology*, **20**, Article ID, 125705.
40. Gnanasekaran, D., Madhavan, K., and Reddy, B.S.R. (2009) *J. Sci. Ind. Res.*, **68**, 437–464.
41. Fina, A., Tabuani, D., Peijs, T., and Camino, G. (2009) *Polymer*, **50**, 218–226.
42. Wan, C., Zhao, F., Bao, X., Kandasubramanian, B., and Duggan, M. (2009) *J. Polym. Sci., Part B: Polym. Phys.*, **47**, 121–129.
43. Liu, Y.L. and Lee, H.C. (2006) *J. Polym. Sci., Part A: Polym. Chem.*, **44**, 4632–4643.
44. Mehl, G.H. and Saez, I.M. (1999) *Appl. Organomet. Chem.*, **13**, 261–272.
45. Fonga, H., Dickens, S.H., and Flaim, G.M. (2005) *Dent. Mater.*, **21**, 520–529.
46. Baney, R.H., Makilton, S.A., and Suzuki, T. (1995) *Chem. Rev.*, **95**, 1409–1428.
47. Lin, W.J., Chen, W.C., Wu, W.C., Niu, Y.H., and Jen, A.K.Y. (2004) *Macromolecules*, **37**, 2335–2341.
48. Castaldo, A., Massera, E., Quercia, L., and Francia, G.D. (2007) *Macromol. Symp.*, **247**, 350–356.
49. Asuncion, M.Z. and Laine, R.M. (2007) *Macromolecules*, **40**, 555–562.
50. Soong, S.Y., Cohen, R.E., Boyce, M.C., and Mulliken, A.D. (2006) *Macromolecules*, **39**, 2900–2908.
51. Feher, F.J., Budzichowski, T.A., and Ziller, J.W. (1997) *Inorg. Chem.*, **36**, 4082–4086.
52. Edelmann, F.T., Gunko, Y.K., Giessmann, S., and Olbrich, F. (1999) *Inorg. Chem.*, **38**, 210–211.
53. Zhou, J., Hua, Z., Liu, Z., Wu, W., Zhu, Y., and Shi, J. (2011) *ACS Catal.*, **1**, 287–291.
54. Heinemann, H. (1981) *Catal. Rev. Sci. Eng.*, **23**, 315–328.
55. Komori, Y. and Hayashi, S. (2003) *Langmuir*, **19**, 1987–1989.
56. Densakulprasert, N., Wannatong, L., Chotpattananont, D., Hiamtup, P., Sirivat, A., and Schwank, J. (2005) *Mater. Sci. Eng., B*, **117**, 276–282.
57. Egerton, T.A. and Vickerm, J.C. (1973) *J. Chem. Soc., Faraday Trans.*, **69**, 39–49.
58. Zhang, Z., Desilets, F., Felice, V., Mecheri, B., Licoccia, S., and Tavares, A.C. (2011) *J. Power Sources*, **196**, 9176–9187.
59. Wang, J., Zheng, X., Wu, H., Zheng, B., Jiang, Z., Hao, X., and Wang, B. (2008) *J. Power Sources*, **178**, 9–19.
60. Wu, H., Zheng, B., Zheng, X., Wang, J., Yuan, W., and Jiang, Z. (2007) *J. Power Sources*, **173**, 842–852.
61. Corma, A. and Garcia, H. (2004) *Chem. Commun.*, **2004**, 1443–1459.
62. Fukahori, S., Ichiura, H., Kitaoka, T., and Tanaka, H. (2003) *Environ. Sci. Technol.*, **37**, 1048–1051.
63. Wagner, T., Haffer, S., Weinberger, C., Klaus, D., and Tiemann, M. (2013) *Chem. Soc. Rev.*, **42**, 4036.
64. Huo, Q., Margolese, D., Ciesla, U., Feng, P., Gier, T.E., Sieger, P., Leon, R., Petroff, P., Schuth, F., and Stucky, G.D. (1994) *Nature*, **368**, 317.

65. Zhao, D., Feng, J., Huo, Q., Melosh, N., Frederickson, G.H., Chmelka, B.F., and Stucky, G.D. (1998) *Science*, **279**, 548.
66. Tiwari, A. and Dhakate, S.R. (2009) *Int. J. Biol. Macromol.*, **44**, 408–412.
67. Lüftl, S., Visakh, P.M., and Chandran, S. (2014) *Polyoxymethylene Handbook: Structure, Properties, Applications and their Nanocomposites*, John Wiley & Sons, ISBN: 9781118385111.
68. Tiwari, A. and Tiwari, A. (2013) *Nanomaterials in Drug Delivery, Imaging and Tissue Engineering*, John Wiley & Sons, ISBN: 9781118290323.
69. Aumelas, A., Serrero, A., Durand, A., Dellacherie, E., and Leonard, M. (2007) *Colloids Surf., B*, **59**, 74.
70. Bertholon, I., Hommel, H., Labarre, D., and Vauthier, C. (2006) *Langmuir*, **22**, 5485.
71. Bravo-Osuna, I., Schmitz, T., Bernkop-Schnürch, A., Vauthier, C., and Ponchel, G. (2006) *Int. J. Pharm.*, **316**, 170.
72. Janes, K.A., Fresneau, M.P., Marazuela, A., Fabra, A., and Alonso, M.J. (2001) *J. Controlled Release*, **73**, 255.
73. Liu, J., Wang, F.H., Wang, L.L., Xiao, S.Y., Tong, C.Y., and Tang, D.Y. (2008) *J. Cent. South Univ. Technol.*, **15**, 768.
74. Marty, J.J. (1977) The preparation, purification and properties of nanoparticles, D. Pharm. Thesis, Victorian College of Pharmacy, Parkville, p. 30.
75. Hubbe, M.A., Rojas, O.J., Lucia, L.A., and Sain, M. (2008) *BioResources*, **3**, 929.
76. Santos, T.M., Souza Filho, M.M., Caceres, C.A., Rosa, M.F., Morais, J.P.S., Alaídes, M.B.P., and Azeredo, H.M.C. (2014) *Food Hydrocolloids*, **41**, 113.
77. Nguyen, V.Q., Ishihara, M., Mori, Y., Nakamura, S., Kishimoto, S., Hattori, H., Fujita, M., Kanatani, Y., Ono, T., Miyahira, Y., and Matsui, T. (2013) *J. Nanomater.*, **2013**, 1.
78. Madhavan, P. (1992) *Chitin, Chitosan and their Novels Applications*, Science Lecture Series, CIFT, Kochi, p. 1.
79. Nagahama, H., New, R., Jayakumar, S., Koiwa, T., and Tamur, F.H. (2008) *Carbohydr. Polym.*, **73**, 295.
80. Delval, F., Crini, G.G., Bertini, S., Morin-Crini, N., Badot, P.M., Vebrel, J., and Torri, G. (2004) *J. Appl. Polym. Sci.*, **93**, 2650.
81. Lemarchand, C., Couvreur, P., Besnard, M., Costantini, D., and Gref, R. (2003) *Pharm. Res.*, **20**, 1284.
82. Hoover, R., Hughes, T., Chung, H.J., and Liu, Q. (2010) *Food Res. Int.*, **43**, 399.
83. Koo, H.Y., Chang, S.T., Choi, W.S., Park, J.H., Kim, D.Y., and Velev, O.D. (2006) *Chem. Mater.*, **18**, 3308.
84. Tojo, C., Dios, M.D., and Barroso, F. (2010) *Materials*, **4**, 55.
85. Ethayaraja, M., Dutta, K., Muthukumaran, D., and Bandyopadhyaya, R. (2007) *Langmuir*, **23**, 3418.
86. Ma, X., Jian, R., Chang, P.R., and Yu, J. (2008) *Biomacromolecules*, **9**, 3314.
87. Kim, J.Y. and Lim, S.T. (2009) *Carbohydr. Polym.*, **76**, 110.
88. Angellier, H., Molina-Boisseau, S., Lebrun, L., and Dufresne, A. (2005) *Macromolecules*, **38**, 3783.
89. Chen, G., Wei, M., Chen, J., Huang, J., Dufresne, A., and Chang, P.R. (2008) *Polymer*, **49**, 1860.
90. Angellier, H., Molina-Boisseau, S., Dole, P., and Dufresne, A. (2006) *Biomacromolecules*, **7**, 531.
91. Aichayawanich, S., Nopharatana, M., Nopharatana, A., and Songkasiri, W. (2011) *Carbohydr. Polym.*, **84**, 292.
92. Kristo, E. and Biliaderis, C.G. (2007) *Carbohydr. Polym.*, **68**, 146–158.
93. Yu, J., Ai, F., Dufresne, A., Gao, S., Huang, J., and Chang, P.R. (2008) *Macromol. Mater. Eng.*, **293**, 763.
94. Chen, Y., Cao, X., Chang, P.R., and Huneault, M.A. (2008) *Carbohydr. Polym.*, **73**, 8.
95. Zheng, H., Ai, F.J., Chang, P.R., Huang, J., and Dufresne, A. (2009) *Polym. Compos.*, **30**, 474.
96. Perez, E.V., Balkus, K.J. Jr., Ferraris, J.P., and Musselman, I.H. (2009) *J. Membr. Sci.*, **328**, 165.
97. Ordonez, M.J.C., Balkus, K.J. Jr., Ferraris, J.P., and Musselman, I.H. (2010) *J. Membr. Sci.*, **361**, 165.
98. O'Neill, L.D., Zhang, H., and Bradshaw, D. (2010) *J. Mater. Chem.*, **20**, 5720.

99. Rowsell, J.L.C. and Yaghi, O.M. (2004) *Microporous Mesoporous Mater.*, **73**, 3.
100. Yaghi, O.M. and Li, H. (1995) *J. Am. Chem. Soc.*, **117**, 10401.
101. Eddaoudi, M., Kim, J., Rosi, N., Vodak, D., Wachter, J., O'Keeffe, M., and Yaghi, O.M. (2002) *Science*, **295**, 469.
102. Long, J.R. and Yaghi, O.M. (2009) *Chem. Soc. Rev.*, **38**, 1213.
103. Perry, J.J., Perman, J.A., and Zaworotko, M.J. (2009) *Chem. Soc. Rev.*, **38**, 1400.
104. Shimizu, G.K.H., Vaidhyanathan, R., and Taylor, J.M. (2009) *Chem. Soc. Rev.*, **38**, 1430.
105. Bhuiyan, M.A., Pucha, R.V., Worthy, J., Karevan, M., and Kalaitzidou, K. (2013) *Compos. Struct.*, **95**, 80–87.
106. Zare, Y. (2014) *Int. J. Adhes. Adhes.*, **54**, 67–71.
107. Zare, Y. and Garmabi, H. (2014) *Appl. Surf. Sci.*, **321**, 219–225.
108. Zare, Y. and Garmabi, H. (2011) *J. Appl. Polym. Sci.*, **122**, 3188–3200.
109. Zare, Y. (2013) *Waste Manage. (Oxford)*, **33**, 598–604.
110. Zare, Y. and Garmabi, H. (2012) *J. Appl. Polym. Sci.*, **124**, 1225–1233.
111. Zeng, Q., Yu, A., and Lu, G. (2008) *Prog. Polym. Sci.*, **33** (2), 191–269.
112. Valavala, P. and Odegard, G. (2005) *Rev. Adv. Mater. Sci.*, **9**, 34–44.
113. Zhu, R., Pan, E., and Roy, A. (2007) *Mater. Sci. Eng., A*, **447** (1), 51–57.
114. Griebel, M. and Hamaekers, J. (2004) *Comput. Meth. Appl. Mech. Eng.*, **193** (17), 1773–1788.
115. Hu, Y. and Sinnott, S.B. (2004) *J. Mater. Chem.*, **14** (4), 719–729.
116. Mokashi, V.V., Qian, D., and Liu, Y. (2007) *Compos. Sci. Technol.*, **67**, 530–540.
117. Huang, G., Mamedov, A., Gupta, S., Wang, B., and Lu, H. (2006) *J. Appl. Mech.*, **73** (5), 737–744.
118. Liu, Y. and Chen, X. (2003) *Mech. Mater.*, **35** (1), 69–81.
119. Song, Y.S. and Youn, J.R. (2006) *Polymer*, **47** (5), 1741–1748.
120. Gomez-del Rio, T., Poza, P., Rodriguez, J., García-Gutiérrez, M., Hernandez, J., and Ezquerra, T. (2010) *Compos. Sci. Technol.*, **70** (2), 284–290.
121. Ogasawara, T., Ishida, Y., Ishikawa, T., and Yokota, R. (2004) *Composites Part A*, **35** (1), 67–74.
122. Coleman, J.N., Cadek, M., Ryan, K.P., Fonseca, A., Nagy, J.B., Blau, W.J. *et al.* (2006) *Polymer*, **47** (26), 8556–8561.
123. Guzman de Villoria, R. and Miravete, A. (2007) *Acta Mater.*, **55** (9), 3025–3031.
124. Fisher, F., Bradshaw, R., and Brinson, L. (2003) *Compos. Sci. Technol.*, **63** (11), 1689–1703.
125. Bradshaw, R., Fisher, F., and Brinson, L. (2003) *Compos. Sci. Technol.*, **63** (11), 1705–1722.
126. Shao, L., Luo, R., Bai, S., and Wang, J. (2009) *Compos. Struct.*, **87** (3), 274–281.
127. Ciolacu, D. and Popa, V.I. (2011) *Cellulose Allomorphs: Structure, Accessibility and Reactivity*, Chapter 1, Nova Science Publisher, New York, pp. 1–3.
128. Klemm, D., Philipp, B., Heize, T., Heinze, U., and Wagwnknecht, W. (1998) *Comprehensive Cellulose Chemistry: Fundamentals and Analytical Methods*, vol. 1, WILEY-VCH Verlag GmbH, Weiheimem, pp. 167–223.
129. Khalil, H.P.S.A., Davoudpour, Y., Islam, M.N., Mustapha, A., Sudesh, K., Dungani, R., and Jawaid, M. (2014) *Carbohydr. Polym.*, **99**, 649–665.
130. Malainine, M.E., Mahrouz, M., and Dufresne, A. (2005) *Compos. Sci. Technol.*, **65**, 1520–1526.
131. Lee, S.Y., Chun, S.J., Kang, I.A., and Park, J.Y.D. (2009) *J. Indian Eng. Chem.*, **15**, 50–55.
132. Panthapulakkal, S. and Sain, M. (2012) *Int. J. Polym. Sci.*, 1–6.
133. Alemdar, A. and Sain, M. (2008) *Bioresour. Technol.*, **99**, 1664–1671.
134. Frone, A.N., Panaitescu, D.M., Donescu, D., Spataru, C.I., Radovici, C., Trusca, A., and Somoghi, R. (2011) *BioResources*, **6** (1), 487–512.
135. Kamel, S. (2007) *eXPRESS Polym. Lett.*, **1** (9), 546–575.
136. Khalil, H.P.S.A., Bhat, A.H., and Yusra, A.F.I. (2012) *Carbohydr. Polym.*, **87**, 963–979.
137. Samir, M.A.S.A., Alloin, F., and Dufresne, A. (2005) *Biomacromolecules*, **6**, 612–626.

138. Zhang, J. and Zhang, J. (2010) *Acta Polym. Sin.*, **0** (12), 1376–1398.

139. Mathew, A.P., Oksman, K., Pierron, D., and Harmand, M.F. (2012) *Carbohydr. Polym.*, **87**, 2291–2298.

140. Haimer, E., Liebner, F., Potthast, A., and Rosenau, T. (2012) in *Polysaccharide Building Blocks: A Sustainable Approach to the Development of Renewable Biomaterials*, 1st edn (eds Y. Habibi and L.A. Lucia), John Wiley & Sons, Inc., Hoboken, NJ, pp. 367–386.

141. Fang, J.M., Sun, R.C., Tomkinson, J., and Fowler, O. (2000) *Carbohydr. Polym.*, **41**, 379–387.

142. Peng, F., Peng, P., Xu, F., and Sun, R.C. (2012) *Biotechnol. Adv.*, **30**, 879–903.

143. Peng, X., Ren, J., Zhong, L., and Sun, R.C. (2011) *Biomacromolecules*, **12**, 3321–3329.

144. Guan, Y., Zhang, B., Bian, J., Peng, F., and Sun, R.C. (2014) *Cellulose*, **21**, 1709–1721.

145. El Mansouri, N.E. and Salvado, J. (2007) *Ind. Crops Prod.*, **26** (2), 116–124.

146. Malutan, T., Nicu, R., and Popa, V.I. (2008) *BioResources*, **3**, 13–20.

147. Popa, V.I., Capraru, A.M., Grama, S., and Malutan, T. (2011) *Cellul. Chem. Technol.*, **45**, 221–226.

148. Nevárez, L.A.M., Casarrubias, L.B., Celzard, A., Fierro, V., Muñoz, V.T., Davila, A.C., Lubian, J.R.T., and Sánchez, G.G. (2011) *Sci. Technol. Adv. Mater.*, **12**, 1–16.

149. Lin, T.T., Wu, H.J., Lu, Q.F., Ling, Y.H., and He, L.H. (2013) *Acta Polym. Sin.*, **0** (3), 320–326.

2
Chemistry of Nanoscience and Technology

Aftab Aslam Parwaz Khan, Anish Khan, and Abdullah M. Asiri

2.1
Introduction

Nanotechnology is science, engineering, and technology conducted at the nanoscale, which is in the range of about 1–100 nm. In chemistry, this range of size has historically been associated with colloids, micelles, polymer molecules, phase-separated regions in block copolymers, and similar structures typically, very large molecules or aggregates of many molecules. More recently, structures such as buckytubes, silicon nanorods, and compound semiconductor quantum dots have emerged as particularly interesting classes of nanostructures. Nanoscience and nanotechnology are the study and application of extremely small things and can be used across all the other science fields, such as chemistry, biology, physics, materials science, and engineering. This chemistry is used as in nano to micro scale and in macro to mega scale and the material chemistry to obtain nanomaterials with specific sizes, shapes, surface properties, defects, self-assembly properties, designed to accomplish specific functions [1]. The nanotechnology that is already with us is that of microelectronics (where clever engineers have already shown how to extend existing methods for making microelectronic devices to new systems with sub-70-nm wires and components) [2], materials science (where many of the properties of polymers, metals, and ceramics are determined by 1–100 nm structures) [3–5], and chemistry (where nanometer-scale drugs are routinely used to control proteins and signaling complexes, and where macromolecules have dimensions of many nanometers) [6, 7]. These technologies are "evolutionary nano" (Figure 2.1) [8, 9].

The nanotechnology whose form and importance is yet undefined is "revolutionary nano"; that is, technologies emerging from new nanostructured materials, from the electronic properties of quantum dots, and from fundamentally new types of architectures based on nanodevices for use in computation and information storage and transmission. Nanosystems that use or mimic biology are also highly interesting. There is no doubt that revolutionary nanoscience exists in the laboratories of universities now, and that new forms of nanotechnology will be important; it is just not clear at the moment how much of this exciting,

Nanomaterials and Nanocomposites: Zero- to Three-Dimensional Materials and Their Composites,
First Edition. Edited by Visakh P.M. and Maria José Martínez Morlanes.

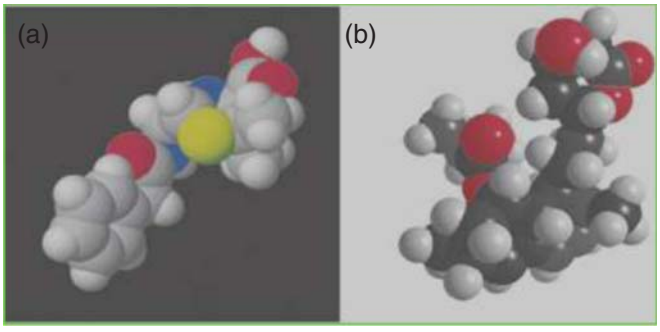

Figure 2.1 Space-filling molecular models of penicillin (a) and lovastatin (b) [8, 9].

revolutionary science will migrate into new technology, and how rapidly this migration will occur. The history of technology suggests, however, that where there is smoke, there will eventually be fire; that is, where there is enough new science, important new technologies will eventually emerge.

It should be bracing to chemists to realize that chemistry is already playing a leading role in nanotechnology. In a sense, chemistry is (and has always been) the ultimate nanotechnology: Chemists make new forms of matter (and they are really the only scientists to do so routinely) by joining atoms and groups of atoms together with bonds. They carry out this sub-nanometer scale activity chemical synthesis on megaton scales when necessary, and do so with remarkable economy and safety. Although the initial interest in nanotechnology centered predominantly on nanoelectronics, and on fanciful visions of the futurists, the first new and potentially commercial technologies to emerge from revolutionary nanoscience seem, in fact, to be in materials science; and materials are usually the products of chemical processes.

Some description follow below.

2.2 Nano

Nano is short form for nanotechnology, and the word itself just means very, very small. Nanotechnology, or more accurately nanotechnologies describe the many ways that scientists can now work with the actual molecules and atoms that make up our world. The study of assembling, controlling, or/and manipulating matter on the molecular or atomic size is called Nanotechnology in brief known as Nano [8–10]. Very commonly, nanotechnology is the study of material of size lesser than 100 nm or smaller in one dimension at least, which comprises constructing devices or materials of that size [11]. Nanotechnology is an extensively wide phenomenon starting from classical device-physics to foremost new methodologies based upon self-assembly of molecules, evolving materials with nanodimensions, and investigation of methods that can directly control matter on an atomic scale.

Nano-(symbol n) as a prefix means 10^{-9}, denoting a factor in the metric system. This is a derivative of the Greek word νᾶνος, meaning dwarf, and has been officially established as a standard in 1960. In 1965, Gordon Moore, head of Intel Corporation, predicted that the number of transistors that could be fitted in a given area would be double in number for every one and half years in the next decade [12]. This came to be a reality and this phenomenon is popularly known as Moore's Law. To this day, the phenomenon according to the above law has continued for the past decade. We have witnessed the fact that there is a significant increase in housing the transistors from a couple of thousand transistors in 4004 processors in the year 1971 to over 700,000 transistors in the Core-2-duo computer mother board. It is noted that there has been a significant decrease in the size of individual electronic elements in modern circuitry, going from millimeters to nanometers. At the same time, the chemistry, biochemistry, and molecular genetics communities are moving in the same direction with the same pace (Figure 2.2).

In the beginning of a new digital era, different powerful technologies have approached the nanoscale technology with the promise of transforming both the fields of biology and electronics. This upcoming field of molecular bio-nanotechnology opens new avenues from basic research in bio-physics and molecular-biology to biosensing, biolabeling, bioinformatics, pharma and medicine, genomics, information storage and energy conversion applications, and also in computing [13–18]. We refer to a talk given by physicist Richard Feynman, a Noble laureate at an American physical society meeting on 29 December 1959, "There is plenty of room at the bottom," [19]. The term "nanotechnology" was first defined by a well-known scientist "Norio Taniguchi" of Science University, Tokyo, in a 1974 paper. In the early 1980s, the research of nanotechnology was stochastic than deterministic. A nanoscale phenomenon was up-held by Dr. K. Eric Drexler for precise handling of individual atoms and molecules theoretically

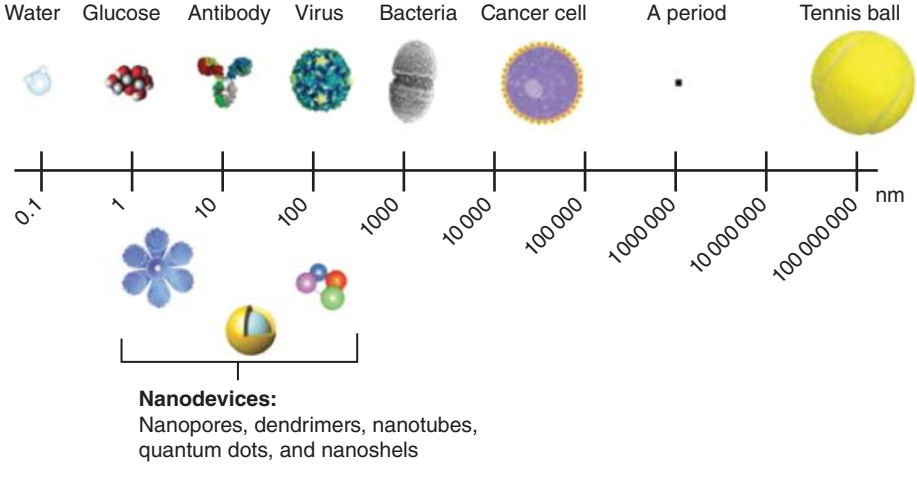

Figure 2.2 Nanometric scale.

[20, 21]. Academic knowledge of nanotechnology in life was given by R. Jones in a book published; "Soft Machines" (nanotechnology and life) [22]. The concept of DNA nanotechnology was invented by a crystallographer, Seeman, in 1980, who demonstrated that a three-dimensional DNA lattice could be used to orient target molecules. In1991, Seeman's laboratory published the synthesis of a DNA cube, the first three-dimensional nanoscale object, for which he was awarded the Feynman Prize in Nanotechnology in 1995 [23]. Although nanotechnology has wonderful future applications, at the other end it raises many issues as is expected in the case of an introduction of any new technology, which includes concern about the toxic impact of nanoresidues on the environment, and their global-economic effects, which predicted many doomsday scenarios. These created apprehensions for the governments and the intellectuals to debate on the necessity of bringing a special regulation for nanotechnology [24].

2.3 Nanomaterials

Materials having one or more dimensions in the range of 100 nm or less may be classified as nanomaterials. The physical and chemical properties of such materials are expected to differ measurably than those of the bulk materials. Figure 2.3 shows some basic nanomaterials available in different morphological forms. The study of nanomaterials envisages the field in which a materials science-based

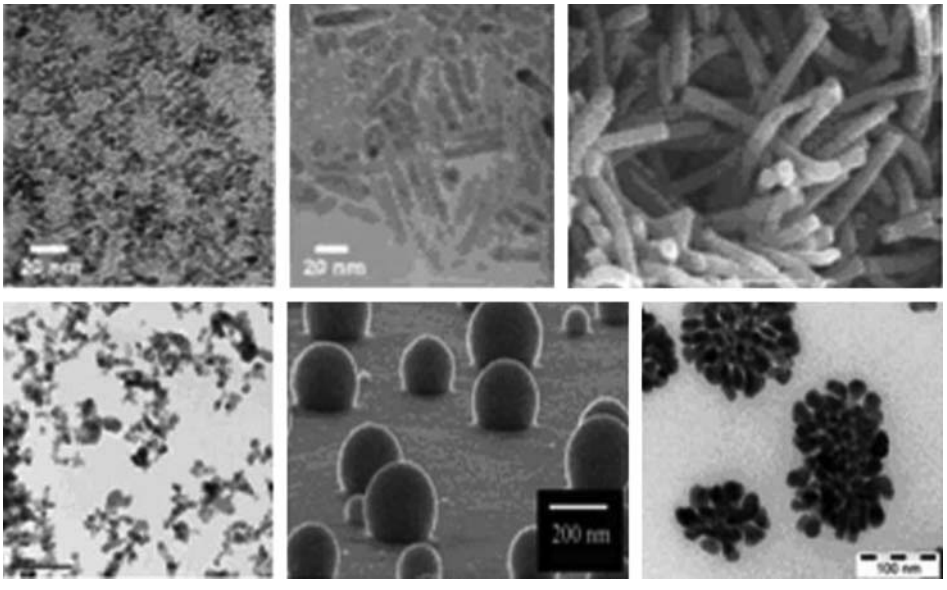

Figure 2.3 Basic morphological forms of nanomaterials.

approach to nanotechnology can be undertaken. It covers the study of materials with morphological features on the nanoscale, especially those materials that have special properties stemming from their nanoscale dimensions. Although, nanoscale is usually defined as smaller than 1/10 of a micrometer in at least one dimension, this term is also used for materials smaller than 1 μm. An important aspect of nanomaterials is the vast increase in the surface area to volume ratio, which incorporates the possibilities of new quantum mechanical effects on such materials. One of the examples of "quantum size effect" is the change in the electronic properties of solids due to the large reduction in particle size. This effect does not come into play by going from macro to micro dimensions but becomes extremely pronounced when the materials reach the nanometer size range. Typically, stable substances can become highly reactive and unstable when the particles become infinitesimal due to their extremely high surface to mass ratio. A series of quantum confinement effects arise that significantly change the way the particles display their behavior such as electrical conductivity, specific heat, band gap, and the wavelengths of light emitted by them. A certain number of physical properties also alter with the change from macroscopic systems to the nano range. Novel mechanical properties of nanomaterials are a subject of research in the field of nanomechanics. Novel catalytic activities were also revealed especially in the interactions and manipulations of biomaterials. Nanoparticles are of great scientific interest as they are effectively a bridge between bulk materials and atoms or molecules. In principle, physical properties of bulk materials are size-independent but deviation occurs when the size reaches to nanoparticles exhibiting a number of special properties relative to bulk material. For example, the bending of bulk copper (wire, ribbon, etc.) occurs with the movement of copper atoms/clusters at about the 50 nm scale. Copper nanoparticles smaller than 50 nm are considered super hard materials that do not exhibit the same malleability and ductility as does bulk copper. The change in properties is not always desirable. Ferroelectric materials smaller than 10 nm can switch their magnetization direction using room temperature thermal energy, thus making them useless for memory storage. Nanoparticles often have unexpected visual properties because they are small enough to confine their electrons and produce quantum effects. For example, gold nanoparticles appear deep red to black in solution. Nanoparticles or nanocrystals made up of metals, semiconductors, or oxides are of particular interest for their mechanical, electrical, magnetic, optical, chemical, and several other properties and they have been used as quantum dots, as chemical catalysts, and so on.

2.4
Quantum Materials

The most important areas of physics to modify are the physical properties. Quantum materials includes as high-temperature superconductivity, the quantum

effect, quantum magnetism for combination with tunable external electric and magnetic fields through self-assembling or lithographic processes. The physical properties of these systems are governed by size quantization effects and energy levels controlled by the Coulomb blockade. An important feature of quantum materials is that it is probable to also influence the spins of the system, which directly relate the quantum materials to the strongly developing field of spintronic. In quantum materials, not only the electronic properties but also the dispersion of the photons and the phonons will be quantized thus that, respectively, confined electromagnetic optical modes or confined optical and acoustic phonons can be studied. In addition, the high quality of man-made quantum dots also allows one to study the influence of size quantization on the crystal morphology and the formation of bulk, interface, and surface states.

One of the most important aspects of quantum materials is superconductivity. Superconductivity is a quantum mechanical phenomenon. Thus, the phenomenon in which the electrical resistance of a substance drops suddenly to zero when it is cooled to a sufficiently low temperature is known as superconductivity. The temperature at which a specimen becomes a superconductor is called as transition temperature or critical temperature. It was discovered by Onnes in the year 1911. They studied mercury, which shows superconductivity at 4 K. Until now, infinite number of researches have been done on nonorganic superconductors and currently, scientists have developed various cuprates superconductors having Tc upto 140 K.

2.4.1 Classification of Superconductor

The most common superconductors are discussed in the following text.

2.4.1.1 Response to a Magnetic Field

Type I Superconductors A type I superconductor consists of basic conductive elements that are used in everything from electrical wiring to computer microchips. Type I superconductors have T_cs between 0.000325 and 7.8 °K at standard pressure. Some other examples of type I include Mercury −4.15 °K, Lead −7.2 °K, Aluminum −1.175 °K, and Zinc −0.85 °K. Roughly, half of the elements in the periodic table are known to be superconductive.

Type II Superconductors A type II superconductor consists of metallic compounds such as copper or lead. The highest T_c reached at standard pressure is 135 °K or −138 °C by a compound ($HgBa_2Ca_2Cu_3O_8$) that falls into a group of

superconductors known as cuprate perovskites. Type II means it has two critical fields, between which it allows partial penetration of the magnetic field.

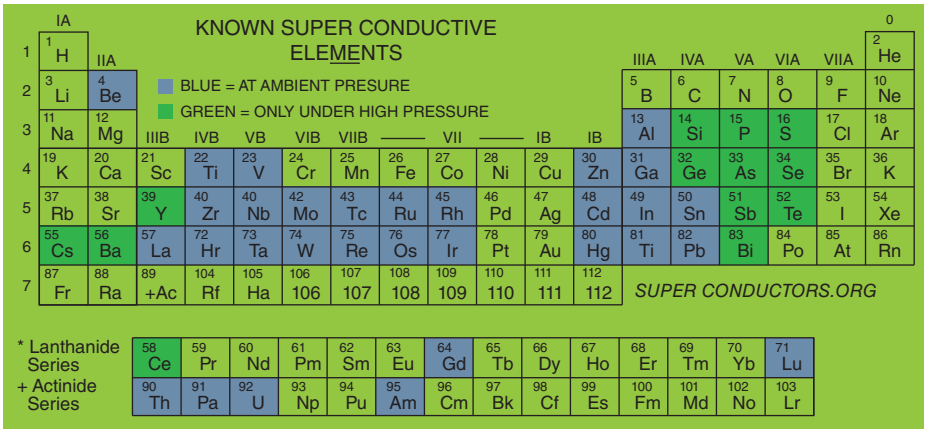

2.4.1.2

By Theory of Operation

It is conventional if it can be explained by the BCS theory or its derivatives, or unconventional, otherwise.

2.4.1.3

By Critical Temperature

A superconductor is generally considered high temperature if it reaches a superconducting state when cooled using liquid nitrogen – that is, at only $T_c > 77\,\mathrm{K}$) – or low temperature if more aggressive cooling techniques are required to reach its critical temperature.

2.4.1.4

By Material

Superconductor material classes include chemical elements (e.g., mercury or lead), alloys (such as niobium-titanium, germanium-niobium, and niobium nitride), ceramics (Yttrium barium copper oxide (YBCO) and magnesium diboride), or organic superconductors (fullerenes and carbon nanotubes (CNTs); though these examples should be included among the chemical elements, as they are composed entirely of carbon). Here, organic superconductor by materials has been explained in detail. An organic superconductor is an organic compound that exhibits superconductivity at low temperatures. The first organic superconductor, tetramethyltetraselenafulvalene (TMTSF) 2PF6 was synthesized by Klaus Bechgaard in 1980 [25]. Here, TMTSF serves as the electron donor and PF6- serves as the electron acceptor. This discovery led to the creation of a wide range of related organic compounds, known as Bechgaard salts, which exhibit a vast array of unique properties. Following a 1964 paper by Little [26], it was hoped that organic

conductors such as Bechgaard salts would be high temperature superconductors, even superconducting at room temperature. However, Bechgaard salts have many other properties that make them very interesting subjects of research. For example, by varying both temperature and pressure, Bechgaard salts can be forced into almost any phase known to condensed matter physicists. Also, because Bechgaard salts are structurally so different from metallic superconductors, it seems that the standard explanation for superconductivity given by the BCS theory of Bardeen, Cooper, and Schrieffer does not apply very well, and as a result there is a lot of work to be done to understand the mechanism behind superconductivity in these materials. Various organic superconductors with their critical temperature are (TMTSF)2PF6-1.1K,(TMTSF)2ClO4-1.4K,(BEDT-TTF)2I4-3.3K,κ-(BEDT-TTF)2Cu[N(CN)2]Br-11.6K,β′(BEDT-TTF)2ICl2-14.2K,κ-(ET)2Cu[N(CN)2]Cl-13.1K,RbCs2C60-33K.

Right now, the highest achieved critical temperature for an organic superconductor at ambient pressure is 33 K, observed in the alkali-doped fullerene RbCs2C60.

2.4.1.5 Fullerene

Among the different new materials with high-temperature superconductivity, fullerene compounds play a significant part. Fullerene is a family of carbon allotropes and was discovered in 1985 by Richard Buckminster Fuller. One of the most significant properties of fullerenes is superconductivity, mainly found in C60.

Apart from the copper oxide superconductor, C60 has the highest superconductivity at ambient pressure 52 K for the highly doped fullerene. Fullerenes is exhibit type 2 and an interesting superconductivity phenomena has been observed in CNTs, but not in the larger common fullerene C70 and C84. Fullerene is a three-dimensional system; actually it is an insulator with a band gap of 1.7 eV, but on doping with alkali metals [27] produces superconductivity with critical temperatures up to 40 K. The general formula for these superconductors is A3C60 where A is an alkali metal. Superconductivity has also been observed in single-walled nanotubes with critical temperatures up to 15 K. The highest measured transition temperature up to 1995 for an organic superconductor in Cs3C60 pressurized with 15 kbar to be $T_c = 40$ K. Until now, the highest critical temperatures observed in organic superconductor in fullerene is via a technique employing a field effect transistor to introduce charge or hole. Hole-doped fullerenes exhibit higher critical temperature than electron-doped fullerenes [28]. Recently, Schon *et al.* found a hole-doped C60 superconducting system C60/CHBr3, which exhibited very high critical temperature $T_c = 117$ K at ambient pressure. It is the greatest T_c for an organic superconductor that has been achieved with a buckyball doped with holes and intercalated with CHBr3 [29]. Field-effect doping exploits the fact that under a strong, static electric field, charge (electrons or holes) will accumulate at the surface of the material, effectively modifying the electronic density in that region. This type of doping avoids imperfections that cause the system to deviate locally [30].

2.5
Forces and Bonding of Nanomaterials

Revealing the chemical bonding and the reorganization of the chemical bonds of any molecular system forms the undisputed foundation of chemistry. Chemical interactions between a protein and a drug, or a catalyst and its substrate, self-assembly of a nanomaterials [31], and also many chemical reactions [32] are dominated by noncovalent interactions, such as hydrogen bonding and metal–ligand coordination, as well as π–π stacking, hydrophobic, ionic, van der Waals forces and London dispersion [33]. The introduction of molecular recognition motifs into these building blocks, such as hydrogen bonding, π–π stacking, electrostatic interactions, and metal–ligand bonds, offers an easy way to access well-defined arrays with novel photo- and electronic properties [34–39]. In this chapter, we summarize our studies on self-assembly systems conducted in the past few years, and focus on the design and properties of the functional assembly systems. As a matter of fact, in the construction of supramolecular systems, many kinds of weak interactions cooperate and coordinate to give rise to subtle structures. Usually, we focus on the leading interaction,as in hydrogen-bonding assemblies π–π stacking, hydrophilic and hydrophobic and metal–ligand interactions. And in the last part of the chapter, novel methods for construction of zero-dimensional, one-dimensional, and two-dimensional nanoscale structures are discussed.

2.5.1
Hydrogen-Bonding Assemblies

A hydrogen bond is an attractive force between the hydrogen attached to an electronegative atom of one molecule and an electronegative atom of a different molecule. Usually, the electronegative atom is oxygen, nitrogen, or fluorine, which has a partial negative charge. A hydrogen bond arises between the donor covalent pair D–H in which a hydrogen atom H is bound to a more electronegative atom D (donor) and another noncovalently bonded nearest neighbor electronegative (acceptor) atom A. Hydrogen bonds play a crucial role in determining the structure of water, the folding of proteins, the pairing of base in DNA, and so on. An important aspect of hydrogen bonds is that they are highly directional. The strongest hydrogen bonds are those in which the donor, hydrogen, and the acceptor atoms are collinear. Hydrogen bonding, has been reported for the design of various molecular assemblies [40–43]. Nanosized aggregates should be very useful for the development of novel functional materials and nanoelectronic devices. Meanwhile, energy- and electron-transfer processes have also been investigated in the assembled supramolecular systems, through the interaction of hydrogen bonds [44, 45]. Hydrogen bonding is one of the most promising methods to fabricate a controllable molecular array and shape for efficient intermolecular energy and electron transfer between donor and acceptor units

[46, 47]. Fullerene has low reorganization energy in electron processes, which leads to a significant acceleration of the charge-separation step and effective deceleration of the energy-wasting charge-recombination step [48–53], and is thereforea promising candidate in applications as excellent photoelectric materials. As mentioned above, hydrogen bonds provide an efficient way to build molecular arrays with efficient intermolecular energy and electron transfer between donor and acceptor units. Much effort has been put into designing the self-assemblies of fullerene derivatives by hydrogen bonds into zero-, one-, and three-dimensional supramolecular architectures. Guldi [54] and Hummelen [55] reported, respectively, the synthesis and photophysical properties of the first quadruple hydrogen-bonded fullerene dimer. Soon thereafter, we reported two assemblies of supramolecules, as shown in Figure 2.4, based on [47] fullerene with three-centered intermolecular hydrogen-bonding bonds, and attempted to analyze the influences of the different structure features on the interactions and stability of molecular aggregates [56, 57]. Well-defined supramolecular ball-like structures were constructed in our work, which could be of interest for the construction of three-dimensional nanomaterials for future applications as photoelectric devices.

In the structure of supra structures, functionalization is the most important objective. Many organic systems have been developed, which exhibit reasonable light-harvesting efficiencies, and many of them show the ability of the energy and electron transfer [47, 58–60] Fullerene (Figure 2.5) has been widely used as a three-dimensional electron acceptor, while porphyrins and pyrene are used as donors. In our previous work, hydrogen-bonding supramolecular assemblies containing [47] fullerene have been constructed to explore the expected outstanding physical and chemical properties.

The response of on-and-off m cycling of the **1**·**2** film is prompt and reproducible, and the photocurrent stability is rather good in the system during the monitored time, as indicated in Figure 2.6. The ball-like supra structure (Figure 2.7), assembled through hydrogen-bond and π–π stacking, could be of importance

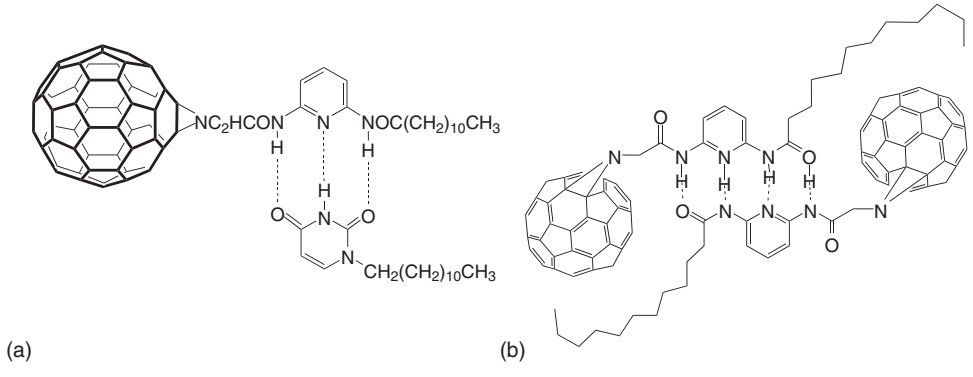

Figure 2.4 Structure of the self-assemblies.

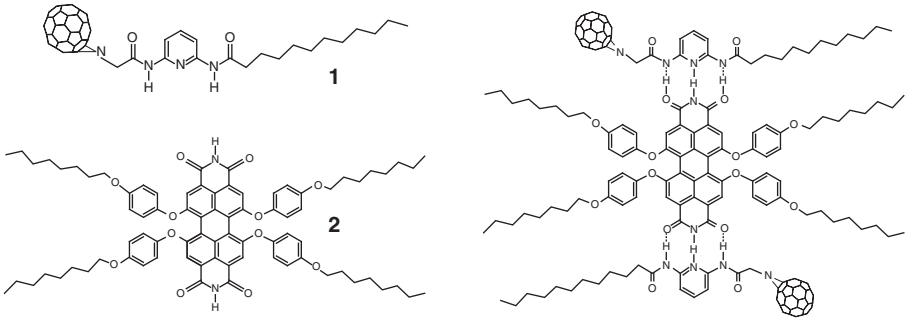

Figure 2.5 Suprastructure of self-assembly of [47] fullerene derivative **1** as acceptor and perylene bisimide **2** as donor by hydrogen bonding [61].

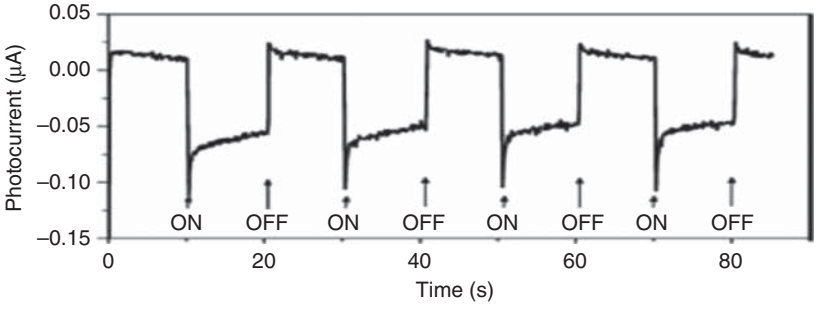

Figure 2.6 Time-dependence of the photocurrent response of the self-assembly film ([1] : [2] = 2 : 1).

for future studies on three-dimensional nanomaterials applied in the field of photoelectric devices. Recently, the first synthesis of 1,1‴-biferrocenediboronic acid (1) demonstrated the usefulness of 1 as a new organo bimetallic building block for the construction of covalent and noncovalent assemblies (Scheme 2.1).

2.5.2
π–π Stacking Assemblies

Two types of π-interactions are common in supramolecular assemblies, namely (i) cation–π interactions and (ii) π–π interactions. More recently, reports on anion-π are also available. Compared to the more conventional noncovalent interactions, the cation–π interaction has been relatively underappreciated. However, it is now an established fact that cation–π interactions have a prominent position among the various noncovalent binding forces that nature uses to assemble the molecules of life. For prototype systems, a simple electrostatic model rationalizes major binding trends, and also provides useful guidelines for understanding more

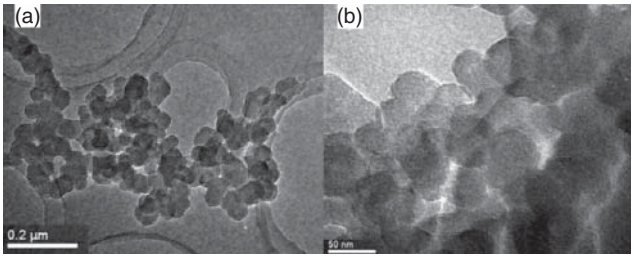

Figure 2.7 (a) TEM images of assemblies ([1] : [2] = 2 : 1). (b) High magnification of the TEM image.

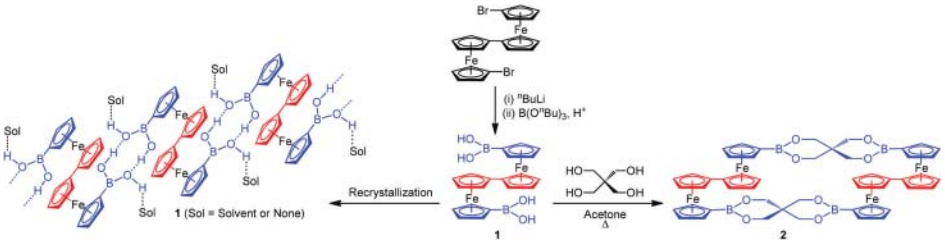

Scheme 2.1 Syntheses of 1′,1‴-biferrocenediboronic acid (**1**), 1D hydrogen-bonded networks and macrocyclic dimer (**2**). Red and blue moieties indicate the first and second ligands, respectively.

complex structures. A clear indication that electrostatics plays an important role in the cation– π interaction comes from a comparison of the binding efficiencies of simple alkali metals to benzene, the trend is Li+ > Na+ > K+ > Rb+. A systematic study by Dougherty *et al.* reveals that the fraction of the total binding energy that is electrostatic varies considerably, depending on the aromatic. Crucial insights into the nature of cation–π interactions have been provided by studies of artificial receptors in aqueous media. π-Systems can also interact favorably with other π-systems. The interactions usually summarized with the term π-stacking are, however, quite complex. Three different π-interactions, namely, *edge-face* π interaction (CH- π), offset π–π interaction, and *face-to-face* π–π interaction are generally observed. Although benzene has no net dipole, it has an uneven distribution of electron density, with higher electron density on the face of the ring and reduced electron density on the edge. The *edge-face* geometry (CH-π) is found to be most stable in benzene. The offset π–π interaction is more common when electron density on the face of one or both rings is reduced. Thus, these edge-face π interaction and offset π–π interaction arise from the attraction between the negatively charged π-electron cloud on the face of benzene ring and the positively charged sigma-framework on the edge of a neighboring molecule (Figure 2.8). A third geometry is the *face-to-face* π–π interaction, where parallel ring systems are separated by about 3.5 Å. This kind of interaction

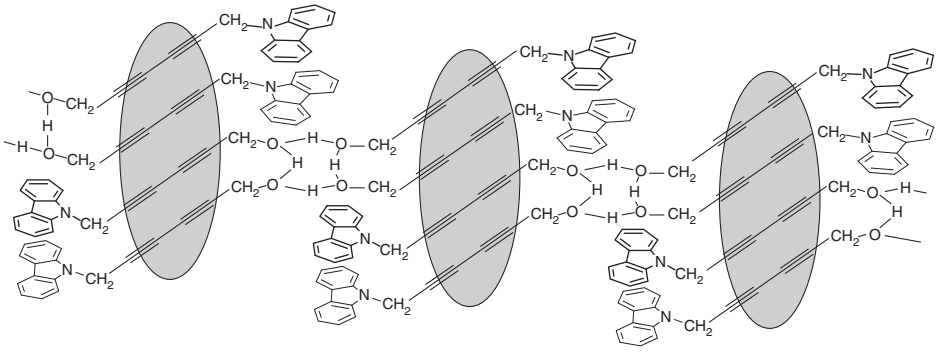

Figure 2.8 Probable self-assembly suprastructure arrangements of CYDIOL.

is commonly observed in donor-acceptors pairs and in compounds having opposite quadrupole moments. The benzene and perfluorobenzene interact in this manner and such interaction was calculated to provide $-15.5\,\mathrm{kJ\,mol^{-1}}$ in stability.

The self-assembly of a conjugated polymer for forming different morphology is currently attracting considerable attention [62–64]. The self-assembly of organic molecules with the assistance of noncovalent forces, such as hydrogen bonding and $\pi-\pi$ stacking interactions, which leads the orientation of molecules in an ordered style, provides an efficient method for creating nanoscopic and mesoscopic structures. In 2005, a small molecule 6-carbazol-9-ylhexa-2,4-diyl-1-ol (CYDIOL) containing diacetylene units which could be self-polymerized by UV light was designed [65]. The CYDIOL molecules are capable of forming low-dimensional nanostructures by the associated effects of self-polymerization and self-assembly (Figure 2.13). The study showed that the association of self-polymerization and self-assembly induces the production of well-defined polydiacetylene nanowires that show excellent field-emission properties (Figures 2.9 and 2.10).

2.5.3
Assemblies by Hydrophilic and Hydrophobic Interactions

The self-assembly of amphiphilic molecules has attracted special attention for a long time, not only for its importance in theoretical studies, but also for its crucial role in biological systems and daily life. Usually, amphiphilic molecules contain hydrophilic and hydrophobic parts at the same time. Because of the different solubility of the hydrophilic and hydrophobic parts, the amphiphilic molecules tend to self-assemble into well-defined structures, and the orphologies may differ in hydrophilic and hydrophobic solvents, to an extent that even the control over specific shapes, dimensions, and pattern formation of supramolecular organization becomes possible. This demonstrates the influence of the environment

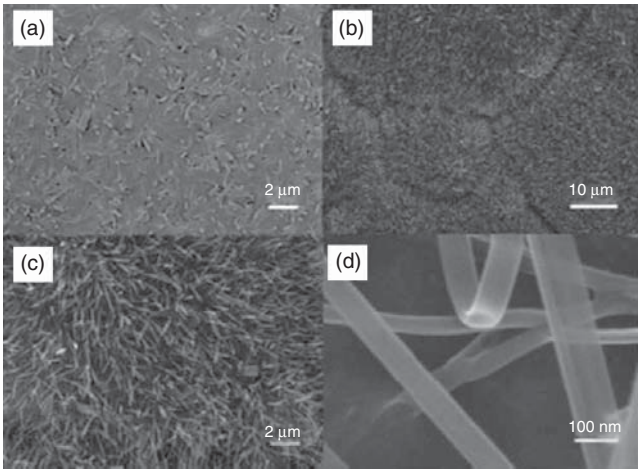

Figure 2.9 Self-assembled nanostructures on copper foils: (a) without polymerization process (b) and (c) large area of ordered polydiacetylene nanowires (d) with some entangled polydiacetylene nanowires.

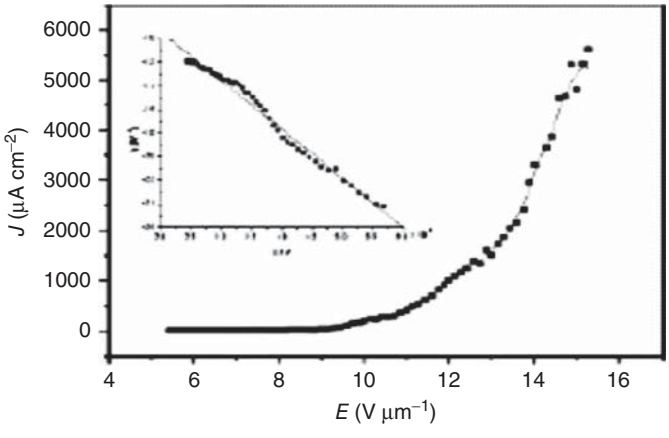

Figure 2.10 Field-emission *J*–*E* curves of the polyCYDIOL nanowires. The inset shows the Fowler–Nordheim plot.

on molecular properties. Hydrophobic effect relies on the minimization of the energetically unfavorable surface between polar/protic and unpolar/aprotic molecules. It is of two types, namely an enthalpic hydrophobic effect and an entropic hydrophobic effect. Enthalpic hydrophobic interactions occur when a guest replaces the water within a cavity. This occurs quite readily as water in such systems do not interact strongly with the hydrophobic cavity of the host molecule and the energy in the system is high. Once the water has been

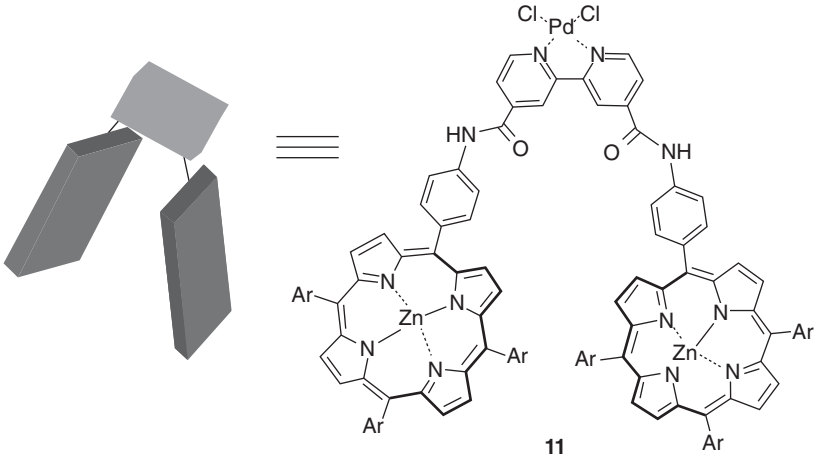

Figure 2.11 Chemical structure of compound **11**.

replaced by a guest, the energy is lowered by the interaction of the former water guest with the bulk solvent outside the cavity. There is also an entropic factor to this process, in that the water that was previously ordered within the cavity becomes disordered when it leaves. An overall increase in entropy favors the process. Various efforts have been made to prepare inorganic and organic hollow capsules, because this kind of nanoscale structure displays unique structural, optical, and surface properties that may lead to a wide range of applications, such as capsule agents for drug delivery, filters, coatings, chemical catalysis, or templates for functional architectural composite materials [66, 67]. Porphyrins have remarkable derivatives and have attracted considerable attention in recent years, especially for the amphiphilic porphyrins, which have been subjugated in the preparation of simple micelles, fibers, and vesicles [66, 68, 69]. V-sharp amphiphilic zinc porphyrin derivative shown in Figure 2.11, could self-assemble into vesicles with a diameter of 200 nm [67]. These vesicles could be controlled to assemble into hollow capsules and worm-like structures as confirmed by scanning electron microscope (SEM) and transmission electron microscope (TEM) (Figure 2.12).

Many researches have been conducted on incorporating chiral moieties [70, 71] or achiral molecules [72, 73] in self-assembling organic molecules with the objective of forming chiral supramolecular structures. Recently, a chiral small-molecule *L*-{2-(4-hydroxy-phenyl)-1-[(pyren-1-ylmethyl)-carbamoxyl]-ethyl}-carbamic acid *tert*-butyl ester (PLBT) was designed and synthesized, which could self-assemble into ball-like particles and helical nanowires with a perfect structure (Figure 2.13) by employing different solvents [74]. The chiral molecule assembled through hydrophilic and hydrophobic interactions and $\pi-\pi$ stacking.

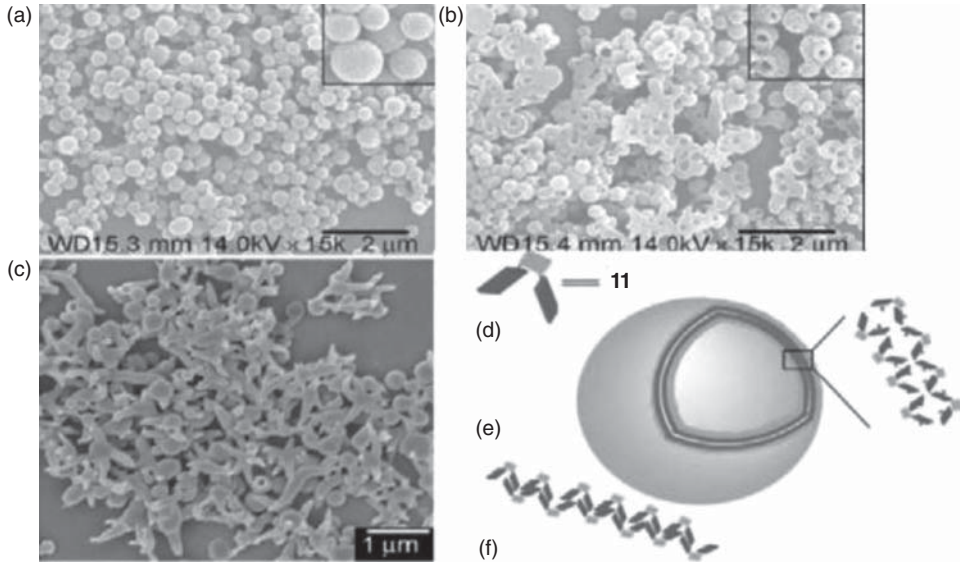

Figure 2.12 Morphology transition of the vesicle heated (a), (b), (c), and (d) SEM image of worm-like aggregates of **11**. (d) Schematic representation of compound **11**. (e) Schematic representation (f) of compound **11** vesicle formed in methanol with a close-up of the vesicle membrane showing the proposed multibilayer structure. (f) Schematic representation of an interdigitated bilayer structure.

2.5.4 Metal–Ligand Interactions

Metal–ligand complexes are the most well studied, having first been brought to the attention of the broader scientific community by Pedersens's work on the ability of cyclic polyethers to complex metal salts, in the late 1960s [5, 6]. In the simplest terms, metal–ligand coordination revolves around the donation of electron density by the electron-rich ligand to the electron-poor metal center. The electron donation of the ligands may arise through a number of modes, such as a negative charge on the ligand, electron density in the π-electron cloud of sp and sp2-hybridized bonds, and the electrons of lone pairs on an organic molecule. Of these metal–ligand interactions, the electron density donated by the lone pairs of the organic molecule will be the focus of this writing. The interaction of electron lone-pairs with metal d-orbitals is observed in σ-donating ligands such as amines and phosphines. One particular example is Co[NH3]6Cl3, a compound whose structure was first elucidated by Werner [7], laying the foundation of the study of coordination chemistry. Upon association of the ligand with the metal, hybridized metal orbitals of the type dxspy form to accept electron density from the ligand, with the integers *x* and *y* depending on the extent of d-orbital filling, ligand properties, and other factors [8]. Often, the partial hybridization of the d-subshell of

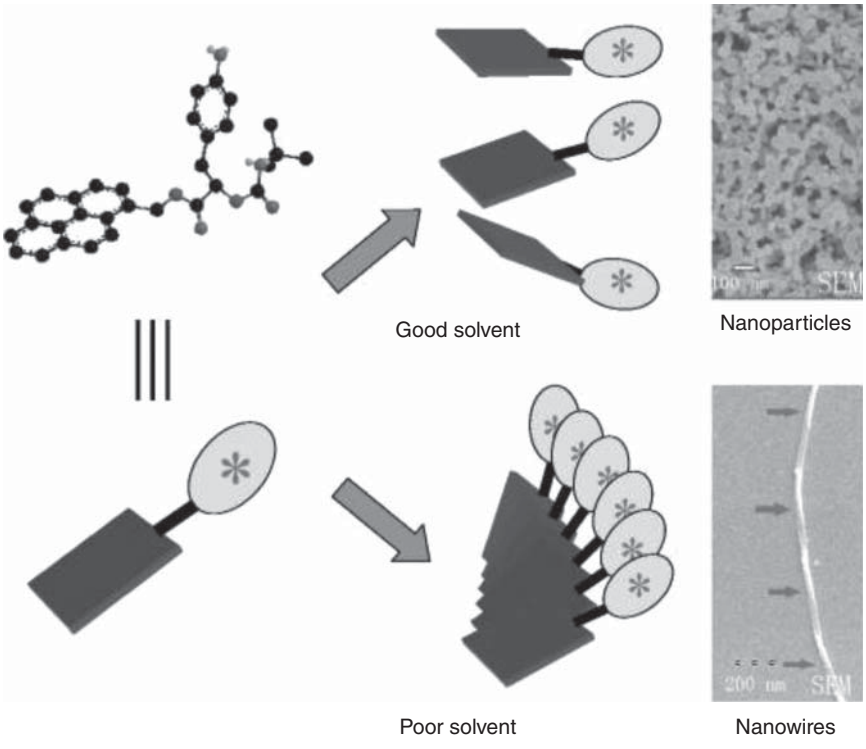

Figure 2.13 Structure of PLBT and schematic representation of self-assembly of compound PLBT.

the metal gives rise to a splitting of the orbital energies, resulting in higher-energy antibonding hybridized orbitals, and lower-energy nonbonding orbitals. This can overcome the pairing energy of the electrons in the orbital, resulting in paired electrons occupying lower-energy orbitals [9]

The metal ligand interactions play an important role in the chiral supramolecular system because of its high directionality [75]. As one of the most known coordination systems, successful assemblies of metal-oligopyridine helices from chiral ligands [76] have been well studied. We also constructed chiral supramolecular assemblies from a novel achiral tripodterpyridine ligand, in which three terpyridine components were introduced into respective sites of silicon core to form tripodal configuration (Figure 2.14) [77]. Chiral coordination architectures were constructed by the self-assembly of the achiral tripod-ligand with silver(I) cations (Figure 2.15), and the possible formation mechanism of the superhelix was exhibited in Figure 2.16. An effective approach of designing ligands of specific configuration was to study the effect of "structure property" in the molecular recognition process.

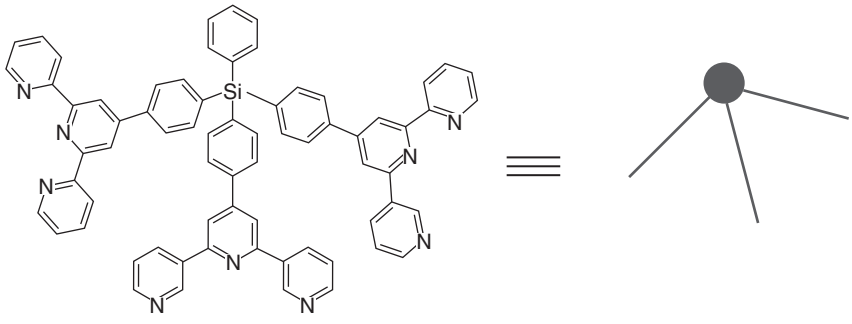

Figure 2.14 Chemical structure of tripod-terpyridine ligand and the proposed "umbrella-shaped" module.

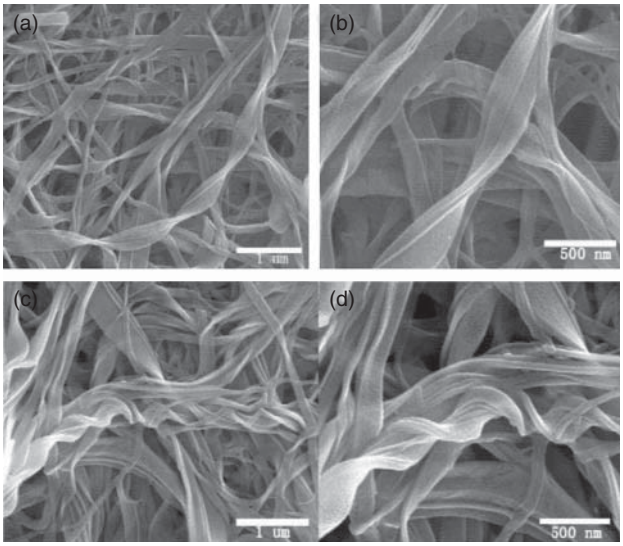

Figure 2.15 SEM (on Pt substrate) images of helical strips of [Ag3L] in different views and magnitude.

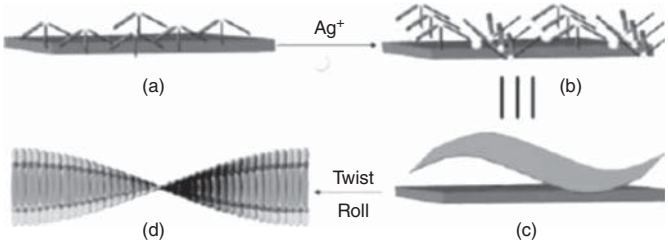

Figure 2.16 Proposed formation mechanism of the superhelix: free ligand molecules in dichloromethane (a), original flat strips with Ag (I) cations (b,c), and twisted strips induced by continuous tilt of coordination planes between ligand and Ag (I) cations (d).

2.5.5
Other Methods for Construction Nanomaterials

Nanostructured materials are materials with the characteristic length scale of the order of a few (typically 1–100) nanometers. The structure refers to the chemical composition, the arrangement of the atoms, and the size of a solid in one, two, or three dimensions; effects controlling the properties of nanostructure materials include size effects (where critical length scales of physical phenomenon become comparable with the characteristic size of the building blocks of the micro structure), changes in the dimensionality of the system, changes in the atomic structure, and alloying of components, for example, elements that are not miscible in the solid or the molten state. The synthesis, characterization, and processing of nanostructure materials are part of an emerging and rapidly growing field. Research and development in this field emphasizes scientific discoveries in the generation of materials with controlled microstructural characteristics. Nanostructured materials may be grouped under nanoparticles, nanointermediates, and nanocomposites. They may be in or far away from a thermodynamic equilibrium. For example, nano-structured materials consisting of nanometer-sized crystallites of Au or NaCl with different crystallographic orientation and chemical compositions vary greatly from their thermodynamic equilibrium. According to Siegel, nanostructured materials are classified as zero-dimensional, one-dimensional, two-dimensional, and three-dimensional nanostructures. Nanomaterials are materials that are characterized by an ultrafine grain size (<50 nm) or by a dimensionality limited to 50 nm. Nanomaterials can be created with various modulation dimensionalities as defined by Richard W. Siegel: zero (atomic clusters, filaments, and cluster assemblies), one (multilayers), two (ultrafine-grained overlayers or buried layers), and three (nanophase materials consisting of equiaxed nanometer sized grains) (Figures 2.17 and 2.18).

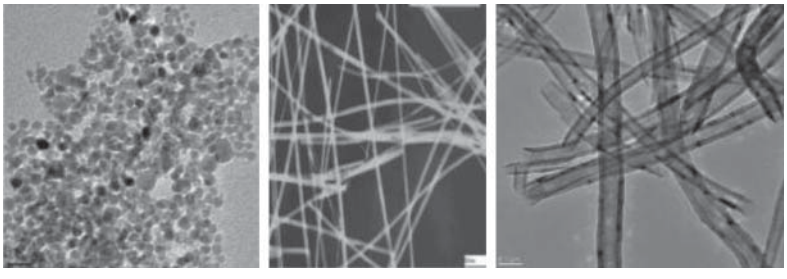

Figure 2.17 (a) 0D: nanoparticles, (b) and (c) 1D: nanowires and nanotubes.

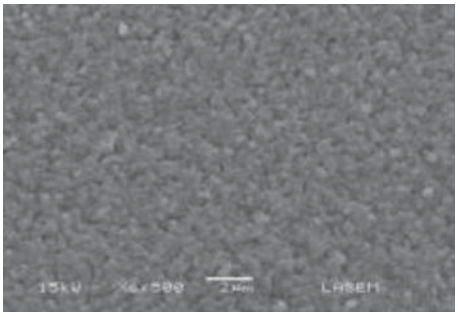

Figure 2.18 2D nanostructure: thin film.

2.6
Zero-Dimensional Nanomaterials

A major feature that discriminates various types of nanostructures is their dimensionality. The word "nano" stems from the Greek word "nanos," which means dwarf [78]. This word "nano" has been assigned to indicate the number 10^{-9}, that is, 1 billionth of any unit. In the past 10 years, significant progress has been made in the field of 0D NSMs. A rich variety of physical and chemical methods have been developed for fabricating 0D NMSs with well-controlled dimensions. Recently, 0D NSMs such as uniform particles arrays (quantum dots), heterogeneous particles arrays, core–shell quantum dots, onions, hollow spheres, and nanolenses have been synthesized by several research groups [79–83]. Figure 2.19 shows the images of different types of 0D NSMs. Moreover, 0D NSMs, such as quantum dots have been extensively studied in light emitting diodes (LEDs) [84], solar cells [85], single-electron transistors [86], and lasers [87].

The template-based method is most widely used to synthesize the 0D NSMs such as core–shell, quantum dots, and hollow sphere nanoparticles [88–91]. Recently, Nash *et al.* [88] reported a template method for synthesizing the temperature-responsive c-Fe2O3-core/Au-shell nanoparticles. For the synthesis of c-Fe2O3-core/Au-shell nanoparticles, they were using the "smart" diblock copolymer micelles as template. The amphiphilic diblock copolymer chains were synthesized using reversible addition–fragmentation chain-transfer with a thermally responsive "smart" poly(*N*-isopropylacrylamide) block. An amine-containing poly(*N*,*N*-dimethylaminoethylacrylamide) block can act as a reducing agent during gold shell formation. Li *et al.* [89] reported template-based synthesis of homogeneous hollow core–shell ferrite (MFe2O4, M = Zn, Co, Ni, Cd). In their report, they synthesized hollow core–shell nanoparticles of spinel ferrites (MFe2O4, M = Zn, Co, Ni, Cd) via carbonaceous saccharide microspheres as template. By adjusting the concentration of metal salts, it was possible to manipulate the core size and shell thickness of hollow spheres. Kim *et al.* [79] applied the template method to prepare the CdSe quantum dots. For the synthesis of CdSe quantum dots, they applied a mesoporous silica thin film template, whose pore structure is composed of 8 nm sized vertical channels in a hexagonal symmetry on

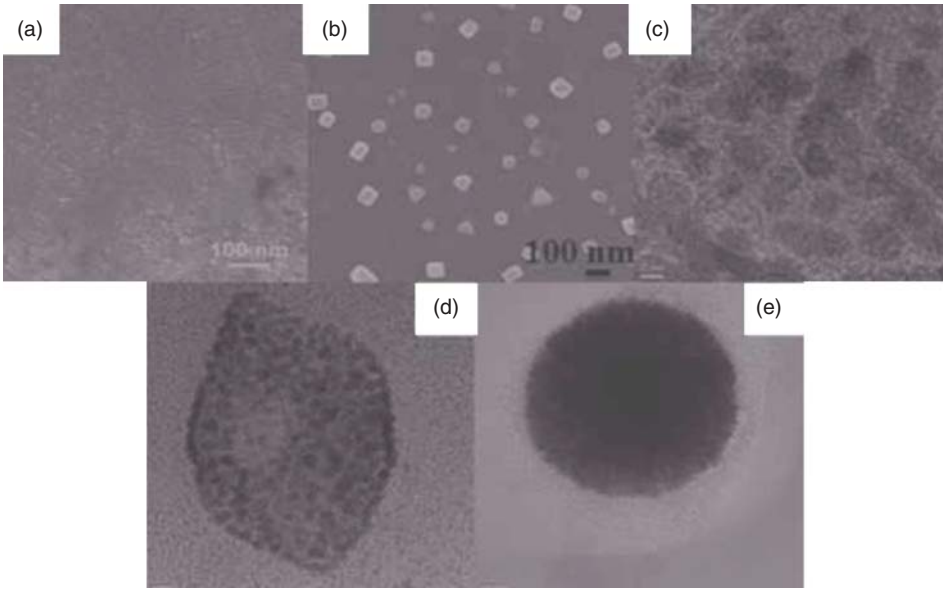

Figure 2.19 Typical scanning electron microscope (SEM) and transmission electron microscope (TEM) image of different types of 0D NSMs, which is synthesized by several research groups. (a) Quantum dots [79], (b) nanoparticles arrays, (c) core–shell nanoparticles, (d) hollow cubes, and (e) nanospheres.

the graphene surface, as a nanoporous mask. The nanochannels exert resistance against the diffusion of electrolytes and, thus, function as a potential-equalizer to suppress the preference for the edge and defect sites. They were able to form CdSe quantum dots into a hexagonal array structure by electrochemically deposited CdSe particles into the pores of the mesoporous silica film template.

Recently, researchers are using a modified Chemical vapor deposition (CVD) technique for the fabrication of 0D NSMs [92–95]. Palgrave and Parkin [92] used aerosol-assisted CVD technique to fabricate the Au nanoparticles on a glass substrate. Toluene is used as a precursor to deposit gold nanoparticles onto glass. The sizes of Au nanoparticles are ~100 nm. Boyd *et al.* [95] developed a new CVD process that can be used to selectively deposit materials of many different types. In this technique, they used the Plasmon resonance in nanoscale structures to create the local heating, which is crucial to initiate deposition when illuminated by a focused low-power laser [95]. Elihn *et al.* [96] synthesized the iron nanoparticles enclosed in carbon shells by laser-assisted chemical vapor decomposition (LCVD) of ferrocene (Fe(C5H5)2) vapor in the presence of the Ar gas. The inner part of a thin carbon shell on the iron core is indicated as a graphitic layer, whereas the outer part of the shell is composed of amorphous carbon. Domingo *et al.* [97] fabricated the Au nanoparticles by LCVD on glass and CaF2 substrates and their potential for providing enhanced Raman and infrared spectra has been investigated by using one of the dithiocarbamate fungicides, thiram, as a test molecule.

Au nanoparticles are prepared on chamber with pressure of $\sim 5 \times 10^{-6}$ mbar, using an ArF excimer laser operating at 20 Hz. However, the development of laser pyrolysis process will open up possibilities in terms of controlling particle-growth mechanisms, that is, the possibility to optimize the experimental conditions (duration, temperature), in order to control the final shape and composition (grain size, crystalline phase, stoichiometry etc.,) of the 0D NSMs [92–101]. Dumitrache *et al.* [98] synthesized the iron-based core–shell nanostructures via laser pyrolysis. In a typical synthesis of iron-based core–shell nanostructures, first by using a cross-flow configuration, the laser radiation heatsa gas phase mixture containing iron pentacarbonyl (vapors) entrained via an ethylene flow. Second, *in situ* passivation of the pyrophoric iron nanoparticles is done by controlled oxidation process. The diameter of iron-based core–shell nanoparticles is ~22 nm. Pignon *et al.* [101] prepared the TiO_2 nanoparticles by laser pyrolysis, with the use of an aerosol of TTIP (titanium tetraisopropoxide) as the main precursor sensitized by C2H4. The TiO_2 nanoparticles had the average diameter in the range from 8 to 20 nm. Thus, laser pyrolysis is used to make the different type of 0D NSMs.

2.7 One-Dimensional Nanomaterials

In the past decade, 1D NSMs have stimulated an increasing interest due to their importance in research and developments and have a wide range of potential applications. One-dimensional nanomaterials has nanoscale sizes along two dimensions and have a rod-like or wire-like appearance. In such nanomaterials, quantum confinement and surface area-related nanoscale effects are more pronounced compared to 2D nanomaterials, at the same time, they can be integrated and connected into device architectures due to single bulk-like dimension that is absent in 0D nanomaterials. Furthermore, their anisotropic morphology makes it possible to exploit the effects of orientation of an ensemble of such nanowires in addition to size and shape-related nano scale effects. The field of 1D NSMs such as nanotubes has attained significant attention after the pioneering work by Iijima [102]. 1D NSMs have a profound impact in nanoelectronics, nanodevices and systems, nanocomposite materials, alternative energy resources, and national security [103]. In Figure 2.20, we show the 1D NSMs, such as nanowires, nanorods, nanotubes, nanobelts, nanoribbons, and hierarchical nanostructures, which have been synthesized in our as well as other laboratories [104–119].

Lyotropic liquid crystal (LLC) template-assisted synthesis is one of the most facile and most applied methods for the synthesis of 1D NSMs such as nanowires, nanorods, nanotubes, nanobelts, nanoribbons, and nanospindles [104, 120–123]. For instance, Huang *et al.* [104] used the LLC template-electrodeposition to fabricate the Cu_2O nanowires with diameter of 25–100 nm.

Later, Kijima *et al.* [123] fabricated the platinum, palladium, and silver nanotubes, with inner diameters of 3–4 nm and outer diameters of 6–7 nm, by the reduction of metal salts confined to lyotropic mixed LCs of two different

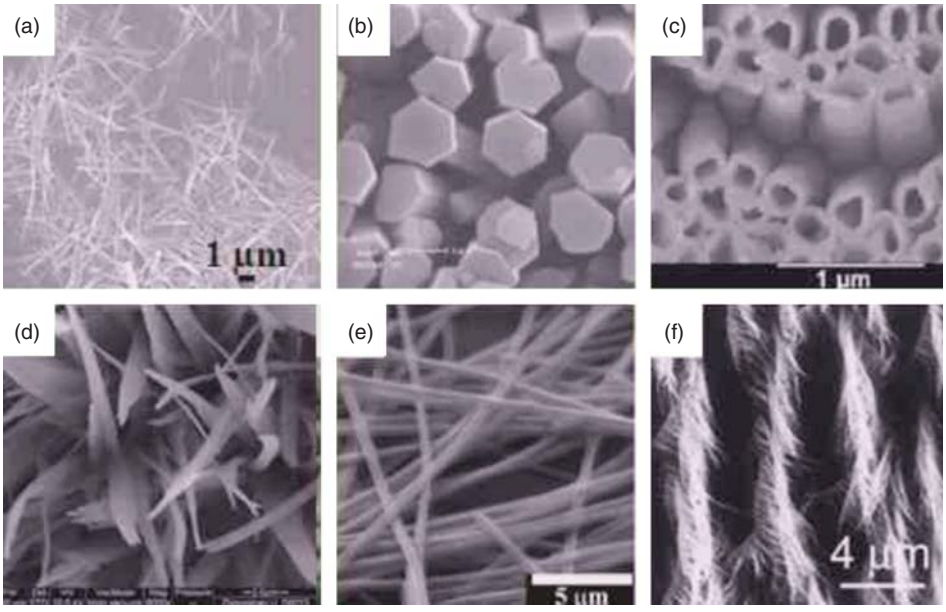

Figure 2.20 (a–f) SEM image of different types of 1D NSMs.

sized surfactants. It is well known that the uniform and consistently sized metal nanotubes are promising for potential applications as electrodes in batteries and fuel cells, and environmental catalysts. From the above results it can be seen that the LLC template-assisted methods are fast, inexpensive, reproducible, and potentially versatile for the fabrication of 1D NSMs. Electrode position processes have a wide range of advantages such as low cost, environmentally friendly, low energy consumption, high growth rate at relatively low temperatures, and have good control of the deposition thickness, shape, and size. Basically, there are two ways to produce the 1D NSMs through the electrode position method. First is the template-assisted electrode position, where the 1D anisotropic growth is realized by using various templates to confine the growth space of the electrodeposits. For example, recently, several groups have been applying the template method pattern to fabricate the 1D NSMs such as nanotubes, nanowires, and nanorods [106, 124–126]. More recently, Xia *et al.* [106] fabricated the MnO_2 nanotube and nanowire arrays via an electrochemical deposition technique using porous alumina templates. Figure 2.21 shows the SEM pictures of MnO_2 nanotube arrays and MnO_2 nanowire arrays after removal of the template. The cross-sectional view of MnO_2 nanotubes shows that the length of the nanotube is 2 μm, as shown in Figure 2.21c. The morphology of the nanotublar nanostructure changes to a wire-like form during prolonged electrochemical deposition (Figure 2.21d, e).

The cross-sectional view of the MnO_2 nanowire arrays shows that the length of the MnO_2 nanowire is ~10 lm (Figure 2.21f). They also report that the MnO_2 nanotube array electrode has a capacitive behavior superior to that of the MnO_2

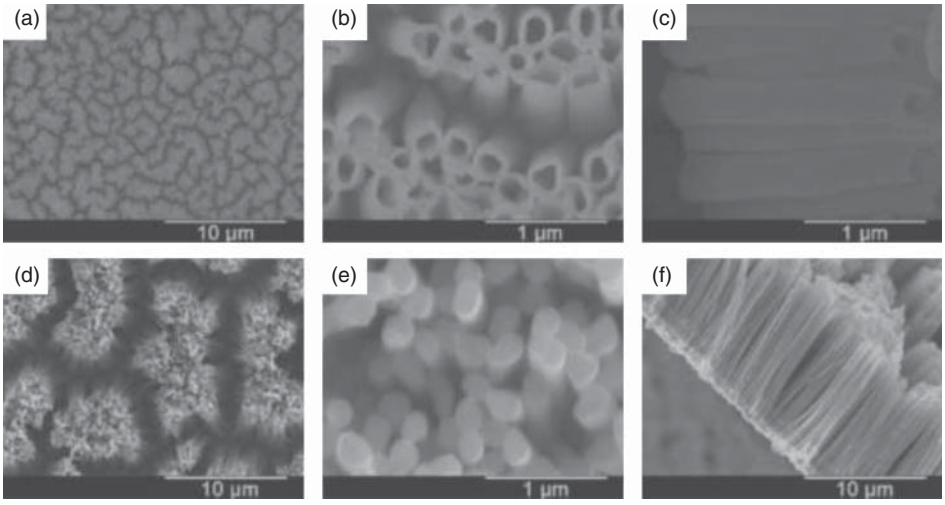

Figure 2.21 (a, b) Plan-view SEM images of MnO_2 nanotube arrays; (c) cross-section view of MnO_2 nanotube arrays; (d, e) plan-view SEM images of MnO_2 nanowire arrays; and (f) cross-section view of MnO_2 nanowire arrays. (Reprinted from Ref. [106].)

nanowire array. The second method is by using template-free electrode position, where the 1D anisotropic – growth is achieved by using the intrinsic anisotropic crystallographic structure of a targeted material [107, 123]. However, only a few 1D NSMs have been made by the template-free electrode position. More recently, Li *et al.* [107] used the electrode position process to fabricate the polyaniline nanobelts.

Figure 2.22 shows the SEM images of the resulting products. The average width and thickness of polyaniline nanobelts are 2 lm and 50 nm, respectively. The length of polyaniline nanobelts is 20 lm. They also had shown that the polyaniline

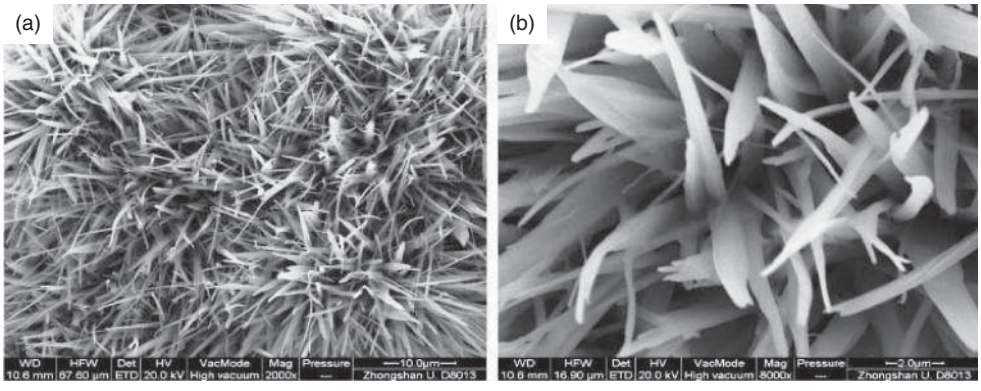

Figure 2.22 Typical (a) low- and (b) high-magnification plan-view SEM images of polyaniline nanobelts. (Reprinted from Ref. [107].)

nanobelts have a high specific capacitance value of 873 F g^{-1} at 10 mV s^{-1}, which is much bigger than that of polyaniline nanospheres.

The hydrothermal technique is an efficient method for the controlled synthesis of 1D NSMs [127–130]. For instance, Tang *et al.* [129] prepared the Si nanowires on Si substrates by the hydrothermal deposition route under low temperature and pressure. The obtained Si nanowire consists of a polycrystalline Si core and an amorphous silica sheath. The diameter and length of Si nanowires were 170 nm and 10 lm, respectively. More recently, Shim *et al.* [130] used the facile hydrothermal method with hydrogen titanate nanowires as the precursor to fabricate the porous TiO_2 nanowires. Figure 2.23 shows the SEM, TEM, HRTEM images and SAED pattern of the pure anatase phase TiO_2 nanowires and an anatase TiO_2 nanowire. They also reported that the porous anatase TiO_2 nanowires demonstrated a good cycling performance and excellent rate capabilities compared with the $H_2Ti_3O_7$ nanowires and the anatase TiO_2 nanowires.

Solvothermal reaction uses a solvent under elevated pressures and temperatures above its critical point to increase the solubility of a solid and to speed up reactions between precursors. In view of several advantages (high purity and good homogeneity) over other techniques, the solvothermal synthesis process has been

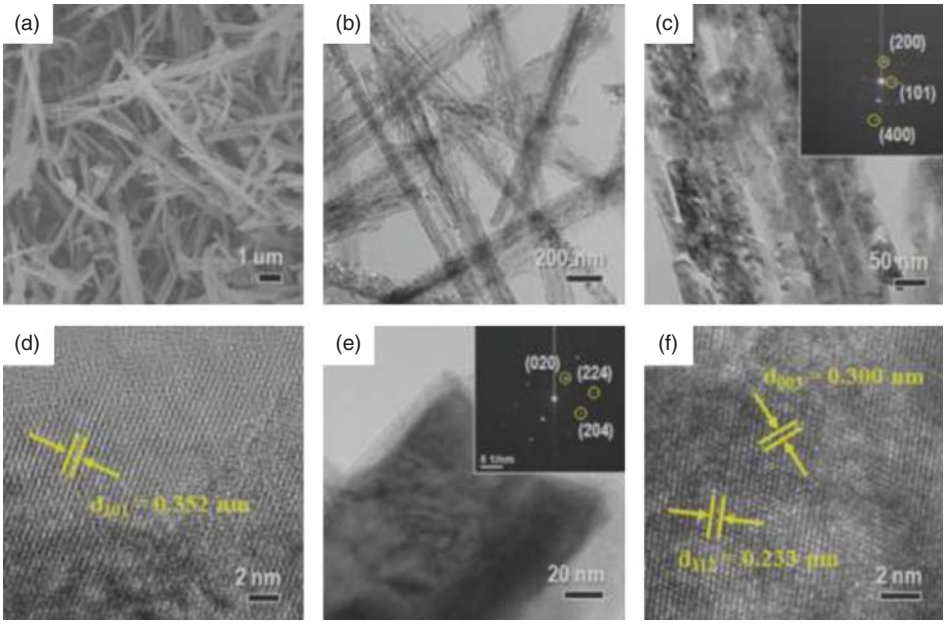

Figure 2.23 (a) SEM and (b) TEM images of the as-made pure anatase phase TiO_2 nanowires growth by hydrothermally dehydrated at 180 °C. (c) TEM image of the pure anatase phase TiO_2 nanowires with porous nanostructures. The inset of image (c) shows the SAED patterns. (d) HRTEM image of a pure anatase phase TiO_2 nanowire. (e) TEM image of an anatase TiO_2 nanowire. The inset of image (e) shows the SAED patterns. (f) HRTEM image of an anatase TiO_2 nanowire. (Reprinted from Ref. [130].)

one of the most important methods for the preparation of 1D NSMs [131–135]. Xu *et al.* [134] fabricated large-scale CdS nanowires by a solvothermal process in a mixed solvent of dodecanethiol and ethylenediamine. Figure 2.24 shows the SEM images of the resulting products. The resulting product is composed of uniform nanowires with an average diameter of 25 nm and lengths of 20–40 lm.

The sol–gel technique is an attractive synthetic method due to its simplicity and flexibility, which allow for optimization and production of bulk 1D NSMs [136–139]. Bitenc *et al.* [139] prepared the ZnO particles with a needle-like shape by the solution-phase method in the autoclave system (oven preheated at 90 °C). Figure 2.25 shows SEM images of the three samples (Samples A–C). As shown in SEM images, the ZnO particles that were prepared in the autoclave had a much higher aspect ratio (20 ± 5) and were needle-like. Hence, the sol–gel method can be applied for the preparation of various types of 1D NSMs.

In the last few years, nanowires formation via CVD is especially attractive because of the relative ease of scaling from research to production-size systems [140–144]. Shimizu *et al.* [143] used the CVD to fabricate the Ge nanowires on Si substrates. Figure 2.26 shows plan-view SEM images of Ge nanowires grown on the Si substrate. The (110) growth direction is dominant in Figure 2.26a–c. The average diameter of the Ge nanowires calculated from Figure 2.33c was 20 nm.

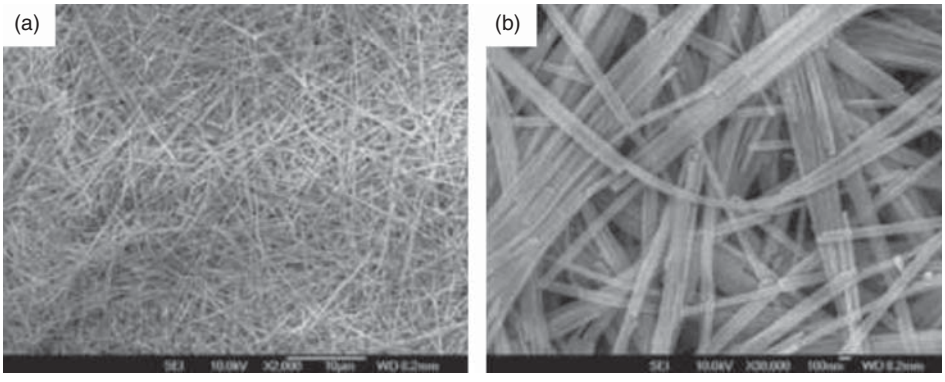

Figure 2.24 (a) Low- and (b) high-magnification SEM pictures of the CdS nanowires. (Reprinted from Ref. [135].)

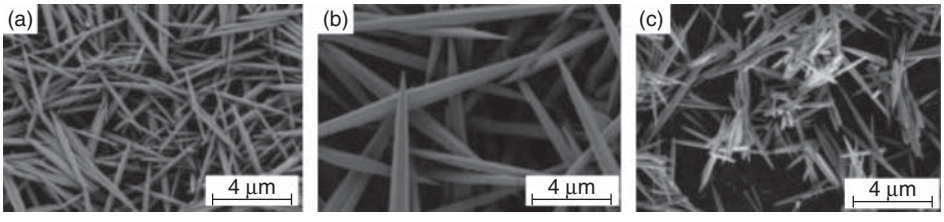

Figure 2.25 SEM images of three samples (a–c) prepared in an autoclave at 90 C. (Reprinted from Ref. [139].)

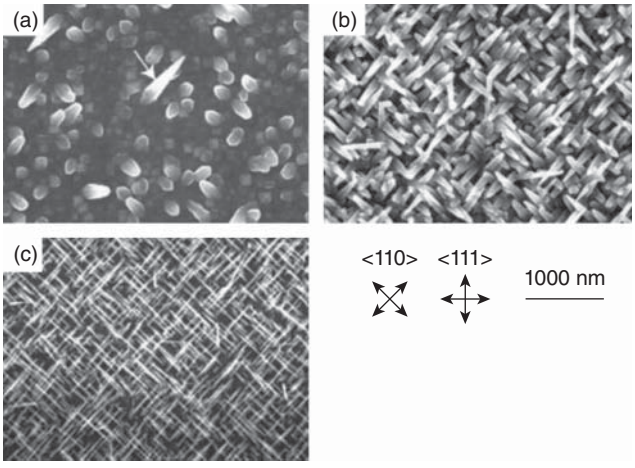

Figure 2.26 Plan-view SEM images of Ge nanowires. The Ge nanowires were grown at various temperatures (a) 450 C, (b) 400 C, and (c) 370 C for duration of 4 min in n-butylgermane. The arrow in (a) indicates a strongly tapered wire. Crossed arrows represent crystal orientations of the Si substrate. It is projection onto the Si (100) surface. Reference [143].

1D NSMs have also been synthesized via LCVD [146–151]. Longtin *et al.* [150] reported the growth of carbon nanofibers on nickel-coated alumina substrates by LCVD. Figure 2.27 indicates the change in the surface morphology of carbon nanofibers with respect to various irradiation times. Longer irradiation times produced a 1 lm-thick carbon coating over most of the irradiated area.

2.8 Two-Dimensional Nanomaterials

In recent years, synthesis of 2D NSMs has become an important area in materials research, owing to their many low-dimensional characteristics that are different from the bulk properties. 2D NSMs with certain geometries exhibit unique shape-dependent characteristics and therefore their subsequent utilization as building blocks for the key components of nanodevices [151–154]. In Figure 2.28, show the 2D NSMs, such as junctions (continuous islands), branched structures, nanoprisms, nanoplates, nanosheets, nanowalls, and nanodisks [155–161].

Nanosheet and nanodisk-like structures were prepared by using cetyltrimethylammonium bromide (CTAB) micelles as a soft template method [157, 162]. Siril*et al.* [157] synthesized the hexagonal Pd nanosheets in ternary emulsions made of water/oil/CTAB and quaternary hexagonal mesophases made of water/oil/CTAB/co-CTAB surfactants. HRTEM revealed that the hexagonal Pd

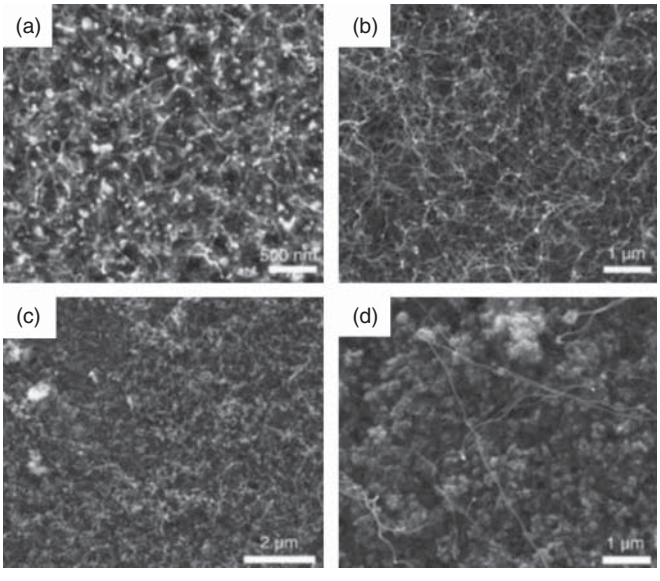

Figure 2.27 Changes in the carbon nanofibers morphology with respect to various irradiation times: (a) 5 s; (b) 120 s; (c) 180 s; (d) 420 s. (Reprinted from Ref. [150].)

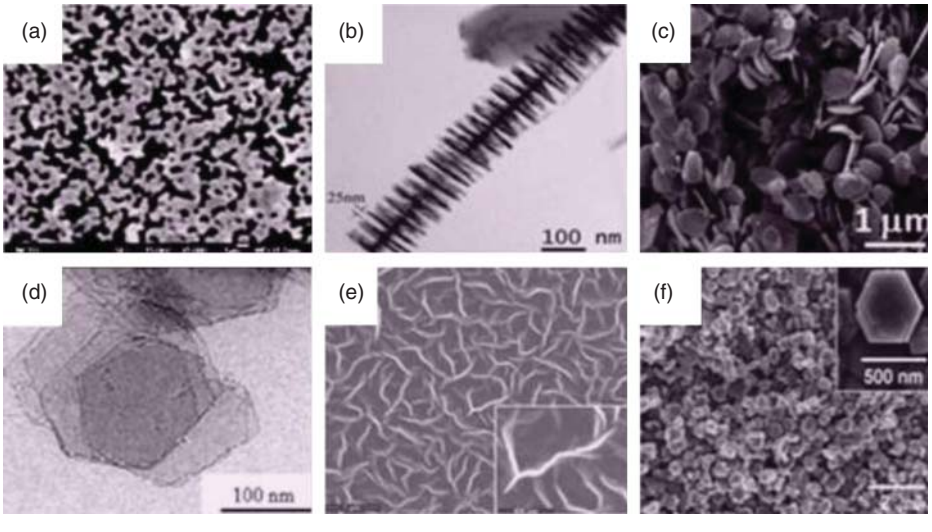

Figure 2.28 Typical SEM and TEM image of different kinds of 2D NSMs, which is synthesized by our and several research groups. (a) Junctions (continuous islands), (b) branched structures [155], (c) nanoplates [156], (d) nanosheets [157], (e) nanowalls [158], and (f) nanodisks [159].

nanosheets were obtained from the CTAB-based emulsions. These hexagonal Pd nanosheets have shown a broad absorption band from the visible to the near infrared region. However, Chen and Carroll [162] also used the CTBA micelles as a soft template to synthesize large quantities of truncated triangular Ag nanoplates. Kawasaki *et al.* [163] synthesized single crystalline platinum (Pt) nanosheets in single or mixed surfactant LLC. They also noticed that the thickness of Pt nanosheets is ~3.5 nm. The Pt nanosheets are surface-smooth and continuous over relatively large length scales of micrometer sizes. Kawasaki *et al.* [163] suggested that the interfacially directed growth of Pt metals within the aqueous shells of the Tween 60 hemicylindrical micelles induces the thin Pt crystals as thick as the aqueous shells. Sakai *et al.* [164] (Figure 2.29) developed a new approach to fabricate single crystalline Pt nanosheets by the chemical reduction of a Pt salt based on the interfacial directed growth of Pt metals within LLC at a graphite/solution interface. Figure 2.29 shows the AFM images obtained for single crystalline Pt nanosheets. AFM images indicated that the thickness of Pt nanosheet is about 11.7 nm. Kijima *et al.* [165] prepared nanohole-structured single-crystalline Pt nanosheets by reduction of Na_2PtCl_6 confined to the LLCs using borohydride as the reductant. Further, Wang *et al.* [166] established a novel method to prepare Au nanoplates from LLC. Another research was carried out by Wang *et al.* [167] to obtain products of controllable shape and size. Single-crystalline Au nanoplates with triangular or hexagonal shapes were synthesized by reducing $HAuCl_4$ in LLC by the addition of a small amount of capping agents. Consequently, all the above results suggest that the hexagonal LLCs-based surfactant cylindrical micelles are available for the formation of 2D metal nanosheets. Another technique that is widely employed to prepare 2D NSM is two- and three-electrode electrochemical cell system [160, 168–171]. Liu *et al.* [169] used a two-electrode electrochemical cell to synthesize the mesoporous hydrous manganese dioxide nanowall arrays.

The following reactions are involved in the deposition of MnO_2 nanowalls. When a voltage was applied, the water electrolysis occurred at the cathode

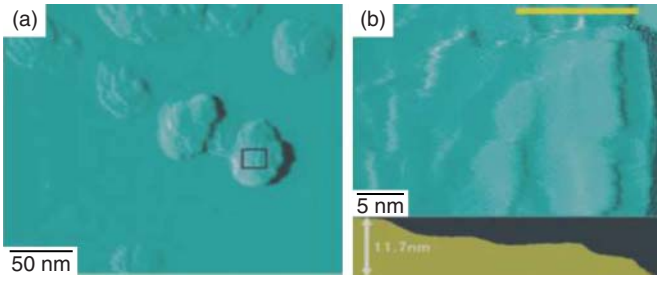

Figure 2.29 (a) AFM image of Pt nanosheets and (b) AFM image of selected region of Pt nanosheets shown in (a). In (b), yellow line shows the scan line for the measured thickness of Pt nanosheets. Bottom of (b) shows the stacking of four nanosheets with a total thickness of 11.7 nm. (Reprinted from Ref. [164].)

surface, generating hydrogen gas and OH-groups:

$$2H_2O + 2e^- = H_2 + 2OH^-$$

Then, the generated OH-groups from bonds with Mn^{2+} ions, caused nanoparticle precipitation:

$$Mn^{2+} + 2OH^- = Mn(OH)_2$$

Figure 2.30 shows the SEM images of manganese oxide film grown on cathodic substrate. The cross-section SEM image (Figure 2.30b) depicts that the nanowall array was deposited with no continuous film at the interface between the Pt film and manganese oxide nanowall arrays.

Jiang *et al.* [172] also applied the electroless process to fabricate Cu microstructures assembled with nanowalls. In Figure 2.31, we can see SEM images of Cu microstructures with net shape consisting of nanowalls. They also found that the morphology of Cu microstructures are controlled by adding NaOH in aqueous solution and by choosing $NaH_2PO_2 \cdot H_2O$ as the reducing agent.

Hydrothermal methods are ideally suited for the rapid synthesis of large quantities of 2D metal oxide or metal nanostructures [145, 173]. For example, MnO_2 nanostructures with different morphologies, such as hexagram-like and dendrite-like hierarchical forms, were successfully synthesized via a facile hydrothermal route (Figure 2.32) [173].

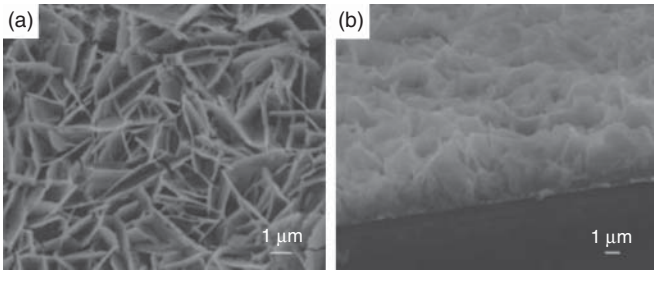

Figure 2.30 The figure shows the SEM images of manganese oxide (a) and (b). (Reprinted from Ref. [169].)

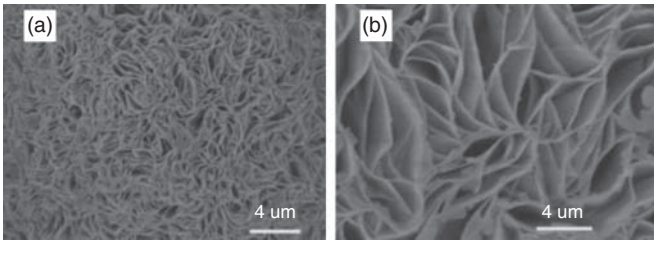

Figure 2.31 SEM images at (a) low- and (b) high-magnifications showing the copper microstructures with net shape consisting of nanowalls. (Reprinted from Ref. [172].)

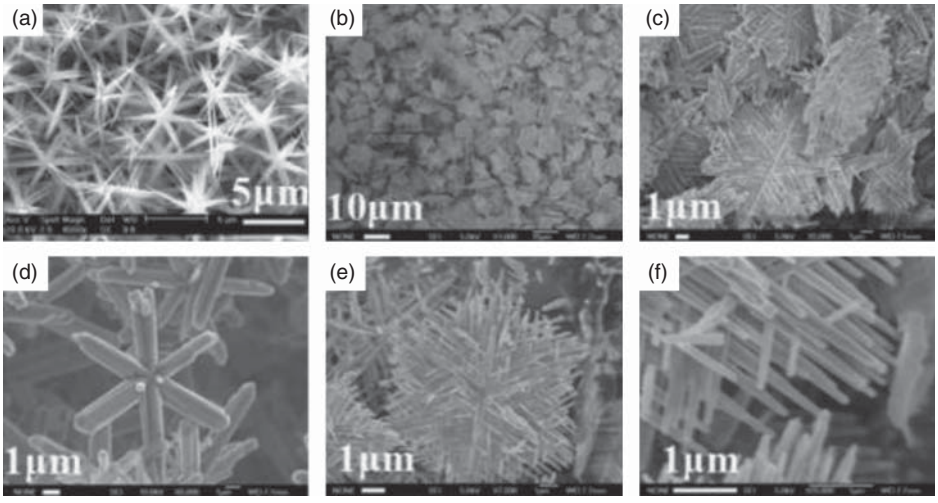

Figure 2.32 (a–f) The figure shows the SEM images of the as-synthesized 2D hexagonal starlike b-MnO_2 and dendritelike hierarchical b-MnO_2 nanostructures. (Reprinted from Ref. [173].)

The solvothermal processes are very facile routes to synthesize 2D NSMs [145, 173]. For example, silver nanosheets, and chain-like sheets have been successfully synthesized by a controlled solvothermal process in the presence of ammonia and $AgNO_3$ [173]. Li *et al.* [145] also used a solvothermal method to fabricate CuS nanoplates by using copper nitrate and sulfur. Figure 2.33 shows the SEM images of CuS architectures prepared in different solvents. According to their results, the CuS products synthesized in DMF were nanoplates and the samples prepared in ethanol exhibited flower-like morphology composed of large numbers of nanoplates, but those synthesized in EG were CuS architectures with high symmetry made up of several nanoplates arranged in a certain mode.

The sol–gel process (or sol–gel deposition) is widely used to synthesize 2D NSMs based on the polymerization of molecular precursors via wet chemical methods [174–176]. For example, Wang *et al.* [175] synthesized 2D MoO_3 nanoplatelets on silicon substrate using a sol–gel process. Figure 2.34 shows the SEM images of 2D MoO_3 nanoplatelets at different magnifications.

Over the past decade, CVD processes have received considerable attention for the synthesis of 2D NSMs. Barreca *et al.* [177] synthesized a 2D zinc oxide nanoplatelets on Si substrate by CVD starting from a second-generation ZnII precursor, Zn(hfa)2·TMEDA (Hhfa = 1,1,1,5,5,5-hexafluoro-2,4-pentanedione; TMEDA = *N*,*N*,*N*0,*N*0-tetramethylethylenediamine). Recently, Gao *et al.* [178] fabricated large quantities of hexagonal boron nitride nanosheets via a CVD process at 1100 and 1300 °C. Figure 2.35 displays the SEM images of boron nitride nanosheets grown at 1100 and 1300 °C. By controlling the synthesis and chemical reaction parameters, the thickness of the BN nanosheets can be adjusted in a range of 25–50 nm.

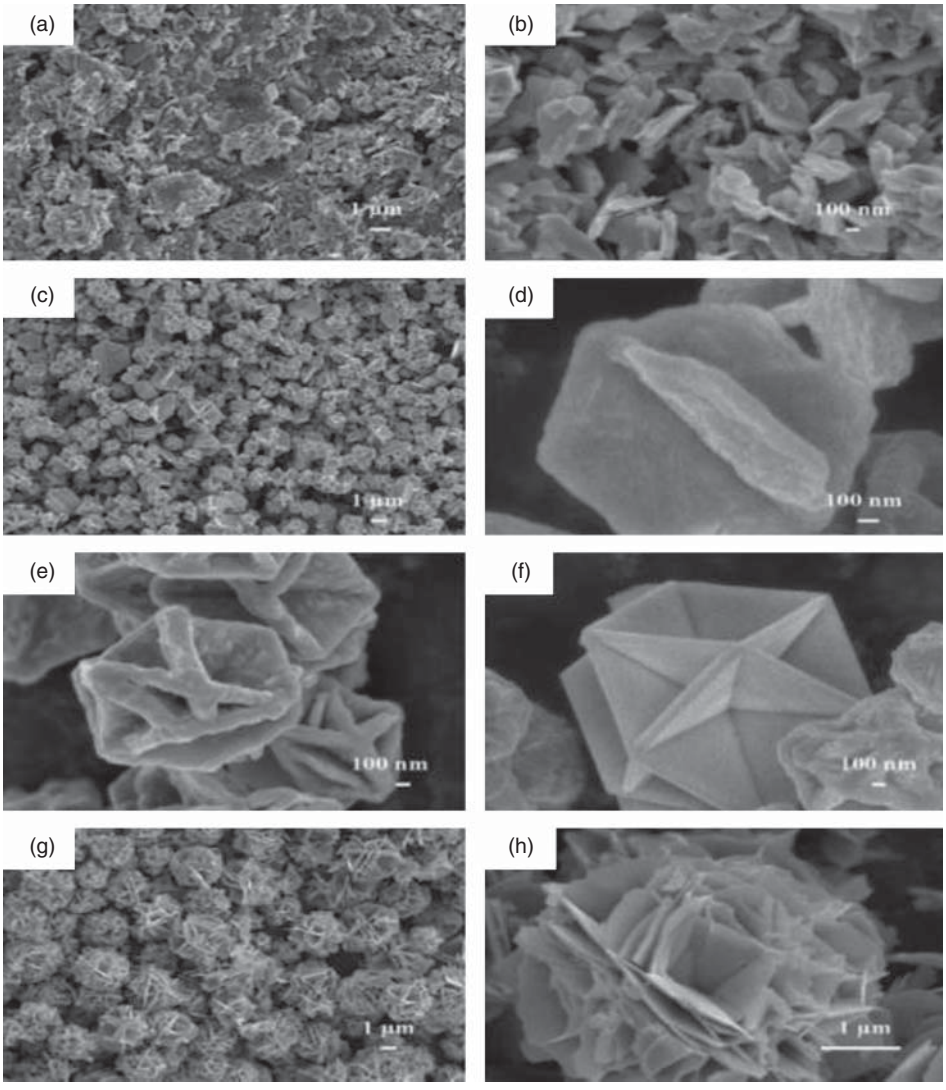

Figure 2.33 SEM images of the CuS architectures prepared in different solvents: (a, b) ethanol, (c–f) ethylene glycol, and (g, h) dimethylformamide. (Reprinted from Ref. [145].)

LCVD has been used to fabricate the 2D NSMs. For instance, Guan *et al.* [179] used LCVD to produce 2D linear arrays of ZnO nanoparticles on a silicon substrate (Figure 2.36).

Consequently, all the above results suggested that the chemical process is a simple and very useful method for the synthesis and fabrication of 2D NSMs. The morphology, particle size, and metallic composition of the 2D NSMs can be tuned based on the precursor solutions, substrate materials, and deposition conditions.

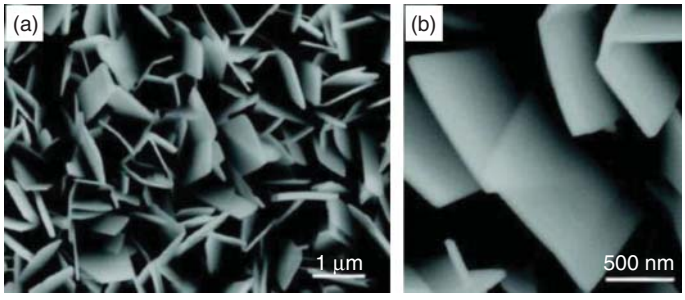

Figure 2.34 SEM images of the 2D MoO_3 nanoplatelets under (a) low- and (b) high-magnifications. (Reprinted from Ref. [175].)

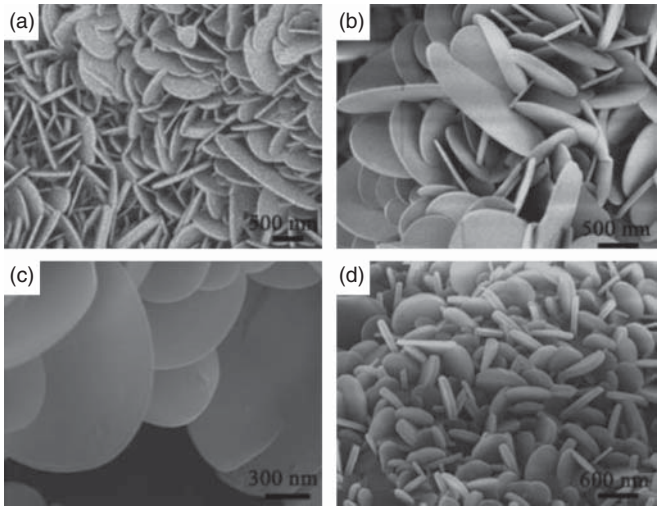

Figure 2.35 Plan-view SEM images of 2D boron nitride nanosheets grown at (a–c) 1300 °C and (d) 1100 °C. (Reprinted from Ref. [178].)

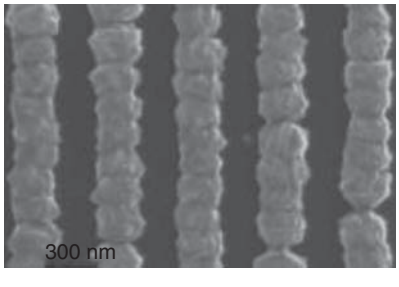

Figure 2.36 SEM images of 2D linear arrays of ZnO nanoparticles. (Reprinted from Ref. [179].)

2.9 Challenges in Nanoscience and Nanotechnology

Nanotechnology may be the ultimate enabling technology, since it deals with the fundamental building blocks of matters and lives. Almost every field of industry will be deeply influenced by the progress in nanotechnology. The most important impact of this nanotechnology revolution may be the new synergy among scientists, engineers, industrialists, and economic development specialists. Nanotechnology creates both challenges and opportunities [180–182].

The major challenges of nanotechnology mainly include technology challenge, industrial cluster, societal and ethical challenge, and military implication.

2.9.1 Challenges for Technological

In nanoscience and nanotechnology, one major technological challenge is the nanomaterial science required for the local growth of nanostructures with desired solid-state or molecular properties, and for the control of local reactions. The second technological challenge concerns nanointerfaces as connections and active components. Another technological challenge deals with the novel components with electronic, mechanical, and chemical functionalities, which can be used for energy and information transfer to autonomous nanosystems [183]. It is expected that nanomechanics and nanochemistry will provide original paths between the "virtual" world of all kinds of data processing, including thermal, mechanical, and chemical processing, and the "real" world of sensing and actuation. Such paths are crucial for the development of integrated sensing, processing, and actuation technologies. Nominally, nanotechnology involves the manipulation of atoms and molecules. Though, like plants and animals, we can manipulate atoms and molecules using biological processes, we cannot freely and accurately control biological processes to perform desired functions. Using our current knowledge and techniques, some biological processes, such as tissue growth, can be guided on a macroscale; however, we cannot yet guide these biological processes in the way viruses and enzymes do. In the research of nanoscience and nanotechnology, one of the most important challenges would be the growth, characterization, and functionalization of nanomaterials and nanostructures. It is still a daunting task to control the material's property and make an ideal metal, semiconductor or insulator with perceived properties. Unlike other well-known aspects of manufacturing, nano design and simulation issues are just beginning to come out from the realms of human imagination.

2.9.2 Challenges and Research for the Social Cluster

Public health and safety is probably the major concern associated with nanotechnology. It is becoming important and urgent to address the societal and

ethical issues related to this emerging area of technology. It is necessary to make sure that fear of nanotechnology be eliminated, and the products of nanotechnology be accepted by the society and are not blocked by the public due to fear. The possible threats of nanotechnology are related to how nanoparticles affect the environment, and more essentially, how nanoparticles interact with the human body. A lot of efforts and resources have been spent in incorporating nanoparticles into products that have already been marketed and accepted by the public. However, the research on health issues related to nanotechnology is very limited, and this is a matter of severe concern. The elements involved in nanotechnology behave quite differently from their counterparts in conventional technology.

Nanotechnologies are positioned not only to initiate the next "industrial revolution," but to also offer technological solutions to many of these problems. Industry and government have in recent years claimed that:

> Nanotechnologies will assist in providing clean water to billions through filtration techniques with their ability to decontaminate dirty water.

2.9.3 The World Is Facing a Water Crisis

The question of whether or not the world is facing a water crisis is beyond dispute: nearly 2 billion people live in water deprived parts of the globe. Pollution, climate change, and ever-increasing populations have made it harder for people to access clean water and adequate sanitation. The consequences for many are deadly:

- Two fifths of the world population lack access to proper sanitation.
- Contaminated water is implicated in 80% of all diseases worldwide.
- Fifty percent of all hospital beds worldwide are occupied by people suffering from easily treatable water borne diseases [184].

In this context, nanotechnologies have been positioned as one of the premier technological solutions to solve some of these problems [185]. Some have even raised the hope that nanotechnologies can assist in achieving the UN Millennium Development Goal of halving the number of people without access to clean water by 2015 [186].

Proponents of this technology claim that nanotechnologies can overcome unresolved challenges associated with the removal of water contaminants, while at the same time being more effective, efficient, durable, and affordable [185]. Potential products using nanotechnologies include:

- Water filtration devices, for example, nanoporous filter and membrane materials to remove contaminants and used in desalination equipment.
- Monitoring devices, for example, sensors for quality and quantity of water resources and the detection of contaminants.

Many different water treatment technologies (chemical and biological, active and passive) already exist for removing various contaminants from water and are achieving different levels of quality, depending on the technology used and the water quality that is required. However, each treatment technology has its own limitations, such as being energy intensive and generating by-products with unintended impacts on the environment and human health. Nanotechnology could assist in meeting the need for safe and affordable water through relatively inexpensive water purification and the rapid and low-cost detection of impurities. The application of nanotechnology in water treatment may vary depending on the scale (local portable systems for central regional treatment facilities) and the quality of water required.

One of the very significant challenges is that a large number of rural communities and informal settlements located near industrial areas need to have access to clean water. In most instances, the water to which the community has access is heavily contaminated, resulting in widespread water-borne diseases such as cholera. This makes the provision of clean water, particularly to rural and arid areas, a real and serious challenge. This necessitates the development of low-cost and portable filters and purifiers. Addressing this challenge could be assisted by nanotechnology research for the

- development of water purification modules;
- development of biodegradable, stimuli-dependent nanoparticles for the delivery of agents that are used in water treatment;
- development of sensors for the detection of pathogens/chemical pollutants in water;
- development of techniques to remove pathogens/chemical pollutants and particulate matter in water; and
- preservation of water cleanliness to ensure that water treated in bulk can remain uncontaminated for a long time.

To enable the exploration of other possible sources of drinking water, we need to explore how nanotechnology can help to

- develop alternative and cost-effective systems for the desalination of sea water;
- create appropriate conditions for rain (such as cloud seeding);
- develop techniques for the maintenance of water levels in dams and rivers (i.e., prevent or minimize water evaporation);
- develop techniques for harvesting and preserving rain water (including excess rain);
- develop systems for water recycling at a point of usage;
- effect an improvement in the portability of water.

Industrial effluence has been the main source of destruction of wet lands. To protect the environment, including the country's wetlands, it has become necessary to investigate cost-effective and efficient means of treating industrial effluence. The challenge is to ensure the sustainable protection of the environment. In addition, industrial waste streams such as those from mines, are responsible

for, among other things, the contamination of ground water. With some communities relying on ground water as their source for water, it is necessary to ensure the remediation of such water sources by using nanoparticles. The remediation of waste streams will not only stop ground water contamination, but also ensure environmental protection. The research focus in this area should be on how nanotechnology can be used to

- develop sensors for the detection of pollutants;
- develop systems for the removal of pollutants (for recovery and/or inactivation);
- beneficiate effluent;
- minimize contaminants through the use of nanoparticles;
- recover water from diluted mine effluent.

One of the greatest challenges of the twenty-first century will be the transition from energy sources based on fossil fuels to sustainable, renewable sources. Climate change and peak oil make it imperative that we find solutions, especially if we want to preserve at least some elements of our current lifestyles. Nanotechnologies are considered by many to be at the forefront for providing solutions for better energy generation, storage, and distribution. Using nanotechnologies to fabricate materials (for instance CNTs) that are lighter and stronger than conventional materials translates to impressive fuel efficiency gains in cars or planes. Use of nanosized catalysts in car engines (e.g., substances that speed chemical reactions) results in using 70–90% less of the same catalyst in bulk form. Storage capacity, lifetime, and safety of batteries are also said to benefit from nanotechnologies. For instance, carbon nanofibers are beginning to be used in lithium-ion batteries to extend the battery's life [187]. While improving efficiency and reducing material use are of course important steps, the existing regulation and testing methods are not able to guarantee the safety performance of any of these products. As such, research questions in the area of energy should aim to address these challenges.

Research could possibly focus on the following things:

- How nanotechnology can be used to develop new sources of energy.
- How nanotechnology can be used to develop/improve existing renewable sources of energy.
- How nanotechnology can be used to effect the production of cleaner and environmentally friendly energy.
- How nanotechnology can be used to effect an improvement in the generation and use of energy.
- How nanotechnology can be used to develop high-capacity energy storage devices,
- How solar energy can be applied to produce hydrogen fuel.
- How nanotechnology can be used for the efficient production of hydrogen by water electrolysis.
- How nanotechnology can be used for hydrogen purification.
- How nanotechnology can be used in both catalysis and fuel cell research.

Energy distribution, particularly to rural communities, has become a serious challenge.

A lack of adequate infrastructure is one of the primary reasons for there being difficulty in distributing energy to such parts of the country. Therefore, it is necessary to investigate the possibility of nanotechnology providing other (and of more effective) means of distributing energy or distributed onsite power generation.

Addressing health-related issues is the basic challenge in this century all over the world.

Almost all countries are facing serious challenges regarding the health of its people. The country has a high rate of HIV-infection that is accompanied by opportunistic infections such as tuberculosis TB, which is placing a tremendous burden on the national health infrastructure and is draining resources that ought to be used in addressing other diseases that are also important and growing in urgency. These diseases include diabetes, cancer, heart disease, malaria, arthritis, and asthma. New solutions are urgently needed to adequately manage these diseases. Relevant research questions in this area would explore the following, among other things:

- The use of nanotechnology in the development of point-of-care diagnostic kits. Point-of-care diagnostic tools are necessary when medical practitioners need to confirm diagnosis during a consultation, thus enabling the rapid identification of pathogens and application of appropriate therapy. Such instances include cases where patients are suffering from infectious diseases that have a rapid disease progression such as meningitis (which can lead to fatality or disability in infants and children), and Ebola (which causes quick and painful death in its patients). Point-of-care diagnostics are also crucial in the management of HIV and TB, because these conditions require rapid detection and treatment to improve the life of the patient, and prevent the spread of these infectious agents. Rapid diagnostic kits for HIV are currently available; however, they have proved not to be selective as they sometimes give false results. Therefore, selective/specific diagnostic tools for HIV are urgently needed. In the case of TB, the current testing methods have a long turn-around time, which makes it difficult for doctors to provide timely and appropriate therapy. In addition, specialized technicians are needed to perform the tests and specialized pathologists to interpret the results. The development of rapid diagnostic kits for TB would enable doctors to quickly confirm the diagnosis of TB, and therefore, administer timely treatment. Therefore, rapid diagnostic kits that are simple and "user friendly" would be beneficial in several instances in the management of infectious diseases. Point-of-care diagnostic kits are also important for the early detection of cancers as this would improve chances of successful therapy.
- Using nanotechnology to improve surgical procedures. Current methods of performing surgery are invasive and cause most patients a great deal of pain during the recovery period. Highly specialized surgeons are required to perform them.

New surgical tools need to be developed to improve on current surgical procedures, and new procedures need to be developed to reduce the invasiveness of surgery and reduce the complexity of surgical procedures.

- The development of nanobiosensors for *in situ* detection of glucose levels in diabetes therapy;
- The ability to functionalize nanoparticles in a simple and efficient manner to confer versatility for biomedical applications.

2.10 Applications of Nanoscience and Technology

Nanoscience and nanotechnology are rapidly growing fields with significant potential to provide a new generation of both scientific and technological approaches and of research and clinical tools and devices. The essence of nanoscience and nanotechnology is the creation and use of molecules, molecular assemblies, materials, and devices in the range of 1 – 100 nm, and the exploitation of the unique properties and phenomena of matter at this dimensional scale.

Nanotechnology comprises both top-down and bottom-up fabrication methodologies. In the former, nanoscale devices and their components draw inspiration from larger, currently known devices and components, while the latter pertains to the assembly of devices from individual atoms, molecules, and supramolecular structures of biological and synthetic origins. Below we list some key current and potential short- and long-term applications of nanomaterials.

2.10.1 Personal Care Products

The use of nanomaterials imparts antibacterial and antiodor functionality to powder, gel, stick, and spray underarm products. They also make them glide smoothly on the skin. Nanogold and nanosilver particles have antibacterial and antifungal characteristics. They are hence used in many personal care products. Silver particles of size less than 10 nm dispersed in soaps impart the double advantage of killing germs and increasing effectiveness in removing dirt particles from the skin. Deodorants and antiperspirants based on nanozinc oxide particles are currently being developed. Silver-doped zinc oxide offers enhancement in odor fighting and antibacterial properties. Nanosized titanium dioxide and zinc oxide are currently used in some sunscreens, as they absorb and reflect ultraviolet (UV) rays and yet are transparent to visible light and so are more appealing to the consumer. Nanosized iron oxide is present in some lipsticks as a pigment but it is our understanding that it is not used by the European cosmetics sector. The use of nanoparticles in cosmetics has raised a number of concerns about consumer safety.


2.10.2 Clays

Clays containing naturally occurring nanoparticles have long been important as construction materials and are undergoing continuous improvement. Clay particle-based composites – containing plastics and nanosized flakes of clay – are also finding applications such as use in car bumpers.

2.10.3 Paints

Incorporating nanoparticles in paints could improve their performance, for example, by making them lighter and giving them different properties. Thinner paint coatings ("lightweighting"), used, for example, on aircrafts, would reduce their weight, which could be beneficial to the environment. It may also be possible to substantially reduce the solvent content of paints, with resulting environmental benefits. New types of fouling resistant marine paint could be developed and are urgently needed as alternatives to tributyl tin (TBT), now that the ecological impacts of TBT have been recognized. Antifouling surface treatment is also valuable in process applications such as heat exchange, where it could lead to energy savings. If they can be produced at a sufficiently low cost, fouling-resistant coatings could be used in routine duties such as piping for domestic and industrial water systems. It remains speculative whether very effective antifouling coatings could reduce the use of biocides, including chlorine. Other novel, and more long-term, applications for nanoparticles might lie in paints that change color in response to change in temperature or chemical environment, or paints that have reduced infra-red absorptivity and so reduce heat loss.

2.10.4 Coatings and Surfaces

Coatings with thickness controlled at the nano- or atomic scale have been in routine production for some time, for example, in MBE or metal oxide CVD for optoelectronic devices, or in catalytically active and chemically functionalized surfaces. Recently developed applications include the self-cleaning window, which is coated in highly activated titanium dioxide, engineered to be highly

hydrophobic and antibacterial, and coatings based on nanoparticulate oxides that catalytically destroy chemical agents. Wear- and scratch-resistant hard coatings are significantly improved by nanoscale intermediate layers between the hard outer layer and the substrate material. The intermediate layers give good bonding and graded matching of elastic and thermal properties, thus improving adhesion. A range of enhanced textiles, such as breathable, waterproof, and stain resistant fabrics, have been enabled by the improved control of porosity at the nanoscale and surface roughness in a variety of polymers and inorganics.

2.10.5 Renewable Energy

Perhaps the greatest challenge for society and humankind is how to meet our ever-increasing demand for energy. Although the primary source of energy on earth is derived from the sun, the fundamental steps for energy conversion, such as the transfer of charge, chemical reactions, transformation of molecular structure, and so on, occur at the nanoscale. Development of nanotechnology has the potential to revolutionize the approaches to energy production. Some of the promising new areas for the use of nanotechnology in this field are the use of nanomaterials to extract hydrogen from water, to harvest energy from the sun and biomass, and to store energy as hydrogen fuel cells, batteries, and capacitors. Nanomaterials are also being used as advanced catalysts for energy conversion. Nanomaterials will also impact the processes for efficient utilization of energy for industries such as transportation, power generation and utilization, water management and purification, and environmental cleanup. A number of studies are underway to deploy nanotechnology to meet future energy needs.

2.10.6 Batteries

With the growth in portable electronic equipment (mobile phones, navigation devices, laptop computers, remote sensors), there is great demand for lightweight, high-energy density batteries. Nanocrystalline materials synthesized by sol–gel techniques are candidates for separator plates in batteries because of their foam-like (aerogel) structure, which can hold considerably more energy than conventional ones. Nickel–metal hydride batteries made of nanocrystalline nickel and metal hydrides are envisioned to require less frequent recharging and to last longer because of their large grain boundary (surface) area.

2.10.7 Fuel Additives

Research is underway on the addition of nanoparticulate ceria (cerium oxide) to diesel fuel to improve fuel economy by reducing the degradation of fuel consumption over time.

2.10.8 Fuel Cells

Engineered surfaces are essential in fuel cells, where the external surface properties and the pore structure affect performance. The hydrogen used as the immediate fuel in fuel cells may be generated from hydrocarbons by catalytic reforming, usually in a reactor module associated directly with the fuel cell. The potential use of nanoengineered membranes to intensify these catalytic processes could enable higher-efficiency, small-scale fuel cells. These could act as distributed sources of electrical power. It may eventually be possible to produce hydrogen locally from sources other than hydrocarbons, which are the feed stock of current attention.

2.10.9 Displays

The huge market for large area, high brightness, flat-panel displays, as used in television screens and computer monitors, is driving the development of some nanomaterials. Nanocrystalline zinc selenide, zinc sulfide, cadmium sulfide and lead telluride synthesized by sol–gel techniques (a process for making ceramic and glass materials, involving the transition from a liquid "sol" phase to a solid "gel" phase) are candidates for the next generation of light-emitting phosphors. CNTs are being investigated for low-voltage field-emission displays; their strength, sharpness, conductivity, and inertness make them potentially very efficient and long-lasting emitters.

2.10.10 Catalysts

In general, nanoparticles have a high surface area, and hence provide higher catalytic activity. Nanotechnologies are enabling changes in the degree of

control in the production of nanoparticles, and the support structure on which they reside. It is possible to synthesize metal nanoparticles in solution in the presence of a surfactant to form highly ordered monodisperse films of the catalyst nanoparticles on a surface. This allows more uniformity in the size and chemical structure of the catalyst, which in turn leads to greater catalytic activity and the production of fewer byproducts. It may also be possible to engineer specific or selective activity. These more active and durable catalysts could find early application in cleaning up waste streams. This will be particularly beneficial if it reduces the demand for platinum-group metals, whose use in standard catalytic units is starting to emerge as a problem, given the limited availability of these metals.

2.10.11 Food

Food packaging can be improved by placing antimicrobial agents directly on the surface of the coated nanocomposite film. The incorporation of nanoscale clay particles in a polymer matrix can result in lower oxygen and water permeation with better recyclability. This can protect food from drying and spoilage (incurred by oxygen access). Silver has been used as an antimicrobial agent for centuries. Recently, nanoscale silver has been introduced in antimicrobial containers to keep food fresh for longer.

2.10.12 Consumer Products

Nanotechnology is impacting the field of consumer goods, by providing products with novel functions ranging from easy-to-clean to scratch-resistant coatings. The most prominent application of nanotechnology in household products is self-cleaning or "easy-to-clean" ceramic or glass surfaces. Nanoceramic particles have improved the smoothness and heat resistance of common household equipment such as the flat iron and cooking pans.

2.10.13 Sports

In the field of sports, nanotechnology is promising to enhance the life and performance of sports gadgets. Nanotechnology has been employed to produce tennis balls that last longer, rackets that are stronger and bowling balls that are harder. Nanoski wax is easier to apply and more effective than standard wax. Nanotechnology-enhanced golf balls can correct their own flight path so that they fly straighter than conventional balls.

2.10.14 Lubricants

Nanospheres of inorganic materials could be used as lubricants, in essence by acting as nanosized "ball bearings." The controlled shape is claimed to make them more durable than conventional solid lubricants and wear additives. Whether the increased financial and resource cost of producing them is offset by the longer service life of the lubricants and parts remains to be investigated. It is also claimed that these nanoparticles reduce the friction between metal surfaces, particularly at high normal loads. If so, they should find their first applications in high-performance engines and drivers; this could include the energy as well as the transport sectors. There is a further claim that this type of lubricant is effective even if the metal surfaces are not highly smooth. Again, the benefits of reduced cost and resource input for machining must be compared against the production cost of nanolubricants. In all these applications, the particles would be dispersed in a conventional liquid lubricant; design of the lubricant system must therefore include measures to contain and manage waste.

2.10.15 Carbon Nanotube

CNTs have exceptional mechanical properties, particularly high tensile strength and light weight. An obvious area of application would be in nanotube-reinforced composites, with performance beyond current carbon-fiber composites. One current limitation to the introduction of CNTs in composites is the problem of structuring the tangle of nanotubes in a well-ordered manner so that use can be made of their strength. Another challenge is generating strong bonding between CNTs and the matrix, to give good overall composite performance and retention during wear or erosion of composites. The surfaces of CNTs are smooth and relatively unreactive, and so tend to slip through the matrix when it is stressed. One approach that is being explored to prevent this slippage is the attachment of chemical side-groups to CNTs, effectively to form "anchors." Another limiting factor is the cost of production of CNTs. However, the potential benefits of such light, high-strength material in numerous applications for transportation are such that significant further research is likely.

2.10.16 Nanosensors

Nanosensors exhibit several distinct advantages over their microscale and macroscale counterparts as listed below:

- Reduction in the overall size and weight of the associated system
- Cost reduction
- Mass production

- Utilization of physical phenomena appearing on the nanoscale
- Low power consumption
- Certain applications require nanoscale systems for functional applications, for example, implanted medical sensors must be in the nanoscale
- Enhanced sensitivity
- Higher level of integration.

Nanoscale sensors can be classified depending on the sensing application as physical, chemical, or biological nanosensors. Also, similarly to the classification of sensors, nanoscale sensors can also be classified according to the energy transduced (Table 2.1).

Other than these, nanosensors can also be classified according to:

- Effect/transduction phenomena
- Measurand
- Material of the sensor element
- Technological aspects.

In particular, nanosensors can be classified depending on the nanostructures employed, such as, nanotubes, nanowires, nanoparticles, nanocomposites, quantum dots, embedded nanostructures, and so on. Though many varieties of sensors exist, no single sensor can effectively sense all interested parameters in all possible environments. Therefore, building up of sensor arrays to consolidate multiple properties in different environments is of current interest. Sensor arrays contain different combinations of uni- and multi-functional sensors, to sense multiple phenomena at one time, like the human sensor system with eyes as the optical sensor, nose as the gas sensor, ear as the acoustic sensor and tongue as the liquid chemical sensor.

This increases data acquisition and multiplication and is used in the chemical or biochemical industries, and so on. Nanosensors and nanoenabled sensors have

Table 2.1 Various nanosensors.

Type	Measured property
Mechanical	Size, velocity, acceleration, mass flow, force, torque, pressure, acoustic wave, piezoelectric, strain, stress
Thermal	Temperature, specific heat, entropy, heat flow, flux
Electrical	Voltage, current, resistance, impedance, inductance, capacitance, dielectric constant, polarization, electric field, frequency, dipole moment
Magnetic	Field strength, flux density, magnetic moment, permeability
Optical	Intensity, frequency, phase, wavelength, polarization, reflectance, transmittance, refractive index
Chemical	Composition, concentration, reaction rate, pH, oxidation/reduction potential

applications in many industries such as transportation, communications, building and facilities, medicine, and safety and national security, including both homeland defence and military operations. There are numerous examples of nanowire sensors that are used, for example, to detect chemicals and biologics: nanosensors are placed in blood cells to aid early detection.

2.10.17 Magnetic Materials

It has been shown that magnets made of nanocrystalline yttrium–samarium–cobalt grains possess unusual magnetic properties due to their extremely large grain interface area (high coercivity can be obtained because magnetization flips cannot easily propagate past the grain boundaries). This could lead to applications in motors, and analytical instruments such as magnetic resonance imaging (MRI), used widely in hospitals and microsensors. Overall magnetization, however, is currently limited by the ability to align the grains' direction of magnetization.

2.10.18 Medical Implants

Current medical implants, such as orthopedic implants and heart valves, are made of titanium and stainless steel alloys, primarily because they are biocompatible. Unfortunately, in some cases these metal alloys may wear out within the lifetime of the patient. Nanocrystalline zirconium oxide (zirconia) is hard, wear-resistant, biocorrosion resistant and biocompatible. It therefore presents an attractive alternative material for implants. Alongwith other nanoceramics, nanocrystalline zirconium oxide can also be made as strong, light aerogels by sol–gel techniques. Nanocrystalline silicon carbide is a candidate material for artificial heart valves primarily because of its low weight, high strength, and inertness.

2.10.19 Machinable Ceramics

Ceramics are hard, brittle, and difficult to machine. However, with a reduction in grain size to the nanoscale, ceramic ductility can be increased. Zirconia, normally a hard, brittle ceramic, has even been rendered superplastic (for example, able to be deformed up to 300% of its original length). Nanocrystalline ceramics, such as silicon nitride and silicon carbide, have been used in such automotive applications as high-strength springs, ball bearings and valve lifters, because they can be easily formed and machined, as well as exhibit excellent

chemical and high-temperature properties. They are also used as components in high-temperature furnaces. Nanocrystalline ceramics can be pressed into complex net shapes and sintered at significantly lower temperatures than conventional ceramics.

2.10.20 Elimination of Pollutants

Nanoscale materials can be used effectively in soil/sediment and water remediation. For sites where refractory organic contamination has penetrated deeply into the soil, it would be cost-effective to develop remediation technologies that do not require excavation. The use of zero-valent iron particles has been shown to be effective in penetrating the required distances, as well as oxidizing selected organic contaminants. Research is underway to examine the fate of those iron particles to make sure they do not cause ancillary problems.

2.10.21 Water Purification

Nanoengineered membranes could potentially lead to more energy-efficient water purification processes, notably in desalination by reverse osmosis.

2.10.22 Textiles

There are several applications of nanotechnology in textiles and fabrics, ranging from antimicrobial, hydrophobic, and self-cleaning applications. When the fabric is mixed with a hydrophobic material, it repels water and is also stain resistant. In the monsoon season, for example, drying such clothes will be much easier, and these clothes will be much more comfortable to wear. Nanoparticles have been incorporated into products such as nylon, polypropylene, and other polymers to impart long-term antimicrobial characteristics even under harsh environmental conditions or after extensive thermal cycling. Nanosocks with nanosilver dispersions are odorless and also possess anti-microbial properties. The demand for minimizing or eliminating microbial growth on a variety of textile-based substrates has increased in healthcare, home furnishings, filtration and apparel sectors, among others. Nanocameras mixed with nanodisplays create an "invisibility coating," which is useful for making camouflage clothing for the military. The above are only a few applications of nanomaterials. Many new applications are being discovered every day and many more are yet to be discovered.

2.10.23
Military Battle Suits

Enhanced nanomaterials form the basis of a state of-the-art "battle suit" that is being developed by the Institute of Soldier Nanotechnologies at Massachusetts Institute of Technology, USA. A short-term development is likely to be energy-absorbing materials that will withstand blast waves; longer-term are those that incorporate sensors to detect or respond to chemical and biological weapons (for example, responsive nanopores that "close" upon detection of a biological agent). There is speculation that developments could include materials that monitor physiology while a soldier is still on the battlefield, and uniforms with potential medical applications, such as splints for broken bones.

2.11 Conclusion

The unique properties of nanomaterials are due to the presence of a high concentration of defects. The word "*nano*" refers to a Greek prefix meaning dwarf or something very small. It depicts 1 billionth (10^{-9}) of a unit. Nanomaterials refer to the class of materials with at least one of their dimensions in the nanometric range. They can be metals, ceramics, polymers, or composites. Nanomaterials exhibit uniquely different physical, chemical, and mechanical properties compared to bulk materials. A number of characterizing tools have been developed over the past decades and have helped in understanding the behavior of nanomaterials and nanostructures. Nanostructured materials may occur in several different geometric configurations including wires, tubes, rods, horns, shells, pores, and so on. Over millions of years, a multitude of nanoparticles and devices have been perfected by nature through the process of evolution. Nanotechnology is bound to have an impact due to large-scale applications in industry and household products. Although nanomaterials have been implicated in causing adverse health effects on exposure to different types, conclusive information is not available at present. There is a need to establish regulatory bodies for establishing guidelines and safe limits for ensuring adoption of nanotechnology without

causing environmental damage or ecological imbalance. In order to substantiate their positive potential, nanotechnological methods and products have to be evaluated for advantages in comparison to conventional alternatives. The risks associated with nanotechnology have to be studied. There is an urgent need to identify and assess possible risks for human health and the environment due to nanotechnology. It is envisaged that nanotechnology will lead to tiny robotic devices, using nanoelectronics, sensors, and MEMS for *in vivo* monitoring and diagnosis of deficiencies and malfunctions of human systems. Despite the many promises that nanotechnology proponents have been making about the ability of nanotechnological solutions to solve our pressing environmental problems and provide for a more sustainable production of goods, few solutions have been delivered to date. Many potentially beneficial solutions in the areas of water treatment and environmental remediation/waste treatment are either in the pilot stage or are being tested in the field. Commercialization on a global scale for these may take 5–10 years in the future. Importantly, many of these products or techniques are being developed without due concern for environmental, health, and safety issues. As the field of nanotoxicology is slowly catching up with technological innovation, the worrying signs of human and environmental toxicity concerns are increasing. However, this also provides an opportunity for environmental NGOs to demand a precautionary approach to the large-scale commercialization of these products.

References

1. Ozin, G.A. and Cademartiri, L. (2009) *Nanochemistry: What Is Next?* Small, vol. 5 (11), Wiley-VCH Verlag GmbH, Weinheim, pp. 1240–1244.
2. Mulkens, J., McClay, J.A., Tirri, B.A., Brunotte, M., Mecking, B., and Jasper, H. (2003) *Proc. SPIE*, **5040**, 753.
3. Shenhar, R. and Rotello, V.M. (2003) *Acc. Chem. Res.*, **36**, 549.
4. Radloff, C., Moran, C.E., Jackson, J.B., and Halas, N.J. (2003) in *Molecular Nanoelectronics* (eds M.A. Reed and T. Lee), p. 229.
5. Baibarac, M., Baltog, I., Lefrant, S., Mevellec, J.Y., and Chauvet, O. (2003) *Chem. Mater.*, **15**, 4149.
6. Hoag, H. (2003) *Nature*, **425**, 880.
7. Lednicer, D. and Mitscher, A. (1998) *The Organic Chemistry of Drug Synthesis*, vol. 6, John Wiley & Sons, Inc., New York.
8. Xiong, X., Hanein, Y., Fang, J., Wang, Y., Wang, W., Schwartz, T.D. *et al.* (2003) *J. Microelectromech. Syst.*, **12** (2), 117.
9. Trevethan, T., Watkins, M., Kantorovich, L.N., Shluger, A.L., Polesel-Maris, L., and Gauthier, S. (2006) *Nanotechnology*, **17** (23), 5866.
10. Roco, M.C. (2007) National nanotechnology initiative – past, present and future, in *Handbook on Nanoscience, Engineering and Technology*, 2nd edn, Taylor & Francis.
11. Borm, P.J.A., Robbins, D., Haubold, S., Kuhlbusch, T., Fissan, H., Donaldson, K. *et al.* (2006) *Part. Fibre Toxicol.*, **3**, 11.
12. Mollick, E. (2006) *IEEE Ann. Hist. Comput.*, **28** (3), 62–75. doi: 10.1109/MAHC.2006.4
13. Ferrari, M. (2005) *Nat. Rev. Cancer*, **5**, 161.
14. Lees, E.E., Gunzburg, M.J., Nguyen, T., Howlett, G.J., Rothacker, J., Nice, E.C. *et al.* (2008) *Nano Lett.*, **8** (9), 2883.
15. Yang, J.Y., Yang, M.Q., Arabnia, H.R., and Deng, Y. (2008) *BMC Genomics*, **9**, I1.
16. Salata, O.V. (2004) *J. Nanobiotechnol.*, **2**, 3.

17. Qi, Y., Jafferis, N.T., Lyons, K. Jr., Lee, C.M., Ahmad, H., and McAlpine, M.C. (2010) *Nano Lett.*, **10** (2), 524.
18. Kumar, R. (2008) *Internet J. Neurol.*, **10**, 1.
19. Feynman, R.P. (1960) There is a plenty of room at the bottom. First published in Engineering and Science Magazine, Vol. 5, p. 22.
20. Taniguchi, N. (1974) On the basic concept of "nano-technology". Proceedings of the International Conference on Production Engineering Tokyo, Part II, Japan Society of Precision Engineering, Vol. 18.
21. Drexler, K.E. (1992) *Nanosystems: Molecular Machinery, Manufacturing, and Computation*, John Wiley & Sons, Inc., New York.
22. Richard, J.A.L. (2004) *Soft Machines: Nanotechnology and Life*, Oxford University Press, New York.
23. Nadrian, C. (2004) *Sci. Am.*, **290** (6), 64.
24. Webster, T.J., Waid, M.C., McKenzie, J.L., Price, R.L., and Ejiofor, J.U. (2004) *Nanotechnology*, **15**, 48.
25. Jérome, D., Mazaud, A., and Ribault, M. (1980) *J. Phys. Lett.*, **41**, 95–98.
26. Little, W.A. (1965) *Sci. Am.*, **212**, 21–27.
27. Shukur, M.M., Kadhim, F.A., and Hassan, M.N. (2012) *Res. J. Chem. Sci.*, **2** (2), 28–34.
28. Szasz, A. (1993) *J. Supercond.*, **6** (2), 99–106.
29. Anju, S.G., Jyothi, K.P., Joseph, S., Suguna, Y., and Yesodharan, E.P. (2012) *Res. J. Recent Sci.*, **1** (ISC-2011), 191–201.
30. Senthil Kumar, A.P., Karthikeyan, P., Selvakumar, B., Jagadheeshwaran, M., Dinesh, J., and Kandasamy, S. (2012) *Res. J. Recent Sci.*, **1** (8), 42–47.
31. Fenniri, H. *et al.* (2001) *J. Am. Chem. Soc.*, **123**, 3854.
32. Sheiko, S.S. *et al.* (2006) *Nature*, **440**, 191.
33. Kollman, P.A. (1977) *Chem. Rev.*, **10**, 365.
34. Lehninger, S., Oleyunk, B., and Stang, J.P. (2000) *Chem. Rev.*, **100**, 853.
35. Mak, C., Bampos, N., Darling, S.L., Montali, M., Prodi, L., and Sanders, J.K.M. (2001) *J. Org. Chem.*, **66**, 4476.
36. Klyszez, A., Lauer, M., Kopaczynska, M., Bottcher, C., Gonzaga, F., and Fuhrhop, J.H. (2004) *Chem. Commun.*, 2358.
37. Tamaru, S.I., Nakamura, M., Takeuchi, M., and Shinkai, S. (2001) *Org. Lett.*, **3**, 3631.
38. Ribo, J.M., Crusats, J., Sagues, F., Claret, J., and Rubires, R. (2001) *Science*, **292**, 2063.
39. Schenning, P.H.J., Benneker, F.B.G., Geurts, H.P.M., Liu, X.Y., and Nolte, R.J.M. (1996) *J. Am. Chem. Soc.*, **118**, 8549.
40. Theobald, J.A., Oxtoby, N.S., Phillips, M.A., Champness, N.R., and Beton, P.H. (2003) *Nature*, **424**, 1029.
41. Moriuchi, T., Tamura, T., and Hirao, T. (2002) *J. Am. Chem. Soc.*, **124**, 9356.
42. Keeling, D.L., Oxtoby, N.S., Wilson, C., Humphry, M.J., Champness, N.R., and Beton, P.H. (2003) *Nano Lett.*, **3**, 9.
43. Archer, E.A., Gong, H., and Krische, M.J. (2001) *Tetrahedron*, **57**, 1139.
44. Credi, A., Balzani, V., Langford, S.J., and Stoddart, J.F. (1997) *J. Am. Chem. Soc.*, **119**, 2679.
45. Pina, F., Melo, M.J., Maestri, M., Passaniti, P., and Balzani, V. (2000) *J. Am. Chem. Soc.*, **122**, 4496.
46. Gunnlaugsson, T., MacDónail, D.A., and Parker, D. (2000) *Chem. Commun.*, 93.
47. Dobrawa, R. and Würthner, F. (2002) *Chem. Commun.*, 1878.
48. Imahori, H. and Sakata, Y. (1997) *Adv. Mater.*, **9**, 537.
49. Fukuzumi, S. and Guldi, D.M. (2001) in *Electron Transfer in Chemistry*, vol. 2 (ed. V. Balzani), Weinheim, pp. 270–326.
50. Page, C.C., Moser, C.C., Chen, X., and Dutton, P.L. (1999) *Nature*, **402**, 47.
51. Gust, D., Moore, T.A., and Moore, A.L. (2001) in *Electron Transfer in Chemistry*, vol. 3 (ed. V. Balzani), Weinheim, pp. 272–336.
52. Li, H., Li, Y., Zhai, J., Cui, G., Liu, H., Xiao, S., Liu, Y., Lu, F., Jiang, L., and Zhu, D. (2003) *Chem.—Eur. J.*, **9**, 6031.

53. Lu, F., Xiao, S., Li, Y., Liu, H., Li, H., Zhuang, J., Liu, Y., Wang, N., He, X., Li, X., Gan, L., and Zhu, D. (2004) *Macromolecules*, **37**, 7444.
54. González, J.J., González, S., Priego, E.M., Luo, C., Guldi, D.M., Mendoza, J., and Martin, N. (2001) *Chem. Commun.*, 163.
55. Rispens, M.T., Sánchez, L., Knol, J., and Hummelen, J.C. (2001) *Chem. Commun.*, 161.
56. Shi, Z., Li, Y., Gan, H., Li, M., Xiao, S., Li, H., Liu, H., Xiao, S., and Zhu, D. (2002) *Org. Lett.*, **4**, 1179.
57. Xiao, S., Li, Y., Fang, H., Li, H., Liu, H., Shi, Z., Jiang, L., and Zhu, D. (2002) *Org. Lett.*, **4**, 3063.
58. Ego, C., Marsitzky, D., Becker, S., Zhang, J., Grimsdale, A.C., Müllen, K., Mackenzie, J.D., Silva, C., and Friend, R.H. (2003) *J. Am. Chem. Soc.*, **125**, 437.
59. Peeters, E., Hal, P.A.V., Meskers, S.C.J., Janssen, R.A.J., and Meijer, E.W. (2002) *Chem.—Eur. J.*, **8**, 4470.
60. Gust, D., Moore, T.A., and Moore, A.L. (1993) *Acc. Chem. Res.*, **26**, 198.
61. Liu, Y., Xiao, S., Li, H., Li, Y., Liu, H., Lu, F., Zhuang, J., and Zhu, D. (2004) *J. Phys. Chem. B*, **108**, 6256.
62. Liu, H., Zhao, Q., Li, Y., Liu, Y., Lu, F., Zhuang, J., Wang, S., Jiang, L., Zhu, D., Yu, D., and Chi, L. (2005) *J. Am. Chem. Soc.*, **127**, 1120.
63. Khan, A., Müller, S., and Hecht, S. (2005) *Chem. Commun.*, 584.
64. Dubus, S., Marceau, V., and Leclerc, M. (2002) *Macromoleculee*, **35**, 9296.
65. Gan, H., Liu, H., Li, Y., Zhao, Q., Li, Y., Wang, S., Jiu, T., Wang, N., He, X., Yu, D., and Zhu, D. (2005) *J. Am. Chem. Soc.*, **127**, 12452.
66. Charvet, R., Jiang, D.L., and Aida, T. (2004) *Chem. Commun.*, 2664.
67. Li, Y., Li, X., Li, Y., Liu, H., Wang, S., Gan, H., Li, J., Wang, N., He, X., and Zhu, D. (2006) *Angew. Chem. Int. Ed.*, **45**, 3639.
68. Guilard, R., Senglet, N., Liu, Y.H., Sazou, D., Findsen, E., Faure, D., Des Courieres, T., and Kadish, K.M. (1991) *Inorg. Chem.*, **30**, 1898.
69. Tamaru, S., Takeuchi, M., Sano, M., and Shinkai, S. (2002) *Angew. Chem. Int. Ed.*, **41**, 853.
70. Mateos-Timoneda, M.A., Crego-Calama, M., and Reinhoudt, D.N. (2004) *Chem. Soc. Rev.*, **33**, 363.
71. Jonkheijm, P., Miura, A., Zdanowska, M., Hoeben, F.J.M., De Feyter, S., Schenning, A.P.H.J., De Schryver, F.C., and Meijer, E.W. (2004) *Angew. Chem. Int. Ed.*, **43**, 74.
72. Enomoto, M., Kishimura, A., and Aida, T. (2001) *J. Am. Chem. Soc.*, **123**, 5608.
73. Kaes, C., Hosseini, M.W., Rickard, C.E.F., Skelton, B.W., and White, A.H. (1998) *Angew. Chem. Int. Ed.*, **37**, 920.
74. Xiao, J., Li, Y., Song, Y., Jiang, L., Li, Y., Wang, S., Liu, H., Xu, W., and Zhu, D. (2007) *Tetrahedron Lett.*, **48**, 7599.
75. Leininger, S., Olenyuk, B., and Stang, P.J. (2000) *Chem. Rev.*, **100**, 853.
76. Mamula, O. and Von Zelewsky, A. (2003) *Chem. Rev.*, **242**, 87.
77. He, X., Li, Q., Li, Y., Wang, N., Song, Y., Liu, X., Yuan, M., Xu, W., Liu, H., Wang, S., Shuai, Z., and Zhu, D. (2007) *J. Phys. Chem. B*, **111**, 8063.
78. Fang, M., Zeisberg, W.M., Condon, C., Ogryzko, V., Danchin, A., and Mechold, U. (2009) *Nucleic Acids Res.*, **37**, 5114.
79. Kim, Y.T., Han, J.H., Hong, B.H., and Kwon, Y.U. (2010) *Adv. Mater.*, **22**, 515.
80. Zhang, G. and Wang, D. (2008) *J. Am. Chem. Soc.*, **130**, 5616.
81. Wang, J., Lin, M., Yan, Y., Wang, Z., Ho, P.C., and Loh, K.P. (2009) *J. Am. Chem. Soc.*, **131**, 11300.
82. Gautam, U.K., Vivekchand, S.R.C., Govindaraj, A., Kulkarni, G.U., Selvi, N.R., and Rao, C.N.R. (2005) *J. Am. Chem. Soc.*, **127**, 3658.
83. Lee, J.Y., Hong, B.H., Kim, W.Y., Min, S.K., Kim, Y., Jouravlev, M.V. *et al.* (2009) *Nature*, **460**, 498.
84. Stouwdam, J.W. and Janssen, R.A.J. (2008) *J. Mater. Chem.*, **18**, 1889.
85. Lee, W., Kang, S.H., Kim, J.Y., Kolekar, G.B., Sung, Y.E., and Han, S.H. (2009) *Nanotechnology*, **20**, 335706.
86. Mokerov, V.G., Fedorov, Y.V., Velikovski, L.E., and Scherbakova, M.Y. (2001) *Nanotechnology*, **12**, 552.
87. Ustinov, V.M. *et al.* (2000) *Nanotechnology*, **11**, 397.

88. Nash, M.A., Lai, J.J., Hoffman, A.S., Yager, P., and Stayton, P.S. (2010) *Nano Lett.*, **10**, 85.
89. Li, Z., Lai, X., Wang, H., Mao, D., Xing, C., and Wang, D. (2009) *J. Phys. Chem. C*, **113**, 2792.
90. Ding, J.H. and Gin, D.L. (2000) *Chem. Mater.*, **12**, 22.
91. Yamauchi, Y., Momma, T., Yokoshima, T., Kuroda, K., and Osaka, T. (2005) *J. Mater. Chem.*, **15**, 1987.
92. Palgrave, R.G. and Parkin, I.P. (2006) *J. Am. Chem. Soc.*, **128**, 1587.
93. Zhang, Z., Wei, B.Q., and Ajayan, P.M. (2001) *Appl. Phys. Lett.*, **79**, 4207.
94. Seipenbusch, M. and Binder, A. (2009) *J. Phys. Chem. C*, **113**, 20606.
95. Boyd, D.A., Greengard, L., Brongersma, M., El-Naggar, M.Y., and Goodwin, D.G. (2006) *Nano Lett.*, **6**, 2592.
96. Elihn, K., Landström, L., Alm, O., Boman, M., and Heszler, P. (2007) *J. Appl. Phys.*, **101**, 034311.
97. Domingo, C., Resta, V., Sanchez-Cortes, S., Garcia-Ramos, J.V., and Gonzalo, J. (2007) *J. Phys. Chem. C*, **111**, 8149.
98. Dumitrache, F., Morjan, I., Alexandrescu, R., Ciupina, V., Prodan, G., Voicu, I. *et al.* (2005) *Appl. Surf. Sci.*, **247**, 25.
99. Maskrot, H., Leconte, Y., Herlin-Boime, N., Reynaud, C., Guelou, E., Pinard, L. *et al.* (2006) *Catal. Today*, **116**, 6.
100. Jäger, C., Huisken, F., Mutschke, H., Henning, T., Poppitz, W., and Voicu, I. (2007) *Carbon*, **45**, 2981.
101. Pignon, B., Maskrot, H., Ferreol, V.G., Leconte, Y., Coste, S., Gervais, M. *et al.* (2008) *Eur. J. Inorg. Chem.*, 883.
102. Iijima, S. (1991) *Nature*, **354**, 56.
103. Kuchibhatla, S.V.N.T., Karakoti, A.S., Bera, D., and Seal, S. (2007) *Prog. Mater Sci.*, **52**, 699.
104. Huang, L., Wang, H., Wang, Z., Mitra, A., Zhao, D., and Yan, Y. (2002) *Chem. Mater.*, **14**, 876.
105. Okada, T., Kawashima, K., Nakata, Y., and Ning, X. (2005) *Jpn. J. Appl. Phys.*, **44**, 688.
106. Xia, H., Feng, J., Wang, H., Lai, M.O., and Lu, L. (2010) *J. Power Sources*, **195**, 4410.
107. Li, G.R., Feng, Z.P., Zhong, J.H., Wang, Z.L., and Tong, Y.X. (2010) *Macromolecules*, **43**, 2178.
108. Park, J.M., Nalwa, K.S., Leung, W., Constant, K., Chaudhary, S., and Ho, K.M. (2010) *Nanotechnology*, **21**, 215301.
109. Cao, L.M., Tian, H., Zhang, Z., Zhang, X.Y., Gao, C.X., and Wang, W.K. (2004) *Nanotechnology*, **15**, 139.
110. Yoon, S.M., Hwang, I.C., Kim, K.S., and Choi, H.C. (2009) *Angew. Chem. Int. Ed.*, **48**, 2506.
111. Wang, Y., Lee, J.Y., Kim, J.S., Kim, G.H., and Kim, K.S. (2007) *Chem. Mater.*, **19**, 3912.
112. Wang, Y.W., Hong, B.H., Lee, J.Y., Kim, J.S., Kim, G.H., and Kim, K.S. (2004) *J. Phys. Chem. B*, **108**, 16723.
113. Hong, B.H., Bae, S.C., Lee, C.W., Jeong, S., and Kim, K.S. (2001) *Science*, **294**, 348.
114. Hong, B.H., Lee, J.Y., Lee, C.W., Kim, J.C., Bae, S.C., and Kim, K.S. (2001) *J. Am. Chem. Soc.*, **123**, 10748.
115. Hong, B.H. *et al.* (2005) *Proc. Natl. Acad. Sci. U.S.A.*, **102**, 14155.
116. Hong, B.H., Lee, J.Y., Beetz, T., Zhu, Y., Kim, P., and Kim, K.S. (2005) *J. Am. Chem. Soc.*, **127**, 15336.
117. Hwang, I.C. *et al.* (2010) *J. Phys. Chem. B*, **114**, 7216.
118. Kim, K.S. *et al.* (2002) *J. Am. Chem. Soc.*, **124**, 14268.
119. Kim, W.Y., Choi, Y.C., and Kim, K.S. (2008) *J. Mater. Chem.*, **18**, 4510.
120. Huang, L.M., Wang, H.T., Wang, Z.B., Mitra, A., Bozhilov, K.N., and Yan, Y.S. (2002) *Adv. Mater.*, **14**, 61.
121. Kijima, T., Ikeda, T., Yada, M., and Machida, M. (2002) *Langmuir*, **18**, 6453.
122. Murali, S., Xu, T., Marshall, B.D., Kayatin, M.J., Pizarro, K., Radhakrishnan, V.K. *et al.* (2010) *Langmuir*, **26**, 11176.
123. Kijima, T., Yoshimur, T., Uota, M., Ikeda, T., Fujikawa, D., Mouri, S. *et al.* (2004) *Angew. Chem. Int. Ed.*, **43**, 228.
124. Cheng, F.L., Wang, H., Sun, Z.H., Ning, M.X., Cai, Z.Q., and Zhang, M. (2008) *Electrochem. Commun.*, **10**, 798.
125. Zhang, X.Y., Dong, D.H., Li, D., Williams, T., Wang, H.T., and

Webley, P.A. (2009) *Electrochem. Commun.*, **11**, 190.
126. Baber, S., Zhou, M., Lin, Q.L., Naalla, M., Jia, Q.X., Lu, Y. *et al.* (2010) *Nanotechnology*, **21**, 165603.
127. Zhao, Y.N., Jin, J., and Yang, X.Q. (2007) *Mater. Lett.*, **61**, 384.
128. Sparta, M., Børve, K.J., and Jensen, V.R. (2006) *J. Phys. Chem. B*, **110**, 11711.
129. Tang, Y.H., Pei, L.Z., Lin, L.W., and Li, X.X. (2009) *J. Appl. Phys.*, **105**, 044301.
130. Shim, H.W., Lee, D.K., Cho, I.S., Hong, K.S., and Kim, D.W. (2010) *Nanotechnology*, **21**, 255706.
131. Tang, K., Qian, Y., Zeng, J., and Yang, X. (2003) *Adv. Mater.*, **15**, 448.
132. Wang, W.Z., Poudel, B., Wang, D.Z., and Ren, Z.F. (2005) *Adv. Mater.*, **17**, 2110.
133. Kar, S. and Chaudhuri, S. (2005) *Mater. Lett.*, **59**, 289.
134. Xu, D., Liu, Z.P., Liang, J.B., and Qian, Y.T. (2005) *J. Phys. Chem. B*, **109**, 14344.
135. Sun, C.W., Li, H., Zhang, H.R., Wang, Z.X., and Chen, L.Q. (2005) *Nanotechnology*, **16**, 1454.
136. Nath, M. and Parkinson, B.A. (2006) *Adv. Mater.*, **18**, 1865.
137. Zhou, Z. and Deng, Y. (2009) *J. Phys. Chem. C*, **113**, 19853.
138. Chaudhuri, M.G., Dey, R., Mitra, M.K., Das, G.C., and Mukherjee, S. (2008) *Sci. Technol. Adv. Mater.*, **9**, 015002.
139. Bitenc, M., Drazic, G., and Orel, Z.C. (2010) *Cryst. Growth Des.*, **10**, 830.
140. Schmitt, A.L., Zhu, L., Schmeisser, D., Himpsel, F.J., and Jin, S. (2006) *J. Phys. Chem. B*, **110**, 18142.
141. Guo, J.Z., Zuo, Y., Li, Z.J., Gao, W.D., and Zhang, J.L. (2007) *Physica E*, **39**, 262.
142. Kamins, T.I., Li, X., and Williams, R.S. (2004) *Nano Lett.*, **4**, 503.
143. Shimizu, T., Zhang, Z., Shingubara, S., Senz, S., and Gosele, U. (2009) *Nano Lett.*, **9**, 1523.
144. Qi, P.F., Wong, W.S., Zhao, H.Z., and Wang, D.W. (2008) *Appl. Phys. Lett.*, **93**, 163101.
145. Takami, S., Hayakawa, R., Wakayama, Y., and Chikyow, T. (2010) *Nanotechnology*, **21**, 134009.
146. Bondi, S.N., Lackey, W.J., Johnson, R.W., Wang, X., and Wang, Z.L. (2006) *Carbon*, **44**, 1393.
147. Duan, X.F. and Lieber, C.M. (2000) *Adv. Mater.*, **12**, 298.
148. Liu, Z., Styers-Barnett, D.J., Puretzky, A.A., Rouleau, C.M., Yuan, D., Ivanov, I.N. *et al.* (2008) *Appl. Phys. A*, **93**, 987.
149. Bachmatiuk, A., Borowiak-Palen, E., Rummeli, M.H., Kramberger, C., Hubers, H.W., Gemming, T. *et al.* (2007) *Nanotechnology*, **18**, 275610.
150. Longtin, R., Fauteux, C., Goduguchinta, R., and Pegna, J. (2007) *Thin Solid Films*, **515**, 2958.
151. Morjan, I. *et al.* (2008) *Infrared Phys. Technol.*, **51**, 186.
152. Jun, J.W., Seo, J.W., Oh, S.J., and Cheon, J. (2005) *Coord. Chem. Rev.*, **249**, 1766.
153. Kim, K.S. *et al.* (2009) *Nature*, **457**, 706.
154. Bae, S. *et al.* (2010) *Nat. Nanotechnol.*, **5**, 574.
155. Nayak, B.B., Behera, D., and Mishra, B.K. (2010) *J. Am. Ceram. Soc.*, **93**, 3080.
156. Mann, A.K.P. and Skrabalak, S.E. (2011) *Chem. Mater.*, **23**, 1017.
157. Siril, P.F., Ramos, L., Beaunier, P., Archirel, P., Etcheberry, A., and Remita, H. (2009) *Chem. Mater.*, **21**, 5170.
158. Vizireanu, S., Stoica, S.D., Luculescu, C., Nistor, L.C., Mitu, B., and Dinescu, G. (2010) *Plasma Sources Sci. Technol.*, **19**, 034016.
159. Jung, S.H., Oh, E., Lee, K.H., Yang, Y., Park, C.G., Park, W. *et al.* (2008) *Cryst. Growth Des.*, **8**, 265.
160. Tiwari, J.N., Pan, F.M., Tiwari, R.N., and Nandi, S.K. (2008) *Chem. Commun.*, 6516.
161. Dong, X., Ji, X., Jing, J., Li, M., Li, J., and Yang, W. (2010) *J. Phys. Chem. C*, **114**, 2070.
162. Chen, S. and Carroll, D.L. (2002) *Nano Lett.*, **2**, 1003.
163. Kawasaki, H., Uota, M., Yoshimura, T., Fujikawa, D., Sakai, G., Annaka, M. *et al.* (2005) *Langmuir*, **21**, 11468.
164. Sakai, G. *et al.* (2007) *Adv. Mater.*, **19**, 237.
165. Kijima, T. *et al.* (2009) *Adv. Funct. Mater.*, **19**, 545.

166. Wang, L., Chen, X., Zhan, J., Sui, Z.M., Zhao, J.K., and Sun, Z.W. (2004) *Chem. Lett.*, **33**, 720.

167. Wang, L., Chen, X., Zhan, J., Chai, Y., Yang, C., Xu, L. *et al.* (2005) *J. Phys. Chem. B*, **109**, 3189.

168. Eliaz, N. and Sridhar, T.M. (2008) *Cryst. Growth Des.*, **8**, 3965.

169. Liu, D.W. *et al.* (2009) *Adv. Funct. Mater.*, **19**, 1015.

170. He, W., Gao, P., Chu, L., Yin, L., and Xie, Y. (2006) *Nanotechnology*, **17**, 3512.

171. Chu, D., Masuda, Y., Ohji, T., and Kato, K. (2010) *Langmuir*, **26**, 14814.

172. Jiang, C.L., Zhang, W.Q., Liu, Y.K., and Qian, Y.T. (2006) *Cryst. Growth Des.*, **6**, 2603.

173. Cheng, F., Zhao, J., Song, W., Li, C., Ma, H., Chen, J. *et al.* (2006) *Inorg. Chem.*, **45**, 2038.

174. Cheng, J.P., Ma, R., Shi, D., Liu, F., and Zhang, X.B. (2011) *Ultrason. Sonochem.* doi: 10.1016/j.ultsonch.2010.12.00

175. Wang, G., Ji, Y., Zhang, L., Zhu, Y., Gouma, P.I., and Dudley, M. (2007) *Chem. Mater.*, **19**, 979.

176. Azimirad, R., Khosravi, P., and Moshfegh, A.Z. (2011) *Surf. Interface Anal.* doi: 10.1002/sia.373

177. Barreca, D., Ferrucci, A.P., Gasparotto, A., Maccato, C., Maragno, C., and Tondello, E. (2007) *Chem. Vap. Deposition*, **13**, 618.

178. Gao, R., Yin, L., Wang, C., Qi, Y., Lun, N., Zhang, L. *et al.* (2009) *J. Phys. Chem. C*, **113**, 15160.

179. Guan, Y.F. and Pedraza, A.J. (2008) *Nanotechnology*, **19**, 045609.

180. Bond, P.J. (2004) *Speech on Challenges to Nanotechnology Development and Commercialization, Delivered to the National Nanotechnology Initiative 2004*, Department of Commerce, Washington, DC.

181. Arnall, A.H. (2003) *Future Technologies, Today's Choices – Nanotechnology, Artificial Intelligence and Robotics; A Technical, Political and Institutional Map of Emerging Technologies*, Greenpeace Environmental Trust, London.

182. Cygnus Business Consultancy and Research (2006) *Emerging Technologies in India*, Cygnus Business Consultancy and Research.

183. Baltes, H., Brand, O., Fedder, G.K., Hierold, C., Korvink, J.G., and Tabata, O. (2005) *Enabling Technologies for MEMS and Nanodevices*, Wiley-VCH Verlag GmbH, Weinheim.

184. Barlow, M. (2007) *Blue Covenant – The Global Water Crisis and the Coming Battle for the Right to Water*, Black Inc., Melbourne.

185. Hillie, T. *et al.* (2007) *Nanotechnology, Water and Development*.

186. Salamanca-Buentello, F. *et al.* (2005) *PLoS Med.*, **2** (5).

187. Ortego, J. (2008) *Nanotechnology: Energizing the Future*. Nanofrontiers Newsletter Fall 2008, Project on Emerging Nanotechnologies, Washington, DC.

3
Carbon Nanotubes and Their Nanocomposites

Sónia Simões, Filomena Viana, and Manuel F. Vieira

3.1
Carbon Nanotubes

3.1.1
Introduction

Carbon nanotubes (CNTs) have generated a great deal of interest, ever since they were observed by Iijima [1] in 1991, due to their unique mechanical, thermal, and physical properties. CNTs consist of tubes formed by rolled sheets of graphene (one atomic layer of graphite). The tubes are arranged in a concentric manner to form single-walled carbon nanotubes (SWCNTs), double-walled carbon nanotubes (DWCNTs), and multi-walled carbon nanotubes (MWCNTs). The atomic arrangement of these tubes, as well as, the number of walls, diameter, length, and density of defects, has a significant impact on CNT properties.

Several processing methods have been reported for the synthesis of CNTs. Depending on the processing method, it is possible to obtain CNTs of better or worse quality, with greater or less density of impurities and defects. However, the process with the most potential to produce high quality CNTs is also the least economically attractive. The key challenges in the synthesis of CNTs are selecting the specific type of CNTs that have to be produced, producing CNTs with fewer defects and impurities and the ability to control the final structure and alignment of CNTs. The perfect technique would be the one that is capable of large-scale production of a single type of CNTs, semiconducting or metallic, preferably with the same chirality and with fewer defects, at low cost.

CNTs are excellent candidates for use in various applications: as biological and chemical sensors, as probe tips for scanning probe microscopy, in nanoelectromechanical systems (NEMSs), and as reinforcement in nanocomposites [2, 3]. The use of CNTs in the area of nanocomposites has been widely explored in recent years. Nevertheless, the full potential of CNTs is compromised due to the poor interfacial interaction with most matrices. Another interesting factor in the field of nanocomposites is the possibility of controlling the length and alignment of the CNTs during production.

Nanomaterials and Nanocomposites: Zero- to Three-Dimensional Materials and Their Composites,
First Edition. Edited by Visakh P.M. and Maria José Martínez Morlanes.

The hydrophobicity and chemical inertness of CNTs frequently hinders their application. Therefore, the graphene sheets that form the CNTs' surfaces are often modified to tailor some of their properties, such as dispersion. Several techniques have been suggested: for example, the incorporation of elements such as oxygen, fluorine, or nitrogen into the exterior walls. The dispersion of CNTs can also be changed without modifying their structure, by the adsorption of surfactants, polymers, or biological molecules. Mechanical dispersion techniques, such as sonication or mechanical mixing, are other techniques suitable for promoting the dispersion of CNTs.

The successful production of nanocomposites reinforced with CNTs depends on the development of processes that promote a dense and uniform dispersion of CNTs, undamaged and well bonded to the matrices, so that the load transfer is effective. These are the essentials factors for obtaining the expected strengthening of nanocomposites.

This chapter will briefly present the structure and properties of CNTs, the principal methods for CNT synthesis and the techniques for surface functionalization of CNTs. The incorporation of CNTs into various types of matrices, the main advantages of this reinforcement, the production processes of these nanocomposites, the microstructural and mechanical characterizations, and the interfacial interaction between the CNT and the matrix will also be explored in this chapter.

3.1.2 Structure of Carbon Nanotubes

CNTs consist of rolled graphene sheets arranged in a concentric mode and are classified according to the number of walls. Figure 3.1 shows schematic illustrations of different types of CNTs. CNTs that consist of only one tube are called SWCNTs, while those with multiple concentric tubes, with interlayer spacing close to the interlayer distance of graphite (0.34 nm), are known as MWCNTs.

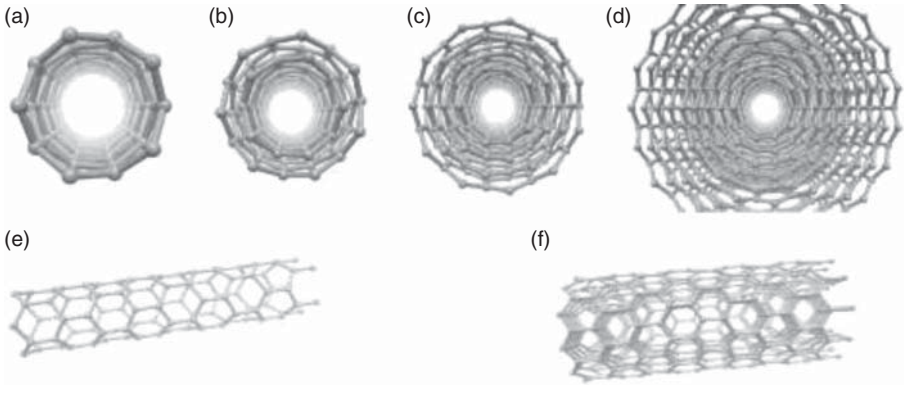

Figure 3.1 Schematic illustrations of carbon nanotubes: (a) SWCNT, (b) DWCNT, (c) FWCNT with four walls, (d) MWCNT with nine walls, (e) SWCNT, and (f) MWCNT.

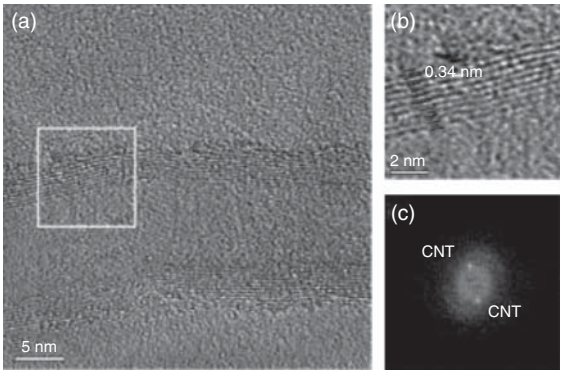

Figure 3.2 (a) HRTEM of a MWCNT, (b) high magnification of area identified in (a) showing 10 walls, and (c) the fast Fourier transform (FFT) revealing the CNT spots.

Recently, other types of CNTs have been reported, including the few-wall carbon nanotubes (FWCNTs) and DWCNTs, which are distinguished by their unusual properties and improved structural integrity. DWCNTs consist of two concentric tubes synthesized with a higher degree of purity [2–4].

Figure 3.2 shows a high resolution transmission electron microscopy (HRTEM) image of an MWCNT. This CNT is characterized by 10 walls that are confirmed in the high magnification image in Figure 3.2b. The spots on the fast Fourier transform (FFT) of Figure 3.2c confirm the spacing of 0.34 nm of the CNT walls.

The properties of the nanotubes are closely related to the number of walls, diameter, and length, but in particular to the way the graphene sheets are rolled, that is, the chirality. The structure of the SWCNTs can be defined through a vector C (chiral vector), which is represented by the integers (n,m) that correspond to graphene vectors $\vec{a}$ and $\vec{b}$. The (n,m) indices determine the diameter and chirality of the CNTs. As shown in Figure 3.3, the nanotubes can be divided into zigzag, armchair, and chiral types for $m = 0$, $n = m$, or $n \neq$ m respectively. Schematic diagrams of armchair (10,10), chiral (10,5), and zigzag (10,0) SWCNTs can be seen in Figure 3.4. In the case of the CNTs with more tubes, the inner tube may be of a different type from the rest. The chirality of the CNT will define its semiconducting or metallic character; for example, a CNT (3,3) is metallic, while a (5,1) is a semiconductor [2,4].

The nanotubes can range in length from a few nanometers to several micrometers, and in outer diameter from about 2.5 to 30 nm.

The production of individual CNTs is quite difficult and depends on which production method is adopted. The most common problems observed in the case of SWCNTs consist in the fact that, in order to minimize energy through the interaction of van der Waals, they usually agglomerate and form bundles (Figure 3.5) and in the case of MWCNTs, they are usually produced in tangles due to their length and to minimize energy. Figure 3.6a shows a scanning electron microscopy (SEM) image of an agglomerate of MWCNTs without any dispersion treatment. The length of the nanotubes is between a few hundred nanometers

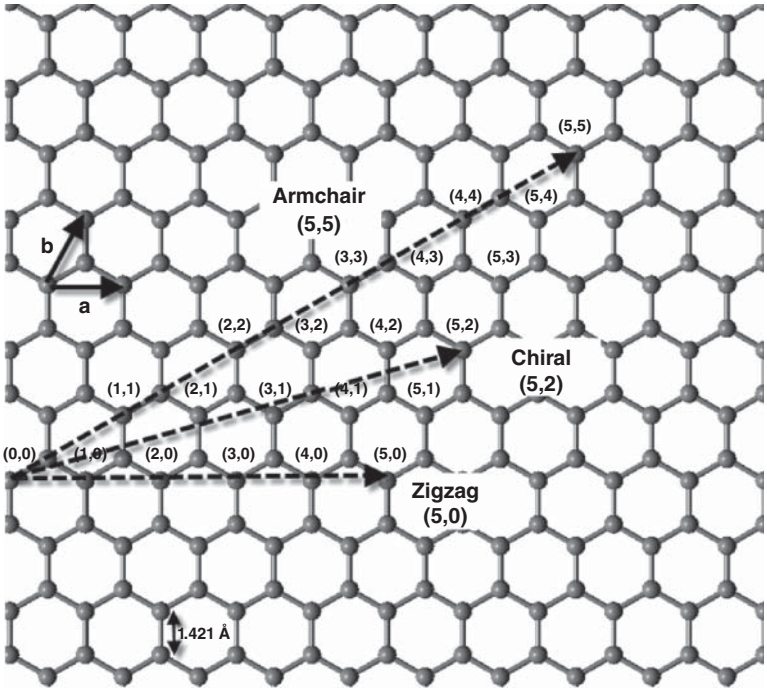

Figure 3.3 Schematic drawing of a sheet of graphene with representation of the chiral vector integers (*n*,*m*) for the construction of different SWCNTs types.

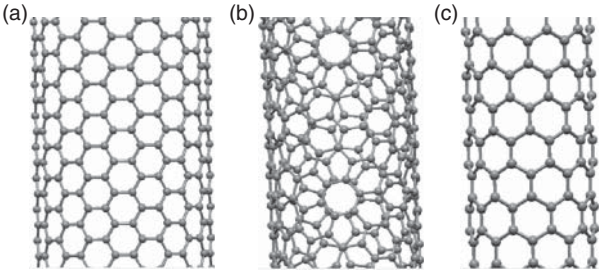

Figure 3.4 Schematic diagrams of SWCNTs with different chiral vectors: (a) armchair (10,10), (b) chiral (10,5), and (c) zigzag (10,0) structures.

and a few micrometers. Due to their length they become entangled. In general, the SWCNTs are defect-free, whereas MWCNTs present defects. The main defects observed include CNTs capped and bent, and particularly in MWCNTs, bamboo structures. A bamboo structure can be viewed as several short-capped nanotubes aligned and assembled. An HRTEM image of an MWCNT with a bamboo structure can be seen in Figure 3.6b. Generally, the CNTs are synthesized with closed ends [2, 3].

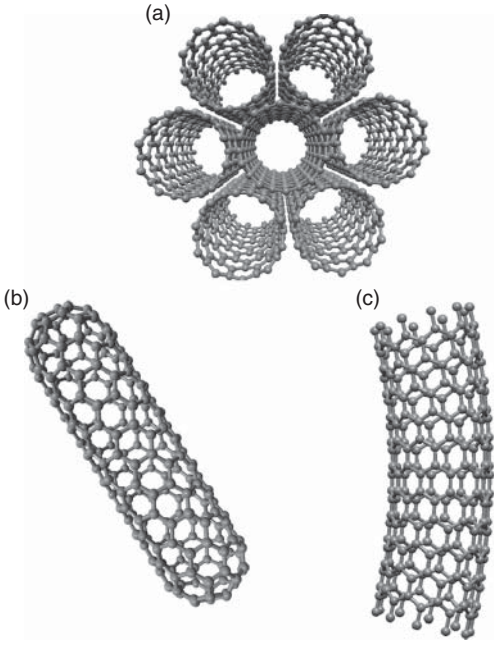

Figure 3.5 Schematic diagrams of different SWCNTs showing defects: (a) bundle of SWCNTs with a structure of (10,0), (b) capped SWCNT with a structure of (10,0), and (c) a SWCNT bend 30° with a structure (10,0).

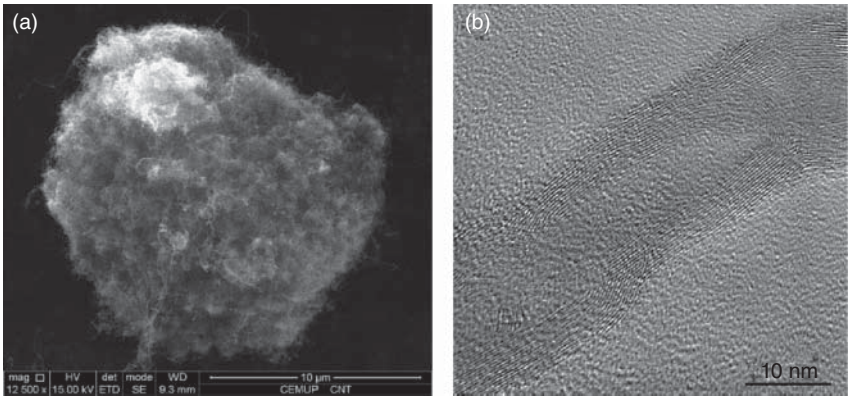

Figure 3.6 (a) SEM image of an MWCNT agglomerate and (b) HRTEM image of an MWCNT with a bamboo structure.

3.1.3
Properties of Carbon Nanotubes

An individual graphene sheet has high strength (130 GPa) and high electrical and thermal conductivities [2–5]. Due to these remarkable properties, it is

expected that since the CNTs consist of rolled graphene sheets, they will also exhibit extraordinary properties. CNTs have generated a great deal of interest in recent years [5–24], due to their unique mechanical, thermal, and physical properties, such as high stiffness, high strength, and high thermal conductivity combined with low weight. The high mechanical properties are related to the sp^2 carbon–carbon bonds.

Due to their nanometric size, the technical difficulties in the manipulation of CNTs make the determination of their properties difficult, when compared to other materials, and therefore, conventional tests cannot be applied. To characterize these properties, it is necessary to combine the results from experimental and simulation studies. Another important aspect to consider is that the properties are very dependent on the type of tube, number of walls, and defects. The literature refers to the results obtained from several tests in transmission electron microscopy (TEM) and atomic force microscopy (AFM). The theoretical results indicate a value of Young's modulus in the range of 0.5–5 TPa [8] for an individual CNT, while experiments performed by Yu *et al.* [9] on TEM equipment reveal Young's modulus of 1.8 and 1.25 TPa for MWCNT and SWCNT, respectively. However, different values are reported by other authors, depending not only on the test method used but also on the CNTs' synthesis process, number of walls, defects, and type of tube, as mentioned previously. MWCNTs produced by arc discharge revealed a higher modulus (1.8 TPa) [10] than those produced by chemical vapor deposition (CVD) (0.35 TPa) [11], which may be explained by the increased number of defects in the CNTs produced by CVD. The thickness and number of walls of CNTs also have a strong impact on Young's modulus, since DWCNTs present a modulus of 1 TPa, which is close to the value of the graphene sheets, while for thicker CNTs this value is reduced to 100 GPa [12]. The decrease in Young's modulus in line with the increase in the number of walls, and consequently in the thickness of the nanotubes, was confirmed by molecular dynamics simulations performed by Liew *et al.* [13].

The elastic response of CNTs to deformation is also extraordinary. Yu *et al.* [9] observed a breaking strain between 3 and 12%, and a tensile strength range from 11 to 63 GPa while simulation results from the experiments of other authors, such as Liew *et al.* [13], measured a higher tensile strength, 150 GPa, and a maximum strain of 28% for an individual SWCNT.

As with mechanical properties, the determination of other properties is also difficult, as different values are measured for a given property depending on the type of CNTs. This is observed, for example, with the determination of conductivities. For MWCNTs, conductivities between 2×10^7 and 8×10^5 S m^{-1} [14, 15] were measured. These values are also influenced by the type of tube, a value of 5×10^7 S m^{-1} [16] being measured for SWCNTs. Films of aligned nanotubes are quite good conductors, with some anisotropy in transport properties for different alignment configurations. The resistivity in the direction perpendicular to the nanotube axis is approximately 10–15 times than that in the parallel direction. Magneto resistance shows that the major contribution to the bulk resistivity of the films comes from intertube contacts [17].

Concerning the thermal conductivity at room temperature, for SWCNTs the measured value varied from 2000 to 10 000 $W\,m^{-1}K^{-1}$ [18, 19] while for MWCNTs the maximum observed value was 3000 $W\,m^{-1}K^{-1}$ [20].

The unique electronic properties of CNTs are a result of the confinement of electrons normal to the nanotube axis, that is, electrons cannot propagate in a parallel to the long axis of the tube, but only along the nanotube axis. CNTs are able to form a perfect spin-transport medium, since electron transport in these is one dimensional and ballistic, with long spin-relaxation time and weak spin-orbital effects. Because of the symmetry and unique electronic structure of graphene, the structure of SWCNTs determines their electrical properties [15, 16].

Due to these properties, the CNTs are good candidates as nanomaterial for a wide range of applications, such as structural materials, electronic devices, conductive components and thermal conductors, biological and chemical sensors, probe tips for scanning probe microscopy, NEMSs, and reinforcement in nanocomposites [2, 3].

3.2
Carbon Nanotubes as Nanomaterials

3.2.1
Synthesis of Carbon Nanotubes

As already mentioned, CNTs can have different structures and properties, which are conditioned by a structure that is influenced by the production method and further processing technologies. A wide variety of processes for the synthesis of CNTs have been developed, though arc discharge, laser ablation, and CVD are those that present the greatest advantages in the production of CNTs. However, there are some drawbacks in this field that need to be overcome. In particular, mass production needs to be made more economically attractive, CNTs need to be of better quality, and there needs to be more effective control over the final structure and alignment of CNTs as well as a better understanding of the mechanism of their growth.

The arc discharge method was the first to be used to produce SWCNTs and MWCNTs. The equipment is quite simple and consists of two electrode graphite rods (cathode and anode) in a chamber with a gas atmosphere (Figure 3.7a). An electric potential difference is applied to the electrodes and a stable arc is achieved. The positive electrode (anode) is consumed and the CNTs are deposited in the cathode. The main factors to be taken into account in this method are the gas atmosphere, pressure, electric current, and efficiency of the cooling system (of the electrodes and the chamber). For the production of MWCNTs, several authors studied the influence of different atmospheres on the morphology of CNTs [25–29]. Wang *et al.* [25] investigated different CH_4 gas pressures and observed the formation of thick nanotubes with high gas pressures and thin and long MWCNTs with a pressure of 6.667×10^3 Pa. Shimotani *et al.* [29] demonstrated that organic atmospheres (ethanol, acetone, and hexane) promote a higher production of CNTs when compared to that obtained using a He

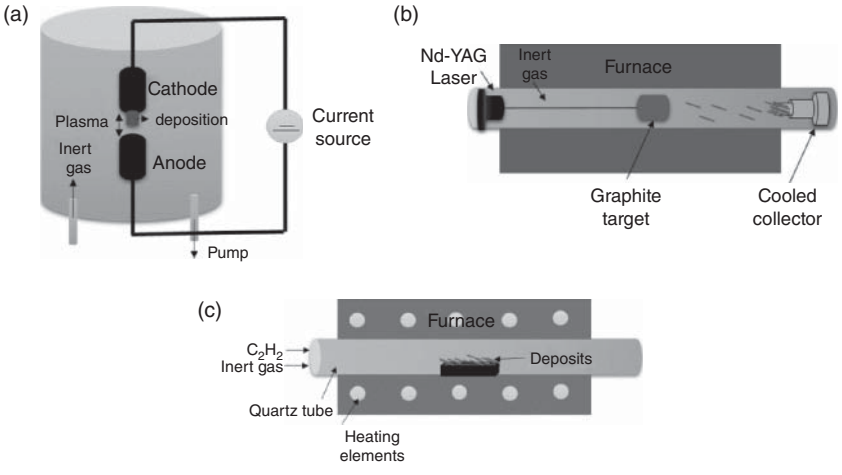

Figure 3.7 Schematic illustrations of (a) arc discharge, (b) laser ablation, and (c) CVD apparatus for CNTs production.

atmosphere, due to the ionization of the organic molecules that contribute to the synthesis of MWCNTs.

In the case of SWCNTs, the production could be obtained with or without catalyst precursors, nickel being the most widely used. The metal catalyst plays a significant role in the process yield. In this process, unwanted products such as MWCNTs or fullerenes are usually produced as well. Several works [30–36] reported the possibility of using different metal catalysts to produce SWCNTs. Recently, new approaches to the production of SWCNTs by means of the arc discharge method have been investigated. Chen *et al.* [36] produced SWCNTs with high crystallinity by using a hydrogen DC arc discharge with a carbon anode containing a 1% Fe catalyst in an atmosphere of H_2 – Ar.

When aiming to produce double-walled nanotubes, the main objective is to eliminate defects, which renders the process more difficult to control.

The large-scale production of SWCNTs was first reported through laser ablation. This method of synthesis involves filling a quartz tube with an inert atmosphere, the target being vaporized at 1200 °C by a laser pulse and deposited in a cooled collector (Figure 3.7b). The main parameters that influence the properties of CNTs are the laser properties, such as power and wavelength, the structural and chemical composition of the target, the chamber pressure, temperature and the chemical composition of the atmospheric gas, the material of the substrate, and the distance to the target.

The main disadvantages of these two methods consist in the production of the entangled CNTs, the large amount of energy consumed during production, and the inability to obtain ordered structures.

CVD is a method that allows large-scale and good-quality production of SWCNTs and MWCNTs along with the possibility of obtaining aligned CNTs. The synthesis technology consists in the reaction of the metal catalyst particles

with the gas (C_xH_x) in a quartz tube filled with an inert atmosphere at temperatures ranging from 500 to 1200 °C (Figure 3.7c). The CNTs grow in the substrate with the metal particles working as nucleation sites. Growth of the CNTs can occur by two different ways [37]; when the catalyst particles stay at the tips of the CNTs during growth when it is referred to as the *tip growth mode*, and when the particles remain at the nanotube base when it is called the *base growth mode*. The most frequently used catalysts are Fe, Co, or Ni [38], and common substrates are Ni, Si, SiO_2, Cu, stainless steel, and glass [39, 40]. Large quantities of high quality CNTs with few impurities can be synthesized by this method.

Recently, several approaches based on the CVD process have been developed in order to improve CNT quality and achieve better control of the entire production process. Seah *et al.* [41] recently wrote a review paper on the production of aligned CNTs by CVD processes. According to these authors, the double step methods, which add the coating of the substrate to the catalyst and CVD of CNTs, provide more control over morphology. An interesting feature of this method is the possibility of controlling the diameter of the nanotube through the catalyst particle size.

CNT production does not end following the synthesis process, unlike CVD or arc discharge. In some cases, a purification step is crucial as a further processing method. The purification process aims to separate the CNTs and the impurities, such as amorphous carbon, nanoparticles, or raw materials. This purification can be performed by dry or wet processes or a combination of both [42].

The use of CNTs following production without any changes or additional procedures is very difficult or rare, mainly because the van der Waals forces and the large surface area lead to the formation of bundles or agglomerates instead of individual CNTs. This issue is very critical, especially when CNTs are to be used as reinforcing material in a nanocomposite or have to be incorporated into a component. As expected, the properties of CNTs are compromised when they are in bundles. To overcome this problem, the options may include dispersion techniques or modifications of the CNTs, or a combination of both processes, in order to reduce the energy of van der Waals forces, thereby reducing the tendency to agglomerate. However, dispersion is not the only important factor, the stabilization of the dispersion being equally essential. Many processes are effective in dispersing the CNTs, but these do not address the need for stable dispersion. It is essential to find a compromise between these two factors. Therefore, it is usual to choose modification methods in combination with mechanical dispersion techniques to increase the stability of the dispersion.

The mechanical dispersion methods commonly used to disentangle CNTs are ball milling and ultrasonication.

The ultrasonication method involves the dispersion of the CNTs in liquid by ultrasound energy. It is a very efficient method for obtaining untangled CNTs in liquids such as water, acetone, ethanol, or acids. The efficiency of this dispersion technology depends on the liquid, energy, time, and type of CNTs, an important factor being the time required for dispersion, since a very long time leads to their damage. In Figure 3.8, it is possible to observe the influence of ultrasonication

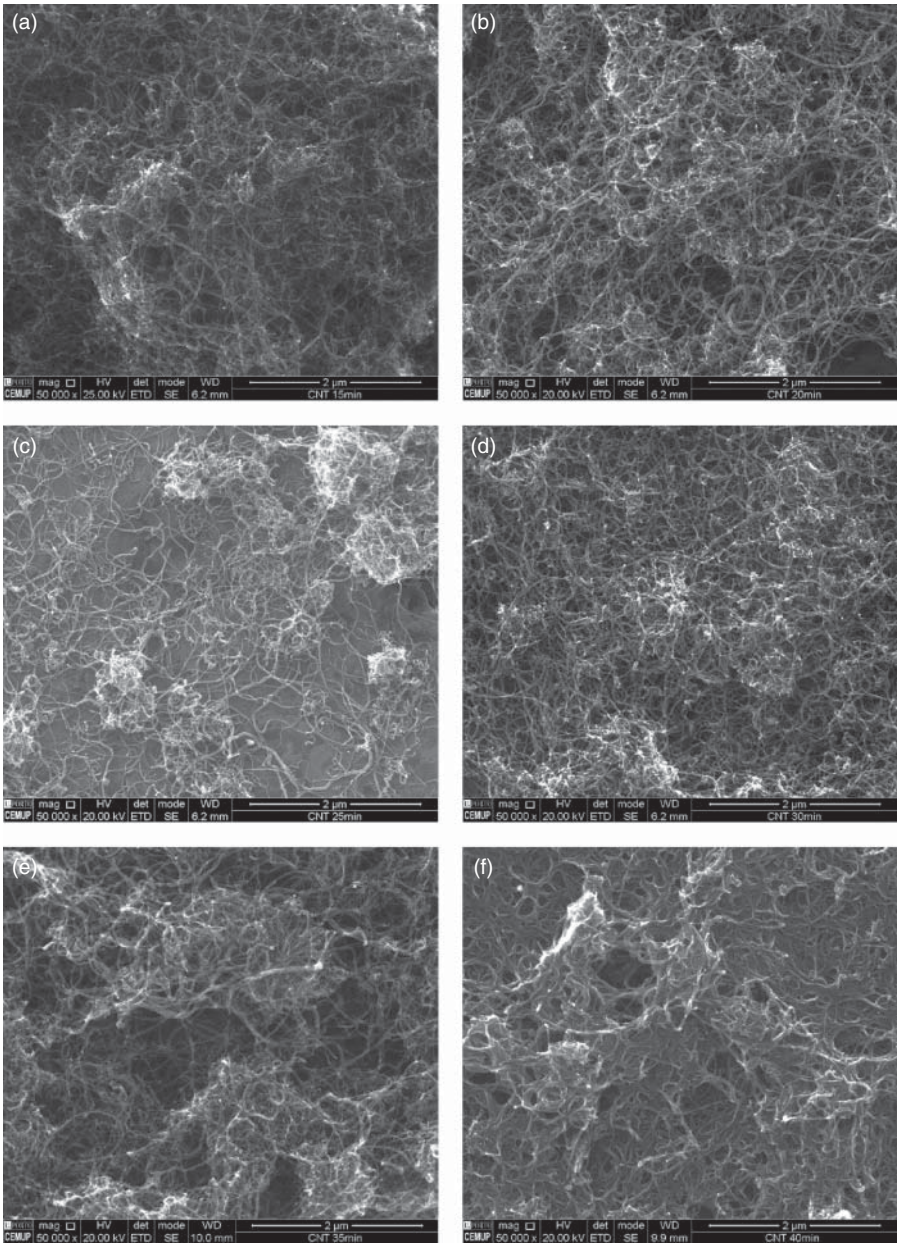

Figure 3.8 SEM images of CNTs dispersed by ultrasonication during (a) 15 min, (b) 20 min, (c) 25 min, (d) 30 min, (e) 35 min, and (f) 40 min.

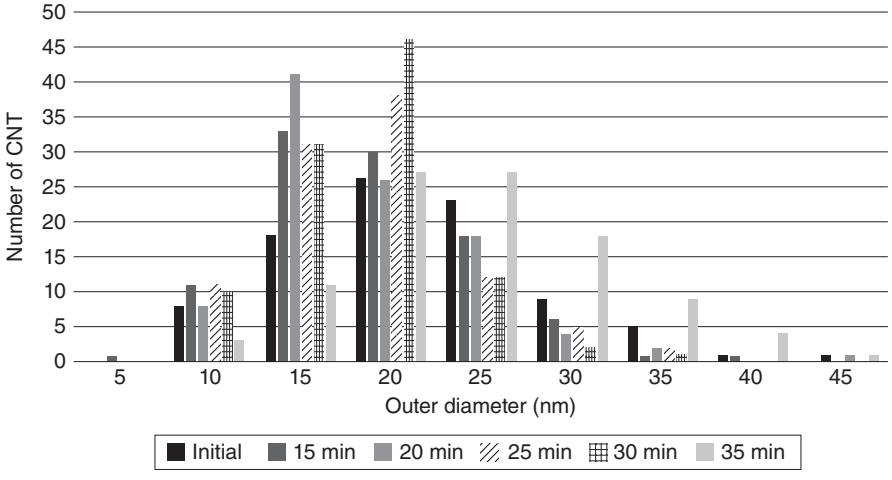

Figure 3.9 The distributions of outer diameters of CNTs, in the as-received condition and after dispersion from 15 to 35 min.

time on their morphology. By increasing the time to 25 min, the dispersion of the nanotubes is improved, but if longer lengths of time are involved, the tubes are destroyed and bind, which is most evident at 35 and 40 min. Figure 3.9 shows the evolution of the outer diameters of MWCNTs with ultrasonication time. It is clear that this treatment causes an increase in the number of small-diameter nanotubes for 15, 20, and 25 min of ultrasonication, resulting in lower average diameters. These results point to the occurrence of an exfoliation process during ultrasonication. For longer times of 30 and 35 min, the number of large-diameter nanotubes is increased, which can be explained by the damage and junction of the nanotubes.

In the ball milling method, a great amount of energy is involved, since the methods involve milling by the collision of dense, rigid balls. Due to this high-energy milling, CNTs' damage occurs, with consequent degradation of properties. Often, this method is a good way of reducing the length of the nanotubes when low energy and shorter time lengths are involved [43].

Another common problem is the production of nanotubes with different chirality, resulting in the need for functionalization in order to separate them.

The CNTs' modification treatments can be a means of solving problems of purification, selection, and dispersion, and can be classified as physical or chemical modification treatments depending on the interaction between the active molecules and the carbon atoms on the CNT surface. In Figure 3.10, a schematic illustration of the principal chemical and physical CNTs' modifications can be observed. Several modification methodologies are reported, all having one thing in common: highly reactive chemical species, which are necessary in order to attack the CNTs, destroying C–C bonds and incorporating new elements. The next section describes the concepts of chemical and physical modifications of CNTs.

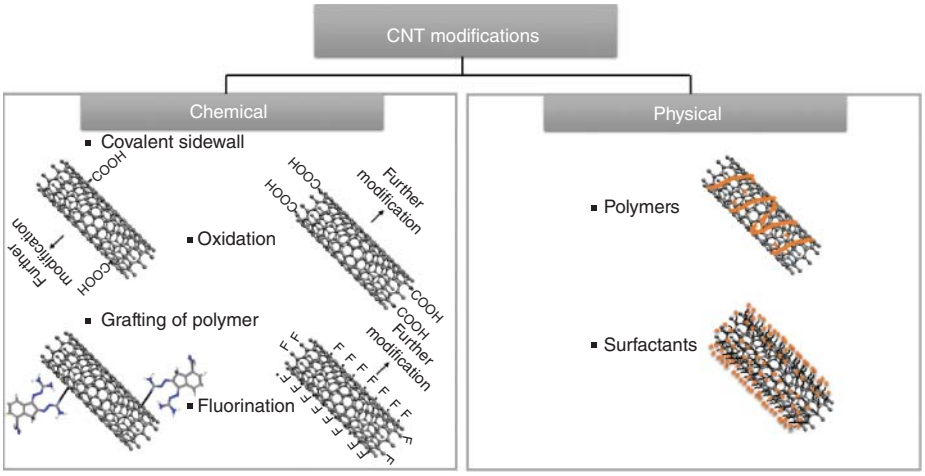

Figure 3.10 Schematic illustration of the principal chemical and physical modifications of CNTs.

3.2.2
Chemical Modifications of Carbon Nanotubes

Chemical modifications are based on the covalent bond between functional groups and CNTs' carbon atoms at the end of the tubes or at their sidewalls. The bonding of functional groups to carbon atoms can occur in a direct mode that is associated with a change of hybridization from sp^2 to sp^3 or in areas with defects, the latter being beneficial, since chemical transformations occur at sites with pre-existing defects.

CNTs possess surfaces of high chemical stability, with the result that few atoms and molecules can interact directly with their walls. The most common way to nucleate bonding sites on CNT walls is through oxidation treatments by concentrated nitric or sulfuric acids. The oxidation treatment creates defect sites (holes in the sidewalls or openings of the tube caps) in CNTs and incorporates carboxylic groups and other oxygen-bearing groups. The stability of this treatment is related not only to the type of CNTs but also to their diameters. However, such an oxidation method usually reduces the electrical conductivity and corrosion resistance of CNTs due to the introduction of a large number of defects. The presence of carboxyl groups leads to a reduction of the van der Waals interaction that facilitates the separation of CNTs [44, 45]. This process of modification through oxidation and the attachment of functional groups can render the nanotubes soluble in aqueous or organic solvents, thus enlarging the number of processing routes.

SEM images in Figure 3.11 reveal that acid treatments destroy the agglomerates by shortening and thinning the nanotubes, while promoting the formation of joints. This treatment was responsible for a reduction from 19 ± 7 to 17 ± 6 nm in the CNTs' average outer diameter as the result of an exfoliation process.

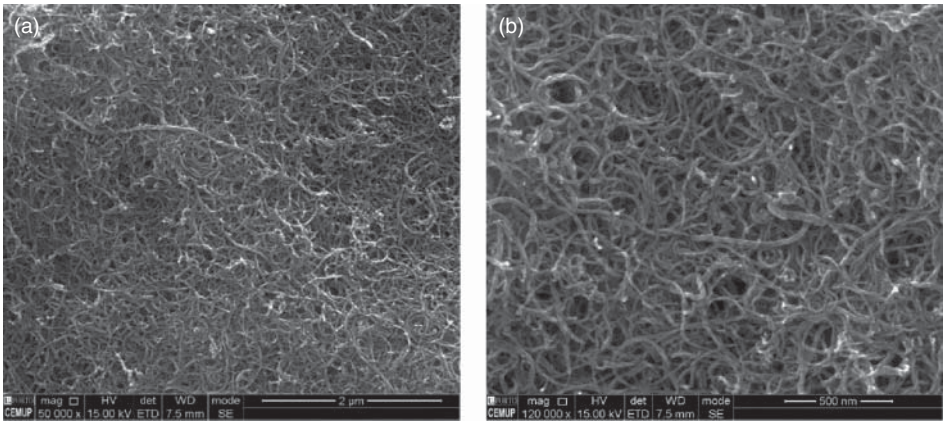

Figure 3.11 SEM images of CNTs modified by oxidation treatments in concentrated nitric and sulfuric acids.

Other types of chemical modifications can occur at CNTs' sidewalls and involve the functionalization by active species (atoms, radicals, carbenes, or nitrenes) [46, 47]. Fluorination is another route that is used to produce tubes that can be further modified to attach polymers. In this case, the fluorine is added most commonly via a high-temperature reaction with fluorine gas [48]. Another route involves grafting polymer molecules on to the surface of CNTs in the presence of active functional groups (–COOH, $–NH_2$, –OH) [49].

Although chemical functionalization has been one of the most preferred methods for the application of CNTs, the treatment conditions (strong acids, longer ultrasonication time, temperature) during functionalization lead to CNT damage, which diminishes electrical conductivity.

3.2.3
Physical Modifications of Carbon Nanotubes

The physical modification of CNTs consists in a noncovalent functionalization by surfactants or polymers. In this type of interaction the absorption of these molecules occurs by means of van der Waals forces at CNTs' sidewalls, at the wrapping of the polymer around the CNTs or the storing of the molecules in their inner cavity. The main advantage of this modification consists in the preservation of the properties of the CNTs, although the force between them and the molecules is weak.

The surfactants are widely used to improve the dispersion of CNTs in an aqueous solution. An efficient coating of the CNTs by surfactants induces a repulsive force that counteracts the attractive van der Waals forces between them. The balance between repulsive and attractive forces creates a thermodynamic equilibrium, which regulates their dispersion and aggregation. The surfactant can be nonionic, ionic, anionic, or cationic according to the corresponding head groups.

The selection of the surfactant type depends on the other aqueous phases; for example, to disperse CNTs in water the use of ionic surfactants is preferable, while for organic solvents nonionic surfactants are preferred [47, 50]. The surfactants most studied are polyoxyethylene octyl phenyl ether (Triton X-series) [51, 52], sodium dodecyl sulfate (SDS) [53, 54], dodecyl trimethyl ammonium bromide (DTAB) [55], and hexadecyl trimethyl ammonium bromide (CTAB) [56].

The adsorption of the surfactant can occur by means of different interactions; for example, Bai *et al.* [51] demonstrated that the Triton X-series surfactants were adsorbed on the CNT's surface by hydrophobic and $\pi-\pi$ interactions. Treatment with a nonionic surfactant improved the formation of CNTs suspensions in water. Composites produced with CNTs modified by these surfactants revealed an improvement in mechanical properties. However, deterioration in electrical conductivity was also observed [56].

Recent studies show that better results can be obtained when this modification technique is combined with ultrasonication. The ultrasonication process is essential for creating the separation of the initially entangled CNTs. The spaces and gaps formed by this process were coated by the surfactants, leading to the separation of the fully coated CNTs – Figure 3.12. Matarredona *et al.* [57] studied the interaction of an anionic surfactant sodium dodecyl benzene sulfonate (SDBS) and SWCNT. The authors observed that the hydrophobic interaction overcomes the Coulomb forces and determines the structure of the surfactant-stabilized CNTs. A monolayer of surfactant molecules was created, oriented vertically on the surface. Sonication proved to be an essential step in separating and obtaining a stable dispersion. This treatment is also important when other surfactants such as SDBS are used [58].

In Figures 3.13 and 3.14, SEM images of CNTs modified with CTAB and SDS surfactants are presented. The average outer diameter of the nanotubes is 21.7 ± 7.9 and 20.8 ± 7.1 nm, respectively. The CNTs agglomerates observed in the low magnification images attest the low dispersion efficiency of ultrasonication

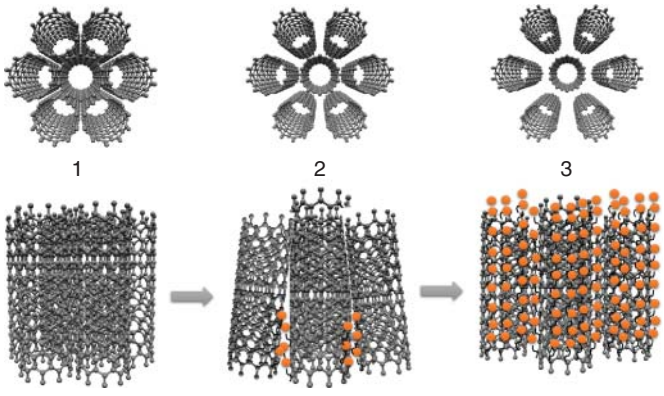

Figure 3.12 Schematic illustration of the combined effect of the sonication treatment with surfactants.

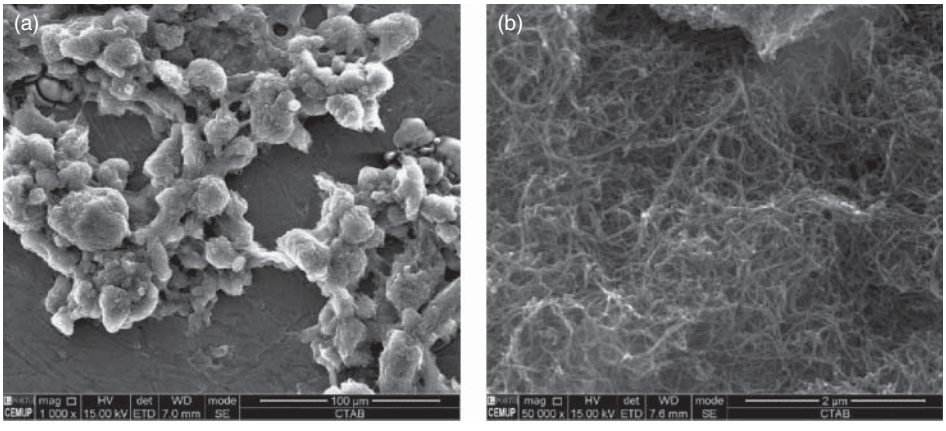

Figure 3.13 SEM images showing the morphology of the CNTs after modification by CTAB.

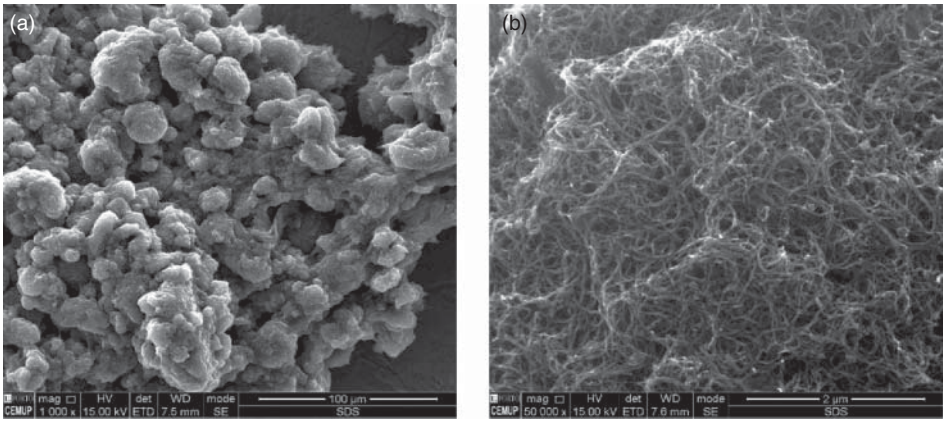

Figure 3.14 SEM images showing the morphology of the CNTs modified by SDS.

combined with physical modification by CTAB and SDS. However, if the nanotubes are treated in acid prior to the physical modification with CTAB, there is a more effective dispersion, as observed in Figure 3.15.

3.3 Carbon Nanotubes Based Nanocomposites

Composites are materials comprising two or more materials with different properties, whose combination exceeds the sum of the properties of its components. Composites consist of a bulk material (the "matrix") and a reinforcement material, added to increase the strength and stiffness of the matrix as well as its electrical conductivity, desirable thermal expansion coefficient and good damping and wear properties, among others [59, 60]. The use of CNTs as a reinforcement has

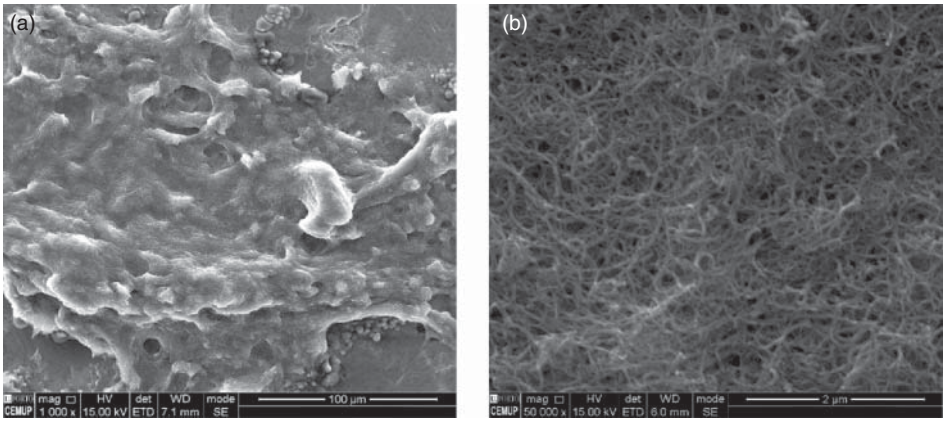

Figure 3.15 SEM images showing the morphology of the CNTs modified by acid treatment followed by physical modification by CTAB.

generated a great deal of interest in recent years [61–75]. Their unique mechanical and physical properties, combined with their low weight, make CNTs an ideal reinforcement material. The CNTs' nanometric dimensions justify the classification of these materials as nanocomposites. The interest in the application of CNTs as reinforcements is related to their potential to produce composites with mechanical properties superior to those obtained by other types of reinforcement material. The successful development of a production process that promotes a uniform dispersion of CNTs in the matrix without CNT damage, with high CNT density and effective load transfer between CNTs and the matrix is essential for obtaining the expected strengthening of the nanocomposites. In addition to the matrix, the reinforcement properties and the uniform dispersion, the interfacial interaction of the reinforcement and matrix also plays an important role in the strengthening of the nanocomposite. An excellent example of this effect is the mechanical behavior of nanotube-filled polymer composite. A noninteracting interface is responsible for weak regions that impair the expected enhancement in mechanical properties.

Production technology is also a crucial factor in this field. The technique should be simple and economical, and should lead to the production of a nanocomposite-free from or with only a small number of defects with a dense and uniform dispersion of CNTs throughout the matrix.

The application of CNTs as reinforcement is very important in any kind of matrix, but is more widely used in polymer matrix composites. The conventional polymer matrix composites exhibit a wide range of application fields due to such properties as low density, reasonable strength, flexibility, and easy processability. However, the search for materials capable of improving the performance of advanced components has triggered the study and production of CNTs-reinforced nanocomposites.

For the production of these nanocomposites, the modification of the CNTs' surfaces is essential, in order to enable their incorporation into the polymer

matrix. Dispersion treatments are crucial to the nanocomposite properties; CNTs agglomerates, bundles, or tangles are defects that lessen the performance of these materials. By contrast, the alignment of the nanotubes in the matrix can enhance the performance of the nanocomposites. The properties of the nanocomposites obtained are significantly influenced by the type and morphology of the CNTs, the modification treatment, the nature of polymer matrices, and the synthesis process. The synthesis processes most commonly used are melting mixing, *in situ* polymerization and solution mixing [59, 61].

CNTs/epoxy nanocomposites have been extensively investigated due to their industrial and technological applications. These nanocomposites are fabricated using melt mixing or solution mixing methods. Zhou *et al.* [62] demonstrated that it is possible to improve the strength and fracture toughness with the incorporation of 0.3 wt% CNTs in the epoxy matrix. Velasco-Santos *et al.* [63] studied the CNTs/Polymethyl methacrylate nanocomposites and observed an increase in the storage modulus of 1135% for composites, with 1 wt% of CNTs dispersed using an *in situ* polymerization at 90 °C.

The works published in the area of CNTs-reinforced nanocomposites are mainly of polymer matrix nanocomposites, due to the ease and low cost of the manufacturing processes. Moreover, these processes involve high pressures and low temperatures that reduce the risk of damage to the CNTs. However, the numbers of works on metal or ceramic matrix nanocomposites have been increasing in recent years, with the development of processing technologies.

Ceramic matrices reinforced with CNTs can provide nanocomposites with, high strength, improved fracture toughness, and higher electrical and thermal conductivities, while metallic matrices reinforced with CNTs are expected to produce nanocomposites of high strength and specific stiffness, which is a desirable coefficient of thermal expansion and good damping properties [60].

In the majority of cases reported, the ceramic matrix nanocomposites reinforced with CNTs were produced by a conventional powder sintering route (mixing, pressing, and sintering). Other technologies, for example, spark plasma sintering (SPS), can be one means of obtaining a nanocomposite with higher densification. However, the mechanical properties are still much lower than expected, and hence more research in dispersion and production techniques is needed [60, 64]. Yamamoto and Hashida [64] developed a new technique to obtain a more homogeneous dispersion of CNTs and improve the bonding to the alumina matrix. This treatment involved the use of a precursor method for the synthesis of an alumina matrix, MWCNTs modified by a covalent functionalization (by a concentrate H_2SO_4 and HNO_3 acid mixture), and the SPS method. By means of this technique the authors observed an improvement in bending strength and fracture toughness.

Several techniques have been suggested as being suitable for the production of metal matrix nanocomposites reinforced with CNTs: thermal spray forming, fusion processing techniques, conventional powder metallurgy, severe plastic deformation, friction stir processing, and electrochemical deposition. Nevertheless, sintering followed by deformation processes, or hot deformation

processes alone, appears to be the most promising techniques [65–75]. The main disadvantage of these processing technologies is the elevated temperature normally necessary for most metals; this high temperature can damage the CNTs or can lead to a reaction between them and the matrix. The stresses imposed by some processes can also damage the CNTs or even align them in the matrix.

The majority of studies on metal matrix composites are those constituted by matrices of Ni, Cu, and Al.

A few studies have revealed that conventional sintering methods can be used to produce CNTs/Al and CNTs/Cu nanocomposites [65, 66]. However, for the composite CNTs/Cu, the high sintering temperature required to achieve a composite with a high density can lead to the damage of the CNTs; other techniques are more suitable for the production of this type of nanocomposite. Pérez-Bustamante *et al.* [65] investigated nanocomposites of MWCNTs/Al produced by uniaxial pressing at 950 MPa followed by conventional sintering at 550 °C for 3 h. Mechanical milling in a high-energy shaker mill in an inert atmosphere mixed the CNTs and Al powders. TEM images of these nanocomposites showed some amorphization due to the milling process. The formation of Al_4C_3 carbide by the reaction of the nanotubes with the Al matrix, usually reported in these nanocomposites, was not detected. The authors found an increase in the hardness of the nanocomposite relative to Al. It was also verified that the use of pressure during the sintering can be one means of obtaining denser composites.

SPS to obtain denser composites also applies to the production of CNTs/Al, CNTs/Ni, and CNTs/Cu. In this process, grain growth is inhibited, often resulting in the mechanical properties obtained being higher than those achieved by conventional sintering. Nguyen *et al.* [67] showed that it is possible to produce ultrafine-grained MWCNTs/Ni composites by SPS with 97% density. The authors used modified CNTs by noncovalent functionalization to improve the cohesion between the CNT and Ni powders. The composites revealed a higher value of hardness than the Ni.

To improve the reinforcement effect of the CNTs in the metal matrix and the density of the nanocomposites, some studies that combine sintering and deformation processes have been conducted by other authors [68, 70]. Kuzumaki *et al.* [68] were the first to fabricate CNTs/Al nanocomposites by adopting hot pressing and hot extrusion processes with 5 and 10 vol% CNTs. Due to the nonuniform dispersion of the CNTs, the tensile strength was similar to the bulk Al. George *et al.* [69] produced nanocomposites with MWCNTs and SWCNTs by sintering at 580 °C for 45 min. followed by hot extrusion at 560 °C. The CNTs were dispersed in ethanol by sonication for 20 min and mixed with Al powders through ball milling at 200 rpm for 5 min. The nanocomposites have shown a tensile strength of 134 and 141 MPa with 0.5% of MWCNTs and SWCNTs, respectively. The strengthening mechanisms were not identified. Kim *et al.* [70] investigated the fabrication of CNTs/Cu by SPS of high-energy ball-milled nanosized Cu powders with MWCNTs followed by cold rolling process. The microstructure of the CNTs/Cu nanocomposite showed clusters of CNTs.

Other authors suggest that production should be carried out only by hot deformation processes. Esawi *et al.* [71, 72] produced Al-2 wt% CNTs nanocomposites using rolling or extrusion processes and obtained a 100% or 50% increase in the tensile strength, respectively. The mixing was performed using high-energy ball milling for 30 min at 400 rpm. The formation of the carbide Al_4C_3 was observed. The authors also observed structural damage of CNTs due to the ball milling process. Kwon and Leparoux [73] obtained a higher strength for CNTs/Al nanocomposites produced by mechanical ball milling followed by a direct powder hot extrusion process. The nanocomposites with 1 vol% of CNTs exhibited a tensile strength that was three times greater than that of Al. These authors detected a small quantity of nanometric Al_4C_3. The increases in mechanical properties of the CNTs-reinforced nanocomposites are more effective when hot deformation processes such as extrusion, rolling, or pressing are used. Quang *et al.* [74, 75] demonstrate that it is possible to produce CNTs/Cu by equal channel angular pressing (ECAE) in cold conditions. By means of this process, the dispersion of the CNTs and the density of the composites are improved with increasing number of extrusion passes. However, the damage or fracture of CNTs during the ECAE is a crucial factor that needs to be characterized.

Despite the scientific and technological advances that have resulted from these studies, there are still some challenges that need to be overcome in the production of these nanocomposites. The dispersion of CNTs in the metal matrix is the greatest one. It is necessary to develop new techniques to obtain a better dispersion of larger amounts of CNTs in the matrix, without damaging them. Most studies have used the ball milling process, which apparently permits a good dispersion among the metal powders but causes damage to the CNTs. Recently, some studies have reported new improved dispersion methods [76, 77]. For example, Jiang *et al.* [76] used a flake powder metallurgy to achieve a uniform distribution of CNTs, while Noguchi *et al.* [77] developed a new mixing method called *nanoscale dispersion*, which disperses the CNTs with a metal powder using natural rubber as a mixing medium. The results have shown that these processes improve the dispersion while causing minor structural damage to the CNTs, thus increasing its mechanical properties of the nanocomposite.

The increase in mechanical properties by CNTs reinforcement is very promising, but the implementation of these nanocomposites on an industrial scale is only possible if they are produced by simple and cost-effective technology, if possible by using conventional procedures. The development of new dispersion technologies that enable the application of conventional powder metallurgical routes (mixing, pressing, and sintering) to the production of composites with higher mechanical properties is essential.

One possibility consists in the junction of the dispersion and the mixture of CNTs and metallic powders in a single step, by ultrasonication in isopropanol. Figure 3.16 shows the SEM images of CNTs/Al nanocomposites produced in a dispersion/mixing single step, followed by uniaxial pressing with 300 MPa and sintering at 640 °C for 90 min in a vertical furnace under a vacuum of 10^{-2} Pa.

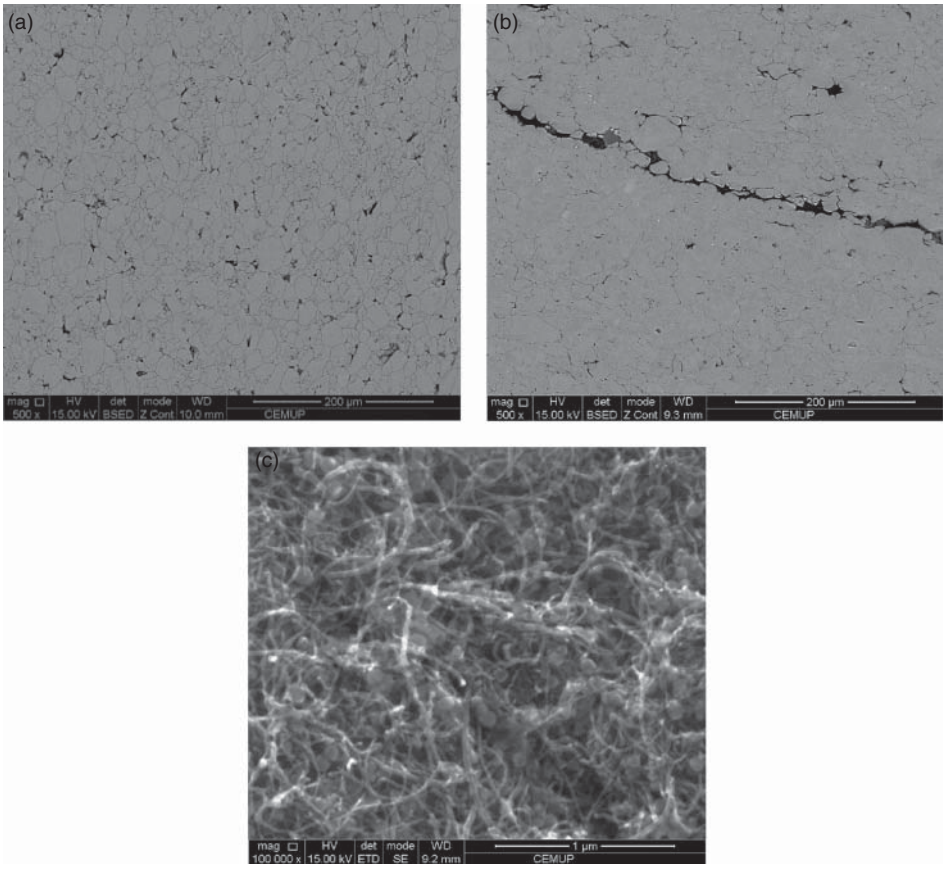

Figure 3.16 SEM images of CNTs/Al nanocomposites: (a) 0.75% of CNTs, (b) 1.0% of CNTs, and (c) high magnification of a CNT cluster of CNTs/Al nanocomposite.

The concentration of CNTs has a major influence on their dispersion in the Al matrix; composites with high concentrations show several clusters of CNTs as a result of poor dispersion. The nanocomposites produced with 0.75% reveal a microstructure with the well-dispersed CNTs through the Al matrix.

In TEM and HRTEM images, it is possible to identify individual CNTs dispersed inside the grains of aluminum (Figure 3.17a,b) of the 0.75 wt% of CNTs nanocomposites.

The strengthening effect of CNTs on these nanocomposites was evaluated by microhardness and tensile tests, the results of which are presented in Table 3.1. By observing these, it is possible to note that the hardness increases with CNT concentrations of up to 0.75 wt%, decreasing for higher concentrations.

In fact, this reduction was expected, since, as observed in the SEM images, the nanocomposite Al–1.0% CNTs showed a poorer dispersion than those with lower concentration of CNTs. The highest hardness value of 50 ± 2 HV0.01 was determined in nanocomposites with 0.75 wt% CNTs. This 50% increase relative

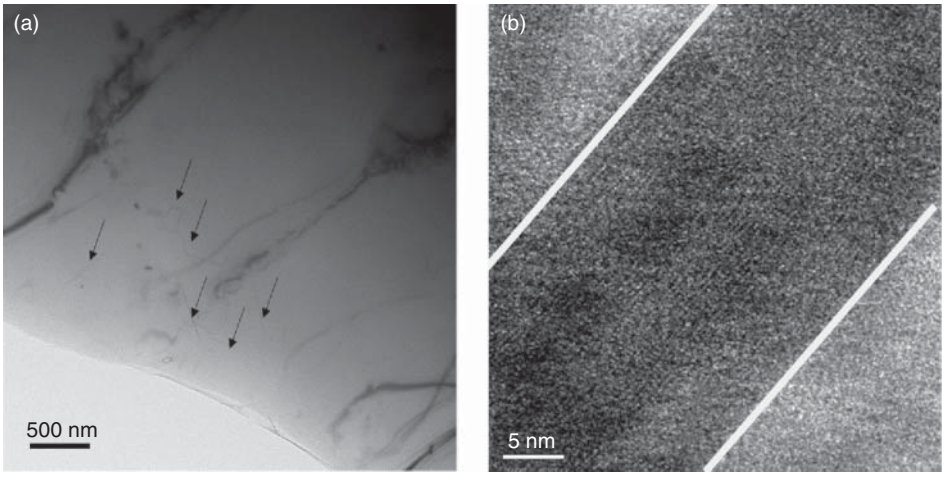

Figure 3.17 (a) TEM and (b) HRTEM images image of CNTs/Al nanocomposites with 0.75% of CNTs showing the CNTs embedded in the aluminum grains.

Table 3.1 Hardness value and tensile properties of pure aluminum and CNTs/Al nanocomposites.

Material	Hardness (HV0.01)	Tensile strength (MPa)	Elongation (%)
Al	34	66	27.6
Al–0.25 CNTs	43	—	—
Al–0.5 CNTs	44	—	—
Al–0.75 CNTs	50	196	3.4
Al–1.0 CNTs	43	—	—
Al–2.0 CNTs	39	—	—

to the hardness of the Al attests the strengthening effect of the CNTs. The efficiency of the dispersion technique developed was confirmed by the results of the tensile tests. The nanocomposite produced with 0.75 wt% of CNTs exhibits a 200% increase in tensile strength relative to the Al. This increase is slightly higher than the maximum increase reported in the literature, 150% for 1.0 wt% of CNTs in nanocomposites produced by hot extrusion [73]. Therefore, through this new dispersion treatment it is possible to increase the mechanical properties of the nanocomposites produced by conventional powder metallurgy production processes.

These mechanical properties are strongly influenced by microstructural features such as grain size and texture. To confirm the effect of CNTs, these microstructural characteristics have been evaluated with and without the incorporation of the reinforcement. The grain size distribution of the nanocomposites with different concentrations of CNTs and pure aluminum is presented in Figure 3.18. The average grain size of nanocomposites does not vary significantly with the

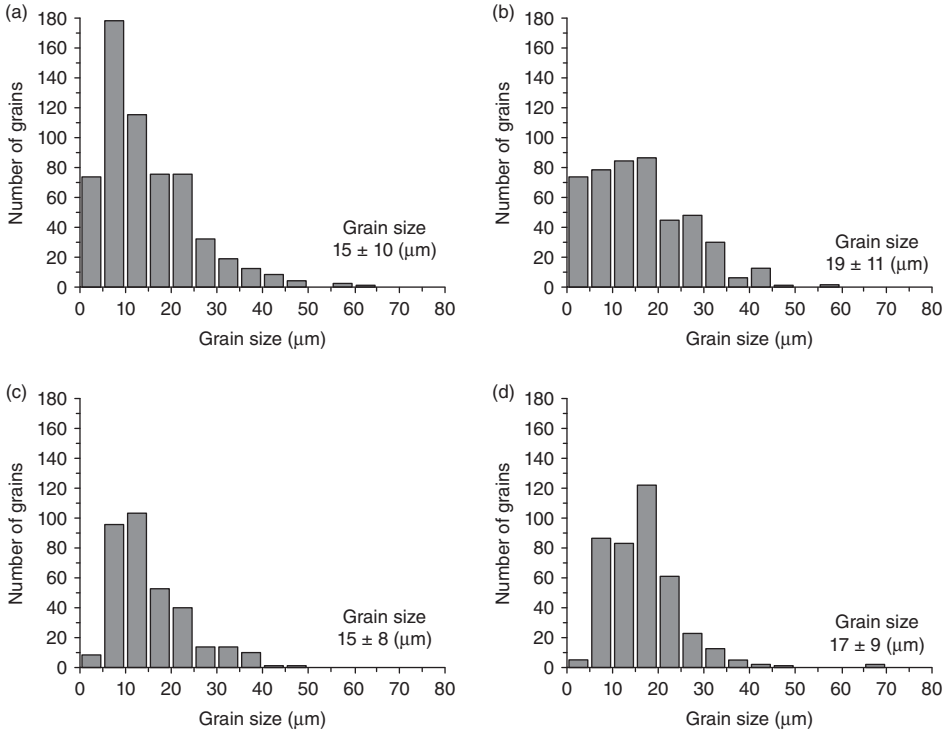

Figure 3.18 Grain size distribution of (a) aluminum and of nanocomposites with (b) 0.5% of CNTs, (c) 0.75% of CNTs, and (d) 1.0% of CNTs.

incorporation of CNTs and is close to that of pure aluminum produced under the same conditions.

The texture of the nanocomposites was evaluated by electron backscatter diffraction (EBSD). The EBSD maps, inverse pole, and pole figures for Al and CNTs/Al nanocomposites with 0.75% CNTs are presented in Figure 3.19. The colors of the EBSD maps indicate the crystallographic orientation of each grain. In the presence of materials with texture, these maps show predominant colors, the results showing that neither the pure aluminum nor the nanocomposite present texture. The hardening effect is only related to the incorporation of the CNTs and not to the alteration of other microstructural features.

3.3.1
Interfacial Interaction of Carbon Nanotubes in Nanocomposites

The interfacial interaction of CNTs with the matrix in nanocomposites is fundamental for effective reinforcement. For all types of matrices, this is a key factor for the successful production of nanocomposites. Interfacial bonding of the embedded CNTs to the matrix is essential for load transferring and reinforcement phenomena. The atomic structure of CNTs consisting of sp^2 hybridized

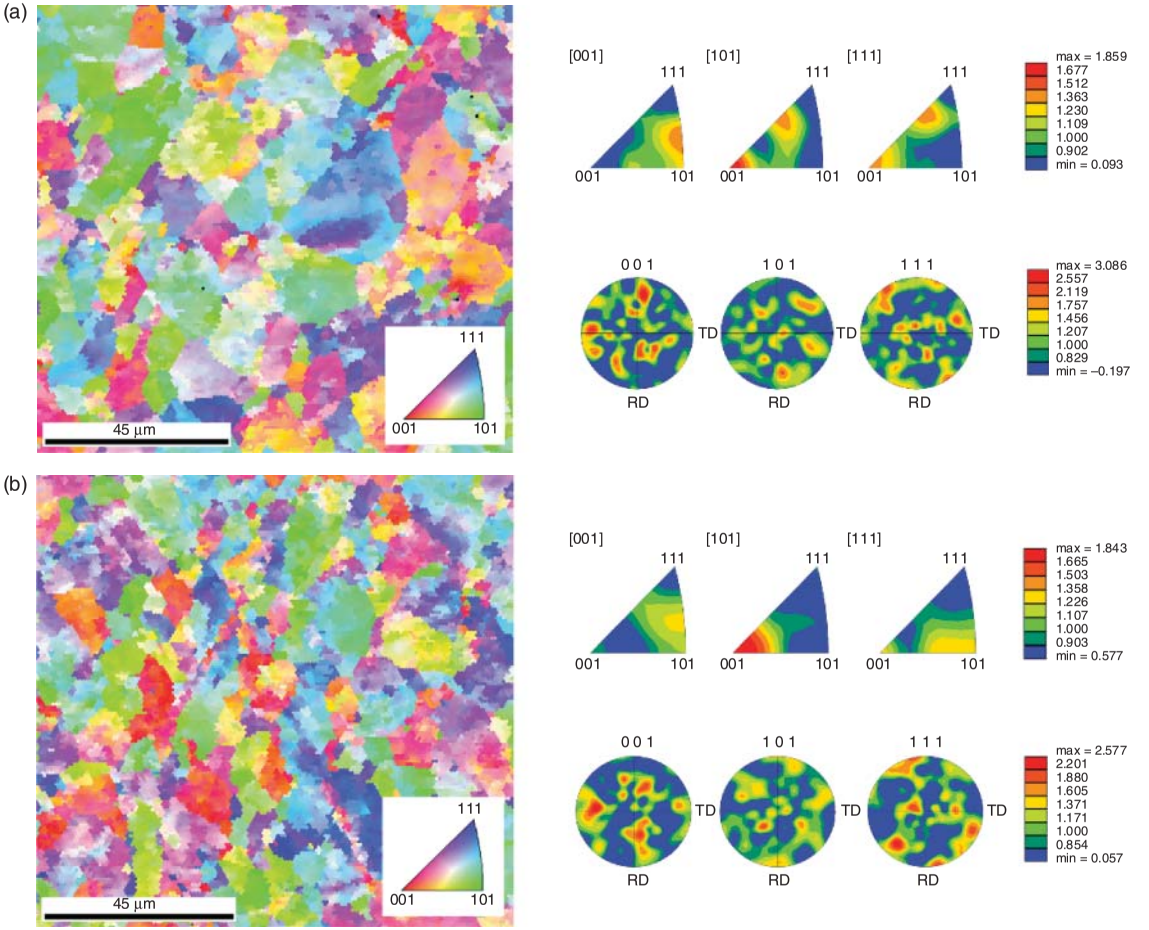

Figure 3.19 Inverse pole figure maps of (a) aluminum and (b) nanocomposites with 0.75% of CNTs produced in the same conditions.

carbon bonds hinders the formation of strong covalent bonds with the surrounding matrix.

For polymer matrix nanocomposites, the interaction of CNTs depends on the matrix being amorphous or semicrystalline. As regards amorphous polymer, the configuration of a polymer is changed by the adsorption of polymer chains onto nanotubes. The polymer chain configuration can be modified by the impenetrability of the nanotube surface; the interface composition of the polymer will only alter if covalent bonds form by introducing CNTs. A strongly interacting surface changes the conformation of a chain near this surface. The attraction between the polymer and the CNT can be improved by the addition of functional groups, which increases the surface energy of nanotubes [59, 61, 78–80]. The entanglement of the nanotubes with the bulk polymer is facilitated if the functional groups at the CNT walls and the polymer are of the same type or are compatible. In this case, the configuration and dynamics of polymer chains are affected. The chain dynamics can be evaluated by the glass transition temperature (T_g) of the polymer; an increase in T_g indicates a reduction in chain mobility, while a decrease in T_g indicates a corresponding increase. An increase in T_g caused by a surface that interacts strongly with the polymer has been observed, either because of grafting of polymer onto the CNTs' surfaces [81] or because of the strong adsorption of the polymer by the surface [82].

The incorporation of CNTs into a semicrystalline polymeric matrix affects the rate of crystal formation, which in turn affects properties such as the crystallite size or shape. A solid surface affects the crystal growth both dynamically and spatially; dynamically, the ability of polymer chains to diffuse to the growing crystal face will be affected, and spatially, a growing crystal encountering a solid has three options: to stop growing, change its growth direction, or force a change in the position of the solid [83, 84].

The chemical modification of CNTs can be one means of improving the covalent cross-link between the carbon atoms of CNTs and the polymer molecules. However, this functionalization can create defects in the structure of CNTs due to the formation of sp^3 hybridized sites and can compromise the mechanical properties of CNTs. The use of physically modified CNTs can lead to stronger bonds without degradation of properties. In this case, the strength of the interfacial bonds will depend on the geometrical conformation of the polymer with respect to the CNTs and the polymer adhesion to CNTs.

For ceramic matrix composites, the poor compatibility and wettability between CNTs and a matrix can result in weak interfacial strength. For an effective load transfer a strong bond between CNTs and ceramic matrix is necessary. Physical or chemical modification of the CNTs can be one means of improving the bonding; covalent and noncovalent bonds can be established with CNTs treated with acid, by fluorination or by using surfactants [85–88]. The main disadvantage of surfactants is the introduction of undesirable impurities that can affect the sintering process and have a negative impact on the properties.

Other dispersion processes, such as molecular-level mixing [89], aqueous colloid [90–93], and polymer-derived ceramics [94], can lead to a homogenous

dispersion of CNTs and also promote a strong bond with the matrix. Fan *et al.* [92] reported a fracture toughness twice that of monolithic alumina for SWCNTs/alumina nanocomposites. They attributed this increase to the strong interfacial CNTs–alumina bonding obtained by heterocoagulation.

The chemical reaction that can occur between the CNTs and metallic matrix can promote the formation of carbides that affect mechanical properties. This effect is not always negative and will depend on the type, number, and size of the carbides.

The joining of the dispersion and mixture processes in a single step, by ultrasonication, was effective in the formation of a uniform dispersion of CNTs through an Al matrix of the nanocomposites. CNTs are embedded in the grains of Al, which is essential for effective load transfer from the matrix to the reinforcement, and improves the mechanical properties of the nanocomposite. This technique is responsible for damaging the CNTs by exfoliation and fracture, reducing its external diameter and length. CNTs become shorter and disentangled, which improves the dispersion. The influence of the dispersion procedure on the quality of CNTs was confirmed by Raman spectroscopy. The ratio of the intensity of D band (ID) to that of intensity of G band (IG) is an indicator of the CNTs' quality [95]. An increase in this ratio indicates a growing number of defects, while a decrease indicates a change in the structure of the CNTs. Figure 3.20 shows the Raman spectrum curves obtained for CNTs with dispersion and for nanocomposites. The results show a slight increase in the ID/IG ratio, which means an increase in the defects in the CNTs due to this dispersion technique and these production processes.

In order to understand the formation of these defects, composites with CNTs embedded in the aluminum matrix were observed by HRTEM (Figure 3.21). These observations revealed, in some localized areas adjacent to the CNTs, the presence of nanoparticles of aluminum carbide, the Al_4C_3 phase. The carbide was identified

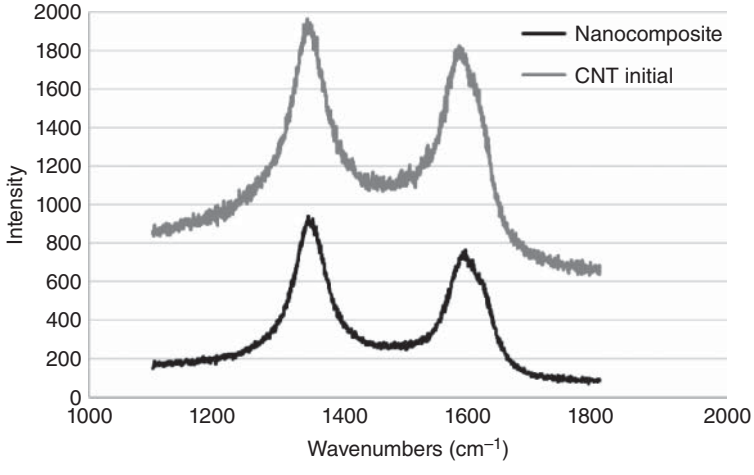

Figure 3.20 Raman spectrum curves obtained for CNTs with dispersion and for nanocomposites with 0.75% of CNTs.

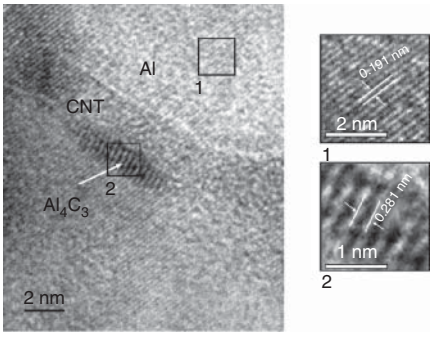

Figure 3.21 HRTEM images of CNTs/Al nanocomposites with 0.75% of CNTs showing the formation of Al_4C_3 at walls of CNTs.

by the interplanar spacing of 0.281 nm measured in high-resolution images, which corresponds to the spacing of the planes (01.2) of Al_4C_3. The nanosized Al_4C_3 phase was formed by the reaction between the CNTs and Al at the CNTs' walls. The production processes promote the formation of this phase, fully (when the CNTs are completely consumed by the reaction), or partially (when the carbide forms only at the CNTs' walls). The formation of this phase at the CNTs' walls can be the cause of the slight increase in the ID/IG ratio observed.

In some studies, the formation of the Al_4C_3 phase in small amounts is mentioned as being beneficial for obtaining a more effective load transfer, so it does not have an adverse effect on strengthening. Know and Leparoux [73] associated the improvement in tensile strength with CNTs and Al_4C_3 implanted into the aluminum matrix in nanocomposites produced by sintered spark plasma followed by hot extrusion.

Different mechanisms are reported in the literature as being responsible for the CNT strengthening effect in Al matrix nanocomposites. The hypotheses that are considered are: the inhibitions of dislocation motion by the presence of second phase particles, CNTs and Al_4C_3, and the mismatch between thermal expansion coefficients of CNTs and aluminum. The greater contraction of the aluminum matrix during cooling from the sintering temperature promotes adhesion at the CNT/Al interface.

Hence, the hardness and tensile strength enhancement observed in CNTs/Al nanocomposites can be related to an improved dispersion of CNTs in the Al matrix and to a strong adhesion between the CNT and the aluminum matrix provided by the partial formation of the Al_4C_3 phase.

3.4 Conclusion

CNTs have been widely investigated as a reinforcing material for various types of matrices. The potential for reinforcement of CNTs is very promising due to their

unique mechanical, thermal, and physical properties associated with low density. However, the properties of CNTs are strongly dependent on their morphological characteristics, such as number of walls, diameter, chirality, length, and density of defects.

There are several processing methods for synthesizing CNTs. Depending on the processing method, it is possible to obtain CNTs of better quality, and with fewer impurities and defects. However, the process with the greatest potential for producing CNTs of highest quality is also the least attractive economically.

The use of CNTs as the reinforcement phase in nanocomposites has been widely explored in recent years. The greatest challenge in this field is to achieve a dense and uniform dispersion of CNTs in the matrix, without damaging them, while at the same time obtaining a good interfacial interaction between the nanotube and the matrix. An efficient dispersion of CNTs normally involves its surface functionalization (by chemical or physical modifications) or/and mechanical dispersion using techniques such as sonication or mechanical mixing. However, these procedures can lead to damage in CNTs and must be carefully conducted in order to preserve their integrity. It is essential to overcome these challenges so as to establish new production technologies that will be capable of developing the full strengthening effect of CNTs.

Acknowledgments

This research is sponsored by FEDER funds through the program COMPETE – Programa Operacional Factores de Competitividade – and by national funds through FCT – Fundação para a Ciência e a Tecnologia, under the project PEst-C/EME/UI0285/2013 and the project PTDC/EME-TME/122472/2010. The authors are grateful to CEMUP – Centro de Materiais da Universidade do Porto for expert assistance with SEM.

References

1. Ijima, S. (1991) Helical microtubules of graphitic carbon. *Nature*, **354**, 56–58.
2. Philip Wong, H.-S. and Akinwande, D. (2011) *Carbon Nanotube and Graphene Device Physics*, Cambridge University Press.
3. Meyyappan, M. (ed.) (2005) *Carbon Nanotubes: Science and Application*, CRC Press, LLC.
4. Grady, B.P. (2011) *Carbon Nanotube-Polymer Composites: Manufacture, Properties, and Application*, John Wiley & Sons, Inc., Hoboken, NJ.
5. Lee, C., Wei, X.D., Kysar, J.W., and Hone, J. (2008) Measurement of the elastic properties and intrinsic strength of monolayer graphene. *Science*, **321** (5887), 385–388.
6. Herasati, S. and Zhang, L.C. (2014) Elastic properties of single-walled carbon nanotube clusters: dependence on hydrostatic pressure. *Comput. Mater. Sci.*, **86**, 93–98.
7. Vijayaraghavan, V. and Wong, C.H. (2013) Shear deformation characteristics of single walled carbon nanotube with water interactions by using molecular dynamics simulation. *Phys. E: Low-Dimens. Syst. Nanostruct.*, **54**, 206–213.
8. Sears, A. and Batra, R.C. (2004) Macroscopic properties of carbon nanotubes

from molecular mechanics simulations. *Phys. Rev. B*, **69**, 235406 (10pp).

9. Yu, M.F., Lourie, O., Dyer, M.J., Moloni, K., Kelly, T.F., and Ruoff, R.S. (2000) Strength and breaking mechanism of multiwalled carbon nanotubes under tensile load. *Science*, **287** (5453), 637–640.
10. Treacy, M.M.J., Ebbesen, T.W., and Gibson, J.M. (1996) Exceptionally high Young's modulus observed for individual carbon nanotubes. *Nature*, **381**, 678–680.
11. Guhados, G., Wan, W.K., Sun, X.L., and Hutter, J.L. (2007) Simultaneous measurement of Young's and shear moduli of multiwalled carbon nanotubes using atomic force microscopy. *J. Appl. Phys.*, **101**, 033514 (6pp).
12. Lukic, B., Seo, J.W., Bacsa, R.R., Delpeux, S., Beguin, F., Bister, G., Fonseca, A., Nagy, J.B., Kis, A., Jeney, S., Kulik, A.J., and Forró, L. (2005) Catalytically grown carbon nanotubes of small diameter have a high Young's modulus. *Nano Lett.*, **5** (10), 2074–2077.
13. Liew, K.M., He, X.Q., and Wong, C.H. (2004) On the study of elastic and plastic properties of multiwalled carbon nanotubes under axial tension using molecular dynamics simulation. *Acta Mater.*, **52** (9), 2521–2527.
14. Dai, H.J., Wong, E.W., and Lieber, C.M. (1996) Probing electrical transport in nanomaterials: conductivity of individual carbon nanotubes. *Science*, **272** (5261), 523–526.
15. Ebbesen, T.W., Lezec, H.J., Hiura, H., Bennett, J.W., Ghaemi, H.F., and Thio, T. (1996) Electrical conductivity of individual carbon nanotubes. *Nature*, **382**, 54–56.
16. Mann, D., Javey, A., Kong, J., Wang, Q., and Dai, H.J. (2003) Ballistic transport in metallic nanotubes with reliable Pd ohmic contacts. *Nano Lett.*, **3** (11), 1541–1544.
17. Baumgartner, G., Carrard, M., Zuppiroli, L., Bacsa, W., de Heer, W.A., and Forró, L. (1997) Hall effect and magnetoresistance of carbon nanotube films. *Phys. Rev. B*, **55** (11), 6704–6707.
18. Pop, E., Mann, D., Wang, Q., Goodson, K., and Dai, H.J. (2006) Thermal conductance of an individual single-wall carbon nanotube above room temperature. *Nano Lett.*, **6** (1), 96–100.
19. Yu, C.H., Shi, L., Yao, Z., Li, D.Y., and Majumdar, A. (2005) Thermal conductance and thermopower of an individual single-wall carbon nanotube. *Nano Lett.*, **5** (9), 1842–1846.
20. Kim, P., Shi, L., Majumdar, A., and McEuen, P.L. (2001) Thermal transport measurements of individual multiwalled nanotubes. *Phys. Rev. Lett.*, **87**, 215502 (4pp).
21. McIntosh, G.C., Kim, G.T., Park, J.G., Krstic, V., Burghard, M., Jhang, S.H., Lee, S.W., Roth, S., and Park, Y.W. (2002) Orientation dependence of magneto-resistance behaviour in a carbon nanotube rope. *Thin Solid Films*, **417** (1-2), 67–71.
22. Cottet, A., Kontos, T., Sahoo, S., Man, H.T., Choi, M.S., Belzig, W., Bruder, C., Morpurgo, A.F., and Schönenberger, C. (2006) Nanospintronics with carbon nanotubes. *Semicond. Sci. Technol.*, **21**, S78–S95.
23. Tyagi, P.K., Misra, A., Manoj, K.S., Misra, D.S., Ghatak, J., Satyam, P.V., and Le Normand, F. (2005) High-resolution transmission electron microscopy mapping of nickel and cobalt single-crystalline nanorods inside multiwalled carbon nanotubes and chirality calculations. *Appl. Phys. Lett.*, **86**, 253110 (4pp).
24. Mykhailenko, O.V., Hui, D., Strzhemechny, Y.M., Matsui, D., Prylutskyy, Y.I., and Eklund, P. (2007) Monte Carlo simulations for carbon nanotubes intercalated with different atomic species. *J. Comput. Theor. Nanosci.*, **4** (6), 1140–1143.
25. Wang, M., Zhao, X.L., Ohkohchi, M., and Ando, Y. (1996) Carbon nanotubes grown on the surface of cathode deposit by arc discharge. *Fullerene Sci. Technol.*, **4** (5), 1027–1039.
26. Zhao, X.L., Wang, M., Ohkohchi, M., and Ando, Y. (1996) Morphology of carbon nanotubes prepared by carbon arc. *Jpn. J. Appl. Phys., Part 1*, **35**, 4451–4456.

27. Zhao, X., Ohkohchi, M., Wang, M., Iijima, S., Ichihashi, T., and Ando, Y. (1997) Preparation of high-grade carbon nanotubes by hydrogen arc discharge. *Carbon*, **35** (6), 775–781.
28. Zhao, X., Ohkohchi, M., Shimoyama, H., and Ando, Y. (1999) Morphology of carbon allotropes prepared by hydrogen arc discharge. *J. Cryst. Growth*, **198-199**, 934–938.
29. Shimotani, K., Anazawa, K., Watanabe, H., and Shimizu, M. (2001) New synthesis of multi-walled carbon nanotubes using an arc discharge technique under organic molecular atmospheres. *Appl. Phys. A: Mater. Sci. Process.*, **73**, 451–454.
30. Ajayan, P.M., Lambert, J.M., Bernier, P., Barbedette, L., Colliex, C., and Planeix, J.M. (1993) Growth morphologies during cobalt-catalyzed single-shell carbon nanotube synthesis. *Chem. Phys. Lett.*, **215** (5), 509–517.
31. Seraphin, S., Zhou, D., Jiao, J., Minke, M.A., Wang, S., Yadav, T., and Withers, J.C. (1994) Catalytic role of nickel, palladium, and platinum in the formation of carbon nanoclusters. *Chem. Phys. Lett.*, **217** (3), 191–198.
32. Saito, Y., Okuda, M., Fujimoto, N., Yoshikawa, T., Tomita, M., and Hayashi, T. (1994) Single-wall carbon nanotubes growing radially from Ni fine particles formed by arc evaporation. *Jpn. J. Appl. Phys., Part 2*, **33**, L526–L529.
33. Zhou, D., Seraphin, S., and Wang, S. (1994) Single-walled carbon nanotubes growing radially from YC2 particles. *Appl. Phys. Lett.*, **65** (12), 1593–1595.
34. Saito, Y., Nishikubo, K., Kawabata, K., and Matsumoto, T. (1996) Carbon nanocapsules and single-layered nanotubes produced with platinum-group metals (Ru, Rh, Pd, Os, Ir, Pt) by arc discharge. *J. Appl. Phys.*, **80** (5), 3062–3067.
35. Saito, Y., Okuda, M., and Koyama, T. (1996) Carbon nanocapsules and single-wall nanotubes formed by arc evaporation. *Surf. Rev. Lett.*, **3**, 863–867.
36. Chen, B., Zhao, X., Inoue, S., and Ando, Y. (2010) Fabrication and dispersion evaluation of single-wall carbon nanotubes produced by FH-arc discharge method. *J. Nanosci. Nanotechnol.*, **10** (6), 3973–3977.
37. Fotopoulos, N. and Xanthakis, J.P. (2010) A molecular level model for the nucleation of a single-wall carbon nanotube cap over a transition metal catalytic particle. *Diamond Relat. Mater.*, **19** (5-6), 557–561.
38. Lee, O., Jung, J., Doo, S., Kim, S.-S., Noh, T.-H., Kim, K.-I.I., and Lim, Y.-S. (2010) Effects of temperature and catalysts on the synthesis of carbon nanotubes by chemical vapor deposition. *Met. Mater. Int.*, **16** (4), 663–667.
39. Afolabi, A.S., Abdulkareem, A.S., Mhlanga, S.D., and Iyuke, S.E. (2011) Synthesis and purification of bimetallic catalysed carbon nanotubes in a horizontal CVD reactor. *J. Exp. Nanosci.*, **6** (3), 248–262.
40. Dumpala, S., Jasinski, J.B., Sumanasekera, G.U., and Sunkara, M.K. (2011) Large area synthesis of conical carbon nanotube arrays on graphite and tungsten foil substrates. *Carbon*, **49** (8), 2725–2734.
41. Seah, C.-M., Chai, S.-P., and Mohamed, A.R. (2011) Synthesis of aligned carbon nanotubes. *Carbon*, **49** (14), 4613–4635.
42. Hou, P.-X., Liu, C., and Cheng, H.-M. (2008) Purification of carbon nanotubes. *Carbon*, **46** (15), 2003–2025.
43. Smart, S.K., Ren, W.C., Cheng, H.M., Lu, G.Q., and Martin, D.J. (2007) Shortened double-walled carbon nanotubes by high-energy ball milling. *Int. J. Nanotechnol.*, **4** (5), 618–633.
44. Balasubramanian, K. and Burghard, M. (2005) Chemically functionalized carbon nanotubes. *Small*, **1** (2), 180–192.
45. Pan, R.Q., Xu, Z.J., Zhu, Z.Y., and Wang, Z.X. (2007) Thermal conductivity of functionalized singlewall carbon nanotubes. *Nanotechnology*, **18** (28), 285704 (4pp).
46. Banerjee, S., Hemraj-Benny, T., and Wong, S.S. (2005) Covalent surface chemistry of single-walled carbon nanotubes. *Adv. Mater.*, **17** (1), 17–29.
47. Vaisma, L., Wagner, H.D., and Marom, G. (2006) The role of surfactants in dispersion of carbon nanotubes. *Adv. Colloid Interface Sci.*, **128-130**, 37–46.

48. Mickelson, E.T., Huffman, C.B., Rinzler, A.G., Smalley, R.E., Hauge, R.H., and Margrave, J.L. (1998) Fluorination of single-wall carbon nanotubes. *Chem. Phys. Lett.*, **296** (1-2), 188–194.
49. Coleman, J.N., Khan, U., Blau, W.J., and Gun'ko, Y.K. (2006) Small but strong: a review of the mechanical properties of carbon nanotube-polymer composite. *Carbon*, **44** (9), 1624–1652.
50. Tkalya, E.E., Ghislandi, M., de With, G., and Koning, C.E. (2012) The use of surfactants for dispersing carbon nanotubes and graphene to make conductive nanocomposites. *Curr. Opin. Colloid Interface Sci.*, **17** (4), 225–232.
51. Bai, Y., Lin, D., Wu, F., Wang, Z., and Xing, B. (2010) Adsorption of Triton X-series surfactants and its role in stabilizing multi-walled carbon nanotube suspension. *Chemosphere*, **79** (4), 362–367.
52. Geng, Y., Liu, M.Y., Li, J., Shi, X.M., and Kim, J.K. (2008) Effects of surfactant treatment on mechanical and electrical properties of CTN/epoxy nanocomposites. *Composites: Part A*, **39** (12), 1876–1883.
53. Shi, Y., Ren, L., Li, D., Gao, H., and Yang, B. (2003) Optimization conditions for single-walled carbon nanotubes dispersion. *J. Surf. Eng. Mater. Adv. Technol.*, **3** (1), 6–12.
54. Zhang, J. and Gao, L. (2007) Dispersion of multiwall carbon nanotubes by sodium dodecyl sulfate for preparation of modified electrodes toward detecting hydrogen peroxide. *Mater. Lett.*, **61** (17), 3571–3574.
55. Hashemnia, S., Khayatzadeh, S., Moosavi-Movahedi, A.A., and Ghourchian, H. (2011) Direct electrochemistry of catalase in multiwall carbon nanotube/dodecyl Trimethylammonium Bromide film covered with a layer of nafion on a glassy carbon electrode. *Int. J. Electrochem. Sci.*, **6**, 581–595.
56. Yang, Y.J. and Li, W. (2014) CTAB functionalized graphene oxide/multiwalled carbon nanotube composite modified electrode for the simultaneous determination of ascorbic acid, dopamine, uric acid and nitrite. *Biosens. Bioelectron.*, **56**, 300–306.
57. Matarredona, O., Rhoads, H., Li, Z., Harwell, J.H., Balzano, L., and Resasco, D.E. (2003) Dispersion of single-walled carbon nanotubes in aqueous solutions of the anionic surfactant NaDDBS. *J. Phys. Chem. B*, **107** (48), 13357–13367.
58. Yang, K., Yi, Z.L., Jing, Q.F., Yue, R.L., Jiang, W., and Lin, D.H. (2013) Sonication-assisted dispersion of carbon nanotubes in aqueous solutions of the anionic surfactant SDBS: the role of sonication energy. *Chin. Sci. Bull.*, **58** (17), 2082–2090.
59. Ajayan, P.M., Schadler, L.S., and Braun, P.V. (eds) (2003) *Nanocomposite Science and Technology*, WILEY-VCH Verlag GmbH Co, KGaA, Weinheim.
60. Tjong, S.C. (2009) *Carbon Nanotube Reinforced Composites Metal and Ceramic Matrices*, WILEY-VCH Verlag GmbH & Co. KGaA, Weinheim.
61. Vikas, M. (ed.) (2010) *Polymer Nanotube Nanocomposites Synthesis, Properties, and Applications*, John Wiley & Sons, Inc., Hoboken, NJ, and Scrivener Publishing, LLC, Salem, MA.
62. Zhou, Y., Pervin, F., Lewis, L., and Jeelani, S. (2008) Fabrication and characterization of carbon/epoxy composites mixed with multi-walled carbon nanotubes. *Mater. Sci. Eng. A*, **475** (1-2), 157–165.
63. Velasco-Santos, C., Martínez-Hernández, A.L., Fisher, F., Ruoff, R., and Castaño, V.M. (2003) Dynamical–mechanical and thermal analysis of carbon nanotube–methyl-ethyl methacrylate nanocomposites. *J. Phys. D: Appl. Phys.*, **36** (12), 1423–1428.
64. Yamamoto, G. and Hashida, T. (2012) in *Carbon Nanotube Reinforced Alumina Composite Materials, Composites and Their Properties* (ed. N. Hu), In Tech, Rijeka, pp. 483–502.
65. Pérez-Bustamante, R., Estrada-Guel, I., Antúnez-Flores, L., Miki-Yoshida, M., Ferreira, P.J., and Martínez-Sánchez, R. (2008) Novel Al-matrix nanocomposites reinforced with multi-walled carbon nanotubes. *J. Alloys Compd.*, **450** (1-2), 323–326.
66. Pham, V.T., Bui, H.T., Tran, B.T., Nguyen, V.T., Le, D.Q., Than, X.T., Nguyen, V.C., Doan, D.P., and Phan, N.M. (2011) The

effect of sintering temperature on the mechanical properties of a Cu/CNT nanocomposite prepared via a powder metallurgy method. *Adv. Nat. Sci.: Nanosci. Nanotechnol.*, **2**, 015006 (4pp).

67. Nguyen, J., Holland, T.B., Wen, H., Fraga, M., Mukherjee, A., and Lavernia, E. (2014) Mechanical behavior of ultrafine-grained Ni–carbon nanotube composite. *J. Mater. Sci.*, **49** (5), 2070–2077.
68. Kuzumaki, T., Miyazawa, K., Ichinose, H., and Ito, K. (1998) Processing of carbon nanotube reinforced aluminum composite. *J. Mater. Res.*, **13** (9), 2445–2449.
69. George, R., Kashyap, K.T., Rahul, R., and Yamdagni, S. (2005) Strengthening in carbon nanotube/aluminium (CNT/Al) composites. *Scr. Mater.*, **53** (10), 1159–1163.
70. Kim, K.T., Cha, S.I., Hong, S.H., and Hong, S.H. (2006) Microstructures and tensile behavior of carbon nanotube reinforced Cu matrix nanocomposites. *Mater. Sci. Eng., A*, **430** (1-2), 27–33.
71. Esawi, A.M.K. and El Borady, M.A. (2008) Carbon nanotube-reinforced aluminium strips. *Compos. Sci. Technol.*, **68** (2), 486–492.
72. Esawi, A.M.K., Morsi, K., Sayed, A., Taher, M., and Lanka, S. (2010) Effect of carbon nanotube (CNT) content on the mechanical properties of CNT-reinforced aluminium composites. *Compos. Sci. Technol.*, **70** (16), 2237–2241.
73. Kwon, H. and Leparoux, M. (2012) Hot extruded carbon nanotube reinforced aluminum matrix composite materials. *Nanotechnology*, **23** (41), 415701 (10pp).
74. Quang, P., Jeong, Y.G., Hong, S.H., and Kim, H.S. (2006) Equal channel angular pressing of carbon nanotube reinforced metal matrix nanocomposites. *Key Eng. Mater.*, **326-328**, 325–328.
75. Quang, P., Jeong, Y.G., Yoon, S.C., Hong, S.H., and Kim, H.S. (2007) Consolidation of 1 vol.% carbon nanotube reinforced metal matrix nanocomposites via equal channel angular pressing. *J. Mater. Process. Technol.*, **187-188**, 318–320.
76. Jiang, L., Fan, G., Li, Z., Kai, X., Zhang, D., Chen, Z., Humphries, S., Hness, G., and Yeung, W.Y. (2011) An approach to the uniform dispersion of a high volume fraction of carbon nanotubes in aluminum powder. *Carbon*, **49** (6), 1965–1971.
77. Noguchi, T., Magario, A., Fukazawa, S., Shimizu, S., Beppu, J., and Seki, M. (2004) Carbon nanotube/aluminium composites with uniform dispersion. *Mater. Trans.*, **45** (2), 602–604.
78. Källrot, N. and Linse, P. (2007) Dynamic study of single-chain adsorption and desorption. *Macromolecules*, **40** (13), 4669–4679.
79. Källrot, N., Dahlqvist, M., and Linse, P. (2009) Dynamics of polymer adsorption from bulk solution onto planar surfaces. *Macromolecules*, **42** (10), 3641–3649.
80. Angelikopoulos, P. and Bock, H. (2010) The differences in surfactant adsorption on carbon nanotubes and their bundles. *Langmuir*, **26** (2), 899–907.
81. Tate, R.S., Fryer, D.S., Pasqualini, S., Montague, M.F., de Pablo, J.J., and Nealey, P.F. (2001) Extraordinary elevation of the glass transition temperature of thin polymer films grafted to silicon oxide substrates. *J. Chem. Phys.*, **115**, 9982–9990.
82. Keddie, J.L., Jones, R.A.L., and Cory, R.A. (1994) Interface and surface effects on the glass-transition temperature in thin polymer films. *Faraday Discuss.*, **98**, 219–230.
83. Li, L.Y., Li, B., Hood, M.A., and Li, C.Y. (2009) Carbon nanotube induced polymer crystallization: the formation of nanohybrid shish-kebabs. *Polymer*, **50** (4), 953–965.
84. Li, L.Y., Li, C.Y., Ni, C.Y., Rong, L.X., and Hsiao, B. (2007) Structure and crystallization behavior of Nylon 66/multi-walled carbon nanotube nanocomposites at low carbon nanotube contents. *Polymer*, **48** (12), 3452–3460.
85. Hernadi, K., Couteau, E., Seo, J.W., and Forró, L. (2003) Al(OH)3/multiwalled carbon nanotube composite: homogeneous coverage of Al(OH)3 on carbon nanotube surfaces. *Langmuir*, **19** (17), 7026–7029.
86. Morisada, Y. and Miyamoto, Y. (2004) SiC coated carbon nanotubes and their application as reinforcements

for cemented carbide. *Mater. Sci. Eng., A*, **381** (1-2), 57–61.

87. Guo, Y., Cho, H., Shi, D., Lian, J., Song, Y., Abot, J., Poudel, B., Ren, Z., Wang, L., and Ewing, R.C. (2007) Effects of plasma surface modification on interfacial behaviors and mechanical properties of carbon nanotube-Al2O3 nanocomposites. *Appl. Phys. Lett.*, **91**, 2619031–2619033.
88. Hwang, G.L. and Hwang, K.C. (2001) Carbon nanotube reinforced ceramics. *J. Mater. Chem.*, **11** (6), 1722–1725.
89. Cha, S.I., Kim, K.T., Lee, K.H., Mo, C.B., and Hong, S.H. (2005) Strengthening and toughening of carbon nanotube reinforced alumina nanocomposite fabricated by molecular level mixing process. *Scr. Mater.*, **53** (7), 793–797.
90. Sun, J., Gao, L., and Jin, X. (2005) Reinforcement of alumina matrix with multi-walled carbon nanotubes. *Ceram. Int.*, **31** (6), 893–896.
91. Poyato, R., Vasiliev, A.L., Padture, N.P., Tanaka, H., and Nishimura, T. (2006) Aqueous colloidal processing of single wall carbon nanotubes and their composites with ceramic. *Nanotechnology*, **17** (6), 1770–1777.
92. Fan, J.P., Zhuang, D.M., Zhao, D.Q., Zhang, G., and Wu, M.S. (2006) Toughening and reinforcing alumina matrix composite with single-wall carbon nanotubes. *Appl. Phys. Lett.*, **89**, 1219101–1219103.
93. Fan, J.P., Zhao, D.Q., Wu, M.S., Xu, Z., and Song, J. (2006) Preparation and microstructure of multi walled carbon nanotubes-toughened composite. *J. Am. Ceram. Soc.*, **89**, 750–753.
94. Bharadwaj, L., Fan, Y., Zhang, L., Jiang, D., and An, L. (2004) Oxidation behavior of a fully dense polymer-derived amorphous silicon carbonitride ceramic. *J. Am. Ceram. Soc.*, **87** (3), 483–486.
95. Keszler, A.M., Nemes, L., Ahmad, S., and Kawasaki, A. (2004) Characterization of carbon nanotube materials by Raman spectroscopy-a case study of multiwalled and single walled samples. *J. Optoelectron. Adv. Mater.*, **6** (4), 1269–1274.

4
Graphene and Graphene Sheets Based Nanocomposites

Anish Khan, Aftab Aslam Parwaz Khan, and Abdullah M. Asiri

4.1
Introduction

Graphene has become something of a celebrity material in recent years due to its conductive, thermal, and optical properties, which could make it useful in a range of sensors and semiconductor devices. Graphene, a one-atom thick sheet of hexagonally arranged carbon, has existed in theory for the better part of a century, but until 2004 accepted wisdom in physics and chemistry communities was that theory was as far as graphene was destined to evolve. However, in 2004, two scientists, Andre Geim and Konstantin Novoselov, both of whom would later receive the Nobel Prize for their work, overturned conventional wisdom, producing the material in a lab with a very non-lab-like process involving scotch tape and graphite (pencil lead).

Since the discovery, research on graphene has exploded. It has been a primary or subordinate subject in over 100 000 academic papers, and as of September 2012, over 2000 patents involving the material have been applied for or awarded. The attention surrounding the research has been likened to a gold rush, and it has generated more interest commercially than any material since silicon. It is 200 times stronger than steel, thinner than a sheet of paper, and more conductive than copper. Graphene is extraordinarily strong (the strongest material ever known or tested), supernaturally light, and electrically superconductive. Its flexibility and structure also make it the leading candidate as the primary component of next-generation, ultrahigh speed circuitry in everything from computers, to smart phones, to televisions. It is therefore of interest to a range of industries. The question, ultimately, is not if graphene will change everything from computing to manufacturing, but how and when (Figures 4.1 and 4.2).

4.1.1
Structure of Graphene and Graphene Sheets

Rolled sheets of graphene form hyperconductive carbon nanotubes (CNTs). These nanotubes work around the primary limiting factor in microchip

Nanomaterials and Nanocomposites: Zero- to Three-Dimensional Materials and Their Composites,
First Edition. Edited by Visakh P.M. and Maria José Martínez Morlanes.

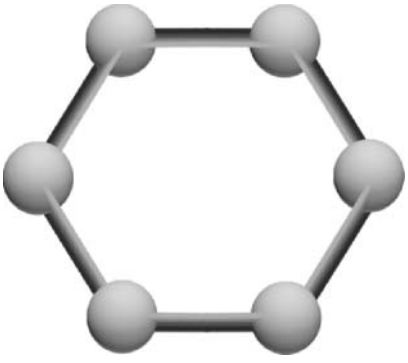

Figure 4.1 The hexagonal structure of a six-way bond between carbon atoms – trillions of which make up a tiny sheet of graphene.

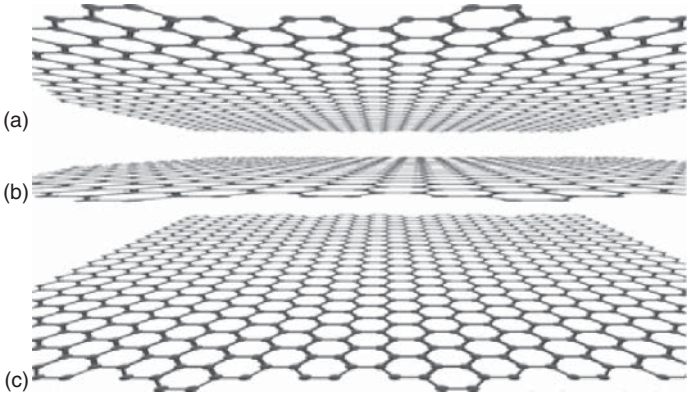

Figure 4.2 Structures of multigraphene sheets.

processing speed by taking chip architecture into the third dimension. There is a lower limit on the size of the essentially flat transistors that make up silicon-based microchips – the devices that allow information processing in everything from phones to computers. Graphene, CNTs can effectively stack transistors on top of one another on microchips, allowing for exponentially more transistors on a chip without increasing the size. More transistors means more operations per second, which means more processing power and faster processing speed. When carbon forms sheets when it bonds to three other carbon atoms they are called *graphene*. Nanotechnology researchers have only recently (2004) been successful in producing sheets of graphene for research purposes. Common graphite is the material in pencil lead, and it is composed of sheets of graphene stacked together. The sheets of graphene in graphite have a space between each sheet and the sheets are held together by the electrostatic force called *van der Waals bonding* (Figure 4.3).

Graphene sheets are composed of carbon atoms linked in hexagonal shapes (Figures 4.3 and 4.4) with each carbon atom covalently bonded to three other carbon atoms. Each sheet of graphene is only one-atom thick, and each graphene sheet is considered to be a single molecule. Graphene has the same structure of

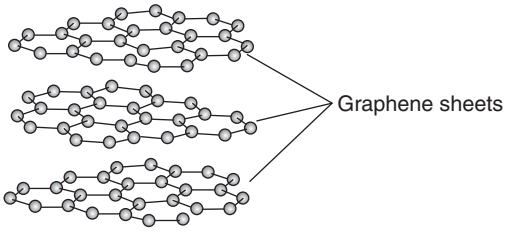

Figure 4.3 Sheets of graphene held together by van der Waals bonding.

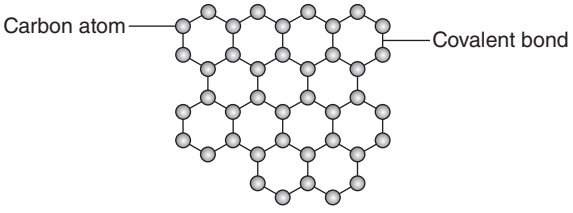

Figure 4.4 A graphene sheet.

carbon atoms linked in hexagonal shapes to form CNTs, but graphene is flat rather than cylindrical.

Because of the strength of covalent bonds between carbon atoms, graphene has a very high tensile strength. (Basically, tensile relates to how much you can stretch something before it breaks.) In addition, graphene, unlike a buckyball or nanotube, has no inside because it is flat. Buckyballs and nanotubes, in which every atom is on the surface, can interact only with molecules surrounding them. For graphene, every atom is on the surface and is accessible from both sides, so there is more interaction with the surrounding molecules.

Finally, in graphene, carbon atoms are bonded to only three other atoms, although they have the capability to bond to a fourth atom. This capability, combined with great tensile strength and the high surface area to volume ratio, makes it very useful in composite materials. Researchers have reported that mixing graphene in an epoxy resulted in the same amount of increased strength for the material as was found when they used 10 times the weight of CNTs. A key electrical property of graphene is its electron mobility (the speed at which electrons move within it when a voltage is applied). Graphene's electron mobility is faster than any known material and researchers are developing methods to build transistors on graphene that would be much faster than the transistors currently built on silicon wafers. Another interesting application being developed for graphene takes advantage of the fact that the sheet is only as thick as a carbon atom. Researchers have found that they can use nanopores to quickly analyze the structure of DNA. When a DNA molecule passes through a nanopore that has a voltage applied across it, researchers can determine the structure of the DNA by the changes in the electrical current. Because graphene is so thin, the structure of a DNA molecule appears at a higher resolution when it passes

through a nanopore cut in a graphene sheet. A visual depiction of the structure of a layered, microscopic segment of graphene. At approximately 200 times stronger than structural steel, given enough layers, graphene would be both harder and stronger than any material ever created, opening the possibility for products and structures that are a fraction of the weight and an exponent of the strength of any existing currently.

4.1.2 Properties of Graphene and Graphene Sheets

4.1.2.1 Electronic Properties

The carbon–carbon bonding length (0.142 nm) as a zero band gap semiconductor, graphene displays an ambipolar electric field effect and charge carriers can be tuned continuously between electrons and holes in concentrations as high as 10^{13} cm^{-2}, with room temperature mobilities of up to 15 000 cm^2 V^{-1} s^{-1} [1–3]. The mobility in graphene remains high even at high carrier density in both electrically and chemically doped devices [4], displaying evidence of ballistic transport on the submicrometer scale [5].

4.1.2.2 Mechanical Properties

The mechanical properties of monolayer graphene including the Young's modulus and fracture strength have been investigated by numerical simulations such as molecular dynamics [6]. The Young's modulus of few-layer graphene was experimentally investigated with force-displacement measurements by atomic force microscopy (AFM) on a strip of graphene suspended over trenches [7]. Circular membranes of few-layer graphene were also characterized by force-volume measurements in AFM [8]. Recently, the elastic properties and intrinsic breaking strength of free-standing monolayer graphene were measured by nanoindentation using an AFM (Figure 4.5a,b). It was reported that defect-free graphene has a Young's modulus of 1.0 TPa and a fracture strength of 130 GPa. CMG was also investigated by a similar AFM indentation method [9]. The CMG obtained by reducing graphene oxide with hydrogen plasma exhibited a mean elastic modulus of 0.25 TPa with a standard deviation of 0.15 TPa; the fracture strength was not reported. A "paper-like" material (Figure 4.5c) made by flow directed assembly of individual graphene oxide platelets has been reported. The average elastic modulus and the highest fracture strength obtained were 32 GPa and 120 MPa, respectively. The mechanical properties of this "graphene oxide paper" were improved by introducing chemical cross-linking between individual platelets using divalent ions [10] and polyallylamine [11]. Instead of preparation by filtration, a self-assembled graphene oxide paper was made at a liquid/air interface by evaporating the hydrosol of graphene oxide [12]. This self-assembled paper showed a slightly lower modulus but a similar tensile strength as compared with those prepared by filtration. In addition, a paper composed of stacked and

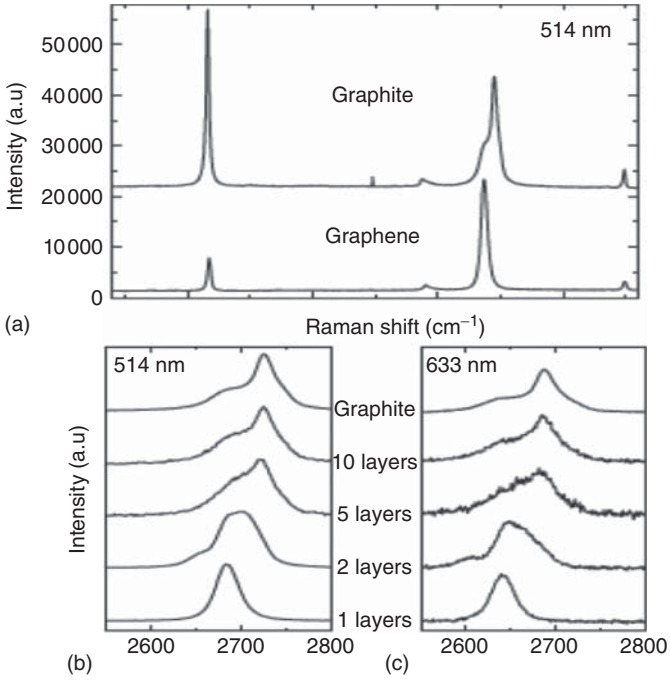

Figure 4.5 (a) Comparison of Raman spectra at 514 nm for bulk graphite and graphene. They are scaled to have similar height of the 2D peak at 2700 cm^{-1}; (b) evolution of the spectra at 514 nm with the number of layers; and (c) evolution of the Raman spectra at 633 nm with the number of layers.

overlapped reduced graphene oxide (rGO) platelets was obtained by controlled reduction of graphene oxide dispersions with hydrazine [13]. After annealing, its stiffness and tensile strength were higher than those of graphene oxide papers that have been reported to date.

4.1.2.3

Optical Properties

The constant transparency (97.7%) has been experimentally observed for graphene in the visible range and the transmittance linearly decreases with the number of layers for *n*-layer graphene [14]. A deviation from this "universal behavior" has been found for incident photons with energy lower than 0.5 eV, which was attributed to the finite temperature and a doping-induced chemical potential shift of the charge-neutrality (Dirac) point [15]. Inter-band optical transitions in graphene have been probed by infrared spectroscopy, and gate-dependent optical transitions have been reported [16]. Due to the low density of states near the Dirac point in graphene, a shift of the Fermi level due to the gate causes a significant variation of charge density, leading to a significant change in transmission. The relaxation and recombination of photo-generated electron–hole pairs in graphene occurs on a timescale of tens of picoseconds,

depending on the carrier concentration of graphene [17, 18]. Given the high carrier transport velocity even under a moderate electrical field, an ultrafast (up to 40 GHz) and efficient (6–16% internal quantum efficiency) photoresponse has been observed for graphene field effect transistors (FETs) [19], suggesting graphene-based high-speed optoelectronic devices for communications, detection, sensing, and so on.

4.1.2.4 Raman Spectroscopy of Graphene

Raman spectroscopy has been used to characterize graphene and several review articles have been published discussing the optical phonon spectrum and Raman spectrum of graphene [20]. The Raman spectra of graphene includes the G peak located at 1580 cm^{-1} and 2D peak at 2700 cm^{-1}, caused by the in-plane optical vibration (degenerate zone center E 2g mode) and second-order zone boundary phonons, respectively. The D peak, located at 1350 cm^{-1} due to first-order zone boundary phonons, is absent from defect-free graphene, but exists in defected graphene. It was proposed that Raman could be used to distinguish the "quality" of graphene and to determine the number of layers for *n*-layer graphene (for *n* up to 5) by the shape, width, and position of the 2D peak [21].

As shown in Figure 4.5, the 2D peak shifts to higher wave number values and becomes broader for an increasing number of layers. The shifting and splitting of Raman modes can be used to analyze mechanical strain in graphene. For example, Raman spectra of epitaxial graphene grown on SiC show a significant phonon "hardening" (blue shift of the G and 2D peaks), mainly due to the compressive strain that occurs when the sample is cooled down after growth [22, 23]. It has been stated that the substrates play a negligible role in the Raman spectrum of micromechanically cleaved graphene transferred onto them, indicating the weak interactions between the transferred graphene and such substrates [24].

4.1.3 Synthesis of Graphene and Graphene Sheets

Creating high-quality graphene in scalable, economical processes is the first step toward practical application of graphene. Work on isolating graphene has progressed over many decades of research [25]. The structure of graphite, and essentially graphene as well, was known since the invention of X-ray diffraction (XRD) crystallography. However, it was unknown whether or not a truly two-dimensional crystal could exist, as extra planar phonons would be entropically overwhelming over long ranges [26]. Solution-based exfoliation of graphite (i.e., via oxidation or graphite intercalation compounds (GICs)) gave an early look at realizing atomic planes of carbon [27]. In the 1960s, Boehm speculated that reducing exfoliated graphite oxide would yield monolayers in solution [28], though the term *graphene* was not coined until 1986 [29] and was formally accepted in 1994 [30]. A number of early studies found monolayers of carbon in graphitic structures, formed on various carbide [31] and transition metal [32]

surfaces, as early as van Bommel in 1975 with SiC [33]. These surface science and chemistry studies did not explore any electronic properties, as the strongly bound metallic surfaces disrupt the perpendicular orbitals, with the exception of SiC. The first electronic measurements of ultrathin graphitic carbon around 2004 required samples sufficiently isolated from its substrate, (e.g., on SiO_2) and ignited an explosion of interest in the field [34]. Synthesis techniques can be categorized into micromechanical exfoliation, solution-based and chemically assisted exfoliation, chemical synthesis, epitaxial growth through sublimated SiC surfaces, and the pyrolysis of hydrocarbons on metal surfaces. Each has its own advantages, challenges, shortcomings, and unique features in terms of processability, quality, scalability, and cost.

4.1.3.1 Exfoliation

Mechanical Cleavage The exfoliation of graphite is a process in which bulk graphite can be separated into single atomic planes. Attempts prior to the development of the so-called "Scotch tape method" were unable to observe isolated single layers. Ever since the first graphene discovered using micromechanical cleavage of bulk graphite, this method has been widely used to prepare high-quality graphene samples, which is less formally called *peeled graphene*. The technique is quite simple: using everyday adhesive tape to repeatedly peel layers off of highly oriented pyrolytic graphite and pressing it onto an appropriate substrate, typically but not limited to oxidized silicon. An initial wet transfer technique was supplanted by a simpler dry transfer from the tape directly onto the oxide. Sizes of individual crystals can reach millimeter range as seen in Figure 4.6a, but production suffers from low throughput. Far from being scalable, these highly crystalline samples are best suited for the study of fundamental properties such as ballistic transport, carrier mobility [36], thermal conductivity, and so on [37]. Although the mechanical exfoliation approach can produce the best quality graphene to probe intrinsic performance limits, it is hardly applicable for any practical applications.

Solution and Chemical Exfoliation Chemical exfoliation of graphite in solution represents one potential approach to high-volume production of graphene. As opposed to direct physical cleavage, chemicals are used to intercalate bulk graphite by inserting reactants between layers that weaken the cohesive van der Waals force [38]. Dai's group was the first to report success in producing high-quality, single-layer graphene (SLG) sheets, stably suspended in organic solvents by steps of chemical intercalation, reintercalation, and sonication [39]. They first heated expandable graphite in sulfuric acid and nitric acid, where most of the exfoliated particles found in the reacted solution are still multiple-layers thick. An oleum treatment followed with tetra-butyl alcohol reintercalation is the key step for high-quality single-layer graphene. About 90% of graphene sheets are in single-layer form after sonication in a surfactant solution based on

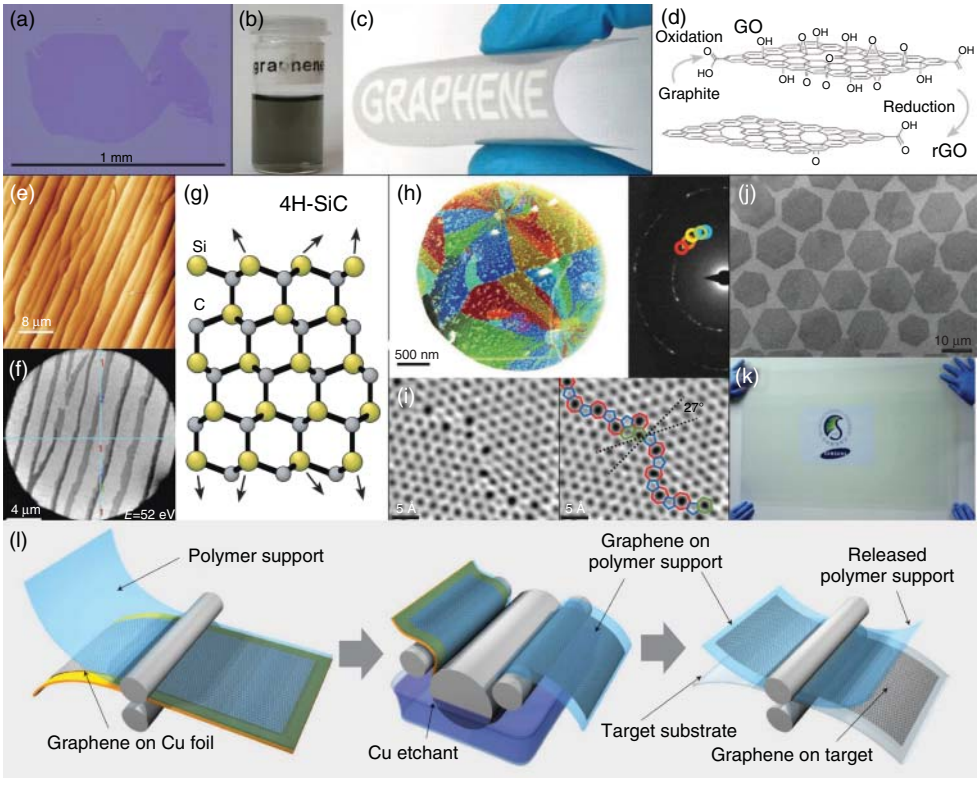

Figure 4.6 Synthesis techniques. (a) Optical microscopy image of a very large micromechanically exfoliated (tape method) monolayer of graphene. Note the considerable contrast for the single atomic layer. (b) Photograph of dispersed graphene by ultrasonic exfoliation of graphite in chloroform and (c) that deposited on a bendable film. (d) Graphene oxide and reduced graphene oxide showing the remaining oxygen-rich functional groups after reduction. (e,f) OM and SEM images of graphene grown epitaxial on SiC. The number of layers is shown in (f), with multiple layers forming at step edges. (g) Crystal structure of 4H–SiC with Si (top) and C (bottom) faces. (h) False-colored dark-field TEM reconstruction of CVD graphene domain patchwork. Each color is a domain with a certain lattice orientation (left), imaged separately using the corresponding diffracted beams for crystal-orientation-dependent contrast (right). (i) High-resolution ADF-STEM of a domain boundary in CVD graphene showing a rotational mismatch of 27 and a series of pentagon–heptagon pairs (Stone–Wales defects) along the boundary. (j) SEM of an array of seeded growth hexagonal domains of CVD graphene on copper. (k) Large-area graphene transferred using roll-to-roll production spanning 30 in. diagonally. (l) Schematic of the roll-to-roll process showing adhesion to a thermal release tape polymer support, run through an etching medium to remove the copper foil, before being released via heat treatment from the polymer support onto the final substrate (a–c) [35].

AFM measurements. A liquid exfoliation approach has also been reported to produce graphene by sonicating graphite powder in *N*-methylpyrroidone [40]. A homogeneous colloidal suspension of graphene sheets or ribbons can be made simply by stirring in surfactant solution [41]. The library of available exfoliating solvents has expanded: some belong to a peculiar class of perfluorinated aromatic molecules and an assortment of other suitable dispersing media [42]. Low-power sonication for weeks at a time to avoid the damage of the graphene sheets yields a high concentration (up to 1.2 mg ml^{-1} up to 4 wt%) of monolayer graphene [43]. Sonication-free, mild dissolution of graphite by synthesizing well-documented GICs achieved large graphene flakes and ribbons [44].

Oxidation and Reduction A more efficient way to obtain large volumes of graphene is by the synthesis of graphite oxide, followed by exfoliation into monolayers, and finally byreduction to remove the oxygen groups (Figure 4.6d) [45]. Each oxidized flake possesses a large number of negative charges and repels one another. The Brodie, Staudenmeier, and Hummers methods are the three most common ways to oxidize graphite. Among these, a slightly modified Hummers method has become the most popular in producing graphite oxide, for its relatively shorter reaction time and absence of toxic side products [46]. After oxidation, the interlayer spacing increases from 0.34 nm in graphite to above 0.6 nm, with weakened van der Waals forces between the layers. Exfoliation is typically augmented with sonication [47], yielding single layers of graphene oxide (GO) [48], which are soluble in water, without the assistance of surfactants, to form a stable colloidal system. Many methods of removing the oxygen from the GO structure through chemical [49], thermal [50], electrochemical [51] or electromagnetic flash [52], and laser-scribe [53] techniques have been successful, but generally resulted in inferior samples and are therefore, more precisely named rGO. GO films reduced via chemical methods typically use highly toxic hydrazine, while less effective but more environmentally friendly alternatives exist such as Vitamin C [54] or *Escherichia coli* (*E. coli*) bacteria [55]. Homogeneous colloidal suspensions of electrically conducting graphene are stable in many organic solutions in the presence of either a polymer or a surfactant. Solutions without these extraneous surfactant agents are also possible by changing to an alkaline condition, with single sheets up to 40 nm in diameter. Chemical reduction usually cannot completely remove all the oxygen in GO, leading to relatively poor electrical quality when compared to pristine graphene [56]. Electrochemical reduction is an ecofriendly and economical option, producing high-quality rGO in large scales. The reduction of GO films on graphite electrodes can be effectively tuned by varying the applied potential. Thermal treatment is another way to reduce GO by heating in alkaline conditions [57] or with microwave irradiation [58]. Thermal reduction can be combined with chemical treatments to achieve more complete removal of oxygen [59]. At room temperature, chemical-free flash reduction process uses an instantaneous photographic camera flash to trigger photothermal reduction [60]. Commercial optical-drive-based laser-scribes were used to pattern as well as for tune

reduction along a disc coated with GO. Photochemical methods were found to effectively reduce GO by UV-irradiation of a mixture with TiO_2 particles suspended in ethanol [61].

4.1.3.2 Epitaxial on Silicon Carbide

Exfoliated-graphene (EG) growth on silicon carbide (SiC) surfaces is an effective bottom-up approach to create carbon-based electronics, which has been demonstrated on wafer scale [62]. The pioneering work on EG was conducted by heating 6H–SiC in ultrahigh vacuum (UHV) in the temperature range of 1200–1600 °C [63]. The silicon atoms on the surface sublimate at high enough temperature and the exposed carbon atoms reconstruct to form graphitic layers (Figure 4.6e–g). EG can grow on both the C-terminated and Si-terminated (0001) surfaces, though films grow much faster on the carbon face [64]. The primary difference between graphene formed on the C-terminated and the Si-terminated surfaces is the weak and strong coupling of both the substrate and successive graphene layers [65]. Selective synthesis of EG on a templated substrate was demonstrated by using patterned AlN caps [66]. Surfaces of cubic 3C–SiC are also capable of epitaxial growth, with low interface interaction, and cheaper, commercialized SiC/Si wafers. Most EG growth is accomplished in UHV; however, larger, several-micrometer domains have been obtained in an argon atmosphere. Direct growth of graphene nanoribbons has been achieved on prefabricated SiC nanofacets, using crystal plane selective growth rates from a lowered surface free energy. SiC offers a suitable insulating structure in which devices can be fabricated with a sufficient buffer layer that isolates the graphene orbitals, keeping the linear dispersion intact. Transferring EG to arbitrary substrates using thermal release tape has been accomplished, without a significant drop in carrier mobility. Industrial scale growth on SiC is primarily limited by the high cost of single-crystal SiC wafers.

4.1.3.3 Chemical Vapor Deposition

Chemical vapor deposition (CVD) method has emerged to be one of the most promising techniques for the large-scale production of single- and multiple-layer graphene films. Uniform, wafer size graphene films have been grown on both single crystal and polycrystalline transition metal surfaces at high temperatures by pyrolysis of hydrocarbon precursors such as methane [67]. Figure 4.6k shows the largest continuous area of CVD graphene reported to date: 30-in. diagonal length, grown on copper foil in an 8-in. diameter quartz tube at low pressure.

The number of graphene layers depends highly on the carbon solubility of the substrate. For metals with relatively high carbon solubility, such as nickel [68], the carbon atoms can dissolve at high temperature, then precipitate onto the metal surface and form single or multilayer graphitic films upon cooling. These nonuniform films with a wide thickness range from 1 to around 10 layers with monolayer domain sizes up to several tens of micrometers in diameter were produced on

nickel substrates [69]. The thickness and crystal ordering can be controlled by the cooling rate and hydrocarbon gas concentration. On the other hand, low carbon solubility in certain transition metals, for instance copper [70] and platinum [71] enables complete monolayer coverage [72]. Under typical atmospheric pressure chemical vapor deposition (APCVD) conditions, the graphene growth is mainly limited by mass transport through the boundary layer, while the surface reaction is the rate-limiting step at low pressure chemical vapor deposition (LPCVD) [73]. The predominantly uniform monolayer graphene grown by the LPCVD method is proposed by the self-limiting nature of the growth process. Lattice mismatch between the metal surface and graphene typically forms a pseudomorphic interface and generally displays a moiré pattern as well as lattice strain. Graphene epitaxial grown on single-crystal metal substrates can avoid surface defects on the metal grain boundaries and help to mitigate orientation mismatch, but will still have significant misaligned domains and grain boundaries [74]. Polycrystalline films offer a more economical alternative that is still capable of large domains without noticeable performance difference within individual domains. Yan and coworkers broke the self-limiting effect of the LPCVD process to enable a second-layer growth on prepared monolayer graphene using a fresh copper foil placed in the high-temperature upstream regime. Bernal AB-stacked bilayer graphene (BLG) is possible with coverage area as high as 67%, which shows typical gate response [75]. Furthermore, Chen and coworkers report the synthesis of controllable mono- and multi-layer graphene films on Cu 0.69 Ni 0.31 alloy foils by LPCVD. By using the alloy of low- and high-solubility catalysts, both thickness and quality of the films can be controlled by the growth temperature and cooling rate [76]. A better understanding of the mechanisms of graphene growth is demanded for controlling domain size and number of layers. Different combinations of temperature and pressure benefit lower nucleation rates as opposed to faster growth and fuller coverage. A two-step CVD synthesis was therefore developed with different parameters for the nucleation and growth phases, yielding domains hundreds of square micrometers large [77] and, later, millimeter sizes [78]. The shape of domains during growth dictates the final morphology, and varies under different conditions between stochastic structures, hexagonal shapes that follow lattice symmetry, and more erratic flower-like structures.

From a practical point of view, it is desirable to reduce growth temperatures. To this end, it has recently been demonstrated that graphene can be grown at a temperature as low as 300 °C using a liquid benzene hydrocarbon source [79]. Plasma-enhanced chemical vapor deposition (PECVD) can achieve growth at moderate temperatures 700 °C [80]. A laser-induced CVD process writes line patterns of graphene directly by irradiation with a focused laser beam (5 W, 532 nm wavelength, 20 m spot size) on a thin foil in a low-pressure system at room temperature [81]. Localized heating decomposes the gas, with a growth rate thousands of times faster than typical thermal CVD. Instead of using the hydrocarbon gases as the carbon precursors, solid state carbon sources such as poly(methyl methacrylate) (PMMA) or even table sugar, virtually any

carbon-based material, is shown to produce graphene on select metal substrates at high enough temperatures [82]. By controlling the Ar/H2 gas flow ratio, monolayer-, bilayer-, or few-layered graphene can be grown using a copper thin film catalyst on SiO_2/Si substrates with a 100 nm thick spin-coated PMMA film at temperatures as low as 800 °C [83]. Graphene grown on metal foils is not particularly useful for electronic applications without transferring it to an insulating substrate. The transfer process adds additional complications to the quality and consistency of samples such as cracking and polymer residue. It would be very desirable if a CVD process eliminates this transfer step (i.e., deposition directly onto arbitrary substrates, particularly insulating oxides).

In order to avoid the extra processing step, some techniques use thin metal films on insulating substrates that are removed during or post growth, or with remote catalyzation by copper atoms in the atmosphere. Other attempts are completely metal-free, which loses the self-limiting catalyzed reaction. A promising approach to isolating CVD graphene from its metallic growth substrate and regaining its intrinsic electronic properties is through intercalation with a buffer layer such as Si. Typically, the convenience and practicality of transfer-free growth is at the expense of quality and performance. Another useful feature of CVD is the ability to dope graphene with substitutional impurities by introducing other gases during growth, such as ammonia (NH_3) or borane (BH_3). This simple approach uses nitrogen and boron to displace normal carbon atoms within the lattice. Alternatively, annealing under ammonia atmosphere or ion bombardment offers post growth routes toward nitrogen-doping.

4.1.3.4 Chemical Synthesis

Another alternative route for the controllable production of graphene is bottom-up organic synthesis. Graphene can be composed of interconnected polycyclic aromatic hydrocarbons (PAHs), which are very small two-dimensional graphene segments. This approach is attractive due to its high versatility and compatibility with various organic synthesis techniques. Müllen and coworkers are pioneers in this field, reporting synthesis of nanoribbon like PAHs with lengths over 30 nm. Recently, the largest stable colloidal graphene quantum dots were synthesized using a benzene-based chemical route, which compose conjugated carbon atoms. However, the size of the as-grown graphene dots is limited due to decreasing solubility as sizes increase. There is also the probability of an increasing number of possible side reactions, which is still a major challenge for organic synthesis of graphene molecules with controllable shapes, sizes, and edge structures.

4.1.4 Chemical Modifications of Graphene and Graphene Sheets

Nethravathi and Rajamathi described that chemically modified graphene sheets are obtained through solvothermal reduction of colloidal dispersions of graphite

oxide in various solvents. Reduction occurs at relatively low temperatures (120–200 °C). Reaction temperature, the self-generated pressure in the sealed reaction vessel, and the reducing power of the solvent influence the extent of reduction of graphite oxide sheets to modified graphene sheets.

Graphene sheets are planar monolayers of sp^2-bonded carbon atoms tightly packed into a two-dimensional honeycomb lattice. These are the basic building blocks of graphitic materials of all dimensionalities [84]. Two-dimensional conducting graphene sheets with extraordinary electronic properties have gained interest as a potent material in high-electron mobility applications [85] and to serve as a nanofiller in composites that can be used in many applications [86, 87]. In 1859, Brodie [88] reported the production of individual graphene sheets by exfoliation of graphite. Since then many routes have been developed to synthesize the metastable two-dimensional graphene sheets. Synthesis routes like chemical exfoliation by intercalation/de-intercalation of guest species in graphite lattice [89], sheets grown epitaxially by CVD of hydrocarbons on metal substrates [90, 91] and thermal decomposition on SiC [92] are unreliable due to low yield and the use of very high temperature, inert atmospheres, and sophisticated instruments. Thermal and chemical reduction of graphite oxide could be used as low-temperature routes to obtain graphene sheets. Though graphene sheets have been obtained on thermal/chemical reduction of GO in composites containing GO [93–95] only recently attempts have been made to synthesize them thermally [96] using GO as a precursor and starting from aqueous colloidal dispersion of GO [97, 98]. GO is derived on oxidation of neutral graphite. It is characterized to be a lamellar solid with unoxidized aromatic regions and aliphatic regions containing phenolic, carboxyl, and epoxide groups as a result of oxidation [99]. Thus the GO platelets are strongly hydrophilic and dispersible in water to form monolayer colloidal dispersions [100]. Alkylamine intercalated GO delaminates to form colloidal dispersions in organic solvents such as alcohols [101]. Delamination of layered solids leads to highly dispersed phases, which forms the basis for the synthesis of layered composites and nanomaterials with unique properties [102, 103]. GO can be delaminated in water and polar protic solvents such as alcohols and the resulting colloidal dispersions are expected to consist of two-dimensional unilamellar/multilamellar GO sheets depending on the nature of the interactions between the GO layers and the solvent. Reduction of these dispersed GO layers results in graphene sheets. Solvothermal reactions have been widely employed in nanomaterial synthesis [104]. Solvothermal reactions due to their unique features such as very high self-generated pressure inside the sealed reaction vessel (autogenous pressure) and containment of volatile products are well suited for the preparation of metastable phases. It would be interesting to see if GO colloidal dispersions could be reduced under solvothermal conditions. Here we report solvothermal synthesis of graphene sheets using colloidal dispersions of GO and alkylamine-modified GO in water and organic solvents (which may also function as reducing agents).

4.1.5 Physical Modifications of Graphene and Graphene Sheets

A variety of physical properties of carbon nanostructures can be obtained by influencing their lattice structure. In addition to the practical significance, the influence of the irradiation on graphene properties is of fundamental scientific interest. One of the methods for modifying the properties of carbon materials is the formation of defects through e-beam irradiation [105]. The effect of the irradiation on bulk graphite has been studied extensively due to graphite applications in thermal nuclear reactors [106, 107]. At the same time, no irradiation data are available for SLG or BLG. In this chapter, we report the investigation of the modification in graphene induced by the low- and medium-energy e-beams. The possible changes due to irradiation include the amorphous, displacement of atoms from the lattice, and excitation of phonons and plasmons, which results in the sample heating. Any of these irradiation effects will lead to modification of the phonon modes. For this reason, we selected the micro-Raman spectroscopy as a main characterization tool. Raman spectroscopy methods are capable of detecting small changes in the crystal structure and have been used extensively in the analysis of the irradiation damage on other carbon materials [108, 109].

The authors report micro-Raman investigation of changes in the single and BLG crystal lattice induced by the low- and medium-energy electron-beam irradiation (5–20 keV). It was found that the radiation exposures result in the appearance of the strong disorder D band around 1345 cm^{-1}, indicating damage to the lattice. The D and G peak evolution with increasing radiation dose follows the amorphization trajectory, which suggests graphene's transformation to the nanocrystalline and then to amorphous form. The results have important implications for graphene characterization and device fabrication, which rely on the electron microscopy and focused ion beam processing.

Zhen Hua Ni and Ting Yu discussed that graphene was deposited on a transparent and flexible substrate, and tensile strain up to ~0.8% was loaded by stretching the substrate in one direction. Raman spectra of strained graphene show significant red shifts of 2D and G band (−27.8 and −14.2 cm^{-1} per 1% strain, respectively) because of the elongation of the carbon–carbon bonds. This indicates that a uniaxial strain has been successfully applied on graphene. We also proposed that, by applying a uniaxial strain on graphene, tunable band gap at K point can be realized. First-principle calculations predicted a band-gap opening of ~300 meV for graphene under 1% uniaxial tensile strain. The strained graphene provides an alternative way to experimentally tune the band gap of graphene, which would be more efficient and more controllable than other methods that are used to open the band gap in graphene. Moreover, our results suggest that the flexible substrate is ready for such a strain process, and Raman spectroscopy can be used as an ultrasensitive method to determine the strain [110].

One of the main obstacles to further industrialization of graphene is the gapless spectrum of quasi-excitations, and thus most of the recent research was devoted to investigation of the electron transport in graphene sheets and possible ways of

generating a controllable mass (energy) gap [111]. On the other hand, the optical properties of monolayer graphene from the beginning proved themselves extraordinary. The very first measurement [14] of optical absorption in graphene revealed a surprisingly huge effect – monoatomic layers absorbed about 2.3% of the incident light, exactly as predicted by the Dirac model; see [112–115]. The quantity and quality of magneto-optical experimental data is growing. In the case of multilayer graphene samples, the first measurements of transmission spectra were reported in [116], and the work was later continued in a series of papers, for example [117–120]. More recently, both the Faraday rotation and transmission in mono- and multilayer-epitaxial graphene were measured in [121]. The Faraday rotation appeared to be unexpectedly large and was dubbed the "giant Faraday effect." The experimental setup permitted a detailed investigation of the so-called cyclotron resonance regime. In this chapter, we recalculated the polarization operator of the Dirac quasi-particles in graphene in an external magnetic field and established a clear connection between its components as well as the optical properties of both suspended and epitaxial graphene. We showed that in a number of different regimes the rotation of polarization of light passing through monolayer graphene samples is gigantic being of the order of 0.1 rad, while the absorption can reach 40%.

4.2
Graphene and Graphene Sheets Based Nanocomposites

Because of graphene's exceptional thermal, mechanical, and electronic properties [122], it stands out as the most promising candidate to be a major filling agent for composite applications. Graphene nanocomposites at very low loading show substantial enhancements in their multifunctional aspects, compared to conventional composites and their materials. This not only makes the material lighter with simple processing, but also makes it stronger for various multifunctional applications [123]. The remarkable properties of graphene are able to improve the physicochemical qualities of the host matrix upon distribution. This helps in strengthening and increasing the interfacial bonds between the layers of graphene and the host matrix. It is this bonding that dictates the emergence of the cumulative properties of graphene in reinforced nanocomposites [124]. Kuilla *et al*. [124], in their extensive review article on graphene-based polymer nanocomposites, have systematically explained the importance and use of graphene in various host materials. They also carried out a remarkable comparison of various nanofillers and listed their important applications in detail. In the world of composites, theoretical analysis plays a crucial role in understanding their mechanisms, molecular interactions, and physical properties and their potential applications. A number of simulation tools provide cumulative or specific results for composite analysis. With the aid of these computational tools, a broad understanding and guide to successful research can be systematically achieved. Such theoretical investigations help the investigators to precisely optimize their case study to perfect the composite product [125].

In recent years, there have been some significant research papers on graphene-based composites with a polymer matrix. Jang and Zhamu [126] reviewed the processing of graphene nanoplatelets (GNPs) for fabrication of composite materials [126]. Mack *et al*. [127] prepared nanocomposites of polyacrylonitrile (PAN) nanofibers strengthened by GNP, which they demonstrated to having improved mechanical qualities [127]. Research by Hansma *et al*. [128] showed successful fabrication of graphene-based nanocomposites. They successfully optimized the amount and combination of adhesives and high-strength nanostructures (graphene) needed to yield a strong, low-density, lightweight, and damage-resistant composite material [128]. Ramanathan *et al*. [129] reported an unprecedented shift in the glass transition temperature (T_g) of a polymer nanocomposite with functionalized graphene sheets (FGSs). They observed that, by the addition of FGSs (1 wt%) to the PAN, the T_g of the composite material increased by 40 °C, whereas, when only 0.5 wt% was added to PMMA, they observed a 30 °C rise in T_g [129]. Also, they observed that by addition of 1 wt% graphene to PMMA, an 80% increase resulted in the elastic modulus and a 20% increase resulted in the ultimate tensile strength. Their comparative research concluded that monolayered functionalized graphene serves as the best nanofiller among all examined nanofillers. Das *et al*. [130] employed the nanoindentation technique to the graphene-reinforced nanocomposite fabricated by using polyvinyl alcohol (PVA) and PMMM. The results showed significant improvement in crystallinity, elastic modulus, and hardness through the addition of only 0.06 wt% of graphene. The authors suggested that the enhancement was due to close mechanical interaction between the host (polymer) matrix and the layers of graphene. This interaction successively provides and dictates a better load transfer within the host matrix and the nanofiller [130]. Yu *et al*. [131] identified that epoxy-based few-layer graphene nanocomposites show fascinating properties suitable for the electronics industry, ideal for the development of thermal-interface-based materials [131]. Zhang *et al*. [132] and Liu *et al*. [133] successfully synthesized graphene–fullerene-based hybrid nanocomposites [132, 133]. Booth *et al*. [134] demonstrated the successful synthesis of robust 100 μm thick macroscopic graphene membranes that can bear heavy loads [134]. According to Luechinger *et al*. [135], the introduction of metal nanoparticles in the host matrix along with graphene has attracted a lot of researchers due to the advantage it provides by facilitating an improved interparticle contact (i.e., contact between the metal particle and the host matrix) [135]. Watcharotone *et al*. [136] fabricated a transparent, electrical conductor by employing a simple sol–gel, spin-coating, chemical reduction, and thermal-curing route. The group used graphene oxide (GO) sheets mixed in the silica solution to obtain metal-encapsulated graphene nanocomposites [136]. In 2008, Chen *et al*. [13] fabricated graphene-conducting paper that was electrically conducting, mechanically strong, and biocompatible. They uniformly dispersed graphene sheets in a solution using vacuum filtration followed by moderate thermal annealing. Recently, Cheng *et al*. [137] synthesized carbon-coated SnO–graphene sheet composites in a green approach via a single-pot hydrothermal route. The composite was fabricated as an anode material for a

Li-ion battery, and it exhibited high storage capacity and improved cyclic performance [137]. Similarly, Perera *et al*. [138] synthesized V_2O_5 nanowire–graphene nanocomposite as an electrode material. The composite electrode exhibited an equilibrated electric double layer (EDL), energy density of 38.8 W kg^{-1}, and pseudo capacitance at a power density of 455 W kg^{-1}, and, also, the composite material showed a high specific capacitance of 80 F g^{-1}. These results clearly indicate that the composite electrode was capable of effective storage and deliverance of charges toward high-energy applications [138]. Lee *et al*. [139] used cryo milling to synthesize fine particles of graphene and chitosan. The mixture was sonicated and layered to form a composite. The graphene particles conferred a cumulative effect in improving the mechanical attributes of the composite and also decreased the agglomeration quotient of graphene during mixing [139]. Guo *et al*. [140] prepared a water-dispersed graphene–tryptophan–PVA nanocomposite for improving tensile strength, modulus, and thermal stability. There was a 23% increase in tensile strength when only a small loading of graphene (0.2 wt%) was introduced in the PVA matrix [140]. Ansari *et al*. [141] studied the DC electrical conductivity retention of their indigenously prepared graphene–PANI–MWCNT nanocomposite in air and also assessed the cyclic aging. They found that PANI–graphene showed higher electrical conductivity and good stability for the DC electrical conductivity retention under isothermal conditions [141]. Jeon *et al*. [142] prepared an exfoliated-graphene (EG) cellulose acetate nanocomposite using the melt compounding method. They found that exfoliated graphene (EG) was uniformly dispersed in the host matrix with lower loadings. They also found that the composite had high thermal stability and improved conductivity and modulus [142]. The great number of application- and property-oriented possibilities suggests that future research and prospects for graphene-based nanocomposites are likely to expand tremendously in every discipline, with many surprises and products in store.

4.2.1
Graphene and Graphene Sheets/Rubber Based Nanocomposites Preparation, Characterization, and Applications

The investigations on graphene or CNT-based polymer composites are mainly focused on plastics matrices such as polyamide 6 (PA6) [143], polycarbonate (PC) [144], epoxy [145], polyurethane (PU) [146], polystyrene (PS) [86, 147], PMMA [148, 149], or poly(styrene-*b*-isoprene-bstyrene) (SIS) block copolymer [150]. There are only a few of studies on graphene or CNTs/rubber composites [151–154]. One important reason is that it is difficult for nanoparticles to be dispersed in rubber matrices because of their high viscosity or low surface energy. Conductive rubbers are critically needed in the fields such as ESD (electrostatic discharge) and EMI (electromagnetic interference) shielding materials, electronics packaging, telecommunication antenna, mobile phone parts, and frequency shielding coatings for aircraft and electronics. However, the physical interaction between rubbers and nanoparticles are weaker than that between plastics and

nanoparticles. It is of importance to understand the mechanism of the dispersion of nanoparticles in rubbers.

Haiqing Hua, and Li Zhao reports a novel, scalable, and inexpensive approach to fully disperse CNTs in silicone rubber by the addition of graphene. In comparison to graphene, the dispersion of multiwalled carbon nanotubes (MWCNTs) in a silicone rubber matrix is extremely difficult although both of them possess similar physical structures. The different dispersion behavior of graphene and MWCNTs could be attributed to the difference in their interaction with polymer matrix and their geometry. Based on SEM, TEM (transmission electron microscopy), and XRD analysis, we find that the dispersion of MWCNTs in silicone rubber is dramatically improved by the addition of graphene. Graphene acts as a compatilizer since it shows strong interaction with both polymer matrix and MWCNTs. This method provides a simple route to enhance the dispersion of CNTs and improve the electrical property of the polymer composites. The synergic effect of the hybrid materials may not be limited to the applications in polymer composites.

The rubber composites were fabricated as follows: (i) Silicone rubber (MVQ, before crosslinking) was dissolved in THF to obtain homogeneous solution. (ii) Graphene (or MWCNTs) was dispersed in THF. The mixture was sonicated for 1 h to get stable suspension. (iii) The above (i) and (ii) suspensions were mixed together and sonicated for 30 min to obtain homogeneous suspension. (iv) THF was evaporated at 50 °C, and the mixture was dried in a vacuum oven. (v)

Curing agent was added to the mixture, and the resulting compound was then moved to a vulcanizing machine for curing followed by vulcanizing at 160 °C for 12 min to obtain the composites [155].

There exists a good interaction between graphene and silicone rubber matrix. On one hand, the eOHe on graphene may form hydrogen bonds with the eOe on silicone rubber. On the other hand, there is huge contact surface area between silicone rubber and graphene because graphene has very large specific surface area and each plane of graphene can contact with silicone rubber. Graphene can be dispersed uniformly in silicone rubber as discussed above. Since graphene has good interaction with silicone rubber and CNTs, graphene plays a role of compatilizer for MWCNTs and silicone rubber, which facilitates the dispersion of MWCNTs in silicone rubber. Based on the aforementioned analysis, we believe that the most important factor for the excellent dispersion of MWCNTs assisted by graphene is the strong interaction between graphene and the matrix as well as the strong interaction between graphene and MWCNTs. Graphene has a large surface area and CNTs have a great aspect ratio. One-dimensional and two-dimensional material cooperates, forming a "conductive bridge" in the silicone rubber as shown in the schematic diagram (Figure 4.7).

Graphene has strong interaction with silicone rubber and also breaks up the agglomeration of MWCNTs. The remarkable enhancement is due to the synergistic effect of graphene and MWCNTs. In this work, we report a simple and effective way to disperse CNTs and graphene in silicone rubber. The excellent dispersion of CNTs can be achieved with the aid of graphene because of the strong interaction

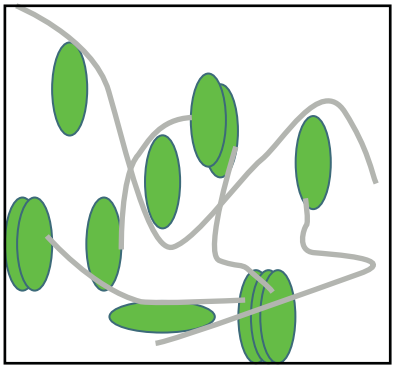

Figure 4.7 Schematic of the synergetic interaction between graphene and carbon nanotubes.

between graphene and silicone rubber matrix as well as the strong interaction between graphene and CNTs.

Huiqin Lian and Shuxin Li studied butyl rubber, IIR nanocomposites based on modified graphene sheets, were fabricated by solution processing followed by compression molding. MG was prepared from natural graphite, and NG through the graphite oxide route. XRD showed that the exfoliated MG was homogeneously dispersed in the IIR matrix with doping levels of 1–10 wt% as evidenced by the lack of the characteristic graphite reflection in the composites. In contrast, the graphite retained its stacking order and showed the sharp characteristic peak in the NG–IIR composites. SEM images of the fracture surfaces of the IIR matrix showed that MG nanofillers exhibited better compatibility than did NG. The mechanical properties of the MG–IIR nanocomposites were significantly improved due to the efficient distribution of the large surface area of the MG sheet. The tensile modulus of nanocomposites with doping level of MG 10 wt% was 16 times that of the pure IIR [156].

The procedure used to prepare the MG–IIR nanocomposite sheets is shown in Figure 4.8. First, based on Hummers' method, the graphite was oxidized by concentrated sulfuric acid to create polar hydrophilic groups (COOH, C¼¼O, OH) on the surface. The GO was dispersed in cetyltrimethylammonium bromide (CTAB) solution (20 wt%) and ultrasonicated for 0.5 h, followed by mechanical stirring at 258 °C for 24 h. During this process, the tertiary amine reacted with the carboxylic groups on the oxidized surface via an acid–base reaction or via hydrogen bonding between the surface OH or C¼¼O group and the amine groups. The suspension was filtrated and washed three times with water and dried at 408 °C in a vacuum for 24 h. The resulting MG was added to the 15 wt% solution of IIR in hexane by sonication for 0.5 h to form a colloidal suspension. Then the mixture was stirred for 6 h at 258 °C. The amounts of MG/NG added were 0, 1, 3, 5, and 10 wt% of the mass of rubber. The composite solution was then coagulated by adding methanol and the precipitated nanocomposite was dried in a vacuum. Finally, sheet samples were prepared by vacuum compression molding using a 2 mm thick spacer at 100 °C under 10 MPa for 10 min. using this procedure, the NG–IIR composite sheets were prepared.

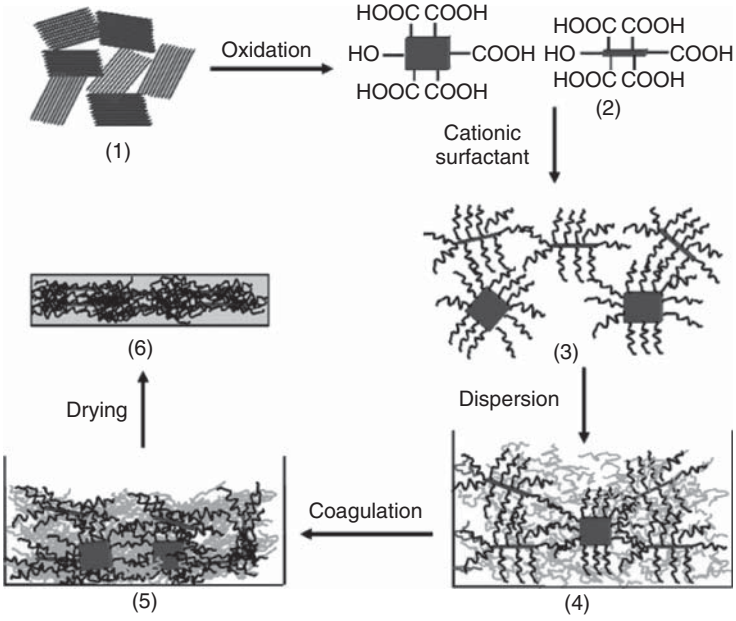

Figure 4.8 Schematic representations of the fabrication of MG-IIR nanocomposite membrane.

The as-made membrane was characterized by XRD (Scintag PAD X diffractometer, Cu Ka source, operated at 45 kV and 40 mA). The samples were scanned with 58/min between 2y of 28–308. SEM observation was performed using Tecnai T12, at an acceleration voltage of 15 kV with gold coating. Composite samples were imaged by first fracturing in liquid nitrogen. TGA was performed using a TA Instrument Q500 attached to an automatic programmer from ambient temperature to 500 °C at a heating rate of 10 °C min^{-1} in a nitrogen atmosphere. A TA instrument Q1000 was used to record the DSC traces at a heating rate of 10 °C min^{-1}. Measurements of mechanical properties were conducted at 25.6–28 °C according to relevant ISO standard (ISO 37).Tensile tests were measured on an Autograph AGS-J SHIMADZU universal testing machine at a crosshead speed of 500 mm min^{-1}. The reported values were the average of five measurements.

Commercial butyl rubber (IIR) is a copolymer of isobutylene and a small amount of isoprene. It is employed in the inner linings of automobile tires and in other specialty applications due to its characteristics of chemical inertness, impermeability to gases, and weatherability. However, due to the presence of isoprene monomer units in the backbone, unsaturated bonds in IIR can be attacked by atmospheric ozone leading to oxidative degradation and chain cleavage. Also, in some fields, such as aerospace, aircraft, and high-vacuum systems, IIR does not meet the extremely high-gas barrier as well as the high mechanical properties requirements. Therefore, there exists a continuous interest

in lowering gas permeability and improving the mechanical properties of IIR by various techniques [157, 158].

Hernández and Bernal [159] described Natural rubber (NR) and FGSs nanocomposites were prepared by conventional two-roll mill mixing. The morphology and structure of the FGS were characterized confirming the successful exfoliation of the FGS. The strong rubber-to-filler interactions accelerate the cross-linking reaction, increase the electrical conductivity, and cause an important enhancement on the mechanical behavior of the NR nanocomposites. The nanofiller does not affect the molecular dynamics of NR, while the presence of vulcanizing additives slows down the segmental motions and decreases slightly the time scale of the global chain dynamics in NR/FGS nanocomposites. These functional properties make NR/FGS nanocomposites a promising new class of advanced materials. The results show that this method produces a better dispersion and exfoliation of graphene in the matrix and contributes to an increase in the tensile strength compared to conventional direct mixing.

Few interesting studies have already been reported illustrating the potential of graphene nanocomposites based on rubber matrices [156, 160–162]. Surprisingly, negligible studies have been conducted in the preparation and characterization of NR/graphene nanocomposites. To the author's best knowledge, only a patent [163] and a recently published work made by Yuan *et al*. [164] have been reported using an NR matrix. Yuan *et al*. have proposed a new method, that is, ultrasonically assisted latex mixing and *in situ* reduction (ULMR) process to prepare NR/graphene composites. GO was dispersed into NR latex using an ultrasonic field and was then reduced*in situ*, followed by latex coagulation to obtain the NR/graphene master batch. The results show that this method produces a better dispersion and exfoliation of graphene in the matrix and contributes to an increase in the tensile strength compared to conventional direct mixing.

4.2.2
Graphene and Graphene Sheets/Thermoplastic Based Nanocomposites Preparation, Characterization, and Applications

Despite the great interest in graphene nanocomposites, most of the work cited in the literature deals with thermoset nanocomposites [165]. Only recently, thermoplastic nanocomposites have been prepared by melt mixing or *in situ* polymerization, using GO itself as catalyst. On the other hand, thermoplastic matrix composites and nanocomposites are finding increasing interest in both academic and industrial research, mainly due to the advantages of thermoplastics in terms of manufacturing costs, impact resistance, and environmental compatibility [166]. Analysis of the materials effect of nanofillers on thermoplastic matrix is rather complex, due to the influence of the nanofiller on the crystallization behavior of the matrix. Therefore, any observed modification of property can be assigned to either the addition of the nanofiller or to the modification of the crystalline structure of the matrix induced by the nanofiller itself.

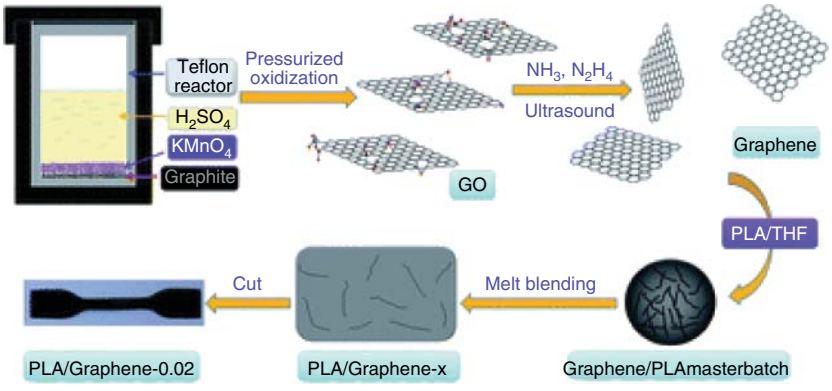

Figure 4.9 Schematic representation of graphene preparation from graphite by pressurized oxidation and multiplex reduction.

Bao *et al.* [167] prepared graphene from graphite by pressurized oxidation and multiplex reduction (Figure 4.9). The pressurized oxidation is advantageous in easy operation and size-control, and the multiplex reduction, based on ammonia and hydrazine, produces single-atom-thick graphene (0.4–0.6 nm thick), which can be directly observed by AFM. A masterbatch strategy, which is feasible in "soluble" thermoplastic polymers, is developed to disperse graphene into poly(lactic acid) by melt blending. The graphene is well dispersed and the obtained nanocomposites present markedly improved crystallinity, rate of crystallization, mechanical properties, electrical conductivity, and fire resistance. The properties are dependent on the dispersion and loading content of graphene, showing percolation threshold at 0.08 wt%. Graphene reinforces the nanocomposites but cuts down the interactions among the polymer matrix, which leads to reduced mechanical properties. Completion of the reinforcing and the reducing causes inflections around the percolation threshold. The roles of the heat barrier and mass barrier effects of graphene in the thermal degradation and combustion properties of the nanocomposites are discussed and clarified.

Ji-Eun An, Gil Woo Jeon [168] have prepared a series of polypropylene/exfoliated graphene (PP/EG) nanocomposite films via efficient melt compounding and compression, and investigated their morphology, structures, thermal transition behavior, thermal stability, electrical, and mechanical properties as a function of EG content. For this purpose, EG, which is composed of disordered graphene platelets as reinforcing nanoscale fillers, is prepared by the oxidation/exfoliation process of natural graphite flakes. SEM images and XRD data confirm that the graphene platelets of EG are well dispersed in PP matrix for the nanocomposites with EG contents less than 1.0 wt%. It is found that thermo-oxidative degradation of PP/EG nanocomposites is noticeably retarded with the increasing of EG content. Electrical resistivity of the nanocomposite films was dramatically changed from ~1016 to ~106 Ω cm by forming electrical percolation threshold at certain EG content between 1 and 3 wt%.

Tensile drawing experiments demonstrate that yielding strength and initial modulus of PP/EG nanocomposite films are highly improved with the increment of EG content.

Zhang *et al.* [153] prepared graphene nanosheets by complete oxidation of pristine graphite followed by thermal exfoliation and reduction. Polyethylene terephthalate (PET)/graphene nanocomposites were prepared by melt compounding. TEM observation indicated that graphene nanosheets exhibited a uniform dispersion in PET matrix. The incorporation of graphene greatly improved the electrical conductivity of PET, resulting in a sharp transition from electrical insulator to semiconductor with a low percolation threshold of 0.47 vol%. A high electrical conductivity of 2.11 S m^{-1} was achieved with only 3.0 vol% of graphene. The low percolation threshold and superior electrical conductivity are attributed to the high aspect ratio, large specific surface area, and uniform dispersion of the graphene nanosheets in PET matrix.

Eswaraiah *et al.* [169] described that graphene–PVDF nanocomposites are synthesized by a simple shear cum solvent casting technique. The homogeneous and stable dispersions of graphene in polymer solution have been attained after functionalization. The 40 morphology of the graphene and graphene–PVDF nanocomposites have been characterized by SEM, which reveals the 3D interconnecting conducting network of graphene in polymer matrix. The analysis of the change in voltages of different nanocomposite films reveal that 2.45 wt% f-G-PVDF composite films show higher strain sensing performance compared with its counterparts based on CNT polymer composites. For higher concentrations of f-G, low strain sensing performance was observed due to the overlap of nanofillers. The rapid changes in contact and tunneling 50 resistances between optimum concentration of graphene nanofillers in PVDF polymer cause high performance in strain sensing and it can be attributed to the 2D nature and flexibility of the graphene.

4.2.3
Graphene and Graphene Sheets/Thermoset Based Nanocomposites Preparation, Characterization, and Applications

The phenylethynyl terminated thermosetting polyimide (PI) and PI/GO nanocomposites were prepared via a polymerization of monomer reactants process. Dimethyl ester of 4,4-oxydiphthalic acid (ODPE) and monomethyl ester of 4-phenylethynylphthalic acid (PEPE) were prepared according to the method of Serafini *et al.* [170] ODPA (1.86 g) and methyl alcohol (MeOH, 20 ml) were placed in a 100-ml flask fitted with a magnetic stirrer and reflux condenser. The mixture was refluxed for 2 h with stirring to yield the dimethyl ester of ODPE solution. The PEPE solution was prepared by refluxing a mixture of PEPA (1.49 g) and MeOH (15 ml) for 3 h. To a solution of ODA (1.8 g) in NMP (7.5 ml) in a 100-ml three-necked flask fitted with stirrer, N2 inlet, and gas outlet, and ODPE and PEPE solution in MeOH were added successively.

The mixture was stirred for 3–5 h at room temperature to yield a homogeneous matrix resin solution with solid content of 30–40 wt% (Figure 4.3). For the

preparation of the PI/GO composite, GO was added to the resin solution at different concentrations by weight and subjected to ultrasonication for 3 h to insure uniform dispersion. The homogeneous matrix resin and composite solution were painted on the steel block and put in an air-circulation oven at 100, 200, 300, and 375 °C for 1 h, respectively, to yield the film specimens.

Thermogravimetric analysis indicated that the incorporation of GO increased the thermal stability of the PI at low filling content. The friction and wear-testing results of the PI and PI/GO nanocomposites under dry sliding condition against GCr15 steel showed that the addition of GO evidently improved the friction and wear properties of PI, which were considered to be the result of the formation of uniform transfer film and the increasing of load-carrying capacity. The friction and wear properties of the PI and PI/GO nanocomposites were investigated on a model ring on-block test rig under dry sliding conditions against the GCr15 steel. Experimental results showed that the addition of GO evidently improved the friction and wear properties of PI, which were considered to be the result of the formation of uniform transfer film and the increase of load carrying capacity. The optimum GO content of nanocomposite for tribological properties is 3 wt%, which could be a potential candidate for tribo-material under dry sliding condition against GCr15 steel.

4.2.3.1

Characterization of GO, PI, and PI/GO Nanocomposites

AFM and TEM were used to characterize the GO as shown in Figure 4.10. Typical AFM image (Figure 4.10a) of GO revealed that the GO sheet had heights of about

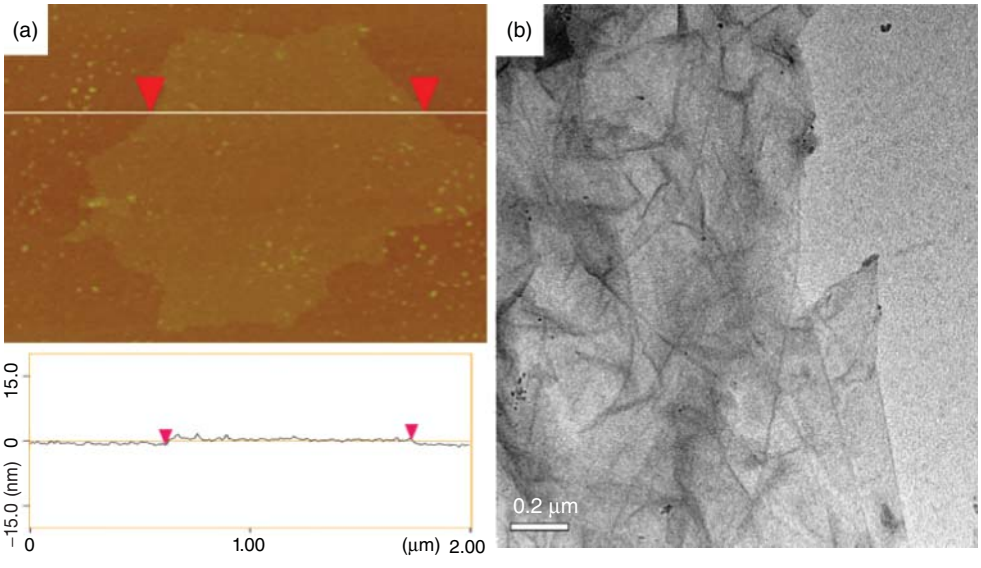

Figure 4.10 (a) Tapping mode AFM topographic image and height profiles of GO and (b) TEM images of layered GO.

1 nm and lengths of about hundreds of nanometers to micrometers, indicating that full exfoliation of GO were indeed achieved by an improved Hummers' method. Chemically modified GO often has oxygen-containing functional groups on its surface, and the GO sheets tend to fold back, thus preventing them from stacking back and from regraphitization. As shown in Figure 4.10b, the TEM image demonstrated that the GO had nanosheet morphology with some corrugations, which was consistent with the result obtained from AFM studies.

The PMR thermosetting PI matrix resin solution was prepared using monomers of PEPE, ODPE, and ODA at a molar ratio of 2:*n* in a mixture of MeOH and NMP at room temperature (Figure 4.11), with n equal to two, giving a calculated molecular weight of about 1600. The PI matrix resin composites solution, which was added to the GO, was thermally cured to yield a cross-linked material after passing through a series of thermal chemical reactions. The cross-linked matrix resin of the composites showed good adhesion to steel, which insures that the film specimens were retained on the steel block in the dry lubricated sliding tribological testing process.

FT-IR experiments were carried out to investigate GO, PI, and the interaction between GO and PI (Figure 4.12). The characteristic absorption bands related to GO are O–H(carboxyl) at about 1423/cm, C═O in carboxylic acid and carboxyl moieties (carboxyl) at 1738/cm, C═C from unoxidized sp^2 cc bonds at 1635/cm, C–O (epoxy or alkoxy) at 1070/cm, and O–H stretching at 3429/cm [171, 172]. Pure PI exhibited obvious absorption peaks arising from the asymmetric and symmetric stretchings of C═O groups in imide rings at about 1779 and 1720/cm. Another characteristic absorption of the imide group arising from C–N stretching appeared at around 1380/cm. The results showed that the PIs matrix had formed through the thermal imidization procedure.

To the 1, 3, and 5 wt% GO content composites, the peaks of GO at 1423/cm of O–H depressed greatly, accompanied by the combination of the C–O–C stretching vibration of PI and epoxy/ether C–O stretch of GO at 1070/cm. This variation indicates that reaction did occur between the PI and the GO. The dispersion state of GO in PI was studied by XRD, which is an important tool for determining the exfoliation of GO in the composites [173, 174]. Figure 4.13 shows the XRD patterns of graphite oxide, PI, and PI/GO composites. The characteristic diffraction peak of graphite oxide appears at about $2h = 11.7°$, corresponding to a *d*-spacing of 0.75 nm. The PI shows a broad peak at around $2h = 18.5°$, revealing its amorphous nature. After GO was incorporated into the PI matrix, the XRD patterns of PI/GO composites were almost the same as pure PI. The disappearance of the characteristic diffraction peak for GO clearly demonstrates that GO was fully exfoliated in the polymer matrix. Low friction coefficient and wear rate and the PI/GO composites of low filler content could be potential candidates for tribo-material under dry sliding condition against GCr15 steel (Figure 4.14) [175].

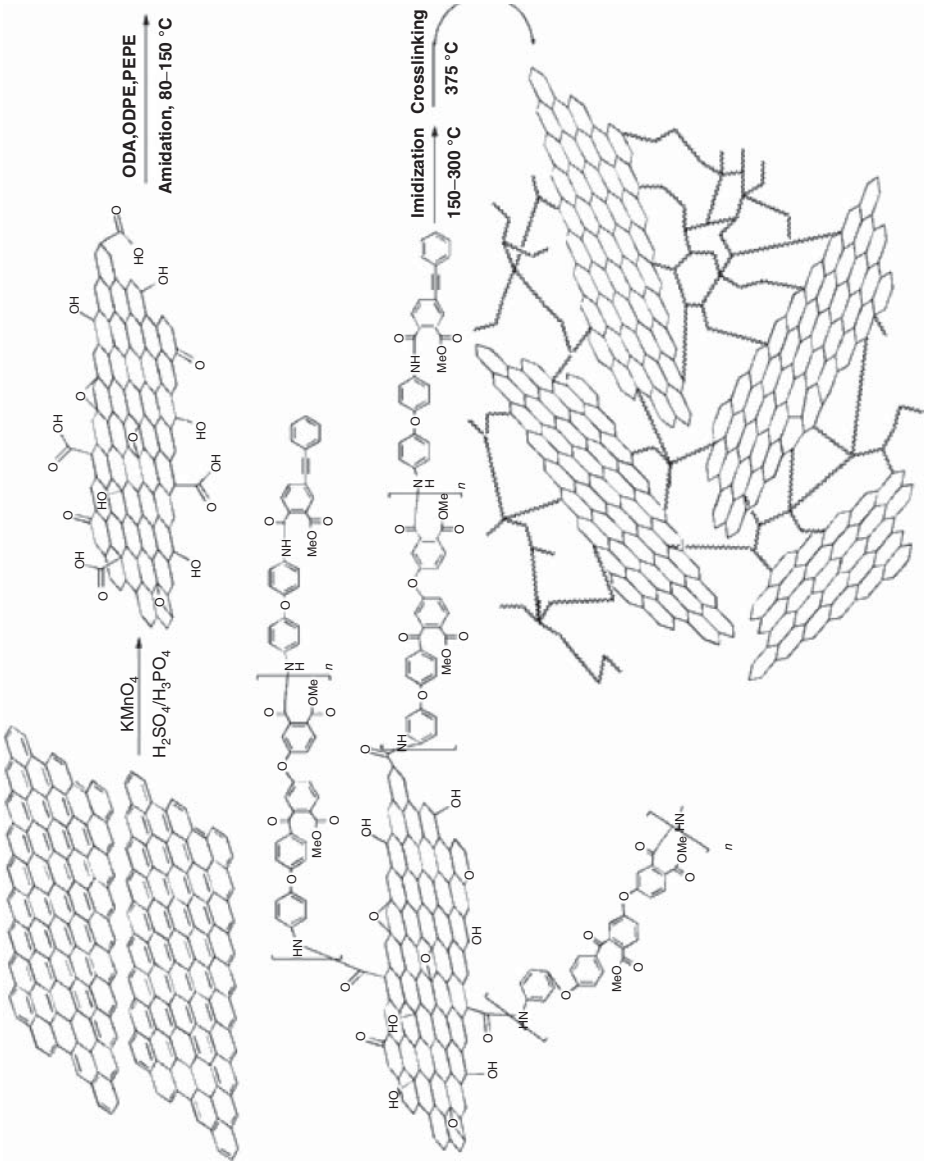

Figure 4.11 Synthesis of thermosetting PMR PI/GO nanocomposites.

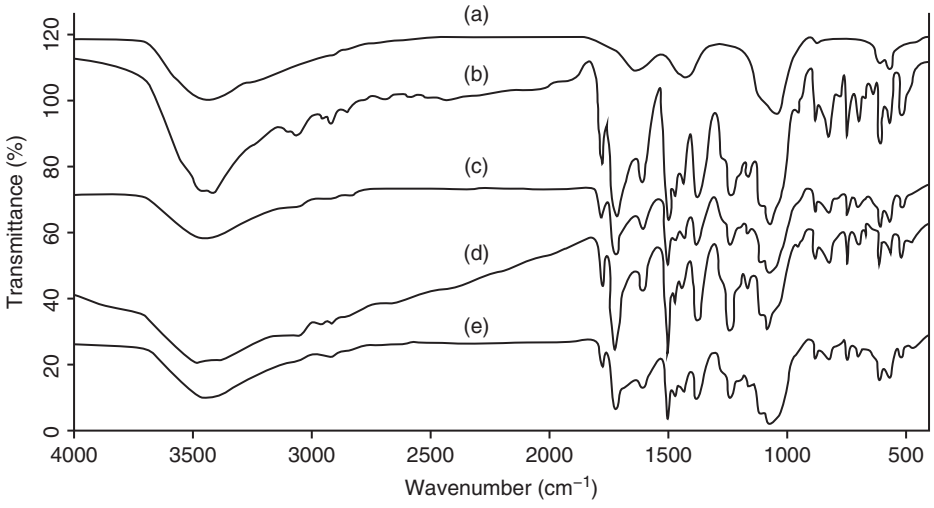

Figure 4.12 FTIR spectra of GO (a), PI (b), and PI/GO composites with GO content of 1 wt% (c), 3 wt% (d), and 5 wt% (e).

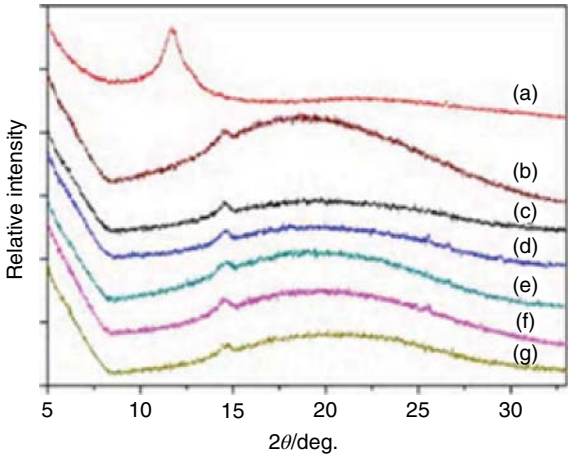

Figure 4.13 XRD patterns (a) Go, (b) PI, (c) 1 wt%, (d) 2 wt%, (e) 3 wt%, (f) 4 wt%, and (g) 5 wt% GO/PI composite.

4.2.4
Interfacial Interaction of Graphene and Graphene Sheets in Nanocomposites

The scenario is not quite ready to develop the graphene polymer nanocomposite (GPN), especially with graphene as the reinforcement filler. Before achieving high performance of GPNs, the following must be considered: (i) homogeneous dispersion or full exfoliation of graphene sheets in polymer matrix and (ii) strong interfacial interaction between the nanosheets and the surrounding polymer host,

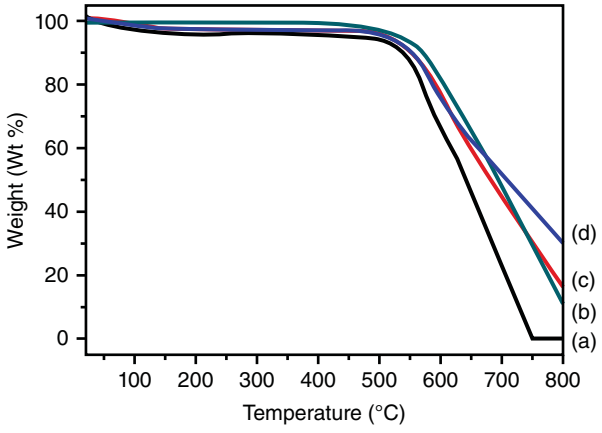

Figure 4.14 TGA curve of PI (a) 1 wt% and (d) 5 wt% GO/PI composites at a heating rate of 10 °C min^{-1} in air.

which is responsible for the effective transfer of external load. Because of the high specific surface area and van der Waals interaction between the interlayers of graphene sheets, graphene tends to form irreversible agglomerates or even restack, which lowers its effectiveness as a nanofiller for reinforcement. Much of current research is focused on dispersion improvement and many methods have been developed such as functionalization of graphene nanosheets to compatibilize the nanofiller with the matrix [176], blending with polymers prior to the chemical reduction of GO [177], *in situ* intercalative polymerization of monomer [178], and so on.

In fact, an individual graphene sheet does not contain any of the functional groups on its surface, while those directly prepared by chemical or thermal reduction of GO bear little functional groups [179], which is not enough to produce strong interfacial adhesion between the nanosheet and polymer matrix. Therefore, knowledge of how to exert the graphene's reinforcement via the strong interfacial adhesion and the transfer of its excellent mechanical property to the polymer matrix in the nanocomposites is very urgent [180]. Until now, few works has concerned the interfacial interaction between graphene sheets and polymer matrix in GNPs [181]. GO, which contains various oxygen functional groups on their basal planes and edges, is hydrophilic and can be easily dispersed as individual sheets in polar solvents to form a stable suspension and graphene/polymer composites are subsequently produced after the reduction of GO [48], where the nanosheet can be completely exfoliated and homogeneously dispersed in the matrix. Whereas, it is necessary to increase the amount of functional groups on the surface of graphene sheets to enhance the interfacial interaction between graphene sheets and polymer matrix for reinforcement improvement. To the best of our knowledge, the most effective approach is to use a chemical bond between the filler and polymer matrix.

For example, the soluble polymer PVA was chosen and partially reduced graphene oxide (PRGO) was prepared by controlled chemical reduction, where a few oxygenated functional groups were preserved for covalent bonding. The graphene/PVA nanocomposites were then prepared via a solution blending using water as the processing solvent. Interfacial interaction was dramatically enhanced due to chemical linkage and hydrogen bondings between graphene and the PVA backbone, which favored an improvement in the thermal and mechanical properties of the nanocomposites [182].

4.3 Graphene and Graphene Sheets in Thermoplastic Based Blends Preparation, Characterization, and Applications

Polymers have been combined with other plastics to form blends mixed with talc and clay to give filled systems, and extruded and molded with fibers and other anisotropic reinforcements to yield composite and hybrid materials. This simple mix-and-match approach has allowed the plastics engineer to use a small library of polymers to produce a bewildering array of useful products that are capable of possessing extremes of property values. The latest addition to this palette is graphene, a single atomic layer of carbon whose existence had been known for a long time but which was produced and identified only as recently as 2004. Andre K. Geim and Konstantin S. Novoseloe of the University of Manchemer, UK, were awarded the 2010 Nobel Prize in Physics for their success in isolating this single sheet of carbon atom. As a result of their accomplishment, the landscape of polymer nanocomposites is changing. It is true that carbon-based materials such as diamond, lonsdaleite, and graphite have been known to mankind for ages. However, renewed enthusiasm in the polymer nanocomposites research community is primarily due to the special properties of graphene that can he transferred to plastics and the fact that graphene is derived from inexpensive precursors. The advantages of price and performance of graphenes challenge carbon nanotubes (CNTs) in nanocomposites, coatings, sensors, and energy-storage device applications. And then there are applications that can only be dreamed about. Indeed, in the words of Andre Geim, "Graphene is a wonder material with many superlatives to its name". This is evident from the huge singe of studies in the current literature. Why such an interest in graphene? Is this simply graphene "hype," or are there application opportunities for graphene based composite structures [183].

Vikas Mittal and Nadejda Matsko described the synthesis of PE-CPE blends and their graphene oxide nanocomposites with reduced low-temperature brittleness (Figure 4.15). To generate blend samples, PE was melt mixed with CPE25 and CPE35 polymers in mini-twin conical screw extruder (MiniLab HAAKE Rheomex CTW5, Germany) using a mixing temperature of 170 °C for 3 min at 60 rpm (batch size of 5 g). Pure polymer was also similarly melt processed at 170 °C. To achieve nanocomposites, CPE was dissolved in *p*-xylene (3% solid content) at 100 °C under reflux and was mixed with sonicated graphene oxide suspension in *p*-xylene at

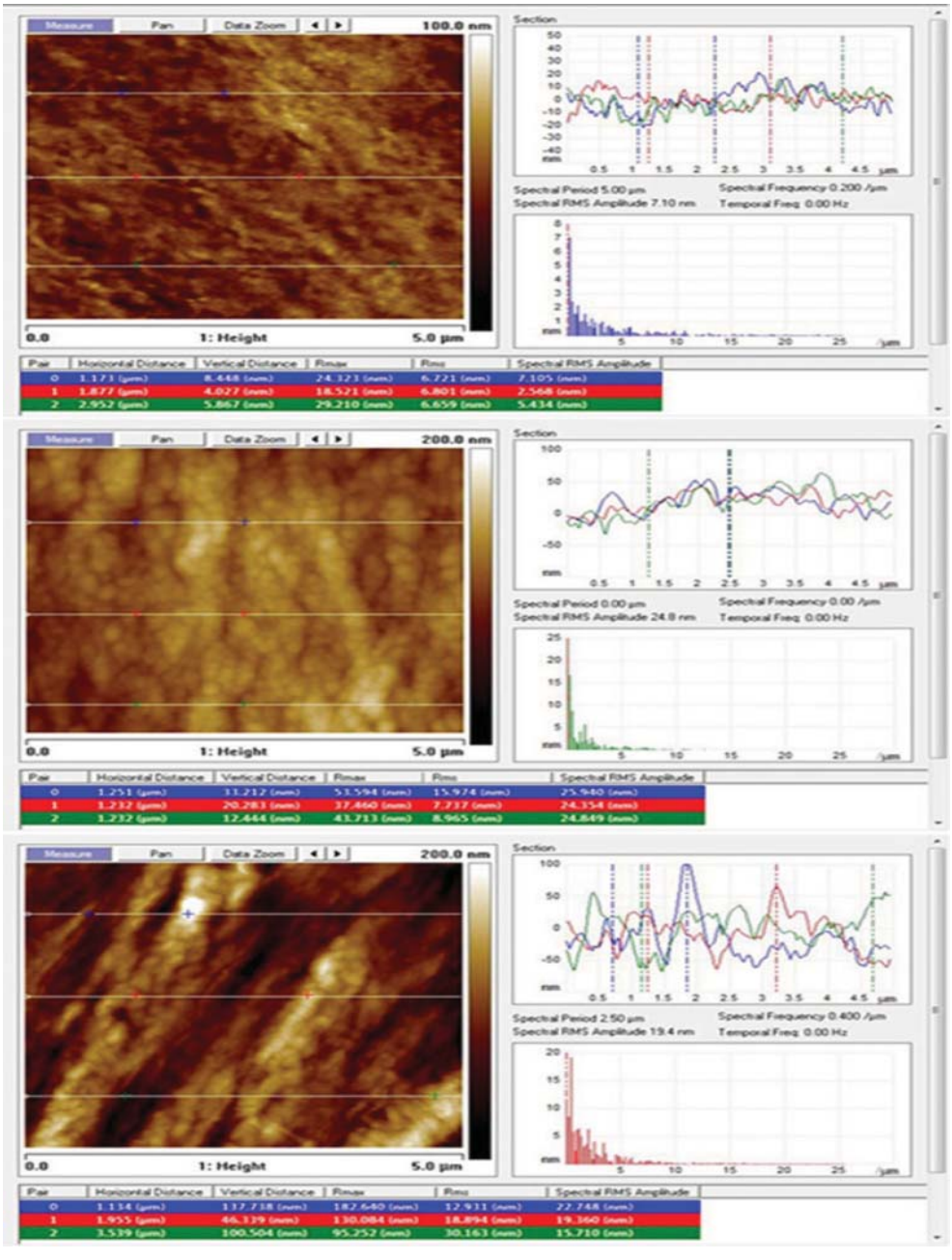

Figure 4.15 AFM height images and corresponding height corrugation analysis for PE (top), PE + 5% CPE25 (middle), and PE + 5% CPE35 (bottom) when sectioned at −140 °C.

100 °C. The mixture was cooled to room temperature and was kept overnight at ambient conditions followed by 40 °C for 24 h. The generated CPE graphene oxide masterbatches were melt mixed with PE at 190 °C using mini-twin screw extruder using the similar processing conditions that were used to form blends. The amount of graphene oxide in the nanocomposites was fixed at 0.1 wt%. Melt mixing of PE–graphene oxide was also similarly performed at 190 °C for comparison. Disc-shaped test samples for rheological characterization were prepared using mini-injection molding machine (HAAKE MiniJet, Germany) at a processing temperature of 170 °C for pure polymer and PE-CPE blends, whereas the temperature was 190 °C for nanocomposites. The injection pressure was maintained at 700 bar for 6 s; whereas, holding pressure was 400 bar for 3 s while the temperature of the mold was kept at 50 °C. The fracture testing bars with dimensions 2.5 cm in length, 0.4 cm breadth, and 0.2 cm thickness were also similarly injection molded. For the characterization methods for the microscopy analysis, the composite samples were mounted in special holders, which at the same time fit in the microtome and were suitable for the examination of the block face by AFM. Block faces of the composite samples were obtained using a Leica Ultracut E microtome (Leica, Austria) equipped with a diamond knife (Diatome, Switzerland) at −140 and −180 °C. The block faces of specimens after cryo-ultramicrotomy were investigated at ambient conditions using Dimension 3100 AFM/SPM (Veeco, USA) atomic force microscope. AFM images were collected in tapping mode using silicon nitride cantilevers with natural frequencies in the 300-kHz range (force constant, 20 N m^{-1}; tip radius, 10 nm (NT-MDT, Russia)). AFM image processing was performed using Nanoscope v720 software (Veeco, USA).

Miscibility analysis of the samples was carried out by using the rheological data obtained from AR 2000 rheometer from TA Instruments. Injection-molded disc shaped samples with 25-mm diameter and 2-mm thickness were measured at 185 °C using a gap opening of 1.2 mm. Initially, the strain sweep scans were recorded for the samples at $\omega = 1$ rad s^{-1} from 0.1 to 100% strain. As the samples were observed to be shear stable up to 10% strain, a strain of 4% was chosen to generate frequency sweep scans of all the samples from $\omega = 0.1$ to 100 rad s^{-1}. Fracture analysis of the sample bars was performed by equilibrating the samples at −140 and −195 °C for 5 min. The bars were then removed from the cooling medium and were subjected to sudden bending along the length in order to study their fracture behavior.

Wissert *et al.* [184] prepared the graphene nanocomposites by chemical reduction of graphite oxide dispersion with vitamin C in the presence of SAN latex followed by melt compounding. In this process, GO is well dispersed in an aqueous SAN emulsion before reduction. During reduction, the SAN latex is adsorbed on the graphene sheets of the chemically reduced graphene oxide (CRGO). After melt compounding of such hybrid particles with SAN, the nanocomposites show uniform dispersion of CRGO in SAN resulting in improved stiffness with respect to SAN/graphite. The reduction of GO in the presence of polymer latex represents a versatile route to graphene masterbatches and does not require either drying of GO or thermal GO expansion at high

temperatures. Also *in situ* emulsion polymerization in the presence of GO was reported for styrene butyl acrylate copolymer [185] and for polyaniline [186].

4.4 Graphene and Graphene Sheets in Rubber–Rubber Blends Preparation, Characterization, and Applications

Graphene oxide/styrene–butadiene rubber (GO/SBR) composites with complete exfoliation of GO sheets were prepared by aqueous-phase mixing of GO colloid with SBR latex and a small loading of butadiene–styrene–vinyl-pyridine rubber (VPR) latex, followed by their co-coagulation [187]. Graphite oxide was prepared from flake graphite by a modified Hummers method. Then a mild ultrasonic treatment of graphite oxide in water results in its exfoliation to form stable GO colloid. Proper ratio of the GO colloid containing 0.35 wt% solid with 1-nm thick sheets, SBR latex containing 20.0 wt% solid with 60 nm diameters, and VPR latex containing 5.0 wt% solid with 70 nm diameters were mixed by vigorous stirring for 30 min. The GO/VPR/SBR emulsion was then coagulated by a 1.0 wt% sulfuric acid solution. The coagulated composites were washed with water until the pH of the filtered water reached [188] and then dried in an oven at 50 μC for 24 h. The dried composites were compounded with rubber ingredients on an open two-roll mill and subjected to compression in a standard mold at 150 μC and 15 MPa for an optimum time, which was determined by a disc.

Figure 4.16 shows the fabrication process of GO/SBR composite. By aqueous-phase mixing of GO colloid with SBR and VPR latexes, the GO/VPR/SBR mixture is obtained. The zeta potential of the mixture is 260 mV. As is well known from colloidal science, zeta potential values more negative than 230 mV are generally considered to represent sufficient mutual repulsion to ensure dispersion stability [189]. It indicates that the initial GO/VPR/SBR mixture exists as a stable state (Figure 4.16a). A cryo-TEM image shows that colloidal particles with different sizes are individually dispersed in the mixture. However, no aggregates of GO sheets is observed, indicating that GO sheets may be isolated by rubber colloidal particles within the mixture dispersion (Figure 4.16b).

By adjusting the pH value of the mixture to 4.0 with sulfuric acid (H_2SO_4), the size distribution of colloidal particles in the mixture becomes narrow compared with that at pH 6.3 and no GO aggregates can be found (Figure 4.16d). It is supposed that the majority of the remaining colloidal particles could be SBR but not VPR, which is verified by zeta potential analysis (Figure 4.16h). At pH 4.0, the zeta potential of SBR is pH, and in aqueous dispersions at 0.5, 5, and 5 wt% of GO, SBR, and VPR, respectively. It can be seen that it is still more negative than 230 mV. Meanwhile, the zeta potential of VPR becomes positively charged, and it is suggested that the VPR molecules are first released from colloidal particles, and then the N atoms in the pyridine of VPR molecules combine with H1 to form positively charged groups. Herein, the acidified VPR molecules will be strongly attracted to electronegative GO sheets to form VPR-modified GO sheets (Figure 4.16g).

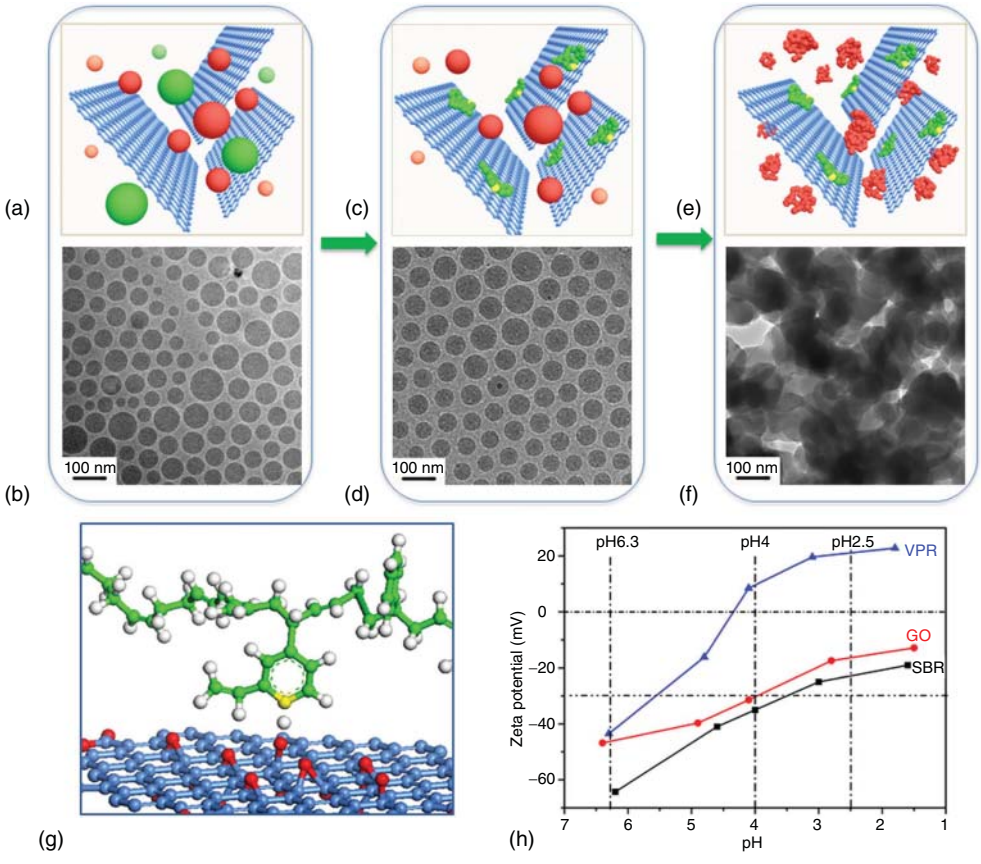

Figure 4.16 Fabrication process of GO/SBR composite. (a,b) GO/VPR/SBR stable emulsion of 0.5 wt% of GO sheets in an aqueous emulsion of 1 wt% VPR and 9 wt% SBR (159 w/w VPR-SBR) at pH 6.3. In the schematic representation (a), SBR and VPR colloidal particles are presented as red and green balls respectively. The cryo-TEM image of the corresponding GO/VPR/SBR stable emulsion is shown in (b). (c,d) By adjusting pH value of mixture to 4.0 with sulfuric acid (H_2SO_4), the VPR colloidal particles are demulsified first, and the released VPR molecules are preferentially adsorbed onto the surfaces of the GO sheets because the acidified pyridine groups of VPR can interact with the ionized carboxylic acid and phenolic hydroxyl groups from the surfaces of the GO sheets. In the schematic representation (c), the released VPR molecules are represented as green random coil. The cryo-TEM image of the corresponding GO/VPR/SBR mixture is shown in (d). Ball-and-stick illustration of a model structure of the interaction between VPR and GO sheets is shown in (g). Yellow, red, and gray are used to represent N, O, and H atoms, respectively. (e,f) When the pH is lower than 3.0, the SBR colloidal particles are further demulsified and then co-coagulated with VPR-modified GO sheets to form the GO/SBR composite. In the schematic representation (e), the demulsified SBR molecules are represented as red random coil. (h) The cryo-TEM image of the corresponding GO/VPR/SBR mixture is shown in (f).

In addition, the electrostatic repulsion between negative charged SBR colloidal particles ensure that the VPR-modified GO sheets be separated uniformly in the mixture instead of being aggregated (Figure 4.16c). When the pH approaches 2.5, the spherical morphology of SBR particles is destructed (Figure 4.16f), indicating that the SBR colloidal particles finally de-emulsificate and co-coagulate with the VPR-modified GO sheets to form the GO/SBR composite (Figure 4.16e). This process makes the exfoliated GO sheets to be strongly combined by VPR chains, effectively preventing the aggregation of GO sheets [190] and obtaining maximal amount of individual GO sheets in the GO/SBR composite, similar to those in the GO/VPR/SBR mixture. In our experiments, we tried to coagulate the SBR latex and GO aqueous solution without VPR, but failed to get a GO/SBR composite with homogeneous dispersion of GO sheets. This result suggests that the electrostatic repulsion between the GO sheets is weaker than that between the GO sheets and SBR colloidal particles. Moreover, there is a strong steric repulsion between GO sheets and SBR colloidal particles. Therefore, GO sheets are strongly adsorbed by H1 ions, and the SBR latex particles between the GO sheets are expelled, resulting in large GO aggregates in the final composite. The dispersion state of GO sheets in GO/SBR composites was observed by SEM and the images are shown in Figure 4.17a–c. No GO aggregates are observed on the cross-section of the composite (see Figure 4.17a). Some wrinkled GO sheets are pulled out of the SBR matrix, as pointed out by the arrows in Figure 4.2c. The GO-based sheets in the rubber matrix are much thicker than the original GO sheets as determined by AFM because their surfaces are coated with VPR rubber. TEM was used to determine the dispersion structure of GO sheets. Extensive high-resolution phase-contrast images of GO/SBR composite at different GO loadings (Figure 4.17d–g) show no evidence of multilayer stacks. At a GO loading of 0.4 vol%, the composite is entirely filled with the GO.

The three peaks at 1.5, 3.0, and 4.6 nm indicate a typical high-order lamellar structure with a long period of 4.2 nm. The weak and broad peak at 7.8 nm [191] indicates a distance of 0.8 nm. The inset shows the interlayer distance of the sandwich structure of GO/SBR composite. In the schematic representation of "layer-by-layer" sandwich structures consisting of GO sheets and rubber, the GO sheets are presented as a blue lattice structure and the rubber between GO sheets are presented as green chains sheets owing to the extremely large surface area of the sheets. In contrast to the typically flat GO sheets observed by AFM, the GO sheets in the GO/SBR composite are crumpled and folded.

The structures of the GO sheets dispersed in the rubber matrix include both individual GO sheets and "layer-by-layer" sandwich structures consisting of GO sheets and rubber. Small-angle/wide-angle X-ray scattering (SWAXS) was performed to further verify the structures of GO sheets dispersed in the SBR matrix in nanoscale. The SWAXS profile of the composite shows four scattering peaks at 1.5, 3.0, 4.6, and 7.8 nm21. The three peaks at 1.5, 3.0, and 4.6 nm21 indicate a typical high-order lamellar structure with a long period of 4.2 nm, which is 4.5 times longer than the layers' distance ($d = 50.96$ nm) in pure GO. The weak and broad peak at 7.8 nm21 indicates a distance of 0.8 nm, which is very close to the interlayer

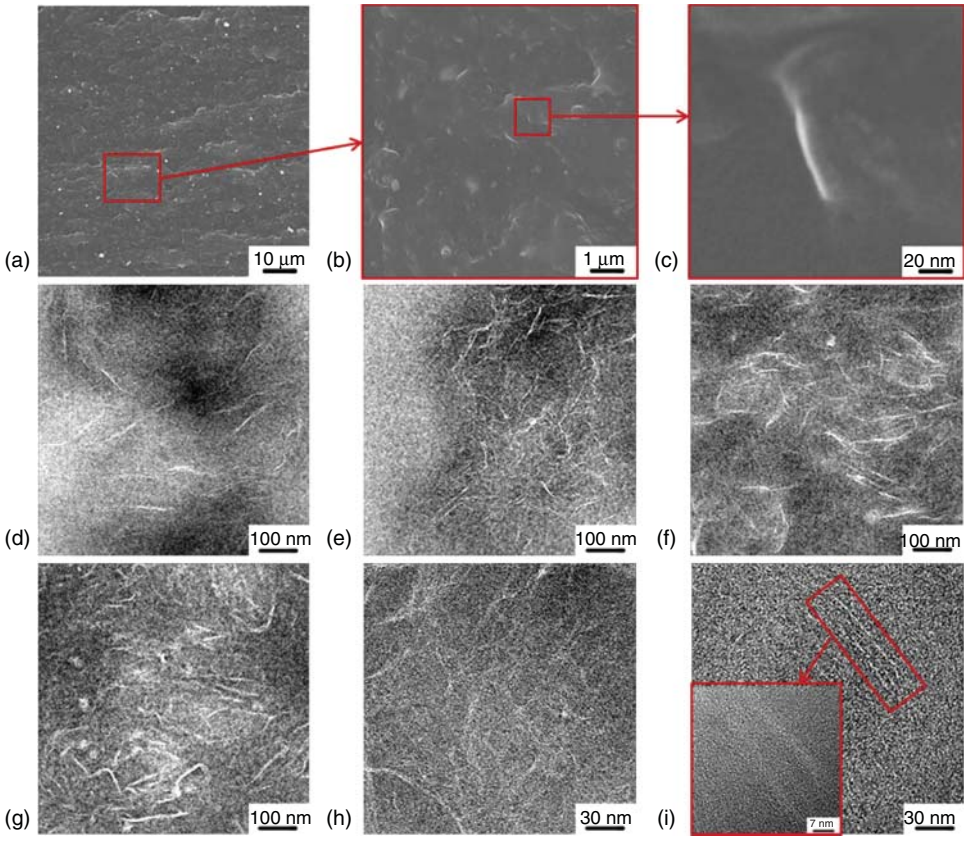

Figure 4.17 Morphology images of GO/SBR composite. (a–c) SEM images ((a) 10 003 magnification; (b) 200 003 magnification; and (c) 2 000 003 magnification) of tensile sections of GO/SBR composite with 2.0 vol% of GO. (d–g) TEM images of microtomed SBR/GO composites revealing different morphologies of GO sheets, including crumpling and folding, at different concentrations (vol%): (d) 0.2; (e) 0.4; (f) 1.2; and (g) 2.0. (h, i) High-resolution phase-contrast images of different regions of microtomed GO/SBR composite sample (2.0 vol% of GO) at different magnifications. These high-resolution images show individual sheets and/or layer-by-layer sandwich structures of GO (Figure 4.18).

distance of GO. These results indicate that different microstructures were formed in the GO/SBR composite. Most GO sheets were dispersed in the rubber matrix as individual sheets. However, owing to the strong electric attraction and nanoscaled effect between the GO sheets, the aggregation of GO sheets is kinetically favored during the co-coagulation process. It is worth pointing out that only sandwich structures (see inset of Figure 4.18), instead of aggregates, were formed in the GO/SBR composite, evidence that well-dispersed individual GO sheets in aqueous solution can be first modified with VPR chains released from latex particles to form a unique GO/VPR meso-structure. This GO/VPR meso-structure can play

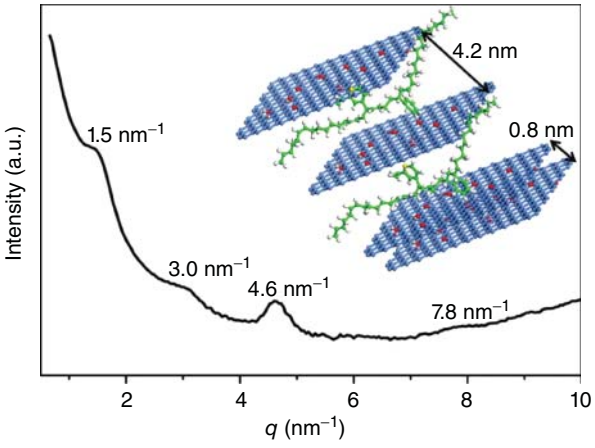

Figure 4.18 SWAXS pattern of GO/SBR composite.

a key role in protecting the original structures of the highly dispersed individual GO sheets in the aqueous solution from re-aggregation during the co-coagulation process.

Rubbers, generally acknowledged as strategic materials, can be tailored by adding fillers to meet the demands of versatile industrial applications. Carbon black (CB) as a carbon nanomaterial has been widely used in rubber reinforcement for over 150 years. Nowadays, CB faces severe challenges because it is derived from crude oil and generates excessive wastes and greenhouse gas emissions. In order to tackle this global issue, new oil-independent fillers have received increasing attention for replacement of CB. Recently, graphene oxide (GO) [38, 192–197] has emerged as a new layered carbon material with nanosize effects and unique physical properties, implying that GO is a potential material for replacing CB for reinforcement of rubbers. Furthermore, graphite as the precursor of GO is oil-independent and naturally abundant. For successful application of GO in rubber industries, especially in the tire industry, two criterions should be fulfilled: (i) commodity rubbers are selected as a matrix, such as SBR and NR, because these two kinds of rubbers account for over 60% of the total rubber market in the world and are mainly reinforced by CB and (ii) the fabrication method is large scale and environment-friendly. The GO/SBR composites formed by this route exhibit unprecedented reinforcing efficiency of GO toward SBR. The GO/SBR composites with small GO loadings have superior mechanical characteristics comparable with those of CB-filled SBR composites at high CB volume fractions, and also show low air permeability and low mass density. In addition, our preparation method is water-mediated, green, and large scale, which is appropriate for preparing various GO-based rubber composites since GO sheets can form well-dispersed aqueous colloid in water [198–200] and most rubbers can exist in latex form.

4.5
Graphene and Graphene Sheets Based Micro and Macro Composites

Three-dimensional graphene-based frameworks (3DGFs) such as aerogels, foams, and sponges are an important class of new-generation porous carbon materials, which exhibit continuously interconnected macroporous structures, low mass density, large surface area, and high electrical conductivity [201]. These materials can serve as robust matrix for accommodating metal, metal oxide, and electrochemically active polymers for various applications in ECs [202, 203], batteries [204], and catalysis [205]. However, 3D-GFs generally lack well-defined mesopores and/or micropores, which substantially limits the efficiency of mass transport and charge storage for ECs through the small pores. Therefore, it is highly attractive to build up hierarchical porous architectures for 3D-GFs by integrating small mesoporous channels within interconnected macroporous frameworks. Considerable efforts have been devoted to fabricating high-performance ECs based on hierarchical porous carbons with macro-/meso- [206], meso-/micro- [207], macro-/micro- [208], and macro-/meso-/micropores [209]. For these porous materials, the macropores can act as a bulk buffering reservoir for electrolytes to minimize the diffusion distances to the interior surfaces of the pores, while the mesopores can provide a large accessible surface area for ion transport/charge storage, and micropores can continuously increase charge accommodation. These features are desirable for applications in high-power ECs.

Herein, Wu *et al.* [210] present the fabrication of hierarchical macro- and mesoporous 3D-GFs. Specifically, the interconnected macropores are derived from 3D graphene aerogels (GAs) that can be prepared by hydrothermal assembly of graphene oxide (GO), while the mesopores can be introduced by the silica networks uniformly grown on the graphene surface. The as-prepared 3D graphene aerogel-based mesoporous silica composites (GA-SiO_2) exhibit tunable thickness of mesoporous silica walls, narrow mesopore size distribution (2–3.5 nm), interconnected macroporous networks, and low mass density. These features render the GASiO_2 as a promising template for creating other 3D porous materials. For instance, 3D graphene aerogel-based mesoporous carbon (GAMC) and metal oxide (GA-Co_3O_4, GA-RuO_2) hybrids can be successfully constructed via a nanocasting technology [211]. Remarkably, 3D GA-MC shows outstanding specific capacitance (226 F g^{-1}), high rate capability, and excellent cycling stability (no capacitance loss after 5000 cycles) when it is applied in ECs, demonstrating a synergistic effect of macro- and mesopores. The overall synthetic procedure leading to GA-SiO_2 is illustrated in Figure 4.19. First, GAs with high macroporosity and good mechanical properties were produced from hydrothermal assembly of GO in an aqueous suspension (1.5 mg ml^{-1}), followed by a freeze-drying process 10. Afterward, the resulting monolithic GAs were immersed into a solution containing CTAB, ethanol, NaOH, and deionized water [212]. Within this step, the surfactant cations (CTA^+) are expected to be electrostatically adsorbed and assembled on the negatively charged surface of GAs. Subsequently on tetraethoxysilane.

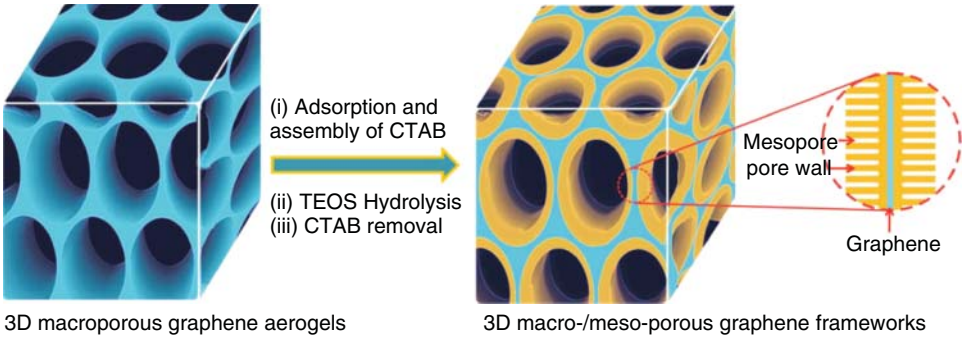

Figure 4.19 Fabrication of hierarchical macro- and mesoporous GA-SiO_2 frameworks: (i) electrostatic adsorption and assembly of CTAB on the surface of 3D GAs, (ii) TEOS hydrolysis for nucleation and growth of mesoporous silica on the surface of CTA^+-adsorped GAs, and (iii) CTAB removal through ethanol washing, drying, and thermal annealing.

Graphene-based mesoporous carbon and metal oxide materials show enhanced supercapacitive performance, such as high specific capacitance, good rate capability, and excellent cycling stability. By adjusting the shell thickness and the mesopore size, it is believed that this approach can provide a variety of new 3D hierarchical porous materials for application in a broad range of ECs, batteries, sensors, catalysis, adsorbents, and fuel cells.

4.6 Conclusion

Much progress has been made in the preparation, functionalization, and applications of graphene nanocomposites. The global upsurge in energy research is paving the way to practical and industrial applications of graphene nanocomposites, leading to the next generation of energy conversion and storage devices. The great potential of graphene nanocomposites in energy has been emphasized by the large amount of exciting research being performed in photovoltaic and photoelectrochemical devices, artificial synthesis, LIBs, super capacitors, and fuel cells. In particular, graphene nanocomposite-based LIBs and supercapacitors are highly promising for energy storage devices. However, there are still many challenges to address before real industrial applications become possible. First of all, large-scale production of graphene nanocomposites with high and uniform quality is still challenging. Energy devices from graphene nanocomposites work well in lab-scale tests. To achieve high-performance devices on an industrial level needs large amounts of high-quality graphene nanocomposites, which should possess environmentally stable electronic and chemical characteristics during operation. Secondly, the efficiencies of photovoltaic and photoelectrochemical devices based on graphene nanocomposites are still low in most prototype

devices. There is still a lot work to do to optimize materials and device fabrication to improve their photoconversion efficiencies. Thirdly, regarding environmental applications, graphene nanocomposites show great potential in the detection of heavy metal ions and bacteria, and organic species degradation. The photodegradation of organic pollutants by graphene nanocomposites is the most attractive feature considering the increase in water pollution by organic species in developing countries. However, it is still premature to envision large-scale applications of these nanocomposites in environmental monitoring and remediation because the fundamental questions over the influence, both in the short- and long-term, of graphene on the ecosystem and human living environments remain largely unaddressed. Although it faces these challenges, graphene nanocomposites, however, are still one of the most exciting platforms for energy and environmental studies. The large-scale application of graphene-based devices in electrochemical energy storage and transparent electrodes in photovoltaics and optoelectronics may be achieved in the near future. More revolutionary applications based on graphene and graphene nanocomposites, with the advancement in both fundamental physics and chemistry as well as in practical techniques, will expand the horizons of graphene nanocomposites and open up new windows in human life.

References

1. Novoselov, K.S., Geim, A.K., Morozov, S.V., Jiang, D., Zhang, Y., Dubonos, S.V., Grigorieva, I.V., and Firsov, A.A. (2004) *Science*, **306**, 666.
2. Novoselov, K.S., Geim, A.K., Morozov, S.V., Jiang, D., Katsnelson, M.I., Grigorieva, I.V., Dubonos, S.V., and Firsov, A.A. (2005) *Nature*, **438**, 197.
3. Zhang, Y.B., Tan, Y.W., Stormer, H.L., and Kim, P. (2005) *Nature*, **438**, 201.
4. Schedin, F., Geim, A.K., Morozov, S.V., Hill, E.W., Blake, P., Katsnelson, M.I., and Novoselov, K.S. (2007) *Nat. Mater.*, **6**, 652.
5. Du, X., Skachko, I., Barker, A., and Andrei, E.Y. (2008) *Nat. Nanotechnol.*, **3**, 491.
6. Van Lier, G., Van Alsenoy, C., Van Doren, V., and Geerlings, P. (2000) *Chem. Phys. Lett.*, **326**, 181.
7. Frank, I.W., Tanenbaum, D.M., Van Der Zande, A.M., and McEuen, P.L. (2007) *J. Vac. Sci. Technol., B*, **25**, 2558.
8. Poot, M. and Van Der Zant, H.S.J. (2008) *Appl. Phys. Lett.*, **92**, 063111.
9. Gomez-Navarro, C., Burghard, M., and Kern, K. (2008) *Nano Lett.*, **8**, 2045.
10. Park, S., Lee, K.S., Bozoklu, G., Cai, W., Nguyen, S.T., and Ruoff, R.S. (2008) *ACS Nano*, **2**, 572.
11. Park, S., Dikin, D.A., Nguyen, S.T., and Ruoff, R.S. (2009) *J. Phys. Chem. C*, **113**, 15801.
12. Guo, P., Song, H.H., and Chen, X.H. (2009) *Electrochem. Commun.*, **11**, 1320.
13. Chen, H., Muller, M.B., Gilmore, K.J., Wallace, G.G., and Li, D. (2008) *Adv. Mater.*, **20**, 3557.
14. Nair, R.R., Blake, P., Grigorenko, A.N., Novoselov, K.S., Booth, T.J., Stauber, T., Peres, N.M.R., and Geim, A.K. (2008) *Science*, **320**, 1308.
15. Mak, K.F., Sfeir, M.Y., Wu, Y., Lui, C.H., Misewich, J.A., and Heinz, T.F. (2008) *Phys. Rev. Lett.*, **101**, 196405.
16. Wang, F., Zhang, Y.B., Tian, C.S., Girit, C., Zettl, A., Crommie, M., and Shen, Y.R. (2008) *Science*, **320**, 206.
17. George, P.A., Strait, J., Dawlaty, J., Shivaraman, S., Chandrashekhar, M., Rana, F., and Spencer, M.G. (2008) *Nano Lett.*, **8**, 4248.
18. Rana, F., George, P.A., Strait, J.H., Dawlaty, J., Shivaraman, S.,

Chandrashekhar, M., and Spencer, M.G. (2009) *Phys. Rev. B*, **79**, 115447.
19. Xia, F., Mueller, T., Lin, Y.-m., Valdes-Garcia, A., and Avouris, P. (2009) *Nat. Nanotechnol.*, **4**, 839.
20. Ferrari, A.C. (2007) *Solid State Commun.*, **143**, 47.
21. Ferrari, A.C., Meyer, J.C., Scardaci, V., Casiraghi, C., Lazzeri, M., Mauri, F., Piscanec, S., Jiang, D., Novoselov, K.S., Roth, S., and Geim, A.K. (2006) *Phys. Rev. Lett.*, **97**, 187401.
22. Rohrl, J., Hundhausen, M., Emtsev, K.V., Seyller, T., Graupner, R., and Ley, L. (2008) *Appl. Phys. Lett.*, **92**, 201918.
23. Ni, Z.H., Chen, W., Fan, X.F., Kuo, J.L., Yu, T., Wee, A.T.S., and Shen, Z.X. (2008) *Phys. Rev. B*, **77**, 115416.
24. Wang, Y.Y., Ni, Z.H., Yu, T., Shen, Z.X., Wang, H.M., Wu, Y.H., Chen, W., and Wee, A.T.S. (2008) *J. Phys. Chem. C*, **112**, 10637.
25. Dreyer, D.R., Ruoff, R.S., and Bielawski, C.W. (2010) *Angew. Chem. Int. Ed.*, **49**, 9336.
26. Mermin, N.D. (1968) *Phys. Rev.*, **176**, 250.
27. Dresselhaus, M.S. and Dresselhaus, G. (1981) *Adv. Phys.*, **30**, 139.
28. Boehm, V.H.P., Clauss, A., Fischer, G.O., and Hofmann, U. (1962) *Z. Naturforschg.*, **17**, 150.
29. Boehm, H.P., Setton, R., and Stumpp, E. (1986) *Carbon*, **24**, 241.
30. Boehm, H.P., Setton, R., and Stumpp, E. (1994) *Pure Appl. Chem.*, **66**, 1893.
31. Stefan, P.M., Shek, M.L., Lindau, I., Spicer, W.E., Johansson, L.I., Herman, F., Kasowski, R.V., and Brogen, G. (1984) *Phys. Rev. B*, **29**, 5423.
32. Oshima, C., Bannai, E., Tanaka, T., and Kawai, S. (1977) *Jpn. J. Appl. Phys.*, **16**, 965.
33. Van Bommel, A.J., Crombeen, J.E., and Van Tooren, A. (1975) *Surf. Sci.*, **48**, 463.
34. Zhang, Y., Small, J., Pontius, W., and Kim, P. (2005) *Appl. Phys. Lett.*, **86**, 073104.
35. Weiss, N.O., Zhou, H., Liao, L., Liu, Y., Jiang, S., Huang, Y., and Duan, X. (2012) *Adv. Mater.*, **24**, 5782–5825.
36. Morozov, S.V., Novoselov, K.S., Katsnelson, M.I., Schedin, F., Elias, D.C., Jaszczak, J.A., and Geim, A.K. (2008) *Phys. Rev. Lett.*, **100**, 016602.
37. Berciaud, S., Ryu, S., Brus, L.E., and Heinz, T.F. (2009) *Nano Lett.*, **9**, 346.
38. Soldano, C., Mahmood, A., and Dujardin, E. (2010) *Carbon*, **48**, 2127.
39. Li, X.L., Zhang, G.Y., Bai, X.D., Sun, X.M., Wang, X.R., Wang, E.G., and Dai, H.J. (2008) *Nat. Nanotechnol.*, **3**, 538.
40. Hernandez, Y., Nicolosi, V., Lotya, M., Blighe, F.M., and Sun, Z. (2008) *Nat. Nanotechnol.*, **3**, 563.
41. Lotya, M., Hernandez, Y., King, P.J., Smith, R.J., Nicolosi, V. *et al.* (2009) *J. Am. Chem. Soc.*, **131**, 3611.
42. Bourlinos, A.B., Georgakilas, V., Zboril, R., Steriotis, T.A., and Stubos, A.K. (2009) *Small*, **5**, 1841.
43. Khan, U., O'Neill, A., Lotya, M., De, S., and Coleman, J.N. (2010) *Small*, **6**, 864.
44. Valles, C., Drummond, C., Saadaoui, H., Furtado, C.A., He, M. *et al.* (2008) *J. Am. Chem. Soc.*, **130**, 15802.
45. Moon, J.S., Curtis, D., Hu, M., Wong, D., McGuire, C. *et al.* (2009) *IEEE Electron Device Lett.*, **30**, 650.
46. Compton, O.C. and Nguyen, S.T. (2010) *Small*, **6**, 711.
47. Si, Y. and Samulski, E.T. (2008) *Nano Lett.*, **8**, 1679.
48. Dreyer, D.R., Park, S., Bielawski, C.W., and Ruoff, R.S. (2010) *Chem. Soc. Rev.*, **39**, 228.
49. Park, S., An, J., Jung, I., Piner, R.D., An, S.J. *et al.* (2009) *Nano Lett.*, **9**, 1593.
50. Rafiee, M.A., Rafiee, J., Wang, Z., Song, H., Yu, Z.-Z. *et al.* (2009) *ACS Nano*, **3**, 3884.
51. Shao, Y., Wang, J., Engelhard, M., Wang, C., and Lin, Y. (2010) *J. Mater. Chem.*, **20**, 743.
52. Cote, L.J., Cruz-Silva, R., and Huang, J. (2009) *J. Am. Chem. Soc.*, **131**, 11027.
53. Strong, V., Dubin, S., El-Kady, M.F., Lech, A., Wang, Y. *et al.* (2012) *ACS Nano*, **6**, 1395.
54. Gao, J., Liu, F., Liu, Y., Ma, N., Wang, Z., and Zhang, X. (2010) *Chem. Mater.*, **22**, 2213.
55. Akhavan, O. and Ghaderi, E. (2010) *ACS Nano.*, **4**, 5731
56. Gilje, S., Han, S., Wang, M., Wang, K.L., and Kaner, R.B. (2007) *Nano Lett.*, **7**, 3394.

57. Fan, X., Peng, W., Li, Y., Li, X., Wang, S., Zhang, G., and Zhang, F. (2008) *Adv. Mater.*, **20**, 4490.
58. Chen, W., Yan, L., and Bangal, P.R. (2010) *Carbon*, **48**, 1146.
59. Wang, X., Zhi, L., and Muellen, K. (2008) *Nano Lett.*, **8**, 323.
60. Gilje, S., Dubin, S., Badakhshan, A., Farrar, J., Danczyk, S.A., and Kaner, R.B. (2010) *Adv. Mater.*, **22**, 419.
61. Williams, G., Seger, B., and Kamat, P.V. (2008) *ACS Nano*, **2**, 1487.
62. Guo, S. and Dong, S. (2011) *Chem. Soc. Rev.*, **40**, 2644.
63. Rollings, E., Gweon, G.-H., Zhou, S.Y., Mun, B.S., McChesney, J.L. *et al.* (2006) *J. Phys. Chem. Solids*, **67**, 2172.
64. Shivaraman, S., Barton, R.A., Yu, X., Alden, J., Herman, L. *et al.* (2009) *Nano Lett.*, **9**, 3100.
65. Hass, J., de Heer, W.A., and Conrad, E.H. (2008) *J. Phys. Condens. Matter*, **20**, 323202.
66. Camara, N., Rius, G., Huntzinger, J.-R., Tiberj, A., Mestres, N. *et al.* (2008) *Appl. Phys. Lett.*, **93**, 123503.
67. Dedkov, Y., Shikin, A., Adamchuk, V., Molodtsov, S., Laubschat, C., Bauer, A., and Kaindl, G. (2001) *Phys. Rev. B*, **64**, 035405.
68. Cai, W., Piner, R.D., Zhu, Y., Li, X., Tan, Z., Floresca, H.C., Yang, C., Lu, L., Kim, M.J., and Ruoff, R.S. (2009) *Nano Res.*, **2**, 851.
69. Reina, A., Jia, X., Ho, J., Nezich, D., Son, H., Bulovic, V., Dresselhaus, M.S., and Kong, J. (2009) *Nano Lett.*, **9**, 30.
70. Lopez, G. and Mittemeijer, E. (2004) *Scr. Mater.*, **51**, 1.
71. Selman, G.L., Ellison, P.J., and Darling, A.S. (1970) *Platinum Met. Rev.*, **14**, 14.
72. Bhaviripudi, S., Jia, X., Dresselhaus, M.S., and Kong, J. (2010) *Nano Lett.*, **10**, 4128.
73. Liu, L., Zhou, H., Cheng, R., Chen, Y., Lin, Y.-C., Qu, Y., Bai, J., Ivanov, I.A., Liu, G., Huang, Y., and Duan, X. (2012) *J. Mater. Chem.*, **22**, 1498.
74. Jian-Hua, G., Keisuke, S., Masayo, K., Ming-Sheng, X., Satoru, M., and Daisuke, F. (2012) *Nanotechnology*, **23**, 055704.
75. Yan, K., Peng, H., Zhou, Y., Li, H., and Liu, Z. (2011) *Nano Lett.*, **11**, 1106.
76. Chen, S., Cai, W., Piner, R.D., Suk, J.W., Wu, Y., Ren, Y., Kang, J., and Ruoff, R.S. (2011) *Nano Lett.*, **11**, 3519.
77. Li, X., Magnuson, C.W., Venugopal, A., An, J., Suk, J.W. *et al.* (2010) *Nano Lett.*, **10**, 4328.
78. Li, X., Magnuson, C.W., Venugopal, A., Tromp, R.M., Hannon, J.B. *et al.* (2011) *J. Am. Chem. Soc.*, **133**, 2816.
79. Li, Z., Wu, P., Wang, C., Fan, X., Zhang, W. *et al.* (2011) *ACS Nano*, **5**, 3385.
80. Wang, J., Zhu, M., Outlaw, R., Zhao, X., Manos, D. *et al.* (2004) *Appl. Phys. Lett.*, **85**, 1265.
81. Park, J.B., Xiong, W., Gao, Y., Qian, M., Xie, Z.Q. *et al.* (2011) *Appl. Phys. Lett.*, **98**, 123109.
82. Ruan, G., Sun, Z., Peng, Z., and Tour, J.M. (2011) *ACS Nano*, **5**, 7601.
83. Sun, Z., Yan, Z., Yao, J., Beitler, E., Zhu, Y., and Tour, J.M. (2010) *Nature*, **468**, 549.
84. Geim, A.K. and Novoselov, K.S. (2007) *Nature*, **6**, 183.
85. Kotov, N.A. (2006) *Mater. Sci. Nat.*, **442** (7100), 254.
86. Stankovich, S., Dikin, D.A., Dommett, G.H.B., Kohlhaas, K.M., Zimney, E.J. *et al.* (2006) *Nature*, **442**, 282.
87. Cassagneau, T., Guerin, F., and Fendler, J.H. (2000) *Langmuir*, **16**, 7318.
88. Brodie, B.C. (1859) *Philos. Trans. R. Soc. London*, **149**, 249.
89. Chung, D.D.L. (1987) *J. Mater. Sci.*, **22**, 4190.
90. Land, T.A., Michely, T., Behm, R.J., Hemminger, J.C., and Comsa, G. (1992) *Surf. Sci.*, **264**, 261.
91. Nagashima, A., Nuka, K., Itoh, H., Ichinokawa, T., Oshima, C., and Otani, S. (1993) *Surf. Sci.*, **291**, 93.
92. Berger, C., Song, Z., Li, T., Li, X., Ogbazghi, A.Y., Feng, R. *et al.* (2004) *J. Phys. Chem. B*, **108**, 19912.
93. Matsuo, Y., Tahara, K., and Sugie, Y. (1997) *Carbon*, **35**, 113.
94. Morishige, K. and Hamada, T. (2005) *Langmuir*, **21**, 6277.
95. Kotov, N.A., Dekany, I., and Fendler, J.H. (1996) *Adv. Mater.*, **8**, 637.
96. Matsuo, Y. and Sugie, Y. (1998) *Carbon*, **36**, 301.

97. Bourlinos, A.B., Gournis, D., Petridis, D., Szabo, T., Szeri, A., and Dekany, I. (2003) *Langmuir*, **19**, 6050.
98. Stankovich, S., Dikin, D., Piner, R.D., Kohlhaas, K.A., Kleinhammes, A., Jia, Y. *et al.* (2007) *Carbon*, **45**, 1558.
99. Lerf, A., He, H., Forster, M., and Klinowski, J. (1998) *J. Phys. Chem. B*, **102**, 4477.
100. Croft, R.C. (1960) *Q. Rev.*, **14**, 11.
101. Nethravathi, C. and Rajamathi, M. (2006) Delamination. *Carbon*, **44**, 2635.
102. Nethravathi, C., Ravishankar, N., Shivakumara, C., and Rajamathi, M. (2007) *J. Power Sources*, **172**, 970.
103. Venugopal, B.R., Shivakumara, C., and Rajamathi, M. (2007) *Solid State Sci.*, **9**, 287.
104. Rajamathi, M. and Seshadri, R. (2002) *Curr. Opin. Solid State Mater. Sci.*, **6**, 337.
105. Takeuchi, M., Muto, S., Tanabe, T., Arai, S., and Kuroyanagi, T. (1997) *Philos. Mag. A*, **76**, 691.
106. Niwase, K. (2002) *Philos. Mag. Lett.*, **82**, 401.
107. Zaiser, M. and Banhart, F. (1997) *Phys. Rev. Lett.*, **79**, 3680.
108. Brunetto, R., Baratta, G., and Strazzulla, G. (2004) *J. Appl. Phys.*, **96**, 380.
109. Compagnini, G. and Baratta, G. (1992) *Appl. Phys. Lett.*, **61**, 1796.
110. Ni, Z.H., Yu, T., Lu, Y.H., and Wang, Y.Y. (2008) *ACS Nano*, **2**, 2301.
111. Das Sarma, S., Adam, S., Hwang, E.H., and Rossi, E. (2011) *Rev. Mod. Phys.*, **83**, 407.
112. Kuzmenko, A.B., van Heumen, E., Carbone, F., and van der Marel, D. (2008) *Phys. Rev. Lett.*, **100**, 117401.
113. Ando, T., Zheng, Y., and Suzuura, H. (2002) *J. Phys. Soc. Jpn.*, **71**, 1318.
114. Falkovsky, L.A. and Pershoguba, S.S. (2007) *Phys. Rev. B*, **76**, 153410.
115. Stauber, T., Peres, N.M.R., and Geim, A.K. (2008) *Phys. Rev. B*, **78**, 085432.
116. Sadowski, M.L., Martinez, G., Potemski, M., Berger, C., and de Heer, W.A. (2006) *Phys. Rev. Lett.*, **97**, 266405.
117. Sadowski, M.L., Martinez, G., Potemski, M., Berger, C., and de Heer, W.A. (2007) *Int. J. Mod. Phys. B*, **21**, 1145.
118. Witowski, A.M. *et al.* (2010) *Phys. Rev. B*, **82**, 165305.
119. Orlita, M. *et al.* (2009) *Solid State Commun.*, **149**, 1128.
120. Orlita, M. *et al.* (2008) *Phys. Rev. Lett.*, **101**, 267601.
121. Grassee, I., Levallois, J., Walter, A.L., Ostler, M., Bostwick, A., Rotenberg, E., Seyller, T., van der Marel, D., and Kuzmenko, A.B. (2011) *Nat. Phys.*, **7**, 48.
122. Potts, J.R., Dreyer, D.R., Bielawski, C.W., and Ruoff, R.S. (2011) *Polymer*, **52**, 25.
123. Winey, K.I. and Vaia, R.A. (2007) *MRS Bull.*, **32**, 314.
124. Kuilla, T., Bhadra, S., Yao, D., Kim, N.H., Bose, S., and Lee, J.H. (2010) *Prog. Polym. Sci.*, **35**, 1350.
125. Zhang, T., Xue, Q., Zhang, S., and Dong, M. (2010) *Nano Today*, **7**, 180.
126. Jang, B.Z. and Zhamu, A. (2008) *J. Mater. Sci.*, **43**, 5092.
127. Mack, J.J., Viculis, L.M., Ali, A. *et al.* (2005) *Adv. Mater.*, **17**, 77.
128. Hansma, P.K., Turner, P.J., and Ruoff, R.S. (2007) *Nanotechnology*, **18**, Article ID, 044026.
129. Ramanathan, T., Abdala, A.A., Stankovich, S. *et al.* (2008) *Nat. Nanotechnol.*, **3**, 327.
130. Das, B., Eswar Prasad, K., Ramamurty, U., and Rao, C.N.R. (2009) *Nanotechnology*, **20**, Article ID, 125705.
131. Yu, A., Ramesh, P., Itkis, M.E., Bekyarova, E., and Haddon, R.C. (2007) *J. Phys. Chem. C*, **111**, 7565.
132. Zhang, X., Huang, Y., Wang, Y., Ma, Y., Liu, Z., and Chen, Y. (2009) *Carbon*, **47**, 334.
133. Liu, Z., Xu, Y., Zhang, X., Zhang, X., Chen, Y., and Tian, J. (2009) *J. Phys. Chem. B*, **113**, 9681.
134. Booth, T.J., Blake, P., Nair, R.R. *et al.* (2008) *Nano Lett.*, **8**, 2442.
135. Luechinger, N.A., Booth, N., Heness, G., Bandyopadhyay, S., Grass, R.N., and Stark, W.J. (2008) *Adv. Mater.*, **20**, 3044.
136. Watcharotone, S., Diking, D.A., Stankovich, S., Pinery, R. *et al.* (2007) *Nano Lett.*, **7**, 1888.
137. Cheng, J., Xin, H., Zheng, H., and Wang, B. (2013) *J. Power Sources*, **232**, 52.

138. Perera, S.D., Liyanage, A.D., Nijem, N., Ferraris, J.P., Chabal, Y.J., and Balkus, J.K.J. (2013) *J. Power Sources*, **30**, 30.
139. Lee, J.H., Marroquin, J., Rhee, K.Y., Park, S.J., and Hui, D. (2013) *Composites B*, **45**, 682.
140. Guo, J., Ren, L., Wang, R., Zhang, C., Yang, Y., and Liu, T. (2011) *Composites B*, **42**, 2130.
141. Ansari, M.O., Yadav, S.K., Cho, J.W., and Mohammad, F. (2013) *Composites B*, **47**, 155.
142. Jeon, G.W., An, J., and Jeong, Y.G. (2012) *Composites B*, **43**, 3412.
143. Steurer, P., Wissert, R., Thomann, R., and Mulhaupt, R. (2009) *Macromol. Rapid Commun.*, **30**, 316.
144. Kim, H. and Macosko, C.W. (2009) *Polymer*, **50**, 3797.
145. Zaman, I., ThanhPhan, T., Kuan, H., Meng, Q., La, L.T., Luong, L. *et al.* (2011) *Polymer*, **2**, 1603.
146. Tkalya, E., Ghislandi, M., Alekseev, A., Koning, C., and Loos, J. (2010) *J. Mater. Chem.*, **20**, 3035.
147. Kim, H., Miura, Y., and Macosko, C.W. (2010) *Chem. Mater.*, **22**, 3441.
148. Das, B., Prasad, E.K., Ramamurty, U., and Rao, C.N.R. (2009) *Nanotechnology*, **20**, 125701.
149. Layek, R.K., Samanta, S., Chatterjee, D.P., and Nandi, A.K. (2010) *Polymer*, **51**, 5846.
150. Peponi, L., Tercjak, A., Verdejo, R., Lopez-Manchado, M.A., Mondragon, I., and Kenny, J.M. (2009) *J. Phys. Chem. C*, **113**, 17973.
151. Verdejo, R., Bernal, M.M., Romasanta, L.J., and Lopez-Manchado, M.A. (2011) *J. Mater. Chem.*, **21**, 3301.
152. Jiang, M.J., Dang, Z.M., and Xu, H.P. (2007) *Eur. Polym. J.*, **43**, 4924.
153. Zhang, H., Zheng, W., Yan, Q., Yang, Y., Wang, J. *et al.* (2010) *Polymer*, **51**, 1191.
154. Prud'homme, R.K., Ozbas, B., Aksay, I.A., Register, R.A., and Adamson, D.H. (2008) Functional Graphene–Rubber Nanocomposites. International patent WO 2008/045778 A1.
155. Hu, H., Zhao, L., Liu, J., Liu, Y., and Cheng, J. (2012) *Polymer*, **53**, 3378.
156. Lian, H., Li, S., Liu, K., Xu, L., Wang, K., and Guo, W. (2011) *Polym. Eng. Sci.*, **51**, 2254.
157. Takahashi, S., Goldberg, H.A., Feeney, C.A., Karim, D.P., Farrell, M., O'Leary, K., and Paul, R. (2006) *Polymer*, **47**, 3083.
158. Liang, Y., Cao, W., Li, Z., Wang, Y., Wu, Y., and Zhang, L. (2008) *Polym. Test.*, **27**, 270.
159. Hernández, M., del-Mar Bernal, M., Verdejo, R., Ezquerra, T.A., and López-Manchado, M.A. (2012) *Compos. Sci. Technol.*, **73**, 24.
160. Bhattacharya, M., Maiti, M., and Bhowmick, A.K. (2009) *Polym. Eng. Sci.*, **49**, 81.
161. Verdejo, R., Barroso-Bujans, F., Rodriguez-Perez, M.A., de Saja, J.A., and López-Manchado, M.A. (2008) *J. Mater. Chem.*, **18**, 2221.
162. Liang, J.J., Xu, Y.F., Huang, Y., Zhang, L., Wang, Y. *et al.* (2009) *J. Phys. Chem. C*, **113**, 9921.
163. Prud'homme, R., Ozbas, B., Aksay, I., Register, R., and Adamson, D. (2010) Functional graphenerubber nanocomposites. US7745528B2 ed, vol. US7745528B2 US: The Trustees of Princeton University, 2010, p. 80.
164. Zhan, Y.H., Wu, J.K., Xia, H.S., Yan, N., Fei, G.X., and Yuan, G.P. (2011) *Macromol. Mater. Eng.*, **296**, 590.
165. Rallini, M., Monti, M., Natali, M., Puglia, D., Kenny, J.M., and Torre, L. (2012) Graphene nanoplatelets as conductive fillers for strain sensing in epoxy nanocomposite. International SAMPE Technical Conference, Baltimore, MD, p. 21.
166. Greco, A., Gennaro, R., and Maffezzoli, A. (2012) *Wiley Encyclopedia of Composites*, John Wiley & Sons, Inc., New York, p. 1.
167. Bao, C., Song, L., Xing, W., Yuan, B., Wilkie, C.A., Huang, J., Guo, Y., and Hu, Y. (2012) *J. Mater. Chem.*, **22**, 6088.
168. An, J.E., Jeon, G.W., and Jeong, Y.G. (2012) *Fibers Polym.*, **13**, 507.
169. Eswaraiah, V., Balasubramaniam, K., Ramaprabhu, S. (2012) *Nanoscale*, **4**, 1258.

170. Serafini, T.T., Delvigs, P., and Lightsey, G.R. (1972) *J. Appl. Polym. Sci.*, **16**, 905.
171. Marcano, D.C., Kosynkin, D.V., Berlin, J.M., Sinitskii, A., Sun, Z.Z., and Slesarev, A. (2010) *ACS Nano*, **4**, 4806.
172. Guo, H.L., Wang, X.F., Qian, Q.Y., Wang, F.B., and Xia, X.H. (2009) *ACS Nano*, **3**, 2653.
173. Liang, J., Huang, Y., Zhang, L., Wang, Y., Ma, Y., Guo, T. *et al.* (2009) *Adv. Funct. Mater.*, **19**, 2297.
174. Ansari, S., Kelarakis, A., Estevez, L., and Giannelis, E.P. (2010) *Small*, **2**, 200900765.
175. Liu, H., Li, Y., Wang, T., and Wang, Q. (2012) *J. Mater. Sci.*, **47**, 1867.
176. Cao, Y., Feng, J., and Wu, P. (2010) *Carbon*, **48**, 1670.
177. Zhao, X., Zhang, Q., Chen, D., and Lu, P. (2010) *Macromolecules*, **43**, 2357.
178. Wang, S., Tambraparni, M., Qiu, J., Tipton, J., and Dean, D. (2009) *Macromolecules*, **42**, 5251.
179. Loh, K.P., Bao, Q., Ang, P.K. *et al.* (2010) *J. Mater. Chem.*, **20**, 2277.
180. Gong, L., Kinloch, I.A., Young, R.J., Riaz, I., Jalil, R., and Novoselov, K.S. (2010) *Adv. Mater.*, **22**, 2694.
181. Liang, J., Huang, Y., Zhang, L., Wang, Y., Ma, Y. *et al.* (2009) *Adv. Funct. Mater.*, **19**, 1.
182. Yuan, X. (2011) *Polym. Bull.*, **67**, 1785.
183. Mukhopadhyay, P. and Gupta, R.K. (2011) *Plast. Eng.*, 32.
184. Wissert, R., Steurer, P., Schopp, S., Thomann, R., and Mulhaupt, R. (2010) *Macromol. Mater. Eng.*, **295**, 1107.
185. Zhang, R., Hu, Y., Xu, J., Fan, W., and Chen, Z. (2004) *Polym. Degrad. Stab.*, **85**, 583.
186. Zheming, G., Ling, Z., and Chunzhong, L. (2009) *J. Macromol. Sci. Part B: Phys.*, **48**, 226.
187. Y. Mao, S. Wen, Y. Chen, F. Zhang, P. Panine, *et al. Sci. Rep.* **3**: 2508, doi:10.1038/srep02508.
188. Yan, L. *et al.* (2012) *Chem. Soc. Rev.*, **41**, 97.
189. Everett, D.H. (1988) *Basic Principles of Colloid Science*, Royal Society of Chemistry, London, p. 20.
190. Shen, J.X. *et al.* (2011) *Langmuir*, **27**, 15213.
191. Wan, C. and Chen, B.J. (2012) *J. Mater. Chem.*, **22**, 3637.
192. Geim, A.K. and Novoselov, K.S. (2007) *Nat. Mater.*, **6**, 183.
193. Dreyer, D.R. *et al.* (2009) *Chem. Soc. Rev.*, **39**, 228.
194. Bai, H. *et al.* (2001) *J. Phys. Chem. C*, **115**, 5545.
195. Rao, C. *et al.* (2009) *Angew. Chem. Int. Ed.*, **48**, 7752.
196. Wei, W. and Qu, X. (2012) *Small*, **8**, 2138.
197. Scharfenberg, S. *et al.* (2011) *Appl. Phys. Lett.*, **98**, 091908.
198. Li, D. *et al.* (2008) *Nat. Nanotechnol.*, **3**, 101.
199. Niyogi, S. *et al.* (2006) *J. Am. Chem. Soc.*, **128**, 7720.
200. Patil, A.J. *et al.* (2009) *Adv. Mater.*, **21**, 3159.
201. Worsley, M.A., Pauzauskie, P.J., Olson, T.Y., Biener, J., Satcher, J.H., and Baumann, T.F. (2010) *J. Am. Chem. Soc.*, **132**, 14067.
202. Wu, Z.S., Winter, A., Chen, L., Sun, Y., Turchanin, A., and Feng, X. (2012) K. Müllen. *Adv. Mater.*, **24**, 5130.
203. Choi, B.G., Yang, M., Hong, W.H., Choi, J.W., and Huh, Y.S. (2012) *ACS Nano*, **6**, 4020.
204. Chen, W.F., Li, S.R., Chen, C.H., and Yan, L.F. (2011) *Adv. Mater.*, **23**, 5679.
205. Wu, Z.S., Yang, S.B., Sun, Y., Parvez, K., Feng, X.L., and Müllen, K. (2012) *J. Am. Chem. Soc.*, **134**, 9082.
206. Wang, Z.Y. and Stein, A. (2008) *Chem. Mater.*, **20**, 1029.
207. Raymundo-Pinero, E., Cadek, M., and Beguin, F. (2009) *Adv. Funct. Mater.*, **19**, 1032.
208. Backov, R. (2006) *Soft Matter*, **2**, 452.
209. Wang, D.W., Li, F., Liu, M., Lu, G.O., and Cheng, H.M. (2008) *Angew. Chem. Int. Ed.*, **47**, 373.
210. Wu, Z.S., Sun, Y., Tan, Y.Z., Yang, S., Feng, X., and Müllen, K. (2012) *J. Am. Chem. Soc.*, **134**, 19532.
211. Yang, S.B., Feng, X.L., Wang, L., Tang, K., Maier, J., and Müllen, K. (2010) *Angew. Chem. Int. Ed.*, **49**, 4795.
212. Yang, S.B., Feng, X.L., Wang, X.C., and Müllen, K. (2011) *Angew. Chem. Int. Ed.*, **50**, 5339.

5
Nanocomposites of Polyhedral Oligomeric Silsesquioxane (POSS) and Their Applications

Dhorali Gnanasekaran

5.1
Introduction

5.1.1
Nanocomposites

Now, immense interest is being shown in the development of nanomaterials for a wide variety of reasons, and these materials offer exciting new challenges and opportunities in all major branches of science and technology (Figure 5.1). It is now widely recognized that reduction in the size of component particles influences the interfacial interactions between them and this can, in turn, enhance the material properties to an appreciable extent. The word "nanocomposites" implies that materials consist of various phases with different compositions, and at least one constituent phase has one dimension less than 100 nm (Figure 5.2). Consequently, it is also possible to develop materials that are completely discontinuous, that is, containing both organic and inorganic phases. Such materials exhibit nonlinear changes in properties with respect to macroscopic composites that are made up of the same component phases. The development of nanomaterials comprising organic and inorganic skeletons will provide a new class of nanocomposites with a variety of improved properties [1]. These materials can serve as bridges between molecules in the polymer due to their quantum-scale sizes. This nature allows them to exhibit different properties from conventional microcomposites. Nanocomposites can be considered to be solid structures with nanometer-scale repeat distances between different phases that constitute the structure. These materials typically consist of an inorganic (host) solid containing an organic component or vice versa. The definition of nanocomposite material has broadened significantly to encompass a large variety of systems such as one-dimensional, two-dimensional, three-dimensional as well as amorphous materials made of distinctly dissimilar components and mixed at the nanometer scale [2].

Organic/inorganic composite materials have been extensively studied for a long time. When inorganic phases in organic/inorganic composites become nanosized, they are called *nanocomposites*. Nanocomposites can be considered

Nanomaterials and Nanocomposites: Zero- to Three-Dimensional Materials and Their Composites,
First Edition. Edited by Visakh P.M. and Maria José Martínez Morlanes.

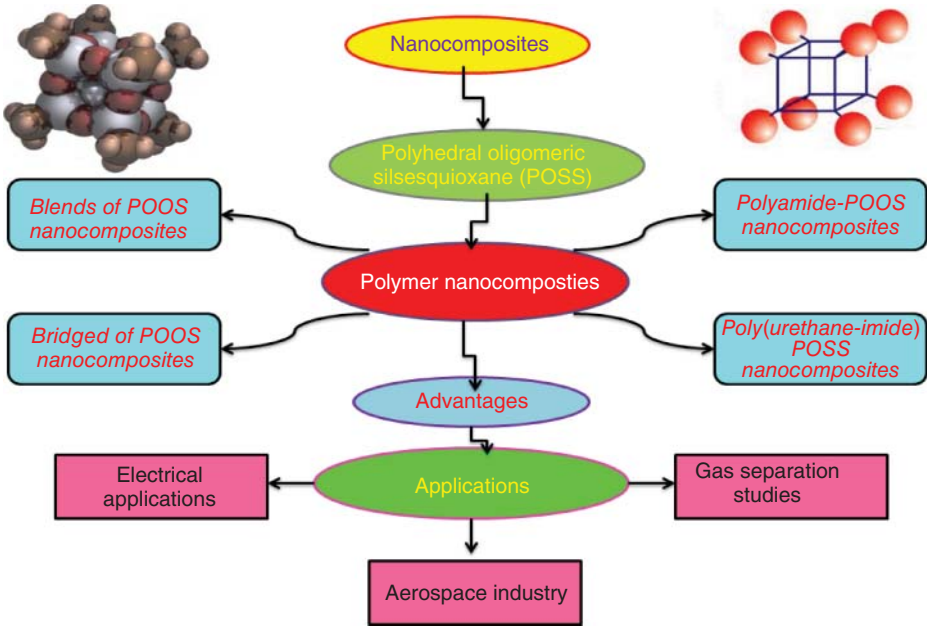

Figure 5.1 Schematic representation and conspectus of this chapter.

solid structures with nanometer-scale repeat distances between different phases that constitute the structure. These may consist of two or more inorganic/organic phases in some combinatorial form with the constraint that at least one of the phases or features is in the nanosize. This type of material combines the advantages of the inorganic material (e.g., rigidity and thermal stability) and the organic polymer (e.g., flexibility, dielectric, ductility, and processability) [3]. The development of nanomaterials opens the possibility for new materials with outstanding properties compared to classical engineering materials. These materials can find applications in different fields such as medical treatment or structural mechanics. Nanocomposite materials are formed by mixing two or more dissimilar materials at the nanoscale in order to control and develop new and improved structures and properties. The properties of nanocomposites depend not only on the individual components used but also on the morphology and the interfacial characteristics. Nanocomposite coatings and materials are one of the most exciting and fastest growing areas of research, and novel properties that are previously unknown in the constituent materials are being continuously developed.

Experimental work has shown that virtually all types and classes of nanocomposite materials lead to new and improved properties, when compared to their macrocomposite counterparts. They tend to drastically improve the electrical conductivity, specifically, the ionic conductivity, and thermal conductivity of the

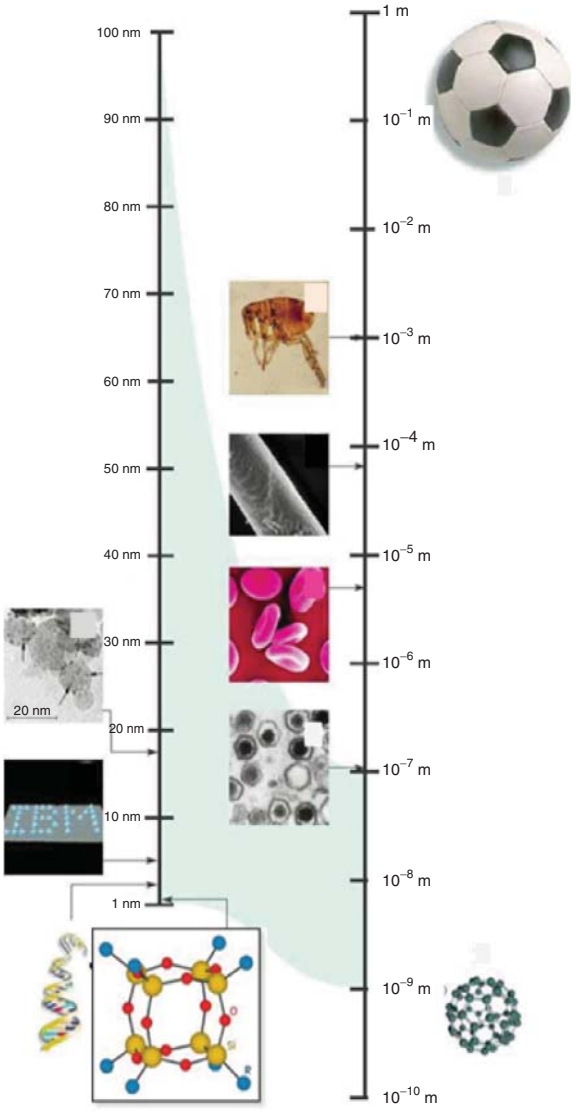

Figure 5.2 How big is a 1 nm length scale?

original material as well as the mechanical properties, for example, strength, modulus, and dimensional stability. Therefore, nanocomposites promise new applications in many fields such as gas separation, aerospace industry, electrical application, mechanically reinforced lightweight components, nonlinear optics, battery cathodes and solid state ionics, nanowires, sensors, and many others. Much effort is going on to develop more efficient combinations of materials and to impart multifunctionalities to the nanocomposites.

Carbon nanofibers, carbon nanotubes (mainly MWCNTs), and polyhedral oligomeric silsesquioxanes (POSSs) are also being used commercially in nanocomposites, and they are gaining ground fast with improvements in cost/performance and processability characteristics.

5.1.2 *How Nanocomposites Work?*

Nanoparticles have an extremely high surface to volume ratio, which dramatically changes their properties when compared with their bulk-sized equivalents. It also changes the way in which the nanoparticles bond with the bulk material. The result is that the composite can be many times improved with respect to the component parts. Some nanocomposite materials have been shown to be 1000 times tougher than the bulk component materials.

5.1.3 Applications

Nanocomposites are currently being used in a number of fields and new applications are being continuously developed. Applications for nanocomposites include:

- Thin-film capacitors for computer chips
- Solid polymer electrolytes for batteries
- Automotive engine parts and fuel tanks
- Impellers and blades
- Gas barriers
- Food packaging.

5.1.4 Polyhedral Oligomeric Silsesquioxane (POSS)

Zero-dimensional nanostructured materials (0DNSMs) are those in which all the dimensions are measured within the nanoscale (no dimensions, or 0D, are larger than 100 nm). The most common representation of a zero-dimensional nanomaterial is the POSS nanoparticle.

Owing to their large specific surface area and other properties that are superior to those of their bulk counterparts arising from the quantum size effect, 0DNSMs have attracted considerable research interest and many of them have been synthesized in the past 10 years [2, 3]. It is well known that the behavior of NSMs (nanostructured materials) depends strongly on their sizes, shapes, dimensionality, and morphologies, which are therefore the key factors that give rise to their ultimate performance and applications. It is therefore of great interest to synthesize 0DNSMs with a controlled structure and morphology. In addition, 0DNSMs are important materials due to their wide range of applications in the areas of catalysis, as magnetic materials, and as electrode materials for batteries.

Moreover, 0DNSMs have recently attracted intensive research interest because the nanostructures have a larger surface area and supply enough absorption sites for all involved molecules in a small space. On the other hand, their having porosity in three dimensions could lead to better transport of molecules.

In this context, hybridizing POSS derivatives with industrially valuable polymeric components can lead to new chemical feedstock technology for the development of interphased nanohybrid materials. There is already evidence to support the belief that modification of polymeric materials using derivatives of POSS is expected to upgrade many of their useful properties namely thermal stability [4], oxidation resistance [5], resistance to atomic oxygen in low Earth orbit [6], glass transition temperature [7], tensile strength [8], fracture toughness [9], abrasion resistance, dimensional stability, dielectric, optical properties, and weather resistance [10].

POSS (Figures 5.3 and 5.4) [11] is a class of organic–inorganic hybrid 0DNSM constituted of inorganic silica, which consists of a rigid, crystalline silica-like core, having the general formula $(RSiO_{1.5})_a(H_2O)_{0.5b}$, where R is a hydrogen atom or an organic group and a and b are integers ($a = 1, 2, 3, \ldots$; $b = 0, 1, 2, 3, \ldots$), with $a + b = 2n$, where n is an integer ($n = 1, 2, 3, \ldots$) and $b \leq a + 2$. POSS is unique in

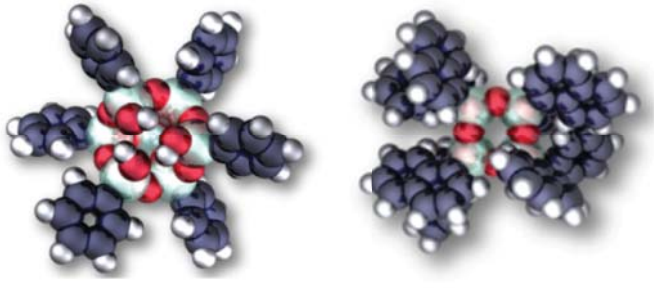

Figure 5.3 Trisilanolphenyl POSS and octanaphthyl POSS.

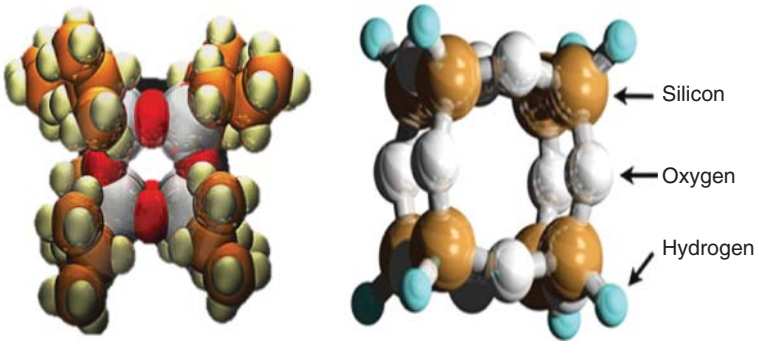

Figure 5.4 Structure of polyhedral oligomeric silsesquioxane.

size (0.5 nm in core diameter) when compared to other nanofillers and can functionally tailor to incorporate a wide range of reactive groups [12].

POSS derivatives have two unique features.

1) POSS chemical composition ($RSiO_{1.5}$) was found to be intermediate between that of silica (SiO_2) and siloxane (R_2SiO).
2) POSS compounds can be tailored to have various functional groups or solubilizing substituents that can be attached to the POSS skeleton.

POSS-based compounds are thermally and chemically more stable than siloxanes. Of several structures of silsesquioxanes (random, ladder, and cage), cage structures contain eight silicon atoms placed at cube vertices. Cubic structural compounds are commonly represented based on the number of silicon atoms present in the cubic structure (Figure 5.5).

One of the most popular branches of silsesquioxanes is POSS including T_8 cage (Figure 5.6), T_{10} cage, T_{12} cage, and other partial cage structures. Tamaki *et al.* [13] and Choi *et al.* [8] have synthesized many kinds of organic–inorganic composites based on POSS.

5.1.5
Hybrid Properties

POSS allows the creation of materials exhibiting hybrid properties. The silica core of the POSS is inert and rigid whereas the surrounding organic groups provide compatibility with the matrix as well as processability. Conceptually, POSS may be thought of as an organic–inorganic hybrid (Figure 5.7). Similarly, POSS is sometimes considered to be a filler and sometimes a molecule. For example, POSS is rigid and inert like inorganic fillers, but unlike those conventional fillers, POSS can molecularly dissolve in a polymer.

Normal fillers and especially nanofillers suffer from agglomeration. The agglomerates formed when using conventional fillers lead to weak points in the polymer (stress concentrations) and this gives poor impact resistance and are susceptible to breakage. As a molecule, POSS dissolves in polymer as 1–3 nm cages and this gives performance advantages that are not seen with fillers. When normal organic molecules are added to a polymer they act as plasticizers, reducing modulus, yield strength, and HDT/Vicat softening temperature. Due to the rigid (high modulus) silica cage structure, POSS addition does not have a detrimental effect on modulus

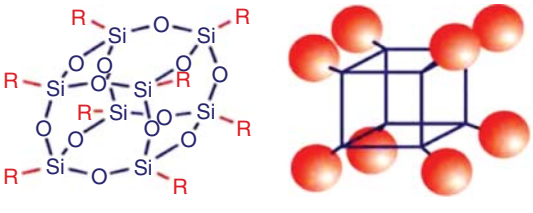

Figure 5.5 Silsesquioxanes Q_8 ($Q = SiO_{2/2}$); R = H, vinyl, epoxy, acetylene, and acrylate.

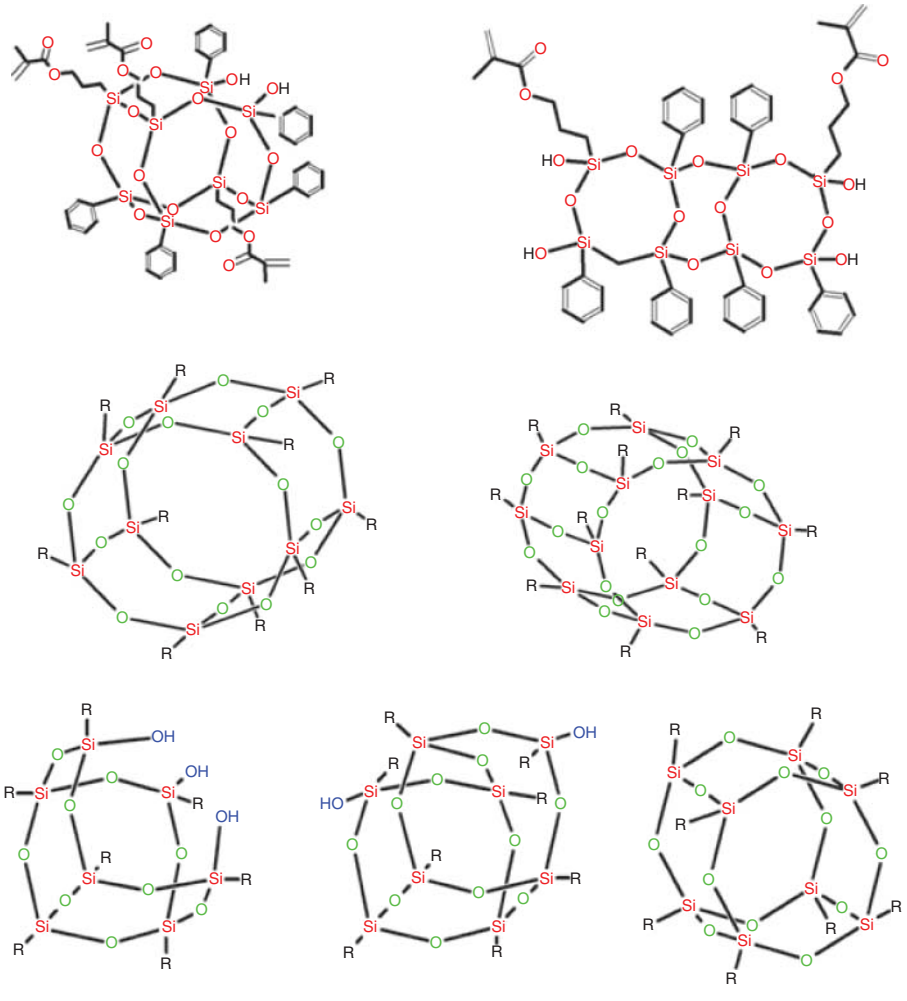

Figure 5.6 Chemical structures of different types of silsesquioxanes.

and normally we see retention of yield strength. The modulus of octacyclohexyl POSS has been calculated as 10–12 GPa. Polymers are normally 1–3 GPa and mineral fillers 15–40 GPa (Figure 5.8).

5.1.6
Polymer Nanocomposites

Polymer nanocomposites are defined as polymers having small amounts of nanometer-size fillers that are homogeneously dispersed by only several weight percentages. The systematic representation of polymer nanocomposites is shown in Figure 5.9.

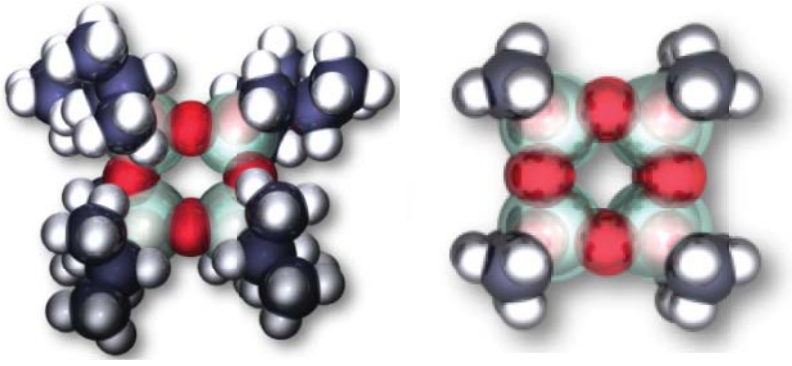

Figure 5.7 Three-dimensional representation of Polyhedral oligomeric silsesquioxane.

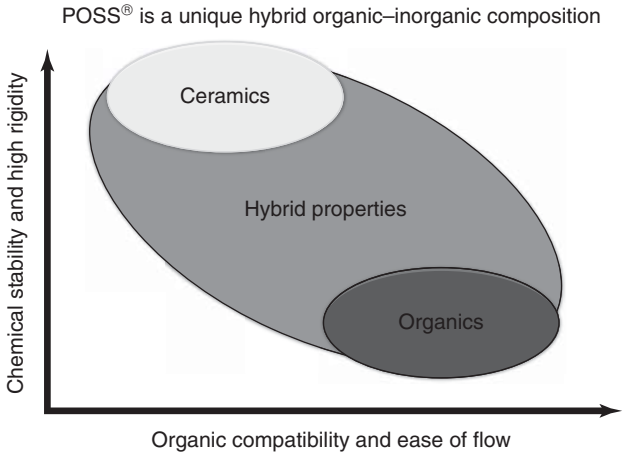

Figure 5.8 The hybrid nature of polyhedral oligomeric silsesquioxane.

Typically 10–100 Å in at least one dimension, addition of even a few weight percent of the nanofillers has a profound impact on the physical, chemical, mechanical, and electrical properties of polymers. Such changes are often favorable for engineering applications. A polymer nanocomposite with a filler having a small size leads to a dramatic increase in interfacial area as compared with traditional composites. This interfacial area creates a significant volume fraction of interfacial polymer with properties different from the bulk polymer even at low loadings [14–18]. While developing a polymer nanocomposite, the attachment of organic groups to nanosized materials can have wide-ranging implications on the interactions occurring at the interfaces between the inorganic

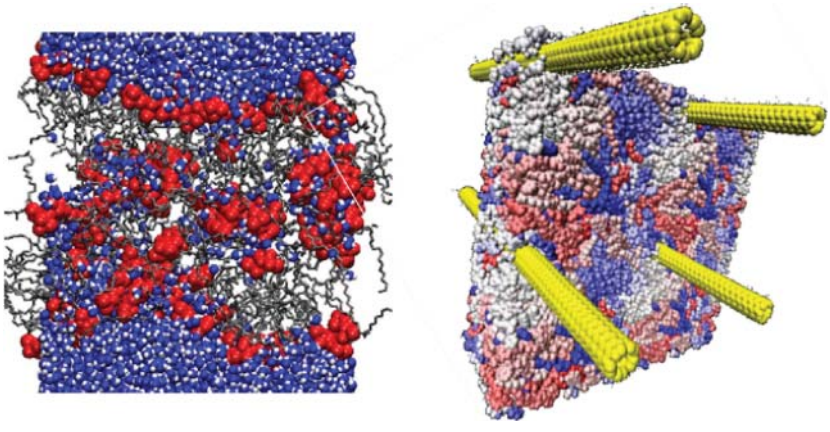

Figure 5.9 Systematic representation of polymer nanocomposites.

composite particles and the organic polymer matrices. These include increased modulus and strength, outstanding barrier properties, improved solvent and heat resistance, and decreased flammability.

The major advantages of incorporating POSS into polymers are as follows:

1) Solubility can be significantly enhanced, which facilitates processability.
2) POSS molecule would influence the chain and segmental mobility, which will affect the local molecular interactions and topology expecting better gas separation properties.
3) Creates entirely new composition with unique properties, which offer specific advantages for the preparation of artificial membranes exhibiting high selectivity and flux, as well as good thermal and chemical resistance.

5.1.7
Hybrid Nanocomposites from Silsesquioxane Monomers

5.1.7.1
Polyamide-POSS Hybrid Nanocomposites

Introduction Recently, many researchers have reported the synthesis of nanocomposites-incorporated polymers and found that these nanocomposites have potential applications because of enhanced processability and solubility with controlled mechanical and thermal properties [19, 20]. Nanocomposites, based on organic/inorganic materials, may combine the advantages of each material such as processability, high solubility, and lower T_g. POSS has a cubic octameric molecule with an inner inorganic silicon and oxygen framework, which

is surrounded by organic functions [21]. Monofunctionalized POSS is suitable for the synthesis of linear thermoplastic hybrid nanocomposites. POSS containing polymers received good attention during the last decade as a novel category of nanoscale structured materials. Incorporation of bulky POSS particles into linear thermoplastic polymers can impart better organo-solubility because of the introduction of bulky POSS pendent group by decreasing the intermolecular forces between the polymer chains. This appears to improve the solubility and processability of polymers significantly[22, 23].

Review of Literature Fina *et al.* [19] prepared the maleic anhydride-grafted polypropylene (PP-g-MA)/POSS hybrids by POSS grafting during a one-step reactive blending process. Thermal, rheological, and mechanical properties improved in the case of the grafting process with respect to simple melt blending. The PA6-POSS (polyamide 6-polyhedral oligomeric silsesquioxane) nanocomposites by *in situ* ring opening polymerization of ε-caprolactam with aminoethylaminopropylisobutyl-POSS contained both primary and secondary amino groups. The TGA results showed that POSS incorporation does not enhance the thermal resistance of PA6/POSS nanocomposites [20].

Polyamide 12/trisilanolphenyl–POSS composites were prepared via melt compounding. The effect of POSS on crystalline structure and crystalline transition of PA12 were studied and enhanced the tensile strength and thermal stability of PA12 [24]. Reversible Addition-Fragmentation Transfer (RAFT) of POSS was successfully prepared using aminopropylisobutyl POSS. The POSS-containing RAFT agent was further applied in the RAFT polymerization of *N*-isopropylacrylamide (NIPAM) to produce tadpole-shaped organic/inorganic hybrid, poly(*N*-isopropylacrylamide) (PNIPAM). The thermal properties of PNIPAM were enhanced by the presence of POSS molecule, until sufficient molecular weight was achieved to dilute the effect of POSS. The self-assembly behavior of the tadpole-shaped inorganic/organic hybrid, PNIPAM was investigated by AFM [25]. POSS-tethered aromatic polyamide nanocomposites with various POSS fractions were prepared through Michael addition between maleimide-containing polyamides and amino-functionalized POSS. A recent study by Gnanasekaran and Reddy [26] reported the preparation of aromatic polyamide–POSS hybrid nanocomposites. Ricco *et al.* [27] prepared polyamide-6/POSS nanocomposites through the polymerization of ε-caprolactam in the presence of ε-caprolactam-functionalized POSS. The POSS fractions in the nanocomposites were tailored by the PA-MI polymer maleimide contents and showed great influence on the thermal and mechanical properties of the polyamide–POSS nanocomposites [28].

The synthesized linear PA-POSS hybrid nanocomposites contains the hexafluoroisopropylidene moiety in diacid part, which offers the expected variation in the physico-chemical properties of polyamides. The solubility and processability problems were thus expected to be solved by introducing the hexafluoroisopropylidene moiety and POSS into polymer. The bulky POSS macromer with ordered

and self-assembled features in the polymer matrix would be expected to play a significant role in improving the physical and chemical properties.

Synthesis of Poly(amic acid) (PAA) PAA was prepared by conventional polycondensation reaction of diamine and dianhydride. 2,2-Bis(3,4-dicarboxyphenyl) hexafluoropropane dianhydride (1 g) was added to dry THF (10 ml) solution containing 2,2-bis[4-(4-aminophenoxy)phenyl]-1,1,1,3,3,3-hexafluoropropane (1.16 g). The mixture was then stirred for 24 h under nitrogen at room temperature (RT) (25 °C) and the resulting solution gradually became light gray viscous. The clear PAA solution was isolated by precipitating the PAA into toluene/hexane (1 : 1 V/V, 100 ml) mixture. The PAA was extensively washed with a toluene/hexane (1 : 1 V/V, 100 ml) mixture, filtered, and dried under vacuum for 24 h at 70 °C.

Synthesis of Aminopropyl Heptacyclopentyl-Polyhedral Oligomeric Silsesquioxane (AP-POSS) Aminopropyl heptacyclopentyl-polyhedral oligomeric silsesquioxane (AP-POSS) was prepared as reported in the literature [29].

Synthesis of Polyamide-POSS Hybrid Nanocomposites (PA-POSS) The mixture of PAA (1 g) and thionyl chloride dissolved in dry DMF (2 ml) was refluxed for 2 h and then the solution was refluxed for a further period of 3 h. The unreacted $SOCl_2$ was removed by adding hexane (10 ml), heated for 20 min and was then distilled off to leave a deep yellow viscous liquid. A mixture of five different mole % of AP-POSS, along with five different mole % of 3-(trifluoromethyl)aniline (TFA) and triethylamine (2 ml) in dry THF (4 ml) was added drop wise to the deep yellow viscous liquid and stirred for 3 h at 0 °C. The resulting solution was precipitated using methanol (100 ml) and filtered. It was then washed thoroughly with methanol (20 ml) and dried at 50 °C for 10 h (yield 80%). The path of this preparation is given in Scheme 5.1.

Results and Discussion The ^{1}H NMR spectra of PAA and PA-POSS hybrid nanocomposites have been shown for comparison in Figure 5.10a,b. It was observed from Figure 5.10b that there was a single chemical shift for amide N–H protons at 10.2 ppm. The disappearance of amine absorption shift at 3.2 ppm and the presence of methylene proton shifts of the AP-POSS chain were observed at 1.9, 1.7, and 1.3 ppm. The incorporation of AP-POSS into the PAA main chain through amidation reaction in the presence of TEA was also confirmed by the presence of an amide group in the polymers. The graphical representation of PA-POSS has been shown in Figure 5.11.

Morphological Studies AFM was employed to investigate the physical characterization such as surface morphology and topological structure of the PA-POSS hybrid nanocomposites in the tapping (contact) mode as shown in Figure 5.12. By increasing the POSS content in the hybrid nanocomposites there is an increase

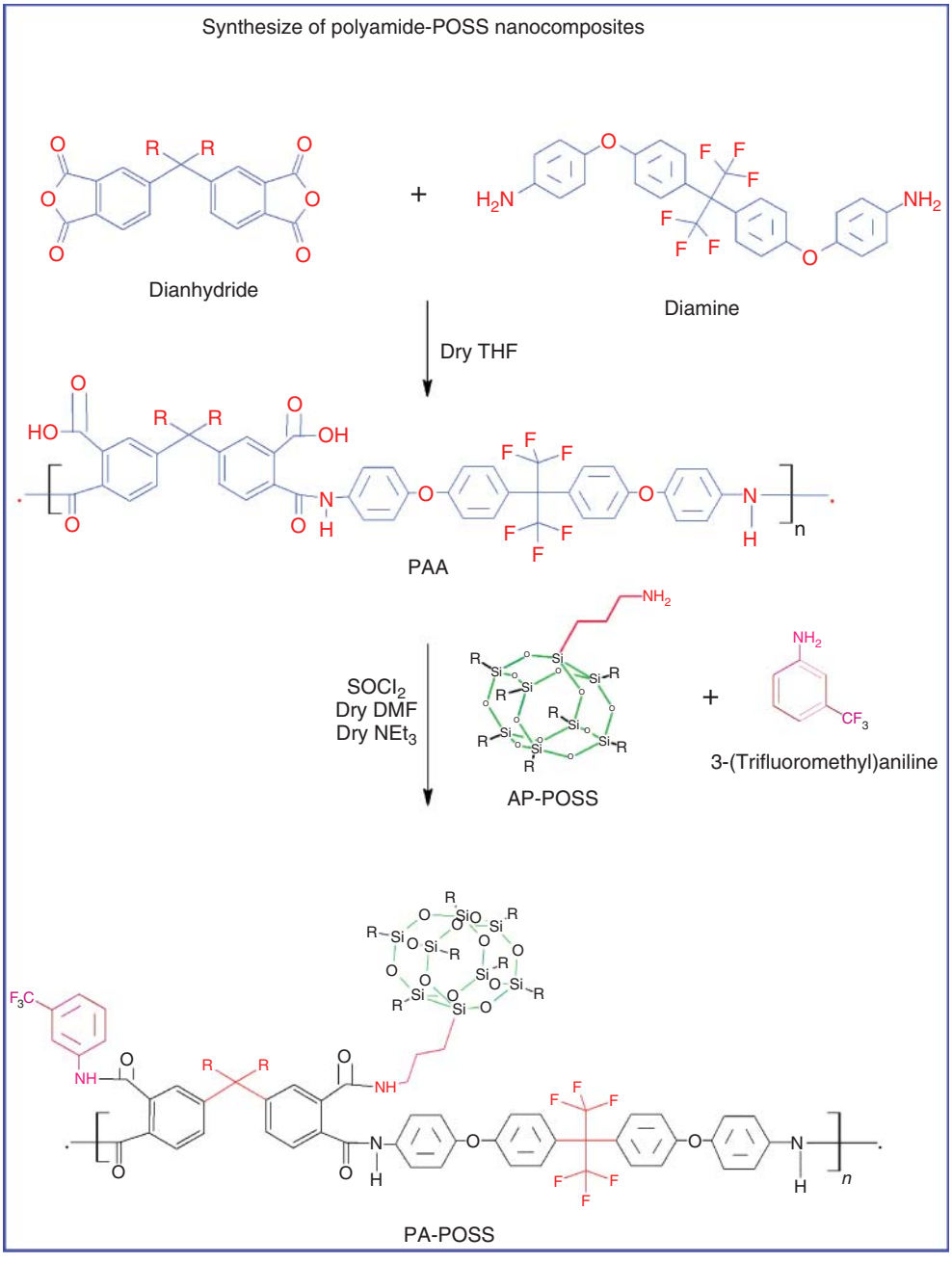

Scheme 5.1 Synthesis of polyamide-POSS nanocomposites (PA-POSS).

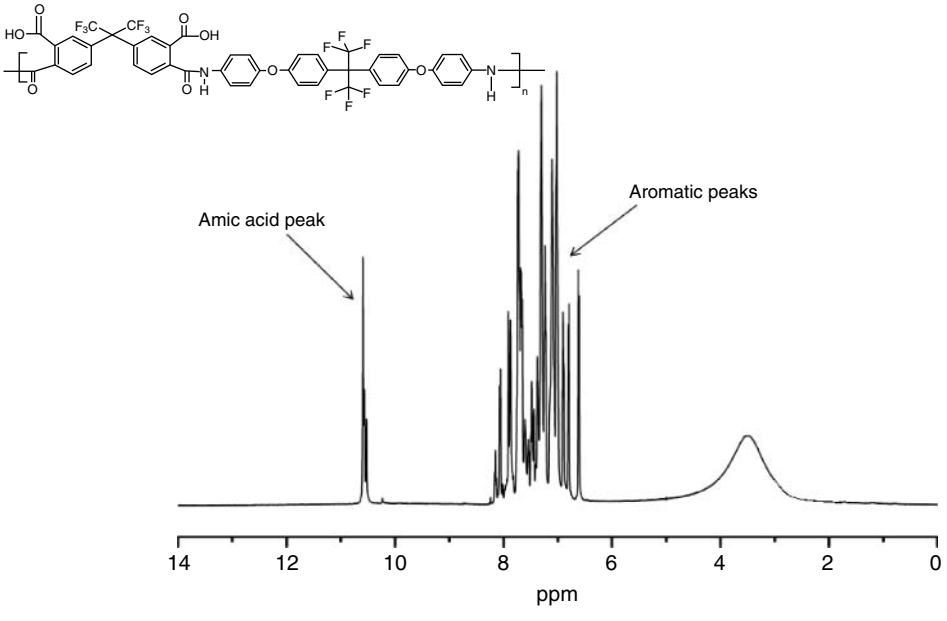

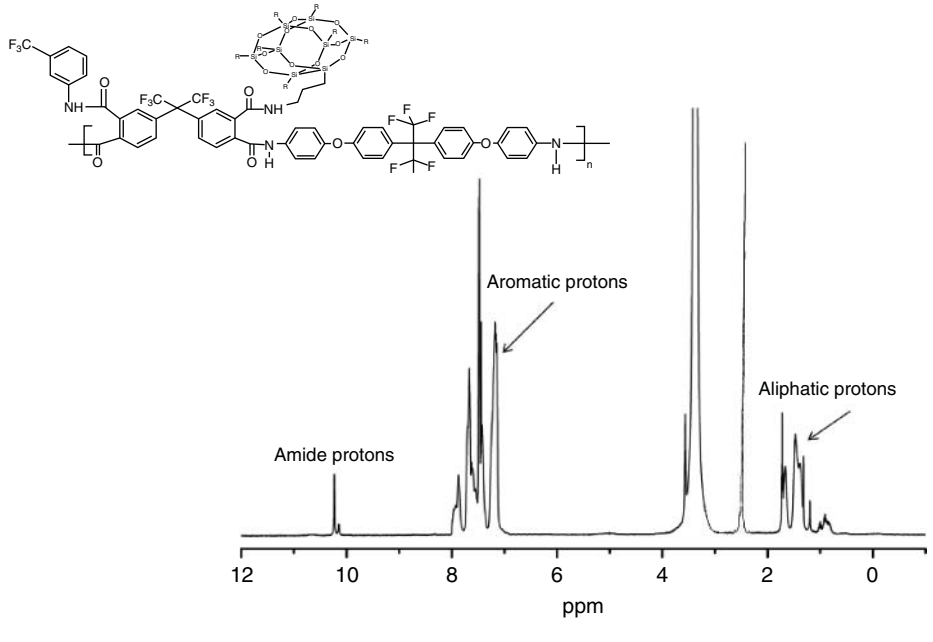

Figure 5.10 (a) ^{1}H NMR of polyamic acid (PAA). (b) ^{1}H NMR PA-POSS nanocomposites.

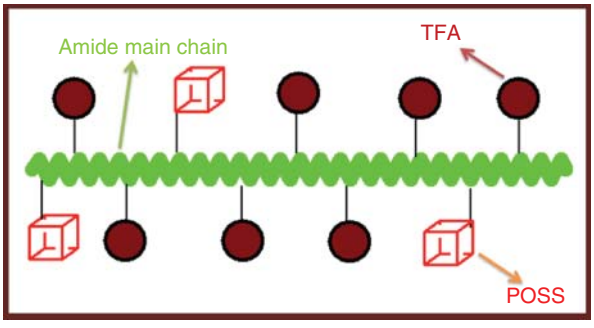

Figure 5.11 Systematic representations of PA-POSS hybrid nanocomposites.

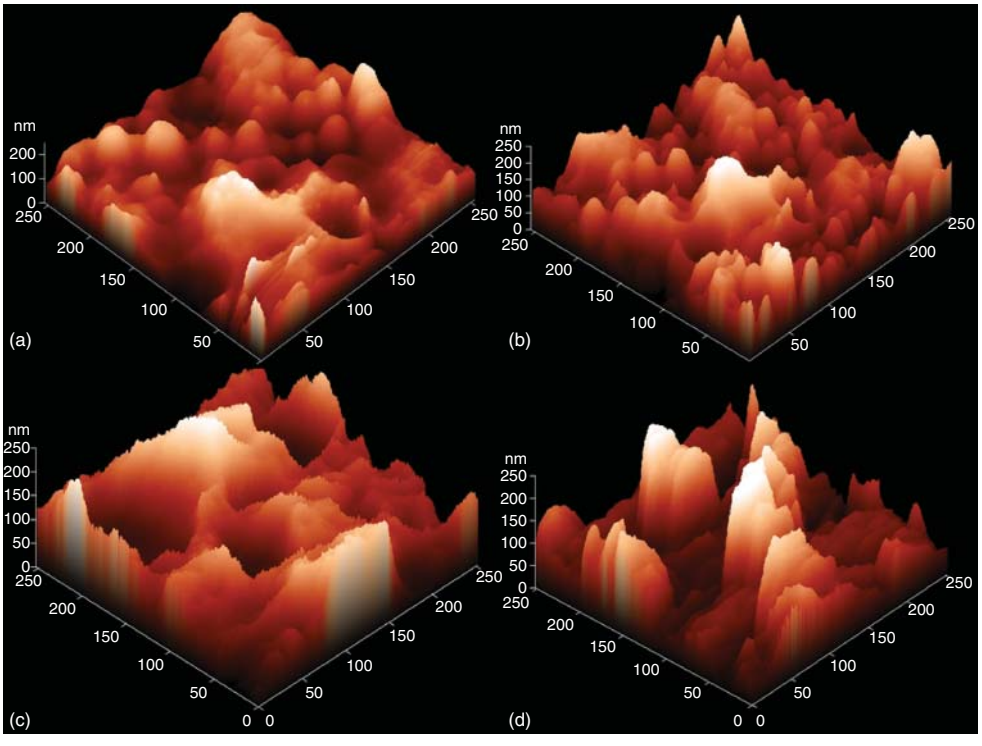

Figure 5.12 Atomic force microscopy of PA-POSS nanocomposites.

in the roughness on the surface of the PA-POSS hybrid nanocomposites as well as larger raised features on the surface. Similar type of observations was reported by Misra *et al.* [30]. According to the viscoelasticity and volume fraction of POSS in the hybrid, it was plausible to propose that the light region in the micrographs was ascribed to the POSS portion, whereas the dark region was ascribed to the

PA matrix. This could be perhaps related to the nanostructures present in the PA-POSS hybrid nanocomposites.

The microphase separation of the PA-POSS hybrid nanocomposites were confirmed by SEM analysis. The microphase separations in the SEM pictures were due to the distribution of POSS (i.e., physical and chemical bonding) in the polymer matrix. The inorganic silicon particles (POSS) were shown as bright dots and may be due to the physical interaction like dipole–dipole interaction between POSS and organic polyamides. Moreover, Liu *et al.* [31] indicated that the formation of homogeneous phase is attributed to the covalent linkage between the amide and POSS domains.

TEM was also used to characterize the morphology of PA-POSS hybrid nanocomposites. This was similar to the reported values by Feng *et al.* [32] in the case of PAS-POSS. According to the difference in transmitted electronic density between organic amide polymer and POSS component, it was assumed that the dark area represents POSS domains, and the white region represents amide matrix. An analysis of WAXD patterns showed that POSS group was present in the PA-POSS hybrid nanocomposites. The X-ray powder pattern of POSS shows two main characteristic diffraction peaks at 7.9° and 18.9° (2θ).

These values are typical for the crystal structure of the POSS. In each case, diffraction patterns of the PA-POSS hybrid nanocomposites with 0.1 and 0.3 mol% POSS have only a broad amorphous peak at 25.6° (2θ), corresponding to the amorphous PA matrix peak.

The appearance of this characteristic diffraction peak in the PA-POSS shows that the POSS nanoparticles have aggregated in the hybrid nanocomposites and the degree of aggregation increases with further increase in the POSS content [33]. This is validated by the results of the WAXD and TEM. The conspectus of this PA-POSS preparations and its characterization has shown in Figure 5.13.

5.1.7.2 Poly(urethane-imide) POSS Hybrid Nanocomposites (PUI-POSS)

Review of Literature Avadhani *et al.* [34] prepared novel poly(urethane-imide) by using diisocyanates containing built-in imide group. Yeganeh and colleagues [35] have synthesized poly(urethane-imide) by reacting isocyanate-terminated PU (prepolyurethane) prepolymer with glycols containing imide function as a chain extender. Zuo and coworkers [36, 37] have reported a novel approach to prepare PUIs (poly(urethane-imides)). Their approach was based on the reaction of PU prepolymer and poly(amic acid) (PAA), which was a precursor of polyimide (PI), providing PUIs with a network structure and improved thermal stability and solvent resistance. They attempted to prepare PI-PUI (polyimide-poly(urethane-imide)) copolymers as semi-interpenetrating networks via *in situ* coimidization between PI and PUI precursors [38].

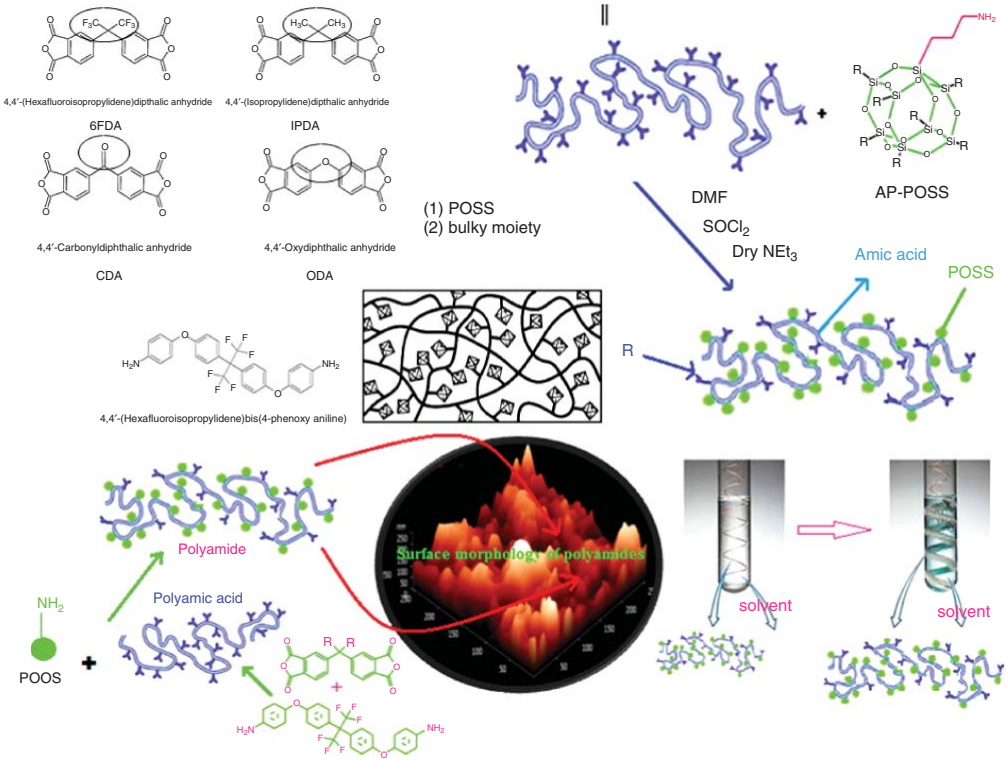

Figure 5.13 Graphical representation of prepared PA-POSS nanocomposites.

An imide containing disuccinic anhydride was synthesized and successfully used as a chain extender for NCO-terminated polyurethane prepolymers. Using this method, four imide structures (two rigid aromatic and two flexible aliphatic ones) per repeating unit of final polymers were introduced as a hard segment. Investigation of physical and thermal properties showed that in comparison to conventional polyurethanes, the thermal stability of PUIs was enhanced considerably and simultaneously good mechanical properties and processability were preserved [39]. Chattopadhyay *et al.* [40] synthesized two different sets of PU-imide/clay hybrids from two types of polyester polyols. CTAB-modified montmorillonite (MMT) clay was introduced to get fine clay dispersion into the polyester matrix by ultrasonication method before the reaction with toluene diisocyanate (TDI) and isophorone diisocyanate (IPDI). The excess isocyanate available in the NCO-terminated prepolymers was reacted with PMDA.

Synthesis of Fluorinated Prepolyimide (FPI) 4,4′-(Hexafluoroisopropylidene) diphthalic anhydride (6FDA) in 5 ml of THF was placed in a flask equipped with a nitrogen inlet and stirred using a magnetic stirrer until a clear solution was obtained. To the clear solution, hexamethylene diisocyanate in 3 ml of THF was added followed by stirring. The reaction mixture was refluxed at 90 °C in 6 h by connecting to a spiral condenser. The synthetic route was given in Scheme 5.2

Synthesis of Prepolyurethane (PU) The NCO-terminated PU was prepared reacting PDMS-OH or PDMS-NH_2 or PPG-OH or PEG-OH or PCL-OH and HMDI in a 50 ml two-necked flask. Hydroxy-terminated soft segments (–OH) and Cy-POSS were reacted with HMDI in 3 ml of THF, followed by adding two drops of DBTDL as a catalyst at RT (35 °C) for 6 h. The synthetic route is given in Scheme 5.2 (I) and Scheme 5.3 (I).

Synthesis of Fluorinated and Mixed Soft Segment Poly(urethane-imide) POSS Membranes (FPUI-POSS) The FPUI-POSS (fluorinated poly(urethane-imide) polyhedral oligomeric silsesquioxane) and MSPUI membranes were prepared by varying the ratios of prepolyimide and PU in the ratio of 0/100, 10/90, 20/80, 30/70, 100/0 and various soft segments such as PDMS-OH or PDMS-NH_2 or PPG-OH or PEG-OH or PCL-OH respectively. THF was used as a solvent for refluxing by using spiral condenser at 90 °C for 6 h. The resulting viscous solution was transferred into a Teflon-coated petridish and was kept at RT for 6 h. Then all the membranes were kept in a hot air oven at 150 °C for 7 h. The model reaction of this polymer is shown in Scheme 5.2.

Gnanasekaran *et al.* [41] and Gnanasekaran and Reddy [42] studied the gas permeation rates of O_2, N_2, and CO_2 gases and selectivity of O_2/N_2 and CO_2/N_2 using synthesized FPUI-POSS. PUI-POSS membranes having different amounts of fluorinated imide and different types of soft segments were synthesized via

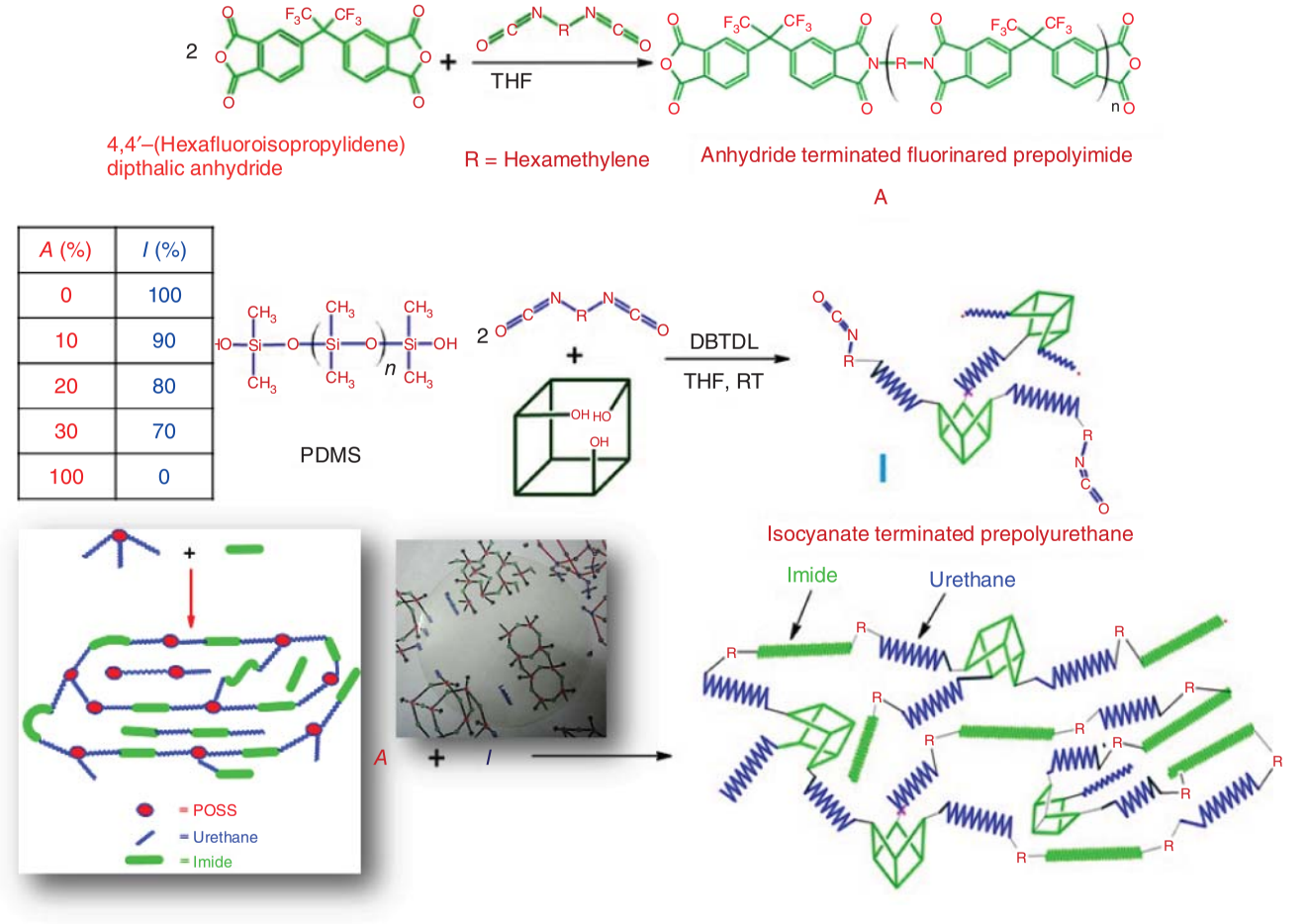

Scheme 5.2 The synthetic route of FPUI-POSS nanocomposite membranes.

I (%)	*A* (%)
PCL+PDMS-OH (90)	10
PPG+PDMS-OH (90)	10
PDMS-NH2+PDMS-OH (90)	10
PDMS-OH (90)	10

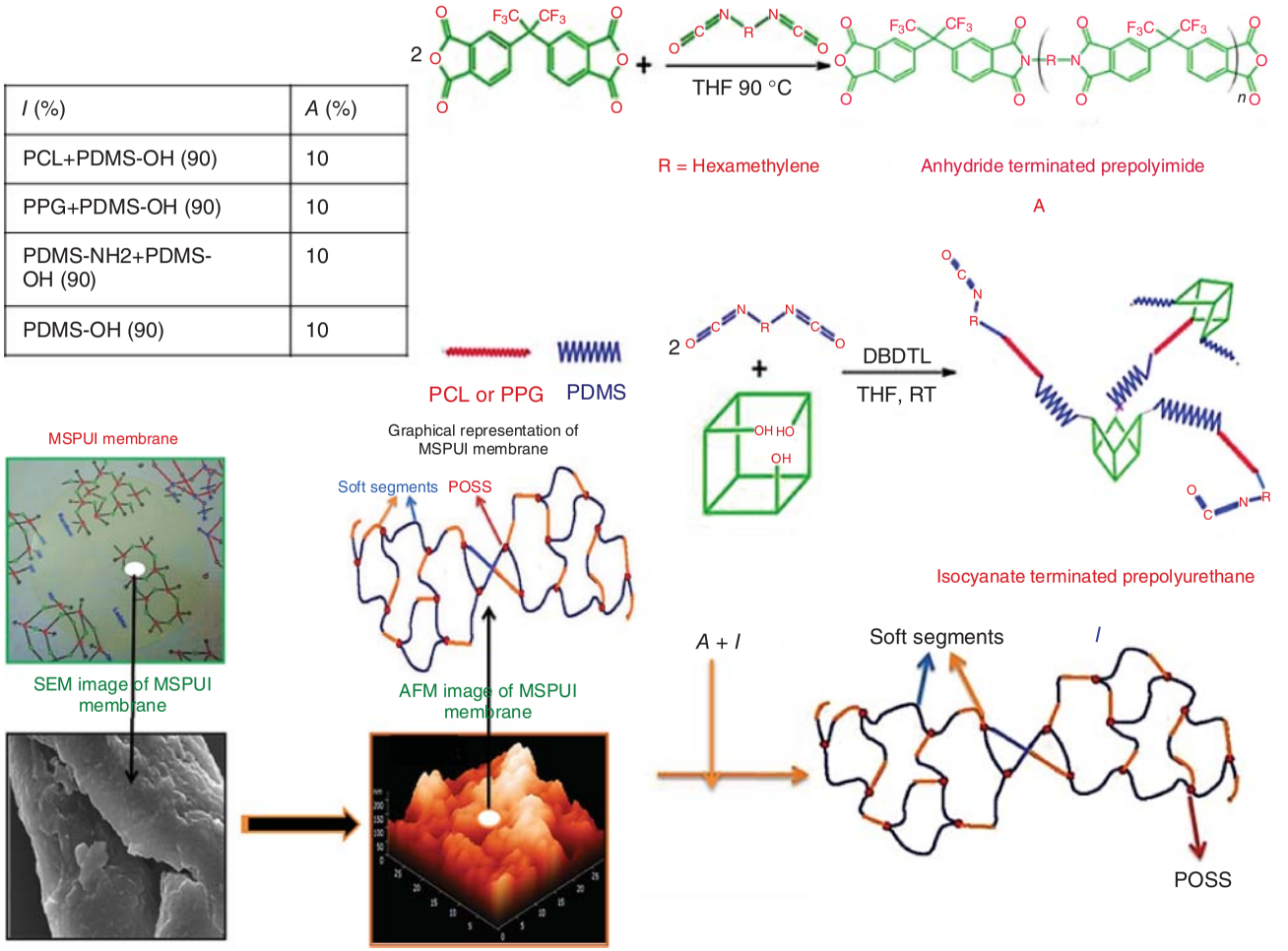

Scheme 5.3 The synthetic route of MSPUI-POSS nanocomposite membranes.

simple condensation reaction of isocyanate-terminated PU and anhydride-terminated fluorinated prepolyimide (FPI). The study on the surface morphology about the extent of compatibility of the polar and nonpolar groups in the network was carried out in order to define the structure–properties relationship. They have introduced POSS and bulky –(C(CF_3)$_2$)– groups into the hybrid membranes by chemically reacting functional groups of POSS molecules and prepolyimide in order to maintain both selectivity and permeability with good thermal properties.

5.1.8
Range of Other POSS Nanocomposites

Crosslinked polysiloxanes were directly synthesized by anionic ring-opening copolymerization of octaisobutyl-POSS as a multifunctional monomer with octamethylcyclotetrasiloxane (D4) using base catalysts (potassium hydroxide (KOH) or tetramethylammonium hydroxide (Me_4NOH) siloxanolate), indicating that crosslinked polysiloxanes exhibit distinct T_g and excellent thermal stability [43]. Synthesis of liquid crystal POSS and specific problems connected with the nature of silsesquioxane cage, and special properties that their geometry imparts to their mesogenic behavior of liquid-crystal polyhedral silsesquioxane materials have been described [44]. Synthesis of these materials is based on a silsesquioxane cage-modification process, starting with a suitably functionalized cage, to which mesogens are attached [45]. Many systems are obtained based on hydrosilylation reaction of hydrido-silsesquioxanes and mesogenic groups [46]. Richardson *et al.* [47] reported a hexadecamer, first-generation, octasilsesquioxane liquid-crystalline dendrimers.

POSS–POSS nanohybrids were synthesized by hydrosilylatively copolymerizing with stoichiometric amounts of octavinylsilsesquioxanes, with T_8H and Q_8M_8H in toluene using Pt catalyst [48]. POSS cubes with longer spacer groups are more reactive than those with no spacer groups. Pores within POSS cube interiors (diameter, 0.3 nm), and pores between cubes (diameter, 1–50 nm) were determined according to nitrogen absorption, positron annihilation lifetime spectroscopy (PALS), and small angle X-ray scattering (SAXS) data. Benzoxazine/POSS hybrids were synthesized by using octafunctional cubic silsesquioxane (CSSQ) (MBZ-POSS) with eight organic benzoxazine tethers as a curing agent [49–51]. In benzoxazine/POSS hybrids, POSS aggregates occur in larger scale at higher POSS contents and the reason for heterogeneous phase separation may be due to less compatibility of inorganic silsesquioxane core with organic benzoxazine species. During the formation of polybenzoxazine (PBA)/POSS hybrids, POSS particles were separated from a PBA-rich region, leading to POSS-rich domains (50–1000 nm). Zheng *et al.* [52] observed that OG was used to prepare PBA/POSS NCs. Crosslinking reactions involved during the formation of PBA/POSS NCs can be divided into two types: (i) ring-opening polymerization of benzoxazine and (ii) subsequent reaction between

in situ-formed phenolic hydroxyls of PBA and epoxy groups of OG. Other PBA/POSS NCs obtained by the reaction of OAPS and 2,2′-(1,3-phenylene)-bis(4,5-dihydro-oxazoles) (PBO) are reported [53]. Dynamic mechanical analyses indicated that NCs exhibited higher T_g values than pristine PBZ and PBZ-PBO resins. Storage modulus of NCs was maintained at higher temperatures even with a small amount of OAPS incorporated into composite systems. Thermal stability of hybrid was also improved by inclusion of OAPS. Crosslinked poly(4-vinylpyridine)/POSS NCs were obtained by the reaction of epoxy group of OG with pyridine ring of poly(4-vinylpyridine) [54].

Amphiphilic silsesquioxane derivative, 1-(1,ω-propylenemethoxy)oligo (ethyleneoxide)-3,5,7,9,11,13,15-heptahydridopentacyclo [9.5.13,9.15,15.17,13] octasiloxane has been prepared by reacting T_8H and allyl functional oligo(ethyleneoxide) ($M_n = 750\,g\,mol^{-1}$) through PCH [55]. Associative behavior of new amphiphilic telechelics containing POSS as an end-group of PEG of varying chain length were investigated using capillary viscometry. Viscosities were strongly affected by solvent composition in THF/water mixtures [56]. POSS modification increased storage modulus and Young's modulus of polyamides slightly decreased their T_g from 312 to 305 °C, and significantly lowered their dielectric constants from 4.45 to 3.35 [28]. Supramolecular inclusion complexations (ICs) of POSS-capped polycaprolactone (PCL) with α-and γ-cyclodextrins (CLs) were derived [57]. Crystallization kinetics of silsesquioxane-based hybrid star, poly(3-caprolactone) was investigated by synthesizing a series of silsesquioxane-based hybrid star poly(3-caprolactone) having different arm lengths through ring-opening polymerization of 3-caprolactone [58].

Poly(alkyl silsesquioxane), PASSQ, copolymers consisting of various chemically linked alkyl units over methyl group as a pore forming moiety, and 1,2-bis-trimethoxysilylethane (BTMSE), were synthesized and their thermo-mechanical and optical properties were investigated [59]. Higher alkyl groups in PASSQ were composed and thereby lower refractive indices from 1.45 to 1.27 due to formation of nanopores in film were achieved. Modulus for BTMSE-based PASSQ films were significantly higher than 3.8 GPa of typical thin film of poly(methyl silsesquioxane). Smith *et al.* [60] synthesized and characterized PFCB aryl ether copolymers and multiblock copolymers with pendant cyclobutyl and *iso*-butyl-functionalized POSS cages. Synthesis of POSS aryl trifluorovinyl ether (TFVE) monomers was accomplished by condensation of commercial monosilanolalkyl-POSS with a TFVE-functionalized chlorosilane. POSS/PFCB aryl ether copolymers demonstrated excellent solution processability, producing optically transparent and flexible films. Incorporation of POSS showed no change in thermal stability as compared to PFCB aryl ether homopolymer.

5.1.8.1 Blends of POSS Nanocomposites

Polysiloxane composites containing POSS were prepared by melt blending. Crosslinking polysiloxane caused changes in POSS solubility that enhanced

phase separation. But cross-links caused constraints, which decreased domain sizes of precipitated phases [61]. Octamethyl-POSS-HDPE NCs were prepared by melt mixing route (Figure 5.14). Joshi *et al.* [62] observed that POSS does not interfere with crystallization of HDPE. At low concentrations (0.25 – 0.5 wt%), POSS particles act as lubricants, lead to decrease in complex viscosity as compared to neat HDPE, show significantly high storage modulus and also enhance thermomechanical properties than HDPE.

Composites of poly(methyl vinylsiloxane) with POSS were prepared by melt blending showing that highly crystalline POSS macromers could undergo condensation reactions at 230 °C in air, leading to partially amorphous structures. Also, POSS crystals apparently dissolved in polysiloxane at high temperatures and POSS crystals with hexahedral or flake-like structures recrystallized upon cooling. Both crystallites and POSS molecules coexisted in these blends, with the amount of dispersed molecular POSS increasing at higher temperatures. POSS molecules exhibited some physical interactions with free polysiloxane chains that are not cross-linked. However, cross-linking induced phase separation. During the curing process, POSS molecules could react with polysiloxane, resulting in decreases in cross-link density. Original POSS crystals could also be dissolved in polysiloxane during the initial curing stages, but recrystallization upon cooling gave regenerated crystals that were roughly spherical [63]. Thermal properties and morphological development of isothermally crystallized isotactic polypropylene (IPP) blended with nanostructured POSS molecules at very small loading of POSS were studied [64].

Maitra *et al.* [65] grafted various oligomeric PEOs with different chain lengths ($n = 2$, 4, 8, 12) onto Q_8M_8H, and reported that silica surface affects the thermal behavior of oligomeric PEOs. A most dramatic effect was observed for PEO($n = 4$), where the original crystalline material became completely amorphous; 4 PEO repeat units were insufficient for crystallization to occur at the surface and PEO oligomers crystallized with increasing side chain length.

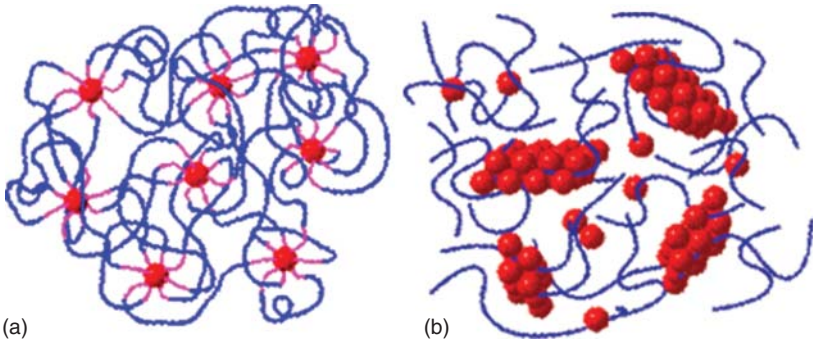

Figure 5.14 Graphical representation of both octafunctioalized POSS (a) and blended polymer nanocomposites (b).

Maxima in ion conductivity observed for PEO chain lengths ($n = 4$ and 8) have been attributed to the absence of crystallinity as well as enhanced mobility of short side chains in comb-like polymers. Mya *et al.* [66] discussed crystallization behavior of star-shaped poly(ethylene oxide) with CSSQ.

5.1.8.2

Bridged Polysilsesquioxanes

Bridged polysilsesquioxanes (BSSs) represent a class of highly cross-linked hybrid organic–inorganic polymers, which are derived from hydrolytic polycondensation of organo-bridged silsesquioxane precursors having general molecular formula $(RO)_3$–Si–R′–Si–$(OR)_3$, where R and R′ are organic groups [67, 68]. BSSs, prepared by sol–gel polymerization of organo-bridged trialkoxysilane precursors, are network polymers, in which the basic building block contains two silicons directly attached to a hydrocarbon bridging group. The remaining three bonds to each silicone are siloxane linkages as shown in Figure 5.15. By connecting two or more silsesquioxane groups to R′, a material with as many as six siloxane linkages (Si–O–Si) per monomer unit can be prepared, as opposed to just four in tetraalkoxy silanes. By introducing hydrocarbon spacers into a siloxane network, the properties (hydrophobicity, surface area, pore size, UV-visible absorption, and fluorescence) can be significantly modified [69, 70]. These materials allow to have properties (porosity, permeability, permselectivity, chemical functionality, and chemical, mechanical, and thermal stability) to be fine-tuned because of the vast variety of synthetically available monomers [71, 72]. Honma *et al.* [73, 74] synthesized a protonic conductive polysilsesquioxane membrane containing PEG, polypropylene oxide, and polytetramethylene oxide bridging groups functionalized with isocyanatopropyltriethoxysilane and condensed in the presence of phosphotungstic acid or monododecyl phosphate. Khiterer *et al.* [75] reported BSSs containing covalently bound sulfonic acid group materials that were used to prepare mechanically stable gel membranes for fuel cell application. BSS molecules are used as precursors for

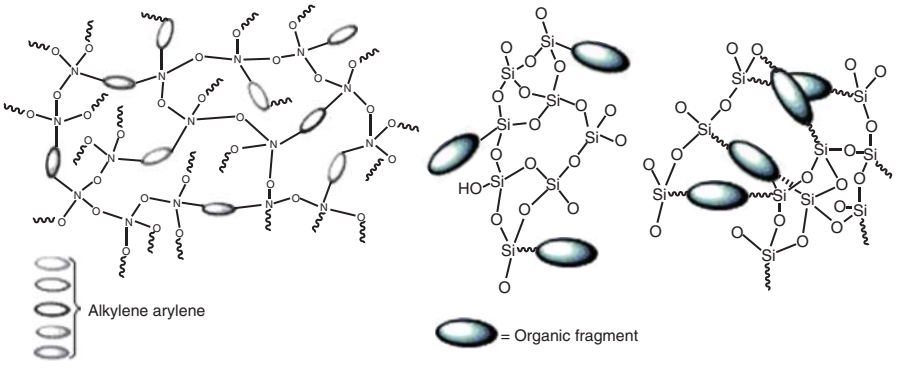

Figure 5.15 Systematic representation of bridged polysilsesquioxanes nanocomposites.

the synthesis of periodic mesoporous organosilicas (PMOs) or bifunctional PMOs. A new methodology was adopted for the preparation of PMOs films by adopting evaporation-induced self-assembly procedure to obtain spherical NPs from the initially developed basic aqueous medium precipitation procedure [76].

Surfactant-directed self-assembly [77, 78] and self-directed assembly [79, 80] methods have been successfully developed for fabrication of BSSs with well-organized structures. Self-directed assembly that takes advantage of weak interactions, such as H bonding and hydrophobic interactions between bridging groups (R′), provides a very easy method for fabricating a hierarchical structure. By judicious choice of organic substructure (R′) in precursor, new intrinsic nanomaterials including both the nature of molecules and their collective properties within an aggregate can be realized [79]. All mesoporous organosilicas contain aliphatic organic groups with relatively short chains (ethane or ethylene) or aromatic (arylene, thiophene, and biphenylene) moieties [81–84]. Very few reports are available for amines and thiols incorporated PMOs [85].

5.2 Advantages of POSS Nanocomposites

- POSS molecule will influence the chain and segmental mobility, which will affect the local molecular interactions and topology expecting better gas separation properties.
- The POSS-incorporated polymers have high thermal and oxidative resistance as well as reduction in flammability.
- The POSS cages can act as cross-linking points in the network if the multifunctional POSS molecules are used as nanosized fillers in the molecular building-block approach to the design of organic–inorganic hybrid materials.
- Hybrid formulations exhibit better properties such as improved thermal stability, mechanical barrier properties, decreased thermal conductivity, reduced flammability, improved corrosion resistance, and reduced solvent (or water) absorbance than those of conventional polymers due to stronger interfacial forces of attraction between the nanometer-sized domains.

Hence, the idea behind the planning of this chapter is to synthesize new polymeric materials containing silsesquioxane nanoparticles. Polyamide has been chosen as the core material to study the contribution of POSS molecule incorporated into the polymer on morphological, thermal, and gas transport properties. The combination of POSS and amide has better improved thermal and mechanical properties than the individual polymers. The objective of this is to design polyamide-POSS and to study the effect on morphological, thermal, and surface properties.

5.3
Applications

5.3.1
Gas Separation Studies

Natural gas plays an important role in today's energy production and is one of the fastest growing fossil fuels. It has been widely used as the energy source as the energy source for electricity generation as well as for natural gas for powered vehicles, domestic appliances, and in the manufacture of metals and chemicals. According to available statistics, the United States produces 50% of this domestic consumption of electricity through the combustion of natural gas. There is every possibility that there will be a dramatic increase in the use of natural gas in the next 20–30 years. The main reason being that natural gas offers many environmentally friendly properties such asno production of sulfur oxides (SO_x), low levels of nitrogen oxides (NO_x) and relatively lower emissions of carbon dioxide than those of other fossil fuels such as coal and oil. CO_2 is a major component contributing to the sweetening of natural gas and causing the greenhouse effect. Therefore, the separation of CO_2 from natural gas is of utmost importance as this may dramatically reduce the pipeline corrosions and enhance the efficiency of high-purity energy products [86–88]. According to acceptable pipeline requirements for optimizing corrosion, the concentration specification of CO_2 must be <2%. Amine absorption is a main strategy that is currently employed in the industry to facilitate CO_2 removal from natural gas [89]. In contrast, membrane separation processes have been proven to be technically and economically far superior in view of their versatile properties, simplicity, and ease of installation and operation, low maintenance requirements, and reduced cost, than the gas separation model as shown in Figure 5.16. Asunction and Liane [90] demonstrated that POSS-epoxy membranes provide excellent O_2 barrier properties that are of potential use for a wide variety of packaging applications and have also shown that O_2 barrier increases on increasing the cross-linking density of the POSS-epoxy membrane. Tejerina and Gordon [91] explained both theoretically and experimentally that the POSS molecule offers high barrier to N_2 diffusion than O_2 gas. Lin and Freeman [92] reported that the POSS molecule in the membrane decreases the permeability of gases. Despite these observations, the exact role of POSS molecule in the gas transport mechanism is still not known clearly. To confirm this, I have decided to direct our basic research toward the synthesis of polysilsesquioxanes derivatives and toward their membranes to determine the exact mechanism of silsesquioxane nanoparticles on transport properties as well as to find the usage of these membranes in commercial gas separation processes.

5.3.2
Aerospace Industry

The aerospace industry is interested in materials that will reduce the mass of the vehicles, thereby making them less expensive to operate (Figure 5.17). Recent

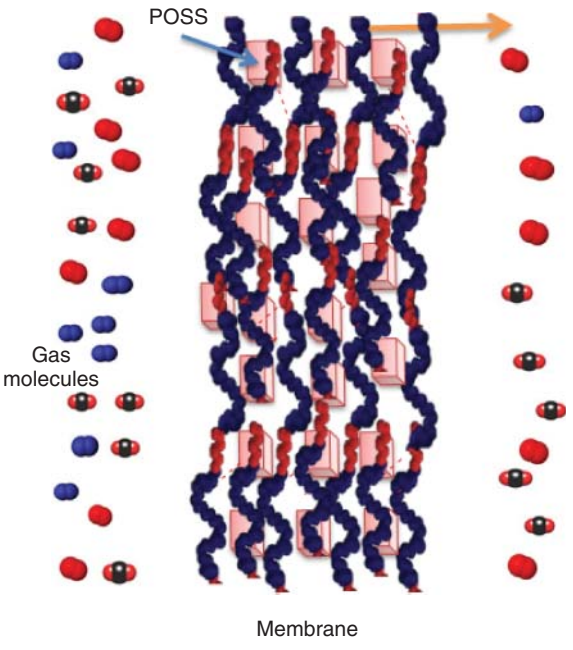

Figure 5.16 Schematic representation of gas permeation model.

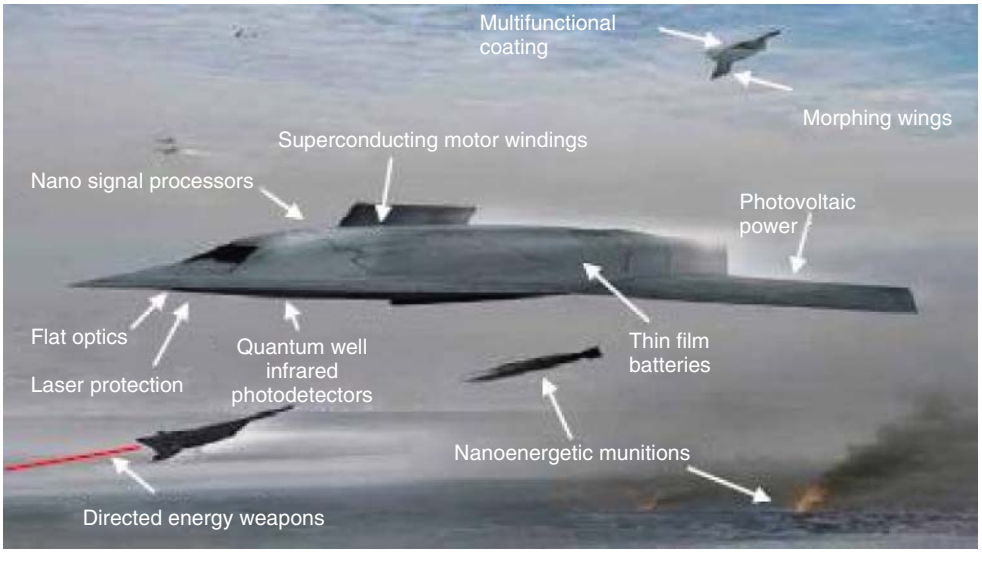

Figure 5.17 Graphical representation of aeronautic applications.

aerospace research focused on combining POSS nanofillers with various polymers to decrease the payload's mass and improve fuel efficiency without sacrificing heat resistance. POSS nanofillers with large area-to-volume ratios are suspected to be more easily dispersed than other fillers, such as micron scale glass. Also, POSS nanofillers should provide better adhesion with matrix materials in high-performance composites. In addition, the aerospace industry is interested in POSS fillers in their capacity to act as heat transfer agents, provide electromagnetic shielding, and control conductivity in electronic applications [93].

5.3.3 Electric Applications

The dielectric constant values of CFPA-POSS, CHPA-POSS, CAPA-POSS, and OXPA-POSS are 3.29, 3.33, 3.45, and 3.75 respectively at 100 kHz. CFPA-POSS had a lower dielectric constant than that of the other polyamides because of the presence of trifluoromethyl group. It was showed that the polyamides containing bulky POSS and fluoro groups can effectively decrease dielectric constants of the polyamides. Such type of results could be ascribed to the small dipole and the low polarizability of the C–F bond as well as the increase in the free volume [94, 95]. Moreover, the polyamides with bulky POSS groups increase the free volume of polyamide and further lower the values of dielectric constant, which may be due to the decrease in the number of polarizable groups per unit volume [96]. Therefore, the CFPA-POSS nanocomposites can be used as low dielectric materials in the field of microelectronic applications. The graph shown in Figure 5.18 suggests

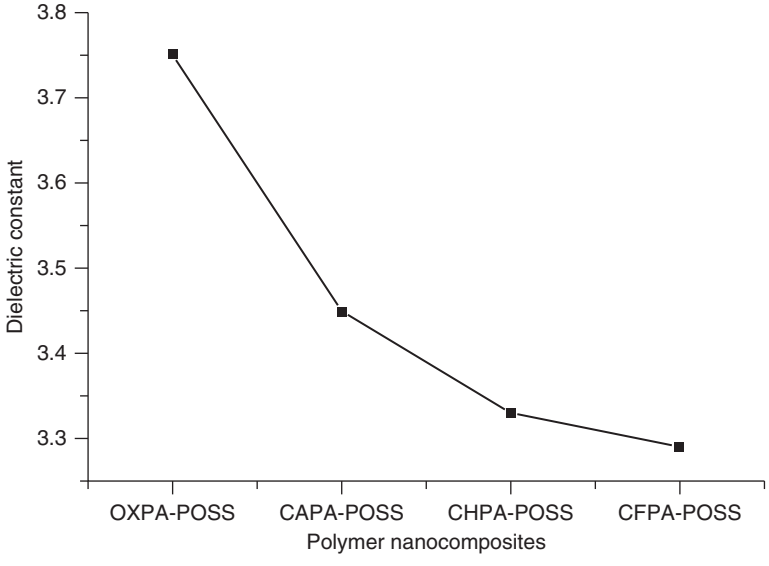

Figure 5.18 Dielectric constant of polymer nanocomposites.

that the fluorinated groups in the polymer composites play an important role in improving the dielectric property.

5.3.4 Other Applications

Poly(carbonate-urea)urethane (PCU)/(POSS) NCs were potentially used in cardiovascular bypass grafts and microvascular components of artificial capillary beds. POSS NCs possess greater thromboresistance than do polytetrafluoroethylene and poly(carbonate-urethane), making them ideal material for construction of both bypass grafts and microvessels [97, 98]. Kaneshiro *et al.* [99] reported that L-lysine dendrimers with an octa(3-aminopropyl)silsesquioxane core (OAS) with fourth generation is a suitable candidate for controlled *in vitro* gene delivery and transfection in human breast carcinoma cells (MDAMB-231 cells). Preliminary toxicity evaluation predicted that L-lysine dendrimer is an excellent biocompatible NC. Polyhedral oligomeric silsesquioxane-maleic anhydride monomer (POSS-MA) was used as a novel dental restorative composite to replace commonly used dental base monomer 2,2′-bis-[4-(methacryloxypropoxy)-phenyl]-propane (Bis-GMA) [100]. Amino-functionalized silsesquioxane provide curl retention for hair [101].

Polyfluorenes/POSS NC shows maximum luminescence intensity and quantum efficiency, which is almost twice as good as those of a PFO EL device, and is an excellent material for optoelectronic applications [102]. Introduction of POSS moieties into PPVs improves the EL properties of PPV derivatives. Improvement in EL properties of POSS-incorporated PPV is due to the formation of suitable insulation domains of POSS moieties in conjugated polymer matrices, resulting in a balance of charge carriers of electrons and holes [103]. Castaldo *et al.* [104] presented polymeric NC sensors, based on a POSS by selecting a proper matrix such as poly[(propylmethacryl-heptaisobutyl-POSS)-*co*-(*n*-butylmethacrylate)] and a suitable choice of other external home-made fillers (graphite, copper, silicon, zinc, and their alloys). Hybrids could be used in sensing of both polar and apolar analytes. Sulfonic acid containing bridged POSS hybrid materials is used as proton-exchange membranes for fuel cell applications, while electrolyte materials are suitable materials in the automotive industry.

Polyphenyl silsesquioxane is used as interlayer dielectrics and protective coatings films for semiconductor devices, liquid crystal display elements, magnetic recording media, and optical fiber coating [100]. Polymethyl silsesquioxane is used as an additive material in cosmetics, polypropylene films, and methacrylic resins. Polymethyl silsesquioxane with epoxy-containing siloxanes adheres well to rubber and plastics and could be used to provide nonsticking, water repellant, and abrasion-resistant films on paper, rubber, plastics, and metals [100]. Poly(aminopropyl silsesquixane) and specific carbonyl compounds of silsesquioxane act as antitumor agents [100]. Silsesquioxane films, particularly OAPS/imide and OAPS/epoxide films, provide excellent O_2 barrier properties, and are ideal candidates in packaging applications [90]. In PVC, POSS behaves

as a plasticizer like dioctyl phthalate (DOP) and could be used as a plasticizer [105]. Metal-containing POSS cages (gallium-containing cage silsesquioxanes and aluminosilsesquioxane) [106, 107] have been synthesized, for the use of silica-supported metal catalysts.

5.4 Conclusions

As we have seen, the POSS family of molecules is interesting and has been the focus of a great deal of research. One or two very niche applications exist already and it can be expected that new applications will gradually be found over the coming decades. Unfortunately, the commercial potential of POSS is very much limited in three ways. Firstly, the high cost, which cannot be further lowered because the raw materials used to make POSS are themselves expensive ($10–20/lb in bulk for the least expensive types). Secondly, as discussed, the marketing efforts are focused on applications that make no sense in terms of cost or performance. Lastly, commercial exploitation of new technologies takes in the order of 10–20 years. Even if Hybrid Plastics can somehow survive that long, by that time the key patents would have expired and other companies could step in and take over the market for POSS. Should a market for POSS have developed by that time, the natural outcome would be for the producers of the organosilanes raw materials to step in and produce POSS themselves and at a price that would be impossible to match. Each specific POSS can behave differently in a specific resin and is attributed to the size of the POSS cage, nature of organic periphery, number of reactive functionalities, and concentration and solubility of POSS in the resin. These factors determine whether POSSs are incorporated as isolated and uniformly dispersed molecules, unreacted and phase separated particles, or matrix-bound aggregates. Different morophologies affect the physical and mechanical properties of the final material. There has been enormous growing application for POSS NCs. POSS monomers and some copolymers of POSS are commercially available in Hybrid Plastics Company (http://www.hybridplastics.com/), Fountain Valley, CA.

References

1. Reddy, B.S.R. and Gnanasekaran, D. (2011) in *Advances in Nanocomposites – Synthesis, Characterization and Industrial Applications* (ed B.S.R. Reddy), InTech, Croatia, pp. 195–226.
2. Gnanasekaran, D., Madhavan, K., Tsibouklis, J., and Reddy, B.S.R. (2011) Ring opening metathesis polymerization of polyoctahedral oligomeric silsesquioxanes (POSS) incorporated oxanorbornene-5,6-dicarboximide: synthesis, characterization, and surface morphology of copolymers. *Aust. J. Chem.*, **64**, 1–7.
3. Zou, H., Wu, S., and Shen, J. (2008) polymer/silica nanocomposites: preparation, characterization, properties, and applications. *Chem. Rev.*, **108**, 3893–3957.
4. Choi, J., Tamaki, R., Kim, S.G., and Laine, R.M. (2003) Organic/inorganic

imide nanocomposites from aminophenylsilsesquioxanes. *Chem. Mater.*, **15**, 3365–3375.
5. Brunsvold, A.L., Minton, T.K., Gouzman, I., Grossman, D., and Gonzalez, R. (2004) An investigation of the resistance of polyhedral oligomeric silsesquioxane polyimide to atomic-oxygen attack. *High Perform. Polym.*, **16**, 303–318.
6. Phillips, S.H., Haddad, T.S., and Tomezak, S.J. (2004) Developments in nanoscience: polyhedral oligomeric silsesquioxane (POSS)-polymers. *Curr. Opin. Solid State Mater. Sci.*, **8**, 21–29.
7. Choi, J., Yee, A.F., and Laine, R.M. (2003) Organic/inorganic hybrid composites from cubic silsesquioxanes. Epoxy resins of octa(dimethylsiloxyethyl cyclohexylepoxide) silsesquioxane. *Macromolecules*, **36**, 5666–5682.
8. Choi, J., Harcup, J., Yee, A.F., Zhu, Q., and Laine, R.M. (2001) Organic/inorganic hybrid composites from cubic silsesquioxanes. *J. A. Chem. Soc.*, **123**, 11420–11430.
9. Choi, J., Yee, A.F., and Laine, R.M. (2004) Toughening of cubic silsesquioxane epoxy nanocomposites using core–shell rubber particles: a three-component hybrid system. *Macromolecules*, **37**, 3267–3276.
10. Vasilopoulou, M., Tsevas, S., Douvas, A.M., Argitis, P., Davazoglou, D., and Kouvatsos, D. (2005) Characterization of various low-k dielectrics for possible use in applications at temperatures below 160 °C. *J. Phys. Conf. Ser.*, **10**, 218.
11. Brick, C.M., Ouchi, Y., Chujo, Y., and Laine, R.M. (2005) Robust polyaromatic octasilsesquioxanes from polybromophenylsilsesquioxanes, Br_xOPS, via Suzuki coupling. *Macromolecules*, **38**, 4661–4665.
12. Zudo, H., Yamamoto, M., Nishikubo, T., and Moriya, O. (2006) Novel materials for large change in refractive index: synthesis and photochemical reaction of the ladderlike poly(silsesquioxane) containing norbornadiene, azobenzene, and anthracene groups in the side chains. *Macromolecules*, **39**, 1759–1765.
13. Tamaki, R., Tanaka, Y., Asuncion, M.Z., Choi, J.W., and Laine, R.M. (2001) Octa(aminophenyl) silsesquioxane as a nanoconstruction site. *J. Am. Chem. Soc.*, **123**, 12416–12417.
14. Balazs, A.C., Emrick, T., and Russell, T.P. (2006) Nanoparticle polymer composites: where two small worlds meets. *Science*, **314**, 1107–1110.
15. Krishnamoorti, R. and Vaia, R.A. (2007) Polymer nanocomposites. *J. Polym. Sci. Part B: Polym. Phys.*, **45**, 3252–3256.
16. Caseri, W. (2004) in *Encyclopedia of Nanoscience and Nanotechnology*, vol. 6 (ed. H.S. Nalwa), American Scientific Publishers, Stevenson Ranch, CA, pp. 235–247.
17. Schadler, L.S. (2003) *Nanocomposite Science and Technology*, Chapter 2, Wiley-VCH Verlag GmbH, Weinheim.
18. Schaefer, D.W. and Justice, R.S. (2007) How nano are nanocomposites? *Macromolecules*, **40**, 8501–8517.
19. Fina, A., Tabuani, D., Peijs, T., and Camino, G. (2009) POSS grafting on PPgMA by one-step reactive blending. *Polymer*, **50**, 218–226.
20. Ramasundaram, S.P. and Kim, K.J. (2007) In-situ synthesis and characterization of polyamide 6/POSS nanocomposites. *Macromol. Symp.*, **249–250**, 295–302.
21. Gnanasekaran, D., Madhavan, K., and Reddy, B.S.R. (2009) Developments of polyhedral oligomeric silsesquioxanes (POSS), POSS nanocomposites and their applications: a review. *J. Sci. Ind. Res.*, **68**, 437–464.
22. Kim, S.H., Kim, Y.H., Ahn, S.K., and Kwon, S.K. (2003) Synthesis and characterization of highly soluble and oxygen permeable new polyimides bearing a noncoplanar twisted biphenyl unit containing tert-butylphenyl or trimethylsilyl phenyl groups. *Macromolecules*, **36**, 2327–2332.
23. Yang, C.P., Su, Y.Y., Wen, S.J., and Hsiao, S.H. (2006) Highly optically transparent/low color polyimide films prepared from hydroquinone- or resorcinol-based bis(ether anhydride) and trifluoromethyl-containing bis(ether amine)s. *Polymer*, **47**, 7021–7033.

24. Wan, C., Zhao, F., Bao, X., Kandasubramanian, B., and Duggan, M. (2009) Effect of POSS on crystalline transitions and physical properties of polyamide-12. *J. Polym. Sci. Part B: Polym. Phys.*, **47**, 121–129.
25. Zhang, W., Liu, L., Zhuang, X., Li, X., Bai, J., and Chen, Y. (2008) Synthesis and self-assembly of tadpole-shaped organic/inorganic hybrid poly(N-isopropylacrylamide) containing polyhedral oligomeric silsesquioxane via reversible addition-fragmentation transfer polymerization. *J. Polym. Sci. Part A: Polym. Chem.*, **46**, 7049–7061.
26. Gnanasekaran, D. and Reddy, B.S.R. (2012) A highly soluble Polyamide-POSS nanocomposite: synthesis and characterization. *Polym. Compos.*, **33**, 1197–1205.
27. Ricco, L., Russo, S., Monticelli, O., Bordo, A., and Bellucci, F. (2005) ε-Caprolactam polymerization in presence of polyhedral oligomeric silsesquioxanes (POSS). *Polymer*, **46**, 6810–6819.
28. Liu, Y.L. and Lee, H.C. (2006) Preparation and properties of polyhedral oligosilsequioxane tethered aromatic polyamide nanocomposites through michael addition between maleimide-containing polyamides and an amino-functionalized polyhedral oligosilsequioxane. *J. Polym. Sci., Part A: Polym. Chem.*, **44**, 4632–4643.
29. Wheeler, P.A., Fu, B.X., Lichtenhan, J.D., Weitao, J., and Mathias, L.J. (2006) Incorporation of metallic POSS, POSS copolymers, and new functionalized POSS compounds into commercial dental resins. *J. Appl. Polym. Sci.*, **102**, 2856–2862.
30. Misra, R., Fu, B.X., and Morgan, S.E. (2007) Surface energetics, dispersion, and nanotribomechanical behavior of POSS/PP hybrid nanocomposites. *J. Polym. Sci. Part B: Polym. Phys.*, **45**, 2441–2455.
31. Liu, Y.L., Chang, G.P., Wu, C.S., and Chiu, Y.S. (2005) Preparation and properties of high performance epoxy–silsesquioxane hybrid resins prepared using a maleimide–alkoxysilane compound as a modifier. *J. Polym. Sci. Part A: Polym. Chem.*, **43**, 5787–5798.
32. Feng, Y., Jia, Y., Guang, S., and Xu, H. (2010) Study on thermal enhancement mechanism of POSS-containing hybrid nanocomposites and relationship between thermal properties and their molecular structure. *J. Appl. Polym. Sci.*, **115**, 2212–2220.
33. Gnanasekaran, D., Madhavan, K., Tsibouklis, J., and Reddy, B.S.R. (2013) Nanocomposites based on copolymers of fluorinated imide and POSS macromonomer for biomedical applications: microstructure and Morphology studies. *Polym. Int.*, **62**, 190–195.
34. Avadhani, C.V., Wadgaonkar, P.P., Khisti, R.S., Gunjikar, V.G., and Vemekar, S.P. (1990) Synthesis and characterization of imide containing diisocyanates and poly(imide-urethane)s therefrom. *Polym. Bull.*, **23**, 163–169.
35. Yeganeh, H., Barikani, M., and Khodabadi, F.N. (2000) Synthesis and properties of novel thermoplastic poly(urethane-imide)s. *Eur. Polym. J.*, **36**, 2207–2211.
36. Zuo, M., Xiang, Q., and Takeichi, T. (1998) Preparation and properties of novel poly(urethane-imide)s. *Polymer*, **39**, 6883–6889.
37. Zuo, M. and Takeichi, T. (1997) Novel method for the preparation of poly(urethane–imide)s and their properties. *J. Polym. Sci. Part A: Polym. Chem.*, **35**, 3745–3753.
38. Yeganeh, H. and Shamekhi, M.A. (2004) Poly(urethane-imide-imide), a new generation of thermoplastic polyurethane elastomers with enhanced thermal stability. *Polymer*, **45**, 359–365.
39. Behniafar, H. (2006) Direct synthesis of new soluble and thermally stable poly(urethane-imide)s from an imide ring-containing dicarboxylic acid using diphenylphosphoryl azide. *J. Appl. Polym. Sci.*, **101**, 869–877.
40. Chattopadhyay, D.K., Mishra, A.K., Sreedhar, B., and Raju, K.V.S.N. (2006) Thermal and viscoelastic properties of polyurethane-imide/clay hybrid coatings. *Polym. Degrad. Stab.*, **91**, 1837–1849.

41. Gnanasekaran, D., Ajit Walter, P., Asha Parveen, A., and Reddy, B.S.R. (2013) Polyhedral oligomeric silsesquioxane–based fluoroimide–containing poly(Urethane-Imide) membranes: synthesis, characterization and gas-transport properties. *Sep. Purif. Technol.*, **111**, 108–118.
42. Gnanasekaran, D. and Reddy, B.S.R. (2013) A facile synthesize of mixed soft segmented poly(urethane-imide)-POSS and their structure-transport relationship studies. *Polym. Int.*, **2014** (63), 507–513.
43. Li, H., Zhang, J., Xu, R., and Yu, D. (2006) Direct synthesis and characterization of crosslinked polysiloxanes via anionic ring-opening copolymerization with octaisobutyl-polyhedral oligomeric silsesquioxane and octamethylcyclo tetrasiloxane. *J. Appl. Polym. Sci.*, **102**, 3848–3856.
44. Mehl, G.H. and Saez, I.M. (1999) Polyhedral liquid crystal silsesquioxanes. *Appl. Organomet. Chem.*, **13**, 261–272.
45. Kim, K.M. and Chujo, Y. (2001) Liquid-crystalline organic–inorganic hybrid polymers with functionalized silsesquioxanes. *J. Polym. Sci., Part A: Polym. Chem.*, **39**, 4035–4043.
46. Zhang, C., Bunning, T.J., and Laine, R.M. (2001) Synthesis and characterization of liquid crystalline silsesquioxanes. *Chem. Mater.*, **13**, 3653–3662.
47. Saez, I.M., Goodby, J.W., and Richardson, R.M. (2001) A liquid-crystalline silsesquioxane dendrimer exhibiting chiral nematic and columnar mesophases. *Chem. - Eur. J.*, **7**, 2758–2764.
48. Zhang, C., Babonneau, F., Bonhomme, C., Laine, R.M., Soles, C.L., Hristov, H.A., and Yee, A.F. (1998) Highly porous polyhedral silsesquioxane polymers. Synthesis and characterization. *J. Am. Chem. Soc.*, **120**, 8380–8391.
49. Lee, Y.J., Kuo, S.W., Huang, C.F., and Chang, F.C. (2006) Synthesis and characterization of polybenzoxazine networks nanocomposites containing multifunctional polyhedral oligomeric silsesquioxane (POSS). *Polymer*, **47**, 4378–4386.
50. Lee, Y.J., Huangb, J.M., Kuoa, S.W., Chena, J.K., and Chang, F.C. (2005) Synthesis and characterizations of a vinyl-terminated benzoxazine monomer and its blending with polyhedral oligomeric silsesquioxane (POSS). *Polymer*, **46**, 2320–2330.
51. Lee, Y.J., Kuo, S.W., Su, Y.C., Chen, J.K., Tu, C.W., and Chang, F.C. (2004) Syntheses, thermal properties, and phase morphologies of novel benzoxazines functionalized with polyhedral oligomeric silsesquioxane (POSS) nanocomposites. *Polymer*, **45**, 6321–6331.
52. Liu, Y. and Zheng, S. (2006) Inorganic–organic nanocomposites of polybenzoxazine with octa(propylglycidyl ether) polyhedral oligomeric silsesquioxane. *J. Polym. Sci., Part A: Polym. Chem.*, **44**, 1168–1181.
53. Chen, Q., Xu, R., Zhang, J., and Yu, D. (2005) Polyhedral oligomeric silsesquioxane (POSS) nanoscale reinforcement of thermosetting resin from benzoxazine and bisoxazoline. *Macromol. Rapid Commun.*, **26**, 1878–1882.
54. Liu, Y., Meng, F., and Zheng, S. (2005) Poly(4-vinylpyridine) nanocrosslinked by polyhedral oligomeric silsesquioxane. *Macromol. Rapid Commun.*, **26**, 920–925.
55. Knischka, R., Dietsche, F., Hanselmann, R., Frey, H., and Mulhaupt, R. (1999) Silsesquioxane-based amphiphiles. *Langmuir*, **15**, 4752–4756.
56. Kim, B.S. and Mather, P.T. (2006) Amphiphilic telechelics with polyhedral oligosilsesquioxane, (POSS) end-groups: dilute solution viscometry. *Polymer*, **47**, 6202–6207.
57. Chan, S.C., Kuo, S.W., and Chang, F.C. (2005) Synthesis of the organic/inorganic hybrid star polymers and their inclusion complexes with cyclodextrins. *Macromolecules*, **38**, 3099–3107.
58. Xu, J. and Shi, W. (2006) Synthesis and crystallization kinetics of silsesquioxane-based hybrid star poly(3-caprolactone). *Polymer*, **47**, 5161–5173.
59. Cham, B.J., Kim, B., and Jung, B. (2006) Characteristics of poly(alkyl

silsesquioxane) thin films prepared from chemically linked alkyl units. *J. Non-Cryst. Solids*, **352**, 5676–5682.

60. Iacono, S.T., Budy, S.M., Mabry, J.M., and Smith, D.W. (2007) Synthesis, characterization, and surface morphology of pendant polyhedral oligomeric silsesquioxane perfluorocyclobutyl aryl ether copolymers. *Macromolecules*, **40**, 9517–9522.
61. Liu, L., Ming, T., Liang, G., Chen, W., Zhang, L., and Mark, J.E. (2007) Polyhedral oligomeric silsesquioxane (POSS) particles in a polysiloxane melt and elastomer dependence of the dispersion of the poss on its dissolution and the constraining effects of a network structure. *J. Macromol. Sci.: Pure Appl. Chem.*, **A 44**, 659–664.
62. Joshi, M., Butola, B.S., Simon, G., and Natalia, K. (2006) Rheological and viscoelastic behavior of hdpe/octamethyl-poss nanocomposites. *Macromolecules*, **39**, 1839–1849.
63. Liu, L., Tian, M., Zhang, W., Zhang, L., and Mark, J.E. (2007) Crystallization and morphology study of polyhedral oligomeric silsesquioxane (POSS)/polysiloxane elastomer composites prepared by melt blending. *Polymer*, **48**, 3201–3212.
64. Yu, S., Wong, T.K.S., Hu, X., and Pita, K. (2003) The comparison of thermal and dielectric properties of silsesquioxane films cured in nitrogen and in air. *Chem. Phys. Lett.*, **380**, 111–116.
65. Maitra, P. and Wunder, S.L. (2002) Oligomeric Poly(ethyleneoxide)-functionalized silsesquioxanes: interfacial effects on Tg, Tm, and ¢Hm. *Chem. Mater.*, **14**, 4494–4497.
66. Mya, K.Y., Pramoda, K.P., and He, C.B. (2006) Crystallization behavior of star-shaped poly(ethylene oxide) with cubic silsesquioxane (CSSQ) core. *Polymer*, **47**, 5035–5043.
67. Shea, K.J., Loy, D.A., and Webster, O.W. (1992) Arylsilsesquioxane gels and related materials. New hybrids of organic and inorganic networks. *J. Am. Chem. Soc.*, **114**, 6700–6710.
68. Corriu, R.J.P., Moreau, J.J.E., Thepot, P., and Chi Man, M.W. (1992) New mixed organic-inorganic polymers: hydrolysis and polycondensation of bis(trimethoxysilyl)organometallic precursors. *Chem. Mater.*, **4**, 1217–1224.
69. Loy, D.A. and Shea, K.J. (1995) Bridged polysilsesquioxanes: highly porous hybrid organic-inorganic materials. *Chem. Rev.*, **95**, 1431–1442.
70. Cerveau, G., Corriu, R.J.P., and Framery, E. (2001) Nanostructured organic-inorganic hybrid materials: kinetic control of the texture. *Chem. Mater.*, **13**, 3373–3388.
71. Oviatt, H.W., Shea, K.J., and Small, J.H. (1993) Alkylene-bridged silsesquioxane sol-gel synthesis and xerogel characterization. Molecular requirements for porosity. *Chem. Mater.*, **5**, 943–950.
72. Shea, K.J. and Loy, D.A. (2001) Bridged Polysilsesquioxanes. Molecular-engineered hybrid organic-inorganic materials. *Chem. Mater.*, **13**, 3306–3319.
73. Honma, I., Takeda, Y., and Bae, J.M. (1999) Protonic conducting properties of sol-gel derived organic/inorganic nanocomposite membranes doped with acidic functional molecules. *Solid State Ionics*, **120**, 255–264.
74. Honma, I., Nishikawa, O., Sugimoto, T., Nomura, S., and Nakajima, H. (2002) A sol-gel derived organic/inorganic hybrid membrane for intermediate temperature PEFC. *Fuel Cells*, **2**, 52–58.
75. Khiterer, M., Loy, D.A., Cornelius, C.J., Fujimoto, C.H., Small, J.H., Mcintire, T.M., and Shea, K.J. (2006) Hybrid polyelectrolyte materials for fuel cell applications: design, synthesis, and evaluation of proton-conducting bridged polysilsesquioxanes. *Chem. Mater.*, **18**, 3665–3673.
76. Lu, Y., Fan, H., Doke, N., Loy, D.A., Assink, R.A., LaVan, D.A., and Jeffrey, B.C. (2000) Evaporation-induced self-assembly of hybrid bridged silsesquioxane film and particulate mesophases with integral organic functionality. *J. Am. Chem. Soc.*, **122**, 5258–5261.
77. Kapoor, M.P., Yang, Q., and Inagaki, S. (2002) Self-assembly of biphenylene-bridged hybrid mesoporous solid with molecular-scale periodicity in the

pore walls. *J. Am. Chem. Soc.*, **124**, 15176–15177.

78. Guan, S., Inagaki, S., Ohsuna, T., and Terasak, O. (2000) Cubic Hybrid organic-inorganic mesoporous crystal with a decaoctahedral shape. *J. Am. Chem. Soc.*, **122**, 5660–5661.
79. Moreau, J.E.E., Vellutini, L., Chi Man, M.W., Bied, C., Bantignies, J.L., Dieudonne, P., and Sauvajol, J.L. (2001) Self-organized hybrid silica with long-range, ordered lamellar structure. *J. Am. Chem. Soc.*, **123**, 7957–7958.
80. Moreau, J.E.E., Pichon, B.P., Chi Man, M.W., Bied, C., Pritzkow, H., Bantignies, J.L., Dieudonn, P., and Sauvajol, J.L. (2004) A better understanding of the self-structuration of bridged silsesquioxanes. *Angew. Chem. Int. Ed.*, **43**, 203–206.
81. Luo, Y., Lin, J., Duan, H., Zhang, J., and Lin, C. (2005) Self-directed assembly of photoactive perylenediimide-bridged silsesquioxane into a super long tubular structure. *Chem. Mater.*, **17**, 2234–2236.
82. Inagaki, S., Guan, S., Fukushima, Y., Ohsuna, T., and Terasaki, O. (1999) Novel mesoporous materials with a uniform distribution of organic groups and inorganic oxide in their frameworks. *J. Am. Chem. Soc.*, **121**, 9611–9614.
83. Yoshina-Ishii, C., Asefa, T., Coombs, N., MacLachlan, M.J., and Ozin, Q.A. (1999) Periodic mesoporous organosilicas, PMOs: fusion of organic and inorganic chemistry 'inside' the channel walls of hexagonal mesoporous silica. *Chem. Commun.*, 2539–2540.
84. Hall, S.R., Fowler, C.E., Lebeau, B., and Mann, S. (1999) Template-directed synthesis of bi-functionalized organo-MCM-41 and phenyl-MCM-48 silica mesophases. *Chem. Commun.*, 201–202.
85. Burleigh, M.C., Markowitz, M.A., Spector, M.S., and Gaber, B.P. (2001) Direct synthesis of periodic mesoporous organosilicas: functional incorporation by co-condensation with organosilanes. *J. Phys. Chem. B*, **105**, 9935–9942.
86. Paul, D.R. and Yampolskii, Y.P. (1994) *Polymeric Gas Separation Membranes*, CRC Press, Boca Raton, FL.
87. Mohammadi, T. (1999) A review of the applications of membrane separation technology in natural gas treatment. *Sep. Purif. Technol.*, **34**, 2095–2111.
88. Li, Y., Chung, T.S., and Kulprathipanja, S. (2007) Novel Ag+-zeolite/polymer mixed matrix membranes with a high CO_2/CH_4 selectivity. *AlChE J.*, **53**, 610–616.
89. Yeh, J.T., Pennline, H.W., and Resnik, K.P. (2001) Study of CO_2 absorption and desorption in a packed column. *Energy Fuels*, **15**, 274–278.
90. Asunction, M.Z. and Liane, R.M. (2007) Silsesquioxane Barrier Materials. *Macromolecules*, **40**, 555–562.
91. Tejerina, B. and Gordon, M.S. (2002) Insertion Mechanism of N_2 and O_2 into T_n(n = 8, 10, 12)-Silsesquioxane frameork. *J. Phys. Chem. B*, **106**, 11764–11770.
92. Lin, H.Q. and Freeman, B.D. (2003) Novel nanocomposite membrane structures for hydrogen separations novel nanocomposite membrane structures for hydrogen separat. 2003 DOE University Coal Research Contractors' Meeting, Pittsburgh, Pennsylvania, http://www.netl.doe.gov/publications/proceedings/03/ucr-hbcu/Freeman.pdf (accessed 1 November 2015).
93. Yang, Y. and Heeger, A.J. (1994) A new architecture for polymer transistors. *Nature*, **372**, 344–346.
94. Gatos, K.G., Martinez Alcazar, J.G., Psarras, G.C., Thomann, R., and Karger-Kocsis, J. (2007) Polyurethane latex/water dispersible boehmite alumina nanocomposites: thermal, mechanical and dielectrical properties. *Compos. Sci. Technol.*, **67**, 157–167.
95. Bera, D., Dasgupta, B., Chatterjee, S., Maji, S., and Banerjee, S. (2012) Synthesis, characterization, and properties of semifluorinated organo-soluble new aromatic polyamides. *Polym. Adv. Technol.*, **23**, 77–84.
96. Son, M., Ha, Y., Choi, M.C., Lee, T., Han, D., Han, S., and Ha, S.K. (2008) Microstructure and properties of polyamideimide/silica

hybrids compatibilized with 3-aminopropyltriethoxysilane. *Eur. Polym. J.*, **44**, 2236–2243.

97. Kannan, R.Y., Salacinski, H.J., Groot, J.D., Clatworthy, I., Bozec, L., Horton, M., Butler, P.E., and Seifalian, A.M. (2006) The antithrombogenic potential of a polyhedral oligomeric silsesquioxane (POSS) nanocomposite. *Biomacromolecules*, **7**, 215–223.

98. Kannan, R.Y., Salacinski, H.J., Edirisinghe, M.J., Hamilton, G., and Seifalian, A.M. (2006) Polyhedral oligomeric silsequioxane–polyurethane nanocomposite microvessels for an artificial capillary bed. *Biomaterials*, **27**, 4618–4626.

99. Kaneshiro, T.L., Wang, X., and Lu, Z.R. (2007) Synthesis, characterization, and gene delivery of poly-l-lysine octa(3-aminopropyl)silsesquioxane dendrimers: nanoglobular drug carriers with precisely defined molecular architectures. *Mol. Pharmaceutics*, **4**, 759–768.

100. Fonga, H., Dickens, S.H., and Flaim, G.M. (2005) Evaluation of dental restorative composites containing polyhedral oligomeric silsesquioxane methacrylate. *Dent. Mater.*, **21**, 520–529.

101. Baney, R.H., Makilton, S.A., and Suzuki, T. (1995) Silsesquioxanes. *Chem. Rev.*, **95**, 1409–1428.

102. Lin, W.J., Chen, W.C., Wu, W.C., Niu, Y.H., and Jen, A.K.Y. (2004) Synthesis and optoelectronic properties of starlike polyfluorenes with a silsesquioxane core. *Macromolecules*, **37**, 2335–2341.

103. Zang, J.M., Cho, H.J., Lee, J., Lee, J.I., Lee, S.K., Cho, N.S., Hwang, D.H., and Shim, H.K. (2006) Highly bright and efficient electroluminescence of new ppv derivatives containing polyhedral oligomeric silsesquioxanes (POSS) and their blends. *Macromolecules*, **39**, 4999–5008.

104. Castaldo, A., Massera, E., Quercia, L., and Francia, G.D. (2007) Filled polysilsesquioxanes: a new approach to chemical sensing. *Macromol. Symp.*, **247**, 350–356.

105. Soong, S.Y., Cohen, R.E., Boyce, M.C., and Mulliken, A.D. (2006) Rate-Dependent deformation behavior of poss-filled and plasticized poly(vinyl chloride). *Macromolecules*, **39**, 2900–2908.

106. Feher, F.J., Budzichowski, T.A., and Ziller, J.W. (1997) Synthesis and characterization of gallium-containing silsesquioxanes. *Inorg. Chem.*, **36**, 4082–4086.

107. Edelmann, F.T., Gunko, Y.K., Giessmann, S., and Olbrich, F. (1999) Silsesquioxane chemistry: synthesis and structure of the novel anionic aluminosilsesquioxane $[HNEt_3][\{Cy_7Si_7O_9(OSiMe_3)O_2\}2Al]$ C_6H_{14} (Cy) c-C_6H_{11}). *Inorg. Chem.*, **38**, 210–211.

6
Zeolites and Composites

G. Gnana kumar

6.1
Introduction

Zeolites are a series of crystalline microporous aluminosilicates found on earth's surface and in number of environments, including soils, seafloor deposits, hydrothermal alteration products, altered volcanic deposits, sediments, etc., [1]. Natural zeolites were discovered by the Swedish mineralogist Axel Fredrik Cronstedt in 1756, and the name has been derived from the Greek words "zeo" and "lithos", meaning "to boil" and "stone" [2]. Zeolites have not been considered as the *new class of materials* and have been investigated for more than 250 years. Until now, more than 40 natural zeolites have been identified, of which clinoptilite, chabazite, mordenite (MOR), and tectosilicate have received more attention, owing to their abundant presence and microporous properties [3]. The general chemical composition of zeolite is $M^{n}_{x/n}Si_{1-x}Al_xO_2{\cdot}yH_2O$, where $M = Na^+/K^+/Li^+/Ag^+/NH_4{}^+/H^+/Ca_2{}^+/Ba_2{}^+$. Natural zeolites exhibit a Si/Al ratio of 4.66 (mol mol^{-1}) and the corresponding ratio of (Na + K)/Ca is 1.85 [4]. A typical natural zeolite clinoptilolite exhibits the chemical composition of $Na_{0.1}$ $K_{8.57}$ $Ba_{0.04}$ $(Al_{9.31}$ $Si_{26.83}$ $O_{72})\cdot 19.56$ H_2O and the Si/Al ratio ranges between 4 and 5.5. On the other side, the low- and high-silica members of natural zeolites exhibited higher amount of Ca and K, Na, and Mg. It is shown that roughly 70% of a natural zeolite comprises of clinoptilolite and plagioclase, mica, quartz, and smectite.

Apart from natural zeolites, artificial zeolites have also been synthesized and 150 zeolites have been reported so far. The large-scale synthesis of zeolites laid the foundation for the rapid development of zeolite industries during the twentieth and twenty-first centuries [5]. According to the database of International Zeolite Association (IZA), the development of diversified unique microporous frameworks has been rapidly achieved and the number of reported synthetic zeolites has reached 174 in 2007 [3]. The physical properties such as bandgap, luminescence, pore size, surface area, ion exchange, and chemical stability can be effectively tuned by the chemical composition of zeolites. To improve the pore properties and catalytic activity of synthetic zeolites, researchers have synthesized different

Nanomaterials and Nanocomposites: Zero- to Three-Dimensional Materials and Their Composites,
First Edition. Edited by Visakh P.M. and Maria José Martínez Morlanes.

types of zeolite materials by varying the chemical composition of a parent gel. Wise *et al.*, Lillerud *et al.*, and Gao *et al.*, reported the different zeolites such as offretite [$(K_2, Ca, Mg)_{2.5}$ Al_5 $Si_{13}O_{36}\cdot 15-16\ H_2O$], erionite [$(K_2, Na_2, Ca, Mg)_{2.1}$ $Al_{4.2}$ $Si_{13.8}$ $O_{36}\cdot 15\ H_2O$], and levyne [$(Ca, Na_2, K_2)_3Al_6Si_{12}O_{36}\cdot 18\ H_2O$], by varying the metal compositions [6]. In most cases, the chemical composition of three minerals Ca, Na, and K are nonstoichiometric in nature and the ions are easily exchangeable.

In general, zeolites are constructed by the framework of [SiO_4^{4-}] and [AlO_4^{5-}] tetrahedra linked together at all their corners via sharing of O atoms, which generates an infinite lattice with the same unit cells [7]. It has been explored that each individual O–T–O angle in a zeolite framework is very small, specifying that framework is composed of rigid $T-O_4$ units (T is Si^{4+} or Al^{3+} ion) linked through highly flexible "ball joints" [8]. The structural building units of zeolites have been classified as primary, secondary, and characteristic cage-building units. In general, these structural building units and frameworks of zeolites are effectively fabricated with the crystallographic unit cells having larger size [9]. Zeolites have attained maximized molecular diffusions, while the thickness of crystal has been contracted to the single unit cell dimension. It is specified that the propagation of unit cell dimensions is the essential factor that influences the change in morphology of materials. The reduction in the dimension thickness of a single unit cell with three-, two-, and one-spatial dimensions leads to the zero-dimensional crystal structure, nanowires, and nanosheets, respectively. Each cubic unit cell of all these aluminosilicates holds 192 (Si, Al) O_4 tetrahedrons [10, 11].

Different framework structures lead to the formation of different aperture sizes of pores in zeolites. On the basis of volume and size of pores, zeolites are classified as microporous (diameter <2 nm), mesoporous (2–50 nm), and macroporous (>50 nm) materials [1]. These unique inherent pore structures of zeolites are negatively charged that allows the positively charged species to pass through, and causes others to be trapped inside their chambers. In addition, the created nanoscale labyrinths in zeolites can be filled with water or other guest molecules. Among the varieties of porous materials studied, zeolites exhibit unique advantages that include less or noncorrosive nature, no waste or disposal problems, abundance, low cost, high thermostability, great adaptability to practically all types of catalysis, great acid strength, easier scale up for continuous processes, and so on. Hence, zeolites find applications in sorbents, water purification, ion exchange beds, catalysts, optically active materials, polymerization science, separation technology, micro-electronics, photoelectrochemical applications in solar cells, thin-film sensors, encapsulation of drugs, and biomolecules for targeted or controlled-release applications [12].

However, the significant loss in its surface due to the vigorous trapping of bulky molecules in pores and cavities may limit its applications. In general, zeolites possess relatively many apertures, trapping the bulky molecules of products inside the cavities, which may deactivate the catalyst. On the other side, the size of synthesized molecule is obviously limited by the size of pore apertures and cavities. In addition, these materials easily lose their active sites with relatively

small amounts of coke [13]. In order to overcome the aforementioned significant limitations, the composite form of zeolites has been developed with metals, metal oxides [14], polymers [15], active carbon materials [16], clay, coordination complexes [17], Schiff bases [18], etc., and the resultant composite materials have been effectively applied in diversified fields. Although a number of research activities on the fabrication of porous structures of zeolites and their composite materials, have been reported pertinent mechanisms involved in the preparation of zeolite composites, different ratio of alumino and silicates on zeolite composite materials, influence of porous structures on the activity of zeolite composites, etc., have been explored, they have not been detailed yet. This chapter asserts the significant efforts achieved so far on the implementation of zeolite-based catalysts on diversified domains, progress and evaluation of zeolite materials, porous nature of zeolites, types of zeolite materials, chemical and porous structures of zeolites and their composites, significances of composites over the bare zeolites, preparation strategies for enhancing the accessibility of pores in zeolites, specific properties, and applications of zeolites and their composites on diversified domains.

6.2 Progress of Zeolite Materials

6.2.1 Natural Zeolites

The first natural microporous aluminosilicate, known as *natural zeolite*, was discovered more than 200 years ago [19]. However, extensive investigations on natural zeolites started in the middle of last century, owing to the enhanced demand for sorption capacity materials for nuclear waste management and long-term practical applications. Natural zeolites were first discovered in vugs or cavities in basaltic and volcanic rocks at a minimum level [20]. In 1962, remarkable amounts of zeolites were discovered in sedimentary deposits in Western United States [21]. Recent statistics show that diversified sorts of natural zeolites such as MOR, clinoptilolite, analcime, heulandite, natrolite, chabazite, erionite, thomsonite, stilbite, and laumontite have been discovered in China. Among the aforementioned materials, chabazite, erionite, MOR, and clinoptilolite have been commercialized for adsorbent applications [22].

Generally, these natural zeolites are formed as a result of many geological reactions. Since these zeolites usually existed near the earth's surface, it can be easily and directly obtained by simple treatments [23]. In general, natural zeolites are generated at optimum temperature and pressure, which is the rationale behind choosing the simple hydrothermal process for synthesizing the zeolite materials. Japan is the largest consumer of natural zeolites that exhibit good potential for applications especially in the fields of agriculture and environmental protection, with affordable cost [21]. Volcanic sediments in alkaline soils, closed alkaline and

saline lake systems, and hydrothermal/low-temperature alteration of marine sediments are the major sources of natural zeolite.

6.2.2 Artificially Synthesized Zeolites

Artificial synthesis of zeolites was achieved at the end of nineteenth century through mimicking the geothermal conditions, i.e., hydrothermal reactions. In 1966, zeolite was primarily synthesized by Barrer using the hydrothermal crystallization method [24]. Following Barrer, a number of research groups have synthesized various sorts of zeolite materials such as zeolite socony mobil-5 (ZSM-5), zeolite X (X = La, Ba) (Si/Al ratio = 1.4), zeolite Y (Y = K, Ca) (Si/Al 2.4), Linde Type A zeolite (LTA), etc., with different chemical compositions. When compared with natural zeolites, artificial zeolites exhibit numerous advantages such as high purity, uniform pore size, and better ion-exchange abilities. The New York based Permutit company launched the first synthetic zeolites as efficient water softeners, which exhibited higher efficiency over natural zeolites [25].

6.2.3 Low-Silica Zeolites

In 1940s, low-silica zeolites were synthesized within the range of Si/Al ratio of 1 – 1.5 and were largely developed during 1954 – 1980. However, the synthesis process of low-silica zeolites is tedious and can not be performed by simply altering the component ratio of Si/Al. Special approaches such as using a structure directing agent (SDA) or choosing the secondary synthesis process are essential for their preparation. Moreover, low-silica types of zeolites serve as the superior adsorbent for gas separation and cleaning and are employed in a number of industrial applications [23].

6.2.4 High-Silica Zeolites

In 1960s, high-silica zeolites (Si/Al ratio is >3) were synthesized by using organic amines and quaternary alkyl ammonium cations as templates in hydrothermal technique, which has been considered as a milestone in zeolite synthesis [26]. Consequently, varieties of high-silica zeolite materials such as ZSM-5, ZSM-23, Theta-1, ferrierite (FER), ZSM-39, Mazzite (MAZ), Levyne (LEV), etc., have been synthesized. The rapid progress in the synthesis of high-silica zeolites facilitated the exploration of zeolite synthesis. However, the presence of structural defects and residual aluminum in high-silica materials may complicate the interpretation of dispersion forces. During the formation of high-silica zeolites, the surface of crystal becomes hydrophobic, leading to a partial penetration of organic molecules into the cage or channel of zeolites, which increased the thermo-kinetic stability of zeolite frameworks [27].

6.3 Classification of Zeolites

In general, zeolites are classified on the basis of various parameters including, effective pore structure, ring structure, structural building units, crystal structure, and Si/Al ratio.

6.3.1 Classification Based on the Pore Structure

6.3.1.1 Microporous Zeolites

The distinct structural characters of microporous zeolites including pore volume, pore size, cation sites, channel dimensionality, numbers, etc., provide a number of unique properties such as ion exchange and catalytic activity as well as their roles as hosts in nanocomposite materials. Melanophlogite (MEP), Merlinoite (MER), MOR, and ZSM-5 have been considered as the common microporous zeolites, which exhibit an average pore size of 2.6 A and pore volume of 0.09 ml g^{-1} [28]. In general, microporous zeolites have been largely synthesized via hydrothermal methods and spin-coating techniques and synthesized microporous zeolites have been extensively used as heterogeneous catalysts in oil refining and petrochemical industries. However, the significant limitation of mass transport properties inhibited their widespread applications.

6.3.1.2 Mesoporous Zeolites

In general, nanosized and ultralarge-pore zeolites and zeolite analogs have been used in diversified industrial applications. However, the use of these materials is limited, owing to the tedious separation process of nanosized zeolite crystals from the reaction mixture, complexity of templates used for the synthesis of ultralarge-pore zeolites, and low thermal stability of zeolite analogs. Hence, keen focus has been directed toward mesoporous zeolites, which exhibit a pore size and a pore volume of 5–50 nm and 1.01 ml g^{-1}, respectively [29]. The mesopores in prepared materials were extensively developed by the solid templating, supramolecular templating, or indirect templating and nanocasting methods. In recent days, interest on the carbon-templated one-step hydrothermal process for the preparation of mesoporous structures with pore range of 5–40 nm has become vibrant. The generation of mesopores in zeolites enhances the accessibility to the internal surface and mesopore-modified zeolites exhibit promising properties (activity and selectivity) in catalytic processes. In general, the high crystalline material exhibits irregular pore size distribution, and finds its applications in heterogeneous catalysis systems [30].

6.3.2 Classification Based on Structural Building Units

On the basis of structural building units, zeolites have been classified as primary, secondary, and sodalite (SOD) cage-building units.

6.3.2.1 Primary Building Unit (PBU)

The individual tetrahedral (TO_4) unit of zeolite is termed as the primary building unit (PBU), where T is either Si or Al and the 3D chemical scaffold of zeolite is purely dependent upon PBU. The pore sizes and topologies of prepared zeolites could be varied by the coordination of metal ion with the oxygen atoms [31]. It has also provided significant information on the surface structure of zeolites, which is based on the dominant behavior of PBU in the scattering pattern. In general, PBUs exist in the inorganic walls of mesoporous zeolites and the corresponding structure effectually determines the high hydrothermal stability of the material. According to the Lowenstein's rule, the PBU structure is made up without the involvement of Al–O–Al linkages and leads to the linkages such as P–O–P, P–O–Si, Al–O–Al, Me–O–Al, and Me–O–Me (where Me = metal) [32]. With the number of tetrahedrons linked by oxygen atoms, the center of only one of them can be occupied by Al and other centers are occupied by Si or other small ions having an electrovalence of four.

6.3.2.2 Secondary Building Unit (SBU)

The secondary building unit (SBU) comprises simple geometric arrangements of primary TO_4 such as 4, 6, 8, 10, or more complicated membered rings and is known as *characteristic configurations of tetrahedral* [33]. The concept of SBU (infinite component units) was introduced by Meier and Smith and 18 types of SBUs have been found out so far, which occur in tetrahedral frameworks. In general, SBU consists up to 16 tetrahedrally coordinated atoms and 9 SBUs are influential enough to describe the known structures of zeolite. In general, the SBUs consist of 4, 6, and 8-membered single rings, 4–4, 6–6, and 8–8 member double rings, and 4–1, 5–1, and 4 to 4–1 branched rings [34].

6.3.2.3 Sodalite Cage Building Units

The SBU is linked to form various polyhedrons such as hexagonal prisms or cuboctahedra and generate the networks of regular channels and cavities and the SOD cage is considered as the major polyhedron. It exhibits a cage of diameter of 6.5 A and is accessible through six-membered rings of oxygen atoms. SOD cage exhibits an aluminosilicate framework in which SiO_4 and AlO_4 tetrahedra exist in approximately equal numbers. The fourfold or sixfold rings of these tetrahedral may form channels, which accommodate sodium and chloride ions [35].

6.3.3 Classification Based on the Ring Structure

The pore diameter of zeolites is purely dependent upon the number of TO_4 existing in the ring aperture and is effectually tuned by the ring structures. The small, medium, and large pore openings of zeolites are based upon the 8-, 10-, and 12-membered ring structures, respectively. The small pore zeolites (3.0–4.5 A) are generated by the eight TO_4 connected with eight oxygen atoms [36]. Ten I-atom rings constitute the medium pore zeolites with the pore size of 4.5–6.0 A and 12 or more T-atoms in rings constitute the large-pore zeolites with the pore diameter of 8.0 A or more [37]. On the basis of ring structure, the common zeolites (including both natural and synthetic zeolites) are listed in Table 6.1.

6.3.4 Classification Based on Si/Al Ratio

On the basis of Si/Al ratio, zeolites have been classified into three types: namely, low- silica, intermediate-silica, and high-silica zeolites. The thermal stability and cation content of zeolites are directly and inversely proportional to the Si/Al ratio, respectively. The low- and high-silica zeolites exhibited a thermal stability up to 700 and 1300 °C, respectively [38]. The existence of a maximum number of cation exchange sites in low-silica zeolite balances the framework and high-silica zeolite exhibits the heterogeneous hydrophilic surface within the porous crystal. The classification of zeolites based on the Si/Al is given in Table 6.2.

Table 6.1 Classification of based on pore size.

Small pore zeolite	Medium pore zeolite	Large pore zeolite
Linde A	Dachiardite	Cancrinite
Bikitaite	Epistilbite	Linde X, Y, L, EMT
Brewsterite	Ferrierite	Gmelinite
Chabazite	Heulandites	Mazzite
TMA-E	Laumonitite	Mordenite
Edingtonite	ZSM-5; 11, 22, 23, 25, 39, 57	ZSM-12
Erionite	EU-1 and 2	Omega
Gismondine	Stilbite	Beta
ZK-5		
Levynite		
Merlinoite		
Paulingtite		
Natrolite		
Phillipsite		
Rho		

Table 6.2 Classification of zeolites based on the Si/Al ratio.

S. No	Name	Si/Al ratio	Examples
1.	Low silica zeolites (Si/Al – 1–1.5)	(Si/Al – 1–1.5)	A, X
2.	Intermediate silica zeolites	(Si/Al – 2–5)	(a) Natural zeolites: erionite, chabazite, clinoptilolite, mordenite (b) Synthetic zeolites: L, Y, omega, large port mordenite
3.	High-silica zeolites	(Si/Al = 10–4000)	(a) By direct synthesis: ZSM-5, ZSM-1I, EU-I, EU-2, Beta (b) By then no chemical framework modification: mordenite, erionite, highly silicious variant of Y
4.	All silica "zeolite"	Si/Al = 1000 to ∝	Silicate

6.3.5
Classification of Zeolites Based on the Crystal Structure

In general, zeolites consist of seven groups and each group exhibits a common subunit structure, which is a specific array of $(Al_2Si)O_4$ tetrahedra. In general, three classification schemes are widely adopted for the zeolite structures [39]. The first structural classification of zeolites is based on the framework topology and the second structural method is based on a concept termed *secondary building units*. The PBU for zeolites is the tetrahedron and the SBUs are the geometric arrangements of tetrahedral and have the tendency to tune the morphology of zeolites. Figure 6.1 shows the formation of secondary and different cage-building units through the combination of single tetrahedral units (PBU). The classification of zeolites on the basis of group and crystal structure is given in Table 6.3.

6.4
Molecular Sieves

The dehydrated forms of synthetic zeolites are termed as *molecular sieves*, which play a vital role on diversified domains through their unique physicochemical properties [26]. The crystalline nature of molecular sieves effectually determines the pore size, dimensionality of pore system, pore shape, surface properties and pore configuration. The aforementioned properties allow the material to recognize, discriminate, and organize molecules with precision that can be less than 1 A. The specific advantages of molecular sieves include high thermal stability, pure crystallinity, robustness, immense capacity for selective absorption, shape-selective sensing, rapid catalyzing ability, and precise pore structure [40]. The molecular sieve materials have received more attention as an effectual host for quantum particles and wires in nanotechnology.

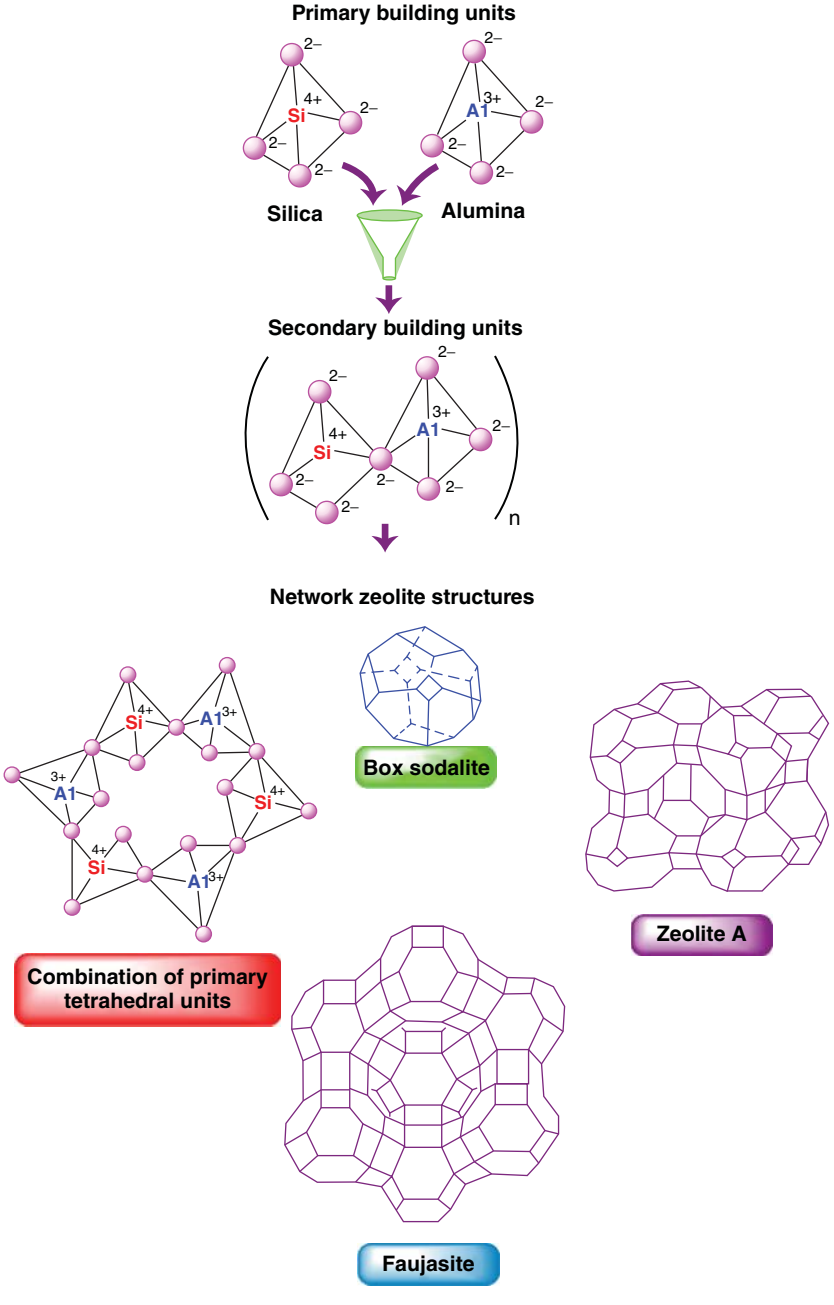

Figure 6.1 Primary, secondary, and cage building units of zeolites.

Table 6.3 Classification of zeolites on the basis of group and crystal structure.

Name of the group	Name of material	Chemical composition	Geometry	Crystal structure
Analcime group	Wairakite	$Ca(AlSi_2O_6)\cdot 2H_2O$	—	Monoclinic
	Pollucite	$Ca(AlSi_2O_6)\cdot xH_2O$	Tetragonal,	—
	Leucite	$K(AlSi_2O_6)$	Tetragonal	—
	Viseite	$NaCa_5(Al_{10}Si_3,P_5O_{30}\ (OH)_{18})\cdot 8H_2O$	—	—
Sodalite group	Linde A	$Na_{12}(Al_{12}Si_{12}O)\cdot 27H_2O$	—	—
	Faujasite	$(Na_2, Ca)_{30}(AlSi_{192}O_{308})\cdot 260H_2O$	—	—
chabazite group	Gmelinite near	$Na_2(Al_2Si_4O_{12})\cdot 6H_2O$	Hexagonal	—
	Erionite	$(Ca, etc.)_{4.5}(Al_9Si_{27}O_{72})\cdot 27H_2O$	Hexagonal	—
	Levyne	$Ca(Al_2Si_4O_{12})\cdot 6H_2O$	—	Rhombohedral
Natrolite group	Scolecite	$Ca(Al_2Si_3O_{10})\cdot 3H_2O$	—	Monoclinic
	Mesolite	$Na_2Ca_2(Al_2Si_3O_{10}),\cdot 8H_2O$	—	Monoclinic
	Edingtonite	$Ba(Al_2Si_3O_{10})\cdot 3H_2O$	Pseudo-tetragonal	Probably orthorhombic
	Thomsonite	$NaCa_2(Al_5Si_5O_{20})\cdot 6H_2O$	—	Orthorhombic
	Gonnardite	$(Ca, Na)_{68}(Si,Al_{20}O_{40})\cdot 12H_2O(Al{\sim}9)$	—	Orthorhombic
	Metanatrolite	—	—	Monoclinic
Phillipsite group	Harmotome	$Ba_2(Al_4.Si_{12}O_{32})\cdot 12H_2O$	—	Monoclinic
	Gismondine	$Ca(Al_2,Si_2O_8)\cdot 4H_2O$	—	Monoclinic
	Garronite	$(NaCa_{2.5})(Al_6Si_{10}O_{32}\ 13_{1/2}H_2O$	Tetragonal	—
	NaPl	$Na_2(Al_2,Si_3O_{10})\cdot 5H_2O$	—	—
Mordenite group	Dachiardite	$(Na_2,Ca)_2(Al_4,Si_{20}O_{48})\cdot 12H_2O$	—	Monoclinic
	Ptilolite	$Na(AlSi_5O_{12})\cdot 3H_2O$	—	Orthorhombic
Zeolites with unknown structure	Paulingite	$(K, Ca, Na)_{120}(Al,Si)_{580},0_{1160}\cdot 690H_2O$	—	—
	Shcroftine	$(K,Na,Ca)_{120}(Al_{160}Si_{200})O_{720}\cdot 320H_2O$	Tetragonal	—
	Thaumasite	$Ca_3\ H_2(CO_3)(SO_4)(SiO_4)\cdot 13H_2O$	Hexagonal	—
	Ferrlerite	$(Na,K)_4,Mg_2(Al_6Si_{30})O_{72}(OH)_2\cdot 18H_2O$	—	Orthorhombic
	Heulandite and clinoptilolite	$(Ca,K,Na)(Al_2,Si_7)O_{18}\cdot 6H_2O$	—	Monoclinic
	Laumontite	$(Ca, Na, K)(Al_2Si_4)O_{12}\cdot 4H_2O$	—	Monoclinic
	Brewsterite	$(Sr, Ba, Ca)(Al_2,Si_6)O_{16}\cdot 5H_2O$	—	Monoclinic
	Stilbite	$Na_2Ca_4(Al_{10}Si_{26})O_{12}\cdot 28H_2O$	—	Monoclinic
	Epistilbite	$Ca(Al_2Si_6)O_{10}\cdot 5H_2O$	—	Monoclinic
	Rhodesite	$(Ca, Na, K)_8Si_{16}O_{40}\cdot 11H_2O$	—	Orthorhombic
	Mountainite	$(Ca, Na, K)_8\ Si_{16}O_{40}\cdot 12H_2O$	—	Monoclinic

6.5
Synthesis of Zeolites

6.5.1
History of Zeolite Synthesis

In 1756, Swedish mineralogist discovered the first natural zeolite stilbite [41]. It is proceeded by the preparation of LEV and "analcime" (ANA), which were achieved by St Claire Deville and de Schulten, respectively [42, 43]. Although extensive progress was made during the successive years, the early synthetic work was not very well established, owing to the lack of essential data for identification. In the late 1940s, the systematic synthesis of zeolites was achieved by Richard Barrer. Without the use of a natural counterpart, Barrer synthesized the first zeolite in 1948 using the conversion of known mineral phases in strong salt solutions at high temperatures (about 170–270 °C) (KFI structured zeolite ZK-5) [44]. The zeolites A, B (now known as *Na–P*), and X were synthesized by using more reactive starting materials under mild conditions by Robert Milton and coworkers in 1949. In 1953, 20 zeolites were synthesized by Milton and his colleagues, of which 14 zeolites have not contained any natural counter parts. Milton and coworkers have also initiated the large-scale synthetic methodologies of zeolite technology. In 1961, Barrer and Denny exploited the quaternary ammonium cations in zeolite synthesis. The significant framework of Si/Al ratio was increased with the inclusion of organic components in aluminosilicate gels [45]. The significant advancements in zeolite synthesis were achieved by the use of organic components; specifically, the tremendous growth has been reported for the siliceous zeolites and a number of new high-silica zeolites were successfully crystallized using organic cations with aluminosilicate gels at 100–200 °C. In the 1960s, extensive efforts were initiated to understand the synthesis process, which triggered the number of new dimensions in the synthetic strategies of novel zeolites, investigation of the mechanism, and detailed characterizations of the resultant products.

6.5.2
Conventional Synthesis Approaches

6.5.2.1
Hydrothermal Synthesis

Among the pioneering techniques on zeolites synthesis, hydrothermal method is most attractive, owing to its simplicity, cost effectiveness, less energy, fast reaction kinetics, etc., Hydrothermal synthesis of aluminosilicate zeolites involves the few elementary steps by which a mixture of Si and Al species, metal cation, organic molecules, and water are converted into a microporous crystalline aluminosilicate via an alkaline supersaturated solution. However, both the crystallization process and understanding the exact mechanism involved in hydrothermal synthesis is yet to be understood, owing to the complicated chemical reactions, growth of crystals under heterogeneous conditions, and variation in the

processes with time. The hydrothermal synthesis briefly described as follows: the aqueous mixture of amorphous reactants containing silica and alumina by mixing together in a basic medium is heated in a sealed autoclave; after rising to the synthesis temperature, the reactants remain amorphous. The principle for the formation of aluminosilicate gel contains two important steps such as nucleation and growth of zeolite crystals from the reaction mixture**.** Upon the induction period, the gel and species are formed from the continuous variation of monomers and clusters and the formation and disappearance of clusters occur through the inhomogeneities through the condensation and hydrolysis reactions [24].

The amount and combination of clusters with cations are increased further and the prepared particles become stable during the course of this reaction. Nuclei of certain dimensions are formed and are preceded by the crystallization process. During the formation of highly supersaturated gels, heterogeneous nucleation occurs to a certain extent. Crystal growth is preceded through a series of depolymerization – polymerization reactions, which is catalyzed by the excessive hydroxyl ions.

A mixture of pulverized fuel ash (PFA) and potassium hydroxide (KOH) solution was taken in an inner Teflon vessel, which was placed in a stainless steel autoclave (30 cm^3) and heated to 160 °C for 1 h to 3 days. After the completion of a reaction, the autoclave was cooled at room temperature and the obtained K–H zeolite precipitate was filtered and finally dried at 40 °C [46].

6.5.2.2 Solvothermal Synthesis

The principle involved in the solvothermal technique is similar to hydrothermal method, in which water is replaced by the organic solvents. The large single and perfect crystals of zeolites were effectively tuned by the lower polarity and larger viscosity of the organic solvents. By the use of organic solvents such as alcohol, amine, etc., a number of possibilities for the formation of H-bonding or coordination interactions are initiated. Although the aforementioned properties of organic solvents do not facilitate the dissolution and diffusion of reactants, it may decrease the nucleation rate and crystal growth rate, which in turn facilitates the slow crystallization process, inducing the formation of large single and perfect crystals. The templated synthesis approach has been considered to be the most common method for the preparation of zeolite nanocrystals and many templates including quaternary ammonium compounds, tertiary amines, and other organic compounds have been reported for the synthesis of several nanocrystalline zeolites, leading to the specific and unique structure of zeolites. The advantages of template synthesis such as particle size control, morphology, colloidal stability, and surface reactivity increase the competence of solvothermal synthesis further [47].

An active form of silica (fumed silica) and NaOH were used as the starting materials and ethylene glycol or propanol were used as an organic solvent for nonaqueous hydrothermal treatment for the preparation of silica-SOD. The typical

reactant molar composition maintained for the preparation is $2SiO_2$:3NaOH:40 EG or Pr-OH and silica-SOD was formed from this mixture after 15–25 days at 150 °C [48].

6.5.3 Green Approaches

6.5.3.1 Ionothermal Synthesis

The use of organic solvents initiates the strong hydrogen bond, which prevents the nucleation of zeolites. To tackle the aforementioned significant issue, a new type of solvothermal synthesis has been introduced in which an ionic liquid (1-ethyl-3-methylimidazolium bromide ([EMIm]Br)) or eutectic mixture was used as both the solvent and SDA for aluminophosphate zeolites. The said synthesis strategy is termed as *ionothermal synthesis* and has received immense interest in the zeolite synthesis field. Ionothermal synthesis exhibits unique advantages over the conventional methods including single agent as a solvent and template, inclination of pressure issues, novel chemical environment for the reagents, and so on [49].

The preparation of new forms of SIZ-1 zeotypes, a Teflon-lined autoclave (Volume 23 ml) was charged with ionic liquid [EMIm]Br, $Al[OCH(CH_3)_2]_3$, phosphoric acid (H_3PO_4), and distilled water (or) Hydrogen fluoride (HF) acid (if required) and the optimized composition is 1.0 $Al(OiPr)_3$:3.0 H_3PO_4:0 HF:43 IL. The SIZ-1 zeotypes were formed at 150 °C for 66 h [50].

6.5.3.2 Microwave-Assisted Synthesis

Microwave-assisted synthesis is generally a much faster, cleaner, and energy efficient technique in comparison with conventional methods. The dipole interaction and ionic conductions are the two specific mechanisms for the materials and microwaves interaction. In principle, the chemical reaction is accelerated by the microwave dielectric heating, ionic conduction loss, and local superheating effect. It significantly varies the kinetics and selectivity of zeolite synthesis with unique advantages including high heating and crystallization rates and uniform temperature distribution, and the heating changes the association between reaction species in the reaction mixtures [51]. Microwave-assisted hydrothermal synthesis has been extensively exploited for the synthesis of a number of zeolites, such as LTA, faujasite (FAU), SOD, ANA, beta (BEA), ZSM-5, and cloverite (CLO).

A NaA zeolite crystal coated alumina (Al_2O_3) disk was vertically placed in a polyethylene bottle and was immersed in the reaction mixture of $5SiO_2$:Al_2O_3:$50Na_2O$:$1000H_2O$. The crystallization of zeolites was carried in a microwave oven at 2450 Hz and the temperature of mixture was quickly raised from room temperature to 90 ± 5 °C in 60 s. After the completion of a reaction, the membrane was washed with water and dried at 150 °C for 3 h [52].

In addition to the conventional microwave process, microwave-enhanced ionothermal synthesis of zeolites has also been widely adopted.

The silicoaluminophosphate molecular sieve was prepared by mixing tetraethyl ortho silicate (TEOS) with the product derived from the ionothermal method and the typical compositions of reaction mixtures for ionothermal synthesis is 40 ([bmim]Br):1.8 H_3PO_4 (85 wt%):1.06 $Al(OPr)_3$. The final product was heated at 100 °C for 20 min and then heated to 150 °C under microwave irradiation [53].

6.5.4 Recent Synthesis Approaches

6.5.4.1 Dry Gel Conversion

The conversion of aluminosilicate dry gels into zeolites under the vapors of organic templating agents and water has received keen interest, owing to the unique properties such as development of new structures, reduction of limitations on chemical compositions, improvement in catalytic activity, reduced consumption of organic solvent, complete conversion of gel into uniform crystalline zeolites, and high yield. It has been classified into two major sections such as Vapor-Phase Transport and Steam-Assisted Crystallization method [54] and the used systems are schematically illustrated in Figure 6.2.

The mixture of volatile organic SDA and water is vaporized by heating and reached a dry aluminosilicate gel state and attained crystallization.

The aluminosilicate gel with a composition of $10Na_2O{:}25SiO_2{:}A1_2O_3$ was prepared and the alumina support had an average pore diameter of 0.1 μm, which was immersed in the parent gel for a day. The obtained material was taken out of the gel and dried for 2 h at 90 °C and the dried product was placed in an autoclave with triethyl-amine and ethylenediamine. The obtained gel was crystallized under autogenous pressure at 180 °C for 4 days [55].

In the second case, the dry gel consisting of nonvolatile SDA-like tetraethylammonium hydroxide (TEAH) and steam was provided from the vapor phase. The products obtained from the SAC method exhibited a higher thermal stability

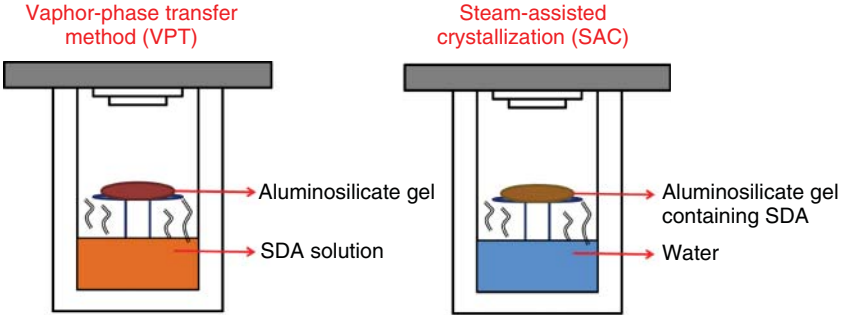

Figure 6.2 The system used for vapor-phase and steam assisted crystallization of zeolites.

over the other zeolites synthesized through the conventional hydrothermal synthesis.

For the synthesis of EMT zeolites, the chemical composition of $10SiO_2$:Al_2O_3:xNa_2O:0.75 (18-crown-6):$140H_2O$ ($x = 2.1 - 3.3$) was used. 18-Crown-6 was applied as the SDA for EMT. The Al-containing mixture was dropped into the Si-containing slurry and aged for 1 h in an ice bath and the resultant gel was dried at 35 °C for 72 h then 80 °C for 1 h and crushed into powder. The powder was crystallized at 105 – 145 °C for 7 days in an autoclave with the droplet of water at the bottom [56].

6.5.4.2 Synthesis of Zeolites under Microgravity Environment

The zeolite synthesis under regular gravity method exhibits certain limitations such as less pure and imperfect crystals formation, owing to the nonhomogeneities in the distribution of temperature and chemical composition. It focused the attention toward the synthesis of zeolites under the microgravity environment and the growth of zeolites in this environment is effectively free from convection and sedimentation, which enhanced perfection and provided highly pure crystals of zeolites. The slower crystallization rate exhibited by the microgravity environment provided perfect crystals to the synthesized material, which is attributed to the decreased mass-transport rate caused by a decreased convection rate [57].

Sodium aluminate Ludox (LS) (30% SiO_2), tetramethylammonium hydroxide, sodium hydroxide, potassium hydroxide, and de-ionized water were loaded in a three chamber reactor containing rotating valves and heated at 75 °C [58] and the resultant products were collected by drying at 100 °C.

6.5.5 Droplet-Based Synthesis Method

6.5.5.1 Microemulsion-Based Synthesis

If the micrometer-sized zeolites could be reduced to a nanometer scale, a significant variation in the properties of obtained zeolites could be visualized. The emulsion method based on hydrothermal technique offers controlled growth, high purity, narrow size distribution small size, etc., In general, the surfactant molecule used in the process exhibits a polar (hydrophilic) head group and a long-chained aliphatic (hydrophobic) tail and their interactions are optimized by residing at the oil/water interface, which considerably reduces the interfacial tension. When the microdroplets were collided with each other, the coalescence and fusion of the droplets occured, which was followed by the disintegration into droplets [59].

For synthesis of silicalite-1, the appropriate amounts of heptane, surfactant, and butanol were mixed together in a Pyrex screw-cap test tube at room temperature. To the mixture, tetrapropyl ammonium hydroxide (TPAOH), H_2O, and TEOS (1TEOS:0.36TPAOH:$20H_2O$) were added and vigorously shaken. After the

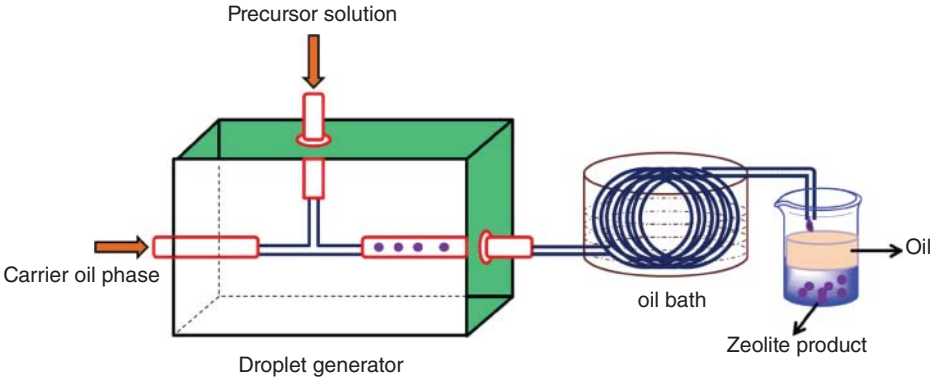

Figure 6.3 The system used for droplet–microfluid formation of zeolites.

stipulated time, the product was obtained via filtration and washed with ethanol, acetone, and water, and dried [60].

6.5.5.2

Droplet-Microfluid Synthesis

Droplet microfluidics is primarily aimed at transporting and manipulating monodisperse aqueous droplets within a carrier oil stream in microfluidic devices, which provides unique advantages such as high surface area to volume ratio at the microscale, fast mass and heat transfer, homogeneous heating, short diffusion distance, dispersion, and rapid mixing of reactants [61]. Zeolite formation via Droplet microfluid method is schematically illustrated in Figure 6.3.

For the synthesis of ZSM-5 zeolites, a mixture of TEOS/TPAOH/sodium aluminate ($NaAlO_2$)/KOH/H_2O/1-butyl-3-methylimidazoliumchloride (C_4MimCl) = 8 : 1.05 : 0.1 : 0.85 : 64 : 20 solution was aged for 0–15 h at room temperature. The mixture was allowed to flow to the reactor channel at a flow rate of 2–8 µl min^{-1}. Fluorocarbon oil was introduced at a flow rate of 12–48 µl min^{-1} and the reactor was immersed in a silicon oil bath at 150 °C. The obtained product was collected via centrifugation and dried at 100 °C [62].

6.5.6

Other Synthesis Approaches

6.5.6.1

Seed-Induced Synthesis

Seed-induced crystallization is an economically viable and facile technique for synthesizing the highly crystalline zeolite materials. In general, the attention on seed-induced crystallization is justified, owing to its ability to increase the rate of crystallization, declination of undesired phases, and perfect tuning of the particle size. The extended cumulative external surface area of seeds induced the crystallization rate and enhanced the uniform distribution of zeolite particles [63].

Preparation of nanosized ZSM-5 zeolites:

To prepare the new forms of ZSM-5 zeolites, sodium aluminates ($NaAlO_2$), de = ionized water, and sodium hydroxide (NaOH) were homogeneously mixed with agitation. In a separate vessel, a silica gel (30% SiO_2 in water) solution was gradually added to the $NaAlO_2$ and NaOH mixture and the 5.0 wt% seed suspension of aluminum isopropoxide (AIP) TPAOH, de-ionized water, and TEOS was then added to the reaction mixture and was magnetically stirred. A hydrothermal treatment was later performed at 180 °C for 24 h and the obtained solid was recovered by high-speed centrifugation, followed by re-dispersion in water [64].

6.5.6.2 Centrifugation-Assisted Grinding

The centrifugation-assisted grinding is an effortless, convenient, and facile technique for synthesizing zeolites with uniform morphology. In this method, milder mechanical grinding converted micro-sized particles into nanosize. After the grinding process, the nanocrystals with various sizes are separated by using centrifugation and are dried further [63].

An Al_2O_3 bowl mill (diameter, 90 mm; power, 51 W; rotation speed, 22 rpm; stroke number 110 spm) was filled with an appropriate amount of previously prepared zeolite microparticles. After grinding for 3 h, the milled zeolite powder was dispersed in de-ionized water under ultrasonication for 30 min. The large particles were then removed by centrifugation at 2000 rpm for 20 min [65].

6.5.7 Zeolite Composites

In general, the composite formation of zeolites is achieved by two significant strategies, that is, *ex situ* and *in situ* formation methods.

6.5.7.1 *Ex situ* Composite Formation

Ko *et al.* prepared the TiO_2/natural zeolite (TiO_2/NZ) composite from sol–gel-derived nano-titania colloids and zeolite powder. Under vigorous magnetic stirring, natural zeolite was mixed with titania sol. Finally, TiO_2-anchored natural zeolite was filtered and dried at 110 °C followed by calcination at 300–800 °C. Liu *et al.*, synthesized the germanium/zeolites composites via hydrothermal technique. TEOS, germanium oxide, hexamethonium hydroxide, and hexamethonium bromide were placed in stainless-steel Teflon-lined autoclaves and heated at 175 °C for 2 weeks. The bifunctional catalyst, $Cu–ZnO–Al_2O_3$/zeolite, was prepared by Prasad *et al.*, through coprecipitation technique. To synthesize the composite, the metal precursor solution containing copper acetate, zinc acetate, and aluminum nitrate was added with slurry of previously prepared zeolite powder. The sodium carbonate solution was also added to this mixture for

maintaining the pH at 11.0 and the temperature was maintained at 70 °C during the precipitation.

6.5.7.2 *In situ* Composite Formation

Vitale *et al.*, prepared the Ni-incorporated ZSM-5 as follows: an appropriate amount of nickel and aluminum chloride salts was dissolved in diluted sulfuric acid solution followed by the addition of tetra-propyl ammonium bromide (TPABr). Under vigorous stirring, sodium silicate was added to the above mixture. NaOH was added to attain basic pH of 11 and this mixture was homogenized and transferred into the Teflon-lined reactor, which was maintained at 190 °C for 40 h. The crystallized product was filtered, washed, and calcined at 550 °C for 6 h. Jianfeng Yu *et al.* synthesized the silica X zeolite/ceramic composites using the mixture of NaOH, KOH, sodium aluminate, and silicic acid. This homogeneously mixed solution was placed into Teflon-lined reactor containing pretreated ceramic honeycomb and aged for 24 h at 25 °C, followed by heating at 100 °C. The obtained product was filtered and calcined at 500 °C for 5 h.

6.6 Properties

6.6.1 Physical Properties

6.6.1.1 Thermal Properties

The studies on thermal properties of zeolites are highly important, owing to the change in catalytic and sorptive properties and molecular sieve effects, which are enhanced by the dehydrated and calcined state. The following factors such as Si/Al ratio, ionic potential/size of exchangeable cations and framework topology, and so on [66], effectually determine the thermal behavior of zeolites. Structural frameworks of low-silica zeolites are degraded at high temperatures of ~700 °C, whereas, siliceous silicates are highly stable up to 1300 °C. When zeolites are completely dehydrated, they undergo irreversible structural and framework topology variations due to the weaker linkages in the framework. The calcination of zeolites at higher temperature exhibited the following structural changes including change in cell volume contraction, phase transformation, T–O–T bonds formation and breakage, complete amorphization or recrystallization, etc., [27]. Furthermore, the inclusion of different rare earth cations with heavy groups such as, Tb, Ho, Er, and Tm increases the thermal stability of zeolites and increases the structural collapse temperature, which is ascribed to the continuation of RE–O–RE bonds in the interior of SOD cavities [67]. On the basis of higher thermal stability, Lanthanide-exchanged Zeolite Y has been extensively used as high-performance petroleum refinery catalysts [68].

6.6.1.2

Hydrophobicity

The hydrophobic properties of zeolites are effectively tuned by high Si/Al ratio, low hydroxyl content, silanol groups (≡SiOH) and ≡Si–O–Si≡ bonds [69]. In general, the physisoprtion of water vapor is usually achieved only at silanol sites, whereas ≡Si–O–Si≡ exhibits the homopolar and hydrophobic structure [70]. The hydrophobic properties of zeolites are effectively controlled by the dealumination process, which removes the charged cations present in the zeolite structure and effectively diminishes the surface charges. Also, the hydrophobic siloxane surfaces on zeolites were established by the cross-condensation process [71]. The hydrophobic surfaces of cages and zeolites are employed for the adsorption of volatile organic compounds such as trichloroethylene, phenol, benzene, carbon tetrachloride, and *n*-hexane by using the adsorption/separation method [69]. In addition, the hydrophobic MCM-41 was successful in encapsulating the larger organic molecules with little diffusion resistance for the removal of VOCs present in high concentrations and high-humidity streams [72].

6.6.1.3

Optical Properties

The photophysical properties of a zeolite are purely dependent upon the presence of cations in the zeolite framework and adsorbed water molecules over its surfaces [73]. Since the donor strength of guest molecules affects the absorption band of chromophores of strong electron acceptors, the optical property of chromophores can be effectively tuned by the direct interaction with cations. Zeolites with semiconducting nanostructures such as CdS, ZnO, and TiO_2 exhibited excellent optical properties, owing to small-size or quantum-size effects arising from the confinement of ordered channels [74]. The variation in the optical properties in three-dimensional interconnection along the zeolites indicates the progression toward a semiconductor supercluster with the behavior of intermediate between those of the nanostructure semiconductors and bulk semiconductors [75]. Semiconductor clusters in zeolites exhibited promising photocatalytic activity toward hydrogen generation from the water and CdS/ETS-4 (titanosilicate zeolite) has been reported as an efficient catalyst in the photocatalytic hydrogen-production field [74].

6.6.1.4

Electrical Properties

The electrical properties of zeolites are associated with the composition and content variation of zeolite, pore size, and ion exchange capacity [76]. The movement of positive ions into the pore distribution along the zeolite varies with electrical conductivity. The hydration of zeolites leads to an electrostatic interaction along the zeolite framework and decreases the barriers of ion migration, resulting the increased electrical conductivity. Also, the cation diffusion into the nanosized pores of zeolite framework enhanced the electrical conductivity [77]. The

electrical conductivity of zeolite is increased by the inclusion of excess electrons into the zeolite hosts; for example, the adsorption of large amount of alkali metals forms metal cluster, thereby accelerating the production of the larger number of extra electrons in the unit volume. The metal cluster material undergoes transition from insulator to conductor, owing to the increased concentration of excess electrons [78]. The development of zeolite-encapsulated electroluminescent guest can be effectively used for microelectronic applications.

6.6.1.5

Magnetic Properties

The location of charge-balancing cations in zeolites exhibited excellent magnetic properties, owing to their unpaired electrons, influenced by the distribution of silicon and aluminum ions within the aluminosilicate framework [79]. The magnetic interaction of zeolite network depends upon the charged cations and the distance between two charged species along the framework. Metal ions such as Fe^{2+}, Co^{2+}, and Ag^{+} are introduced into the zeolite by the ion exchange process and can be converted into the metallic state by thermal reduction, resulting the excellent magnetic properties of zeolites. The increasing weight percentage of magnetic iron nanoparticles on zeolite surfaces dramatically increases the magnetization of iron-impregnated zeolite composites [80].

6.6.1.6

Pore Properties

The highly interconnected micropores in zeolites find wide applications in catalysis, separation field, and environmental field [1]. On the basis of pore sizes, the conventional labeling of zeolites is termed as *molecular sieves*, which is a significant property of zeolites because of their size discriminating at the molecular level. A number of zeolite sieves are available depending on the variation in pore sizes [81]. The mesoporous zeolites are prepared by dealumination, sequential desilication–dealumination process, which are non-templating methods, and hard and soft templating methods [1]. Upon the variation in the specific conductivity of the building blocks, zeolites form three-dimensional lattices that are perforated by microporous channels or cavities of various sizes and shapes. The microelectronic device fabrication is achieved by the mesoporous zeolite films and the mesoporous activity of zeolites are broadly applicable in heterogeneous catalysis such as petroleum refining to produce fuels and chemicals, as adsorbents for separation processes, and as ion exchangers [82].

6.6.2

Chemical Properties

6.6.2.1

Basicity

On the basis of acid–base concept of solution chemistry, the basicity of zeolite is well developed. In general, zeolites exhibit microporous silicates with negatively

charged lattices, owing to the isomorphous substitution of Si^{4+} by Al^{3+} in the lattice. This negative charge was effectively neutralized by the exchangeable cations and protons. In zeolite matrix, the protons and exchangeable cations are served as acid sites, whereas the existing oxygen served as basic sites [83]. The negatively charged oxygen atoms bound with the protons via the covalent bond formation as the acid hydroxyl groups are able to donate protons to the incoming base molecules and are categorized as bronsted acid sites. Lewis acidity and Lewis basicity were related with exchangeable cations and lattice oxygen present in the zeolite matrix. In general, the Lewis basicity can be investigated by the spectral changes of adsorbed molecules such as CO_2, pyrrole, methanol, and methyl iodide, and nitrous oxide (N_2O_4) by the immobilization of exchangeable cations [83].

6.6.2.2
Adsorption

The pore sizes and geometry of size-selective zeolites facilitate the adsorption selectivity of various components. The inner walls of the micropores behave as active sites, where the catalytic adsorption takes place and selective adsorption occurs by adjusting the size of micropores and cavities. The adsorption ability of zeolites is varied by the chemical composition and surface cations, which can be altered by the Si/Al ratio [84]. The flexibility of zeolite framework influences the adsorption properties of hydrocarbons into the zeolite silicalite, which consists of zigzag and straight channels. The interaction of linear and branched alkanes with zeolite is dominated by the dispersive interactions with the oxygen atoms, which is present on the zeolite surface [85]. The ion-exchanged forms of zeolites are extensively used for the adsorption of inorganic materials including mercury, sulfur, and phosphorous. Although the complete dehydration collapses the structure of zeolites minerals, it can adsorb gases such as CH_4, Ar, Kr, Xe, O_2, N_2, CO, CO_2, and NH_3 with proper partial activation energies [86].

6.6.2.3
Ion-Exchange

The presence of Al atoms in the zeolite framework generates negative charges over the zeolite surfaces and can be counter-balanced by the external cations, which provide an excellent ion-exchange capability for zeolites [87]. In addition, the framework of zeolite exhibits large number of exchangeable cations per unit cell and these cations effectively improve the ion-exchange process [88]. The ion-exchange properties of zeolite are dependent upon the hydrating capacity, surface charge, and size. The ion-exchange properties of univalent and divalent exchange forms of the zeolites are decreased due to the increasing cation radius by hydration process. The unfavorable charge distribution along the zeolite framework exhibits the steric factor, which decreases the ion exchange properties. The larger sized ions are expelled in the zeolite through the ion-sieve effect, that completely hinders the ion exchange properties [89].

6.7 Applications

6.7.1 Fuel Cells

Fuel cell is one of the most significant electrochemical devices in which the role of zeolites as catalysts and fillers in membranes are highly imperative. Zeolite serves as a better alternative for porous materials (employed in fuel cells), owing to its unique advantages such as high electrical and thermal conductivity, high chemical and physical stability, extended surface area and porosity, low cost, etc., Baglio *et al.*, prepared Nafion/MOR composite membrane through the solution-casting technique and exploited as an electrolyte membrane in DMFCs. The prepared composite membrane exhibited a maximum power density of 390 mW cm^{-2}, which is higher than that of Chabazite and the Clinoptilolite-modified Nafion membrane. The maximum power output obtained for the Nafion/MOR composite is attributed to the high adsorption density ($OH-H^+$), excellent water adsorption and retention abilities, and prompt proton conduction properties of MOR [90]. Zhang *et al.*, exploited the Nafion/FAU composite membrane in DMFC applications, which was prepared through the solution-casting method by using. FAU zeolite powder and Nafion. The maximum power density achieved for the Naf/FAU membrane was 17.8 mW cm^{-2}, which was much higher than that of bare Nafion membrane. The obtained higher efficiency is attributed to the lower methanol crossover and excellent proton conductivity attained through the water up-taking ability of zeolites [91]. Chen *et al.* employed Nafion/acid-functionalized zeolite Beta (NAFB) as the electrolyte membrane in DMFCs. The number of charges on Nafion gets enhanced with the acid-functionalized zeolites that facilitate the charge (proton) transfer between the anode and cathode chambers of DMFC. As a consequence, the highest power density obtained for NAFB composite membrane was 120 mW cm^{-2}, which was twofold higher than that of Nafion 115 membrane (62 mW cm^{-2}) [92]. Wang *et al.* developed chitosan-incorporated zeolite (CS/zeolite) membrane by solution-casting technique and used as an electrolyte membrane in DMFCs. The prepared composite membranes exhibited desirable thermal and mechanical stabilities due to the presence of strong H-bonds between CS and zeolite. The prepared composite membrane exhibited a methanol permeability of 1.026×10^{-6} cm^2 s^{-1}, which is lower than that of bare CS membrane. The obtained lower methanol permeability is attributed to the high diffusion resistance of the membrane achieved by the smaller pore size (0.3 A) and inorganic nature of zeolites [93]. The mordenite/poly vinyl alcohol (MOR/PVA) composite was prepared by the solution-casting technique and exploited as the electrolyte membrane in DMFC by Libby *et al.* The maximum proton conductivity-permeability selectivity ratio was obtained for the MOR/PVA composite membrane, which was 20-fold higher than that of the Nafion membrane. The exhibited maximum proton selectivity of composite membrane is attributed to the defined pore size of MOR [94]. Wu

et al. developed NaX/graphite felt anode composite through the hydrothermal method and exploited as an anode in microbial fuel cells. The maximum power density obtained for NaX zeolite/graphite anode was $215.3 \pm 6.4\,mW\,m^{-2}$, which was approximately 1.5 times higher than that of the bare graphite felt anodes ($85.4 \pm 6.3\,mW\,m^{-2}$). The improved performance of anode was achieved by the higher surface area and porosity of zeolites for bacterial adhesion [95]. Eguizábal *et al.* prepared NaY/polybenzimidazole (PBI) composite membrane through the solution-casting technique and exploited in PEMFC applications. The proton conductivity exhibited by the prepared membrane is $54\,mS\,cm^{-1}$, which is higher than that of bare PBI membrane obtained, which higher proton conductivity is attributed to the effectual H-bonding type interaction between the PBI and NaY attained by the charged species onNaY [96]. The significant fuel cell performances obtained for the zeolite-based materials are given in Table 6.4.

6.7.2 Dye Sensitized Solar Cells (DSSCs)

A dye sensitized solar cell (DSSC) is a sort of photovoltaic device, which converts light energy into electrical energy. The effectual use of DSSC is an appropriate way to minimize environmental concern. In order to improve the efficiency of DSSC components (electrode), modification with porous materials is crucial. Among the various porous materials, zeolites received significant attention, owing to their high dye adsorption capacity, high conducting ability, and cage-like structure. Atienzar *et al.*, prepared titanium/zeolite (TiO_2/zeolite) composite through the sol–gel technique and exploited as a photoactive anode in DSSCs. The fill factor achieved by the prepared composite is 0.34, which is closer to the commercially available TiO_2 (0.64). However, the dye molecule adsorption capacity of composite is higher than that of bare TiO_2, which is attained by the larger pore volumes and internal voids of zeolites, suggesting that zeolites can be considered as suitable material for anode modification in DSSCs [97]. Alvaro *et al.*, used the N-doped zeolite-encapsulated TiO_2 composite (N–TiO_2@Y) as an anode catalyst in DSSC

Table 6.4 Zeolite composite materials used in fuel cells.

Zeolite composite	Preparation method	Type of fuel cell	Proton conductivity ($S\,cm^{-1}$)	Methanol permeability ($cm^2\,s^{-1}$)	Power density ($mW\,m^{-2}$)	References
Nafion/MOR	Solution-casting	DMFC	—	—	390	[90]
Nafion/FAU	Solution-casting	DMFC	0.130	—	17.8	[91]
NAFB	—	DMFC	0.080	1.40×10^{-6}	120	[92]
CS/zeolite	Solution-casting	DMFC	0.017	1.02×10^{-6}	—	[93]
MOR/PVA	Solution-casting	DMFC	0.400	1.00×10^{-6}	—	[94]
NaX/graphite felt	Hydrothermal	MFC	2.58	9.04×10^{-7}	215.3	[95]
NaY/PBI	Solution-casting	PEMFC	0.054	—	—	[96]

and the composite material was prepared by *ex situ* method. The open circuit voltage and fill factor exhibited by the N–TiO_2@Y are 270 and 0.4 mV, respectively. Although these values are lower in comparison with those exhibited in the current dye-sensitized TiO_2 solar cells, these findings could open up a gate for a stimulating extensive research activities on the photovoltaic activity of zeolite-based host–guest solids [98]. Kim *et al.*, exploited cadmium sulfide (CdS) and lead sulfide (PbS) quantum dots loaded zeolite Y composite as electrodes in DSSC. PbS QD-loaded zeolite Y counter electrode exhibited a threefold increment in overall efficiency of the cell. Under this condition the incident-photon-to-current conversion efficiency (IPCE) value at 398 nm was 42% and the absorbed photon-to-current conversion efficiency (APCE) value at 405 nm was observed to be 82%. The obtained high efficiency is attributed to the electrolyte-mediated high interdot-charge transport achieved by the extended channel dimensionality and electrical conductivity of zeolites [99]. The significant solar cell performances obtained for the zeolite-based materials are given in Table 6.5.

6.7.3 Batteries

The importance of energy on various domains has driven technological advances in energy storage devices. A battery is a transducer that converts chemical energy into electrical energy in which the role of zeolites as the electrode catalyst and membrane is vibrant. Pereira *et al.*, prepared the NaY/poly(vinylidene fluoride–trifluoroethylene) composite membrane via solution-casting technique and exploited as the separator in Li-ion batteries. The incorporated NaY fillers improved the mechanical strength, electrochemical stability, uptaking capacity, pore connectivity, and decreased tortuosity of the membrane. The higher ionic conductivity achieved by the composite membrane is 2.33×10^{-6} S cm^{-1}, which is attributed to the large surface area of the zeolites that reduces the growth rate of the resistive layer on the electrode surface and helps to trap residual traces of impurities [100]. Coetzer developed the zeolite–sulfur/graphite (Z–S/graphite) composite electrode by hot-pressing technique and employed as cathode in Li–sulfur batteries. The Z–S/graphite composite cathode exhibited a maximum power output of 0.50 W cm^{-2}, which is higher than that of bare graphite. The obtained higher power output is attributed to the larger electrical conductivity

Table 6.5 Zeolite composite materials used in DSSCs.

Zeolite composite	Preparation method	Solar cell type	Fill factor	References
TiO_2/zeolite	Sol–gel technique	DSSC	0.34	[97]
N–TiO_2@Y	—	DSSC	0.4	[98]
PbS quantum dots loaded zeolite Y	—	DSSC	—	[99]

attained by the effectual immobilization of sulfur on zeolites [101]. Dalas *et al.*, fabricated the polyaniline/zeolite (PANI/zeolite) composite electrode and utilized as cathode in primary dry cells. The prepared composite cathode showed the energy density 6.34 mWh cm^{-3}, which is higher that of polypyrrole/lithium air batteries (PPY/Li) cathode (5.1 mWh cm^{-3}) and closer to In_2S_3/PVA–KCl/Mg cathode (8.1 mWh cm^{-3}). The obtained effectual performance of composite is attributed to the adsorption, intercalation, and cation exchange characteristics of zeolites [102]. The significant energy storage performances obtained for the zeolite-based materials are given in Table 6.6.

6.7.4 Oil Refining

The exploitation of zeolite-based catalysts in the oil refining process is considered as the key activity in large-scale industries, owing to the highly active, selective, durable, and environmentally benign nature of zeolites. Furthermore, the extended and large cavities, wide pore windows and tremendous number of channels of zeolites provide an excellent activity toward oil refining and zeolites have been extensively exploited for the various sorts of oil refining processes such as reforming, fluid catalytic cracking, isomerization, hydrocracking, aromatization, hydrotreating, and so on [68]. Corma *et al.*, prepared the ITQ-21 through the hydrothermal crystallization technique and utilized as catalyst in oil refining process. The maximum oil cracking ability exhibited by ITQ-21 is 85, which is higher than that of other beta (83.9). The obtained high catalytic cracking ability is attributed to the high pore topology, crystal dimensionality, high pore interconnectivity and acidity of ITQ-21 [103]. Boyas *et al.*, exploited the bifunctional Pt/zeolite (Pt–H–Y) as the catalyst in the hydrocracking of rapeseed oil. The time consumed by the Pt–H–Y catalyst for cracking the rapeseed oil is 3 h, which is lower than that of other catalysts. The obtained swift catalytic activity of composite is ascribed to the strong acid sites of zeolites [104]. Verboekend *et al.*, prepared the mesoporous bi-functional Pt/NaOH–HCl zeolite catalyst by incipient wetness impregnation technique and employed as catalyst in hydroisomerization of *n*-alkane. The yield obtained with Pt/NaOH–HCl zeolite

Table 6.6 Zeolite composite materials used in energy storage devices.

Zeolite composite	Preparation method	Battery type	Ionic conductivity (S cm^{-1})	Power out-put (W cm^{-2})	References
NaY/poly(vinylidene fluoride-trifluoroethylene)	Solution casting technique	Li-ion batteries	2.33×10^{-6}	—	[100]
Z–S/graphite	Hot-pressing technique	Li-sulfur batteries	—	0.50	[101]
PANI/zeolite	—	Primary dry cells	—	6.34	[102]

is 70%, which is greater than that of Pt/ZSM-22 (60%), suggesting that acid–base functionalized zeolites exhibited strong ability toward isomerization than do bare zeolites [105]. Landau *et al.*, used the Pt/H-beta Al_2O_3 catalyst with different sizes (200–500 nm (Z1) and 10–30 nm (Z2)) for the hydrocracking of heavy vacuum gas oil (HVGO) and the catalyst was prepared through hydrothermal method. The yield exhibited by Z2 is 50% higher than that of Z1, which is attributed to the smaller size and high surface area of Z2 composite [106]. The significant oil refining performances obtained for the zeolite-based materials are given in Table 6.7.

6.7.5 Photocatalysts

In general, the attention on photocatalysts is attractive, owing to their potential applications on diversified domains such as solar cells, dye degradation, hydrogen production, water splitting, and so on. Although zeolites exhibited unique photocatalytic activity with excellent molecular selectivity and higher photostability, the lower quantum size effects, less photosensitizing ability, and requirement of a favorable polar environment for the photoinduced electron transfer hampered their promotion to the next level. It urges the modification of zeolites either in framework or in channels. Zeolite-based photocatalysts are promising material for the abatement of air and water pollution by using solar light, photoreduction of CO_2 by H_2O, photo-oxygenation of saturated hydrocarbons, photosplitting of water into hydrogen and oxygen, photogeneration of hydrogen peroxide, and other photo processes [107]. Fukahori *et al.*, synthesized the TiO_2/zeolite sheets through papermaking techniques and the prepared material was exploited as photocatalyst in the degradation of bisphenol A (BPA). The TiO_2/zeolite sheets exhibited a higher efficiency for BPA removal than that of bare TiO_2 sheets. The obtained higher efficiency is ascribed to the reversible adsorption, free movement of BPA molecules on composite attained by the cage-like structure and pore connectivity of zeolites [108]. Tayade *et al.*, used silver ion-exchanged TiO_2/NaY (Ag/TiO_2/NaY) as the efficient catalyst for the degradation of organic

Table 6.7 Zeolite composite materials used in oil refining.

Zeolite composite	Preparation method	Maximum oil cracking ability (%)	Cracking time (h)	References
ITQ-21	Hydrothermal crystallization	85	3	[103]
Pt–H–Y	—	—	—	[104]
Pt/NaOH–HCl zeolite	Incipient wetness impregnation	70	—	[105]
Pt/H-beta Al_2O_3	—	50	—	[106]

contaminants such as nitrobenzene (NB), acetophenone (AP), methylene blue (MB), and malachite green (MG) under UV light irradiation. The degradation percentage of NB is 55–60% and AP is 88–90%, while complete degradation of dyes was achieved within 2–3 h for both the MB and MG using the $Ag/TiO_2/NaY$ catalysts, which is much lower than that of bare TiO_2 particles [109]. Alvaro *et al.*, prepared the 2,4,6-triphenylthiapyrylium (TPTP) cations encapsulated zeolites Y (TPTP@Y) through ship-in-a-bottle synthesis and exploited as the photocatalyst for the oxidative degradation of organic contaminants. The TPTP@Y catalyst exhibited the maximum degradation efficiency in comparison with TPTP@β, TPTP@Y, P-25, TP@β, and TP@Y, which is attributed to the lower reduction potential of the composite attained by the large number of metal ions on zeolites Y [110].

6.7.6 Hydrogen (H_2) Storage

Vigorous incineration of fossil fuels is an ever-growing environmental concern and hydrogen fuels are the pertinent alternatives for the aforementioned significant crisis. Recently, lightweight materials with zeolites have been potentially applied for the adsorption of homonuclear diatomic gases such as H_2, O_2, and N_2. These materials exhibited infrared absorption spectra and no permanent electric dipole moment. Zeolites A, X, Y, and RHO, contain a range of different pore geometries, are extensively applied for H_2 storage [111]. Li and Yang, prepared the low silica type X zeolites (LSX, silicon:aluminum = 1) by ion-exchange method and utilized as catalyst for the H_2 storage. The maximum H_2 storage ability shown by Li-LSX is 1.5 wt%, which is higher than that of other porous materials. The obtained high storage capacity of composites is attributed to the radius and the density of cations located on the zeolites [112]. Palomino *et al.*, prepared the magnesium-exchanged zeolites by ion-exchange method and utilized for H_2 storage. The (Mg,Na)–Y catalyst exhibited 7.5 wt% H_2 uptake capacity, which is due to the high H_2 adsorption enthalpy value of $-17.5\ kJ\ mol^{-1}$ that facilitated the H_2 storage. The obtained higher H_2 storage capacity was attributed to the high polarizing power of the Mg^{2+}, H_2 interaction with alkali-metal cations, and porous structure [113]. Dong *et al.*, prepared the Na-LEV, H-OFF, Na-MAZ, and Li-ABW by hydrothermal method. The aforementioned materials were effectively utilized for H_2 storage at 16 bar pressure and a temperature of −196 °C. The maximum H_2 uptakes of 2.07, 1.75, 1.64, and 1.02 wt% were obtained for each material. The obtained higher H_2 uptake capacity was ascribed to an optimal channel diameter, and large cage volume contributed to the H_2 storage capacity [114]. Bae *et al.*, introduced organic ions, such as pyridine hydrochloride and pyridinium chlorochromate into the pores of ion-exchanged zeolite-Y (OZ) for the application of H_2 storage. These modifications effectively improved the hydrogen uptake capacity of 0.15–0.34 wt% at 25 °C and 10 MPa and the bare Na–Y, having no significant efficiencies. The obtained higher efficiency is attributed to the

Table 6.8 H_2 storage capacity of zeolite composites.

Zeolite composite	Preparation method	Storage capacity (wt%)	References
Li-LSX	Ion-exchange	1.5	[112]
(Mg,Na)-Y	Ion-exchange	7.5	[113]
Na-LEV	Hydrothermal method	2.07	[114]
OZ	—	0.34	[115]

changes of porosities near the zeolite cavities, selective organic molecules, and the electrostatic field gradients to improve the OZ [115]. The significant H_2 storage performances obtained for the zeolite-based materials are given in Table 6.8.

6.7.7
CO_2 Capture

The increasing concentration of CO_2 on the earth's atmosphere leads to many environmental perturbation, global warming, depletion of ozone, increment in sea water level, etc., which urges the reduction CO_2 in the atmosphere. Zeolites exhibit pore cavities and cages on its surface that assist effectual capturing of CO_2. Ranjani *et al.*, exploited the different zeolite materials as adsorbents for the capture of CO_2 at 120 °C and the exhibited CO_2 adsorption capacity of zeolite 13X is 0.70 mol kg^{-1}, which is greater than that of other zeolites (4 A, 5 A, APG-II, WE-G 592). The obtained high adsorption capacity is attributed to the extended number of pores and channels in the zeolites [116]. Sanchez *et al.*, used the FAU as the material for the adsorption of CO_2 at the temperature ranging from 253 to 298 K and at 120 kPa. The FAU exhibited maximum adsorption capacity than that of other zeolites such as LTA, MFI, owing to the topology, bigger cages, cavities, and high Si/Al ratio (2.5 (54 Na per unit cell)) of the zeolites [117]. Siporin *et al.*, prepared the zeolite X (X = K, Ba, or La) by the postmodification of commercial zeolites with different ions. The prepared material was exploited as the host for CO_2 capture. The CO_2 adsorption capacity of zeolite K is higher than that of zeolite Ba, and La, which is ascribed to the high BET surface area (602 $m^2\ g^{-1}$) and pore volume (0.251 $cm^3\ N_2\ g^{-1}$) [118].

6.8
Future Perspectives of Zeolites and Their Composites

Although zeolites and their composites find wide applications in a number of fields, the following improvements may improve their potential applications further.

- In general, zeolites and their composites have been extensively applied in powder form. However, the technologies including gas removal, ion separation, ion exchange, and fuel cells are mainly based upon the macro/meso/microporous fibers, membrane, and films. Hence, an apt technology has to be identified for the fabrication of zeolite composites thinfilms, in which the extensive research activities have to be devoted toward the emulsion, co-axial, and melt electrospinning techniques to fabricate the core–shell/hollow fiber membranes and films as free-standing materials for the said applications.
- Zeolite synthesis based on microwave irradiation is mainly focused on thermal effects, which hampers the understanding of the exact formation mechanism of zeolites. Hence, the non-equilibrium thermodynamics and molecular dynamics analysis may be adopted to elucidate the exact formation mechanism.
- In petroleum industries, bi-functional hydrocracking catalysts are extremely valuable, owing to their increasing hydroprocessing process and can be achieved through high-level basic nitrogen and sulfur incorporation on zeolite matrices, which may act as bi-functional catalysts.
- Recently, researchers have focused on mixed matrix membranes, which exhibit high permeability with better selectivity on the basis of inorganic particles in the matrices. The developments on the fabrication of mixed matrix membranes containing zeolite composites in polymeric membranes have to be extended, which may promote the efficiency of gas separation.
- The energy production devices have thrust on electricity production, owing to the increasing population and energy demand for a long time. Although the different energy devices have been developed, the problems could not be shortened due to the inefficient resources for their devices such as catalysts, electrode material, membrane, etc., Fuel cell studies showed that increasing surface area and introducing the redox materials on their respective electrode materials will enhance the power production. The fine pores and change in framework compositions of zeolites-based ORR catalysts will ensure the extended fuel cell performances. Hence, a proper focus on zeolites-based ORR catalysts has to be improved.
- Although the use of zeolite filler–polymer membranes is attractive in fuel cells, the optimization of filler–polymer compatibility, dispersion level, interaction and loading of zeolite fillers in zeolite filler-polymer membranes have not been analyzed in detail. A complete study on the above will bring forth the large-scale applications of the above membranes.
- The perfectly tuned porous network structures, increased surface area and the inclusion of biocompatible materials along the zeolite matrices will be beneficial to increase the bacterial adhesion, biofilm formation, and convenient electron transferences in MFCs.
- The applications of zeolites and their composites are purely dependent upon the pore sizes, pore shapes, pore networks, framework compositions, and cations of zeolite materials. Proper analytical tools have to be effectively developed and the aforementioned significant characteristics effectively tuned for the betterment of zeolite and its composite applications in the highly potential fields.

6.9 Conclusion

In the sophisticated technological civilization, zeolitic materials have received continuously increasing interest, owing to their unique properties. However, the limited understanding of the synthesis strategies, involved mechanisms, and the influence of chemical composition in tuning the physical properties of zeolites and their composites has hampered their extensive applications. Hence, the foremost aim of this chapter is to afford a detailed overview concerning zeolites chemistry in a single tool. The progress and classification of zeolites based on the pore structure, building unit ring structure, Si/Al ratio and crystal structure, have been reviewed in detail. In this contribution, the limitations of conventional techniques for the synthesis of zeolites have been detailed and have also paved the way toward the exploration of novel techniques to tune the perfect crystals. The salient features in tuning the unique properties of zeolites such as reduced consumption of organic solvents, high pure zeolite crystal, controlled growth, high surface to volume ratio, perfect tuning of particle size, uniform morophology, and so on, have been discussed to a considerable extent. The physical and chemical properties of zeolites are effectually tuned by changing the chemical composition, molecular sieve effects, and quantum size effects and the strategies involved in tuning the aforementioned significant properties have been elaborated to a greater level. Zeolites have been extensively applied in a number of green energy sources such as fuel cells, photocatalysis, hydrogen storage, oil refining, solar cells, super capacitors, etc., The reasons and salient features behind in choosing zeolites and zeolite composites in the aforementioned applications, the mechanisms that provoke the excellent performances of zeolites and their composites, equipped devices, and the recent efforts achieved on the above have been well documented in this chapter. Hence, this chapter has elaborated on the aforesaid significant aspects of zeolites and their composites and will hopefully be a boon for researchers not only to materialize their theoretical knowledge to the experimental level but also to extend their aspirations for large-scale applications.

References

1. Zhou, J., Hua, Z., Liu, Z., Wu, W., Zhu, Y., and Shi, J. (2011) Direct synthetic strategy of mesoporous ZSM-5 zeolites by using conventional block copolymer templates and the improved catalytic properties. *ACS Catal.*, **1**, 287–291.
2. Flanigen, E.M., Broach, R.W., and Wilson, S.T. (2010) *General Introduction on Zeolites*. ISBN: 978-3-527-32505-4.
3. Xu, R., Pang, W., Yu, J., Huo, Q., and Chen, J. (2007) *Chemistry of Zeolites and Related Porous Materials: Synthesis and Structure*. ISBN 978-0-470-82233-3.
4. Erdem, E., Karapinar, N., and Donat, R. (2004) The removal of heavy metal cations by natural zeolites. *J. Colloid Interface Sci.*, **280**, 309–314.
5. Marcilly, C. (2001) Evolution of refining and petrochemicals: what is the place of zeolites. *Oil Gas Sci. Technol.*, **56**, 499–514.
6. Wise, W.S. and Tschernich, R.W. (1976) Chemical composition of ferrierite. *Am. Mineral.*, **6**, 853–886.

7. Bouizi, Y., Rouleau, L., and Valtchev, V.P. (2006) Factors controlling the formation of core-shell zeolite-zeolite composites. *Chem. Mater.*, **18**, 4959–4966.
8. Blasco, T., Corma, A., Cabaas, M.J.D., Rey, F., Moya, J.A.V., and Wilson, C.M.Z. (2002) Preferential location of Ge in the double four-membered ring units of ITQ-7 zeolite. *J. Phys. Chem. B*, **106**, 2634–2642.
9. Georgiev, D., Bogdanov, B., Angelova, K., Markovska, I., and Hristov, Y. (2009) Synthetic zeolites – structure, classification, current trends in zeolite synthesis: review. *Techn. Stud.*, **4**, 1–5.
10. Choi, M., Na, K., Kim, J., Sakamoto, Y., Terasaki, O., and Ryoo, R. (2009) Stable single-unit-cell nanosheets of zeolite MFI as active and long-lived catalysts. *Nature*, **461**, 246–249.
11. Lutz, W. 2014. Zeolite Y: synthesis, modification, and properties—A case revisited, *Adv. Mater. Sci. Eng.*, **2014**, Article ID 724248, doi: 10.1155/2014/724248.
12. Heinemann, H. (1981) Technological applications of zeolites in catalysis. *Catal. Rev.: Sci. Eng.*, **23**, 315–328.
13. Perot, G. and Guisnet, M. (1990) Advantages and disadvantages of zeolites as catalysts in organic chemistry. *J. Mol. Catal.*, **61**, 173–196.
14. Ko, S., Fleming, P.D., Joyce, M., and Gur, P.A. (2009) High performance nano-titania photocatalytic paper composite. Part II: preparation and characterization of natural zeolite-based nano-titania composite sheets and study of their photocatalytic activity. *Mater. Sci. Eng., B*, **164**, 135–139.
15. Sancho, T., Soler, J., and Pina, M.P. (2007) Conductivity in zeolite–polymer composite membranes for PEMFCs. *J. Power Sources*, **169**, 92–97.
16. Jha, V.K., Matsuda, M., and Miyake, M. (2008) Sorption properties of the activated carbon-zeolite composite prepared from coal fly ash for Ni^{2+}, Cu^{2+}, Cd^{2+} and Pb^{2+}. *J. Hazard. Mater.*, **160**, 148–153.
17. Tabares, L.C., Navarro, J.A.R., and Salas, J.M. (2001) Cooperative guest inclusion by a zeolite analogue coordination polymer. Sorption behavior with gases and amine and group 1 metal salts. *J. Am. Chem. Soc.*, **123**, 383–387.
18. Qi, B., Lu, X.H., Fang, S.Y., Lei, J., Dong, Y.L., Zhou, D., and Xia, Q.H. (2011) Aerobic epoxidation of olefins over the composite catalysts of Co-ZSM-5 (L) with bi-/tridentate Schiff-base ligands. *J. Mol. Catal. A*, **334**, 44–51.
19. Jana, D. (2007) A new look to an old pozzolan: clinoptilolite – a promising pozzolan in concrete. Proceedings of the Twenty-Ninth Conference on Cement Microscopy Quebec City, PQ, Canada, May 20–24, pp. 168–206.
20. Mumpton, F.A. (1999) *La rocamagica*: Uses of natural zeolites in agriculture and industry. *Proc. Natl. Acad. Sci. U.S.A.*, **96**, 3463–3470.
21. Mumpton, F.A. and Fishman, P.H. (1977) The application of natural zeolites in animal science and aquaculture. *J. Anim. Sci.*, **45**, 1188–1203.
22. Ackley, M.W., Rege, S.U., and Saxena, H. (2003) Application of natural zeolites in the purification and separation of gases. *Microporous Mesoporous Mater.*, **61**, 25–42.
23. Neuhoff, H.S., Fridriksson, T., Arnórsson, S., and Bird, D.K. (1999) Porosity evolution and mineral paragenesis during Low-grade metamorphism of basaltic lavas at Teigarhorn, eastern iceland. *Am. J. Sci.*, **299**, 467–501.
24. Cundy, C.S. and Cox, P.A. (2003) The Hydrothermal synthesis of zeolites: history and development from the earliest days to the present time. *Chem. Rev.*, **103**, 663–701.
25. Tiger, H.L. and Sussman, S. (1943) Demineralizing solutions by a two-step ion exchange process. *Ind. Eng. Chem.*, **35**, 186–192.
26. Davis, M.E. and Lobo, R.F. (1992) Zeolite and molecular sieve synthesis. *Chem. Mater.*, **4**, 756–768.
27. Cruciani, G. (2006) Zeolites upon heating: factors governing their thermal stability and structural changes. *J. Phys. Chem. Solids*, **67**, 1973–1994.
28. Bates, S.P., Well, W.J.M., Santen, R.A., and Smit, B. (1996) Energetics of

n-Alkanes in zeolites: a configurational-bias montecarlo investigation into pore size dependence. *J. Am. Chem. Soc.*, **118**, 6753–6759.

29. Cho, K., Cho, H.S., Menorval, L.C.D., and Ryoo, R. (2009) Generation of mesoporosity in LTA zeolites by organosilane surfactant for rapid molecular transport in catalytic application. *Chem. Mater.*, **21**, 5664–5673.
30. Xiao, F.S., Wang, L., Yin, C., Lin, K., Di, Y., Li, J., Xu, R., Su, D.S., Schlgl, R., Yokoi, T., and Tatsumi, T. (2006) Catalytic properties of hierarchical mesoporous zeolites templated with a mixture of small organic ammonium salts and mesoscale cationic polymers. *Angew. Chem. Int. Ed.*, **118**, 3162–3165.
31. Li, Y., Shi, J., Hua, Z., Chen, H., Ruan, M., and Yan, D. (2003) Hollow spheres of mesoporous aluminosilicate with a three-dimensional pore network and extraordinarily high hydrothermal stability. *Nano Lett.*, **3**, 609–612.
32. Meier, W.M. (1986) Zeolites and zeolite-like materials. *Pure Appl. Chem.*, **58**, 1323–1328.
33. Eddaoudi, M., Moler, D.B., Li, H., Chen, B., Reineke, T.M., Okeeffe, M., and Yaghi, O.M. (2001) modular chemistry: secondary building units as a basis for the design of highly porous and robust metal-organic carboxylate frameworks. *Acc. Chem. Res.*, **34**, 319–330.
34. Murugavel, R., Walawalkar, M.G., Dan, M., Roesky, H.W., and Rao, C.N.R. (2004) Transformations of molecules and secondary building units to materials: a bottom-up approach. *Acc. Chem. Res.*, **37**, 763–774.
35. Weitkamp, J., Fritz, M., and Ernst, S. (1995) Zeolites as media for hydrogen storage. *Int. J. Hydrogen Energy*, **20**, 967–970.
36. Davis, M.K. (2002) Ordered porous materials for emerging applications. *Nature*, **417**, 813–821.
37. Bu, X., Feng, P., Gier, T.E., Zhao, D., and Stucky, G.D. (1998) Hydrothermal synthesis and structural characterization of zeolite-like structures based on gallium and aluminum germinates. *J. Am. Chem. Soc.*, **120**, 13389–13397.
38. Meng, Y., Genuino, H.C., Kuo, C.H., Huang, H., Chen, S.Y., Zhang, L., Rossi, A., and Suib, S.L. (2013) One-step hydrothermal synthesis of manganese-containing MFI type zeolite, MN – ZSM-5, characterization, and catalytic oxidation of hydrocarbons. *J. Am. Chem. Soc.*, **135**, 8594–8605.
39. Smith, B. and Ouden, C.J. (1998) Topochemistry of zeolites and related materials. 1. Topology and geometry. *J. Phys. Chem.*, **92**, 7169–7171.
40. Wilson, S.T., Lok, B.M., Messina, C.A., Cannan, T.R., and Flanigen, E.M. (1982) Alumino phosphate molecular sieves: a new class of microporous crystalline inorganic solids. *J. Am. Chem. Soc.*, **104**, 1146–1147.
41. Masters, A.F. and Maschmeyer, T. (2011) Zeolites – from curiosity to cornerstone. *Microporous Mesoporous Mater.*, **142**, 423–438.
42. Mondale, K.D., Carland, R.M., and Aplan, F.M. (1995) The comparative ion exchange capacities of natural sedimentary and synthetic zeolites. *Miner. Eng.*, **8**, 535–548.
43. Schulten, A. (1882) The hydrothermal formation of silicates, a review. *Bull. Soc. Min.*, **5**, 7–9.
44. Barrer, R.M. (1948) *Hydrothermal Chemistry of Zeolites*, Journal of Chemical Society, Academic Press, London, pp. 251–305.
45. Barrer, R.M. and Denny, P.J.J. (1961) Hydrothermal chemistry of silicates. 9. Nitrogenous aluminosilicates. *J. Am. Chem. Soc.*, 971.
46. Mimura, H., Yokota, K., Akiba, K., and Onodera, Y. (2001) Alkali Hydrothermal synthesis of zeolites from coal fly ash and their uptake properties of cesium ion. *J. Nucl. Sci. Technol.*, **38**, 766–772.
47. Walton, R.I. (2002) Subcritical solvothermal synthesis of condensed inorganic materials. *Chem. Soc. Rev.*, **31**, 230–238.
48. Bibby, D.M. and Dale, M.P. (1985) Synthesis of silica –sodalite from non-aqueous systems. *Nature*, **317**, 157–158.

49. Parnham, E.R. and Morris, R.E. (2007) Ionothermal synthesis of zeolites, metal–organic frameworks, and inorganic–organic hybrids. *Acc. Chem. Res.*, **40**, 1005–1013.
50. Cooper, E.R., Andrews, C.D., Wheatley, P.S., Webb, P.B., Wormald, P., and Morris, R.E. (2004) Ionic liquids and eutectic mixtures as solvent and template in synthesis of zeolite analogues. *Nature*, **430**, 1012–1016.
51. Li, Y. and Yang, W. (2008) Microwave synthesis of zeolite membranes: a review. *J. Membr. Sci.*, **316**, 3–17.
52. Xu, X., Yang, W., Liu, J., and Lin, L. (2001) Synthesis of NaA zeolite membrane by microwave heating. *Sep. Purif. Technol.*, **25**, 241–249.
53. Xu, Y.P., Tian, Z.J., Wang, S.J., Wang, Y.H.L., Wang, B.C., Ma, Y.C., Hou, L., Yu, J.Y., and Lin, L.W. (2006) Microwave-Enhanced ionothermal synthesis of aluminophosphate molecular sieves. *Angew. Chem. Int. Ed.*, **118**, 4069–4074.
54. Matsukata, M., Ogura, M., Osaki, T., Rao, P.R.H.P., Nomura, M., and Kikuchi, E. (1999) Conversion of dry gel to microporous crystals in gas phase. *Top. Catal.*, **9**, 77–92.
55. Nishiyama, N., Ueyama, K., and Matsukata, M. (1995) A defect-free mordenite membrane synthesized by vapour-phase transport method. *J. Chem. Soc. Commun.*, 1967–1968.
56. Matsukata, M., Kizu, K., Ogura, M., and Kikuchi, E. (2001) Synthesis of EMT zeolite by a steam-assisted crystallization method using crown ether as a structure-directing agent. *Cryst. Growth Des.*, **1**, 509–516.
57. Coker, E.N., Jansen, J.C., Martens, J.A., Jacobs, P.A., DiRenzo, F., Fajula, F., and Sacco, A. (1998) The synthesis of zeolites under micro-gravity conditions: a review. *Microporous Mesoporous Mater.*, **23**, 119–136.
58. Akporiaye, D.E., Stocker, M., and Junggreen, H. (1995) Results of the crystallisation of zeolite molecular sieves under microgravity conditions during the EURECA-1 mission. *Adv. Space Res.*, **16**, 55–58.
59. Sharma, P., Han, M.H., and Cho, C.H. (2014) An emulsion-based droplet hydrothermal synthesis method for the production of uniform sized zeolite nanocrystals. *J. Colloid Interface Sci.*, **422**, 45–53.
60. Lee, S. and Shantz, D.F. (2005) Zeolite growth in nonionic micro emulsions: synthesis of hierarchically structured zeolite particles. *Chem. Mater.*, **17**, 409–417.
61. Teh, S.Y., Lin, R., Hung, L.H., and Lee, A.P. (2008) Droplet microfluidics. *Lab Chip*, **8**, 198–220.
62. Hoang, P.H., Park, H., and Kim, D.P. (2011) Ultrafast and continuous synthesis of unaccommodating inorganic nanomaterials in droplet- and ionic liquid-assisted microfluidic system. *J. Am. Chem. Soc.*, **133**, 14765–14770.
63. Mintova, S. (2013) *Zeolite Nanoparticles*, Elsevier, doi: 10.1016/B978-0-08-097774-4.00512-X.
64. Wu, G., Wu, W., Wang, X., Zan, W., Wang, W., and Li, C. (2013) Nanosized ZSM-5 zeolites: seed-induced synthesis and the relation between the physicochemical properties and the catalytic performance in the alkylation of naphthalene. *Microporous Mesoporous Mater.*, **180**, 187–195.
65. Kong, C. and Tsuru, T. (2010) Zeolite nanocrystals prepared from zeolite microparticles by a centrifugation-assisted grinding method. *Chem. Eng. Process.*, **49**, 809–814.
66. Joshi, U.D., Joshi, P.N., Tamhankar, S.S., Joshi, V.P., Idage, B.B., Joshi, V.V., and Shiralkar, V.P. (2002) Influence of the size of extra framework monovalent cations in X-type zeolite on their thermal behavior. *Thermochim. Acta*, **387**, 121–130.
67. Trigueiro, F.E., Monteiro, D.F.J., Zotin, F.M.Z., and Aguiar, E.F.S. (2002) Thermal stability of Y zeolites containing different rare earth cations. *J. Alloys Compd.*, **344**, 337–341.
68. Primo, A. and Garcia, H. (2014) Zeolites as catalysts in oil refining. *Chem. Soc. Rev.*, **43**, 7548–7561.
69. Tsai, W.T., Hsu, H.C., Su, T.Y., Lin, K.Y., and Lin, C.M. (2006) Adsorption characteristics of bisphenol-A in aqueous

solutions onto hydrophobic zeolite. *J. Colloid Interface Sci.*, **299**, 513–519.
70. Chen, N.Y. (1978) Hydrophobic properties of zeolites. *J. Phys. Chem.*, **80**, 60–64.
71. Cheng, H. and Reinhard, M. (2006) Sorption of trichloroethylene in hydrophobic micropores of dealuminated Y zeolites and natural minerals. *Environ. Sci. Technol.*, **40**, 7694–7701.
72. Zhao, X.S., Ma, Q., and Lu, G.Q. (1998) VOC removal: comparison of MCM-41 with hydrophobic zeolites and activated carbon. *Energy Fuels*, **12**, 1051–1054.
73. Komori, Y. and Hayashi, S. (2003) Reversible color change of chromophores in zeolites by direct interaction with alkali metal cations. *Langmuir*, **19**, 1987–1989.
74. Sathish, M., Viswanathan, B., and Viswanath, R.P. (2006) Alternate synthetic strategy for the preparation of CdS nanoparticles and its exploitation for water splitting. *Int. J. Hydrogen Energy*, **31**, 891–898.
75. Herron, N., Wang, Y., Eddy, M.M., Stucky, G.D., Cox, D.E., Moller, K., and Beid, T. (1989) Structure and optical properties of CdS superclusters in zeolite hosts. *J. Am. Chem. Soc.*, **111**, 530–540.
76. Densakulprasert, N., Wannatong, L., Chotpattananont, D., Hiamtup, P., Sirivat, A., and Schwank, J. (2005) Electrical conductivity of polyaniline/zeolite composites and synergetic interaction with CO. *Mater. Sci. Eng., B*, **117**, 276–282.
77. Orbukh, V.I., Lebedeva, N.N., Ozturk, S., and Salamov, B.G. (2013) Electrical properties of the zeolite composites prepared by using zeolite and copper powders. *Superlattices Microstruct.*, **54**, 16–25.
78. Anderson, P.A., Bell, R.G., Catlow, C.R.A., Chang, F.L., Dent, A.J., Edwards, P.P. (1996) Matrix-bound nanochemical possibilities. *Chemistry of Materials* **8**, 2114–2120.
79. Egerton, T.A. and Vickerman, J.C. (1973) Magnetic studies of zeolites. Part 2.—magnetic properties of NiA, NiX and NiY. *J. Chem. Soc., Faraday Trans.*, **69**, 39–49.
80. Liu, M., Xi, B., Hou, L., and Yu, S. (2013) Magnetic multi-functional nanofly ash-derived zeolite composites for environmental applications. *J. Mater. Chem. A*, **1**, 12617–12626.
81. Moller, K. and Bein, T. (2013) Mesoporosity – a new dimension for zeolites. *Chem. Soc. Rev.*, **42**, 3689–3707.
82. Zhu, K., Sun, J., Liu, J., Wang, L., Wan, H., Hu, J., Wang, Y., Peden, C.H.F., and Nie, Z. (2011) Solvent evaporation assisted preparation of oriented nanocrystalline mesoporous MFI zeolites. *ACS Catal.*, **1**, 682–690.
83. Schoonheydt, R.A., Geerlings, P., Pidko, E.A., and Santen, R.A. (2012) The framework basicity of zeolites. *J. Mater. Chem.*, **22**, 18705–18717.
84. Smith, J.V. (1988) Topochemistry of zeolites and related materials. 1. Topology and geometry. *Chem. Rev.*, **88**, 149–182.
85. Vlugt, T.J.H. (2002) Influence of framework flexibility on the adsorption properties of hydrocarbons in the zeolite silicalite. *J. Phys. Chem. B*, **106**, 12757–12763.
86. Kiselev, A.V. and Du, P.Q. (1981) Molecular statistical calculation of the thermo dynamic adsorption characteristics of zeolites using the atom-atom approximation. *J. Chem. Soc., Faraday Trans.*, **77**, 1–15.
87. Dyer, A. (2005) Ion-exchange properties of zeolites. *Stud. Surf. Sci. Catal.*, **157**, 181–204. ISBN: 978-0-444-53063-9.
88. Barrer, R.M., Davies, J.A., and Rees, L.V.C. (1969) Comparison of the ion exchange properties of zeolites X and Y. *J. Inorg. Nucl. Chem.*, **31**, 2599–2609.
89. Barrer, R.M. and Klinowski, J. (1972) Influence of framework charge density on ion-exchange properties of zeolites. *J. Chem. Soc., Faraday Trans.*, **68**, 1956–1963.
90. Baglio, V., Arico, A.S., Blasi, A.D., Antonucci, P.L., Nannetti, F., Tricoli, V., and Antonucci, V. (2005) Zeolite-based composite membranes for high temperature direct methanol fuel cells. *J. Appl. Electrochem.*, **35**, 207–212.

91. Zhang, Z., Desilets, F., Felice, V., Mecheri, B., Licoccia, S., and Tavares, A.C. (2011) On the proton conductivity of Nafion–Faujasite composite membranes for low temperature direct methanol fuel cells. *J. Power Sources*, **196**, 9176–9187.
92. Chen, Z., Holmberg, B., Li, W., Wang, X., Deng, W., Munoz, R., and Yan, Y. (2006) Nafion/zeolite nanocomposite membrane by in situ crystallization for a direct methanol fuel cell. *Chem. Mater.*, **18**, 5669–5675.
93. Wang, J., Zheng, X., Wu, H., Zheng, B., Jiang, Z., Hao, X., and Wang, B. (2008) Effect of zeolites on chitosan/zeolite hybrid membranes for direct methanol fuel cell. *J. Power Sources*, **178**, 9–19.
94. Libby, B., Smyrl, W.H., and Cussler, E.L. (2003) Polymer-zeolite composite membranes for direct methanol fuel cells. *AlChE J.*, **49**, 991–1001.
95. Wu, H., Zheng, B., Zheng, X., Wang, J., Yuan, W., and Jiang, Z. (2007) Surface-modified Y zeolite-filled chitosan membrane for direct methanol fuel cell. *J. Power Sources*, **173**, 842–852.
96. Eguizábal, A., Lemus, J., and Pina, M.P. (2013) On the incorporation of protic ionic liquids imbibed in large pore zeolites to polybenzimidazole membranes for high temperature proton exchange membrane fuel cells. *J. Power Sources*, **222**, 483–492.
97. Atienzar, P., Valencia, S., Corma, A., and Garcia, H. (2007) Titanium-containing zeolites and microporous molecular sieves as photovoltaic solar cells. *ChemPhysChem*, **8**, 1115–1119.
98. Alvaro, M., Carbonell, E., Atienzar, P., and Garcia, H. (2006) A novel concept for photovoltaic cells: clusters of titanium dioxide encapsulated within zeolites as photoactive semiconductors. *ChemPhysChem*, **7**, 1996–2002.
99. Kim, H.S., Jeong, N.C., and Yoon, K.B. (2011) Photovoltaic effects of CdS and PbS quantum dots encapsulated in zeolite Y. *Langmuir*, **27**, 14678–14688.
100. Pereira, J.N., Lopes, A.C., Costa, C.M., Rodrigues, L.C., Silva, M.M., and Méndez, S.L. (2013) Microporous membranes of NaY zeolite/poly(vinylidene fluoride–trifluoroethylene) for Li-ion battery separators. *J. Electroanal. Chem.*, **689**, 223–232.
101. Coetzer, J. (1978) High temperature lithium/sulphur batteries: a preliminary investigation of a Zeolite-sulphur cathode. *Electrochim. Acta*, **23**, 787–789.
102. Dalas, E., Vitoratos, E., Sakkopoulos, S., and Malkaj, P. (2004) Polyaniline/zeolite as the cathode in a novel gel electrolyte primary dry cell. *J. Power Sources*, **128**, 319–325.
103. Corma, A., Cabanas, M.J.D., Triguero, J.M., Rey, F., and Rius, J. (2002) A large-cavity zeolite with wide pore windows and potential as an oil refining catalyst. *Nature*, **418**, 514–517.
104. Boyas, R.S., Liu, Y., and Minowa, T. (2011) Renewable diesel production from the hydro treating of rapeseed oil with Pt/zeolite and $NiMo/Al_2O_3$ catalysts. *Ind. Eng. Chem. Res.*, **50**, 2791–2799.
105. Verboekend, D., Thomas, K., Milina, M., Mitchell, S., Ramırez, J.P., and Gilson, J.P. (2011) Towards more efficient mono dimensional zeolite catalysts: n-alkane hydro-isomerisation on hierarchical ZSM-22. *Catal. Sci. Technol.*, **1**, 1331–1335.
106. Landau, M.V., Vradman, V., Valtchev, V., Lezervant, J., Liubich, E., and Talianker, M. (2003) Hydrocracking of heavy vacuum gas oil with a Pt/H-beta-Al_2O_3 catalyst: effect of zeolite crystal size in the nanoscale range. *Ind. Eng. Chem. Res.*, **42**, 2773–2782.
107. Corma, A. and Garcia, H. (2004) Zeolite-based photocatalysts. *Chem. Commun.*, **2004**, 1443–1459.
108. Fukahori, S., Ichiura, H., Kitaoka, T., and Tanaka, H. (2003) Photocatalytic decomposition of bisphenol A in water using composite TiO_2-zeolite sheets prepared by a paper making technique. *Environ. Sci. Technol.*, **37**, 1048–1051.
109. Tayade, R.J., Surolia, P.K., Lazar, M.A., and Jasra, R.V. (2008) Enhanced photocatalytic activity by silver metal ion exchanged NaY zeolite photocatalysts for the degradation of organic contaminants and dyes in aqueous medium. *Ind. Eng. Chem. Res.*, **47**, 7545–7551.

110. Alvaro, M., Carbonell, E., Garcia, H., Lamaza, C., and Pillai, M.N. (2014) Ship-in-a-bottle synthesis of 2,4,6-triphenylthiapyrylium cations encapsulated in zeolites Y and beta: a novel robust photocatalyst. *Photochem. Photobiol. Sci.*, **3**, 189–193.

111. Dalebrook, A.F., Gan, W., Grasemann, M., Moret, S., and Laurenczy, G. (2013) Hydrogen storage: beyond conventional methods. *Chem. Commun.*, **49**, 8735–8751.

112. Li, Y. and Yang, R.T. (2006) Hydrogen storage in low silica type X zeolites. *J. Phys. Chem. B*, **110**, 17175–17181.

113. Palomino, G.T., Carayol, M.R.L., and Arean, C.N. (2006) Hydrogen adsorption on magnesium-exchanged zeolites. *J. Mater. Chem.*, **16**, 2884–2885.

114. Dong, J., Wang, X., Xu, H., Zhao, Q., and Li, J. (2007) Hydrogen storage in several microporous zeolites. *Int. J. Hydrogen Energy*, **32**, 4998–5004.

115. Bae, D., Park, H., Kim, J.S., Lee, J.B., Kwon, O.Y., Kim, K.Y., Song, M.K., and No, K.T. (2008) Hydrogen adsorption in organic ion-exchanged zeolites. *J. Phys. Chem. Solids*, **69**, 1152–1154.

116. Ranjani, V.S., Shen, M.S., and Fisher, E.P. (2005) Adsorption of CO_2 on zeolites at moderate temperatures. *Energy Fuels*, **19**, 1153–1159.

117. Sanchez, A.G., Ania, C.O., Parra, J.B., Dubbeldam, D., Vlugt, T.J.H., Krishna, R., and Calero, S. (2009) Transferable force field for carbon dioxide adsorption in zeolites. *J. Phys. Chem. C*, **113**, 8814–8820.

118. Siporin, S.E., McClaine, B.C., and Davis, R.J. (2003) Adsorption of N_2 and CO_2 on zeolite X exchanged with potassium, barium, or lanthanum. *Langmuir*, **19**, 4707–4713.

7
Mesoporous Materials and Their Nanocomposites

Vijay K. Tomer, Sunita Devi, Ritu Malik, and Surender Duhan

Porous materials are ubiquitous around the world, and nearly all the earth's solid contents are porous to some extent. The application of clay, wood, and other porous materials do not have any well-documented beginnings, but certainly date back to prehistoric times. These porous solids in the form of natural material or with heat treatment were already used by early humans. Nowadays, the synthesis, characterization, and application of novel porous materials have been strongly encouraged globally due to their wide range of applications in adsorption, separation, catalysis, sensors, drug delivery, and environmental pollution control. The design, synthesis, and modification of porous materials are in some aspects more challenging than the synthesis of dense materials. The increasing interest in porous materials is because of their ability to interact with atoms, ions, molecules, and nanoparticles not only at their surfaces, but throughout the bulk of the materials. Therefore, the presence of pores in nanostructured materials greatly promotes their physical and chemical properties. Thanks to innovative synthesis strategies, an evolution toward structured materials with larger pores could be obtained. After the first reports that introduced the M41S family of ordered mesoporous silicas at the beginning of the 1990s, the synthesis of advanced mesoporous materials has undergone explosive growth. Recently, the understanding, design, and manipulation of pores have significantly advanced science and technology, and have been playing increasingly important roles in modern society.

7.1
Introduction of Mesoporous Materials

Zeolites, the first primitive porous material, were first discovered in 1756 by the Swedish scientist Axel Fredrik Cronstedt. Zeolites have aluminosilicate frameworks, and small micropores inside it and were synthesized via nonsurfactant-assisted route employing single molecule template. The ever increasing demands in industrial and academic applications such as the encapsulation of metal complexes into a framework, the introduction of nanoparticles

Nanomaterials and Nanocomposites: Zero- to Three-Dimensional Materials and Their Composites,
First Edition. Edited by Visakh P.M. and Maria José Martínez Morlanes.

into a zeolite molecular sieve for optical and electronic properties, and the separation and selective adsorption of large organic molecules from contaminated water has driven the interest in expanding the pore size of zeolites material from the micropore region to the mesopore region. This task was made possible by scientists of Mobil Oil Corporation (USA) in 1992 [1] when they first reported the successful synthesis of a novel M41S family of mesoporous silica with large uniform pore size through self-assembled molecular aggregation or through supramolecular assembly of surfactant molecules such as cetyltrimethylammonium cation as the structure-directing agent (SDA), rather than the conventional single-amine-molecule-template microporous structures. This surfactant-assisted templating pathway or soft templating strategy opens a new class of materials named as mesoporous materials resulting in a worldwide research in this field. The templating agent used is no longer a single, solvated organic molecule, or metal ions, but rather a self-assembled surfactant molecule. Following the breakthrough discovery of the mesoporous silica M41S in the early nineties, the area of periodic mesoporous materials has been growing steadily. The material possessed regular arrays of uniform channels whose diameter could be tailored through the choice of surfactant and reaction conditions. This was the start of a new era in material science. Important findings appear in the literature on a regular basis, providing new opportunities for further innovations, as well as creating new areas of research.

7.2 IUPAC Classification of Porous Materials

The definition of porous materials relates to the existence of voids in between the solid network framework of materials. A material can be classified as porous if its internal voids can be filled with gas, liquid, or even with a solid. Generally, pores are classified into two types (Figure 7.1): closed pores that are isolated from the outside and open pores that connect to the outside of the material. Porous materials have lower density and higher surface area compared to dense materials. According to IUPAC International Union of Pure and Applied Chemistry classification [2], based on the framework building blocks, porous materials can be classified as: purely inorganic, hybrid organic–inorganic and organic porous polymers, and carbonaceous materials. Depending on the predominant pore size, the porous materials are further classified into three different types (Figure 7.2).

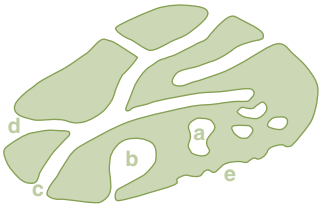

Figure 7.1 Definition of pores in a solid material: (a) closed pore, (b) ink-bottle shape, (c) cylindrical shape, (d) funnel shape, and (e) surface roughness.

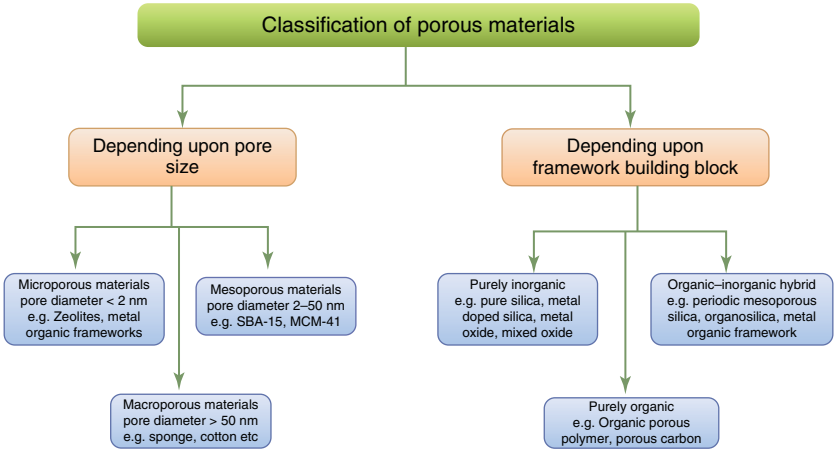

Figure 7.2 Schematic of classification of porous materials.

- Microporous material, pore diameter <2 nm
- Mesoporous material, pore diameter between 2 and 50 nm
- Macroporous material, pore diameter >50 nm.

Among the above-mentioned materials, mesoporous materials are of specific importance due to their high stability, surface areas, and large pore volumes, which make them the most suitable candidates as adsorbents, ion-exchangers, catalysts, catalyst supports, and in many other related applications [3].

7.3 Synthesis Pathways for the Formation of Mesoporous Materials

In the burgeoning field of mesostructured materials, synthesized through the self-assembly of inorganic polymeric species and SDA, a precise control over the morphology and orientation of the pore channels is needed to realize the promising applications of these materials. The pore channels can be modulated during the synthesis by controlling the reaction time and temperature, by using swelling organic molecules (e.g., aromatic hydrocarbons and trialkylamines), by adjusting the surfactant and co-cation concentration, by postsynthesis treatment (e.g., water-amine treatment), or by changing the calcination conditions [4]. The control of the morphology has been explained by the influence of defects during the nucleation and growth process or by the formation mechanism.

7.4 Role of Structure Directing Agents/Surfactants

Surfactants (surface active agents) are amphiphilic molecules, having both hydrophilic (head) and a hydrophobic (tail) part (Figure 7.3). Surfactants are classified according to the charge on their head group: anionic, cationic, zwitterionic,

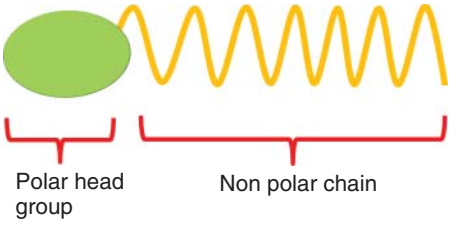

Figure 7.3 Schematic picture of a surfactant.

and nonionic and the lipophilic part is generally a hydrocarbon chain [5]. The tail can be linear or branched; aliphatic, aromatic or a mixture of both; short or long (typically between 8 and 16 carbons). Due to their amphiphilicity, the surfactants form micelles in oil or aqueous solutions to lower the free energy in the system. If the solvent has two immiscible phases, the surfactants are located in the oil/water interface with the hydrophilic part toward the water and the lipophilic part in the oil. A list of common surfactants commonly used in the synthesis of mesoporous materials is shown in Table 7.1.

The high surface activity of surfactants results in that they preferably locate themselves at interfaces, for example, at the air/water interface when dissolved in water. At a critical micelle concentration (CMC) the surfactants start to aggregate into micelles, because of the hydrophobic effect [6]. With increasing concentration of surfactants more micelles are formed and at some point micelles come in direct contact. This intermicellar state leads to aggregation of micelles into ordered structures called lyotropic liquid crystals (LLCs).

Table 7.1 List of common surfactants for mesoporous materials.

Surfactants	
Anionic	
Sulfates	$C_nH_{2n+1}OSO_3^-Na^+$
Sulfonates	$C_nH_{2n+1}SO_3H$
Phosphates	$C_nH_{2n+1}OPO_3H_2$
Carboxylates	$C_nH_{2n+1}COOH$
Cationic	
Alkylammonium salts	$C_nH_{2n+1}(CH_3)NX$ [X = OH, Cl, Br, HSO_4]
Dialkylammonium salts	$(C_{16}H_{33})_2(CH_3)_2N^+Br^-$
Non ionic	
Primary amines	$C_nH_{2n+1}NH_2$
Polyethylene oxides	$HO(CH_2CH_2O)_nH$

7.4.1
Lyotropic Liquid Crystals (LLCs)

LLCs have a long-range order, but are disordered at the short-range molecular level. Depending on the molecular structure of the amphiphile, different LLCs can be formed; where single-chain surfactants commonly aggregate into cubical or hexagonal structures and double-chain surfactants self-assembly into lamellar or reversed hexagonal structures [7]. In general, the interplay of the relative bulkiness of the hydrophilic and hydrophobic domains of the amphiphile influences the LLCs formed. In order to predict the structure of the aggregate, a simplified molecular model of the surfactants can be used, which is based on geometrical parameters as is illustrated in Figure 7.4.

$$\text{Critical Packing parameter} : \text{CPP} = V_{\text{H}}/a_0 L_{\text{c}}$$

where V_{H} is the volume of the hydrophobic part, a_0 is the surface area of the hydrophilic part, L_{c} ($L_{\text{c}} \leq 1.5 + 1.265n$) is the critical chain length and depends on the chain shape, and n is the number of carbon atoms [8] (Table 7.2).

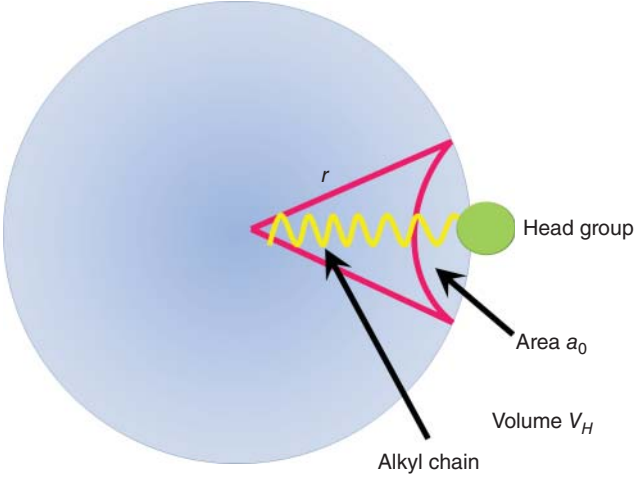

Figure 7.4 The preferred aggregate structure of amphiphiles can be estimated using the CPP, which is based on the geometric shape of the amphiphile.

Table 7.2 CPP ratios and their corresponding geometry of micelles.

CPP	Surfactant	Micelle shape
<0.33	Linear chain, large head	Spherical
0.33–0.5	Linear chain, small head	Cylindrical
0.5–1.0	Two chains, large head	Bilayers

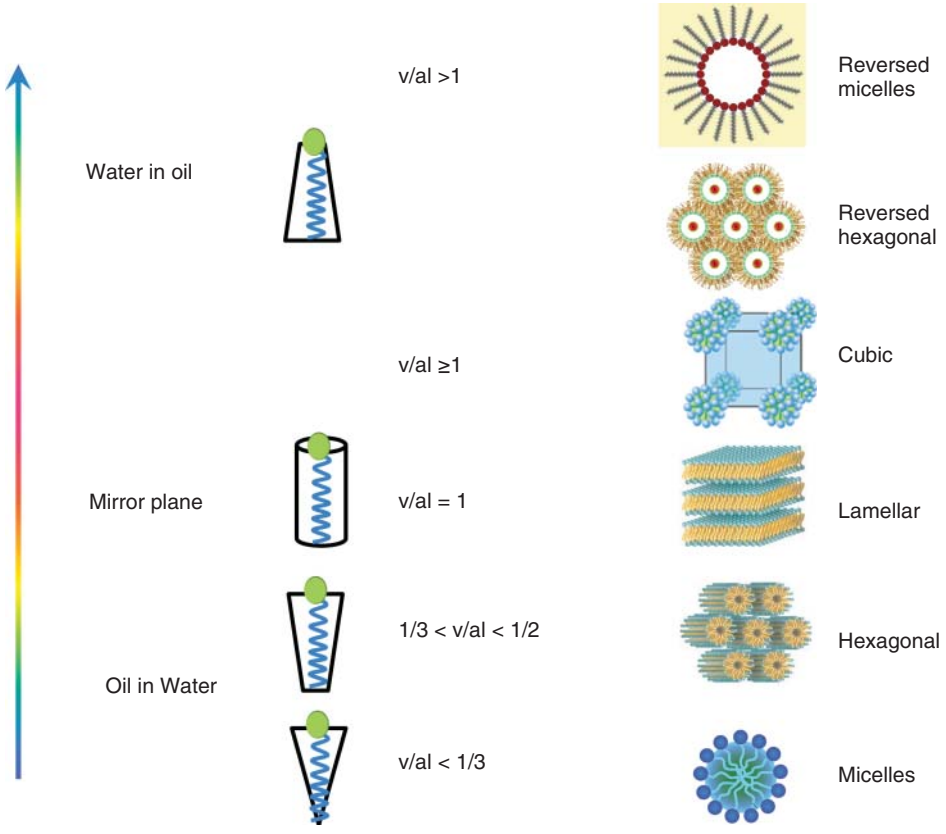

Figure 7.5 The relationship between the preferred aggregate structure and the critical packing parameter (CPP) of surfactant molecules [8].

In Figure 7.5, the relationship between the CPP and different self-assembly structures, including micells, cubic, hexagonal, and lamellar structures, are illustrated.

Another factor that determines the LLCs that are being formed is the surfactant concentration. An increased surfactant concentration results in a change of LLCs, typically from micellar, to hexagonal, to cubic structure, and so on. Surfactants in LLCs of hexagonal, cubic, and lamellar orientation, are aligned in a bilayer with the hydrophobic tails pointing to each other such that the pore dimension or the distance between lamellar sheets corresponds to twice the length of the hydrophobic tail (Figure 7.6). For triblock copolymers, the pore dimension or the distance between the lamellar sheets equals the length of the hydrophobic block, Polyethylene Oxide (PO).

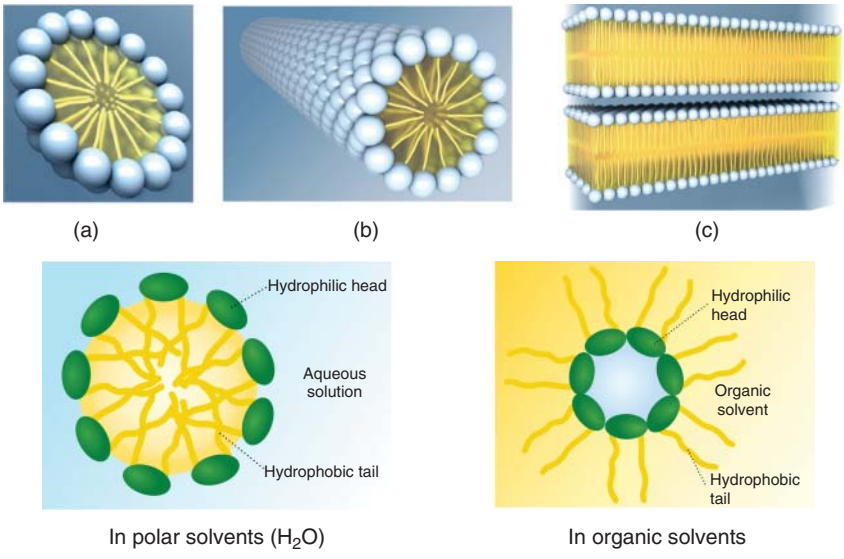

Figure 7.6 Morphologies of surfactants and their behavior in different solvents.

7.5 Type of Surfactants

There are basically two types of surfactants involved in the synthesis of mesoporous or nanoporous silicates and other metal oxides with narrowly distributed pore diameters of 2–50 nm. These are charged (cationic and anionic) and neutral surfactants wherein the mesophase formation is based on the electrostatic interaction and hydrogen-bonding interactions, respectively.

7.5.1 Charged Surfactant Template

According to Mobil's technology, the energy of long-chain quaternary ammonium surfactants in solution gets minimized by assembling into micelles. Under suitable conditions, these micelles adopt a rod-like shape and even organize into long-range hexagonal arrays with the hydrophilic head groups pointing toward the solution and hydrophobic chains pointing toward the center of the micelles. The ability of the long-chain quaternary ammonium cations to form rod-like micelles and long-range hexagonal arrays in aqueous solutions has been known for a very long time. The formation of the hexagonal arrays of micellar rods is strongly dependent on the surfactants' nature of the halide counter-ion, concentration, temperature of the solution, and alkyl chain length. Upon the addition of a silicate precursor, for example, tetraethyl orthosilicate (TEOS), the negatively charged silica species (I^-) condense and polymerize on the surface of the positively charged micelles (S^+), giving rise to the corresponding

hexagonal S^+I^- organic–inorganic complex. The final hexagonal solid framework of the mesoporous molecular sieve (MCM-41, Mobil Composition of Matter) is achieved by removing the surfactants during calcination.

Ionic surfactant templating pathways to ordered mesostructures use assemblies of charges surfactant ions (S^+ or S^-) as templates to organize an inorganic framework from charged inorganic oxide precursors (I^- or I^+). These charged templates are strongly bonded to the charged inorganic framework, and are difficult to recover. In general, the electrostatically bonded templates are removed from the framework of MCM-41 materials by either a calcination process or by an ion-exchange reaction with an ion donor solution. Also, electrostatic-templated MCM-41 materials have relatively low degree of framework cross-linking and small framework wall thickness that influences the hydrothermal and mechanical stability of these molecular sieves. As a consequence, the materials often have limited thermal and chemical stability and structure collapse during calcination in which further condensation of silanol groups occurs.

7.5.2 Neutral Surfactant Templates

Mesoporous materials prepared using neutral surfactants as templates possess improved stability. In case of primary amine (with carbon tail lengths between C_8 and C_{18}) as templates, the pore size of the final mesoporous silicas can be tuned by changing the hydrophobic tail length of the amines. The hydrogen bonding interactions and self-assembly between neutral primary amine micelles (S_o) and neutral inorganic precursors (I_o) direct the formation of mesophases. The template can be removed by solvent extraction or by calcination. The mesoporous materials have greater wall thickness (1.7–3.0 nm) due to the absence of electrostatic or charge-matching effects and therefore, have higher thermal stability than M41S materials. However, the materials exhibit only short-range hexagonal ordering. The high cost and toxicity of amines also limit their use in large-scale production.

Nonionic pluronic surfactants are a convenient alternative to primary amines and have demonstrated advantages in solving the problems of ionic surfactant, since the pluronic surfactants are neutral, nontoxic, and biodegradable. In this S_oI_o templating pathway, hydrogen bonding interactions between the hydrophilic surfaces of flexible rod- or worm-like micelles and intermediate hydrolysis products are the driving force in the formation of the mesophases. The pore size of the materials can be tuned by varying the length and structure of the surfactant molecules. This approach allows for the preparation of mesoporous molecular sieves with large framework wall thickness, small particle sizes, and textural mesoporosity. In addition, the S_oI_o approach allows for cost reduction by employing less expensive reagents and mild reaction conditions while providing for the effective and environmentally benign recovery and recyclability of the template. The use of polyethylene oxide (PEO) copolymers as templates has led to inorganic materials with pore diameters extending from mesoporous to macroporous range.

7.6
Role of Templates

In the synthesis of mesoporous materials, two kinds of templates are generally used: supramolecular aggregates such as surfactant micelle arrays (soft-templating method), and preformed mesoporous solids such as silicates and carbons (hard-templating or nanocasting method). Two classes of ordered mesoporous materials are thus obtained: continuous framework structures with cylindrical or spherical mesopores and their counter-replica structures, which can also be regarded as nanowire/nanosphere arrays.

7.6.1
Soft Templates

In the soft-templating method, the ordered mesopore arrangement is achieved by the cooperative assembly of amphiphilic surfactant molecules and guest species are driven by the spontaneous trend of reducing interface energy. The constituents and properties of the molecule templates are critical for mesostructures. Therefore, these molecules are also called *structure-directing agents*. Aqueous solution synthesis and evaporation induced self-assembly (EISA) routes are normally adopted [9]. In a solution synthesis route, the key issue is that the guest species ought to have a controllable aqueous sol–gel process, while, in an EISA synthesis, the use of nonaqueous solvent media greatly slows down the hydrolyzation and condensation rate of metal species, which greatly benefits the formation of their ordered mesostructures. In both cases, a strong interaction between SDAs and precursors is necessary to assemble ordered target materials and avoid the macroscale phase separation.

7.6.2
Hard Templates

The hard-templating method is also known as *nanocasting* because the entire manufacturing procedure is similar to the traditional casting method but in nanoscale. In this approach, the regular arrangement comes from the preformed ordered mesoporous template (mesoporous silica, or mesoporous carbon). The small mesotunnels inside the template's pore wall are necessary for nanocasting. They can be replicated to form small nanorods and thus support the nanowire/nanospheres that are replicated from the primary mesopores, to form stable mesostructured replica arrays (Figure 7.7). Otherwise, the obtained replicas cannot maintain their mesostructures once the templates are removed, resulting in isolated nanowires/nanospheres or low-symmetry mesostructured products. This synthesis strategy avoids the control of the cooperative assembly of SDAs and guest species and the sol–gel process of guest species, making it quite successful in plenty of materials. Siliceous, metal oxides, and carbon-based

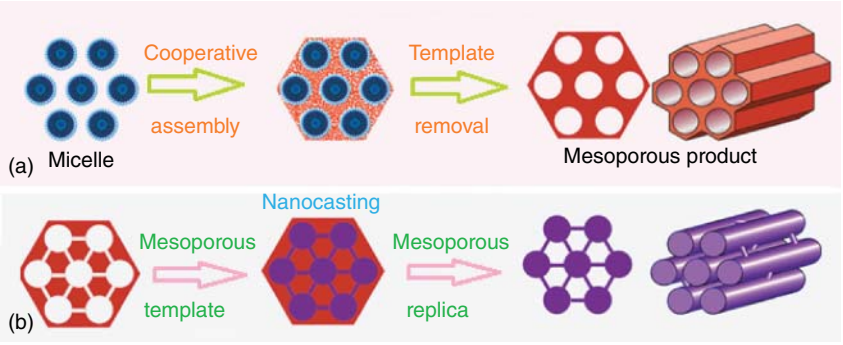

Figure 7.7 Scheme of two representative synthesis routes for ordered mesoporous materials: (a) soft-templating method and (b) hard-templating (nanocasting) method.

materials dominate the research society of mesoporous materials due to plenty of practicable precursors and controllable sol–gel processes for these materials.

7.7
Types of Mesoporous Materials: Structure and Properties

7.7.1
Mesoporous Silica

The basic interest in mesoporous silica stems from the presence of a well-ordered structure that provides high surface area and accessibility to molecular species through the channels. In addition, the possibility of synthesizing different types of mesostructures with multiple pore architecture further enhances their versatility for different applications. It is possible to synthesize mesoporous silica via the alkaline or the acidic routes using surfactants such as SDAs with the properties of mesoporous silica strongly dependent on the maintained synthesis conditions just as hydrolysis/condensation of silica is strongly influenced by the pH of the synthesis sol.

Since the first report of mesoporous silica (MCM-41) synthesized by the liquid crystal template, the soft-templating method has become a general pathway for the synthesis of ordered mesoporous materials. Even though better condensation of the silanol groups occurs in mesoporous silica obtained under alkaline conditions, a rich morphology in shapes is achievable in acidic conditions. Of particular mention is the remarkable findings by Zhao *et al.* in 1998, regarding the preparation of large-pore ordered mesoporous silica with a 2D hexagonal structure by using triblock copolymers as templates, which is popularly known as *SBA-15*, an acronym for Santa Barbara Amorphous. During acid synthesis (with pH < 2), the silica species in solution are positively charged (I^+). The surfactant (S^+) and silica interaction as mediated by the counterion X becomes $S^+X^-I^+$, and

this micelle-counterion interaction is in thermodynamic equilibrium [10]. There are various factors such as ion exchange equilibrium of X^- on micellar surface, surface-enhanced concentration of I^+, and proton-catalyzed silica condensation near micellar surface, phase separation, colloid stability, and micelle aggregation, which are responsible for directing the shapes of mesoporous silica.

A large number of soft templates, including cationic, anionic and nonionic surfactants, and mixed surfactant systems, have been used to synthesize ordered mesoporous silica with controllable structures and tunable pore architecture. Mesoporous silica materials based on MCM-41 and SBA-15 show excellent thermal, hydrothermal, and hydrolytic stabilities. The walls of the channels are amorphous SiO_2 and the porosity can be as high as 80% of their total volume. The diameter of the pore channels can be controlled by changing the length of the template molecule. The growth of a mesoporous silica particle in specific shape is believed to be through the firstly formed precursor silica-surfactant nanoparticles that grow through aggregation of silica/surfactant micelle. Small changes in acidity and specific kind of dislocations defects are responsible for the production of characteristic shapes such as curved morphologies, and so on. Moreover, changing the surfactants (e.g., Pluronics (P123 and F127), hexadecylamine (HDA), and cetyltrimethylammonium bromide (CTAB)) and silica source (e.g., fused silica, colloidal silica, TEOS, tetramethyl orthosilicate (TMOS), and sodium silicate), synthesis procedure (sol–gel, hydrothermal method), or reaction conditions (solvent, temperature, aging time, hydrothermal conditions, reactant mole ratio, and pH of the medium) leads to the production of new mesoporous systems. At the same time, these changes also affect the thermal, hydrothermal, and mechanical stabilities of the materials. By varying the above parameters, a variety of mesoporous silica materials have been developed such as MCM-41, MCM-48, SBA-15, SBA-16, KIT-6, (Korea Institute of Technology-6) and so on.

7.7.1.1 M41S Materials

The M41S materials enjoy the status of first being called as *mesoporous materials*. M41S is the generic term for the various types of MCM (Mobil Composition of Matter) materials in the mesoporous range. All M41S materials have well-defined uniform pores that are ordered in the long range. The Mobil researchers introduced self-assembling surfactants as SDAs to direct the formation of the SiO_2 mesostructured materials. The three most important M41S materials are: MCM-41 (hexagonal), MCM-48 (cubic), and MCM-50 (lamellar) (Figure 7.8).

M41S materials are generally synthesized in a basic environment with quaternary ammonium salts or gemini surfactants. The key parameters for the M41S synthesis are the hydrogel composition, type and length of the surfactant, alkalinity, temperature, and the synthesis time. The type of mesophase that will be obtained after a specific M41S synthesis with quaternary ammonium salts can be predicted by the packing factor (g-factor), which is a measure for

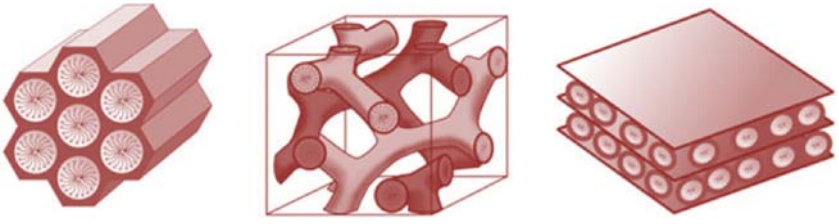

Figure 7.8 Structure of M41S materials (a) MCM-41, (b) MCM-48, and (c) MCM-50.

the local effective surfactant packing. It includes the hydrophobic–hydrophilic balance and therefore describes the tendency of the alkyl chains to minimize their water contact and maximize their interorganic interactions. When the polar head group has a large surface area, spherical structures are obtained. On the other hand, lamellar or rod packing occurs when the head groups are packed tightly with large aggregation numbers. By changes in the synthesis conditions, the g packing factor and therefore, also the ordering of the materials can be altered.

MCM-41 MCM-41 is the most widely studied among the M41S family of material. It is often used as a model to compare with other materials or to study the fundamental aspects in sorption, catalysis, and so on [11]. This is due to the simplicity and ease in its preparation with negligible pore-networking and pore-blocking effects. It consists of an amorphous silicate framework forming hexagonal pores. MCM-41 has high surface areas of up to 1200 $m^2 g^{-1}$ and large pore volumes. The pores are unidirectional and uniform causing narrow pore size distributions and are arranged in a honeycomb structure over micrometer length scales. For classical MCM-41, the pores can be tailored to diameters between 1.5 and 20 nm. The largest pores can only be obtained with the addition of swelling agents. The pore walls are quite thin with a thickness between 1 and 1.5 nm and are the major cause of low chemical and hydrothermal stabilities. Hence, to improve the stability of these materials, various techniques have been used like addition of various salts, post-modification methods (ion exchange, treatment in acid, grafting of organosilane functional groups to produce hydrophobic organic chains on the surface, etc.).

MCM-48 Due to the smaller synthesis regime for MCM-48 when applying quaternary ammonium salts, the MCM-48 structure has been far less studied than MCM-41. MCM-48 could be obtained only with surfactant to silica ratios higher than 1. However, gemini surfactants have the intrinsic ability to favor a cubic symmetry over a wide variety of conditions [12]. MCM-48 is cubic and has surface areas, pore sizes, and volumes similar to MCM-41. The wall thickness of the pores is thin for MCM-48 causing only limited chemical and hydrothermal

stabilities. The structure of MCM-48 is of particular interest since the pores are three-dimensional.

7.7.1.2

SBA-X Materials

In 1998, a new family of highly ordered mesoporous silica materials have been synthesized in an acid medium by the use of nonionic triblock copolymers ($EO_nPO_mEO_n$) with large PEO and polypropylene oxide (PPO) blocks. Different materials with a diversity of periodic arrangements have been prepared and denoted as SBA materials (the acronym for Santa Barbara Amorphous) [13]. A wide variety of SBA materials have been reported in the literature, such as SBA-1 (cubic), SBA-11 (cubic), SBA-12 (3D hexagonal network), SBA-14 (lamellar), SBA-15 (2D hexagonal), and SBA-16 (cubic cage-structured).

SBA-15 SBA-15 is a combined micro- and mesoporous material with hexagonally ordered tunable uniform mesopores (4–30 nm). It consists of thick microporous silica pore walls (0.3–4 nm) responsible for the high hydrothermal stability of SBA-15 compared to other mesoporous materials like MCM-41 and MCM-48 with thin pore walls [14]. The size of the micropores was found to be dependent on the synthesis conditions. The micropores in the walls of the SBA-15 mesopores originate from the PEO blocks in the triblock copolymers that are directed to the aqueous solution, whereas the PPO blocks are more hydrophobic and give rise to the internal structure of the mesopore. SBA-15 materials with short or straight channels can be synthesized as well by decreasing the stirring time or adding salts during the synthesis, respectively. Moreover, the short channel of SBA-15 materials also gives rise to smaller, less aggregated particles. The shape and curvature of the pores are found to be important for the diffusion of molecules through the structure and the ultimate adsorption capacity. X-ray diffraction patterns of the SBA-15 materials reveal the 2D hexagonally structured pores (*p6mm* space group) at low angles, whereas no diffraction pattern can be observed at high angles due to the amorphous nature of the pore walls. A typical process depicting the structure and synthesis of SBA-15 using micelles has been shown in Figure 7.9.

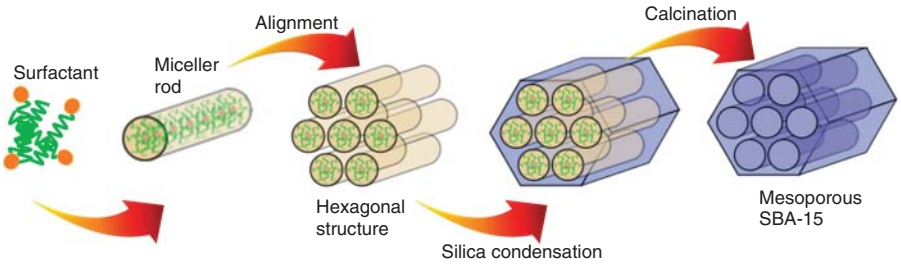

Figure 7.9 Schematic of process for synthesis of SBA-15.

By changing the length of the PEO blocks, different amounts of micropores and changes in the pore wall thickness could be obtained. Moreover, the ratio of the number of PEO units to the number of PPO units directs the mesophase (lamellar, hexagonal, cubic, etc.) of the structure. On the other hand, altering the length of the PPO blocks will result in different mesopore diameters. Furthermore, synthesis parameters like temperature, pH, and the addition of additives such as co-surfactants, swelling agents, electrolytes, salts, and so on, will allow pore size engineering and tuning of the general properties and morphologies of SBA-15 to a large extent.

The synthesis of SBA-15 is often straightforward and relatively easy. During a standard synthesis the surfactant, P123, is dissolved in hydrochloric acid where the micelles continue to elongate and form long thread-like micelles. During this step, spherical and cylindrical micelles are coexisting. This coexistence indicates the presence of two phases: concentrated phase and dilute phase where the spherical micelles exist. At the mild synthesis temperatures (35–45 °C), the micelles are always spherical, even at strongly acidic conditions. When the TEOS is added, an emulsion of hydrophobic TEOS droplets is formed, although this emulsion is only present until the TEOS is completely hydrolyzed. The hydrolysis of TEOS occurs at the water/TEOS interface, and the condensation process starts as soon as hydrolyzed spices are available. The silica precursor penetrates into the core of the micelles, although this seems unlikely, considering that no expansion of the micelles was observed. As soon as the hydrolyzed silica oligomers start to interact with the corona, the micelles undergo a sphere-to-rod transition, forming short, cylindrical micelles. Upon further condensation of the silicate oligomers, micelles become straighter and less flexible, and finally the hexagonal structure is formed. The elongation of micelles is due to the decrease of the curvature of the corona, and swelling of the hydrophobic core. The silicate oligomers interact with the PEO chains in the core–corona interface, and decrease the effective volume of the PEO chains. The main interaction between the silicate oligomers and the PEO is the formation of hydrogen bonds between them. The reaction process travels from the core–corona region and outward with time. Also, ethanol is a decay product of TEOS, and within the relevant temperature range, PPO is soluble in ethanol and insoluble in water. When the ethanol goes into the hydrophobic core of the micelles, the core volume expands and the CPP increases. The diameter of the PPO core is equal to the pore size of SBA-15. During the formation of cylindrical micelles, the radius of the PPO core decreases initially. This is most probably due to the interaction of silica and PEO in the core/corona region where the silica can partly penetrate into the core and remove water, causing a contraction of the core. During the formation of the hexagonal structure, the voids between the cylindrical micelles decrease, and the solvent in the voids is replaced with silicate species. The solution is stirred for 20 h at 35–40 °C, and at this step the material's pore structure and morphology are determined. This is followed by hydrothermal treatment where the material is heated to 95–105 °C for 24–48 h in order to finalize the condensation of TEOS and complete the pore formation. Finally, the product is collected by filtration and calcinated at 550 °C to remove the surfactants. There

are several ways to control the pore size, microporosity, and particle morphology to obtain the optimal product, for example, addition of salt, swelling agents, and/or temperature variations.

SBA-16 When block copolymers with larger ethylene oxide (EO) chains (e.g., $EO_{106}PO_{70}EO_{106}$ = F127) are used as templates under acidic conditions, SBA-16 is formed at room temperature. The large EO chains favor the formation of globular aggregated structures. SBA-16 is obtained in a narrow range of diluted surfactant concentration (3–5%). Similarly to SBA-15, the template are removed by calcination at elevated temperatures. After template removal, a combined micro- and mesoporous material is obtained due to the presence of PEO and PPO chains that are responsible for the formation of the micropores and mesopores, respectively. The narrow pore size distributions, mesopore sizes around 6 nm, high surface areas, large total pore volumes, and thick pore walls (4–6 nm) of SBA-16 resemble those of SBA-15. The thick pore walls of SBA-16 results in high chemical, thermal, and hydrothermal stabilities. As in the case of SBA-15, the total pore volume, pore size, and relative fraction of micro- and mesopores can be controlled by changes in the synthesis conditions (time, temperature, Si/surfactant ratio, pH, type of surfactant, additives, co-surfactants, etc.). Moreover, a wide variety of morphologies such as spheres, cubes, rods, and so on, can be formed by careful control of the synthesis method.

7.7.2
Mesoporous Metal Oxides

Metal oxides have found applications in catalysis, sensors, and electrode materials because of their excellent magnetic, electrical, dielectric, optical, Lewis acid–base, and redox behaviors. Synthesis of mesoporous metal oxides with high surface area, crystalline frameworks, and well-connected uniform pores is particularly important to achieve improved application performances. Similar to that for silica-based mesoporous materials, the synthesis of mesoporous metal oxides is mainly accomplished through the soft-templating approach. However, due to the intrinsic properties of their elements, the precursors of metal oxides, such as metal chlorides and alkoxides, display much faster hydrolysis–condensation kinetics compared to silica precursors, which makes it difficult to assemble the metal oxides and the amphiphilic templates into ordered mesostructures. Until now, many strategies have been developed to achieve a well-controlled assembly of template molecules and metal oxides without phase separation, including the use of complex molecules or acids as stabilizing agents, nonaqueous synthesis, assembly of presynthesized nanocrystals with template molecules, and so on.

Ordered mesoporous materials with different compositions from pure inorganic or pure organic frameworks to organic–inorganic hybrid frameworks have been widely reported in the past two decades. For example, mesoporous metal oxides and mixed oxides with semicrystalline frameworks, such as TiO_2,

ZnO, WO_3, SnO_2, Al_2O_3 are successfully prepared by a direct synthesis strategy using amphiphilic copolymer templates. A metal oxide prepared by "soft templating" usually exhibits poor crystallinity and lower structural stability upon being exposed to higher temperatures than those present during the synthesis. Also, the crystallinity and stability of porous metal oxides prepared by soft templating can be enhanced by filling of the pores with carbon and subsequent high-temperature treatment under oxygen-free conditions; the carbon serves as a "backbone" to prevent structural disintegration of the metal oxide and can later be removed. As an alternative to soft-templating route, "nanocasting" (hard-templating) method [15], facilitates the synthesis of a much larger variety of mesoporous metal oxides (Figure 7.10). This method comprises a solid, mesoporous structure matrix, most frequently silica, which is used as the porogen. The desired product is created inside the pores of the matrix that is selectively removed later. Hence, the product remains as a negative replica of the matrix. For the synthesis of mesoporous metal oxides by this structure replication procedure, a precursor compound, typically a metal salt, is filled into the pores of the silica matrix. The precursor compound is then converted into the metal oxide by thermal decomposition, sometimes preceded by a pH-induced conversion into an intermediate phase (such as a hydroxide species). The silica matrix is then removed by chemical etching with either hydrofluoric acid (HF) or with a strong base, for example, concentrated sodium hydroxide (NaOH) solution. Instead of silica, mesoporous carbon is sometimes used as the structure matrix, especially in those cases where the desired metal oxide is not stable against either HF or NaOH (as used for the etching of silica).

7.7.3 Mesoporous Carbon

Mesoporous carbon, another member from the family of porous materials, was first reported in 1999. Since then they have been widely studied due to their unique applications in water and air purification, shape-selective catalysts, gas

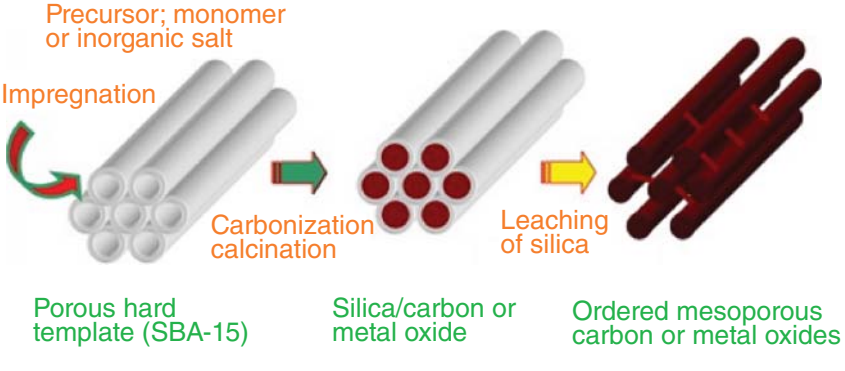

Figure 7.10 Schematic of process for synthesis of mesoporous metal oxide/carbon.

hosts, templates, and components of electrodes for electrochemical double-layer capacitors [16]. Their surface characteristics are similar to that of ordered porous materials as they exhibit a wide open and highly interconnected pore structure in addition to very large conductive surface areas. Since their discovery, mesoporous carbons have been used as potential matrix for the immobilization of biomolecules [17]. The widespread applications of porous carbons are attributed to their remarkable physicochemical properties, including the hydrophobicity of their surfaces, high corrosion resistance, good thermal stability, high surface area, large pore volume, good mechanical stability, easy handling, and low cost of manufacture. Thus, the designed synthesis of mesoporous carbon materials with controlled surface properties and structural ordering is important from a fundamental and application point of view.

Mesoporous carbon is usually prepared according to a template carbonization route. Both hard-templating (mesoporous silica templates, i.e., nanocasting method) and soft-templating (polymeric surfactants) approaches have been applied but the nanocasting approach is generally more used. The preparation of ordered mesoporous carbon by nanocasting involves the following successive steps, as shown in Figure 7.11:

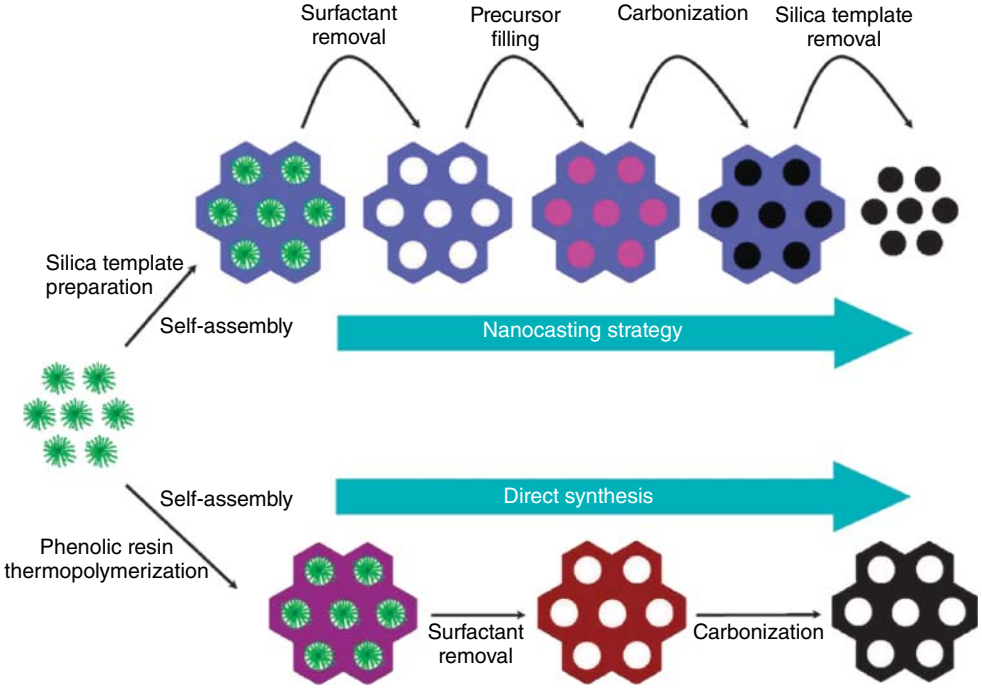

Figure 7.11 Two typical methods for the preparation of ordered mesoporous carbon materials: the nanocasting strategy from mesoporous silica hard templates and the direct synthesis from block copolymer soft templates [18].

1) The preparation of a mesoporous silica matrix with controlled architecture;
2) The introduction of a suitable carbon precursor into the mesopores (by either wet impregnation or chemical vapor deposition);
3) The polymerization of the resulting organic–inorganic composite and its carbonization at high temperature; and
4) The removal of the silica mold (by etching in HF or alkaline dissolution).

As the space once occupied by the host hard template is transferred into the pores of the carbon material, the resulting structure is a replica of the mesoporous silica one. Until now, mesoporous carbon, CMK-1 and CMK-3 (acronym for Carbon Mesoporous Korea) have been obtained from cubic MCM-48 and hexagonal SBA-15 respectively, or analogous solids, and are the main materials used in electrochemistry [19]. As a consequence of different thicknesses of the silica walls in the starting mesoporous silica molds (i.e., thinner in MCM-48 and thicker in SBA-15), the average pore sizes of the resulting replica CMK-1 and CMK-3 materials were also distinct but the pore size distribution remained narrow in both cases. Mesoporous silicas with tunable wall thickness (such as SBA-15) are particularly attractive templates, as they enable finetuning of the mesoporous carbon pore sizes. As expected, the carbon replica mesostructures were of similar geometry (i.e., cubic or hexagonal) to the starting mesoporous silica templates. Sucrose is most often used as the carbon precursor source to generate uniform mesoporous carbons. Both the precursor nature and concentration have proven to have a significant influence on the physico-chemical characteristics of the final materials. For instance, the CMK-3 because of its high specific surface areas ($900-1500\,m^2\,g^{-1}$), total pore volume ($1.1-1.7\,cm^3\,g^{-1}$), and pore sizes (3.3–5.0 nm) is used for electroanalytical purposes. Ordered mesoporous carbonaceous frameworks can also be prepared by soft templating, based on supramolecular aggregates as templates (mainly block copolymers). Both the aggregates of block copolymers and the assembling with thermosetting resins have the ability to organize the ordered mesostructures. This usually involves several steps: (i) formation of supramolecular arrangement of molecules, (ii) templating, (iii) cross-linking, (iv) removal of templates, and (v) carbonization. Compared to mesoporous carbons obtained by nanocasting, which can suffer from some limitations (only a few cases are partially graphitized, the pore size distribution is relatively wider than the mother silica template, and the use of mesoporous silica as a scaffold makes the process expensive, somewhat complicated, and time-consuming), the soft-templating route is likely to circumvent some of these limitations, notably via the generation of mesoporous carbons with improved electrical conductivity (graphitized mesoporous carbons).

7.7.4
Hybrid Organic–Inorganic Mesoporous Materials

An organic/inorganic hybrid material is one that consists of an inorganic support (silica) with organic functionalities either on the silicate surface, inside the silicate wall, or trapped within the channels. Organic functionalization of these solids

permits the tuning of surface properties (e.g., hydrophilicity, hydrophobicity, binding to guest molecules), alteration of the surface reactivity, protection of the surface from attack, and modification of the bulk properties of the materials, and at the same time stabilizing the materials toward hydrolysis. Typical advantages of organic functionalities are flexibility, low density, toughness, and formability whereas inorganic ceramics have excellent mechanical and optical properties such as surface hardness, modulus, strength, transparency, and high refractive index. Introduction of organic moieties within the silicate framework increases the flexibility of mesoporous films and fibers and reduces the brittleness of monoliths. Organic/inorganic hybrid materials are important because they can be designed at a molecular level to perform many processes including catalysis, adsorption, separation, drug delivery, and sensing. They are also used as supports of which one may construct more complex materials such as dendrons and organometallic catalysts. Due to their many different building blocks as well as the countless ways to combine the building blocks together, organic/inorganic hybrid materials are known to be the materials of the future.

7.7.4.1

Inorganic Support Material: Silica

The inorganic portion of the organic/inorganic hybrid material plays an important role in the overall properties of the material. The silica possesses the following key attributes as support materials.

- inert to chemical reactions with the solvent,
- robust over a wide range of reaction temperatures and pressures,
- easily functionalized without destruction of the material, and
- low in cost.

Amorphous silica materials are common supports that satisfy these requirements. The most important characteristic of silica materials is the ease with which one can tether organic functionalities onto the support material. The silica surface has highly reactive silanol (Si – OH) groups onto which organic functionalities may be reacted (Figure 7.12), allowing for the formation of organic/inorganic hybrid materials. The silica material can have a mixture of isolated silanols (1.1A), geminal silanols (1.1B), vicinal silanols (1.1C), and siloxane bridges (1.1D). All of these surface species can be modified to form organic/inorganic hybrid materials.

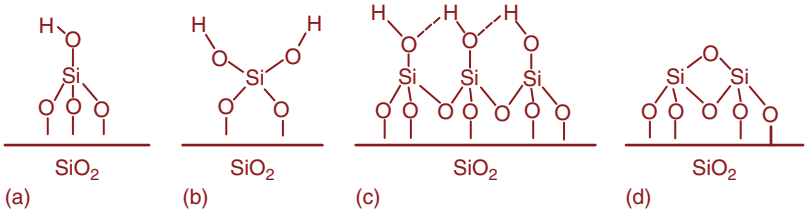

Figure 7.12 Types of silica surface Si–O species.

The synthesis of hybrid mesoporous silica materials with controlled functionality and hydrophobicity has opened up new avenues in organometallic chemistry, catalysis, and organic–inorganic host–guest chemistry. The major driving forces behind the intense activities in this area are the new and different properties of the nanocomposites, which the traditional macroscale composites and traditional materials do not have. For example, unlike the traditional composite materials that have macroscale domain sizes of millimeter and even micrometer scale, most of the organic/inorganic hybrid materials are nanometers, typically 1–100 nm, as the minimum size of the components or phases. Therefore, they are often still optically transparent materials although microphase separation may exist. Based on the structural distinction, there are two classes of organic–inorganic hybrid materials:

- Class I corresponds to hybrid systems in which weak interactions such as van der Waals forces and hydrogen bonds or electrostatic interactions are created between organic and inorganic phases.
- Class II corresponds to hybrid organic–inorganic compounds where both organic and inorganic components are bonded through strong covalent chemical bonds. Hybrid materials made in this way are termed *creamers* (ceramic polymers), *ormosils* (organically modified silicates), or *ormocers* (organically modified ceramics).

Through the combinations of different inorganic and organic components in conjunction with appropriate processing methods, various types of primary and secondary bonding have been developed leading to materials with unique combination of properties that cannot be achieved by other materials. Organic functionalization of silicates permits precise control over the surface properties, modification of the hydrophilic/hydrophobic of the surface, alteration of the surface reactivity, protection of the surface from attack, modification of the bulk properties of the materials and at the same time stabilizing the materials toward hydrolysis. For example, mesoporous silica having surfaced bonded thiol groups showed high adsorption for heavy metals such as Hg^{2+}, Ag^{+} ions from contaminated solutions. Sulfonic acid groups grafted mesoporous materials exhibited high catalytic activity for selective formation of bulky organic molecules. Porous silica gel particles bonded with alkyl, phenyl, amines, nitro, nitrile, diol, and sulfonates made a tremendous impact in separation science by high performance liquid chromatography.

The hybrid materials are generally synthesized via two methods. The first is the one-pot method that is currently the most common and direct synthesis route to the introduction of the organic groups into the silica network. It provides better control over the amount of organic groups incorporated into the matrix and ensures the uniform surface coverage with organic groups under mild conditions. It also provides better control over the amount of organic groups incorporated in the structure. However, products obtained by post-synthesis grafting are often structurally better defined and hydrolytically more stable. Although pore sizes can be controlled to some extent by both methods, it is more easily achieved by

grafting. The second is the post-synthesis method in which pore wall surface of the prefabricated inorganic mesoporous materials is modified with organosilane compounds after surfactant removal. The original structure of the mesoporous support is usually maintained after modification. The mesoporous surface can be altered with both passive (i.e., alkyl and phenyl) and reactive (i.e., amines, nitriles, etc.) surface groups. In order to minimize involvement of the external surface in reaction processes and to optimize selectivity, researchers have tried to modify the external surface first through passive groups, before functionalizing the internal silanol groups.

7.8
Chemical Modification of Mesoporous Materials: Functionalization

The polarity of the pore surfaces of an inorganic matrix can be modified by the addition of organic building blocks, which considerably extends the range of materials for applications in separation, absorption, sensing, catalysis, and drug delivery. The surface functionalization of mesoporous silica with organic functional groups such as alcohols, thiols, sulfonic, carboxylic acids, amines, and so on, is used to carry out biochemical reactions on a stable solid inorganic matrix (Figure 7.13). The pathways available for the surface modification of porous hybrid materials are based on organosilica units: (i) the modification of the pore surface of a purely inorganic silica material ("grafting") and (ii) the simultaneous condensation of corresponding silica and organosilica precursors ("co-condensation").

7.8.1
Grafting Method

Grafting refers to the subsequent modification of the inner surfaces of mesostructured silica phases with organic groups. This process is carried out primarily by the reaction of organosilanes of the type $(R'O)_3SiR$ with the free silanol groups of

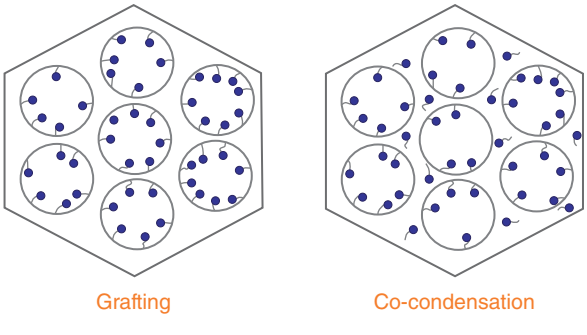

Figure 7.13 Schematic of co-condensation and grafting process.

the pore surfaces. In principle, functionalization with a variety of organic groups can be realized in this way by variation of the organic residue R. This method of modification has the advantage that under the synthetic conditions used, the mesoporous structure of the starting silica phase is usually retained, whereas the lining of the walls is accompanied by a reduction in the porosity of the hybrid material.

7.8.2 Co-condensation Method

An alternative method to synthesize organically functionalized mesoporous silica phases is the co-condensation method (one-pot synthesis). It is possible to prepare mesostructured silica phases by the co-condensation of tetraalkoxysilanes [$(RO)_4Si$ (TEOS or TMOS)] with terminal trialkoxy organosilanes of the type $(R'O)_3SiR$ in the presence of SDAs. This will lead to the materials with organic residues to be anchored covalently to the pore walls. By using SDAs known from the synthesis of pure mesoporous silica phases (e.g., MCM or SBA silica phases), organically modified silica can be prepared in such a way that the organic functionalities project into the pores. Since the organic functionalities are direct components of the silica matrix, pore blocking is not a problem in the co-condensation method. Furthermore, the organic units are generally more homogeneously distributed than in materials synthesized with the grafting process.

7.9 Mesoporous Silica/Polymer Nanocomposites

Mesoporous silica has a large surface area and a lot of constrained space in the form of nanochannels. Polymers grown within the constrained space of periodic mesoporous silica may exhibit unusual mechanical, electronic, magnetic, and optical properties. The spatial control of the growth process is limited by the channel network of the silica host, which allows the fabrication of materials with designed shapes, particularly nanofibers, wires, and porous particles. These nanochannels of the mesoporous silica are also used as nanoreactors for polymerization. Polystyrene, polyethylene, polyaniline (PANI), polyacrylonitrile, polymethyl methacrylate (PMMA), and polyesters have been polymerized in mesoporous nanochannels to form mesoporous silica/polymer nanocomposites. For example, MCM-41 was used as a container for polymerization of ethylene, aniline, acrylonitrile, methyl methacrylate, and phenol-formaldehyde. The monomers were first adsorbed from the gas phase into the inorganic host and then polymerized inside the channeled networks using initiators such as benzoyl peroxide or anhydrous HCl vapor. The resulting polymer fibers did not exhibit the same properties as bulk polymers, for example, polystyrene fibers constrained inside the channels of MCM-41 silica did not exhibit a glass transition temperature.

Mesoporous silica/polymer nanocomposites can be categorized as four different groups, which are shown in Figure 7.14. The first category is surface modification, where organic components such as $R–Si(OR')_3$ can be used to functionalize the mesoporous silica surface. The second category is framework modification, which produces nanocomposites called periodic mesoporous organosilica (PMO), where the organic functional group is in the silica species having the form of $(OR')_3Si–R–Si(OR')_3$ which is hydrolyzed and polymerized in water and, thus, organic functional groups are also in the frame of mesoporous structure. Different PMO can be synthesized by just changing the structure of R. The third category is polymer composite in pore void, where catalysts or initiators that are grafted onto the inner walls of the mesoporous silica nano-pores can initiate the polymerization and form polymers in the void. The last category is framework polymer composites which are formed during the formation of mesoporous silica through sol-gel method. In these composites, the constituent polymer crosses the framework of the mesoporous silica as shown in Figure 7.14(d).

Mesoporous silica/polymers nanocomposites are synthesized with extrusion polymerization and are found with special properties [20]. The reason is that the nanoreactor gives space constraints on polymer chains when they grow inside the nanochannels. For example, polyethylene made with this method had ultrahigh molecular weight, high melting temperature, and only extended chain crystals rather than folded chain crystals because of the space constraint that controlled the formation of crystals. For mesoporous silica/organic nanocomposites, organic features introduce flexibility into the framework, and the inorganic silica provides structural, mechanical, and thermal stability.

Currently, there are two methods to initiate extrusion polymerization inside nano channels of mesoporous materials. The first method is to evaporate the mixture of initiator and monomer inside the nanochannels, and polymerization is initiated under certain conditions. The second method is to graft catalysts inside the nanochannels and then polymerization is initiated. However, not all polymers can be initiated from the nanochannels with the two methods because it is impossible to graft some kind of catalysts onto the surface of mesoporous silica. To overcome the limitations of these two polymerization methods, a third method was proposed wherein the initiator was grafted onto the surface of the

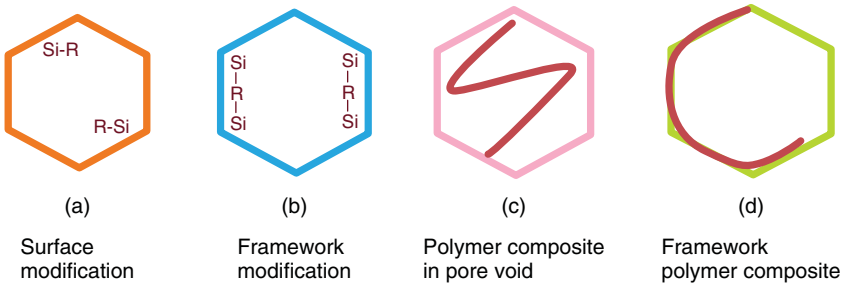

Figure 7.14 Conceptual schemes of nanocomposite materials of mesoporous silica with organic components.

walls of nanochannels. Unlike the two currently reported methods by which polymers are initiated and propagated inside the nanochannels without producing covalent bonds with the surface of mesoporous silica, the third method can connect the silica surface and synthesized polymer using covalent bonds because polymers are initiated and propagated from the initiator which is covalent bonded with silica surface through grafting steps. Thus this method introduces one more route to produce mesoporous silica/polymer nanocomposites. Mesoporous silica/polymer nanocomposites can also be made through entrapping polymers in the nanochannels of mesoporous silica through the hydrogen bonding between the silanol groups on the silica surface and the groups in the polymer chain. So, groups which can form a hydrogen bond with silanol groups are very necessary for a certain polymer if high loading of polymers needs to be trapped. The hydrogen-donating property of silanol moieties is so strong that organic polymers having hydrogen-accepting groups, such as amide moieties, form hydrogen bonds with silanol groups. Transparent and homogeneous polymer hybrids could be obtained from amide-containing polymers such as poly(2-methyl-2-oxazoline), poly(*N*-vinylpyrrolidone), and poly(*N*,*N* dimethyl-acrylamide).

On the other hand, most composites materials consist of a thermoplastic matrix and particulate fillers with a method of mechanically blending components of the composites above the melting temperature of the polymer. However, the physical blending can not produce a homogeneous mixture of polymer matrix and the filler, and the organic and inorganic phases are easily phase separated; the direct connection of the polymer with the surface of the filler is also a potential method to overcome the disadvantages of the current methods. An azo-initiator is needed to be grafted onto the surface of mesoporous silica through several surface grafting steps so that it can initiate free radical polymerization of most monomers with vinyl groups. With this azo-initiator-immobilized mesoporous silica, different monomers with vinyl get initiated and propagated through free radical polymerization under specific conditions. Some vinyl monomers with strong polar functional groups and cyclic monomers can not be initiated through free radical polymerization and therefore, anionic polymerization should be used. The catalysts of anionic polymerization are alkali metals and strong anions, most of which can not be grafted onto the silica surface. Initiator grafting onto the silica surface also provides a very good method to initiate anionic polymerization inside the nanochannels of mesoporous silica. Nylon is a very common engineering plastic with special properties, such as high toughness, high tensile strength, high elasticity, high resistant to abrasion and chemicals, and so on, and can be polymerized through anionic ring-opening polymerization of epsilon–caprolactam with alkali metal as catalysts [21]. Nylon/silica nanocomposites have been synthesized by the physical blending method and their excellent mechanical properties have been identified. To initiate the anionic ring-opening polymerization inside the nanochannels, a new synthesis route with initiator surface grafting steps has been designed to achieve mesoporous silica/nylon 6 nanocomposites. Through grafting initiator of *N*-acyllactam onto the surface of mesoporous silica, epsilon caprolactam is expected to be initiated inside the nanochannels. This initiator surface

grafting method also provides a third choice to initiate a kind of polymerization where no catalysts can be grafted onto a silica surface.

At present, the common method to graft functional groups onto a silica surface is through postsynthesis procedures which can not distribute the functional groups onto a silica surface very well. If polymer with certain functional groups can be introduced into the mesoporous silica framework in a well-distributed manner, this kind of mesoporous silica/polymer nanocomposites will have great potential in the fields of catalysts, fuel cell, drug delivery, and so on. With the sol–gel method, polyethylene, polyacrylate, and Nafion resin are successfully interpenetrated into the mesoporous silica framework.

7.10
Mesoporous Carbon/Polymer Nanocomposites

Ordered mesoporous carbon (OMC) materials (CMK-3) exhibit higher surface area, larger pore volume, and higher mechanical stability and electric conductivity than pure mesoporous silica. Therefore, mesoporous carbon have been used as attractive hosts for conducting polymers, PANI, to generate novel composite systems with special properties like improved electro-rheological effects and interaction of the p-conjugated networks. PANI has attracted a great deal of interest in recent years due to its low cost, ease of preparation, excellent environmental stability, and high electrical conductivity. Therefore, encapsulation of PANI into OMCs gives rise to unique properties of the final composite system. Figure 7.15 shows the synthesis route for CMK-3 and PANI nanocomposite. Firstly, CMK-3 was synthesized by the nanocasting method from SBA-15 using HF for silica template removal. Then the CMK-3 was suspended in aniline monomer for a day under ambient conditions. This solution was further allowed to polymerize and thus mesoporous CMK-3 and PANI nanocomposites were obtained.

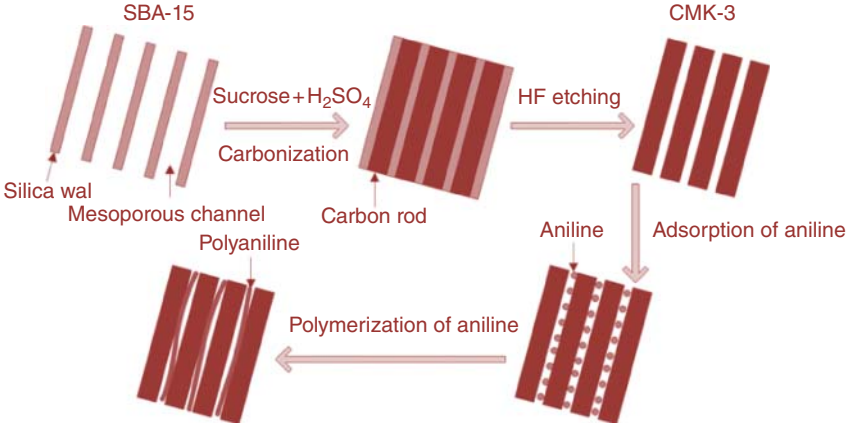

Figure 7.15 Schematic representation for the synthesis of PANI–CMK-3 nanocomposite.

7.11
Mesoporous Silica/Metal (Oxides) Nanocomposites

Mesoporous silica has been extensively modified with metal/metal oxides for their efficient use in sensing, catalysis, drug delivery, and as adsorbents for heavy ions. There are generally two methods followed to obtain the nanocomposites: direct synthesis, wherein the dopants (metal/metal oxides) are introduced simultaneously into the reaction mixture and wet impregnation (post synthesis) in which the silica is soaked into the salt solution of aqueous dopant solution. Recently, our group has synthesized the nanocomposites of WO3 [22] and SnO_2 [23] with SBA-15 by using the direct synthesis method. The obtained nanocomposites have shown promising behavior in humidity-sensing applications.

7.12
Applications

7.12.1
Drug Delivery

A drug delivery system is one which is capable of releasing a carried bioactive agent in a specific location at a specific rate. The main aim of this type of system is to facilitate the dosage and duration of the drug effect, causing minimal harm to the patient and improving human health, since they aid in reducing dosage frequency. Mesoporous materials are promising candidates because of the following features:

- effective drug targeting specificity,
- lowering systemic drug toxicity,
- improving treatment absorption rates, and
- providing protection for pharmaceuticals against biochemical degradation.

Mesoporous materials thus provide improved delivery systems for biomolecules, which have local and sustained release over time, while simultaneously protecting the biopharmaceutical agent from degradation. These delivery systems maintain the concentration of drugs in the precise sites of the body within optimum range and under the toxicity threshold, improve the therapeutic efficacy, and reduce toxicity [24]. Mesoporous silica materials like SBA-15 are very promising materials and offers several advantages as drug delivery systems as they have inert behavior in human beings or living creatures, are biocompatible, and are degradable in an aqueous solution, and thus problems related to the removal of the material after use can be avoided. The reasons for such a high impact of these materials in the field of biotechnological research are based on their following properties:

1) their high pore volume, which allows the confinement of a large amount of drug or biologically active species;

2) their large surface area, which means high potential for drug adsorption;
3) their well-ordered pore distribution, which favors the homogeneity and reproducibility on the drug adsorption and release stages; and
4) their high density of silanol groups at the surface, which brings the possibility of undergoing, through an easy chemical modification of the pore walls, modification of the surface chemistry to allow a better control over drug loading and release.

7.12.2 Adsorption

The most important requirement for a good adsorbent is a large interface. Adsorption is a fundamental process involving the enrichment of guest species at the interface of a certain adsorbent. Mesoporous materials, especially those composed of silica and carbon frameworks, have attracted global interest because of their high specific surface areas, regular and tunable pore sizes, large pore volumes, as well as stable and interconnected frameworks with active pore surface for easy modification or functionalization, thereby meeting the requirements as promising adsorbents for trapping heavy metal ions. In order to specifically bind different heavy metal ions, the basic principle lies on the different behaviors of complex chemistry; for example, soft metal ions (e.g., Hg^{2+}) are more likely to form stable complexes with ligands carrying soft electron donor atoms (e.g., thiol), and vice versa. Ordered mesostructures favor fast mass transport than disordered structures, and functional groups obtained by post graft are more easily accessible than those by co-condensation. Similarly, analogous materials grafted with terminal amino-based (amine, urea, polyamidoamine, etc.) or carboxylic groups have shown efficient binding properties to many hard heavy metal ions (such as Cu^{2+}, Zn^{2+}, Cr^{3+}, Fe^{3+}, Cd^{2+}, and Ni^{2+}). The main adsorption process of heavy metal ions is found to relate to surface complexation.

7.12.3 Catalysis

Mesoporous materials are promising candidates for catalysis because of their relatively large pores that facilitate mass transfer and the very high surface area that allows a high concentration of active sites per mass of material. Mesoporous silicas are not often used as catalysts as such due to their high intrinsic band gap, so they are generally modified with additional catalytic functions by incorporation of active sites in the silica walls or by deposition of active species on the inner surface of the material. The deposition of catalytically active nanoparticles on support materials with high dispersion is an important and effective strategy for the design of catalysts. Metal ion incorporated in the framework acts as acid or redox active site and is used for different classes of catalytic reactions. These active sites can be constructed by both direct loading or via post-synthesis procedures by a multitude of pathways, which means that the properties of these active sites

are variable and controllable, depending on the synthetic procedure. Compared to other support materials, the ordered mesoporous solids have the advantage of stabilizing metal or metal oxide particles, since they cannot grow to sizes larger than the pore size unless they move to the external surface of the particles. Compared to the microporous solids with their narrow and well-defined pores, they allow the access of bulky reagents. The number of combinations of different modifications of ordered mesoporous materials with noble metal nanoparticles or metal oxides is high, since many properties can be changed independently of each other.

7.12.4 Sensors

Sensors can be thought of as extensions of human senses. Sensors usually generate electrical signals that can easily be processed and transmitted by manufactured devices or systems of devices. With the ever-growing need for sensors in science and medicine, the demand for sensors in environmental monitoring [25] and food safety [26] is also increasing rapidly. The performance of sensors is significantly influenced by the morphology and structure of sensing materials, resulting in a great obstacle for gas sensors based on bulk materials or dense films to achieve highly sensitive properties. The sensors are expected to work at low parts per billion. Therefore, it is highly desirable that sensors have a large surface area, so as to adsorb as much of the target analyte as possible on the surface, giving a stronger and more measurable response (especially at low concentration. Gas sensors based on mesoporous materials are promising candidates due to their enhanced gas sensing properties like sensitivity, selectivity, and response speed. Mesoporous materials due to their large surface area, possesses uniform channels that ensure the presence of abundant diffusion sites for gas molecules to desorb on the material's surface and also provide easy and free movement of gaseous molecules across the material. The gas sensors are usually based on the interaction of the gas molecules with the surface of a solid material. Therefore, with the development of new functional materials with well-defined surface properties, efficient gas sensors can be developed. Nowadays, mesoporous Silica/metal oxides (SBA-15, ZnO, SnO_2, WO_3, etc.) have been widely used in portable gas detection systems because of their advantages such as low cost, easy production, compact size, simple measuring electronics, and laboratory-scale synthesis methods.

7.13 Conclusion and Outlook

Tremendous progress has been made in the past two decades for novel synthesis strategies using block copolymers, which has led to the discovery of a large number of porous materials (pore size 10–50 nm) with controlled architectures and pore sizes in the mesoporous range, and has also opened avenues to many new materials of relevance to large molecule catalysis, separation, sensors, drug

delivery, and environmental remediation. The narrow and uniform pore size of mesoporous materials with extremely high surface area has held much promise for the development of novel solid materials The future design of tailored hierarchical architectures, and control over the connectivity between different pore dimensions, requires the continued development of new templates and motifs for self-assembly. Incorporation of elements in inorganic walls, impregnation of active components, and immobilization of active species with a predetermined structure can create well-isolated sites with uniform properties. The synthetic procedure can be easily tuned by variation of pH during the synthesis process and a series of mesoporous nanocomposites with increased levels of mesoporosity can be generated.

Synthesis of novel surfactants that exhibit predictable mesophase play a valuable role in achieving different mesoporous structures. The CMC of block copolymer surfactant is a powerful criterion for the experimental design of synthesis of ordered mesoporous materials. While applications of these mesoporous materials are currently being extensively explored, their full potential has not yet been achieved. The large accessible pore size, high surface areas, and easy functionalization of the silica wall provide many opportunities to use these highly ordered channels and pore size as nanoreaction vessels for chemical/biological reactions. Functionalization of the surface of these mesoporous materials with organic or inorganic functional groups leads to new physical and chemical properties. Organic moieties and molecules are usually introduced into the inorganic framework of mesostructures, or bonded onto the pore surfaces via one-pot synthesis such as co-condensation, or by post grafting, inner pore surface modifications, and direct solution or vapor impregnations. Introduction of organic groups in the mesoporous materials permits the tuning of surface properties, alteration of the surface reactivity, protection of the surface from chemical attack, hydrophobization of the surface by silylation to preclude water attack, and modification of the bulk properties of the materials, while at the same time stabilizing the materials toward hydrolysis. The diversity of organic species in mesoporous materials could lead to many different and special properties, such as light emission, catalytic and photo-catalytic activities, and photo- and chemo-environmental sensitivities. Nanocasting using hard templates is another useful method in fabrication of mesoporous materials other than those of silica. The principal issues in the nanocasting synthesis include template composition and mesostructure, pore surface chemistry, precursor selection, processing, and template removal. However, template composition/removal and precursor/processing are of little importance for most cases of the nanocast carbon or metal oxides.

Despite great progress on the synthesis of the ordered mesoporous nonoxide materials, until now, a simple, facile, and easily repeatable synthesis method from all commercial available chemicals, like that for mesoporous silicas, has not been achieved. A new and general approach is still required to extend compositions, improve crystallinity and purity, control morphology, and achieve low-cost and large-scale preparation. Hence, the rational design of optimized mesoporous nanocomposites framework requires significant improvements in kinetic models

for the relevant chemistry. Such optimization requires collaboration between chemists, materials scientists, chemical engineers, and experts in molecular simulation in order to take full advantage of new material syntheses to fine-tune the morphology, texture, connectivity, and surface area of hierarchical porous nanocomposite materials. The future of these mesoporous materials and their nanocomposites in commercial applications rests on the high degree of control over composition, pore properties, processability, hierarchical structure, and function that they provide relative to the well known and studied amorphous silica phases and crystalline zeolites. We believe that the ordered mesoporous composite materials provide a promising research field and there lies ample opportunities for design of new multifunctional materials and hence much more efforts should be put on them in the future.

References

1. Kresge, C.T., Leonowicz, M.E., Roth, W.J., Vartuli, J.C., and Beck, J. (1992) *Nature*, **359**, 710–712.
2. Sing, K.S.W., Everett, D.H., Haul, R.A.W., Moscou, L., Pierotti, R.A., Rouquerol, J., and Siemieniewska, T. (1985) *Pure Appl. Chem.*, **57**, 603–619.
3. Adhyapak, P.V., Meshram, S.P., Tomer, V.K., Amalnerkar, D., and Mulla, I.S. (2013) *Ceramics International*, **39**, 7367.
4. Feng, P., Bu, X., and Pine, D.J. (2000) *Langmuir*, **16**, 5304–5310.
5. Holmberg, K., Jönsson, B., Kronberg, B., and Lindman, B. (2003) *Surfactants and Polymers in Aqueous Solution*, 2nd edn, John Wiley & Sons, Ltd, Chichester.
6. Evans, D.F. and Wennerstrom, H. (1999) *The Colloidal Domain: Where Physics, Chemistry, Biology and Technology Meet*, 2nd edn, Wiley-VCH Verlag GmbH, New York.
7. Attard, G.S., Bartlett, P.N., Coleman, N.R.B., Elliott, J.M., Owen, J.R., and Wang, J.H. (1997) *Science*, **278**, 838.
8. Israelachvili, J.N. (1992) *Intermolecular and Surface Forces*, 2nd edn, Academic Press.
9. Brinker, C.J., Lu, Y.F., Sellinger, A., and Fan, H.Y. (1999) *Adv. Mater.*, **11**, 579.
10. Huo, Q., Margolese, D., Ciesla, U., Feng, P., Gier, T.E., Sieger, P., Leon, R., Petroff, P., Schuth, F., and Stucky, G.D. (1994) *Nature*, **368**, 317.
11. Albero, J.S., Ruiz, J.C.S., Escribano, A.S., and Reinoso, F.R. (2008) *Appl. Catal. A: Gen.*, **135**, 16.
12. Collart, O., Van Der Voort, P., Vansant, E.F., Desplantier, D., Galarneau, A., Di Renzo, F., and Fajula, F. (2001) *J. Phys. Chem. B*, **105**, 12771.
13. Zhao, D., Feng, J., Huo, Q., Melosh, N., Frederickson, G.H., Chmelka, B.F., and Stucky, G.D. (1998) *Science*, **279**, 548.
14. Khodakov, Y., Zholobenko, V.L., Bechara, R., and Durant, D. (2005) *Microporous Mesoporous Mater.*, **79**, 29.
15. Tomer, V.K., and Duhan, S. (2016) *Sensors and Actuators B: Chemical*, **223**, 750.
16. Korenblit, Y., Rose, M., Kockrick, E., Borchardt, L., Kvit, A., Kaskel, S., and Yushin, G. (2010) *ACS Nano*, **4**, 1337.
17. Tiwari, A. and Dhakate, S.R. (2009) *Int. J. Biol. Macromol.*, **44**, 408–412.
18. Ma, T.Y., Liu, L., and Yuan, Z.Y. (2013) *Chem. Soc. Rev.*, **42**, 3977.
19. Wang, P.Y., Zhao, L., Wu, R., Zhong, H., Zou, H.F., Yang, J., and Yang, Q.H. (2009) *J. Phys. Chem. C*, **113**, 1359.
20. Lüftl, S., Visakh, P.M., and Chandran, S. (2014) *Polyoxymethylene Handbook: Structure, Properties, Applications and their Nanocomposites*, John Wiley & Sons, Inc., ISBN: 9781118385111.
21. Thomas, S. and Visakh, P.M. (2011) *Handbook of Engineering and Specialty*

Thermoplastics: Nylons: 4 (Wiley-Scrivener), vol. 4, John Wiley & Sons, Inc., ISBN: 978-0470639252.

22. Tomer, V.K., and Duhan, S. (2015) *App. Phy. Lett.*, **106** (6), 063105.
23. Tomer, V.K., Malik, R., Jangra, S., Nehra, S.P., and Duhan, S. (2014) *Mater. Lett.*, **132**, 228–230.
24. Tiwari, A. and Tiwari, A. (2013) *Nanomaterials in Drug Delivery, Imaging and Tissue Engineering*, John Wiley & Sons, Inc., ISBN: 9781118290323.
25. Duhan, S. and Tomer, V.K. (2014) *Advanced Sensor and Detection Materials*, Wiley-Scrivener Publishing, ISBN: 9781118773482.
26. Visakh, P.M., Iturriaga, L.B., and Ribotta, P.D. (2014) *Advances in Food Science and Nutrition*, Wiley-Scrivener Publishing, ISBN: 9781118137093.

8
Bio-based Nanomaterials and Their Bionanocomposites

Dipali R. Bagal-Kestwal, Rakesh M. Kestwal, and Been H. Chiang

8.1
Introduction for Bio-based Nanomaterials

Natural materials develop functionality, flexibility, and high mechanical strength/weight performance by exploiting hierarchical structure design that spans nanoscale to macroscopic dimensions [1] (Figure 8.1). Bio-based nanocomposites are composite materials that are made up of particles in the range of 1–100 nm in size from renewable natural sources. These bio-based nanomaterials such as building blocks, particles, fiber, and resin, are combined to engineer new materials with enhanced properties. These new immerging "nano–bio" materials comprise exotic, dynamic, and fascinating features that make them smart futuristic biodegradable material. These bio-based nanomaterials and their composites also attract attention due to their environmentally friendly renewable properties, reduced carbon footprint, and tremendous resources on this biosphere. These smart, high-value materials also offer new challenges/problems due to their high strength. The main reason for increased use of biopolymers is due to the fear of depleting fossil resources and limited sustainable solution for a green world. Scientists are looking for these bio-based nanomaterials in the hope of replacing petrochemical-based polymers. These bionanomaterials and their composites are being explored for a variety of biomedical applications such as for drug delivery, bioimaging, tissue engineering, and biosensors. Nanomaterials have attracted the attention of many researchers and scientists to create many new novel materials, and the research is continuing at a rapid pace. The biological materials developed are superior to micron-scale materials due to differences in their physical phenomena. Bio-based materials will help to develop the new bioeconomy, while also helping rural development. Nanomaterials from agriculture residue and forestry have attracted attention due to the abundance of the bio-based materials.

Cellulose is the most abundant polymer in nature, after which comes hemicellulose followed by lignin. This makes scientists to discover new possibilities for biological materials in the rapidly expanding field of nanotechnology. Lignin has many different applications, including being used as a composite material. Hemicellulose has already been used in food applications but there are possibilities for

Nanomaterials and Nanocomposites: Zero- to Three-Dimensional Materials and Their Composites,
First Edition. Edited by Visakh P.M. and Maria José Martínez Morlanes.

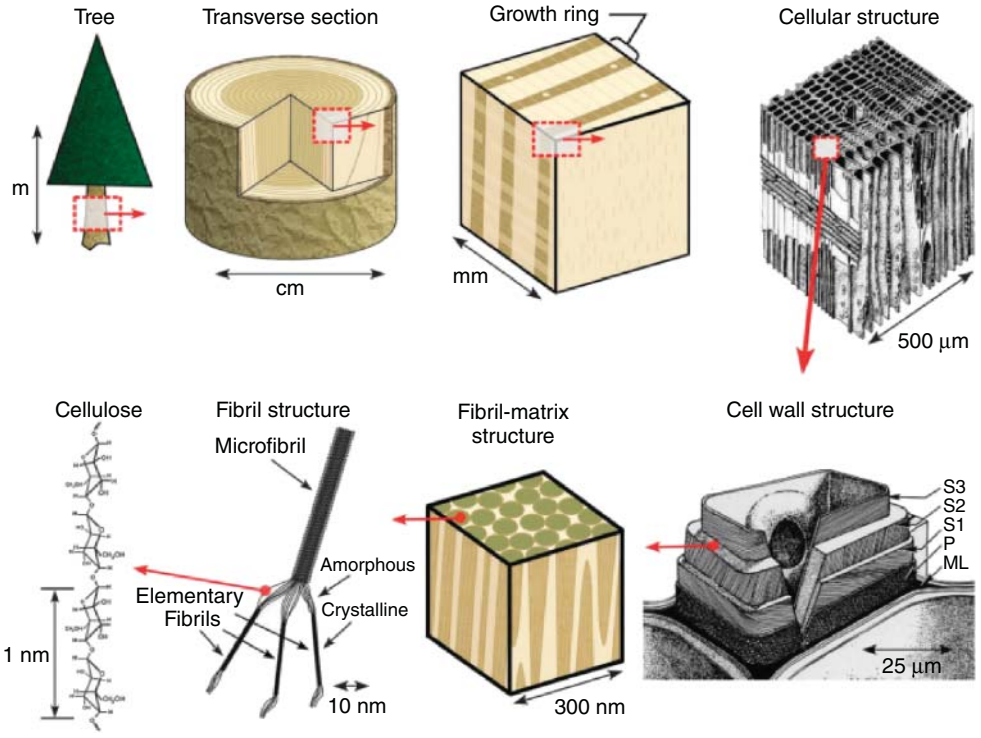

Figure 8.1 Schematic of the tree hierarchical structure [1]. (Reproduced with permission.)

new polymer production as well. Likewise, many researchers have also prepared nanoparticles (NPs)using other natural compounds such as chitosan, dextran, gelatin, alginate (ALG), albumin, and starch [2–7]. NPs have been reported using the process of reversible swelling of macromolecules [7, 8] using gelatin [8], human serum albumin [8], bovine serum albumin [9], and casein [8]. In this chapter, we intend to explore the research and development in bio-based nanomaterials and their potential applications.

8.2 Cellulose

Cellulose is the most common organic compound and biopolymer on earth. About 33% of all plant matter is cellulose. Cellulose occupies a unique place in the annals of polymers. Cellulose is the most ubiquitous and abundant polymer on the planet, given its widespread industrial use in the present age, but also in the past for ropes, sails, paper, timber for housing, and many other applications [10]. As early as 1838, Payen recognized cellulose as a definitive substance, which still could be broken

down into its basic units of glucose and coined the name "Cellulose" [11]. Payen named this new substance "cellulose" because he had obtained it from the cell walls of plants [11].

The cellulose content of cotton is 90%, while that of wood is 50% [12]. Cellulose, a linear polysaccharide composed of β-1-4-linked D-glucopyranose repeating units, exhibits a number of desirable properties and has become one of the most promising renewable polymeric materials. Besides the application of unmodified cellulose products, cellulose can be converted into regenerated cellulosic materials, which have been widely applied in many fields [13, 14]. In spite of its poor solubility characteristics, cellulose is used in a wide range of applications including composites, netting, upholstery, coatings, packing, and is important in the manufacture of numerous products, such as paper, textiles, pharmaceuticals, explosives, and so on.

Over the past several decades there has been extensive research in cellulose, cellulose-based particles, and cellulose-based composites [1]. There have been several review articles and books describing the various aspects of cellulose: cellulose structure, its processing into nanosize, bacterial cellulose, regenerated cellulose, chemical modification of cellulose surfaces, rheological behavior of cellulose suspensions, and so on. This current section is built on the adequate information of cellulose from previous reviews that have been summarized and referenced out [1].

8.2.1
Structure and Properties of Cellulose

Cellulose can be extracted from a broad range of plants and animals, and there is a wide range of cellulose particle types that are being studied for myriad commercial applications. Cellulose can be obtained from fibers of plant tissues. Generally, the natural fibers are composed of glucose chains, hemicellulose, and lignin. Cellulose is a polysaccharide formed by large glucose chains and it is non-watersoluble due to its β 1 → 4 glycosidic linkage and interactions of hydrogen bonds between the glucose chains. The linear chain of ringed glucose molecules has a flat ribbon-like conformation (2–20 nm diameter and 100–40 000 nm long). The repeat unit (Figure 8.2) comprises two anhydroglucose rings ($[C_6H_{10}O_5]_n$; $n = 10\,000–15\,000$, where n is depended on the cellulose source material) linked together through an

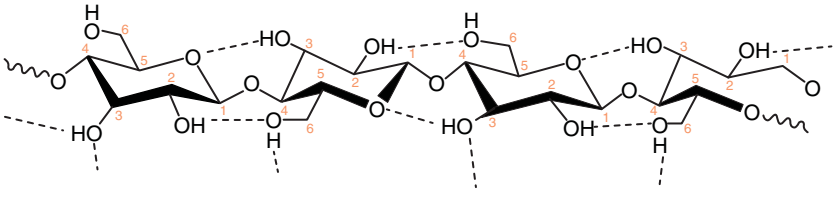

Figure 8.2 Schematics of cellulose chain structure with repeat units.

oxygen covalently bonded to C1 of one glucose ring and C4 of the adjoining ring (1 → 4 linkage) and is called the β 1 → 4 glucosidic bond. The intrachain hydrogen bonding between hydroxyl groups and oxygens of the adjoining ring molecules stabilizes the linkage and results in the linear configuration of the cellulose chain. During cellulose formation, van der Waals and intermolecular hydrogen bonds between hydroxyl groups and oxygens of adjacent molecules promote aggregation of multiple cellulose chains forming fibrils [15]. The intra- and inter-chain hydrogen-bonding network makes cellulose a relative stable polymer, and gives the cellulose fibrils high axial stiffness. Within these cellulose fibrils, the cellulose chains are arranged in a highly ordered crystalline structure and regions that are low order or amorphous regions [16].

Cellulose structure presents crystalline and amorphous regions, which allow the formation of micelles. The polymorphy of cellulose and its derivatives has been well documented by many researchers [1, 12, 16–18]. Cellulose that is produced by plants is typically called cellulose-I. This cellulose I crystal form, or native cellulose, also comprises two allomorphs, namely cellulose Iα and Iβ which is the crystal structure with the highest axial elastic modulus. Triclinic Iα allomorph is predominant in algal-bacterial celluloses whereas the cotton-ramie types of celluloses are highly rich in the monoclinic Iβ form. Cellulose II, which generally occurs in marine algae, is a crystalline form that is formed when cellulose I is treated with aqueous sodium hydroxide. A liquid ammonia treatment and subsequent thermal treatments of cellulose I and cellulose II give crystalline cellulose III and cellulose IV forms [19]. Several excellent reviews and papers concerning the nature of cellulose structure and biosynthesis have appeared and some of the unifying features are recounted [20–22].

8.2.1.1 Biological Function of Cellulose

Cellulose is the structural component of the primary cell wall of green plants. It is the basic building blocks of the cell wall of plants. In plants, microfibers form through parallely aligned chains of cellulose bound by hydrogen bridges formed by the hydroxyl groups of glucose. Around 80 aligned chains form a microfiber. These microfibers form superimposed storeys of cellulose, with other fibers running transversely in multiple layers. The main function of cellulose in plants is to keep the stems, stalks, and trunks of a plant rigid. It provides mechanical rigidity to plants to maintain these structures. The fibers are further cross-linked by hemicellulose and are suspended in the gel-like pectin. The primary cell wall directly protects the cell's plasma membrane. Outside the primary cell wall there is just a thin layer of pectin, wax, and cutin to provide some padding, called the middle lamella. In some plants a secondary cell wall, mostly made up of cellulose forms during the adult stages as an extra protection. In addition, a very thin cellulose tertiary layer is sometimes formed.

Most animals including humans can not digest cellulose because it is very hard to break down. Animals that eat only plants (herbivores) have special sacs or specialized guts with fermentation chambers in their digestive system to help break

down cellulose. Symbiosis with microorganisms, such as bacteria, protozoans, and fungi results in fermentation of cellulose in these chambers where the indigestible cellulose is converted into digestible nutrients via the process of fermentation. Cellulose is not digestible by humans and is often referred to as "dietary fiber" or "roughage," which acts as a hydrophilic bulking agent, reducing the likelihood of colon cancer. Cellulose has many uses as an anticake agent, emulsifier, stabilizer, dispersing agent, thickener, and gelling agent but these are generally subsidiary to its most important use of holding on to water.

8.2.1.2 Industrial Application of Cellulose

Being the most abundant organic compound derived from biomass, cellulose's worldwide production is estimated to be between 10^{10} and 10^{11} tons each year [23]. Of this, only about 6×10^9 tons is processed by industries such as paper, textile, material, and chemicals. For human industrial use, cellulose is mainly obtained from wood pulp and cotton. It is primarily used to produce cardboard and paper; and to a smaller extent it is converted into a wide variety of derivative products such as cellophane and rayon. Semisynthetic derivatives of cellulose with different physicochemical and mechanical properties are extensively used in pharmaceutical and cosmetic industries. The production of new cellulose derivatives and finding new applications for the existing compounds by pharmaceutical researchers are of great interest.

8.2.2 Origin of Cellulose

Cellulose from wood (over 50%) and cotton (over 94%) as primary sources is renewable, biodegradable, as well as nontoxic [24]. Wood and plants are cellular hierarchical biocomposites produced by nature, and are essentially semicrystalline cellulose microfibril-reinforced amorphous matrices made of hemicellulose, lignin, waxes, extractive, and trace elements [25]. In the oceans, most of the cellulose is produced by unicellular plankton or algae using the same type of carbon dioxide fixation found in photosynthesis of land plants. In fact, it is believed that these organisms, the first in the vast food chain, represent nature's largest resource for cellulose production [20]. Without photosynthetic microbes, all animal life in the oceans would cease to exist. Several animals, fungi, and bacteria can assemble cellulose. Tunicates are the only animals known to produce cellulose microfibrils. Tunicates are a family of sea animals that have a mantle consisting of cellulose microfibrils embedded in a protein matrix [1]. Most research has used a class of tunicates that are commonly known as "sea squirts" (*Ascidiacea*). There are over 2300 species of Ascidiacea and some of the most frequently studied species have been *Halocynthia roretzi* [26], *Halocynthia papillosa* [27, 28], and *Metandroxarpa uedai* [29].

Among bacteria, one of the most advanced types of cellulose producing bacteria is the common vinegar bacterium, *Acetobacter*. However, these organisms are

devoid of photosynthetic capacity and usually require glucose or some organic substrate synthesized by a photosynthetic organism to assemble their cellulose. Very few genera of bacteria can synthesize cellulose, but the gram-negative bacterium *Gluconacetobacter xylinus* (Formerly known as *Acetobacter xylinum*) and *Agrobacterium tumefaciens* secretes large quantities of cellulose as microfibrils [30–32]. *Dictyostelium discoideum*, a soil-living amoeba, also synthesizes cellulose at various stages of life cycles [33]. The reason why the bacteria generate cellulose is unclear, but it has been suggested that it may be necessary for their survival, such as to guard against ultraviolet (UV) light, or to act as a barrier to fungi, yeasts, and other organisms [1].

Several species of algae (green, gray, red, yellow-green, etc.) produce cellulose microfibrils within the cell wall. In both red and brown algae the cellulose content is rather low [34]. Most green algae (*Micrasterias denticulate* [35, 36], *Micrasterias rotate* [35], *Valonia ventricosa* [37], *Caldophora* [37], *Boergesenia* [37]) have a cellulosic wall, with cellulose content ranging up to 70% of the dry weight [38]. There are considerable differences in the cellulose microfibril structure between the various algae species, which are caused by differences in the biosynthesis process.

8.2.3 Cellulose Nanomaterials

In plants, about 36 individual cellulose molecules are brought together into larger units known as elementary fibrils or microfibrils, which are further packed into larger units called microfibrillated cellulose (MFC) [39]. The latter are in turn assembled into familiar cellulose fibers. The diameter of elementary fibrils is about 5 nm whereas the MFC (also called nanofibrillated cellulose or nanofibers cellulose (NFC)) has diameters ranging from 20 to 50 nm. The microfibrils (several micrometers in length) are formed during the biosynthesis of cellulose and each microfibril can be considered as a flexible hair strand with cellulose crystals linked along the microfibril axis by disordered amorphous domains [40]. The ordered regions are cellulose chain packages that are stabilized by a strong and complex network of hydrogen bonds that resemble nanocrystalline rods [39]. This is why the two main types of nanocellulose are (i) cellulose nanocrystals (CNCs) and (ii) cellulose microfibrils. Further, depending on the source, the various forms of nanomaterials that can be produced from cellulose are often collectively referred to as cellulosic nanomaterials or nanocellulose [41]. For example, the extraction of cellulose nanofibrils (CNFs) and CNCs from plants, bacteria, and some animals (e.g., tunicates) is leading to a wide array of worldwide research to use these nanomaterials in product applications [39, 42–45]. Nanocellulose in its various forms contains unique structures and self-assembly features that we can exploit to develop new nano-enabled green products.

It is a natural nanomaterial that seems to give a range of opportunities to obtain superior material properties for different end products. The cellulose

particle nomenclature has not been standardized and because of this there is an inconsistent use of terms in the literature to describe a given set of cellulose particles. Cellulose nanoparticles of various kinds can be extracted, owing to various available cellulose sources and processes for NP extraction. Each particle type is distinct, having a characteristic size, aspect ratio, morphology, crystallinity, crystal structure, and properties. We use the term cellulose nanoparticles (CN) to broadly refer to several of the particle types that have at least one dimension in the nanoscale. Nine particle types are considered to describe the main cellulose-based particles, which typically differ from each other based on cellulose source materials and the particle-extraction method. There are wood fiber (WF) and plant fiber (PF), microcrystalline cellulose (MCC), MFC, NFC, CNCs, tunicate cellulose nanocrystals (t-CNCs), algae cellulose nanocrystals (AC), and bacterial cellulose particles (BC) [1].

8.2.3.1

Preparation, Characterization, and Applications

Cellulose nanoparticles (CNs) are ideal materials on which to base a new biopolymer composites industry. CNs have high aspect ratio, low density, and a reactive surface of –OH side groups that facilitates grafting chemical species to achieve different surface properties (surface functionalization). Surface functionalization allows the tailoring of particle surface chemistry to facilitate self-assembly, controlled dispersion within a wide range of matrix polymers, and control of both the particle–particle and particle–matrix bond strength.

8.2.3.2

Synthesis and Isolation of Cellulose Nanoparticles

Manipulating cellulose molecules in nanosize ranges to create excellent nanomaterials is the frontier of cellulose science. Cellulose nanoparticles (CNPs) or nanocellulose (NC) can be extracted from this naturally occurring polymer using a top-down, mechanically or chemically induced, deconstructing strategy. Due to the potential of cellulosic nanoparticles as special functional nanomaterials [46], as well as bio-based reinforcing nanofiller, they have attracted significant interest over the past 20 years [1, 10, 40].

The main important and widely used methods for cellulose nanofibers isolation include mechanical (such as crushing, cryocrushing), chemical (such as acid hydrolysis, alkaline hydrolysis, organic solvent treatment, and ionic liquid treatment), physical (such as ultrasonication, microwave, gamma rays irradiation), and biological (cellulose degrading enzyme extracted from various organisms) treatments or a hybrid of the above.

The isolation of cellulose particles from cellulose source materials occurs in two stages. The first stage is a purification and homogenization pretreatment of the source material so that it reacts more consistently in subsequent treatments. The particular pretreatment is dependent on the cellulose source material and to a lesser degree on the desired morphology of the starting cellulose particle for

the second stage treatments. The pretreatments for wood and plants involve the complete or partial removal of matrix materials (hemicellulose, lignin, etc.) and the isolation of individual complete fibers (WF, PF). For tunicates the pretreatment involves the isolation of the mantel from the animal and the isolation of individual cellulose fibrils with the removal of the protein matrix. There are three alternatives: (i) limit the hydrogen bonds, and or (ii) add a repulsive charge, and or (iii) decrease the degree of polymerization (DP) or the amorphous link between individual MFCs. Enzymatic pretreatment and 2,2,6,6-tetramethylpiperidine-1-oxyl radical (TEMPO) mediated oxidation pretreatment are the most commonly used pretreatments for oxidation of cellulose fibers. However, carboxymethylation and acetylation is the chemical method used to increase the anionic charges in the formation of carboxyl groups on the surface of the MFC [41]. Pretreatments for algal cellulose sources typically involve culturing methods, and then purifying steps for removal of algal wall matrix material. Bacterial cellulose pretreatments focus on culturing methods for cellulose microfibrillar growth and then washing to remove the bacteria and other media. Detailed descriptions of several of these pretreatments are available within the respective references for the following source materials, that is, wood [47], plant [48], tunicate, algae, and bacteria [49].

The second stage involves the separation of these "purified" cellulose materials into their microfibrillar and/or crystalline components. There are several approaches for isolating cellulose particles and these have been previously reviewed [50]. The three basic separation approaches are mechanical treatment, acid hydrolysis, and enzymatic hydrolysis. These approaches can be used separately, though in practice to obtain the desired particle morphology several of these methods are used in sequence or in combination. Here, we will briefly describe the two most common approaches for isolating cellulose particles, mechanical treatment, and acid hydrolysis.

Acid Hydrolysis A controlled strong acid hydrolysis treatment can be applied to cellulosic fibers allowing dissolution of amorphous domains and therefore longitudinal cutting of the microfibrils. The ensuing NPs are generally called cellulose nanocrystals and are obtained as an aqueous suspension. With respect to the morphology of the particles, a combination of both sulfuric and hydrochloric acid during the hydrolysis step appears to generate spherical CNCs instead of rod-like nanocrystals when carried out under ultrasonic treatment [51–54].

CNCs have been obtained from hard and soft wood by traditional acid hydrolysis methods [55]; however, for the black spruce pulp, longer hydrolysis time resulted in shorter cellulose rods with narrow particle length distribution. The optimization of extraction process has been carried out by Bondeson *et al.* [55], from Norway Spruce (*Picea abies*) through monitoring the effect of hydrolysis time, temperature, and the ultrasonication treatment.

TEMPO-mediated oxidation of wood celluloses has a high possibility of becoming a breakthrough in nanotechnology to bridge biomass/forest refining

and high-tech/cutting-edge fields, and to contributing to the establishment of sustainable societies and environmentally friendly systems based on renewable resources to partly replace fossil resources [56]. Araki *et al.* [57] prepared cellulose whiskers by acid hydrolysis with HCl, from Whatman CF11 cellulose powder. The aqueous suspensions of nanocrystals were carboxylated by NaClO oxidation catalyzed by TEMPO. The carboxylation of CNCs was followed by amidation with a single amidated PEG-Polyethylene glycol (PEG-NH_2) using a water-soluble carbodiimide. Saito *et al.* [58, 59], have proposed a new process to obtain MFC based on the TEMPO reaction and strong mixing to obtain individualized MFCs with 3–4 nm width and few microns of length.

Mechanical Treatment/Processing While for mechanical methods, which include high-intensity ultrasonication [60], high-pressure refiner [61], or grinder treatment [54], the main product generated is not a single fiber and has been referred as nanofibrils. However, these two techniques of extracting nanocellulose from plants are time consuming and very costly [62]. They also involve high consumption of energy for processes such as mechanical treatments [63], which can cause dramatic decrease in both the yield and fibril length down to 100–150 nm and also introduce damage to the environment, as in the case of chemical treatments [64].

Cryocrushing Cryocrushing has also been used to extract nanocellulose from WF, PF, MCC, tunicate, algae, and bacterial source materials. Cryocrushing is often used to manufacture MFC from agricultural crops and by-products and consists of the crushing of frozen pulp with liquid nitrogen [61]. Ice crystals within the cells are then formed, and under mechanical crushing, they slash the cellular wall and release wall fragments. In general, these processes produce high shear that causes transverse cleavage along the longitudinal axis of the cellulose microfibrillar structure, resulting in the extraction of long cellulose fibrils, termed microfibrillated cellulose [1]. The nanocellulose spheres with size 60–570 nm were synthesized by mild acid hydrolysis and mechanical stirring. Quasi-spherical cellulose nanoparticles from *Agave atrovirens* fibers were hydrolyzed and purified by means of heat, sonication, and dialysis. Sain and his research team successfully extracted MFC from wheat straw and soy hulls via cryocrushing [48, 61, 65, 66]. Sixty percentage of the MFC obtained had a diameter in the range of 30–40 nm and lengths of several thousand nanometers. This group also obtained MFC from flax, hemp, and rutabaga fibers via the same technique (with diameters of 5–80 nm). They also applied this process to soybean stock to produce MFCs with diameters in the range of 50–100 nm.

8.2.3.3 Characterization and Properties of Nanocellulose

The ultrastructure of cellulose derived from various sources has been extensively studied. Techniques such as transmission electron microscopy (TEM),

scanning electron microscopy (SEM), atomic force microscopy (AFM), wide angle X-ray scattering (WAXS), small incidence angle X-ray diffraction and solid state 13C cross-polarization magic angle spinning (CP/MAS), field-emission scanning electron microscopy (FE-SEM), and nuclear magnetic resonance (NMR) spectroscopy have been used to characterize nanocellulose morphology. These methods have typically been applied for the investigation of dried nanocellulose morphology.

Microfibrillated Cellulose (MFC) The term "microfibril" is generally used to describe the 2–10 nm thick fibrous ribbon-like cellulose structures with a length of several tens of microns formed during cellulose biosynthesis in higher plants [67]. However, in the literature "Nanofibril (NF)" and "nanofiber (NF)" cellulose are also used as synonyms for "microfibril (MF)" which may also lead to some confusion [1, 42, 67]. The MFC particles are considered to contain multiple elementary fibrils each consisting of 36 cellulose chains arranged in Iβ crystal structure. They have a high aspect ratio (10–100 nm wide, 0.5–10 mm in length) are 100% cellulose, and contain both amorphous and crystalline regions. Depending on their origin, the MF diameters may vary. In wood, for example, the lateral dimension for microfibrils is around 3–5 nm [68]. However, cellulose microfibrils also form intertwined aggregates with widths of 20–25 nm in the parenchyma cell wall [63]. MFC is produced via mechanical refining of highly purified WF and PF pulps. Typically, the Valonia microfibrils consists of ∼1000 cellulose chains, have a square cross-section (∼20 nm by 20 nm), high crystallinity, and a high fraction of Iα crystal structure. MFCs have been used as a thickening agent in the food and cosmetics industries.

Cellulose Nanocrystals (Nanowhiskers) The CNCs are rod-like or whisker-shaped particles with transverse dimensions as small as 3–30 nm, giving a high surface to volume ratio, also called cellulose nanowhiskers (CNWs). These particles have also been named nanocrystalline cellulose, cellulose whiskers, CNWs and cellulose microcrystals (in early literature). They can be generated from various plant sources such as WF, PF, MCC, MFC, or NFC by harsh acid hydrolysis [51, 69, 70]. CNCs have a high aspect ratio (3–5 nm wide, 50–500 nm in length), are ∼100% cellulose, highly crystalline (54–88%), and contain a high fraction of Iβ crystal structure (68–94%).

The morphology of CNs along the axis of the crystal presents different features, depending on the source of the nanocrystals [39]. For example, CNCs from wood are 3–5 nm in width and 100–200 nm in length, while those for *Valonia*, a sea plant, are reported to be 20 nm in width and 1000–2000 nm in length. While cotton CNCs are of 5–10 nm in width and 100–300 nm long with an aspect ratio between 10 and 30 and tunicate, a sea animal is about 10–20 nm in width and 500–2000 nm in length, with an aspect ratio of about 70 [39, 71].

Ideally, CNCs are reminiscent of the crystalline regions within the elementary fibrils of the wood and plant cellulose biosynthesis process and are considered to consist of 36 cellulose chains arranged in Iβ crystal structure and have a square cross-section with $[110]_m$ and $[110]_m$ terminating surfaces (Figure 8.3) [27]. Alternatively, for maize cellulose, Ding and Himmel have proposed a 36 cellulose chain elementary fibril having a hexagonal shaped cross-section with $[100]_m$, $[110]_m$, and $[110]_m$ terminating surfaces and heterogeneous structure containing a Iβ crystalline core and layers of subcrystalline sheaths [72].

The formation of a colloidal suspension of CNCs/whiskers, produced by sulfuric acid hydrolysis was first reported by Ranby and Ribi [73, 74]. The dimensions of CNWs do depend on the initial source and temperature, agitation, and time during acid hydrolysis treatment (Figure 8.4). Different other methods have also been reported to produce CNCs from various sources. For instance, enzymatic-mediated production of nanocrystals from recycled pulp; ionic liquid preparation of nanowhiskers from microcrystalline cellulose; sonochemical-assisted hydrolysis for CNs preparation; and combined mechanical shearing, enzymatic, and acid hydrolysis extraction of CNCs from plants have been mentioned [40, 75–80].

Potential applications of CNCs include barrier films, antimicrobial films, transparent films, flexible displays, reinforcing fillers for polymers, biomedical implants, pharmaceuticals, drug delivery, fibers and textiles, templates for electronic components, separation membranes, batteries, super-capacitors, electro-active polymers, and many others [80]. The author recommends reading

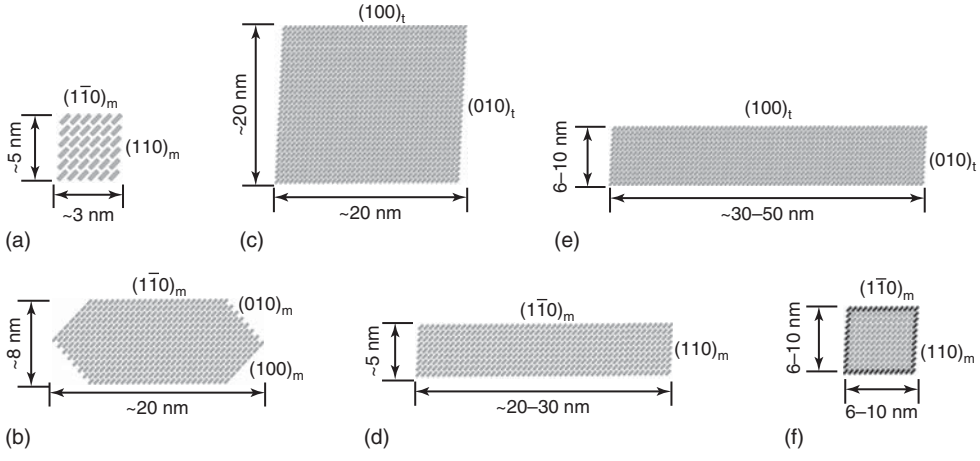

Figure 8.3 Schematics of idealized cellulose particle cross-sections showing terminating surfaces and crystal structure (m, monoclinic, t, triclinic) for (a) wood CNC and elementary fibril (or NFC) cross-section, (b) t-CNC, (c) AC *Valonia*, (d) AC *Micrasterias*, (e) unmodified – BC – *Acetobacter*, and (f) modified – BC – *Acetobacter*. Each gray box represents a cellulose chain looking down the chain-axis [1]. (Reproduced with permission.)

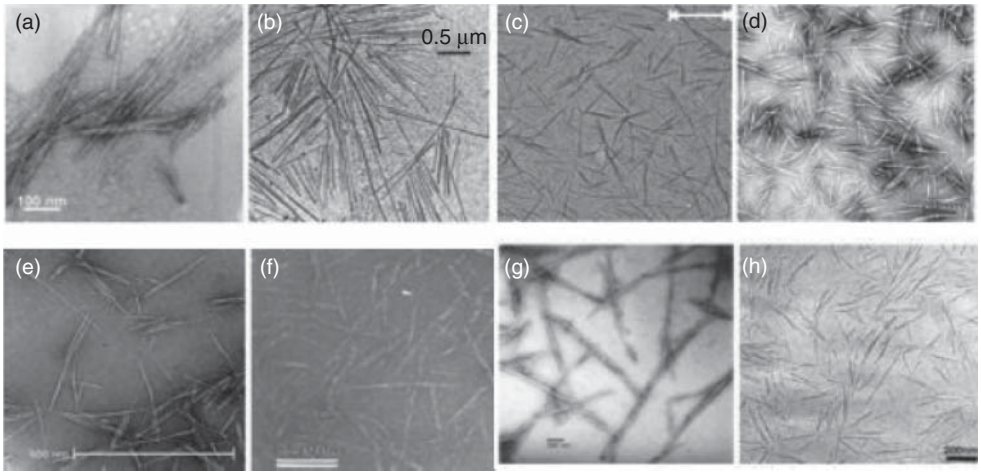

Figure 8.4 TEM images of cellulose whiskers obtained from acid hydrolysis of (a) microcrystalline cellulose, (b) tunicate, (c) cotton, (d) ramie, (e) sisal, (f) straw, (g) bacterial cellulose, and (h) sugar beet [10]. (Reproduced with permission.)

recent review articles, which include details of new developments in CNCs/CNWs production, properties, and their applications [1, 41, 56, 64, 68, 81, 82].

Nanofibrillated Cellulose/Nanofibers (NFC) NFC refers to cellulose fibers that have been fibrillated to achieve agglomerates of cellulose microfibril units obtained by mechanical disintegration. NFC has nanoscale (<100 nm) diameter and typical length of several micrometers. NFC is described as a long and flexible cellulosic nanomaterial and is obtained from cellulose fiber by mechanical disintegration. Several denominations are used to describe this nanocellulose material and most often nanofibrillated cellulose/microfibrillated cellulose (NFC/MFC) is used [83–85]. Therefore, we will also keep the NFC denomination throughout the chapter for better understanding. The first successful isolation of cellulose microfibrils was reported 30 years ago by Herrick *et al.* [86] and Turbak *et al.* [87] using a Gaulin laboratory homogenizer from softwood pulp. Since the 1980s, other mechanical treatments have been performed and different raw materials, pretreatments or post-treatments have been incorporated in the mechanical refining of WF and PF including softwood sulfite, oat straw, wheat straw (*Triticum* sp.), beech wood, and so on [83, 88].

NFCs are reminiscent of elementary fibrils in the wood and plant cellulose biosynthesis process and are considered to consist of 36 cellulose chains arranged in Iβ crystal structure, have a high aspect ratio (4–20 nm wide, 500–2000 nm in length), are ~100% cellulose, and contain both amorphous and crystalline regions [1] (Figure 8.5). In the literature, diverse nonwood sources have already been used to produce NFC. For example, it can be extracted from sugar beet pulp

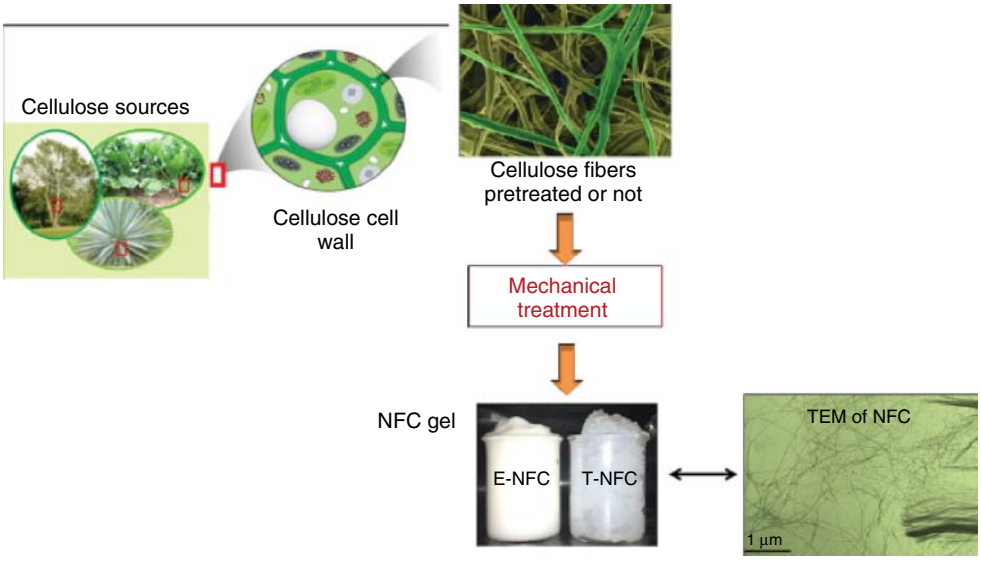

Figure 8.5 Description of classical process to obtain nanofibrillated cellulose (NFC). Different cellulose sources (wood or annual plant) followed by extraction of cellulose fibers from the cell wall, using different mechanical treatments, thus yielding an NFC gel suspension [83]. (Copyright Allowed: Open Access Article.)

[89, 90], wheat straw and soy hulls [91], sisal [92], bagasse [93], palm trees [94, 95], ramie, carrots [96], luffa cylindrica [97], and so on.

The differentiation of NFC from MFC is based on the fibrillation process that produces finer particle diameters [1]. NFCs are lightweight material, which can build network structures with high strength and stiffness. This renewable resource is transparent, translucent biodegradable material with high water storage capacity, high reactivity, and barrier properties. NFCs also act as rheology modifier with high surface area and aspect ratio when used to prepare novel nanocomposite materials.

NFCs display two main drawbacks that are associated with their intrinsic physical properties. The first one is the high number of hydroxyl groups, which lead to strong hydrogen interactions between two nanofibrils, eventually leading to the gel-like structure once produced. The second drawback is the high hydrophilicity, which limits its uses in several applications such as in paper coating (increase of dewatering effect) or composites (tendency to form agglomerates in petro-chemical polymers) [83].

Consequently, NFC modification is of interest in order to limit its natural phenomenon and open up new applications. NFC surface modification not only helps to introduce new functionalities but also to produce "active" NFC. The surface of cellulose nanoparticles can be modified and tuned either (i) by physical interactions or adsorption of molecules or macromolecules onto their surface or

(ii) by using a chemical approach to achieve covalent bonds between cellulosic substrates and the grafting agent [83]. NFCs with and without modification are widely used in polymer industry especially for polymer applications in packaging, biomedicine, adhesives, fibers, electronics, and automotives. The potential for these applications has been shown and discussed in various recent publications [88–101].

Tunicate Cellulose Nanocrystals (t-CNCs) Particles produced from the acid hydrolysis of tunicates are called "t-CNCs." t-CNCs are different from other CNCs in terms of particle morphology, crystal structure, and mechanical properties (Figure 8.6). The ribbon-shaped t-CNCs have a height of ~8 nm, a width of ~20 nm, and a length of 100–4000 nm (typical aspect ratios 70–100), are ~100% cellulose, highly crystalline (85–100%), and contain a high fraction (76–90%) of Iβ crystal structure [1]. The advantage of t-CNCs is that they are highly crystalline and have the largest aspect ratio of any CNC. The ideal morphology is a parallelogram-shaped cross-section, and a Iβ crystal structure, but it has been shown that acid hydrolysis used to extract the t-CNC partially erodes the parallelogram-shaped hexagon with $[110]_m$, $[010]_m$, and $[100]_m$ terminating surfaces and the $[110]_m$ being the largest facet [27]. Along the crystal length there is a 180° twist with a pitch of 2.4–3.2 mm. t-CNCs are also observed to agglomerate such that they stack in parallel [26].

Tunicate cellulose exhibits high surface area, an ultrafine fibrous network, highly crystalline structure and aspect ratio, high-purity monoclinic cellulose Iβ allomorph, low density, and remarkable mechanical strength [58, 101–108].

Algae Cellulose Particles (AC) AC particles are the microfibrils extracted from the cell wall of various algae by acid hydrolysis and mechanical refining (Figure 8.6g). The resulting microfibrils are microns in length, have a large aspect ratio (>40) with morphology depending on the algae: two contrasting examples are *Valonia* and *Micrasterias* [109, 110], *Valonia* microfibrils have a square cross-section (~20 nm by ~20 nm) with $(100)_t$ and $(010)_t$ terminating surfaces, with primarily Iα crystal structure (Figure 8.6c). *Micrasterias* microfibrils have a rectangular cross-section (~5 nm by ~20–30 nm) with $[110]_m$ and $[110]_m$ terminating surfaces, where $[110]_m$ is the largest facet, with primarily Iβ crystal structure (Figure 8.6d). Along the crystal length there is a 180° twist with a pitch of 700 nm [111].

Bacterial Cellulose (BC) Particles BC particles are microfibrils secreted by various bacteria that have been separated from the bacterial bodies and growth medium [1]. It is obtained in pure form, free from other plant parts such as lignin, hemicellulose, and wax. The resulting microfibrils are microns in length (normally up to 1 μm), have a large aspect ratio (>50) with morphology, depending on the specific bacteria and culturing conditions. Typically, Acetobacter microfibrils have a rectangular cross-section (6–10 nm by 30–50 nm), terminating surfaces of $(010)_t$, and $(100)_t$ with $(100)_t$ being the largest facet, and have primarily Iα crystal structure (Figure 8.6e). However, by altering the

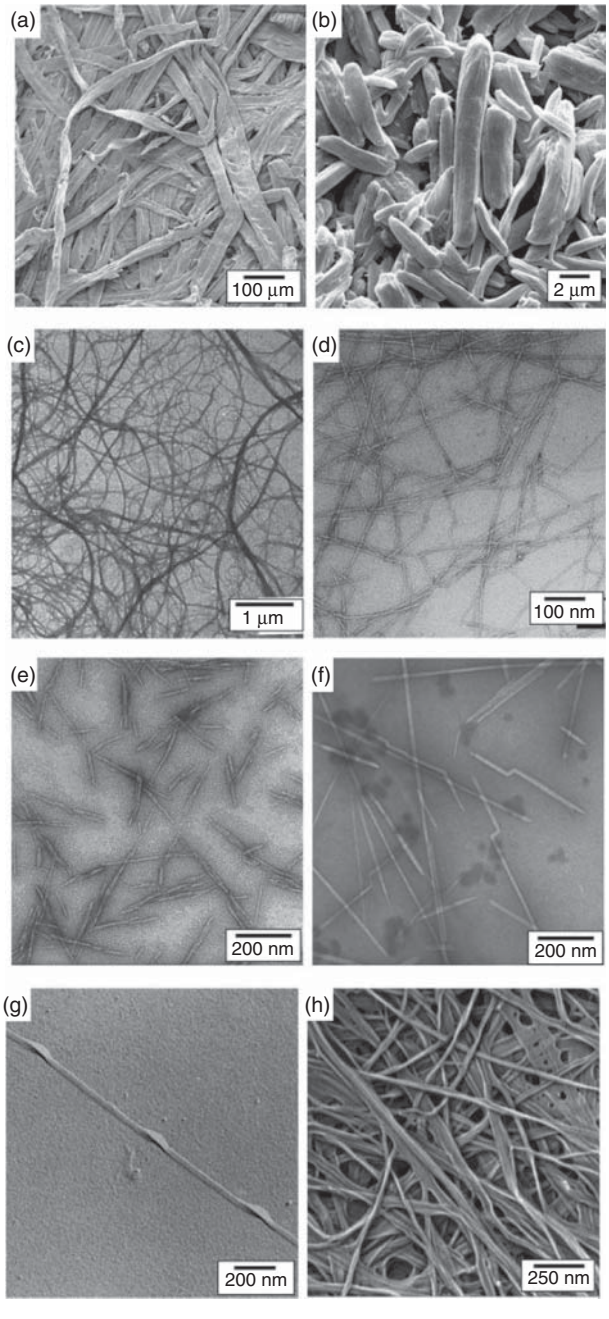

Figure 8.6 Several cellulose particle types, (a) SEM image of WF, (b) SEM image of MCC that has been deagglomerated, (c) TEM image of MFC, (d) TEM image of TEMPO-NFC, (e) TEM image of wood CNCs, (f) TEM image of t-CNC, (g) TEM of AC, and (h) SEM image of BC [1]. (Reproduced with permission.)

culture conditions (stirring, temperature, and additives) it is possible to alter the Iα/Iβ ratio and the width of the microfibrils [112, 113]. Additives have been shown to interfere with the aggregation of the elementary fibrils into the normal ribbon assembly [114] and these modified BC microfibrils have a square cross-section (~6–10 nm cross-section) with $(110)_m$, and $(110)_m$ terminating surfaces, and have primarily Iβ crystal structure (Figure 8.6f) [113–116]. This change in morphology has been linked to the decrease in the proportion of Iα in the microfibril [117], in which the Iβ preferentially forms in the isolated elementary fibrils that are free from the constraint present when aggregated in the normal microfibril ribbon assembly. It has been suggested that this added constraint is necessary for the formation of the metastable Iα phase [115].

AC and BC nanocellulose can also be used to make aerogels/foams. Due to their mechanical properties, film-forming properties, viscosity, and so on, they are considered to be interesting material for the paper, food, medical, cosmetic, and pharmaceutical industries.

8.2.4 Cellulose Nanocomposites

Nanocomposites can be described as engineered structures consisting of various materials with different physical or chemical properties of which one component has at least one dimension in the nanometer scale. These composites are materials made of two or more types of components: the matrix whose role is to support and protect the filler materials and transmit and distribute the applied load to them and the mentioned fillers, which are the stronger and stiffer components reinforcing the matrix. It is well known that the properties of nanocomposite materials depend not only on the properties of their individual components but also on the morphological and interfacial characteristics arising from the combination of distinct materials [117–125]. The combination of these building blocks allows creating and designing new composite materials with high flexibility and improvement in their properties, far beyond the possibilities of their constituting, single components [119–125].

This section focuses on the use of nanocellulose as the matrix in the production of nanocomposites. Now, in the era of nanotechnologies, the reinforcing materials are nanoscaled. The pioneer work on nanocomposites that was initiated by researchers at Toyota in the early 1990's created nanoclay-reinforced polymers, opening a new research path on composites. Shortly after, researchers started working on cellulose whiskers-reinforced polymers [12, 25, 46, 126]. Nanocellulose composites offer new possibilities for unaccountable applications in day-to-day life. Unlike cellulose, nanostructured cellulose provides a large variety of options for chemical and engineering material applications. Fundamental domain structures with high intrinsic strength, high melting temperature,

directional rigidity, and ease of chemical modification can provide high reinforcement and scaffold in formation of nanocomposites [47, 126]. Therefore, cellulose-based materials including CNWs and CNFs are excellent candidates for biocompatible nanocomposites with good mechanical properties. They are used as reinforcement materials/nanofillers in polymeric nanocomposites and porous foams.

8.2.4.1 Nanocomposites Preparations

Combination of nanotechnology and biopolymer technology is imperative in merging multifunctional attributes in a single, ideal, and unique polymer matrix to address the shortcomings of already existing nano or biomaterials. The possibility of dispersing cellulosic nanofibers in nonaqueous media has been investigated using surfactants or chemical grafting and it opens other possibilities for nanocomposites processing. Cellulose nanoparticles possess a reactive surface covered with hydroxyl groups, providing the possibility to extensive chemical modification. Although this strategy decreases the surface energy and polar character of the NPs, thereby improving the adhesion with nonpolar polymeric matrix, a detrimental effect is generally reported for the mechanical performances of the composite. The hydrophilic nature of cellulose causes irreversible agglomeration during drying and aggregation in nonpolar matrices because of the formation of additional hydrogen bonds between amorphous parts of the NPs. Therefore, the preparation of cellulose whiskers-reinforced polylactic acid (PLA) nanocomposites by melt extrusion was carried out by pumping the suspension of nanocrystals into the polymer melt during the extrusion process [127, 128]. An attempt to use poly vinyl alcohol (PVA) as a compatibilizer to promote the dispersion of cellulose whiskers within the PLA matrix was reported [129]. Organic acid chlorides-grafted cellulose whiskers were extruded with LDPE [130]. The homogeneity of the ensuing nanocomposite was found to increase with the length of the grafted chains. Polycaprolactone-grafted CNCs obtained by ring-opening polymerization (ROP) of the corresponding lactone were also used as "masterbatches" by melt blending with a matrix [40]. In another attempt, Lin *et al.*, used gelatin and its enzymatically modified gelatin (EMG) to prepare nanocellulose nanocomposites in an attempt to enhance the property of rehydration ability of nanocellulose [131]. Porous networks and thickened cellulose ribbons could be found in these two (low and high) gelatin/nanocellulose composites [131].

Impressive mechanical properties as well as reinforcing capability, abundance, low weight, and biodegradability of CNCs make them ideal candidates for the processing of polymer nanocomposites [40, 47, 131]. An attempt to use a recently patented concept (Dispersed nanoobjects protective encapsulation – DOPE process) intended to disperse carbon nanotubes in polymeric matrices was reported. Physically cross-linked ALG capsules were successfully formed in the presence of either cellulose whiskers or MFC [132]. The ensuing capsules have been extruded with a thermoplastic material.

The feasibility of using metallic nanomaterials like silver nanoparticles (AgNPs) in the development of antimicrobial food packaging materials was critically checked by many researchers where AgNPs were blended with cellulose matrix [45, 116, 133, 134]. Properties and application of cellulose–metal nanocomposites have been summarized in Table 8.1.

Hydroxypropyl methyl cellulose (HPMC) based hybrid nanocomposites reinforced with bacterial cellulose nanocrystals (BCNCs) and AgNPs had been prepared and characterized. Ternary nano-biocomposite films based on PLA with modified CNCs and synthesized AgNPs have been prepared and characterized by Fortunati, *et al.* The combination of CNC and silver particles increased the barrier properties and a significant antibacterial activity due to the Ag effect [159]. Cai and Kim have three different methods to prepare nanocellulose/PEG composites. In the first method, PEG was incorporated in nanocellulose hydrogels by adding PEG solution to the culture medium for *G. xylinus* [160]. In the second method, suspensions of microbial cellulose nanofibers were mixed with PEG solution with mechanical stirring followed by a freezing–thawing process. The composite is a hydrogel and can be used for soft tissue replacement devices. In the third method, a previously produced nanocellulose hydrogel was soaked in PEG solution, allowing the PEG molecules to penetrate the nanocellulose [161]. Such nanocomposite materials can be used to develop a composite scaffold for bone regeneration. Nanocellulose has also been augmented by immersion in solutions of polyacrylamide and gelatin, yielding hydrogels with improved toughness [162]. Similarly, immersion of nanocellulose into PVA has yielded hydrogels having a wide range of mechanical properties of interest for cardiovascular implants [163]. In this study, authors reported Cai and Kim's third method. SEM images showed that PEG molecules were not only coated on the nanocellulose fibrils surface but also penetrated into the nanocellulose fiber networks. Recently, a hybrid bionanocomposite of PVA in combination with CNCs and poly D,L-lactide-co-glycolide (PLGA) NPs loaded with bovine serum albumin was synthesized [164]. This bionanocomposite in the form of films is found to be to adult bone marrow mesenchymal stem cells and thus represents a new tool for drug delivery strategies.

8.2.4.2 NW Nanocomposites

Studied showed that CNWs with a high aspect ratio can enhance the mechanical properties of nanocomposites when they are used as nanofillers. One of the first reports on nanocomposites containing cellulose whiskers was presented in 1995 [165]. Since then, both natural and synthetic polymers were explored as the matrix for new nanocomposite formation. CNW-reinforced nanocomposites showed significantly improved mechanical properties and elastic modulus, for both of the natural and synthetic polymer matrix. Natural polymers such as poly (β-hydroxyoctanoate) [166–168], rubber [169], starch [170], silk Fibroin [171], and cellulose acetate butyrate reinforced with CNWs were reported in the literature [172]. Poly-(styrene-co-butyl acrylate)

Table 8.1 Properties and application of cellulose–metal nanocomposites.

Type of cellulose	Metal ion	Nanocomposite properties	Possible application	References
CNPs	Fe_3O_4NPs	Hybrid nanoparticle average diameter of 8 nm. Method of preparation: coating polymerization process	For the removal of traces of heavy metal ions in solution	[135]
CF	AgNPs	Hybrid material for controlled barrier	Antibacterial food-packaging materials	[136–140]
NFC	Ag nanoclusters	High surface area, excellent antibacterial property	Fluorescence, antibacterial hydrbid material, wound-healing pads	[141, 142]
NFC	Metal Ag nanoclusters	—	Fabrication of novel material	[142, 143]
NFC	AgNPs	Highly reinforced hybrid network structures	Potential wound-dressing material, hydrogel, aerogels, and films formation	[144]
BC	AgNPs	Preparation method-TEMPO process, self-supporting functionalized smooth hydrofilms	Detection of amino acids	[145]
BC	AgNPs	High water-holding capacity and biocompatibility	Antimicrobial wound dressing materials for chronic wounds and burns	[146, 147]
NC	AgNPs	Simple and low-cost methodology	Fabrication of fuel cells	[148]
Hydroxypropyl methyl cellulose/BCNC	AgNPs	Hydrophobic nanocomposite film	Eco-friendly food packaging applications	[149]
Nanoporous cellulose gel	AgNPs, AuNPs, PtNPs	Areogel, electrostatic interactions for preparation of nanocomposite, high transmittance, porosity, surface area, moderate thermal stability, and good mechanical strength	Synthesis of metallic nanoparticles, matrix for metal NPs immobilization, biosensor application	[134]
BC	AuNPs	Enzyme immobilization	Biosensor application glucose biosensors in human blood samples	[150–152]

(*continued overleaf*)

Table 8.1 (*Continued*)

Type of cellulose	Metal ion	Nanocomposite properties	Possible application	References
NFC	ZnO	Semiconducting property, bactericidal activity against gram positive (*Staphylococcus aureus* and *Bacillus cereus*) and gram negative (*Klebsiella pneumoniae*) bacteria	Paper-coating formulations for the production of antibacterial papers	[153]
BC	CuNPs	*In situ* and *ex situ* method of preparation	Diverse applications such as packaging or paper coatings, antimicrobial materials	[116]
VC	CuNWs	Pathogen test for *S. aureus* and *Klebsiella pneumonia*		
RC	CuNPs	One-step reduction method, film antibacterial activity against *S. aureus* and *E. coli*	Nanocomposite film in biomedical, catalysis, packaging, and electronics	[154]
BCNF	CdS NPs	Nanosized CdS crystals with 8 nm, *in situ* method, high thermal stablity	Potential application as photocatalyst, novel luminescence, and photoelectron transfer devices	[155]
BCNF	CdSNPs	CdSNPs with hexagonal wurtzite structure, 10–20 nm diameter for 3 h reaction, high photocatalytic activity nanofibers with high-efficiency photocatalysis with 82% methyl orange (MO) degradation after 90 min irradiation and good recyclability	As robust visible light-responsive photocatalysts	[156]
NFC	Fe_3O_4/Ag nanocomposites	Role: support matrix, nanocomposite aerogel, and film, catalytic and antibacterial activity	Medical and environmental applications	[157]
CNCs	Ag/Pd	10 nm bimetallic quantum dots, carboxylated cellulose nanocrystals as platforms carrying Ag–Pd alloy nanoparticles	Labels for electrical detection of DNA hybridization	[158]

RC, regenerated cellulose; VC, vegetable cellulose.

(poly(S-co-BuA)) [127, 164], poly(vinyl chloride) [173], polypropylene [174], waterborne epoxy [175], acetate butyrate [176], and poly(oxyethylene) [40, 177] were used as synthetic matrixes. Nanocomposites containing CNWs and PLA were prepared by extrusion. The whiskers were prepared by swelling MCC in *N*,*N*-dimethylacetamide/lithium chloride to avoid the problem of aggregation [55]. A linear increase of the Young's modulus with increasing MFC content was reported for these novel nanocomposites. For example, Helbert *et al.* [127] reported that a poly(S-co-BuA) latex film containing 30 wt% of wheat straw cellulose whiskers presented a rubbery Young's modulus value more than 1000-times higher than that of the bulk matrix. This effect was ascribed not only to the geometry and stiffness of the whiskers, but also to the formation of H-bonded whiskers network. The incorporation of CNCs into the nanocomposite provides a physical barrier through the creation of a tortuous path for the permeating moisture. The possibility of surface chemical modification and nanosized dimensions of cellulose nanoparticles have been extensively used in a wide variety of applications, for example, packaging, adhesives, and electronic display materials.

8.2.4.3 NFC Nanocompostites

In 1998, the preparation of nanocomposites containing NFC and starch as a matrix was reported [178]. Novel bionanocomposite films with improved thermal and mechanical properties were prepared by casting water-based suspensions of pullulan and NFC [179]. In the last few years, research on nanocomposites containing NFC has been noticeably intensified. Xiong *et al.* [157], have demonstrated a facile and environmentally friendly approach to prepare Fe_3O_4/Ag@ NFC nanocomposites which enables tunability from highly porous, flexible aerogels to solid, and stiff films. In the procedure, NFC acts as a biocompatible support for the magnetic AgNPs as well as a reducing agent for the silver ions.

Other hydrophilic polymer matrices like PVA or hydroxypropyl cellulose (HPC) were used to prepare nanocomposites containing NFC. Tests showed that there was a significant increase in both the tensile strength and modulus of elasticity upon addition of NFC to the polymer matrices [180]. In addition, more hydrophobic polymers such as polyurethane were used as a matrix for the preparation of nanocomposites. In a film-stacking method, thin films of dried NFC and polyurethane were stacked and compression molded. Also for this method, the thermal stability of the composite was found to be clearly increased as compared to the neat polyurethane. Again, this was attributed to the percolating network of NFC [181].

NFC and their nanocomposites are thixotropic, biodegradable, dimensionally stable thickeners (stable against temperature and salt addition) and can be used in low-calorie food applications, as thickeners in cosmetics, in pharmaceuticals (tablet binder, diagnostics: bioactive paper), as pickering stabilizer for emulsions and in particle stabilized foams, paint formulations, and so on.

8.2.4.4

Characterization and Applications of Nanocomposites

The nanocomposite characterization is a very essential part of research as it highlights the structural, chemical, electrical, and optical properties of the novel material and its possible application of new material. Cellulose nanocomposite with its characteristics like nanofibers size and distribution, mechanical properties, compatibility, and ability to mold, make it a unique biomaterial indispensable in health area. The nanocellulose composite scaffolds are biocompatible with less rejection with cellular contact and blood contact cells interaction to be a promising biomaterial and may be suitable for cell adhesion/attachment suggesting that these scaffolds can be used for wound-dressing or tissue-engineering scaffolds [45]. TEM, SEM, AFM, WAXS, FE-SEM, and NMR spectroscopy have been used to study the structure of these nanocomposites. Further, the mechanical properties including tensile strength, flexural strength, modulus, impact force/performance, fatigue behavior, and compressive force have also been studied for different cellulose nanocomposites.

The potential of nanocomposites in various sectors of research and application is promising and attracting increasing investments. Applications of nanocellulose are mainly considered to be in paper and packaging products, although applications in construction, automotives, furniture, electronics, pharmacy, and cosmetics are also being considered. For companies producing electroacoustic devices, nanocellulose is used as a membrane for high quality sound. Additionally, nanocellulose is applied in membranes of combustible cells (hydrogen); additives for high-quality electronic paper (e-paper); ultrafiltrating membranes (water purification); membranes used to retrieve mineral and oils, and nowadays, they are being greatly discussed and researched in a huge variety of applications. The high strength and stiffness as well as the small dimensions of nanocellulose may well impart useful properties to composite materials reinforced with these fibers, which could subsequently be used in a wide range of applications [182].

Metal nanocomposites with nanocellulose have applications in drug delivery strategies, food-packaging material [136–139], dressing materials, [133, 147] bactericidal papers for water treatment [136], and so on. The addition of metal NPs with cellulose blend adds new functionalities such that these structured materials may be of interest in diverse applications such as electronics, sensors, wound dressings, catalysis, and selective filtration.

8.3 Chitin/Chitosan

Chitin $(C_8H_{13}O_5N)_n$ is one of the widely available natural polymers on earth and functions naturally as a structural polysaccharide like cellulose in plants and collagen in animals. Chitin is a long-chain polymer of *N*-acetylglucosamine (GlcNAc), a derivative of glucose, and is found in yeast, fungi, and in the exoskeletons of arthropods like crustaceans and insects as well as in cephalopod molluscs

and marine sponges [183–187]. Chitin is a highly insoluble material resembling cellulose in its solubility and low chemical reactivity. It can be degraded by chitinase. Its immunogenicity is remarkably low, in spite of the presence of nitrogen. Chitin can also be regarded as cellulose with hydroxyl at position C-2 replaced by an acetamido group. Chitin is inelastic, nitrogenous polysaccharide, and a major source of surface pollution in coastal areas [188].

Chitin and chitosan are the collective names for a family of de-*N*-acetylated chitin with different degrees of deacetylation [189–192]. In general, when the number of *N*-acetyl-glucosamine units exceeds 50%, the biopolymer is termed chitin, whereas the term "chitosan" (CS) is used to describe the polymer when the *N*-acetylglucosamine content is less than 50%. Chitosan is the *N*-deacetylated derivative of chitin, although this *N*-deacetylation is almost never complete. A sharp nomenclature with respect to the degree of *N*-deacetylation has not been defined between chitin and chitosan [188, 193, 194].

8.3.1
Structure and Properties of Chitin/Chitosan

The structure of chitin is comparable to the polysaccharide cellulose in plants, forming crystalline nanofibrils or whiskers. In terms of function, it may be compared to the protein keratin in animals. Chitin is a linear, highly crystalline homo polymer of 1,4 GlcNAc. Earlier, it was designated "animal cellulose" because it is structurally similar to cellulose except that the hydroxyl groups had been replaced with acetamide groups at the C-2 position (Figure 8.7). Chitin consists of β-1,4-linked *N*-acetyl glucosamine residues that are arranged in antiparallel and most abundant (α), parallel (β), or mixed (γ) strands. Recent studies have reported that the β form is a variant of α family [196]. Chitosan (CS) is a copolymer composed

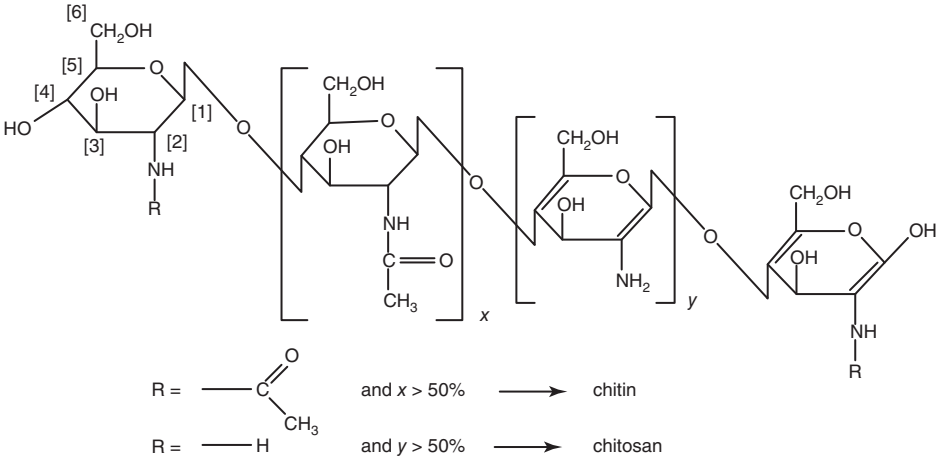

Figure 8.7 Structure of chitin and chitosan [195]. (Reproduced with permission.)

of glucosamine and *N*-acetylglucosamine. The physical properties of CS depend on a number of parameters such as the molecular weight (from approximately 10 000 – 1 million Da), degree of acetylation (in the range of 50 – 95%), sequence of the amino and the acetamido groups, and the purity of the product [196].

8.3.1.1

Physico-Chemical Properties of Chitin/Chitosan

Chitin is a colorless to off-white, hard, inelastic, nitrogenous polysaccharide [188, 197]. The higher degree of acetylation of chitin results in the poor solubility in common solvents [198]. The crystallinity is the hydrogen bonding formed between the arranged strands of chitin. The degree of crystallinity is a function of the degree of deacetylation and the higher the crystallinity, the more stability for chitin molecules [199]. The average molecular weight of chitins range from 1.03×10^6 to 2.5×10^6 Da but the conversion of chitin to chitosan by deacetylation reduces it to 1×10^5 to 5×10^5 [200]. Chitin is insoluble in water as well as in most organic solvents. While it is soluble in dilute organic acids at low pH [201]. Chitin and CS are chemically reactive because they have amino and hydroxyl groups which they easily substitute with other groups. Due to their basic polysaccharide nature, chitin and CS both show chelating activity. Chitin can be easily processed into gels, beads, powders, fibers, membranes, flakes, colloids, films, and so on. Both CS and chitin are remarkably stable in concentrated alkaline solutions even at high temperatures.

8.3.1.2

Biological Properties of Chitin/Chitosan

Chitin and CS and their derivatives are highly eco-friendly and nontoxic and nonallergic. They also possess good biodegradability, bioactivity, biocompatibility, coating ability, and good miscibility. Because of their nonantigenic properties, they are highly compatible with animal as well as plant tissues. They are considered to be bacteriostatic, hemostatic, immunologic, analgesic, anti-ulcer, anti-inflammatory, hyperuricemic, hypocholesterolemic, , anticoagulant, anti-gastritis, antiviral, antibacterial, antifungal, anti-tumor, spermicidal, and having free radical scavenging activity [202 – 204].

8.3.1.3

Applications of Chitin/Chitosan

Chitin and chitosan have drawn much attention in many fields including medicine, pharmaceuticals, and agriculture because of their biocompatibility, biodegradability, and low cost. Chitin and chitosan have been studied as natural cationic biopolymers because of their excellent biocompatibility, biodegradability, nontoxicity, antimicrobial capability, and wound healing stimulation [189]. Both chitin and chitosan materials have found applications as components in different products (cosmetics, textile products, solid state batteries, antibiotics, etc.,) and processes (paper industry, food processing, biomedical treatments, purification of water, chromatographic techniques, etc.) [197, 205]. The development of all these

applications has promoted detailed analysis of the physicochemical properties of chitin and chitosan. These biopolymers have found a plethora of applications in biomedical field due to their biocompatible, biodegradable, and nontoxic nature. Major applications include their use as carriers for drug delivery and as scaffolds for tissue engineering and wound healing [187].

Applications based on the optical properties of chitin and chitosan are emerging. For instance, the development of sensors to detect metal ions and biological structures, based on resonant excitation of surface free electrons oscillations is being considered. In the field of modeling, structural colors related with the metallic or iridescent appearance of several species of animals (birds, butterflies, beetles, spiders, fishes), the optical properties of chitin have entered only through its average refractive index (n_{chitin}) for wavelengths in the visible range. These unique characteristics of chitosan and its derivatives relates to applications in various fields such as water treatment, food industry, cosmetics, agriculture, and biomedicine [203–208].

8.3.2
Origin of Chitin/Chitosan

Chitin occurs in a wide variety of species, from ciliates, amoebae, chrysophytes, some algae, yeasts, and fungi to the lower animals like crustaceans (e.g., crabs, lobsters, and shrimps), worms, insects, and mollusks [198]. Vertebrates, plants, and prokaryotes do not contain chitin [209]. It is also the main component of arthropod exoskeletons, tendons, and the linings of their respiratory, excretory, and digestive systems. It is also found in the reflective material (iridophores) both in the epidermis and the eyes of arthropods and cephalopods (phylum: *Mollusca*). It is found in the cell walls of fungi, exoskeletons of arthropods such as insects, radulas of mollusks, and in the beaks and internal shells of cephalopods, including squid and octopuses. Moreover, there is one report based on lectin binding, endo-chitinase binding, and enzymatic degradation studies, that the epidermal cuticle of a vertebrate named *Paralipophrys trigloides* (fish) is chitinous. Therefore, chitin is not only an essential component of invertebrates but may also be present in vertebrates. Unlike cellulose, chitin can be a source of nitrogen as well as carbon (C:N = 8 : 1). In most organisms chitin is cross-linked to other structural components such as proteins and glucans except for chitin of some centric diatom (chitan) such as *Thalassiosira fluviatilis,* which produce radiating spines that are fully acetylated and are the purest form of chitin known in nature, unlinked with other extracellular components [203].

8.3.3
Chitin Nanomaterials: Preparation, Characterization, and Applications

Chitosan is a natural product and most important derivative of chitin. Chitosan has received attention from the nineteenth century, when Rouget discussed

the deacetylated forms of the parent chitin natural polymer in 1859 [210]. During the past 20 years, a considerable amount of work has been reported on chitosan and its potential use in various bioapplications [211]. Chitosan is more suitable for the bioapplications than chitin because of its better solubility in water and organic solvents [212]. In nanomaterials field, chitosan has gained growing interest due to its biocompatibility, biodegradability, high permeability, cost-effectiveness, nontoxic property, and excellent film forming ability [213–215]. Moreover, its ability to enhance the penetration of large molecules across mucosal surface and its recognition as a mucoadhesive has enabled its use worldwide for the production of nanoparticles [215]. Rod-like nanowhiskers with average size of 200 ± 20 nm in length and 8 ± 1 nm in width have recently been prepared from many chitins of different origins such as squid pen chitin [216], riftia tubes [217], crab shells [218–220], and shrimp shells [221–224]. Other examples are chitosan whiskers from Chitin [225], Silk Fibroin-chitin whisker (CHW) sponge nanocomposite [226], PVA-CHW nanofiber nanocomposite [227, 228], calcium alginate yarn-CHWs nanocomposite fibers [229], and so on.

As chitin and/or chitosan are soluble in acidic aqueous solution, micro- or NPs of chitosan have been produced by techniques such as emulsification (microemulsion) and precipitation, chemical modification (cross-linking), hydrothermal method, and so on [230–236]. Some of the strategies for preparing chitin and chitosan nanomaterials are discussed below.

In 1997, Calvo and co-workers reported the ionic gelation method for the preparation of NPs of hydrophobic polymers. The preparative methods were extremely mild and involved a mixture of two aqueous phases at room temperature. One phase of solvent contained the chitosan and poly-(ethylene oxide), while another phase contained polyanion sodium tripolyphosphate (TPP). Particle sizes of 200–1000 nm and the zeta potentials between +20 and +60 mV for Chitosan nanoparticles (CSNPs) were reported. Such NPs were found to have huge loading capacity of protein (efficiency up to 80%) and were capable of supplying a constant release of the encapsulated protein for 1 week [237].

CS nanoparticles have been reported for a targeted delivery system especially for delivery of the chemotherapeutic drugs Q17 doxorubicin (DOX), N-(trifluoroacetyl) doxorubicin (FDOX), tamoxifen (Tam), 4-hydroxytamoxifen (4-Hydroxytam), endoxifen (Endox), and so on [238]. These drugs and their analogs have been used as antitumor agents against several types of cancers such as acute leukemia, malignant lymphoma, and breast cancer [239–245]. The freeze-drying process plays an important role in improving the shelf-life of the CSNPs. The difference in the shelf-life between the NPs synthesized by freeze drying method and cryo-protective agent method is almost negligible. By using the gelation method, Alonso and co-workers investigated the two different types of chitosan NPs in the form of hydro-chloride salt. The synthesized particle was around 300–400 nm in size with a positive surface charge. These particles were used to address the difficulties in the nasal absorption of insulin. The same group also studied the use of chitosan NPs with relevance to the entrapment and release efficiency of

hydrophilic anthracycline drugs and doxorubicin (DOX) [246–248]. Termsarasab and his team have synthesized DOX-loaded NPs based on polyethylene glycol-conjugated chitosan oligosaccharide-arachidic acid and they further explored their potential application in leukemia (blood cancer) therapy [248]. While in another attempt, miR-34a, a potent endogenous tumor-suppressive molecule in breast cancer, was co-encapsulated with DOX into hyaluronic acid (HA)-chitosan (CS) NPs and simultaneously delivered into breast cancer cells. *In vitro* and *in vivo* experiments showed that miR-34a and DOX can be efficiently encapsulated into HA-CS NPs and delivered into tumor cells or tumor tissues and enhance antitumor effects of DOX by suppressing the expression of nonpump resistance and antiapoptosis proto-oncogene Bcl-2 [249]. In a recent study, γ-polyglutamic acid (γ-PGA) and chitosan (CS) NPs were characterized as a DOX carrier. *In vitro* studies with DOX-loaded NPs with sizes ranging from ∼150 to ∼630 nm demonstrated the cytotoxicity of the NPs against a human oral squamous cell carcinoma cell line [250]. NPs with an average diameter of <200 nm from novel polymer, that is, galactosylated O-carboxymethyl chitosan-graft-stearic acid (Gal-OCMC-g-SA) were synthesized for liver targeting delivery of DOX. Furthermore, *in vitro* release revealed that Gal-OCMC-g-SA/DOX NPs exhibit sustained pH dependent drug release [251]. Self-assembled NPs, formed by polymeric amphiphiles, have been demonstrated to accumulate in solid tumors by the enhanced permeability and retention effect, following intravenous administration. In another study, CS-DOX conjugates were synthesized via carboxylation of doxorubicin and subsequent amidation of succinyl doxorubicin with amine groups on chitosan [252]. Similarly, tamoxifen and its metabolites 4-hydroxytamoxifen and endoxifen known as breast cancer drugs were used in this evaluation.

Ohya *et al.*, synthesized poly (ethylene glycol)-grafted chitosan NPs as drug carriers for peptides. They investigated the NP formation that takes place through the intermolecular hydrogen bonding in aqueous solution. Incorporation property and release behavior of insulin depended upon the degree of introduction of PEG chain on chitosan, which varied with time [253]. In 2000, Yamomoto *et al.* reported the mucoadhesive liposomes-coated chitosan for drug delivery. They investigated the mucoadhesive formulation by mixing chitosan solution with a drug-loaded liposomal suspension prepared by using the thin film hydration method. In their study, they confirmed that these synthesized NPs could play an important role in the release of insulin [254]. Yang *et al.*, identified in their study that the formation of positively charged poly (butyl cyanoacrylate) NPs is stabilized by the chitosan. They found that the size of NPs is influenced by many factors such as pH, concentration, volume, and molecular weight of chitosan [255]. Maitra and co-workers investigated a procedure to prepare the ultrafine cross-linked CSNPs through the sodium bis(ethylhexyl) sulfosuccinate/*n*-hexane reverse micellar system. In this study, it was shown that the particle sizes of synthesized CSNPs were mainly influenced by the degree of cross-linking. At a particle size of 30 nm only 10% $-NH_2$ groups were cross-linked in polymeric chain; when the particles size was 110 nm then all the amino group of the polymeric chain were cross-linked [256]. In 2003, Andersson and Lofroth reported

that heparin/chitosan microemulsion works as a good carrier and is also more suitable for oral administration. They studied this microemulsion with or without the drugs by scattering turbidity, diffusion-NMR, conductivity, and dynamic light scattering (DLS) [257].

Chitin has been known to form microfibrillar arrangements in living organisms [258, 259]. These fibrils with diameters from 2.5 to 25 nm depending on their biological origins are usually embedded in a protein matrix [260]. CHWs can be prepared from chitins isolated from living organisms through hydrolysis in strong acid aqueous medium. On the basis of the preparation of cellulose crystallites suspension, Marchessault *et al.* [261], for the first time reported a route for preparing suspension of chitin crystallite particles in 1959. They found that acid-hydrolyzed chitin spontaneously dispersed into rod-like particles that could be concentrated to a liquid crystalline phase and self-assemble to a cholesteric liquid crystalline phase above a certain concentration [260, 262]. In recent years, chitinous NPs and their properties have been the subject of many studies due to their potential in various applications. Chitinous nanomaterials from species have a promising future in the biomedical nanotechnology area and their properties are enlisted in Table 8.2.

8.3.4 Chitin Nanocomposites: Preparation, Characterization, and Applications

Chitosan is abundant, low cost, environmentally friendly, and biocompatible in nature. Due to its high content of amino ($–NH_2$) and hydroxyl (–OH) groups, chitosan and its derivatives have proved to be an excellent adsorbent for removal of heavy metal ions, fluoride, organic dyes, and so on. Their structure and mechanical properties have been characterized by a variety of techniques including Fourier transform infrared spectroscopy, elemental analysis, FE-SEM, and an Instron universal testing machine. Magnetic separation technique for removing heavy metals has some advantages, such as high efficiency and cost-effectiveness. Magnetic carriers are usually composed of the magnetic cores to ensure a strong magnetic response and a polymeric shell to provide favorable functional groups and features for various applications. In recent years, the magnetic chitosan NPs have been widely used in the field of water purification because of their advantages like rapidity, high separation efficiency, cost-effectiveness, and simple operation process. Chitin derived chitosan offers high biocompatibility for preparation of different composites. It has attracted intense attention as an important biopolymer to effectively stabilize colloidal dispersions of super paramagnetic iron oxide NPs, conferring them with an increased biocompatibility and chemical functionality. In all types of magnetic chitosan NPs, the most widely used is Fe_3O_4/CS NPs due to their good super paramagnetism and low toxicity. These materials find applications in magnetic hyperthermia treatment of cancer, a promising approach to cancer therapy to induce apoptosis of the cells. This therapy involves the introduction of ferromagnetic or super paramagnetic NPs (mainly magnetite, Fe_3O_4) into the tumor tissue and then

Table 8.2 Chitin and chitosan nanoparticles and their properties.

Material	Size (nm)	Method of preparation	IEP/special features	Applications	References
CS–TPP (tripolyphosphate)	100–250	Ionic gelation mechanism	IEP-pH 9.0	Delivery of gene or protein macromolecules	[245]
CSNPs	275–300	—	—	Dorzolamide hydrochloride (Dorzo) and pramipexole hydrochloride (drug delivery)	[263]
CS-polymethacrylic acid copolymers	NA	Grafting polymethacrylic acid	—		[264]
CSNPs	100	Ionic gelation mechanism	—	Encapsulation and drug delivery	[265]
CSNPS	—	Ionotropic gelation technique	—		[266]
CSNPs	10	Water-in-oil microemulsion	—	Enzyme lipase immobilization	[267]
CSNPs	104–148	Emulsification solvent diffusion method	+31.2 zeta potential mucoadhesive	Cyclosporin-A Bioavaiblity of drug	[268]
CSNPs-DNA	50–100	Polyelectrolyte complex	—	Gene delivery	[269]
CSNPs	250–400	Ionotropic gelation procedure	Polydispersity index <0.1, Insulin lading 21 IU kg^{-1}	Nanomedicine: insulin carrier	[270]
CSNPs	5–6	—	Biocompatible, Luminesce at about 670 nm lifetime of 1.353 ns	Live cell imaging	[271]
CSNPs	620	Pregel preparation method	Zeta potential of 29.3 mV, biocompatible	Targeted drug delivery	[272]
GC-AuNPs glycol chitosan-coated gold nanoparticles	99.4 ± 16.8	Reduction method	Zeta potential: $(+34.48 \pm 1.0\,mV)$	Biomedical application-tumor targeting cell imaging	[273]
Chitosan gel	—	Chemical cross-linking in water-in-oil emulsion	—	Entrapping and delivering drugs	[253]
Chitosan nanogel	270–390	Chemical cross-linking using genipin	Positive charge at acidic pH	Biomedical application	[274]

IEP, isoelectric point.

irradiation with an alternating magnetic field (AMF). The particles transform the energy of the AMF into heat by different physical mechanisms, and the transformation efficiency strongly depends on the frequency of the external as well as the nature of the particles such as particle size or surface modification [275]. Several other methods have been developed to prepare magnetic Fe_3O_4/CS NPs (MFe_3O_4/CS NPs).

For example, Li *et al.* [276], have reported that MFe_3O_4/CS NPs were prepared by co-precipitation of Fe^{2+} and Fe^{3+} in a basic environment. In another case, Zhi *et al.* [277], prepared MFe_3O_4/CS NPs via oxidation-precipitation of Fe^{2+} process. However, these methods usually involved either emulsifying agents, or protective gas and high-temperature, thereby requiring relatively complicated facilities. A novel *in-situ* reduction-precipitation method to prepare M Fe_3O_4/CS NPs was proposed by Cao *et al.* [236]. Figure 8.8 schematically represents the formation of M Fe_3O_4/CS NPs.

At first, Fe^{3+} ions in solution are chelated on the chitosan chains by amino ($–NH_2$) and hydroxyl (–OH) groups and then partially reduced to Fe^{2+} ions by sodium sulfite. With the addition of ammonia solution, Fe_3O_4 NPs are formed in about 10 min by reduction-precipitation method [236]. The chelation effect of $–NH_2$ and –OH groups on the chitosan chains could disperse iron ions homogeneously; thus, chitosan chains can hinder the NPs from agglomeration during the growth process. The proposed method is advantageous in its simplicity and rapidity. These new composites can be extensively exploited for biomedical applications, food, and paper industry. Few examples of nanocomposites of chitin and chitosan have been listed in Table 8.3.

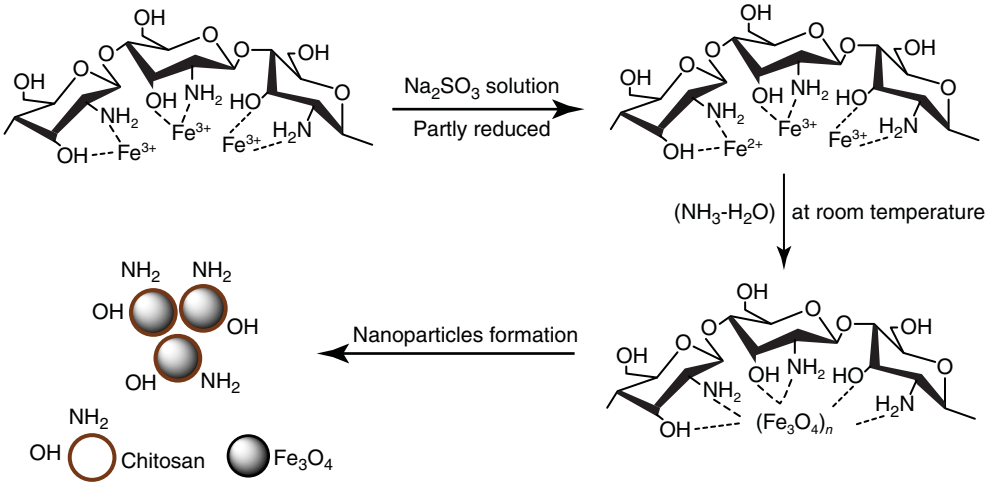

Figure 8.8 Schematic representation of the formation of MFe_3O_4/CS NPs [236]. (Reproduced with permission.)

Table 8.3 List of chitin and chitosan nanocomposites.

Material	Size	Method of preparation	Properties	Application	References
Fe_3O_4-CSNPs	Quasi-spherical, ~7 nm diameter	Reduction-precipitation method	Super paramagnetic property, low toxicity	Trace heavy metal ions removal	[187]
CS–ZnONPs	An average diameter of 60 nm	Polymer-based method	Pesticide dosage range 0.01–1.5 g (permethrin)	Water treatment application: removal of pesticides	[232]
Polyaniline-grafted amine modified chitosan Cu and Ag NPs nanocomposite	Copper – dot-like nanospheres-3 nm Rod-like structure about 2.5 nm diameter and 25 nm length Silver hexagonal 30 nm	Polyaniline grafting	—	Biotemplate in treatment of meat industry wastewater	[233]
Chitosan-coated Mn Fe_3O_4 nanoparticles (CCMNPs)	—	—	pH dependent zeta potential −20 to −30 mV	Trace heavy metal ions removal	[235]
Calcium alginate-CSNPs	161 nm	Pregel preparation	Mean zeta potential of 45 mV Biocompatable, nontoxic to HEK 293 cells, highly stable	Targeted drug delivery, gene delivery	[272]
Fe_3O_4-CSNPs	10–80 nm	Reversed-phase water-in-oil microemulsion	—	Drug delivery carrier, separation materials	[277]
Fe_3O_4-CSNPs	50–92 nm	Reversed-phase water-in-oil microemulsion	—	Biomedical application	[278]
Fe_3O_4-CSNPs	10–20 nm	—	Positively charged NPs Loading capacity-110 mg g^{-1}	Adsorption of bovine serum albumin	[279]

(*continued overleaf*)

Table 8.3 (*Continued*)

Material	Size	Method of preparation	Properties	Application	References
Fe_3O_4-CSNPs	41–64 nm	—	UV irradiation	Possible biomedicine application	[280]
Ethylenediamine-modified magnetic chitosan nanoparticles (EMCNs)	15–40 nm	Microemulsion	Maximum loading capacity for Pt(IV) and Pd(II) = 171 and 138 mg g^{-1}	Removal of metal ions: adsorption platinum(IV) and palladium(II) from aqueous solution	[281]
Chitosan-Ag nanoparticles (CS-AgNPs)	2–16 nm, spherical	Electrochemical oxidation/complexation process followed by UV irradiation reduction	Surface plasmon absorption around 420 nm	Biomedical application	[282]
CS-MNPs	Spherical, size range 10–100 nm	*In situ* sysnthesis and co-precipitation method	pH responsive release, superparamagnetic	Chemotherapeutic drug delivery (doxorubicin)	[283]
CoFe/chitosan	Size-50 nm, spherical	—	Supermagnetic property (24 emu g^{-1}), γ-radiation route in inverse microemulsion system	For drug carrier and cancer-targeted radiotherapy	[284]
Carboplatin-Fe@C-loaded CSNPs	210 ± 26 nm (size range 150–300 nm)	—	Drug loading by physical encapsulation and adsorption Loading capacity	Drug delivery	[285]
CS-AuNPs	40 nm	Electrochemical deposition method	Linear range: 5.0×10^{-5} to 1.30×10^{-3} M, Lower limit of detection = 13 μM	Application in glucose biosensor	[286]
CS-alginate	20–240 nm	—	Ionic cross-linking	Environmentally friendly biosorbent for copper ions	[287]

8.4
Starch

Among the carbohydrate polymers, starch is an abundant, inexpensive, naturally renewable, and biodegradable polysaccharide. Starch is produced by most green plants as an energy store and is the most common carbohydrate in human diets and animal foods [288]. Since starch is a low-cost versatile biopolymer and renewable natural material, it has been widely used in food and in many industrial applications. The world starch market was estimated to be 48.5 million tons, including native and modified starches. The value of the output is worth €15 billion per year, justifying the intentions of industrialists and researchers to seek new properties or high value application. Starch is widely used in food, chemical, textile, papermaking, medicine, and many other industries because of its biodegradability, reproducibility, and cheapness.

8.4.1
Structure and Properties of Starch

Starch or amylum is a carbohydrate consisting of a large number of glucose units joined by glycosidic bonds. Interesting and detailed reviews [288–291] on starch structure have been published and these can be referred for more details. Starch's composition was first determined by studying the residue of its total acid hydrolysis. It consists of mainly two glucosidic macromolecules: amylose (AM) and amylopectins (APs). In most common types of starch the weight percentages of amylose range between 72% and 82%, and the amylopectins range from 18% to 28%. However, some mutant types of starch have very high amylose content (up to 70% and more for amylomaize) and some very low amylose content (1% for waxy maize) [12]. Amylose is essentially a linear α-1,4-linked glucan chain of approximately 1000 residues, whereas amylopectin has numerous branch points that form by α-1,6 linkages joining linear chains, and has a DP up to tens of thousands [292]. The starch structure has been under research for years, and because of its complexity, a universally accepted model is still lacking [288, 289]. The ratio of the two α-glucans in starch granules as well as their molecular structure influences the solubility, gelatinization temperature, viscosity, gelation, and retrogradation properties of starch [293]. In general, the ratio of AM to AP and their structural variability strongly depend on the botanical origin [290]. Native starch is biosynthesized in the form of semicrystalline granules made of these two components. The semicrystalline structure of granules originates from amylopectin chains in double helical configurations [294].

8.4.2
Origin of Starch

Starch is found in plant roots, stalks, crop seeds, and staple crops such as rice, corn, wheat, tapioca, and potato. Worldwide, the main sources of starch are maize

(82%), wheat (8%), potatoes (5%), and cassava (5%) from which tapioca starch is derived [295].

8.4.3 Starch Nanoparticles: Preparation, Characterization, and Applications

Starch nanoparticles (StNPs) are nanosized (1–1000 nm in the pharmaceutical field) particulates of starch prepared by chemically cross-linking starch molecules with appropriate cross-linkers [296–298]. The predominant model for starch is a concentric semicrystalline multiscale structure that allows the production of new nanoelements: (i) StNPs which are amorphous in nature produced from gelatinized starch and (ii) starch nanocrystals (StNCs) resulting from semicrystalline granules by acid hydrolysis [288].

The hydrophilic nature of starch is a major constraint that seriously limits the development of starch-based NPs [299]. A good alternative to solve this problem is the grafting of hydrophobic side chains to the hydrophilic starch backbone [300–304]. However, an important restriction that usually arises from the use of these hydrophobic polysaccharides derivatives to prepare NPs is the necessity to employ organic solvents, such as dichloromethane or dimethyl sulfoxide, with considerable toxicological and other safety risks [301, 302]. Therefore, there is a strong incentive to develop a new strategy for the synthesis of StNPs and conduct research on their properties. Once the starch structure is opened and dispersed by the application of alkali, acid, and enzymes, the formation of the hydrogen bonds can be accelerated through which such NPs can be formed [305, 306]. Synthesis and characterization of starch piperinic ester of nanosize micelles or nanospheres was reported by Han *et al.* [306]. Nanometric and monodisperse starch acetate nanospheres can be prepared through a simple procedure of nanoprecipitation, by drop-wise addition of water to an acetone solution of starch acetate, without any stabilizing agent. This was the first report of preparation of starch-based nanospheres by this method. The size of the nanospheres obtained could be easily controlled by a number of simple and efficient modifications, that is, through regulation of the polymer concentration in acetone, the proportions of the water and organic phases, and the molecular weight, and degree of substitution of the starch esters. A number of reasons are suggested to explain the observed transitions in the particle size. Fluorescence spectroscopic studies proved that these types of nanospheres could be potentially used for the encapsulation of hydrophobic drugs.

Various synthetic methods for synthesis of StNPs such as high-pressure homogenization and miniemulsion cross-linking [296], precipitation/nanoprecipitation [305, 307–309], emulsion [310, 311], and microemulsion [312–314] have been explored by researchers. NPs obtained by the above-mentioned methods are further subjected to geometrical characteristics such as size, dimensions, and shape of NPs or crystals. These properties are highly dependent on the nature of the starch source as well as the preparation conditions such as time, temperature,

along with the purity of the source materials. Different techniques including TEM, AFM, SEM, alkali fluidity number, number average molecular weight, intrinsic viscosity, and so on.

8.4.3.1 Emulsion/Homogenization

High-pressure homogenization is a simple technique and useful for diluted and concentrated samples; however, it requires high number of homogenization cycles and possible contamination of product could occur from metal ions coming off from the wall of the homogenizers [296, 315]. A new and convenient synthetic route using high-pressure homogenization combined with water-in-oil (w/o) miniemulsion cross-linking technique was used to prepare sodium trimetaphosphate (STMP)- cross-linked StNPs [316]. These firm spherical StNPs with good stability, narrow size distribution, and good dispersibility, are expected to be exploited as drug carriers [296]. In another study, a novel ionic liquid microemulsion consisting of 1-octyl-3-methylimidazolium acetate ([Omim] Ac, an ionic liquid), native corn starch, surfactant TX-100, 1-butanol, and cyclohexane was prepared. StNPs with a mean diameter of 96.9 nm and narrow size distribution were confirmed by the results of DLS [317]. StNPs were also prepared by emulsification-diffusion technique for encapsulation and release of three different model drugs, flufenamic acid, testosterone, and caffeine for transdermal drug delivery [297]. Anion StNPs with an average 130 nm diameter were prepared in water-in-oil microemulsion and further used for Doxorubicin loading. Results demonstrated that the system has a potential for the targeted delivery of anticancer drug [318].

8.4.3.2 Nanoprecipitation

Nanoprecipitation is an attractive method for preparing NPs from biomaterials such as starch, as it does not employ toxic chemicals [307, 319, 320]. This method involves dispersion/dissolution of starch material in aqueous media and precipitation. The dispersion of starch material in aqueous alkaline media and the method of precipitation may therefore influence the shapes and sizes of the NPs [298]. StNPs were prepared by delivering ethanol as the precipitant into starch-paste solution dropwise. Citric acid-modified StNPs were fabricated with the dry preparation technique. Ma *et al.* [321], has prepared StNPs by precipitating a starch solution within ethanol as the precipitant. Native starch was mixed with water and completely gelatinized with dropwise addition of ethanol at room temperature and stirred for 50 min. The suspension was then centrifuged with ethanol to remove water, and the settled material was dried at 50 °C to remove ethanol. The resulting NPs were used to prepare a bio-nanocomposite. In another study, spherical or oval shape NPs (diameters in the range of 10–20 nm) were prepared by starch–butanol complex precipitation method [322].

8.4.3.3

Acid Hydrolysis

StNPs have been recommended as good candidates for renewable nanofillers. Kim *et al.* [316], reported the synthesis of NPs from various starches such as wax maize, normal maize, high AM maize, potato, and mung bean. StNPs were obtained using a H_2SO_4 solution (3.16 M) at 40 °C for 7 days by centrifugation. Electron microscopy confirmed that the starch particles had round or oval shapes with diameters ranging from 40 to 70 nm, which possibly represented the starch blocklets in granules.

8.4.3.4

Ultrasonication

Ultrasonic waves generated by converting electrical energy into mechanical vibration result in the intense agitation of the molecules in the medium. Application of ultrasonic irradiation in food processing has been increasing over the past few years because it shortens the processing times required and lowers energy consumption, creating an effective process. Ultrasonication generates ultrasonic cavitation in the solution and causes micro-bubbles [323]. When micro-bubbles collapse, high energy is released and is converted to high pressure and high temperature. This physical method causes degradation of starch or other polymers and/or catalytic acceleration of reactions. The high-intensity ultrasonication is found to be quite rapid, presenting a higher yield and not requiring any chemical treatment as compare to acid hydrolysis [324]. Nano-sized starch particles (NSPs) were prepared from starch granules using an ultrasonic physical treatment method by many researchers [314, 324–329].

An easy and efficient approach has been used for preparation of StNPs. Three StNP samples were produced by one time oxidation followed by ultrasonic treatment (O1U1-StNPs), twice oxidation and twice ultrasonic treatment (O2U2-StNPs) and TEMPO-mediated oxidation with ultrasonic treatment (TEMPO-SNPs), respectively. These different ultrasonic-assisted oxidation methods were used to prepare StNPs with 30–50, 20–50, and 20–60 nm size, respectively with higher carboxyl and carbonyl content and lower crystallinity [323].

8.4.3.5

Schiff Base Reaction

A robust method was reported to synthesize the starch-based NPs (~143 nm) and cross-linked to polyvinylamine to custom hydrogels via a Schiff base reaction *in situ* [329]. Authors used DOX drug as model to investigate the potential application of the novel material as a drug carrier for biomedical applications. StNPs as nontoxic, cheap, and easy to prepare materials have been extensively studied as controlled release nanocarriers.

8.4.3.6

Starch Nanocrystals (StNCs)

Starch crystallite, StNC, microcrystalline starch, and hydrolyzed starch all refer to the crystalline part of starch obtained by hydrolysis [288]. StNCs are crystalline

platelets originating from the breakdown of the semicrystalline structure of starch granules by acid hydrolysis of amorphous parts. In 1996, Dufresne *et al.*, reported a method for producing what they called at the time "microcrystalline starch" and which they reported to be agglomerated particles of a few tens of nanometers in diameter [288]. The morphology of nanocrystals resulting from the disruption of the waxy maize starch granules by acid hydrolysis was revealed for the first time by Putaux *et al.* in 2003 [330]. TEM observations showed: (i) a longitudinal view of lamellar fragments consisting of stack of elongated elements, with a thickness of 5–7 nm and (ii) a planar view of individualized platelets after hydrolysis. Shapes and lateral dimensions were derived from observation of individual platelets in planar view, and marked 60–65° acute angles for parallelepiped blocks with a length of 20–40 nm and a width of 15–30 nm were reported. However, more recent publications reported bigger StNCs with round edges and grape-like aggregates of 1–5 μm [331–336]. The heterogeneity in particle size has been explained by the differences in starch botanic origin, as recently presented, and also by the difficulty to obtain well-defined pictures of nanoaggregated and nanocrystals by authors [337].

8.4.3.7

Preparation of StNCs

StNCs have attracted growing interest not only due to their nanoscaled size but also to their renewable and biodegradable nature [316, 337]. In native starch granules, the crystalline and amorphous phases coexist and together form the onion-like structure of the entire starch granule. The botanical origin of a starch, namely the type of crystallinity and the relative proportion of amylose and amylopectin, determines the structure and morphology of the StNCs [338–340]. Different preparation strategies, analogical characterization, and properties of StNCs have been reported by many researchers [295, 330, 341–344]. Lin *et al.*, in their recent article also provide an overview of aspects related to StNCs, including methods for extraction and preparation, chemical modification (with particular emphasis on the modification methods and strategies), reinforcing effects and mechanisms, and applications and prospects [345] (Figure 8.9). The conditions of hydrolysis during the extraction process (such as the type of acid, acid concentration, temperature, and time) affect the size and yield of StNCs. The preparation methods by different acid hydrolysis (hydrochloric acid, sulfuric acid, etc.) and their direct effect on morphology and yield of StCNs have been extensively studied [347–350].

During the formation of StNCs, carboxyl groups and sulfate esters could be introduced to the surface of the StNCs after H_2SO_4 hydrolysis [295, 350]. The key element in the preparation of StNCs is to not destroy the starch crystalline structure while completely removing the amorphous region of starch granules. At the same time, isolating the nanocrystalline lamellae and obtaining the individual, low degree of self-aggregated platelet StNCs should also be desirably created or maintained [345]. The use of enzymes could be an answer because they are widely used and are available industrially. An attempt to use purely

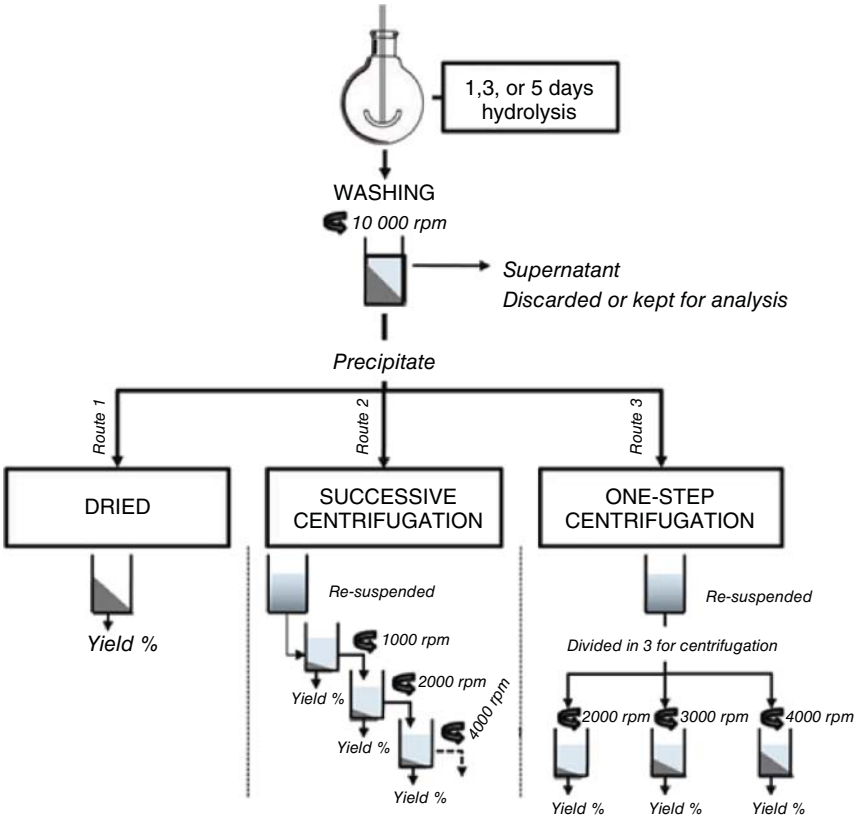

Figure 8.9 Schematic representation of the three different routes chosen for analysis of starch nanocrystals obtained from the 1, 3, or 5 days hydrolysis [346]. (Reproduced with permission.)

enzymatic hydrolysis has been reported by Kim *et al*. [351]. Small starch crystal particles with 500 nm particle size with a yield of 5–6%, was prepared by hydrolyzing waxy rice starch using α-amylase and the ultrasonicating in ethanol [288]. Crystalline square-like platelet StNCs about 10 nm thick and 50–100 nm equivalent diameters were prepared by acid hydrolysis. The isolated nanocrystals from waxy maize, normal maize, high amylose maize, potato, and wheat showed different features including thermal transitions due to different botanic origin [352].

8.4.3.8

Applications of Starch Nanoparticles

Chin *et al.*, reported that curcumin loaded onto StNPs exhibited enhanced solubility in aqueous solution as compared to free curcumin. These StNPs were

prepared by using *in situ* nanoprecipitation method and water-in-oil microemulsion system [353]. Other applications include sweetener production, bakery and antistalling, brewing and beverages, digestive aids, cyclodextrin for food, and drug encapsulation. For instance, propyl StNPs loaded with different types of drugs (flufenamic acid, testosterone, and caffeine) showed enhanced effectiveness upon permeation studies on human skin [297]. Dialdehyde starch nanoparticles (DASNPs) conjugated with 5-fluorouracil (5-Fu) were found to have enhanced breast cancer cell (MF-7) inhibition *in vitro* as compared to free 5-Fu [354]. These StNPs help encapsulate and deliver the hydrophilic drugs to targeted spots, in the absence of which these drugs are sensitive to the environment prevailing in the stomach, intestine, and blood circulation system. The efficacy of drug delivery prolongs the residence time of drugs and reduces drug-related side effects [304–306].

8.4.4
Starch Nanocomposites (StNCs): Preparation, Characterization, and Applications

In recent times, more attention has turned toward understanding and exploiting the unique physical properties of polymer nanocomposites. Polysaccharide nanocrystals which bear three hydroxyl groups in each glucose residue offer the possibility of various reactions and have also been found to be excellent reinforcement materials [335]. This increasing interest can be ascribed to a growing recognition that moves beyond formulating polymers with nanoparticular fillers, and toward really engineered, designed, and functional nanocomposites. Starch nanocomposites are complex systems because they involve interactions at multiple length scales, brought about by the inherent multilevel structure of starch and NP interactions.

Starch bio and other nanocomposites are a mixture of starch-based biopolymers with nanofillers (solid layered clays, synthetic polymer nanofibers, CNWs, and carbon nanotubes) and exhibit significant improvements in mechanical properties, dimensional stability, transparency, improved processibility, and solvent or gas resistance with respect to the pristine polymer. Thus, starch bionanocomposites are a system of much academic interest as well as practical interest for industry. Most work has been oriented toward the use of new environmentally friendly polymers with starch nanocomposites such as natural rubber [342, 343], waterborne polyurethane [331], waxy maize starch [341], cassava starch [355, 356], pullulan [357], PLA [333], PVA [332], and soy protein isolate (SPI) [358]. Angellier *et al.*, and Dufresne and Cavaillé have reported composite preparation by hot pressing [359, 360]. However, this process raises the question of the potential melting of StNCs. Similar issue should be considered if classical polymer processing methods, for example, extrusion or injection molding, are used. With the casting process, it was necessary to decrease the temperature of the polymer matrix before adding waxy maize StNCs to avoid melting [341]. However, other authors report casting-evaporation

at 50 °C after constant stirring of StNCs in thermoplastic starch at 90 °C for half an hour [356]. Most recently, compression molding was used to prepare glycerol-plasticized StNCs composites at 120 °C from a freeze-dried powder [358]; however, the stability of crystalline StNCs is still questionable after this treatment [355].

Starch nanocomposites with strong reinforcing, shows nanometric size effect as compared to conventional composite. Recently, there has been an increase in the interest in polysaccharides with hydrophobically modified derivatives for different applications. Studies have been conducted with nonrenewable inorganic fillers and a petroleum-based matrix. Increasing environmental concerns have led to developing new flexible barrier bio-based packaging and investigating the potential uses of renewable resources for such an application. However, the uses of these materials have been limited by their poor performances, such as brittleness and poor gas and moisture barrier. Bi-polymer starch nanocomposite systems closely related to their structures can be designed for many different applications and environments. The techniques used to manufacture starch bionanocomposites are based largely on following existing techniques for processing nanocomposite materials. The amphiphilic nature imparted upon starch after hydrophobic modification give them a wide and interesting applications spectrum, for instance as rheology modifier, emulsion stabilizer, surface modifier, and as drug delivery vehicles.

However, StNCs are easily self-aggregated and settled in water forming agglomerates on a micrometer scale due to their hydrophilic property [350]. The aggregation behavior of StNCs greatly limits their applications, since a procedure of mixing StNCs aqueous suspensions with matrix solution is needed in the casting fabrication of the nanocomposites. Consequently, a homogeneous dispersion of StNCs is required for high mechanical performance of nanocomposites [361, 362]. The current potential application for StNCs is in bionanocomposites where they are added as nanofillers in a polymeric matrix to improve its mechanical and/or barrier properties [346] Due to its unique properties such as the nanoscale platelet morphology, intrinsic rigidity, high crystallinity, and low permeability, StNCs have been used as reinforcement materials to prepare nanocomposites with matrices of natural polymers and biodegradable polymers [341, 355–360].

8.5 Soy Protein Isolate (SPI)

Among different biopolymers, SPI has been extensively studied due to its low cost, availability, and biodegradability. It is obtained from soybean seeds with 90–95% protein content. It has a wide range of applications in food chemistry, therapeutics, agricultural equipment, automobiles, and civil engineering [362].

8.5.1
Structure and Properties of SPI

The enriched form of soy protein, known as soy protein isolate, has been reported to exhibit high nutritional values and desirable functionalities, and its wide application as a food ingredient has been well documented [362–367]. The major components of SPI are glycinin (Molecular weight = 360 000, approximate 60%) and β-conglycinin (Molecular weight = 180 000, approximate 40%) [364]. These are basically two globular protein fractions differentiated by sedimentation coefficients: 7S (β-conglycinin) and 11S (glycinin) [364]. β-Conglycinin is a trimeric glycoprotein, which consists of three sub-units, α, ά, and β. Glycinin is a hexamer composed of an acidic (A) polypeptide linked by a disulfide bond to a specific basic (B) polypeptide [365].

8.5.2
Origin of Soy Protein Isolate

SPI is obtained from the seeds of an annual plant, *Glycine Max L. Merrill* [367]. Soybean is currently one of the most abundant sources of plant proteins [364]. Soybean proteins are widely used in many foods as functional and nutritional ingredients. It is known that soybean proteins have several physiological functions such as cholesterol-lowering and body-fat reducing effects. Furthermore, the US Food and Drug Administration (FDA) has approved the health claim concerning the role of soy protein in reducing the risk of coronary heart disease [368]. Consumption of soymilk, tofu, and other soy foods is increasing in North America due to an increase in Asian immigrants, greater acceptance by the general population, and increased recognition of the health benefits of soy foods, especially by those who wish to reduce their consumption of animal products [365]. SPIs are derived from delipidated soy flour (90–95%) by elimination of soluble carbohydrates and mineral salts [369]. The conventional procedure for SPI production is based on protein solubilization at neutral or slightly alkaline pH, and precipitation by acidification to the isoelectric region, near pH 4.5. The resulting product is "Isoelectric SPI" (Figure 8.10). Since spray-drying is a common drying method in the production of SPI, the primary physical form of SPI in commerce, is that of fine powders. Structured forms, such as granules, spun fibers, and other fibrous forms are made by further processing [370, 371].

8.5.3
SPI Nanomaterials: Preparations, Characterization, and Applications

Food grade proteins are promising candidates for NP preparation as delivery vehicles. Food proteins possess unique functional properties including their ability to form gels and emulsions, offering the possibility of developing delivery systems for both lipophilic and hydrophilic bioactive compounds [372]. SPI is unique in its high content of hydrophobic amino acids, along with polar and charged residues.

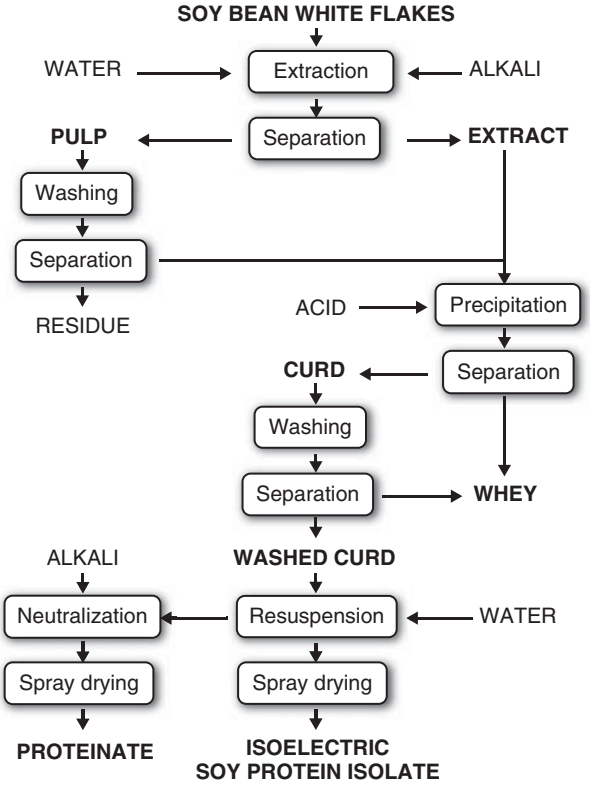

Figure 8.10 Soy protein isolate production outline [370]. (Copyright Allowed without permission.)

The first property enables a strong hydrophobic interaction with encapsulated compounds. The latter feature leads to desirable water solubility as well as facilitates the protein–drug association through electrostatic attraction and hydrogen bonding [373].

Recently, there have been many reports regarding the synthesis and application of SPI nanomaterial. As described by Zhang *et al.* [372], SPI NPs (28–179 nm) were prepared by employing a cold gelation method (Figure 8.11a). They exhibited uniform size distribution and spherical shape with a unique honeycomb-like core structure. As prepared without using toxic reagents, they would provide promising delivery systems for pharmaceutical or food applications. In another report by Teng *et al.*, SPI NPs preparation process consisted of dispersion, desolvation, drug incorporation, cross-linking, and evaporation (Figure 8.11b). Curcumin as a model drug was encapsulated successfully into the NPs. The average size of the curcumin-loaded NPs was 220.1–286.7 nm with high encapsulation efficiency and loading efficiency of 97.2 and 2.7%, respectively [364].

Further, Jong reported SPI NPs produced with a microfluidizer and characterized them in terms of particle size, size distribution, morphology, rheological

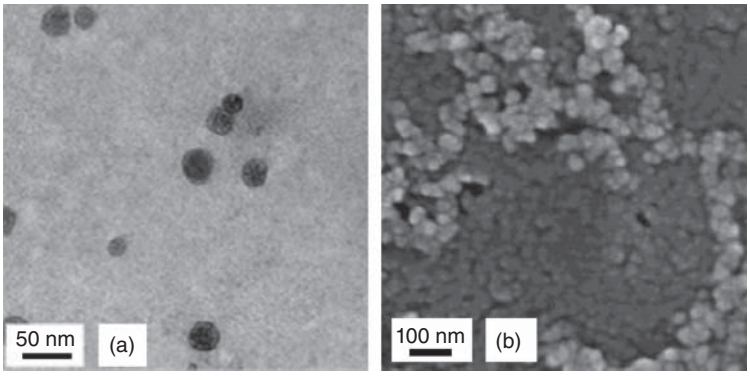

Figure 8.11 (Soy protein isolates nanoparticles reported by Zhang *et al.* [372] (a) and Teng *et al.* [364] (b)). (Reproduced with permission.)

properties, and aggregate structure [374]. Rheological measurements of these soy protein emulsions showed that both viscosity and storage decreased as the aggregate size of soy protein was decreased[abc]. Further, Liu *et al.* reported SPI NPs aggregates that were formed by sequential treatments of heating followed by electrostatic screening [375, 376]. The fabricated NPs (~100 nm size) were having gel-like network that could entrap the oil droplets within the network, indicating that SPI NPs could be used as effective Pickering-like stabilizers [375, 376].

Soy lipophilic proteins were also used to fabricate lipophilic protein NPs as described by Gao *et al.* [377]. The NPs were fabricated by ultrasonication of the soy lipophilic protein, which contains hydrophobic proteins and phospholipids. These lipophilic protein NPs had an improved dispersibility and acted as an emulsifier with a superior physical stability over long-term storage (8 weeks), suggesting that they could be explored to fabricate a stable food emulsion. Further, in a similar report by Gao *et al.*, soy lipophilic protein NPs, fabricated by ultrasonication, were used as a novel delivery vehicle for conjugated linoleic acid (CLA) [378]. They exhibited a mean diameter of 170 ± 0.63 nm with a high loading capacity, oxidation protection, and a sustained releasing profile *in vitro* for CLA.

8.5.4
SPI Nanocomposites: Preparation, Characterization, and Applications

Composite materials are made up of two or more materials with different properties. The properties of composite materials, in general, are superior in many respects to those of the individual constituents. This has provided the main motivation for the research and development of soy protein composite materials [379]. The need for sustainable material supplies calls for other renewable biopolymers such as soy protein, which is an abundant plant-sourced biopolymer. Soy proteins have good film-forming properties but the produced films have poor water vapor permeability and less than optimal mechanical properties. Dispersion of NPs in a biopolymer matrix to produce bionanocomposites has been proposed

as a possible approach to improve film properties [380]. Similar to SPI NPs, SPI nanocomposites have also been explored as novel drug delivery candidates.

In a report by Jhong, composites were formed by mixing hydrolyzed soy protein isolate (HSPI) NP aggregates with styrene butadiene (SB) latex, followed by freeze-drying and compression molding methods [381]. The results show that the fractal dimensions extracted from both linear and nonlinear viscoelastic data have good agreement with each other and the model fitting indicates that HSPI has a greater fractal dimension and highly compact structure. These nanocomposites were found to be having great potential as replacement for petroleum-based fillers (e.g., carbon black) in polymer composites with renewable agricultural based fillers for sustainability.

In another report by Chen and Zhang [382], the soy protein isolate/montmorillonite (SPI/MMT) nanocomposites were successfully prepared, and their structures and properties were characterized (Figure 8.12). The results revealed fine dispersion of the montmorillonite (MMT) layers and strong interactions between SPI and MMT creating significant improvement of the mechanical strength and thermo-stability of the SPI/MMT plastics. Similar works, wherein nanocomposites were prepared based on soy proteins and MMT have also been reported by Jin *et al.* [380] Kumar *et al.* [383], and Echeverría *et al.* [384].

In a different approach, Huang and Netravali [379], fabricated environment-friendly, sustainable, and biodegradable "green" composites using modified soy protein concentrate (SPC) resins and flax yarns and fabrics. The modified SPC resin, prepared by cross-linked SPC with nano-clay particles using glutaraldehyde, showed significantly improved mechanical properties. Flax fiber was used as the reinforcement material, in both yarn and fabric forms, individually, to fabricate "green" composites.

SPI composites have also been explored as potential drug delivery candidates. In one of the reports by Teng *et al.* [385], complex NPs were developed from carboxymethyl chitosan and SPI by a simple ionic gelation method. Vitamin D_3 was successfully incorporated into the polymeric complex, forming particles with

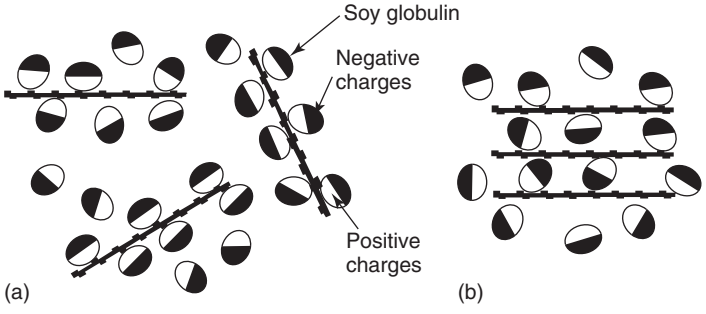

Figure 8.12 Schematic illustration of the electrostatic interaction between soy globulins and MMT, (a) highly exfoliated state and (b) intercalated state. Positively charged domains are colored in white and negatively charged domains are in black [382]. (Reproduced with permission.)

sizes between 162 and 243 nm and zeta potentials ranging from −10 to −20 mV with an encapsulation efficiency of 96.8%. While in another report by Teng *et al.* [373], SPI was conjugated with folic acid to prepare NPs for target specific drug delivery. Curcumin as a model drug was encapsulated successfully (encapsulation efficiency of 92.7%) into folic acid–SPI NPs, evidenced by X-ray diffraction study. Further cell culture study showed that conjugation of folic acid resulted in an increase in cellular uptake by at most 93% in Caco-2 cells, suggesting that nanoconjugate was a potential wall material for encapsulation and enhanced delivery of anticancer drugs.

8.6
Casein (CAS)

Protein-based drug delivery systems hold great promise due to their extraordinary biocompatibility, biodegrability, low toxicity, and natural metabolism as proteins are generally recognized as safe (GRAS) raw materials with high nutritional value and abundant renewable sources. Casein (CAS) proteins are commonly found in mammalian milk, making up 80% of the protein in cow milk and between 20 and 45% of the protein in human milk and rich in proline [386]. Casein has a wide variety of uses, from being a major component of cheese, to use as a food additive, to a binder for safety matches [387]. As a food source, casein also supplies amino acids; carbohydrates; and two inorganic elements, calcium and phosphorus.

8.6.1
Structure and Properties of Casein Nanomaterials

Caseins have high proline content with distinctive hydrophobic and hydrophilic domains and open flexible rheomorphic conformation and can assume any one of several energetically favorable conformations in solution. They can adapt to their environment by altering their conformation, and therefore they are highly flexible than globular proteins [388, 389]. Casein comprises about 94% protein and 6% low molecular weight compounds collectively called "calcium phosphate." Casein from Latin *caseus*, "cheese" is the name for a family of related phosphoproteins (alpha (αS1, αS2), beta (β), and kappa (κ)) with molecular weight of 19–25 kDa, and an isoelectric point (IEP) of 4.2–5.8 [390–392]. Each phosphoprotein has its own amino acid composition, genetic variations, and functional properties [393]. Naturally, casein self-assembles into micelles with diameters ranging from 50 to 500 nm, acting as natural nanovehicles for delivery of calcium, phosphate, and other biomolecules [394–398]. α- and β-CASs are both insoluble in water and are solubilized by the micelle surrounding them. κ-Casein molecules protrude their hydrophilic C-terminal domains into the aqueous environment and stabilize the mycelium structure. Many researchers tried to interpret the internal structure of CAS micelles. Buchheim and Welsch, are the two authors who were the first to propose that caseinate subunits and calcium phosphate can assemble together to form the final casein micelles [399]. Further, Schmidt, Both,

and Walstra developed a model based on casein-submicelles held together by calcium phosphate clusters, which would act as a supramolecular glue to hold together the submicelles [400]. By this time, the κ-casein molecule's role to be confined to the surface of the micelles has been proved [401, 402]. A new model with submicelles with αs- and β-caseins (14 nm size) held together by calcium phosphate nanoclusters were pictured by Walstra in the late 1990s [402]. Yet even now, re-interpretations of the casein structural models continue to flourish and are well reviewed by Mezzenga and Fischer [403].

8.6.2 Origin of Casein

Caseins, the largest protein components in milk, have desirable emulsification, gelation, water binding properties, and block copolymers with high levels of hydrophobic or hydrophilic amino acid residues. Therefore, they exhibit a strong tendency to self-assemble into spherical micelles (50–500 nm in diameter, 150 nm average diameters) [404, 405]. CAS exists in milk as a calcium salt, calcium caseinate. Calcium caseinate has an isoelectric point of pH 4.6 and it is insoluble in solutions with a pH < 4.6. The pH of milk is 6.6; therefore, casein has a negative charge at this pH and is solubilized as a salt. If an acid is added to milk, the negative charges on the outer surface of the casein micelles are neutralized, by protonation of the phosphate groups. The casein micelles destabilize or aggregate because the electric charge is decreased to that of the isoelectric point (pH at which there is no net charge because there are equal number of positive and negative charges present). The casein micelles disintegrate and the casein (the neutral protein) precipitates because it is no longer polar, with the calcium ions remaining in solution. CAS components in the internal micellar nanostructures are held together through hydrophobic interactions, together with the interlocking effect of colloidal calcium phosphate (CCP) that is bound to the phosphorylated serine in the casein side chains (mainly for as αS1, αS2, and β-casein) [406, 407]. As for the external surface of the micelle, k-casein is the dominant component, and is distributed and covers the surface to form a hydrophilic, negatively charged, and diffusible "hairy layer" ensuring the stability of CAS micelles by intermicellar electrostatic and steric repulsion [408]. Generally, the hydrophobic interactions, calcium bridging, and the electrostatic interactions together maintain the structural integrity and prevent the dissociation of CAS micelles.

In addition to its excellent biocompatibility and biodegradability, CAS has pH-responsive structural, conformational, and functional changes, and is heat-stable up to 60–70 °C. These unique structural and physicochemical properties of CAS provide functionality in drug delivery systems. These properties include the ability to bind ions and small molecules; self-assembly properties, excellent surface activity, and emulsion stabilization property. CAS is also a good candidate when it comes to gelation, film-forming capacity, and binding capacities. They are also regarded as a potential film-forming agent for the coating of pharmaceutical dosage forms.

8.6.3
Casein Nanomaterials: Preparation, Characterization, and Applications

Drug delivery systems based on casein have been prepared, for example, via polyelectrolyte ionic complexation, cross-linking and heat gelation, and graft copolymerization [404]. Other mechanisms for NP formation have been based on casein's tendency to self-assemble and form micelles. Casein-based nanoformulations are promising materials for controlled drug delivery applications in pharmaceutics. Spherical NPs of 200 nm were prepared by grafting dextran to casein through the Maillard reaction. The hydrophilic dextran shell with casein core and encapsulated carotene was synthesized by the green process [409]. CAS nanogels were also prepared by enzymatic cross-linking using casein's open tertiary structure. An enzyme transglutaminase creates nanogel particles consisting of a covalently linked casein network from which micellar calcium phosphate (MCP) can be removed without compromising their structural integrity [410]. Furthermore, these nanogel particles can be used potentially for a number of encapsulation and protection technologies, for instance to transport minerals, vitamins, and pharmaceuticals. Polyelectrolyte ionic complexation was used for the formation of electrostatic complexes between sodium caseinate and gum arabic. The slow acidification *in situ* with glucono-δ-lactone (GDL) or titration with HCl resulted in 100–150 nm NPs [411, 412].

8.6.3.1
Casein Nanosized Micelles/Nanocapsules

Casein micelles from milk are in effect nanocapsules created by nature to deliver nutrients, encapsulated hydrophobic nutraceuticals, and bioactive compounds such as calcium, phosphate, and protein, to the neonate [405]. CAS micelles are considered as natural nanocapsules (almost spherical aggregates, 50–500 nm in diameter (150 nm in average)). The micelles are very stable in processing and retain their basic structural identity during processing of milk into various products [404, 405]. They have also gained importance in various fields like food, cosmetics, and medicine. For the delivery of nutraceutical compounds like lipophilic vitamin D_2, they have been nanoencapsulated into the hydrophobic core of CAS micelles to achieve high bioavailability. The micelles not only provide protection to entrapped compound in aqueous environment, but also from heat and UV-light induced degradation [405, 413]. Another hydrophobic nutraceutical omega-3 fatty acid docosahexaenoic acid (DHA) has also been encapsulated into CAS micelles and NPs [404, 414]. DHA loaded CAS micelles as well as NPs displayed remarkable protection against oxidation of DHA [415]. The entrapment of hydrophobic anticancer drugs such as curcumin, mitoxantrone, vinblastine, irinotecan, paclitaxel (Ptx), and docetaxel into casein micelle has been studied by Shapira and colleagues and proved that the CAS micelles can improve thermodynamic stability of the drug significantly [416–419]. The complexation of the poorly soluble chemopreventive agent curcumin with the natural nanostructure of bovine casein micelles and its application in drug delivery to cancer cells was

investigated [406]. The Casein Micelle (CMs) were roughly spherical in shape with an average size of 166.3 nm. In a recent study, Ghasemi and Abbasi [420], have shown that using alkaline pH solely or along with ultrasound treatment (in natural environment of milk) results in creation of natural casein micelle nanocapsules with high encapsulating efficiency while maintaining the natural structure and morphological features.

8.6.3.2 Casein Nanogels

Nanogels can be termed as hydrogels if they are composed of water-soluble and swellable polymer chains. Caseins have excellent gelation properties; especially acid gelation of CASs is based on isoelectric precipitation. Gelation can also be achieved by proteolytic cleavage (rennet-induced gelation) of κ-caseins hydrophilic "hairy layer" to form aggregated micelles. In general, nanogel (1 – 1000 nm) particles are cross-linked gel particles capable of delivering a wide variety of drugs to various parts of body for a sustained period. Genipin is a natural cross-linking reagent that is approximately 10 000 times less toxic than glutaraldehyde. Due to its low toxicity, it provides an alternative to the micelle aggregation. Genipin cross-linked CAS NPs have been prepared by spray-drying and are used in food technology applications [404].

8.6.3.3 Casein-Polyelectrolyte Complex Nanoparticles

Caseins and casein spheres can directly deliver cargos into the cytoplasm of cells making them potential nanoscale cell-penetrating and protein-based drug carriers. Development of nanosized drug carriers that can penetrate the cells themselves and avoid lysosomal degradation is highly desirable, because it would enable effective targeted drug delivery and drastically improve the therapeutic efficacy of encapsulated compounds. Caseins and casein nanospheres hold significant promise in the development of novel drug and gene delivery systems with superior biocompatibility in the future.

The structural features of CAS enable them to form complexes with multivalent cationic as well as anionic macromolecules [411]. The interactions can be either attractive or repulsive. Attractive interactions, which almost always arise from electrostatic interactions between two oppositely charged polymers/biopolymers, induce inter-polymer complexes. The pH and ionic strength are important factors that influence the formation of these complexes, because both of these factors affect the number of charges present on the backbone of polymers/biopolymers, and therefore influence the intensity of electrostatic interactions. Liu *et al.* [421] have prepared cell-penetrating biocompatible hollow casein spheres in aqueous solution based on the molecular self-assembly of casein in the absence of surfactant, organic solvent, template core, or emulsion phase (Figure 8.13). The hollow casein spheres (40 nm sized) were prepared by polymerizing acrylic acid monomers in the presence of caseins and propionic acid, followed by the cross-linking of caseins, and removal of the poly acrylic acid (PAA). Figure 8.13

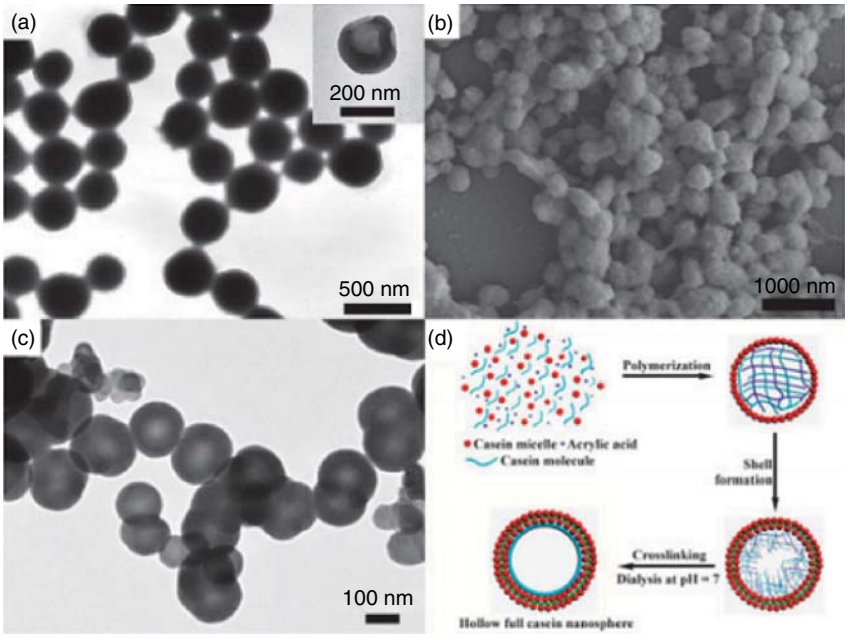

Figure 8.13 (a) TEM image of the uncrosslinked casein-PAA nanospheres, Inset is a cut-section TEM image of the particle; (b) SEM image of the cross-linked casein-PAA nanospheres; (c) cut-section TEM of the full casein nanospheres; and (d) showing the formation of hollow casein spheres [421]. (Reproduced with permission.)

shows the proposed formation mechanism of hollow full casein nanospheres. The generated PAA polymers interacted with the positively charged free CAS monomers, which resulted in the polyelectrolyte complexes used for cisplatin (CDDP) drug loading.

The casein NPs cross-linked by transglutaminase were prepared, and CDDP, as a model antitumor drug, was loaded into the casein NPs. The antitumor effect of CDDP-loaded NPs was evaluated on hepatic H22 tumor-bearing mice model via intravenous administration. It was found that the obtained NPs showed spherical shape with the size of 257 nm, and drug loading content of 10% [422].

8.6.3.4 Characterization of Nanoparticles

Several features can be examined in the physical characterization of NPs, for example, size, morphology, surface area, surface charge, surface hydrophobicity, surface adsorbates, density, and interior structure. Several methods should be used in parallel to support each other and confirm the interpretation of the obtained results. There are many techniques available for the particle size measurements, and the appropriate method is usually selected based on the

purpose of the measurement and mean size distribution of NPs. A combination of two or more techniques is usually needed to obtain reliable results. Light scattering and electron microscopy techniques are among the most widely used techniques for particle size measurements. AFM is a more demanding technique than electron microscopy techniques but ultrahigh resolution is obtainable with this technique. AFM scans can identify large bimodal size distributions regardless of particle shape, and AFM analysis of an unknown particle mixture could serve as a screening technique prior to light scattering analysis.

Another widely used method is confocal fluorescence microscopy. It has been used for the *in vitro* permeability studies of the shell structures of core-shell NPs, and also to study cellular uptake of NPs and the release of encapsulated materials. An array of more specific methods can be used in addition to the above methods, in the characterization of polyelectrolyte complex NPs, to gain information on morphological and structural features or binding behavior. For example, the composition can be analyzed with methods such as high performance liquid chromatography, size exclusion chromatography, infrared spectroscopy, NMR spectroscopy, and quartz crystal microbalance.

8.6.4 Casein Nanocomposites: Preparation, Characterization, and Applications

Casein-based nanocarriers could be excellent in the conservation of sensitive bioactive compounds throughout the shelf-life of pharmaceutical products. PLGA–casein polymer–protein hybrid nanocarrier (190 ± 12 nm) with entrapped chemically distinct combination (hydrophobic/hydrophilic) of model drugs such as Ptx and epigallocatechin gallate (EGCG) was recently reported. A simple emulsion–precipitation route was adopted by authors to prepare nearly monodispersed NPs with distinct core/shell morphology entrapping Ptx in the core and EGCG in the shell, with the intention of providing a sequential and sustained release of these drugs [423]. In another attempt, biocompatible hollow magnetic supraparticles: ultrafast microwave-assisted synthesis, casein-micelle-mediated cavity formation, and controlled drug delivery has reported by Xu *et al.* [424]. Uniform hollow magnetic supraparticles with nanocrystal aggregates in shells are fabricated via a one-pot microwave irradiation process within 10 min, employing casein, as a structure-directing agent. The proposed scheme is shown in Figure 8.14.

In another study, nanosize emulsion of fish oil has been produced by using inulin and CAS as coating material. An ultrasound generator was used to prepare nanoemulsion and further emulsion was converted to powder by lab-scale spray dryer [425]. Casein-based silica nanocomposite film for drug delivery systems has been recently reported by Ma *et al.* [426]. This CAS-based silica nanocomposite was prepared via double *in situ* method, and the as-prepared latex particles were evaluated in terms of their morphology and size through TEM.

In another attempt, CAS-based silica nanocomposite latex as bio-based film-forming material was synthesized from casein, caprolactam, acrylate,

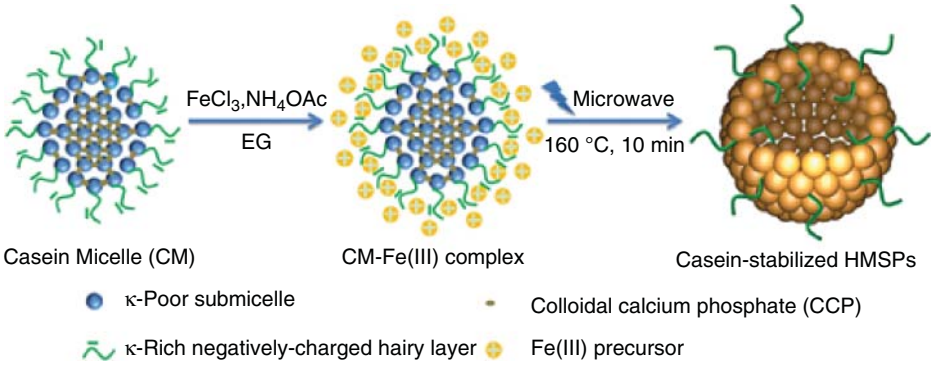

Figure 8.14 Schematic formation mechanism of the casein-micelles-mediated, microwave-assisted hollow magnetic supraparticles [424]. (Reproduced with permission.)

tetraethoxysilane, and silane coupling agent via double-*in situ* emulsion polymerization. The morphology of the resultant composite latex exhibited an evident core-shell structure with the average size of around 80 nm, and the improved shell thickness indicated the encapsulation of silica on the outer layer of the particle, which was verified by TEM results. The hybrid latex film containing silica showed higher hydrophobicity, lower water absorption, enhanced tensile strength, and decreased flexibility [422, 426].

Metal oxides and their CAS nanocomposites are also gaining interest as CAS provides biocompatibility and stability to the metal nanomaterials. AgNPs prepared using two surfactants (sodium dodecyl sulfate and Tween 80) and two natural polymers (casein and gelatin) were used as heterogeneous catalysts in a model reaction based on reduction of 4-Nitrophenol using sodium borohydride under alkaline conditions [427]. A green route based on the casein hydrolytic peptides (CHPs) has been established by Ghodake *et al.* [428], for the synthesis of highly stable and smaller sized (10 ± 5 nm) AgNPs, without producing any type of toxic byproducts. While in another study, milk casein protein coated magnetic iron oxide (IO, that is, Fe_3O_4, γ-Fe_2O_3) NPs with a core size of 15 nm and hydrodynamic diameter 30 nm were prepared and tested for diagnostic and therapeutic applications. These CAS-IONPs exhibited excellent water-solubility, colloidal stability, and biocompatibility and hence can be used as biomarker targeted magnetic NPs for magnetic resonance imaging (MRI) contrast enhancement and related biomedical applications [429]. The magnetic NPs–casein nanocomplexes were prepared by using fractions of milk, namely, whole milk, skimmed milk, and whey (milk serum), and their properties were studied using a variety of experimental tools. These CAS nanocomplexes showed an improved biocompatibility for biomedical applications owing to their easy manipulation using an external stimulus. The interaction of iron oxide NPs with casein micelles was studied using DLS size measurement, Ultraviolet–visible (UV–vis) spectroscopy, Fourier Transform Infrared spectroscopy, Thermo Gravimetric Analysis (TGA),

rheology, and phase contrast microscopy [430]. Casein stabilized s reversible agglomeration of AgNPs to form protein–AgNP composite agglomerates as the pH approaches to the isoelectric point of casein protein. Cytotoxicity and the cellular uptake of these hybrid NPs showed their possible potential in bioapplications [431].

Commercially, Casein is isolated from milk and is industrially important because after dissolving in alkaline solutions and drying, it becomes a sticky substance that can be used in glues, coating of paper, and in the binding of colors in paints and wallpaper. When isolated under sanitary conditions and dissolved in alkaline solutions, casein is also employed in the manufacture of pharmaceutical and nutritional products. Only recently, CAS micelles were harnessed for delivering exogenous hydrophobic bioactives. CAS micelles effectively protected vitamin D_2 and DHA against UV light-induced degradation and oxidation, respectively [405, 413]. In recent years, CAS-based nanoformulations have been prepared to deliver both nutraceuticals and synthetic drugs [395, 404]. The entrapment of hydrophobic anticancer drugs such as curcumin, mitoxantrone, vinblastine, irinotecan, Ptx, and docetaxel into casein micelle has been studied and proved that the CAS micelles can improve thermodynamic stability of the drug significantly [414]. CAS has wide applications as nano-vehicles in drug delivery systems [414], in tablet coating [432, 433], as nanovehicles for oral delivery of chemotherapeutic drugs, and so on [416, 417]. Their interactions with surfactants and polyelectrolytes have been studied systematically [434, 435].

The drug-loading mechanisms into protein NPs include for instance electrostatic attractions, hydrophobic interactions, and covalent bonding. A novel particulate delivery matrix based on ionically cross-linked casein (CAS) NPs was developed for controlled release of the poorly soluble anticancer drug flutamide (FLT). NPs were fabricated via oil-in-water emulsification and then stabilized by ionic cross-linking of the positively charged CAS molecules below their isoelectric point, with the polyanionic cross-linker sodium TPP. With the optimal preparation conditions, the drug loading and incorporation efficiency achieved were 8.73 and 64.55%, respectively [436].

Currently, interest has been focused on the development of various technologies for detecting and measuring the presence of milk allergens in food products by immunoassays. Electrochemical immunosensor for casein based on gold NPs and poly l-arginine/multiwalled carbon nanotubes composite film. This functionalized interface was further successfully applied to the determination casein in cheese samples [390]. Facile preparation of casein micelle stabilized sub-10 nm gold NPs, which are hydrophilic and biocompatible, were synthesized in aqueous medium by chemical reduction of $HAuCl_4$ in the presence of amphiphilic casein micelles protein aggregates, by Liu *et al.* [421]. Soejima *et al.*, reported that gold NPs were fabricated by reduction of highly concentrated Au (III) ions with casein proteins from milk. The gold NPs were converted to NP powders after washing and subsequent vacuum drying without aggregation [437].

8.7
Alginates

Alginates are a family of polymers, containing 1,4-linked p-D-mannuronic and a-L-guluronic acid residues in varying proportions and sequential arrangements. They form gels with divalent ions like calcium, and the gel-forming properties are strongly correlated with those of the L-guluronic acid residues in the polymeric chains [438].

8.7.1
Structure and Properties

Alginates are linear unbranched copolymers that contain homopolymeric blocks of (1,4)-linked b-D-mannuronic acid (M) and its C-5 epimer, a-L-guluronic acid (G) residues, respectively, which are covalently linked together in different sequences or blocks [439]. The blocks are either similar or strictly alternating (MMMMM, GGGGGG, or GMGMGM), and the relative amount depends on the origin of the ALG (Figure 8.15).

Alginates have the property to form gels in the presence of certain divalent (or multivalent) cations, particularly Ca^{2+}. The physical properties of the gel will depend on the ratio of uronic acids within the polysaccharide chains; alginates rich in L-guluronate form strong but brittle gels whereas those rich in D-mannuronate are weaker but more flexible. The ratio of D-mannuronate to L-guluronate (M : G ratio) can be used as an index of the nature of the gel that will be formed in the presence of divalent cations [441].

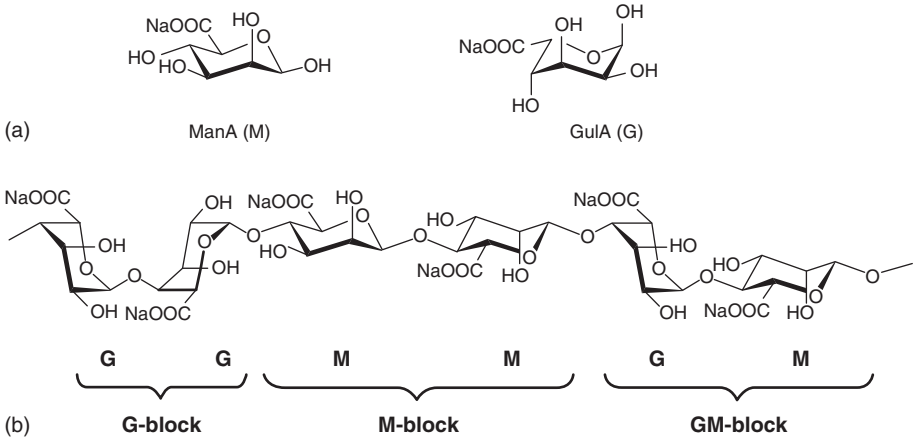

Figure 8.15 Alginate chemical structure: (a) β-D-mannuronic acid (M) sodium salt and α-L-guluronic acid (G) sodium salt. (b) The block composition of alginate with G-blocks, M-blocks, and MG-blocks [440]. (Reproduced with permission.)

8.7.2 Origin of Alginates

Alginates are produced by algae and bacteria. The commercially available alginates are derived primarily from brown algae. ALG is recognized as a structural component of marine algae, where it constitutes up to 40% of the dry matter. It provides the mechanical strength and flexibility of the seaweed. Thus it is regarded as having the same function in algae as those of cellulose and pectins in terrestrial plants [440].

Common algae species that are commercially important include *Laminaria hyperborea, Ascophyllum nodosum,* and *Macrocystis pyrifera*. The commercial production of alginates involves mainly alkaline extraction processes. Brown algae collected are dried and undergo various chemical treatments to remove impurities normally present, (e.g., heavy metals, endotoxin, proteins, other carbohydrates, and polyphenols) before being processed into finished raw material as a powder in the acid or salt form (Sutherland, 1991) [442].

The worldwide annual industrial production of ALG is estimated to be 30 000 metric tons. The main industrial applications of ALG as a natural polymeric material are linked to its stabilizing, viscosifying, and gelling properties and its ability to retain water. ALG is largely used as a viscosifier in textile printing because of its shear-thinning characteristics. In the food industry, ALG is widely used as an additive for the production of low-sugar jam, jellies, and fruit fillings [440]. Among biomedical applications, apart from industrial usealginate hydrogels have been particularly attractive in wound healing, drug delivery, and tissue engineering. These gels have been found to retain structural similarity to the extracellular matrices in tissues and can be manipulated to play several critical roles [443].

8.7.3 Alginates Nanomaterials: Preparation, Characterization, and Applications

Calcium alginate gels have been used for encapsulation and controlled release of peptides and proteins as well as of DNA. Macroscopic calcium alginate beads (1 – 3 mm) can be easily produced by dripping an aqueous solution of ALG into another solution containing calcium ions. However, NPs are more difficult to prepare. Most preparation methods require large input of mechanical energy by, for instance, shearing or ultrasonication, or solvent exchange procedures, to attain a sufficient increase in the surface-to-volume ratio [444].

It has been reported recently that calcium alginate NPs were prepared in the aqueous phase of water-in-oil (w/o) nanoemulsions. The emulsions were produced from mixtures of the nonionic surfactant tetraethylene glycol monododecyl ether, decane, and aqueous solutions of sodium alginate by means of the phase inversion temperature (PIT) emulsification method. NPs collected from the emulsion droplets using a gentle extraction procedure showed a size

in the sub-200 nm range, having potential as drug delivery agents [444]. In a similar study by Nesamony *et al.* [445], 350 nm sized calcium alginate NPs were produced by sonication. The particles were isolated and characterized via low-vacuum SEM. The NPs were evaluated as a drug delivery system by incorporating bovine serum albumin and performing *in vitro* release and sodium dodecyl sulfate-polyacrylamide gel electrophoresis studies [445]. In another report on ALG NPs synthesis using the water-in-oil emulsion method, superparamagnetic sodium alginate NPs with diameter around 25–30 nm were prepared, which has potential in industrial enzyme immobilization [446]. Similar reports of ALG NPs preparation using water-in-oil emulsion method have been reported by Paques *et al.* [447, 448] and Angelescu *et al.* [449, 450].

ALG derivatives were also used for NPs preparation for their potential use in drug delivery. As reported by Li *et al.* [451], hydrophobic alginate derivative was prepared by modification of ALG by acid chloride reaction using oleoyl chloride without organic solvents. The conjugate of oleoyl alginate ester formed self-assembled NPs at low concentrations in aqueous medium, and the NPs retained their structural integrity both in simulated gastric fluid and simulated intestinal fluid. The loading and release results of NPs using vitamin D3 as a model revealed the potential of oleoyl alginate ester NPs as oral carriers for sustained release of nutraceutical [451]. For extensive information on ALG NPs a recent review article by Paques *et al.* [450], is recommended.

8.7.4
Alginates Nanocomposites: Preparation, Characterization, and Applications

Medical and pharmaceutical industries have shown increased interest in alginates in particular because of their usefulness in specific applications, as they enhance efficient treatment of esophageal reflux, create multiquality calcium fibers for dermatology, and stimulate wound healing. They are also used for high and low gel strength dental impression materials. Besides this, ALG is an effective natural disintegrant, tablet binder, and offers an attractive alternative for sustained-release systems [452, 453]. It also offers advantages over synthetic and other polymers as it forms hydrogels under relatively mild pH and temperature and is generally regarded as nontoxic, biocompatible, biodegradable, less expensive, and abundantly available in nature; in addition, ALG meets the important requirement of being amenable to sterilization and storage. All these advantages make alginates very useful materials for biomedical applications, especially for controlled delivery of drugs and other biologically active compounds and for the encapsulation of cells. Calcium alginate is also a natural hemostat, and therefore, ALG-based dressings are indicated for bleeding wounds [454]. ALG nanocomposites using different materials improve the stability of the nanomaterials and can help in regulating the porosity of the membranes. Some of the examples of ALG nanocomposites and their details studies are enlisted in Table 8.4.

Table 8.4 Properties and characterization of alginate nanocomposites.

Type of nanostructures	Nanocomposite properties	Type of characterization	Application	References
Bio-ALG nanocomposites				
CS-ALG nanocomposite	Composite with medical clay – Cloisite 30B	XRD, FTIR, SEM	Drug delivery: curcumin for oral chemotherapy	[451]
CS-ALG NPs	Method of preparation: ionotropic pregelation followed by polyelectrolyte complexation Average diameter: 20–50 nm	FTIR, TEM, HPLC	Nanosystem for delivery of hydrophobic compounds, drug delivery: nifedipine	[452]
CS-ALG NPs	Method of preparation: gelation Average diameter: 200 nm	DLS,TEM, DFA	Controlled drug release system-5-fluorouracil	[453]
CS-SA–CS NPs	Method of preparation: ionic gelation technique Average diameter: 329–505 nm	DLS,SEM, AFM, DFA	Ophthalmic application-5-fluorouracil	[454]
CS-ALG- NPs	Method of preparation: ionic gelation technique Average diameter: 196 ± 12 nm	Gel electrophoresis, drug release kinetics	epidermal growth factor receptor antisense vector	[455]
CS-ALG NPs	Method of preparation: ionotropic pregelation followed by polycationic cross-linking Average diameter: 100 ± 20 nm	Encapsulation efficiency (%), FTIR	Drug delivery applications: curcumin	[456]
Si-ALG-Nanocomposite beads	Method of preparation: template-removing method Average diameter: 160 ± 7, 450 ± 10, 600 ± 25 nm	SEM, Beads stability cell viability assay analysis	3D cell encapsulation and culture system	[457]
Si-ALG-Nanocomposite beads	Method of preparation: Sol–gel process Nanoparticle average diameter: 50–200 nm	TGA, SEM, XRD, magnetic properties	Drug carriers using iron oxide and fluorescein	[458]

CS-ALG NPs	Average diameter: 205–572 nm Zetapotential: 17.6–47.8 mV	TEM, AFM, FTIR, DSC, XRD	Ocular delivery: prolonged topical ophthalmic delivery of antibiotic, gatifloxacin	[459]
NCC-ALG (nanocrystalline cellulose-alginate)	Nanocomposite film with high tensile strength and thermal stability	SEM, FTIR, XRD	Thermostable film formation for food-packaging applications	[460]
Laponite-ALG	Nontoxic, injectable, high mechanical strength composite	FTIR, TGA, XRD, swelling rate	Biomedical application: drug carrier	[461]
Gel-ALG-hydroxyapatite nanocomposite	Biocompatible and biodegradable nanocomposite	FTIR, SEM, XRD	Biomedical applications: drug delivery, tissue engineering, and so on	[462]
Metal nanoparticles-ALG nanocomposites				
AgNPs-ALG-nanocomposite	Electrochemical synthesis: electrostatic extrusion technique	UV–vis spectroscopy, optical microscopy	Biomedical application	[463]
Au-ALG	Method of preparation: γ-irradiation Average diameter: 20–50 nm	UV–vis spectroscopy, FTIR	Biological applications	[464]
FeNPs-CS-ALG nanocomposite film	Average diameter of magnetic nanoparticles: 150–200 nm	UV–vis spectroscopy, TEM, FTIR	Metal-enhanced drug delivery system fabrication	[465]
ZnxCd1–xS–CS-ALG NPs	Method of preparation: spin-coating technique Average diameter: ~2 nm	TEM, AFM, XRD, ultraviolet–visible (UV–vis)	Optoelectronics, solar photovoltaic devices, and chemical/biological sensors	[466]
Synthetic polymer-ALG nanocomposites				
Tetrasodium thiacalix[4]arene tetrasulfonate (TSTC[4]AS-s-SA)-nanogel	Superparamagnetic nanocomposite and nanogel Average diameter: 50 nm	XRD, FTIR, SEM, DSC, TGA, AFM, VSM	Bionanoadsorbents for heavy metal ions different pollutant such as herbicides and fungicides	[467]
ALG-nBGC (bioactive glass ceramic)	Composite pore size: 100–300 nm	SEM, EDAX, AFM, FTIR, XRD, swelling ability	Periodontal tissue regeneration	[468]
GA-ALG NPs	Average diameter: 274.2 nm Zeta potential: −45.6 mV	XPS, TEM, DLS	Liver cancer: liver tumor chemotherapy	[469]
GA-ALG/DOX-ALG NPs	Average diameter: 274.2 nm Zeta potential: −45.6 mV	CAC, FTIR, TEM	Cancer therapy	[470]

XPS, X-ray photoelectron spectroscopy analysis; GA, glycyrrhetinic acid; CAC, critical aggregation concentration; DFA, drug feeding amount.

8.8 Other Polymers

Protein NPs represent a potential system for encapsulation and delivery of bioactive compounds and drugs due to their large surface area. A number of techniques have been employed in the preparation of protein particles, and it is the balance between the attractive and repulsive forces that determines the level of molecular aggregation and the size of the particles. As discussed before, some of these methods include emulsification and solvent extraction, salting out, complex formation, desolvation, and spray drying. Protein NPs for drug delivery have been prepared not only from animal origin proteins such as gelatin, collagen, albumin, milk proteins, silk proteins, and elastin but also plant proteins such as zein, gliadin, soy proteins, and lectins have been used as materials for protein NPs, because plant proteins reduce the risk of spreading animal protein related diseases. Few of these proteins and their nanoforms are discussed in the following text.

8.8.1 Gelatin/Collagen

Collagen (Coll) is the main structural protein of the various connective tissues in animals. Collagen, in the form of elongated fibrils, is mostly found in fibrous tissues such as tendons, ligaments and skin, and is also abundant in corneas, cartilage, bones, blood vessels, the gut, and intervertebral discs. The fibroblast is the most common cell that creates collagen. In muscle tissue, it serves as a major component of the endomysium. Collagen constitutes 1–2% of muscle tissue, and accounts for 6% of the weight of strong, tendinous muscles. Gelatin, which is used in food and industry, is collagen that has been irreversibly hydrolyzed.

Gelatin/Collagen-based matrix and reservoir NPs require cross-linkers to stabilize the formed nanosuspensions, considering that physical instability is the main challenge of nanoparticulate systems. Experimental evidences proved that D-glucose modified gelatin/collagen matrix NPs containing *Calendula officinalis* powder might be proposed as a safer alternative vehicle for anticancer treatments [471]. Coll–NP interactions are vital for many biomedical applications including drug delivery and tissue engineering applications. Iron oxide NPs synthesized using starch templates were functionalized by treating them with gum arabic, a biocompatible polysaccharide, so as to enhance the interaction between NPsurfaces and collagen [472]. Recently, Chen *et al.* [473], reported that collagen-specific peptide conjugated high-density lipoprotein (HDL) NPs as MRI contrast agents to evaluate compositional changes in atherosclerotic plaque regression.

Gelatin is one of the most versatile natural biopolymers widely used in pharmaceutical industries due to its biocompatibility, biodegradability, low cost, and numerous available active groups for attaching targeting molecules. Gelatin has a number of advantages as an NP material: it is a natural macromolecule that is readily available, it possesses a relatively low antigenicity [474] and a great deal of experience exists for its use in parenteral formulations [475]. Selective examples

of gelatin nanoparticles (GelNPs) and their applications are summarized in Table 8.5. The preparation of GelNPs by desolvation was first described in 1978. This methodology is not only very tedious but also causes irreversible aggregation during cross-linking [485]. Therefore, Coester *et al.* [485], used new methods for preparation of Gel NPs and their modification with two fluorescent dyes for cell uptake study. Elzoghby has done detailed overviews of GelNPs as drug and gene delivery systems for three decades. The author recommends reading this article for more insight of the GelNPs, their surface medications, and different applications [486].

8.8.2 Whey Protein

Whey protein NPs could be an appropriate tool for the manufacture of functional food products. In a recent report, whey protein isolate (WPI) nanoparticles (<100 nm), were reportedly prepared by diluting an alkaline solution of protein in ethanol at concentrations varying between 50 and 80% [487]. In another report, nanoparticulation was induced by acidification of diluted polymer dispersions followed by pH neutralization. NPs with a diameter ranging from 100 to 300 nm were produced depending on the pH of aggregation, the added calcium concentration, and the aging time at the aggregation pH (0–75 h) [488]. Sequential enzymatic cross-linking and heat pretreatments were reported by Zhang and Zhong [489] to enhance the heat stability of WPI. In the first route, WPI was cross-linked by transglutaminase before incorporation in microemulsions for heat pretreatment. In the second route, WPI was cross-linked by transglutaminase within microemulsions before thermal pretreatment. Particles produced from the two routes were different in dimension and heat stability and were also affected by the ratio of WPI and enzyme and cross-linking duration. Whey protein NPs with 100–300 nm have been prepared by thermal denaturation, pH cycling, and Ca^{2+} cross-linking [490]. Encapsulation of ethyl hexanoate in whey protein NPs (<300 nm) were prepared by cross-linking denatured whey protein through pH-cycling. The whey protein NPs reduced the mass transfer of aroma at the surface of the matrix and improved its retention [491].

8.9 Conclusions

Biopolymers have attracted a great deal of attention, as they have vast application possibilities in many areas due to their unique renewable and biodegradable properties. Numerous research publications on bionanomaterials and nanocomposites reflect the importance of each material. Their renewable, natural, biodegradable, biocompatible, hydrophilic polymer with nontoxic matrix are desirable properties for unlimited applications in biomedicine, water-treatment, biosensor fabrication, and so on. In this chapter, we tried to report the work

Table 8.5 Selective examples of gelatin nanoparticles and their applications.

Nanomaterial	Average diameter (nm)	Properties/method	Specific application		References
GelNPs-anti-CD3 antibody	250–300	Cross-linking: glutaraldehyde Polydispersity index: 0.02 Method of preparation: two-step desolvation process	Drug delivery	Drug: NeutrAvidin™	[476]
GelNPs	100–200	Cross-linking: glutaraldehyde Entrapment efficiency: 42%	Drug delivery	Drug: doxorubicin	[477]
GelNPs	288.3	Polydispersity index: 0.067 Low cytotoxicity Transfection ability of the loaded nanoparticles was tested on B16 F10 cells	Drug delivery	DNA delivery systems	[478]
GelNPs	100–1000	Drug-loading efficiency: 0.7%	Drug delivery	Intravesical bladder cancer therapy Paclitaxel	[479]
GelNPs thiolated gelatin nanoparticles	200	Zeta potential: −11.97 mV Spherical shape	Drug delivery	Intracellular delivery potential of plasmid DNA using nonviral vectors glutathione	[480]
LBL-GelNPs	200	Breast cancer cell line MBA-MD-231 as potently as free EGCG	Drug delivery	Drug delivery natural polyphenols	[481]
GelNPs	100–200	w/o emulsion drug loading efficiency 86%	Drug delivery	Delivery system for methotrexate	[482]
GelNPs	277.0 288.0 291.0	Avidin Method of preparation : two-step desolvation	Drug delivery	Carriers for biotinylated peptide nucleic acid (PNA) in antisense therapy	[483]
Amphiphilic gelatin–oleic acid (GO)	200–250	—	Drug delivery	Anticancer agents and low bioavailable drugs	[484]

based on the different bio-based polymers and their nanostructures. Effort has been aimed to provide current knowledge to this research area with remarkable development and highly diverse applications in daily life. Different biopolymers such as cellulose, chitin, starch, soy protein, casein, alginates, and other biopolymers and their nanostructure, as well as their properties, characterization, and applications were discussed in detail. In addition, some limitations of each polymer were also enlisted that need to overcome and achieve a wide range of high-tech applications. These biomolecules and their nanostructures such as NPs, nanorods, nanohydrogels, nanosheets, and so on, will serve as new inspirations for innovative technologies in the near future.

List of abbreviations

BC	Bacterial cellulose
BCNCs	Bacterial cellulose nanocrystals
CAC	Critical aggregation concentration
CAS	Casein
CCP	Colloidal calcium phosphate
CNCs	Cellulose nanocrystals
	Carbon nanotubes
CNWs	Cellulose nanowhiskers
DFA	Drug feeding amount
DMAc	*N*,*N*-Dimethylacetamide
DP	Degree of polymerization
EDAX	Energy Dispersive X-ray Spectroscopy
EMG	Enzymatically modified gelatin
	(2,3-Epoxypropyl) trimethylammonium chloride
	Fast Fourier transform
FLT	Flutamide
GA	Glycyrrhetinic acid
	High resolution transmission electron microscopy
	Ionic liquids
IO	Iron oxide
MCC	Microcrystalline cellulose
MFC	Microfibrillated cellulose
NFC	Nanofibrillated cellulose
NPs	Nanoparticles
NWs	Nanowires
	Poly(ethyleneimine)
PF	Plant fiber
	Poly(methacrylic acid)
polyDADMAC	Poly(diallyldimethylammonium chloride)
	Poly(sodium 4-styrenesulfonate)
	Polyvinylpyrrolidone

RC	Regenerated cellulose
SEM	Scanning electron microscopy
	Surface enhanced Raman scattering
	Technical Association of the Pulp and Paper Industry
	Triethanolamine
TEMPO	2,2,6,6-Tetramethylpiperidine-1-oxyl radical
UV	Ultraviolet
VC	Vegetable cellulose
WF	Wood fiber
XPS	X-ray photoelectron spectroscopy analysis

References

1. Moon, R.J., Martini, A., Nairn, J., Simonsen, J., and Youngblood, J. (2011) *Chem. Soc. Rev.*, **40**, 3941.
2. Aumelas, A., Serrero, A., Durand, A., Dellacherie, E., and Leonard, M. (2007) *Colloids Surf. B*, **59**, 74.
3. Bertholon, I., Hommel, H., Labarre, D., and Vauthier, C. (2006) *Langmuir*, **22**, 5485.
4. Bravo-Osuna, I., Schmitz, T., Bernkop-Schnürch, A., Vauthier, C., and Ponchel, G. (2006) *Int. J. Pharm.*, **316**, 170.
5. Janes, K.A., Fresneau, M.P., Marazuela, A., Fabra, A., and Alonso, M.J. (2001) *J. Controlled Release*, **73**, 255.
6. Liu, J., Wang, F.H., Wang, L.L., Xiao, S.Y., Tong, C.Y., and Tang, D.Y. (2008) *J. Cent. S. Univ. Technol.*, **15**, 768.
7. Marty, J.J. (1977) The preparation, purification, and properties of nanoparticles. D. Pharm Thesis, Victorian College of Pharmacy, Parkville, Australia, p. 30.
8. Marty, J.J., Oppenheim, R.C., and Speiser, P. (1978) *Pharm. Acta Helv.*, **53**, 17.
9. Weber, C., Coester, C., Kreuter, J., and Langer, R. (2000) *Int. J. Pharm.*, **194**, 91.
10. Eichhorn, S.J., Dufresne, A., Aranguren, M., Marcovich, N.E., Capadona, J.R., Rowan, S.J., Weder, C., Thielemans, W., Roman, M., Renneckar, S., Gindl, W., Veigel, S., Keckes, J., Yano, H., Abe, K., Nogi, M., Nakagaito, A.N., Mangalam, A., Simonsen, J., Benight, A.S., Bismarck, A., Berglund, L.A., and Peijs, T. (2010) *J. Mater. Sci.*, **45**, 1.
11. Payen, A. (1838) *Comptes Rendus*, **7**, 1052.
12. Klemm, D., Heublein, B., Fink, H., and Bohn, A. (2004) *Angew. Chem.*, **44**, 3358.
13. Mahmoudian, S., Wahit, M.U., Ismail, A.F., and Yussuf, A.A. (2012) *Carbohydr. Polym.*, **88**, 1251.
14. Jiang, G.S., Huang, W.F., Li, L., Wang, X., Pang, F.J., and Zhang, Y.M. (2012) *Carbohydr. Polym.*, **87**, 2012.
15. Poletto, M., Pistor, V., and Zattera, A.J. (2013) in *Cellulose-Fundamental Aspects*, Chpater 2 (eds T. Van de Ven and L. Gdbout), InTech, pp. 45–68.
16. John, M.J. and Thomas, S. (2008) *Carbohydr. Polym.*, **71**, 343.
17. O'Sullivan, A. (1997) *Cellulose*, **4**, 173.
18. Gautam, S.P., Bundela, P.S., Pandey, A.K., Khan, J., Awasthi, M.K., and Sarsaiya, S. (2010) *J. Appl. Natl. Sci.*, **2**, 330.
19. Atalla, R.H. and Vanderhart, D.L. (1984) *Science*, **223**, 283.
20. Sherif, M.A.S.K. (2014) *J. Bioprocess. Biotechniqu.*, **4**, 1000150.
21. Kai, A., Arashida, T., Hatanaka, K., Akaike, T., Matsuzaki, K., Mimura, T., and Kaneko, Y. (1994) *Carbohydr. Polym.*, **23**, 235.
22. Delmer, P.D. and Yehudit, A. (1995) *Plant Cell*, **7**, 987.
23. Clasen, C. and Kulicke, W.M. (2001) *Prog. Polym. Sci.*, **26**, 1839.
24. Dufresne, A. (2013) *Mater. Today*, **16**, 220.

25. Fengel, D. and Wegener, G. (1984) *Wood: Chemistry, Ultrastructure, Reactions*, Walter de Gruyter, Remagen, Kessel Verlag, Berlin, pp. 613–618.
26. Elazzouzi-Hafraoui, S., Nishiyama, Y., Putaux, J.L., Heux, L., Dubreuil, F., and Rochas, C. (2008) *Biomacromolecules*, **9**, 57.
27. Helbert, W., Nishiyama, Y., Okano, T., and Sugiyama, J. (1998) *J. Struct. Biol.*, **124**, 42.
28. Iwamoto, S., Kai, W.H., Isogai, A., and Iwata, T. (2009) *Biomacromolecules*, **10**, 2571.
29. Kimura, S. and Itoh, T. (1996) *Protoplasma*, **194**, 151.
30. Ross, P., Mayer, R., and Benziman, M. (1991) *Microbiol. Rev.*, **55**, 35.
31. Tanaka, M., Murakami, S., Shinke, R., and Aoki, K. (2000) *Biosci. Biotechnol., Biochem.*, **64**, 757.
32. Matthysse, A.G., White, S., and Lightfoot, R. (1995) *J. Bacteriol.*, **177**, 1069.
33. Blanton, R.L. and Northcote, D.H. (1990) *Planta*, **180**, 324.
34. Frei, E. and Preston, R.D. (1964) *Proc. R. Soc. London, Ser. B*, **160**, 314.
35. Kim, N.H., Herth, W., Vuong, R., and Chanzy, H. (1996) *J. Struct. Biol.*, **117**, 195.
36. Hanley, S.J., Revol, J.F., Godbout, L., and Gray, D.G. (1997) *Cellulose*, **4**, 209.
37. Imai, T. and Sugiyama, J. (1998) *Macromolecules*, **31**, 6275.
38. Baldan, B., Andolfo, P., Navazio, L., Tolomio, C., and Mariani, P. (2001) *Eur. J. Histochem.*, **45**, 51.
39. Habibi, Y., Lucia, L.A., and Rojas, O.J. (2010) *Chem. Rev.*, **110**, 3479.
40. Azizi, S.M.A.S., Alloin, F., and Dufresne, A. (2005) *Biomacromolecules*, **6**, 612.
41. Lavoine, N., Desloges, I., Dufresne, A., and Bras, J. (2012) *Carbohydr. Polym.*, **90**, 735.
42. Siro, I. and Plackett, D. (2010) *Cellulose*, **17**, 459.
43. Taniguchi, T. (1998) *Polym. Int.*, **47**, 29.
44. Reddy, J.P. and Rhim, J.W. (2014) *Carbohydr. Polym.*, **110**, 480.
45. Kalia, S., Dufresne, A., Cherian, M.B., Kaith, B.S., Avérous, L., Njuguna, J., and Nassiopoulos, E. (2011) *Int. J. Polym. Sci.*, **2011**, 1.
46. Lin, N., Huang, J., and Dufresne, A. (2012) *Nanoscale*, **4**, 3274.
47. Hubbe, M.A., Rojas, O.J., Lucia, L.A., and Sain, M. (2008) *BioResources*, **3**, 929.
48. Alemdar, A. and Sain, M. (2008) *Bioresour. Technol.*, **99**, 1664.
49. Sugiyama, J., Persson, J., and Chanzy, H. (1991) *Macromolecules*, **24**, 2461.
50. Pandey, J.K., Nakagaito, A.N., and Takagi, H. (2012) *Polym. Eng. Sci.*, **53**, 1.
51. Beck-Candanedo, S., Roman, M., and Gray, D.G. (2005) *Biomacromolecules*, **6**, 1048.
52. Wang, N., Ding, E., and Cheng, R. (2008) *Langmuir*, **24**, 5.
53. Dong, X.M., Kimura, T., Revol, J.F., and Gray, D.G. (1996) *Langmuir*, **12**, 2072.
54. Abe, K., Iwamoto, S., and Yano, H. (2007) *Biomacromolecules*, **8**, 3276.
55. Bondeson, D., Mathew, A., and Oksman, K. (2006) *Cellulose*, **13**, 171.
56. Isogai, A., Saito, T., and Fukuzumi, H. (2011) *Nanoscale*, **3**, 71.
57. Araki, J., Wada, M., Kuga, S., and Okano, T. (1998) *Colloids. Surf., A*, **142**, 75.
58. Saito, T., Nishiyama, Y., Putaux, J.L., Vignon, M., and Isogai, A. (2006) *Biomacromolecules*, **7**, 1687.
59. Saito, T., Kimura, S., Nishiyama, Y., and Isogai, A. (2007) *Biomacromolecules*, **8**, 2485.
60. Wang, S. and Cheng, Q. (2009) *J. Appl. Polym. Sci.*, **113**, 1270.
61. Chakraborty, A., Sain, M., and Kortschot, M. (2005) *Holzforschung*, **59**, 102.
62. Spagnol, C., Rodrigues, F.H.A., Pereira, A.G.B., Fajardo, A.R., Rubira, A.F., and Muniz, E.C. (2012) *Carbohydr. Polym.*, **87**, 2038.
63. Nakagaito, A.N. and Yano, H. (2004) *Appl. Phys. A*, **78**, 547.
64. De Souza, L.M.M. and Borsali, R. (2004) *Macromol. Rapid Commun.*, **25**, 771.
65. Bhatnagar, A. and Sain, M. (2005) *J. Reinf. Plast. Compos.*, **24**, 1259.
66. Wang, B. and Sain, M. (2007) *Compos. Sci. Technol.*, **67**, 2521.

67. Krassig, H.A. (1993) *Cellulose-Structure, Accessibility and Reactivity*, Gordon and Breach Science Publishers, Yverdon, pp. 307–314.
68. Ohad, I. and Mejzler, D. (1965) *J. Polym. Sci. Part A*, **3**, 399.
69. De Rodriguez, N.L.G., Thielemans, W., and Dufresne, A. (2006) *Cellulose*, **13**, 261.
70. Bai, W., Holbery, J., and Li, K.C. (2009) *Cellulose*, **16**, 455.
71. Angles, M.N. and Dufresne, A. (2001) *Macromolecules*, **34**, 2921.
72. Ding, S.Y. and Himmel, M.E. (2006) *J. Agric. Food. Chem.*, **54**, 597.
73. Ranby, B.G. and Ribi, E. (1950) *Cell. Mol. Life Sci.*, **6** (1), 12.
74. Ranby, B.G. (1952) *Tappi*, **35**, 53.
75. Ahola, S., Turon, X., Osterberg, M., Laine, J., and Rojas, O.J. (2008) *Langmuir*, **24**, 11592.
76. Filson, P.B., Dawson-Andoh, B.E., and Schwegler-Berry, D. (2009) *Green Chem.*, **11**, 1808.
77. Man, Z., Muhammad, N., Sarwono, A., Bustam, M.A., Kumar, M.V., and Rafiq, S. (2011) *J. Polym. Environ.*, **19**, 726.
78. Mao, J., Osorio-Madrazo, A., and Laborie, M.P. (2013) *Cellulose*, **20**, 1829.
79. Siqueira, G., Tapin-Lingua, S., Bras, J., da Silva, P.D., and Dufresne, A. (2010) *Cellulose*, **17**, 1147.
80. Ranby, B.G. (1949) *Acta Chem. Scand.*, **3**, 649.
81. Sacui, I.A., Nieuwendaal, R.C., Burnett, D.J., Stranick, S.J., Jorfi, M., Weder, C., Foster, E.J., Olsson, R.T., and Gilman, J.W. (2014) *ACS Appl. Mater. Interfaces*, **6**, 6127.
82. Peng, B.L., Dhar, N., Liu, H.L., and Tam, K.C. (2011) *Can. J. Chem. Eng.*, **89**, 1191.
83. Missoum, K., Belgacem, M.N., and Bras, J. (2013) *Materials*, **6**, 1745.
84. Bilodeau, M. (2012) Potential applications of nanofibrillated cellulose in printing and writing papers. Proceedings of the 2012, TAPPI International Conference on Nanotechnology for Renewable Materials, Montreal, QC, Canada, 4–7 June 2012.
85. Ensor, D. and Nieh, W.L.S. (2012) INSCC workshop on international standards for cellulose nanomaterials. Proceedings of the 2012, TAPPI International Conference on Nanotechnology for Renewable Materials, Montreal, QC, Canada, 4–7 June 2012.
86. Herrick, F.W., Casebier, R.L., Hamilton, J.K., and Sandberg, K.R. (1983) *J. Appl. Polym. Sci.*, **28**, 797.
87. Turbak, A.F., Snyder, F.W., and Sandberg, K.R. (1983) *J. Appl. Polym. Sci.*, **28**, 815.
88. Zimmermann, T., Bordeanu, N., and Strub, E. (2010) *Carbohydr. Polym.*, **79**, 1086.
89. Dinand, E., Maureaux, A., Chanzy, H., Vincent, I., and Vignon, M.R., 1996, Eur. Patent 0726356.
90. Habibi, Y. and Vignon, M. (2008) *Cellulose*, **15**, 177.
91. Siqueira, G., Bras, J., and Dufresne, A. (2008) *Biomacromolecules*, **10**, 425.
92. Bhattacharya, D., Germinario, L.T., and Winter, W.T. (2008) *Carbohydr. Polym.*, **73**, 371.
93. Bendahou, A., Kaddami, H., and Dufresne, A. (2010) *Eur. Polym. J.*, **46**, 609.
94. Siqueira, G., Tadokoro, S., Mathew, A.P., and Oksman, K. (2010) Proceedings of the 2010 TAPPI International Conference on Nanotechnology for the Forest Product Industry, Espoo, Finland, September 27–29, 2010.
95. Siqueira, G., Bras, J., and Dufresne, A. (2010) *BioResources*, **5**, 727.
96. Benhamou, K., Dufresne, A., Magnin, A., Mortha, G., and Kaddami, H. (2014) *Carbohydr. Polym.*, **99**, 74.
97. Haugaard, V.K., Udsen, A.M., Mortensen, G., Hoegh, L., Petersen, K., and Monahan, F. (2001) *Stärke*, **53**, 189.
98. Pandey, J.K., Kumar, A.P., Misra, M., Mohanty, A.K., Drzal, L.T., and Singh, R.P. (2005) *J. Nanosci. Nanotechnol.*, **5**, 497.
99. Wan, W.K., Hutter, J.L., Millon, L., and Guhados, G. (2006) in *Cellulose Nanocomposites: Processing, Characterization, and Properties*, vol. 938 (eds K. Oksman and M. Sain), American Chemical Society, Washington, DC, pp. 221–241.

100. Yano, H., Sugiyama, J., Nakagaito, A.N., Nogi, M., Matsuura, T., Hikita, M., and Handa, K. (2005) *Adv. Mater.*, **17**, 153.
101. Dalmas, F., Chazeau, L., Gauthier, C., Cavaille, J.Y., and Dendievel, R. (2006) *Polymer*, **47**, 2802.
102. Zhang, D., Zhang, Q., Gao, X., and Piao, G. (2013) *Int. J. Polym. Sci.*, **2013**, 175609, 1 pp.
103. Wu, M., Kuga, S., and Huang, Y. (2008) *Langmuir*, **24**, 10494.
104. Berlioz, S., Molina-Boisseau, S., Nishiyama, Y., and Heux, L. (2009) *Biomacromolecules*, **10**, 2144.
105. Kimura, S. and Itoh, T. (2004) *Cellulose*, **11**, 377.
106. Lima, M.M.S. and Borsali, R. (2002) *Langmuir*, **18**, 992.
107. Li, D., Liu, Z., Al-Haik, M., Teharni, M., Tannenbaum, R., and Garmestani, H. (2010) *Polym. Bull.*, **65**, 635.
108. Khandelwal, M. and Windle, A.H. (2013) *Polymer*, **54**, 5199–5206.
109. Revol, J.K. (1982) *Carbohydr. Polym.*, **2**, 123.
110. Sugiyama, J., Harada, H., Fujiyoshi, Y., and Uyeda, N. (1985) *Planta*, **166**, 161.
111. Miao, C. and Hamad, W. (2013) *Cellulose*, **20**, 2221.
112. Tokoh, C., Takabe, K., Fujita, M., and Saiki, H. (1998) *Cellulose*, **5**, 249.
113. Yamamoto, H. and Horii, F. (1994) *Cellulose*, **1**, 57.
114. Haigler, C.H., White, A.R., Brown, R.M., and Cooper, K.M. (1982) *J. Cell Biol.*, **94**, 64.
115. Brown, E.E. and Laborie, M.P.G. (2007) *Biomacromolecules*, **8**, 3074.
116. Pinto, R.J.B., Neves, M.C., Pascoal Neto, C.P., and Trindade, T., (2012) *Nanocomposites – New Trends and Developments, Composites of Cellulose and Metal Nanoparticles*, InTech, Chapter 4, pp. 73–96.
117. Sanchez, C., Rozes, L., Ribot, F., Laberty-Robert, C., Grosso, D., Sassoye, C., Boissiere, C., and Nicole, L. (2010) *C. R. Chim.*, **1**, 3.
118. Bagal, D., Vijayan, A., Aiyer, R.C., Karekar, R.N., and Karve, M.S. (2007) *Biosens. Bioelectron.*, **22**, 3072.
119. Bagal-Kestwal, D.R., Kestwal, R., and Chiang, B.H. (2009) *Biosens. Bioelectron.*, **24**, 2566.
120. Bagal, D., Kestwal, R., Hsieh, B.C., Chen, R.L.C., Cheng, T.J., and Chiang, B.H. (2010) *Biosens. Bioelectron.*, **26**, 118.
121. Bagal-Kestwal, D.R., Kestwal, R., and Chiang, B.H. (2011) *Sens. Actuators, A.*, **160**, 1026.
122. Bagal-Kestwal, D.R., Kestwal, R., and Chiang, B.H. (2011) *J. Biol. Macromol.*, **49**, 894.
123. Bagal, D. and Karve, M.S. (2006) *Anal. Chim. Acta*, **555**, 316.
124. Kestwal, R., Bagal-Kestwal, D.R., and Chiang, B.H. (2012) *Plant food Hum. Nutr.*, **67**, 136.
125. Bagal-Kestwal, D.R., Kestwal, R., Hsieh, W.T., and Chiang, B.H. (2014) *J. Pharm. Biomed.*, **88**, 571.
126. Santos, T.M., Souza Filho, M.M., Caceres, C.A., Rosa, M.F., Morais, J.P.S., Alaídes, M.B.P., and Azeredo, H.M.C. (2014) *Food Hydrocolloids*, **41**, 113.
127. Helbert, W., Cavaille, J.Y., and Dufresne, A. (1996) *Polym. Compos.*, **17**, 604.
128. Bondeson, D. and Oksman, K. (2007) *Composites Part A*, **38** (12), 2486.
129. De Menezes, A.J., Siqueira, G., Curvelo, A.A.S., and Dufresne, A. (2009) *Polymer*, **50**, 4552.
130. Goffin, A.L., Raquez, J.M., Duquesne, E., Habibi, Y., Dufresne, A., and Dubois, P. (2011) *Polymer*, **52**, 1532.
131. Dufresne, A. (2006) *J. Nanosci. Nanotechnol.*, **6**, 322.
132. Dufresne, A. (2006) *Can. J. Chem.*, **6**, 322.
133. Jung, R., Kim, Y., Kim, H.S., and Jin, H.J. (2009) *J. Biomater. Sci., Polym. Ed.*, **20**, 311.
134. Cai, J., Kimura, S., Wada, M., and Kuga, S. (2009) *Biomacromolecules*, **10**, 87.
135. Fidale, C.L., Nikolajski, M., Rudolph, T., Dutz, S., Schacher, F.H., and Heinze, T. (2013) *J. Colloid Interface Sci.*, **390**, 25.
136. Dankovich, T.A. and Gray, D.G. (2011) *Environ. Sci. Technol.*, **45**, 1992.
137. Ngo, Y.H., Li, D., Simon, G.P., and Gamier, G. (2011) *Adv. Colloid Interface Sci.*, **163**, 23.
138. Tankhiwale, R. and Bajpai, S.K. (2009) *Colloid Surf. B-Biointerfaces*, **69**, 164.

139. Fernandez, A., Picouet, P., and Lloret, E. (2010) *Int. J. Food Microbiol.*, **142**, 222.
140. Dallas, P., Sharma, V.K., and Zboril, R. (2011) *Adv. Colloid Interface Sci.*, **166**, 119.
141. Jiang, T., Liu, L., and Yao, J. (2011) *Fibers Polym.*, **12**, 620.
142. Kim, S.S., Park, J.E., and Lee, J. (2011) *J. Appl. Polym. Sci.*, **119**, 2261.
143. Diez, I., Eronen, P., Osterberg, M., Linder, M.B., Ikkala, O., and Ras, R.H.A. (2011) *Macromol. Biosci.*, **11**, 1185.
144. Martins, N.C.T., Freire, C., Pinto, R.J.B., Fernandes, S., Pascoal Neto, C., Silvestre, A., Causio, J., Baldi, G., Sadocco, P., and Trindade, T. (2012) *Cellulose*, **19**, 1425.
145. Hong, D., Snyder, J.F., Tran, D.T., and Leadore, J.L. (2013) *Carbohydr. Polym.*, **95**, 760.
146. Marques, P.A.A.P., Nogueira, H.I.S., Pinto, R.J.B., Neto, C.P., and Trindade, T. (2008) *J. Raman Spectrosc.*, **39**, 439.
147. Tokura, M.T.S. and Rujiravanit, R. (2008) *Carbohydr. Polym.*, **72**, 43.
148. Sharifi, N., Tajabadi, F., and Taghavinia, N. (2010) *Int. J. Hydrogen Energy*, **35**, 3258.
149. George, J., Kumar, R., Sajeevkumar, V.A., Venkata, R.K., Rajamanickam, R., Abhishek, V., and Nadanasabapathy, S.S. (2014) *Carbohydr. Polym.*, **105**, 285.
150. Zhang, T., Wang, W., Zhang, D., Zhang, X., Ma, Y., Zhou, Y., and Qi, L. (2010) *Adv. Funct. Mater.*, **20**, 1152.
151. Wang, W., Li, H.Y., Zhang, D.W., Jiang, J., Cui, Y.R., Qiu, S., Zhou, Y.L., and Zhang, X.X. (2010) *Electroanalysis*, **22**, 2543.
152. Wang, W., Zhang, T.J., Zhang, D.W., Li, H.Y., Ma, Y.R., Qi, L.M., Zhou, Y.L., and Zhang, X.X. (2011) *Talanta*, **84**, 71.
153. Martins, N.C.T., Freire, C.S.R., Neto, C.P., Silvestre, A.J.D., Causio, J., Baldi, G., Sadocco, P., and Trindade, T. (2013) *Colloids Surf., A: Physicochem. Eng. Asp.*, **417**, 111.
154. Jia, B., Mei, Y., Cheng, L., Zhou, J., and Zhang, L. (2012) *ACS Appl. Mater. Interfaces*, **4**, 2897.
155. Li, B., Chen, S., Hu, W., Shi, S., Shen, W., Zhang, X., and Wang, H. (2009) *Carbohydr. Polym.*, **76**, 509.
156. Yang, J., Yu, J., Fan, J., Sun, D., Tang, W., and Yang, X. (2011) *J. Hazard. Mater.*, **189**, 377.
157. Xiong, R., Lu, C., Wang, Y., Zhou, Z., and Zhang, X. (2013) *J. Mater. Chem. A*, **1**, 14910.
158. Liu, H., Wang, D., Shang, S., and Song, Z. (2011) *Carbohydr. Polym.*, **83**, 38.
159. Fortunati, E., Rinaldi, S., Peltzer, M., Bloise, N., Visai, L., Armentano, I., Jiménez, A., Latterini, L., and Kenny, J.M. (2014) *Carbohydr. Polym.*, **101**, 1122.
160. Cai, Z. and Kim, J. (2010) *Cellulose*, **17**, 83.
161. Seves, A., Testa, G., Bonfatti, A.M., Paglia, E.D., Selli, E., and Marcandalli, B. (2001) *Macromol. Mater. Eng.*, **286**, 524.
162. Yasuda, K., Gong, J.P., Katsuyama, Y., Nakayama, A., Tanabe, Y., Kondo, E., Uneno, M., and Osada, Y. (2005) *Biomaterials*, **26**, 4468.
163. Millon, L.E. and Wan, W.K. (2006) *J. Biomed. Mater. Res. B.*, **79**, 245.
164. Rescignano, N., Fortunati, E., Montesano, S., Emiliani, C., Kenny, J.M., Martino, S., and Armentano, I. (2014) *Carbohydr. Polym.*, **99**, 47.
165. Favier, V., Canova, G.R., Cavaille, J.Y., Chanzy, H., Dufresne, A., and Gauthier, C. (1995) *Polym. Adv. Technol.*, **6**, 351.
166. Dubief, D., Samain, E., and Dufresne, A. (1999) *Macromolecules*, **32**, 5765.
167. Dufresne, A., Kellerhals, M.B., and Witholt, B. (1999) *Macromolecules*, **32**, 73961.
168. Dufresne, A. (2003) *Compos. Interfaces*, **10**, 369.
169. Bendahou, A., Habibi, Y., Kaddami, H., and Dufresne, A. (2009) *J. Biobased Mater. Bioenergy*, **3**, 81.
170. Angle's, M.N. and Dufresne, A. (2000) *Macromolecules*, **33**, 8344.
171. Aranda, P. and Ruizhitzky, E. (1992) *Chem. Mater.*, **4**, 1395.
172. Noshiki, Y., Nishiyama, Y., Wada, M., Kuga, S., and Magoshi, J. (2002) *J. Appl. Polym. Sci.*, **86**, 3425.

173. Chazeau, L., Cavaille, J.Y., Canova, G., Dendievel, R., and Boutherin, B. (1999) *J. Appl. Polym. Sci.*, **71**, 1797.
174. Bonini, C. (2000) Mise en e'vidence du role des interactions fibre/fibre et fibre/matrice dans des nanocomposites a' renfort cellulosique et matrice apolaire (atactique et isotactique). PhD thesis. Joseph Fourier University, Grenoble.
175. Ruiz, M., Cavaille, M., Dufresne, J.Y., Graillat, A., and Gerard, C.J.F. (2001) *Macromol. Symp.*, **169**, 211.
176. Ray, S.S. and Okamoto, M. (2003) *Prog. Polym. Sci.*, **28**, 1539.
177. Cavaille, J.Y., Dufresne, A., Paillet, M., Azizi Samir, M.A.S., Alloin, F., and Sanchez, J.Y. French Patent FR2841255.
178. Dufresne, A. and Vignon, M.R. (1998) *Macromolecules*, **31**, 2693.
179. Trovatti, E., Fernandes, S.C.M., Rubatat, L., da Silva Perez, D., Freire, C.S.R., Silvestre, A.J.D., and Neto, C.P. (2012) *Compos. Sci. Technol.*, **72**, 1556.
180. Li, Z., Renneckar, S., and Barone, J.R. (2010) *Cellulose*, **17**, 57.
181. Pereda, M., Dufresne, A., Aranguren, M.I., and Marcovich, N.E. (2014) *Carbohydr. Polym.*, **101**, 1018.
182. Zhou, C. and Wu, Q. (2012) in *Nanocrystals – Synthesis, Characterization and Applications*, Chapter 6 (ed S. Neralla), InTech, pp. 103–120.
183. Ehrlich, H., Maldonado, M., Spindler, K.D., Eckert, C., Hanke, T., Born, R., Goebel, C., Simon, P., Heinemann, S., and Worch, H. (2007) *J. Exp. Zool. B: Mol. Dev. Evol.*, **308**, 347.
184. Dash, M., Chiellini, F., Ottenbrite, R.M., and Chiellini, E. (2011) *Prog. Polym. Sci.*, **36**, 981.
185. Jayakumar, R., Menon, D., Koyakutty, M., Nair, S.V., and Tamura, H. (2010) *Carbohydr. Polym.*, **82**, 227.
186. Rinaudo, M. (2006) *Prog. Polym. Sci.*, **31**, 603.
187. Smitha, K.T., Anitha, A., Furuike, T., Tamura, H., Nair, S.V., and Jayakumar, R. (2013) *Colloids Surf. B: Biointerfaces*, **104**, 245.
188. Ravi Kumar, M.N.V. (2000) *React. Funct. Polym.*, **46**, 1.
189. Nguyen, V.Q., Ishihara, M., Mori, Y., Nakamura, S., Kishimoto, S., Hattori, H., Fujita, M., Kanatani, Y., Ono, T., Miyahira, Y., and Matsui, T. (2013) *J. Nanomater.*, **2013**, 1.
190. Shi, C., Zhu, Y., Ran, X., Wang, M., Su, Y., and Cheng, T. (2006) *J. Surg. Res.*, **133**, 185.
191. Dutta, J., Tripathi, S., and Dutta, P.K. (2012) *Food Sci. Technol. Int.*, **18**, 20.
192. Khoushab, F. and Yamabhai, M. (2010) *Mar. Drugs*, **8**, 1988.
193. Atkins, E.D.T. (1985) *J. Biosci.*, **8**, 375.
194. Muzzarelli, R.A.A. (ed) (1973) *Natural Chelating Polymers*, Pergamon Press, New York, p. 83.
195. Khor, E. (2001) *Chitin: Fulfilling a Biomaterials Promise*, Elsevier Science, Amsterdam.
196. Zikakis, J.P. (ed) (1984) *Chitin, Chitosan and Related Enzymes*, Academic Press, Orlando, FL, p. XVII.
197. Madhavan, P. (1992) *Chitin, Chitosan and Their Novels Applications*, Science Lecture Series, CIFT, Kochi, p. 1.
198. Ceba, A.B. (2011) *Global J. Biotechnol. Biochem.*, **6**, 149.
199. Rathke, T. (1993) *J. Polym. Sci. Polym. Hem. Ed.*, **31**, 749.
200. Lee, V.F. (1974) Solution and shear properties of chitin and chitosan. PhD Dissertation, University of Washington, University Microfilms, Ann Arbor, MI, Microfilm, Vol. 446, p. 74.
201. No, H.K., Meyers, S.P., Prinyawiwatkul, W., and Xu, Z. (2007) *J. Food Sci.*, **72**, R87.
202. No, H.K., Park, N.Y., Lee, S.H., and Meyers, S.P. (2002) *Int. J. Food Microbiol.*, **74**, 65.
203. Jiang, T., James, R., Kumbar, S.G., and Laurencin, C.T. (2014) in *Natural and Synthetic Biomedical Polymers*, Chapter 5 (eds S.G. Kumbar, C.T. Laurencin, and M. Deng), Elsevier Science, pp. 91–113.
204. Okamoto, Y., Watanabe, M., Miyatake, K., Morimoto, M., Shigemasa, Y., and Minami, Y. (2002) *Biomaterials*, **23**, 1975.
205. Nagahama, H., New, R., Jayakumar, S., Koiwa, T., and Tamur, F.H. (2008) *J., Carbohyd. Polym.*, **73**, 295.
206. Díez-Pascual, A.M., Gómez-Fatou, M.A., Ania, F., and Flores, A. (2015) *Prog. Mater Sci.*, **67**, 1.

207. Bashar, M.M. and Khan, M.A. (2013) *J. Polym. Environ.*, **21**, 181.

208. Shukla, S.K. and Mishra, A.K. (2013) *Int. J. Biol. Macromol.*, **59**, 46.

209. Sandford, P.A. (2004) *Carbohydr. Polym.*, **56**, 59.

210. Rouge, C. (1859) *C.R. Hebd. Seances Acad. Sci.*, **48**, 792.

211. Pillai, C.K.S., Paul, W., and Sharma, C.P. (2009) *Prog. Polym. Sci.*, **34**, 641.

212. Mima, S., Miya, M., Iwamoto, R., and Yoshikawa, S. (1983) *J. Appl. Polym. Sci.*, **28**, 1909.

213. Prabaharan, M. and Mano, J.F. (2006) *Carbohydr. Polym.*, **63**, 153.

214. Prabaharan, M., Reis, R.L., and Mano, J.F. (2007) *React. Funct. Polym.*, **67**, 43.

215. Xu, Y. and Du, Y. (2003) *Int. J. Pharm.*, **250**, 215.

216. Paillet, M. and Dufresne, A. (2001) *Macromolecules*, **34**, 6527.

217. Morin, A. and Dufresne, A. (2002) *Macromolecules*, **35**, 2190.

218. Lu, Y., Lihui, W., and Zhang, L. (2004) *Biomacromolecules*, **5**, 1046.

219. Nair, K.G. and Dufresne, A. (2003) *Biomacromolecules*, **4**, 657.

220. Hariraksapitak, P. and Supaphol, P. (2010) *J. Appl. Polym. Sci.*, **117**, 3406.

221. Sriupayo, J., Supaphol, P., Blackwell, J., and Rujiravanit, R. (2005) *Carbohydr. Polym.*, **62**, 130.

222. Sriupayo, J., Supaphol, P., Blackwell, J., and Rujiravanit, R. (2005) *Polymer*, **46**, 5637.

223. Goodrich, J.D. and Winter, W.T. (2007) *Biomacromolecules*, **8**, 252.

224. Phongying, S., Aiba, S., and Chirachanchai, S. (2007) *Polymer*, **48**, 393.

225. Wongpanit, P., Sanchavanakit, N., Pavasant, P., Bunaprasert, T., Tabata, Y., and Rujiravanit, R. (2007) *Eur. Polym. J.*, **43**, 4123.

226. Junkasem, J., Rujiravanit, R., Grady, B.P., and Supaphol, P. (2010) *Polym. Int.*, **59**, 85.

227. Junkasem, J., Rujiravanit, R., and Supaphol, P. (2006) *Nanotechnology*, **17**, 4519.

228. Watthanaphanit, A., Supaphol, P., Tamura, H., Tokura, S., and Rujiravanit, R. (2008) *J. Appl. Polym. Sci.*, **110**, 890.

229. Maitra, A.N., Ghosh, P.K., De, T.K., and Sahoo, S.K. (1999) Process for the preparation of highly monodispersed hydrophilicpolymeric nanoparticles of size less than 100 nm. US patent 5874111.

230. Tiyaboonchai, W. (2003) *Naresuan Univ. J.*, **11**, 51.

231. Sun, J., Rao, S., Su, Y., Xu, R., and Yang, Y. (2011) *Colloids Surf. A*, **389**, 97.

232. Dehaghi, S.M., Rahmanifar, B., Moradi, A.M., and Azar, P.A. (2014) *J. Saudi Chem. Soc.*, **18**, 348.

233. Mostafaa, T.B. and Darwish, A.S. (2014) *Chem. Eng. J.*, **243**, 326.

234. Zhao, Y., Zhou, Y., Wu, X., Wang, L., Xua, L., and Wei, S. (2012) *Appl. Surf. Sci.*, **258**, 8867.

235. Xiao, Y., Liang, H., Chen, W., and Wang, Z. (2013) *Appl. Surf. Sci.*, **285**, 498.

236. Cao, C., Xiao, L., Chen, C., Shi, X., Cao, Q., and Gao, L. (2014) *Powder Technol.*, **260**, 90.

237. Calvo, P., Remunan-Lopez, C., Vila-Jato, J.L., and Alonso, J. (1997) *J. Appl. Polym. Sci.*, **63**, 125.

238. Tajmir-Riahi, H.A., Nafisi, S., Sanyakamdhorn, S., Agudelo, D., and Chanphai, P. (2014) *Methods Mol. Biol.*, **1141**, 165.

239. Carvalho, C., Santos, R.X., Cardoso, S., Correia, S., Oliveira, P.J., Santos, M.S., and Moreira, P.I. (2009) *Curr. Med. Chem.*, **16**, 3267.

240. Minotti, G., Menna, P., Salvatorelli, E., Cairo, G., and Gianni, L. (2004) *Pharmacol. Rev.*, **56**, 185.

241. Turner, A., Li, L.C., Pilli, T., Qian, L., Wiley, E.L., Setty, S., Christov, K., Ganesh, L., Maker, A.V., Li, P., Kanteti, P., Gupta, T.K.D., and Prabhakar, B.S. (2013) *PLoS One*, **8**, e56817.

242. Hejazi, R. and Amiji, M. (2003) *J. Controlled Release*, **89**, 151.

243. Lehr, C.M., Bouwstra, J.A., Schacht, E.H., and Junginger, H.E. (1992) *Int. J. Pharm.*, **78**, 43.

244. Vila, A., Sánchez, A., Tobío, M., Calvo, P., and Alonso, M.J. (2002) *J. Controlled Release*, **78**, 15.

245. Gan, Q., Wang, T., Cochrane, C., and McCarron, P. (2005) *Colloids Surf., B*, **44**, 65.

246. Fernandez-Urrusuno, R., Romani, D., Calvo, P., Vila-Jato, J.L., and Alonso, M.J. (1999) *STP Pharm. Sci.*, **9**, 429.
247. Fernandez-Urrusuno, R., Calvo, P., Remunan-Lopez, C., Vila-Jato, J.L., and Alonso, M.J. (1999) *Pharm. Res.*, **16**, 1576.
248. Termsarasab, U., Yoon, I.S., Park, J.H., Moon, H.T., Cho, H.J., and Kim, D.D. (2014) *Int. J. Pharm.*, **464**, 127.
249. Deng, X., Cao, M., Zhang, J., Hu, K., Yin, Z., Zhou, Z., Xiao, X., Yang, Y., Sheng, W., Wu, Y., and Zeng, Y. (2014) *Biomaterials*, **35**, 4333.
250. Hellmers, F., Ferguson, P., Koropatnick, J., Krull, R., and Margaritis, A. (2013) *Biochem. Eng. J.*, **75**, 72.
251. Guo, H., Zhang, D., Li, C., Jia, L., Liu, G., Hao, L., Zheng, D., Shen, J., Li, T., Guo, Y., and Zhang, Q. (2013) *Int. J. Pharm.*, **458**, 31.
252. Yousefpour, P., Atyabi, F., Vasheghani-Farahani, E., Movahedi, A.M., and Dinarvand, R. (2011) *Int. J. Nanomed.*, **6**, 1977.
253. Ohya, Y., Cai, R., Nishizawa, H., Hara, K., and Ouchi, T. (2000) *STP Pharm. Sci.*, **10**, 77.
254. Yamomoto, H., Takeuchi, H., Hino, T., and Kawashima, Y. (2000) *STP Pharm. Sci.*, **10**, 63.
255. Yang, S.C., Ge, H.X., Hu, Y., Jiang, X.Q., and Yang, C.Z. (2000) *Colloid. Polym. Sci.*, **278**, 285.
256. Sharma, A.M. (2002) *Int. J. Pharm.*, **243**, 93.
257. Andersson, M. and Lofroth, J.E. (2003) *Int. J. Pharm.*, **257**, 305.
258. Zeng, J.B., He, Y.S., Li, S.L., and Wang, Y.Z. (2012) *Biomacromolecules*, **13**, 1–11.
259. Carlström, D. (1957) *J. Biophys. Biochem. Cytol.*, **3**, 669.
260. Revol, J.F. and Marchessault, R.H. (1993) *Int. J. Biol. Macromol.*, **15**, 329.
261. Marchessault, R.H., Morehead, F.F., and Walter, N.M. (1959) *Nature*, **184**, 632–633.
262. Li, J., Revol, J.F., Naranjo, E., and Marchessault, R.H. (1996) *Int. J. Biol. Macromol.*, **18**, 177.
263. Papadimitriou, S., Bikiaris, D., Avgoustakis, K., Karavas, E., and Georgarakis, M. (2008) *Carbohydr. Polym.*, **73**, 44.
264. Saboktakin, M.R., Tabatabaee, R.M., Maharramov, A., and Ramazanov, M.A. (2010) *Carbohydr. Polym.*, **82**, 466.
265. Zhang, H., Oh, M., Allen, C., and Kumacheva, E. (2004) *Biomacromolecules*, **5**, 2461.
266. Bodmeier, R., Chen, H.G., and Paeratakul, O. (1989) *Pharm. Res.*, **6**, 413.
267. Wu, Y., Wang, Y., Luo, G., and Dai, Y. (2010) *Bioresour Technol.*, **101**, 841.
268. El-Shabouri, M.H. (2002) *Int. J. Pharm.*, **249**, 101.
269. Erbacher, P., Zou, S., Steffan, A.M., and Remy, J.S. (1998) *Pharm. Res.*, **15**, 1332.
270. Pan, Y., Li, Y.J., Zhao, H.Y., Zheng, J.M., Xu, H., Wei, G., Hao, J.S., and Cui, F.D. (2002) *Int. J. Pharm.*, **249**, 139.
271. Wang, K., Yuan, X., Guo, Z., Xu, J., and Chen, Y. (2014) *Carbohydr. Polym.*, **102**, 699.
272. Rafiee, A., Alimohammadian, M.H., Gazori, T., Riazi-rad, F., Fatemi, S.M.R., Parizadeh, A., Haririan, I., and Havaskary, M. (2014) *Asian Pac. J. Trop. Dis.*, **4**, 372.
273. Sun, C., Na, J.H., Jeong, S.Y., Kim, D.E., Kwon, I.C., Choi, K., Ahn, C.H., and Ki, K. (2014) *Pharm. Res.*, **31**, 1418.
274. Pujana, M.A., Pérez-Álvarez, L., Iturbe, L.C.C., and Katime, I. (2013) *Carbohydr. Polym.*, **94**, 836.
275. Zamora-Mora, V., Fernández-Gutiérrez, M., Román, J.S., Goya, G., Hernández, R., and Mijangos, C. (2014) *Carbohydr. Polym.*, **102**, 691.
276. Li, Y., Huang, G., Zhang, X., Li, B., Chen, Y., Lu, T., Lu, T.J., and Xu, F. (2013) *Adv. Funct. Mater.*, **23**, 660.
277. Zhi, J., Wang, Y., Lu, Y., Ma, J., and Luo, G. (2006) *React. Funct. Polym.*, **66**, 1552.
278. Zhou, Z., Jiang, F., Lee, T.C., and Yue, T. (2013) *J. Alloys Compd.*, **581**, 843.
279. Wang, Y., Wang, X., Luo, G., and Dai, Y. (2008) *Bioresour. Technol.*, **99**, 3881.
280. Zhang, L., Zhu, X., Sun, H., Chi, G., Xu, J., and Sun, Y. (2010) *Curr. Appl Phys.*, **10**, 828.
281. Zhou, L., Xu, J., Liang, X., and Liu, Z. (2010) *J. Hazard. Mater.*, **182**, 518.

282. Reicha, F.M., Sarhan, A., Abdel-Hamid, M.I., and El-Sherbiny, I.M. (2012) *Carbohydr. Polym.*, **89**, 236.

283. Unsoy, G., Khodadust, R., Yalcin, S., Mutlu, P., and Gunduz, U. (2014) *Eur. J. Pharm. Sci.*, **62**, 243.

284. Kang, B., Chang, S., Dai, Y., and Chen, D. (2007) *Radiat. Phys. Chem.*, **76**, 968–973.

285. Guo, Y.H., Li, F.R., Bao, S.Y., Han, T., Cao, J.J., and Zhou, H.X. (2007) *Curr. Appl Phys.*, **7**, e97.

286. Du, Y., Luo, X.L., Xu, J.J., and Chen, H.Y. (2007) *Bioelectrochemistry*, **70**, 342.

287. Yu, K., Ho, J., McCandlish, E., Buckley, B., Patel, R., Li, Z., and Shapley, N.C. (2013) *Colloids Surf. A*, **425**, 31.

288. LeCorre, D., Bras, J., and Dufresne, A. (2010) *Biomacromolecules*, **11**, 1139.

289. Buleon, A., Colonna, P., Planchot, V., and Ball, S. (1998) *Int. J. Biol. Macromol.*, **23**, 85.

290. Vandeputte, G. and Delcour, J. (2004) *Carbohydr. Polym.*, **58**, 245.

291. Oates, C.G. (1997) *Trends Food Sci. Technol.*, **8**, 375.

292. Yao, Y., Zhang, J., and Ding, X. (2002) *J. Agric. Food. Chem.*, **50**, 7420.

293. Blazek, J. and Copeland, L. (2008) *Carbohydr. Polym.*, **71**, 380.

294. Wang, S. and Copeland, L. (2013) *Food Funct.*, **4**, 1564.

295. Angellier, H., Choisnard, L., Molina-Boisseau, S., Ozil, P., and Dufresne, A. (2004) *Biomacromolecules*, **5**, 1545.

296. Shi, A.M., Li, D., Wang, L.J., Li, B.Z., and Adhikari, B. (2011) *Carbohydr. Polym.*, **83**, 1604.

297. Santander-Ortega, M.J., Stauner, T., Loretz, B., Ortega-Vinuesa, J.L., Bastos-Gonzalez, D., Wenz, G., Schaefer, U.F., and Lehr, C.M. (2010) *J. Controlled Release*, **141**, 85.

298. Juna, S., Hayden, S., Damm, M., Kappe, C.O., and Huber, A. (2014) *Starch/Stärke*, **66**, 316.

299. Delval, F., Crini, G.G., Bertini, S., Morin-Crini, N., Badot, P.M., Vebrel, J., and Torri, G. (2004) *J. Appl. Polym. Sci.*, **93**, 2650.

300. Lemarchand, C., Couvreur, P., Besnard, M., Costantini, D., and Gref, R. (2003) *Pharm. Res.*, **20**, 1284.

301. Rodrigues, J.S., Santos-Magalhães, N.S., Coelho, L.C.B.B., Couvreur, P., Ponchel, G., and Gref, R. (2003) *J. Controlled Release*, **92**, 103.

302. Hornig, S. and Heinze, T. (2007) *Carbohydr. Polym.*, **68**, 280.

303. Simi, C.K. and Emilia Abraham, T. (2007) *Bioprocess. Biosyst. Eng.*, **30**, 173.

304. Deetae, P., Shobsngob, S., Varanyanond, W., Chinachoti, P., Naivikul, O., and Varavinit, S. (2008) *Carbohydr. Polym.*, **73**, 351.

305. Hoover, R., Hughes, T., Chung, H.J., and Liu, Q. (2010) *Food Res. Int.*, **43**, 399.

306. Han, J., Borjihan, G., Bai, R., Chen, X., and Jing, X. (2008) *J. Appl. Polym. Sci.*, **108**, 523.

307. Chin, S.F., Pang, S.C., and Tay, S.H. (2011) *Carbohydr. Polym.*, **86**, 1817.

308. Tay, S.H., Pang, S.C., and Chin, S.F. (2012) *Carbohydr. Polym.*, **88**, 1195.

309. Dai, C.A., Chang, C.J., Chi, H.Y., Chien, H.T., Su, W.F., and Chiu, W.Y. (2008) *J. Polym. Sci., Part A: Polym. Chem.*, **46**, 2536.

310. Koo, H.Y., Chang, S.T., Choi, W.S., Park, J.H., Kim, D.Y., and Velev, O.D. (2006) *Chem. Mater.*, **18**, 3308.

311. Tojo, C., Dios, M.D., and Barroso, F. (2010) *Materials*, **4**, 55.

312. Ethayaraja, M., Dutta, K., Muthukumaran, D., and Bandyopadhyaya, R. (2007) *Langmuir*, **23**, 3418.

313. López-Quintela, M.A. (2003) *Curr. Opin. Colloid Interface Sci.*, **8**, 137.

314. Chingunpituk, J. and Walailak, J. (2007) *Sci. Technol.*, **4**, 139.

315. Sweedman, M.C., Schäfer, C., and Gilbert, R.G. (2014) *Carbohydr. Polym.*, **111**, 918.

316. Kim, H.Y., Lee, J.H., Kim, J.Y., Lim, W.J., and Lim, S.T. (2012) *Starch/Stärke*, **64**, 367.

317. Zhou, G., Luo, Z., and Fu, X. (2014) *Ind. Crops. Prod.*, **52**, 105.

318. Xiao, S.Y., Tong, C.Y., Liu, X.M., Yu, D.M., Liu, Q.L., Xue, C.G., Tang, D.Y., and Zhao, L.J. (2006) *Chin. Sci. Bull.*, **51**, 1693.

319. Tan, Y., Xu, K., Li, L., Liu, C., Song, C., and Wang, P. (2009) *ACS Appl. Mater. Interfaces*, **1**, 956.

320. Juna, S. and Huber, A. (2013) *Starch/Stärke*, **65**, 1029.
321. Ma, X., Jian, R., Chang, P.R., and Yu, J. (2008) *Biomacromolecules*, **9**, 3314.
322. Kim, J.Y. and Lim, S.T. (2009) *Carbohydr. Polym.*, **76**, 110.
323. Sun, Q., Fan, H., and Xiong, L. (2014) *Carbohydr. Polym.*, **106**, 359.
324. Bel Haaj, S., Magnin, A., Petrier, C., and Boufi, S. (2013) *Carbohydr. Polym.*, **92**, 1625.
325. Azhar, A. and Hamdy, K. (1979) *J. Food Sci.*, **44**, 801.
326. Chung, K.M., Moon, T.W., Kim, H.J., and Chun, J.K. (2002) *Cereal Chem.*, **79**, 631.
327. Iida, Y., Tuziuti, T., Yasui, K., Towata, A., and Kozuka, T. (2008) *Innovative Food Sci. Emerg. Technol.*, **9**, 140.
328. Zuo, J.Y., Knoerzer, K., Mawson, R., Kentish, S., and Ashokkumar, M. (2009) *Ultrason. Sonochem.*, **16**, 462.
329. Li, Y., Liu, C., Tan, Y., Xu, K., Lu, C., and Wang, P. (2014) *Carbohydr. Polym.*, **110**, 87.
330. Putaux, J.L., Molina-Boisseau, S., Momaur, T., and Dufresne, A. (2003) *Biomacromolecules*, **4**, 1198.
331. Chen, G., Wei, M., Chen, J., Huang, J., Dufresne, A., and Chang, P.R. (2008) *Polymer*, **49**, 1860.
332. Chen, Y., Cao, X., Chang, P.R., and Huneault, M.A. (2008) *Carbohydr. Polym.*, **73**, 8.
333. Yu, J., Ai, F., Dufresne, A., Gao, S., Huang, J., and Chang, P.R. (2008) *Macromol. Mater. Eng.*, **293**, 763.
334. García, N.L., Famá, L., Dufresne, A., Aranguren, M., and Goyanes, S. (2009) *Food Res. Int.*, **42**, 976.
335. Namazi, H. and Dadkhah, A. (2010) *Carbohydr. Polym.*, **79**, 731.
336. Wang, Y. and Zhang, L. (2008) *J. Nanosci. Nanotechnol.*, **8**, 5831.
337. LeCorre, D., Bras, J., and Dufresne, A. (2009) in *Starch Nanoparticles for Eco-Efficient Packaging: Influence of Botanic Origin. 2nd International Conference on Biodegradable Polymers and Sustainable Composites* (ed A. Jimenez), BIOPOL, Alicante, p. 49.
338. Ren, L., Jiang, M., Wang, L., Zhou, J., and Tong, J. (2012) *Carbohydr. Polym.*, **87**, 1874.
339. Jayakody, L. and Hoover, R. (2002) *Food Res. Int.*, **35**, 665.
340. Gérard, C., Colonna, P., Buléon, A., and Planchot, V. (2002) *Carbohydr. Polym.*, **48**, 131.
341. Angellier, H., Molina-Boisseau, S., Dole, P., and Dufresne, A. (2006) *Biomacromolecules*, **7**, 531.
342. Angellier, H., Molina-Boisseau, S., Lebrun, L., and Dufresne, A. (2005) *Macromolecules*, **38**, 3783.
343. Angellier, H., Molina-Boisseau, S., and Dufresne, A. (2005) *Macromolecules*, **38**, 9161.
344. Angellier, H., Molina-Boisseau, S., Belgacem, M.N., and Dufresne, A. (2005) *Langmuir*, **21**, 2425.
345. Lin, N., Huang, J., Chang, P.R., Anderson, D.P., and Yu, J. (2011) *J. Nanomater.*, **2011**, 1.
346. LeCorre, D., Bras, J., and Dufresne, A. (2011) *Biomacromolecules*, **12**, 3039.
347. Sweedman, M.C., Hasjim, J., Schäfer, C., and Gilbert, R.G. (2014) *Carbohydr. Polym.*, **112**, 85.
348. Singh, V. and Ali, S. (2000) *Carbohydr. Polym.*, **41**, 191.
349. Singh, V. and Ali, S.Z. (2008) *Int. J. Food Prop.*, **11**, 495.
350. Wei, B., Xu, X., Jin, Z., and Tian, Y. (2014) *PLoS One*, **9**, e86024.
351. Kim, J.Y., Park, D.J., and Lim, S.T. (2008) *Cereal Chem.*, **85**, 182.
352. LeCorre, D., Bras, J., and Dufresne, A. (2012) *Carbohydr. Polym.*, **87**, 658.
353. Chin, S.F., Azman, A., and Pang, S.C. (2014) *J. Nanomater.*, **2014**, 1.
354. Xiao, S., Liu, X., Tong, C., Zhao, L., Liu, X., Zhou, A., and Cao, Y. (2012) *Chin. Sci. Bull.*, **57**, 3226.
355. Aichayawanich, S., Nopharatana, M., Nopharatana, A., and Songkasiri, W. (2011) *Carbohydr. Polym.*, **84**, 292.
356. García, N.L., Ribba, L., Dufresne, A., Aranguren, M.I., and Goyanes, S. (2009) *Macromol. Mater. Eng.*, **294**, 169.
357. Kristo, E. and Biliaderis, C.G. (2007) *Carbohydr. Polym.*, **68**, 146–158.
358. Zheng, H., Ai, F.J., Chang, P.R., Huang, J., and Dufresne, A. (2009) *Polym. Compos.*, **30**, 474.

359. Mele, P., Angellier, H., Molina-Boisseau, S., and Dufresne, A. (2011) *Macromolecules*, **12**, 1487.

360. Angellier, H., Putaux, J.L., Molina-Boisseau, S., Dupeyre, D., and Dufresne, A. (2005) *Macromol. Symp.*, **221**, 95.

361. Siqueira, G., Bras, J., and Dufresne, A. (2010) *Polymers*, **2**, 728.

362. Weng, W. and Zheng, H. (2015) *Food Chem.*, **169**, 255.

363. Schmidt, V., Giacomelli, C., and Soldi, V. (2005) *Polym. Degrad. Stab.*, **87**, 25.

364. Teng, Z., Luo, Y., and Wang, Q. (2012) *J. Agric. Food. Chem.*, **60**, 2712.

365. Chen, L., Remondetto, G., Rouabhia, M., and Subirade, M. (2008) *Biomaterials*, **29**, 3750.

366. Poysa, V., Woodrow, L., and Yu, K. (2006) *Food Res. Int.*, **39**, 309.

367. Lodha, P. and Netravali, A.N. (2005) *Compos. Sci. Technol.*, **65**, 1211.

368. Tsumura, K., Saito, T., Tsuge, K., Ashida, H., Kugimiya, W., and Inouye, K. (2005) *LWT - Food Sci. Technol.*, **38**, 255.

369. Agostoni, C., Axelsson, I., Goulet, O., Koletzko, B., Michaelsen, K.F., Puntis, J., Rieu, D., Rigo, J., Shamir, R., Szajewska, H., and Turck, D. (2006) *J. Pediatr. Gastroenterol. Nutr.*, **42**, 352Y361.

370. Berk, Z. (1992) Technology of Production of Edible Flours and Protein Products from Soybeans, Chapter 6, Food and Agriculture Organization of the United Nations, Rome.

371. Lusas, E.W. and Riaz, M.N. (1995) *J. Nutr.*, **125**, 573S.

372. Zhang, J., Liang, L., Tian, Z., Chen, L., and Subirade, M. (2012) *Food Chem.*, **133**, 390.

373. Teng, Z., Luo, Y., Wang, T., Zhang, B., and Wang, Q. (2013) *J. Agric. Food. Chem.*, **61**, 2556.

374. Jong, L. (2013) *J. Dispersion Sci. Technol.*, **34**, 469.

375. Liu, F. and Tang, C.H. (2013) *J. Agric. Food. Chem.*, **61**, 8888.

376. Liu, F. and Tang, C.H. (2014) *J. Agric. Food. Chem.*, **62**, 2644.

377. Gao, Z.M., Wang, J.M., Wu, N.N., Wan, Z.L., Guo, J., Yang, X.Q., and Yin, S.W. (2013) *J. Agric. Food. Chem.*, **61**, 7838.

378. Gao, Z.M., Zhu, L.P., Yang, X.Q., He, X.T., Wang, J.M., Guo, J., Qi, J.R., Wang, L.J., and Yin, S.W. (2014) *Food Funct.*, **5**, 1286.

379. Huang, X. and Netravali, A. (2007) *Compos. Sci. Technol.*, **67**, 2005.

380. Jin, M., Ikeda, S., and Zhong, Q. (2013) *LWT - Food Sci. Technol.*, **51**, 23.

381. Jong, L. (2008) *Mater. Res. Soc. Symp. Proc.*, **1086**, 1086-U08-18.

382. Chen, P. and Zhang, L. (2006) *Biomacromolecules*, **7**, 1700.

383. Kumar, P., Sandeep, K.P., Alavi, S., Truong, V.D., and Gorga, R.E. (2010) *J. Food Eng.*, **100**, 480.

384. Echeverría, I., Eisenberg, P., and Mauri, A.N. (2014) *J. Membr. Sci.*, **449**, 15.

385. Teng, Z., Luo, Y., and Wang, Q. (2013) *Food Chem.*, **141**, 524.

386. Kunz, C. and Lonnerdal, B. (1990) *Am. J. Clin. Nutr. (Am. Soc. Clin. Nutr.)*, **51**, 37.

387. Livney, Y.D. (2010) *Curr. Opin. Colloid Interface Sci.*, **15**, 73.

388. Arora, N., Tarun, G., and Bilandi, A. (2012) *Int. Res. J. Pharm.*, **3**, 41.

389. Horne, D. (2002) *Curr. Opin. Colloid Interface Sci.*, **7**, 456.

390. Cao, Q., Zhao, H., Yang, Y., He, Y., Ding, N., Wang, J., Wu, Z., Xiang, K., and Wang, G. (2011) *Biosens. Bioelectron.*, **26**, 3469.

391. Farrell, H.M. Jr., Jimenez-Flores, R., Bleck, G.T., Brown, E.M., Butler, J.E., Creamer, L.K., Hicks, C.L., Hollar, C.M., Ng-Kwai-Hang, K.F., and Swaisgood, H.E. (2004) *J. Dairy Sci.*, **87**, 1641.

392. Modler, H.W. (1985) *J. Dairy Sci.*, **68**, 2195.

393. Holt, C. and Sawyer, L. (1993) *J. Chem. Soc., Faraday Trans.*, **89**, 2683.

394. Holt, C. and Horne, D.S. (1996) *Neth. Milk Dairy J.*, **50**, 85.

395. Horne, D.S. (2006) *Curr. Opin. Colloid Interface Sci.*, **11**, 148.

396. Holt, C., De Kruif, C.G., Tuinier, R., and Timmins, P.A. (2003) *Colloids Surf.*, **213**, 275.

397. Farrell, H.M. Jr., Malin, E.L., Brown, E.M., and Qi, P.X. (2006) *Curr. Opin. Colloid Interface Sci.*, **11**, 135.

398. Dalgleish, D.G. (2011) *Soft Matter*, **7**, 2265.

399. Buchheim, W. and Welsch, U. (1973) *Neth. Milk Dairy J.*, **27**, 163.
400. Schmidt, D.G. and Both, P. (1982) *Milchwissenschaft—Milk Sci. Int.*, **37**, 336.
401. Parker, T.G. and Dalgleish, D.G. (1981) *J. Dairy Res.*, **48**, 71.
402. Walstra, P. (1999) *Int. Dairy J.*, **9**, 189.
403. Mezzenga, R. and Fischer, P. (2013) *Rep. Prog. Phys.*, **76**, 046601.
404. Elzoghby, A.O., Abo El-Fotoh, W.S., and Elgindy, N.A. (2011) *J. Controlled Release*, **153**, 206.
405. Semo, E., Kesselman, E., Danino, D., and Livney, Y.D. (2007) *Food Hydrocolloids*, **21**, 936.
406. Sahu, A., Kasoju, N., and Bora, U. (2008) *Biomacromolecules*, **9**, 2905.
407. McMahon, D.J. and Oommen, B.S. (2008) *J. Dairy Sci.*, **91**, 1709.
408. De Kruiff, C.G. and Zhulina, E.B. (1996) *Colloids Surf.*, **117**, 151.
409. Pan, X., Yao, P., and Jiang, M. (2007) *J. Colloid Int. Sci.*, **315**, 456.
410. Huppertz, T. and De Kruif, C.G. (2008) *Int. Dairy J.*, **18**, 556.
411. Ye, A., Flanagan, J., and Singh, H. (2006) *Biopolymers*, **82**, 121.
412. Park, J.M., Muhober, B.B., Dubin, P.L., and Xia, J. (1992) *Macromolecules*, **25**, 290.
413. Maham, A., Tang, Z., Wu, H., Wang, J., and Lin, Y. (2009) *Small*, **5**, 1706.
414. Zimet, P., Rosenberg, D., and Livney, Y.D. (2011) *Food Hydrocolloids*, **25**, 1270.
415. Esmaili, M., Ghaffari, S.M., Moosavi-Movahedi, Z., Atri, M.S., Sharifizadeh, A., Farhadi, M., Yousefi, R., Chobert, J.M., Haertlé, T., and Moosavi-Movahedi, A.A. (2011) *Food Sci. Technol.*, **44**, 2166.
416. Shapira, A., Assaraf, Y.G., and Livney, Y.D. (2010) *Nanomedicine*, **6**, 119.
417. Shapira, A., Markman, G., Assaraf, Y.G., and Livney, Y.D. (2010) *Nanomedicine*, **6**, 547.
418. Shapira, A., Assaraf, Y.G., Epstein, D., and Livney, Y.D. (2010) *Pharm. Res.*, **27**, 2175.
419. Shapira, A., Davidson, I., Avni, N., Assaraf, Y.G., and Livney, Y.D. (2012) *Pharm. Biopharm.*, **80**, 298.
420. Ghasemi, S. and Abbasi, S. (2014) *Food Hydrocolloids*, **42**, 42–47.
421. Liu, C., Yao, W., Zhang, L., Qian, H., Wu, W., and Jiang, X. (2010) *Chem. Commun.*, **46**, 7566.
422. Xu, O., Ma, J., and Zhou, J. (2013) *Chem. Eng. J.*, **228**, 281.
423. Narayanan, S., Pavithran, M., Viswanath, A., Narayanan, D., Chandini, C., Manzoor, M.K., and Menon, D. (2014) *Acta Biomater.*, **10**, 2112.
424. Xu, S., Yin, B., Guo, J., and Wang, C. (2013) *J. Mater. Chem. B*, **1**, 4079.
425. Hashemiravan, M., Saberi, M., and Farhadyar, N. (2013) *Int. J. Bio-Inorg. Hybd. Nanomat.*, **4**, 485.
426. Ma, J., Xu, Q., Zhou, J., Zhang, J., Zhang, L., Tang, H., and Chen, L. (2013) *Colloids Surf.*, **111**, 257.
427. Suchomel, P., Panacek, A., Prucek, R., Zboril, R., and Kvitek, L., Brno, Czech Republic, EU (2013) *Nanocon*, **16-18**, 10.
428. Ghodake, G., Lim, S.R., and Lee, D.S. (2013) *Colloids Surf.*, **108**, 147.
429. Huang, J., Wang, L., Lin, R., Wang, A.Y., Yang, L., Kuang, M., Qian, W., and Mao, H. (2013) *ACS Appl. Mater. Interfaces*, **5**, 4632.
430. Sangeetha, J. and Philip, J. (2012) *Colloids Surf.*, **406**, 52.
431. Ashraf, S., Zahoor Abbasi, A., Pfeiffer, C., Hussain, S.Z., Khalida, Z.M., Gil, P.R., Parak, W.J., and Hussain, I. (2013) *Colloids Surf.*, **102**, 511.
432. Diak, O.A., Jaber, A.B., Amro, B., Jones, D., and Andrews, G.P. (2007) *Food Bioprod. Process.*, **85**, 284.
433. Motoki, M., Aso, H., Seguro, K., and Nio, N. (1987) *Agric. Biol. Chem.*, **51**, 993.
434. Warszynska, L.S., Gergely, C., Jarek, E., Cuisinier, F., Socha, R.P., and Warszynski, P. (2009) *Colloids Surf.*, **343**, 118.
435. Elzoghby, A.O., Helmy, M.W., Samy, W.M., and Elgindy, N.A. (2013) *Int. J. Nanomed.*, **8**, 1721.
436. Elzoghby, A.O., Saad, N.I., Helmy, M.W., Samy, W.M., Elgindy, N.A., and European, J. (2013) *Pharm. Biopharm.*, **85**, 444.

437. Soejima, T., Oshiro, S., Nakatsuji, Y., and Ito, S. (2011) *J. Colloid Interface Sci.*, **362**, 325.
438. Martinsen, A., Skjak-Braek, G., and Smidsrsd, O. (1989) *Biotechnol. Bioeng.*, **33**, 79.
439. Augst, A.D., Kong, H.J., and Mooney, D.J. (2006) *Macromol. Biosci.*, **6**, 623.
440. Donati, I. and Paoletti, S. (2009) in *Alginates: Biology and Applications* (ed B.H.A. Rehm), Springer, London, p. 5.
441. Gacesa, P. (1988) *Carbohydr. Polym.*, **8**, 161.
442. Goh, C.H., Heng, P.W.S., and Chan, L.W. (2012) *Carbohydr. Polym.*, **88**, 1.
443. Lee, K.Y. and Mooney, D.J. (2012) *Prog. Polym. Sci.*, **37**, 106.
444. Machado, A.H., Lundberg, D., Ribeiro, A.J., Veiga, F.J., Lindman, B., Miguel, M.G., and Olsson, U. (2012) *Langmuir*, **28**, 4131.
445. Nesamony, J., Singh, P.R., Nada, S.E., Shah, Z.A., and Kolling, W.M. (2012) *J. Pharm. Sci.*, **101**, 2177.
446. Liu, X., Chen, X., Li, Y., Cui, Y., Zhu, H., and Zhu, W. (2012) *J. Nanopart. Res.*, **14**, 763.
447. Paques, J.P., van der Linden, E., van Rijn, C.J.M., and Sagis, L.M.C. (2013) *Food Hydrocolloids*, **31**, 428.
448. Paques, J.P., Sagis, L.M.C., van Rijn, C.J.M., and van der Linden, E. (2014) *Food Hydrocolloids*, **40**, 182.
449. Angelescu, D.G., Anastasescu, M., and Anghel, D.F. (2014) *Colloids Surf. Physicochem. Eng. Asp.*, **460**, 95–103.
450. Paques, J.P., van der Linden, E., van Rijn, C.J., and Sagis, L.M. (2014) *Adv. Colloid Interface Sci.*, **209**, 163.
451. Li, Q., Liu, C.G., Huang, Z.H., and Xue, F.F. (2011) *J. Agric. Food. Chem.*, **59**, 1962.
452. Malesu, V.K., Sahoo, D., and Nayak, P.L. (2011) *Int. J. Appl. Biol. Pharm. Technol.*, **2**, 402.
453. Li, P., Dai, Y.N., Zhang, J.P., Wang, A.Q., and Wei, Q. (2008) *J. Biomed. Sci. Eng.*, **4**, 221.
454. Xing, J., Deng, L., and Dong, A. (2010) *J. Appl. Polym. Sci.*, **117**, 2354.
455. Azizi, E., Namazi, A., Haririan, I., Fouladdel, S., Khoshayand, M.R., Shotorbani, P.Y., Nomani, A., and Gazori, T. (2010) *Int. J. Nanomed.*, **5**, 455.
456. Das, R.K., Kasoju, N., and Bora, U. (2010) *Nanomedicine*, **6**, 153.
457. Mohammadifard, H., Arpanaei, A., Vosoughi, M., Kabirsalmani, M., and Shakibaei, M. (2012) Alginate-silica nanocomposite beads for the 3D cell culture: preparation and study of the mechanical stability and cell proliferation and viability. Proceedings of the 4th International Conference on Nanostructures, Vol. 1, p. 843.
458. Boissiere, M., Allouche, J., Chaneac, C., Brayner, R., Devoisselle, J.M., Livage, J., and Coradin, T. (2007) *Int. J. Pharm.*, **344**, 128.
459. Motwani, S.K., Chopra, S., Talegaonkar, S., Kohli, K., Ahmad, F.J., and Khar, R.K. (2008) *Eur. J. Pharm. Biopharm.*, **68**, 513.
460. Huq, T., Salmieri, S., Khan, A., Khan, R.A., Le Tien, C., Riedl, B., Fraschini, C., Bouchard, J., Uribe-Calderon, J., Kamal, M.R., and Lacroix, M. (2012) *Carbohydr. Polym.*, **90**, 1757.
461. Ghadiri, M., Chrzanowski, W., Lee, W.H., Fathi, A., Dehghani, F., and Rohanizadeh, R. (2013) *Appl. Clay Sci.*, **85**, 64.
462. Brun, F., Turco, G., Accardo, A., and Paoletti, S. (2011) *J. Mater. Sci. Mater. Med.*, **22**, 2617.
463. Stojkovska, J., Zvicer, J., Jovanovic, Z., Miskovic-Stankovic, V., and Obradovic, B. (2012) *J. Serbian Chem. Soc.*, **77**, 1709.
464. Tue Anh, N., Van Phu, D., Ngoc Duy, N., Duy Du, B., and Quoc Hien, N. (2010) *Radiat. Phys. Chem.*, **79**, 405.
465. McGill, S.L., Cuylear, C., Adolphi, N.L., Osinski, M., and Smyth, H. (2014) *Proc. SPIE*, **7189**, 718918-1.
466. Wang, L., Sun, Y., and Yang, X. (2014) *Ceram. Int.*, **40**, 4869.
467. Lakouraj, M.M., Mojerlou, F., and Zare, E.N. (2014) *Carbohydr. Polym.*, **106**, 34.
468. Srinivasan, S., Jayasree, R., Chennazhi, K.P., Nair, S.V., and Jayakumar, R. (2012) *Carbohydr. Polym.*, **87**, 274.
469. Zhang, C., Wang, W., Liu, T., Wu, Y., Guo, H., Wang, P., Tian, Q., Wang, Y., and Yuan, Z. (2012) *Biomaterials*, **33**, 2187.

470. Guo, H., Lai, Q., Wang, W., Wu, Y., Zhang, C., Liu, Y., and Yuan, Z. (2013) *Int. J. Pharm.*, **451**, 1.

471. Lam, P.L., Kok, S.H.L., Bian, Z.X., Lam, K.H., Tang, J.C.O., Lee, K.K.H., Gambari, R., and Chui, C.H. (2014) *Colloids Surf.*, **117**, 277.

472. Kandamchira, A., Selvam, S., Marimuthu, N., Janardhanan, S.K., and Fathim, N.N. (2013) *Mater. Sci. Eng.*, **33**, 4985.

473. Chen, W., Cormode, D.P., Vengrenyuk, Y., Herranz, B., Feig, J.E., Klink, A., Mulder, W.J.M., Fisher, E.A., and Fayad, Z.A. (2013) *JACC: Cardiovascu. Imaging*, **6**, 373.

474. Schwick, H.G. and Heide, K. (1969) *Bibl. Haematol.*, **3**, 111.

475. Haessig, A. and Stampfli, K. (1969) *Bibl. Haematol.*, **33**, 1.

476. Balthasar, S., Michaelis, K., Dinauer, N., Briesen, H.V., Kreuter, J., and Langer, K. (2005) *Biomaterials*, **26**, 2723.

477. Zwiorek, K., Kloeckner, J., Wagner, E., and Coester, C. (2004) *J. Pharm. Pharm. Sci.*, **7**, 22.

478. Leo, E., Vandelli, M.A., Cameroni, R., and Forni, F. (1997) *Int. J. Pharm.*, **155**, 75.

479. Lu, Z., Yeh, T.K., Tsai, M., Au, J.L.S., and Wientjes, M.W. (2008) *Clin. Cancer Res.*, **14**, 1510.

480. Kommareddy, S. and Amiji, M. (2005) *Bioconjugate Chem.*, **16**, 1423.

481. Shutava, T.G., Balkundi, S.S., Vangala, P., Steffan, J.J., Bigelow, R.L., Cardelli, J.A., O'Neal, P., and Lvov, Y.M. (2009) *ACS Nano*, **3**, 1877.

482. Cascone, M.G., Lazzeri, L., Carmignani, C., and Zhu, Z. (2002) *J. Mater. Sci.*, **13**, 523.

483. Coester, C.J., Kreuter, J., von Briesen, H., and Langer, K. (2000) *Int. J. Pharm.*, **196**, 147.

484. Tran, P.H.L., Tran, T.T.D., Vo, T.V., Vo, C.L., and Lee, B.J. (2013) *Int. J. Pharm.*, **455**, 235.

485. Coester, C.J., Langer, K., Von Briesen, H., and Kreuter, J. (2000) *J. Microencapsulation*, **17**, 187.

486. Elzoghby, O.A. (2013) *J. Controlled Release*, **172**, 1075.

487. Gülseren, I., Fang, Y., and Corredig, M. (2012) *Food Hydrocolloids*, **29**, 258.

488. Giroux, H.J., Houde, J., and Britten, M. (2010) *Food Hydrocolloids*, **24**, 341.

489. Zhang, W. and Zhong, O. (2009) *J. Agric. Food. Chem.*, **60**, 9181.

490. ElSalam, M.A.B.D. and El-Shibiny, S. (2012) *Int. Diary Technol.*, **65**, 13.

491. Giroux, H.J., Houde, J., and Britten, M. (2011) *J. Microencapsulation*, **28**, 337.

9
Metal-Organic Frameworks (MOFs) and Its Composites

Ali Morsali and Lida Hashemi

Over the past two decades the fields of gas adsorption and catalysis have greatly benefited from the development of a class of materials called metal-organic frameworks (MOFs). MOFs represent a class of crystalline and highly porous hybrid materials obtained by the assembly of metallic ions and organic ligands. The diversity of metals and organic linkers that can be used to synthesize MOFs makes these materials highly tunable. Besides an application in gas adsorption and catalysis, MOFs exhibit interesting properties for gas separation, gas storage, and drug delivery and could also be used as sensors (luminescent and magnetic properties). To drive MOFs up to the step of industrial/large-scale applications, several drawbacks/limitations must be addressed. The latter include poor stability of selected MOFs in the presence of humidity or upon a solvent removal (one of the steps of their synthesis) and weak dispersive forces for the adsorption of small molecule gases (e.g., ammonia or hydrogen). Moreover, there is a need to produce MOFs, currently available in the form of powder, into "user-friendly" configurations (e.g., membranes, thin films, etc.).

Subtitles:

- *Composites of MOFs with graphite oxide*: GO/MOF composites were formed via interactions between the oxygen groups of GO and metallic centers of MOFs. These composites showed higher ammonia and hydrogen adsorption capacities than those expected for the mixture of MOF and GO.
- *Composites of MOFs with functionalized graphite:* These composites showed higher ammonia and hydrogen adsorption capacities too.
- *Composites of MOFs with carbon nanotubes*: CNTs can act as a template for MOF growth. Surface carboxylate functional groups of a CNT could act as nucleation sites to form MOFs by heterogeneous nucleation and crystal growth.
- *Composites of MOFs with polymers:* Externally accessible nanosized cavities and channels allow for the incorporation of substrates inside the crystal to facilitate the heterogeneous catalytic action of these MOFs.
- *Composites of MOFs with mesoporous silica and alumina:* High micropore volumes and consequently large specific surface areas (SSAs) are desirable for

Nanomaterials and Nanocomposites: Zero- to Three-Dimensional Materials and Their Composites,
First Edition. Edited by Visakh P.M. and Maria José Martínez Morlanes.

many applications. Such narrow pores do not allow for fast diffusion, which limits their uses in adsorption, catalysis, and separations. Thus, the preparation of MOF-based materials with mesopores (pore widths between 2 and 50 nm) is important from a utilitarian viewpoint. One approach is to control the growth of MOF crystals on the surface of silica and alumina.

- *Composites of MOFs with metal nanoparticles*
- *Composites of MOFs with silk*

9.1 Composites

Composites are multicomponent materials comprising multiple different (non-gaseous) phase domains in which at least one type of phase domain is a continuous phase [1]. They are often used in industrial processes, since the composites combine the properties of the phases, and tuning of the properties is possible. Thus, they have been studied, for example, to improve gas sorption properties or in gas separation. In addition, handling of the composites is often easier compared to the crystalline MOFs. Especially in catalysis, composites are of interest since the catalytic activity of the dispersed phase is combined with superior stability of the continuous phase, which also allows the easy recovery of the catalyst.

In the following section, composites will be described containing the MOF as the dispersed phase. The sections are organized according to composites containing an organic or an inorganic matrix. Monoliths, membranes, fibers, or beads were used as the continuous phase. The section does not cover MOF-based composites where the MOF is the continuous phase. Numerous examples for these kinds of composites have been reported, which also include metals [2], magnetic particles [3], CNTs [4], or polymers [5] as the dispersed phase.

9.1.1 MOF-Organic Matrix Composites

MOFs contain metal ions linked by coordinated ligands into an infinite array. This is a general term that incorporates a variety of architectures ranging from simple one-dimensional chains with small ligands to large mesoporous frameworks like MOFs [6–15].

Natural and synthetic polymers were used for the formation of composites composed of an organic matrix and MOF crystals. One study on the use of a monolithic material has been reported. HKUST-1 crystals were deposited within the interconnected voids of a monolithic macro porous hydrophilic poly-HIPE, which was obtained by polymerization of 4-vinylbenzyl chloride and divinylbenzene. Hydrophilization was mandatory to obtain homogenous distribution of the crystals throughout the monolith, which was easily detected by the light blue color of the composite material. The formation of the composite was accomplished by treating the activated monolith with the reaction mixture followed by the solvothermal reaction [16], A HKUST-1 monolithic structure (Figure 9.1a)

Figure 9.1 Digital images of (a) HKUST-1 monolith, (b) ZIF-8/PVP fiber mat, and (c) HKUST-1/PAM beads.

was also manufactured in a two-step process. Presynthesized crystals were first mixed with a liquid-binding agent and a plasticizer in a lab-scale kneader until the molding batch appeared as homogeneous. In a second step, the molding batch was extruded to a monolithic structure [17]. Synthetic polymer-MOF composite membranes have been investigated using a polyimide (Matrimid) and a polysulfone polymer as the matrix. Composite membranes of MOF-5 and ZIF-8 with Matrimid were prepared by the solution blending approach [18, 19]. A dispersion of preformed MOF-5 or ZIF-8 was added to a solution of Matrimid in $CHCl_3$. Dispersion of the MOF crystals was accomplished by sonication. The composite membrane was formed by evaporation of the solvent. Plastic deformation of the composite membrane indicated strong interaction between the polymer matrix and the MOF-5 nanocrystals.

Appling the same approach, composite membranes of HKUST-1, MIL-47, MIL-53, and ZIF 8 with Matrimid or polysulfone were also produced [20, 21]. Better quality composite membranes were formed by pretreatment of the MOF crystals with the silylating agent *N*-methyl-*N*-(trimethylsilyl) trifluoroacetamide. In a similar study, ZIF-8-polysulfone membranes were also obtained by the solution blending approach [22]. The CO_2 diffusion properties of the composite membranes were studied, and the ZIF-8 crystals were shown to improve the transport of the gas through the membrane.

Synthetic polymer fibers were also employed as the substrate, and the composites were obtained by electrospinning. In the first report, ZIF-8/polyvinylpyrrolidone (PVP) composite nanofibers were synthesized starting from a PVP solution with well-dispersed ZIF-8 nanocrystals (Figure 9.1b) [23]. The diameter of the nanofibers in the fiber mat was adjusted by varying the polymer concentration. Using other polymers like polystyrene and polyethylene oxide allowed increasing the fibers' stability. Higher ZIF-8 loadings were achieved by tuning the synthesis parameters and functionalizing the surface of the ZIF-8 nanocrystals with less polar molecules. The second report describes the preparation of the MOF/polymer (MOF: HKUST-1, MIL-100; polymer: PS, PVP, polyacrylonitrile, polypropylene) composite fibers with different mechanical stabilities [24]. A small difference between particle size and fiber diameter led

to a pearl necklace-like morphology with lower MOF loadings. Fortunately, particles in combination with significantly smaller fibers resulted in a spider-like morphology at higher MOF loadings.

Natural polymer fibers were also used to form composites. Differently treated pulps were employed. Addition of the crystalline powder of HKUST-1 to the pulp slurry was found to yield a homogeneous distribution of the powder [25]. Pulp fibers with crystals homogeneously distributed over the surface area were obtained by the direct growth method. In these experiments, the degree of coverage increased with increasing lignin contents in the fibers. This was explained by the presence of carboxyl groups in lignin. PAM beads were used as a matrix, due to their hydrophilicity, in combination with HKUST-1 and Co-CPO-27311 with the goal to enhance mechanical stability and facilitate handling compared to bulk HKUST-1.

Two methods were employed: formation under solvothermal conditions and immersion of the beads into preheated crystallization solutions. Using copper (II) nitrate, HKUST-1/PAM composites (Figure 9.1c) were synthesized under solvothermal conditions, and the presence of

HKUST-1 crystals within the beads was confirmed by scanning electron microscopy (SEM) images. Preswelling of the beads in an ethanol/water (1 : 1) mixture prior to solvothermal treatment led to the growth of the crystals only on the external surface, indicating a large barrier to diffusion compared to the rate of nucleation and crystal growth.

The ratio of MOF: polymer could be adjusted by changing the concentration of the HKUST-1 reaction mixture. The immersion procedure of untreated beads did not lead to the formation of HKUST-1 crystals. Therefore, pretreatment, that is, preswelling of the PAM beads in a solution of copper (II) acetate was carried out, which led to the formation of HKUST-1/PMA composites. Independent of the pretreatment, solvothermally prepared Co-CPO-27/PAM beads exclusively exhibited crystals on the external surface. In addition to pure organic beads, composite SiO_2/PAM beads were also tested. Applying the immersion method, HKUST-1 crystals were grown on SiO_2/PAM beads.

9.1.2 MOF-Inorganic Matrix Composites

Four different types of inorganic matrices – GO, silica, alumina, and cordierite or combinations thereof were employed for the formation of composites. Two studies were reported on the coating of a cordierite monolith [7, 17, 18]. Uniform coatings of Cr-MIL-101 nanocrystals inside the macro pores of a cylindrical cordierite monolithic were accomplished by employing the secondary growth technique [26].

Two methods were employed: (i) a suspension of α-alumina was dip-coated on the substrate prior to seeding with preformed Cr-MIL-101 nanocrystals and (ii) the suspension of α-alumina together with preformed Cr-MIL-101 nanocrystals was dipcoated on the substrate. Dense, uniform coating was observed for

optimized reaction conditions, that is, rotating of the autoclave during the secondary growth step as well as the right choice of the size of seeds and the seeding procedure. The composite was tested in liquid-phase oxidation reactions and showed good stability. In the second study, a cordierite monolith was also used as the substrate [7]. Solvothermal synthesis of HKUST-1 resulted in low crystal coverage on the cutting edges of the honeycomb structure. In order to enhance gas adsorption capacities of GO, composites of MOF-5 [27] and HKUST-1 [28] were synthesized by dispersing GO in the synthesis mixtures prior to the solvothermal reactions. GO/MOF-5 composites with various ratios of the components were obtained. With increased GO content, a decrease in microporosity was observed. The composites likely adopted lamellar structures constructed from alternating layers of GO and MOF, which was explained by possible interactions between the epoxy groups on graphene and the oxide clusters in MOF-5. GO/HKUST-1 composites were also reported, and the porosity of the composite was claimed to exceed that of the parent materials. Unfortunately, a specific surface of 900 $m^2\ g^{-1}$ of HKUST-1 for their material was reported by the authors, which is far below the state-of-the-art values known for HKUST-1. Recently, the formation of GO/Fe-MIL-100 composites was also investigated. In these studies increasing amounts of amorphous phase were observed with higher GO contents [29].

Using a nonionic surfactant, the formation of hierarchical micro- and mesoporous HKUST-1/alumina and HKUST-1/silica composites was investigated. These were prepared by applying MW irradiation to a dispersion containing starting materials of HKUST-1 and the alumina (boehmite) or silica (TEOS) source together with the triblock copolymer Pluronic P123 [30]. Microporosity as well as mesoporosity could be demonstrated for the composites by sorption experiments, and the presence of HKUST-1 was confirmed by XRPD measurements. Silica as well as alumina beads were also employed as substrates for the synthesis of HKUST-1 composites. Monodisperse mesoporous silica beads (Nucleosil 100-3) were impregnated with the starting mixture, and the solvent was evaporated [31].

The monodisperse MOF-silica composites were tested as the HPLC stationary phase and showed good separation properties. In another report [32], silica and SiO_2/Al_2O_3 composite beads were used. Two methods were employed: formation under solvothermal conditions and immersion of the beads into preheated crystallization solutions. No HKUST-1 growth was detected on the silica beads, but growth was observed using mixed SiO_2/Al_2O_3 beads. This was attributed to the more basic properties of the alumina. No information regarding bead surface growth or growth within the macro pores of the beads was reported.

9.1.3
Composites of MOFs with Graphite Oxide

Recently, in the scientific community, great interest has risen in graphene and graphene-based materials [33], owing to the specific and very unique structural, mechanical, and electronic properties of these one-atom-thick sheets. The

common source of grapheme is graphite, which can be considered as 3D crystals consisting of graphene layers. Separation of graphite into graphene layers is not a trivial task and many attempts have been made based on GO. GO is formed by treating graphite with very strong oxidizing agents [34] and has a layered structure and a nonstoichiometric chemical composition. Recently, it has been used to build various nanocomposites, which exhibit enhanced electronic and adsorption properties [35]. The graphene layers of GO are stacked together with an interlayer distance varying from 6 to 12 Å depending on the level of hydration [36]. Oxidation of graphite causes the introduction of epoxy and hydroxyl groups into the graphene layers, as well as the introduction of carboxylic groups mainly located on the edges of the layers [37]. Moreover, strong oxidation leads to defects in the layers in the form of incorporated oxygen atoms or vacancies [38]. This increase in hydrophilicity causes GO to be easily dispersed in water and delaminated in alkaline media or alcohols [39]. Subsequently, the graphite layers can be restacked and their degree of orientation depends on the method of drying.

Another group of materials that have recently opened new possibilities of applications are MOFs [40]. Yaghi and co-workers were the first group to describe the synthesis and properties of MOFs [41]. During recent years, it has been shown that a large variety of 2D and 3D metal–organic networks with high porosity, unusual ion exchange, and adsorptive properties can be designed using intermolecular interactions and metal–ligand co-ordination [42]. The structure of the materials obtained is the result of a maximum degree of freedom in both components, the spherical shape of metal ions, and well-defined points of contacts in the organic linkers [43].

In spite of the very high porosities of MOFs, their open framework is not able to provide strong, nonspecific adsorption forces to retain small molecules at ambient conditions. For this kind of separation process, a surface consisting of a dense arrangement of atoms and a porous network is needed. An ideal situation is present when this dense surface creates an accessible porous framework with pores similar in size to the target molecule. This is not an easy task and, for years, various methods of sorbent synthesis and modifications have been explored to provide the best suitable surface features. To meet the above requirements in adsorption processes, the concept of MOF–GO nanocomposites has been developed. Knowing the ratios of GO and MOF in the composites, it is expected that distorted graphene sheets will contribute to the enhancement in the dispersive interactions, whereas the MOF component will contribute to the expansion of the pore space, in which the adsorbate can be stored. Moreover, taking into account the variety of transition and noble metals, which can be used to form the MOF structure, these materials have a potential to provide active sites for reactive adsorption or heterogeneous catalysis. There are also other unforeseen applications, where the presence of graphene can increase the electrical conductivity of the resulting materials. Examples of MOFs are MOF-n materials (n = integer designating a specific structure), which are built from the extended analogs of molecular metal–carboxylate clusters. They are

stable at rather high temperature and their porosity can reach up to 60% [42]. The preparation of MOFs involves the reaction between solutions of metal ion salts and organic linkers. Besides, as mentioned above, a broad range of transition of noble metals can be used in the synthesis owing to their catalytic properties [44].

Thus, a major objective of this work is to present the synthesis of MOF–GO nanocomposite materials, which combine the favorable attributes of carbonaceous graphene surfaces and MOFs. As a metal–organic framework, MOF-5 was chosen, owing to its relatively small pore size (8 Å) and the chemistry of the linkages. In MOF-5, $(Zn_4O)^{6+}$ tetrahedra occupy the corners of a primitive cubic structure, while benzene carboxylates (1,4-benzenedicarboxylate, BDC) form junctions between these zinc oxide clusters [45]. The formula of the resulting material is $Zn_4O(H\text{-}BDC)_3$ [42]. Since epoxy and carboxylic groups are present on GO, it is expected that they might anchor zinc oxide clusters. Synthesis of the parent materials and the nanocomposites is followed by their surface characterization using a range of experimental methods. Different nanocomposites containing 5, 10, and 20 wt% of GO are presented. The nanocomposites are referred to as MOF-5–GO1, MOF-5–GO2, and MOF-5–GO3, where 1, 2, and 3 represent the 5, 10, and 20 wt% of GO in the samples, respectively. nanocomposites containing GO and MOF-5 have been prepared with various ratios of the two components. The structure of the precursors is preserved in the composites, which show a well-defined and porous structure; where graphene layers from GO alternate with layers of MOF-5. The arrangement of these materials is progressively modified and its porosity decreases when the amount of GO in the composite increases. It is hypothesized that the formation of such structures occurs via interactions between epoxy groups from graphene layers and zinc oxide clusters from MOF-5. Due to their preserved porosity and well-developed and flexible functionality, these materials might be tested for gas-adsorption applications.

In other work, graphene can be decorated with functional groups on either side of its basal plane, giving rise to a bifunctional nanoscale building block that can undergo face-to-face assembly. Benzoic acid-functionalized graphene (BFG) can act as a structure-directing template in influencing the crystal growth of MOFs. BFG is also incorporated into the MOF as a framework linker. Because of the high density of carboxylic groups on BFG, an unusual MOF nanowire that grows in the (220) direction was synthesized. The diameter of the nanowire correlates closely with the lateral dimensions of the BFG. The intercalation of graphene in the MOF imparts new electrical properties such as photoelectric transport in the otherwise insulating MOF. The results point to the possibility of using functionalized graphene to synthesize a wide range of structural motifs in the MOF with adjustable metrics and properties.

Schematic of proposed bonding between functionalized grapheme and an MOF via COOH groups along (220) direction and the assembly into nanowire structure have been shown in Figure 9.2.

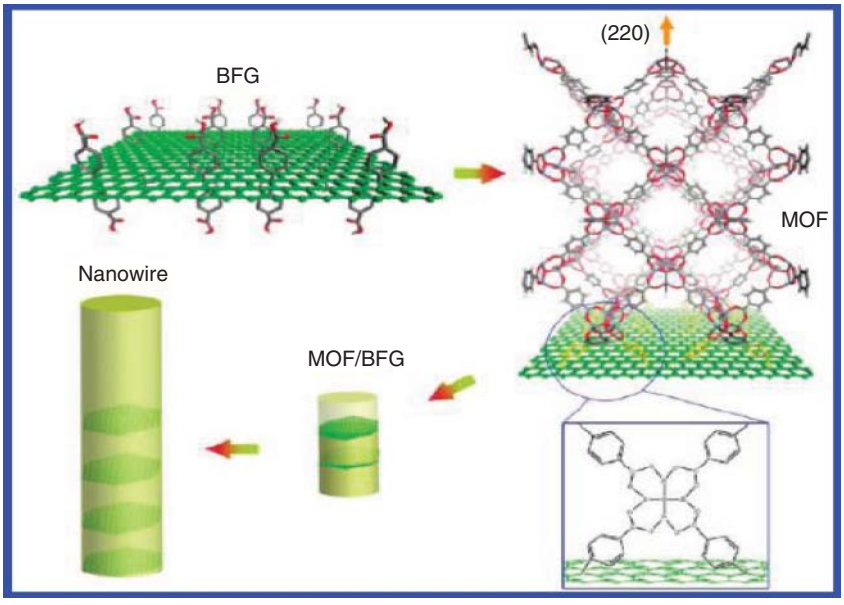

Figure 9.2 Bonding between functionalized grapheme and MOF via –COOH groups along (220) direction and the assembly into nanowire structure.

The sorption properties of the MOF/BFG were investigated by recording the N_2 sorption isotherms. The isotherm reveals that the MOF/BFG samples exhibit typical type I sorption behavior without hysteresis [46]. As derived from the N_2 adsorption data, the Brunauer-Emmett-Teller surface area of MOF/BFG (5 wt%) is higher than that of MOF-5, which indicates that intercalated graphene increases the surface area in porous MOF-5. However, the difference between nitrogen adsorption of nanowire and MOF-5 is not so significant.

BET nitrogen adsorption isotherms were recorded to study the effect of BFG in increasing the surface area of MOF-5. The BET surface area and microporosity of our synthesized MOF-5 is similar to that reported by Petit *et al.* [27]. The results show that the surface area and microporosity of MOF/BFG is only marginally improved over that of MOF-5, due perhaps to the low wt% (5%) of graphene used in the experiments. Although the BET surface area and microporosity of the synthesized MOF-5 is close to that reported by Huang *et al.* [47], it should be noted that the surface area of the MOF-5 reported here is much smaller than 3500 $m^2 g^{-1}$, the highest value reported [48]. This is due to the fact the preparation conditions for the MOF-5 had not been optimized.

9.1.4
Composites of MOFs with Functionalized Graphite

To drive MOFs up to the step of industrial/large-scale applications, several drawbacks/limitations must be addressed. The latter include poor stability of

selected MOFs in the presence of humidity or upon a solvent removal (one of the steps of their synthesis) and weak dispersive forces for the adsorption of small molecule gases (e.g., ammonia or hydrogen). Moreover, there is a need to produce MOFs, currently available in the form of powder, into "user-friendly" configurations (e.g., membranes, thin films, etc.,). Many research efforts have focused on these issues and the deposition of MOF on various supports such as alumina, silica, functionalized self-assembled monolayer (SAM), functionalized graphite, GO, or amorphous carbon have been recently reported as a way to produce MOF-based membranes or composites. These studies indicate that the functionalization of the substrate is important in the preparation of MOF-based composites. In particular, Jahan and co-workers reported the growth of MOF-5 on functionalized graphite and found that the graphite influences the crystal growth of the MOF.

MOF/graphite hybrid materials were prepared using an *in situ* process. Graphite with various chemical and physical features were used, and HKUST-1 was selected as the MOF component. The samples (parent materials and hybrid materials) were characterized by X-ray diffraction (XRD), nitrogen sorption, SEM, Raman spectroscopy, Fourier transform infrared spectroscopy, and thermo gravimetric analysis. Then they were tested as ammonia adsorbents in dynamic conditions. The results indicate that the functionalization of graphite is important to build the hybrid materials with synergistic properties. The lack of functional groups on graphite results in the formation of a simple physical mixture. Besides the surface chemistry of the graphitic component, the physical parameters (porosity and size of flakes) also seem to influence the formation of the hybrid materials. It is observed that the graphite particles disturb the formation of HKUST-1 and induce a different crystal morphology (more defects and increased surface roughness) than the one observed when the MOF is formed in the absence of a substrate. The latter behavior causes less ammonia to be adsorbed on the hybrid materials than is expected for the simple physical mixture of HKUST-1 and graphite. The MOF structure collapses (in HKUST-1 and the hybrid materials) upon ammonia adsorption and leads to the formation of a new species.

This part focuses on MOF/graphite hybrid materials. Graphites with differences in their chemical and physical features are used to prepare the hybrid materials. The MOF selected is HKUST-1 and contains copper ions as the metallic centers and molecules of benzene tricarboxylic (BTC) as the organic ligand [49]. HKUST-1 was chosen owing to its relatively easy synthesis and large porosity, and the presence of unsaturated metallic copper sites capable of binding to ammonia. The samples (parent materials and hybrid materials) were characterized by various techniques and tested for ammonia adsorption in dynamic conditions. The results of this study, along with those obtained on MOF/GO composites, should bring a clearer picture of the role of the substrate's functional groups on the formation of MOF-based composites as well as an indication of the influence of the substrate's physical features. Indeed, in the case of the MOF/GO composites, formation of the composites was proposed to occur as a result of the linkages between the oxygen groups of GO and the metallic centers of the MOF.

It was suggested that these linkages were responsible for an increase in porosity in the composites compared to the parent materials. By studying hybrid materials involving the MOF and graphite and comparing the results to those obtained on the MOF/GO composites, we intend to clearly isolate the effect of the oxygen groups. This will provide a better understanding of their role on the porosity formation. Therefore, by suppressing the effect of the GO functional groups, we can better isolate the influence of the physical parameters of graphite on the formation and structure of the resulting MOF/graphite materials.

The hybrid materials were prepared by adding a graphite powder to the well-dissolved MOF precursors and solvent mixture, which was used for HKUST-1 synthesis. The hybrid materials are referred to as MGrn with $n = 1$, 2, 3, 4, and 5 depending on the graphite used. The estimated graphite contents (from thermal analysis) in MGr1, MGr2, MGr3, MGr4, and MGr5 are 10.6, 10.0, 11.3, 14.9, and 3.5 wt% graphite, respectively.

An important aspect of adsorbents in general and MOFs in particular is the porosity of these materials. Comparison between the measured parameters and the ones calculated enables us to identify any synergistic effect between HKUST-1 and graphite. Although Gr1 and Gr2 are nonporous materials, Gr3 exhibits quite a high surface area and pore volume considering the nonporous nature of the graphite materials in general (222 $m^2 g^{-1}$ and 0.334 $cm^3 g^{-1}$). The porosity of Gr4 and Gr5 are intermediate between those of Gr1 and Gr3 samples. HKUST-1 has a surface area of 984 $m^2 g^{-1}$ and a total volume of pores of 0.514 $cm^3 g^{-1}$. The porosity of the hybrid materials is in the range of that of the MOF; however, a slight decrease is found (except for MGr5) due to the addition of low- or nonporous graphite.

Ammonia removal from air was tested on the parent and hybrid materials in dynamic conditions and at room temperature. It is important to note that the tests were not carried out until whole breakthrough sigmoidal curves were recorded. The breakthrough was monitored until the outlet concentration reached 10% of the inlet concentration, and thus only a rapid increase in the ammonia concentration was observed up to 100 ppm. The decrease in concentration observed afterward corresponds to the desorption curve. During that step, no more ammonia is injected in the system and only air passes through the adsorbent's fixed bed. This part enables to assess the amount of ammonia released and thereby to evaluate the strength of ammonia retention. The steeper the desorption curve, the smaller the amount of ammonia desorbed and thus the stronger the retention process. HKUST-1 and the hybrid materials tested in the dry conditions exhibit steep breakthrough and desorption curves, which indicate the fast kinetics of interactions and the strong adsorption of ammonia, respectively.

In moist conditions however, the desorption curves are much less steep which suggests the weaker retention of ammonia. This has already been observed in the case of MOF/GO composites and attributed to the presence of ammonia dissolved in water [50]. This type of ammonia is easily removed during air purging together with water vapor phase. The results indicate that the oxidation of graphite is important to build MOF/graphite hybrid materials with synergistic properties.

The presence of functional groups on the substrate's surface enables the formation of bonds between the components and thus the composites can be formed. The results suggest that MOF/graphite hybrid materials represent a distorted physical mixture of MOF and graphite. Besides the chemical features of the graphite, the physical parameters, and especially the porosity and size of flakes, also seem to influence the formation of the hybrid materials. Overall, the graphite particles interfere with the formation of HKUST-1 and induce a different crystal morphology (more defects and increased surface roughness) than the one observed when the MOF is formed in the absence of a substrate. The latter behavior results in less ammonia being adsorbed on the hybrid materials than would be expected from the simple physical mixture of HKUST-1 and graphite. As already described in previous studies, ammonia adsorption induces the collapse of the MOF structure and changes in the chemistry of materials, in both HKUST-1 and the hybrid materials.

9.1.5
Composites of MOFs with Carbon Nanotubes

Reduction of the anthropogenic emission of CO_2 is currently a top priority because CO_2 emission is closely associated with climate change. Carbon capture and storage (CCS) [51] and the development of renewable and clean energy sources are two approaches for the reduction of CO_2 emission. One of the most promising alternative fuels is CH_4, which is the major component of natural gas. The efficient storage of CH_4 is still one of the main challenges for its widespread application. Accordingly, the development of more efficient approaches for CO_2 capture and CH_4 storage is critically important. Recently, MOFs (e.g., MOF-210 and NU-100) have shown great potential for gas storage because of their high SSA and functionalized pore walls. However, most MOF materials still show relatively low CO_2 and CH_4 uptakes. To enhance CO_2 and CH_4 adsorption, it is imperative to develop new materials, such as covalent organic frameworks (COFs), or to modify MOFs by using postsynthetic approaches.

One of the modification approaches is incorporation of CNTs into MOFs in order to achieve enhanced composite performance, because of the unusual mechanical and hydrophobicity properties of CNTs. Another approach is doping MOFs or COFs with electropositive metals. Recent studies indicate that the surface carboxylate functional groups of a substrate could act as nucleation sites to form MOFs by heterogeneous nucleation and crystal growth. Both experimental and theoretical investigations indicate that the H_2 adsorption capacities of MOFs can be enhanced significantly by doping alkali-metal ions, in particular Li^+ ions, to the frameworks, owing to the strong affinity of Li^+ ions toward H_2 molecules. Lan *et al.* also showed theoretically that doping of COFs with Li^+ ions can significantly enhance the CH_4 uptake of COFs. Most recently, the multiscale simulations performed by Lan *et al.* indicate that Li is the best surface modifier of COFs for CO_2 capture among a series of metals (Li, Na, K, Be, Mg Ca, Sc, and Ti). Furthermore, their simulations show that the excess CO_2 uptakes of the

lithium-doped COFs can be enhanced by four to eight times compared to the undoped COFs at 298 K and 1 bar.

Motivated by these experimental and theoretical results, hybrid MOF materials by using the two modification techniques outlined above have been synthesized, that is, (i) incorporation of CNTs into $(Cu_3(C_9H_3O_6)_2(H_2O)_3)\cdot xH_2O$ ($(Cu_3(btc)_2)$, HKUST-1; btc = 1,3,5-benzenetricarboxylate), which is an important MOF material owing to its open metal sides and high thermal stabilities, as well as its sorption properties and (ii) doping ($Cu_3(btc)_2$) with Li^+ ions. Has been used from lithium naphthalenide ($Li^+C_{10}H_8^-$) to introduce Li^+ ions into the ($Cu_3(btc)_2$) frameworks. These frameworks have Cu^{2+} sites that become available for interaction with other molecules after removal of H_2O in from Cu^{2+} carbonyl complexes, and can also be easily rehydrated without change of the crystalline nature of the material after exposure to air. Although the btc ligand cannot act as an electron receptor for the electron transfer from the naphthalenide radical anion, the rehydration of the Cu^{2+} sites in the framework makes the electron transfer possible because of the strong nucleophilicity of lithium naphthalenide, which is the main reason for selecting this complex. Furthermore, we also proposed a hypothetical hybrid composite, in which the CNTs with carboxylic groups provide homogeneous nucleation sites to support a continuous copper framework growth, and the Li^+ ions were subsequently introduced into the frameworks.

To better explore the cooperative effects of CNT incorporation and Li doping on the uptakes of CO_2 and CH_4, four different MOF materials have been prepared. The first two MOFs are unmodified ($Cu_3(btc)_2$) MOF (1); lithium-doped ($Cu_3(btc)_2$) (Li@($Cu_3(btc)_2$)). The sample of Li@($Cu_3(btc)_2$) with Li/Cu = 0.07 is denoted as 1·Li, which exhibits the greatest gas uptake of the investigated samples with various Li contents. Also, a carboxylic CNT hybrid composite has been prepared (CNT@($Cu_3(btc)_2$), 2) and lithium-doped CNT@($Cu_3(btc)_2$) (Li@CNT@($Cu_3(btc)_2$); the sample with Li/Cu = 0.001 is denoted as 2·Li).

To determine how modification by CNTs affected the CO_2 and CH_4 capacities of $Cu_3(btc)_2$, gas adsorption measurements have been carried out by using an intelligent gravimetric analyzer (IGA-003). Both CO_2 and CH_4 isotherms for 1 and 2 show good reversibility without hysteresis and are not saturated.

At 298 K and 18 bar, the CO_2 uptake of 2 is 595 mg g^{-1}, which is about twice the uptake of 1 (295 mg g^{-1}) under the same conditions. Similarly, the same behavior occurs for the CH_4 adsorption. At 298 K and 18 bar, the capacity of 2 for CH_4 reaches 120 mg g^{-1}, which is higher than the value for 1 (72 mg g^{-1}). Thus, the incorporation of CNTs in ($Cu_3(btc)_2$) enhances the CO_2 and CH_4 adsorption capacities of 1 significantly.

Both CO_2 and CH_4 isotherms of 1·Li, and 2·Li show good reversibility without hysteresis between adsorption and desorption. This observation suggests that CO_2 and CH_4 are reversibly physisorbed in lithium-doped materials, similar to hydrogen storage. The CO_2 uptake increases from 295 mg g^{-1} (1) to 469 mg g^{-1} (1·Li) at 298 K and 18 bar, while the CH_4 uptake increases from 72 mg g^{-1} (1) to 96 mg g^{-1} (1·Li) under the same conditions. The enhancing effect of Li doping

on gas adsorption is also observed for 2. At 298 K and 18 bar, the CO_2 and CH_4 uptakes of 2·Li reach 660 and 130 mg g^{-1}, respectively, while the uptakes are 595 and 120 mg g^{-1} in 2, respectively, under the same conditions.

Recently, MOFs have been evaluated as promising H_2storage media as MOFs exhibit exceptionally high surface areas and tunable pore size. An additional advantage of MOFs is that preparation is economic as MOFs are synthesized by "one-pot" solvothermal methods under mild conditions. Much effort has been devoted to improving MOF H_2 storage capacities and adopting strategies such as high porosity with appropriate pore size, catenation, and inclusion of open metal sites. For example, Rowsell and colleagues attempted to improve H_2 storage capacity by tailoring organic ligands [52]. These authors obtained (at 77 K and 1 bar) H_2 storage capacities of 1.62, 1.32, and 1.25 wt% from products with Langmuir specific surface areas (L-SSAs) of 1910, 3360, and 4530 m^2 g^{-1}, respectively. This indicates that high surface area is not the only factor influencing adsorbent H_2 storage capacity [43]. Sun and co-workers obtained 1.9 wt% storage at 77 K and 1 bar using interwoven MOFs (of L-SSA 3800 m^2 g^{-1}) in which a single H_2 molecule could interact with several ligand aromatic units [53]. Yaghi and colleagues and Dietzel and coworkers took somewhat different approaches. These authors deliberately introduced open metal sites, or metal centers that were unsaturated from a coordination aspect, to increase the affinity of H_2 molecules for metal sites [54]. Indeed, MOF-505, which contains such open metal sites, exhibited a much improved H_2 storage capacity of about 2.5 wt% at 77 K and 1 bar [46a]. However, H_2 storage by MOFs at room temperature is far below that seen at 77 K and 1 bar. Indeed, interwoven MOFs (with an L-SSA of 303 m^2 g^{-1}) showed 0.3 wt% H_2 storage at 298 K and 65 bar and Ni-based MOFs containing open metal sites (with an L-SSA of 1083 m^2 g^{-1}) had a H_2 storage capacity of 0.3 wt% at 298 K and 90 bar [54]. Thus, structural modifications such as open metal sites, use of non-zinc metal cores, and higher SSA did indeed contribute to enhanced H_2 storage at 77 K, but not necessarily at room temperature. Among reported MOFs, MOF-5 ($Zn_4O(bdc)_3$; bdc = 1,4-benzenedicarboxylate) is the most thermostable, shows the highest porosity, and has a high H_2 capacity, suggesting that MOF-5 is a promising gas storage medium, particularly for hydrogen. However, MOF-5 shows relatively low H_2 storage capacity at 298 K and is extremely water-sensitive, even under atmospheric conditions, showing a sharp reduction in surface area after prolonged exposure to humid air. If H_2 gas adsorption enthalpy and water stability could be improved, MOF-5 would be a very promising candidate for commercialization.

Another hybrid composite is acid-treated multiwalled carbon nanotubes (MWCNTs) and MOF-5 (denoted MOFMC). In a successful synthesis, well-dispersed MWCNTs in dimethylformamide (DMF) were mixed with a DMF solution of zinc nitrate tetrahydrate and terephthalic acid.

The use of CNTs as composite fillers has been investigated in various applications, and enhanced composite performance has been achieved because of the unusual electroconductive, thermoconductive, mechanical, and hydrophobicity properties of CNTs [55]. In particular, CNTs have been considered as useful

composite fillers in H_2 storage research. Synergistic effects such as increases in H_2 storage capacity, lowered desorption temperature, and reductions in charging and discharging time have been obtained by incorporation of CNTs into H_2 storage materials. The MOFMCs obtained had the same crystal structure and morphology as those of virgin MOF-5, but exhibited a much greater L-SSA (increased from 2160 to 3550 $m^2 g^{-1}$), about a 50% increase in hydrogen storage capacity (from 1.2 to 1.52 wt% at 77 K and 1 bar and from 0.3 to 0.61 wt% at 298 K and 95 bar), and much improved stability in the presence of ambient moisture.

Figure 9.3 shows FE-SEM and optical images of MOFMC. The MOFMC morphology is characterized by well-defined cubic crystals 50–250 μm in width. The black stripes on a transparent golden background (Figure 9.3b) indicate that CNTs were incorporated inside MOF-5.

Powder X-ray diffraction (PXRD) patterns of virgin MOF-5 and MOFMC were found to be in perfect agreement with earlier data on MOF-5, confirming that MWCNT incorporation did not disturb or destroy the MOF-5 crystal structure. MWCNTs and MOF-5 exhibited H_2 uptakes of 0.15 and 1.2 wt%, respectively, in good agreement with previous studies [52], but MOFMC showed a somewhat increased capacity of 1.52 wt% at 77 K and 1 bar. Generally, it is recognized that ultramicro pores 0.6–0.7 nm in diameter are more effective in high-level hydrogen uptake than are pores of other diameters.

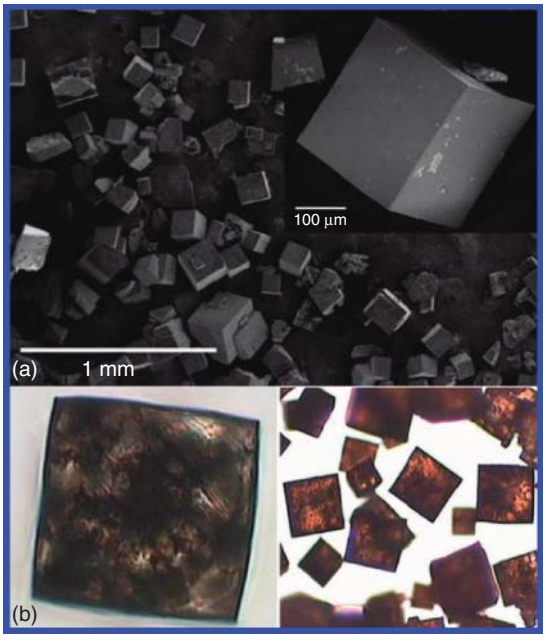

Figure 9.3 (a) FE-SEM images of MOFMC. The inset shows an enlarged view of the crystal. (b) Optical images of MOFMC.

In MOF-5s, extremely high SSAs (over 3000 m^2/g from DEF-based syntheses) are obtained, but pore diameter is usually 1.2–1.3 nm. This is why relatively low hydrogen uptakes of 1.2–1.3 wt% at 77 K (1 bar) and 0.3–0.4 wt% at 298 K (100 bar) are seen, despite high SSAs [43]. With MOFMCs, the ultramicropore volume was significantly increased compared with that of MOF-5s, although MOFMCs' crystal structure was the same as that of MOF-5. Thus, the 1.52 wt% H_2 storage capacity of MOFMC contains a contribution from ultramicropores arising because of MWCNT incorporation. It is particularly noteworthy that, at 298 K and high pressure, the hybrid composite H_2 storage capacity became much more apparent. At low pressure and 298 K, H_2 storage capacity of MOFMC was only slightly higher than those of other materials examined (MOFMC, 0.024 wt%; MOF-5, 0.015 wt%; MWCNT, 0.010 wt%), and the MOFMC isotherm slope indeed suggested enhanced H_2 storage capacity at high pressure. Under higher pressure, up to about 95 bar at 298 K, MWCNTs and MOF-5 had H_2 storage capacities of 0.2 and 0.3 wt%, almost the same as in previous reports. However, the hybrid composite had a twofold greater H_2 storage capacity (0.61 wt%) than did MOF-5. Furthermore, adsorption at each tested pressure was reversible, and equilibrium was obtained within 10 min (data not shown). These observations imply that additional micropore development within MOFMC enhanced H_2 storage capacity at 77 K, particularly at 298 K, over a wide pressure range.

An interesting feature of the MOF-5/MWCNT hybrid composite is enhanced moisture stability under ambient conditions. Moisture stability tests on MOF-5 and MOFMC were carried out at 33% relative humidity and 23 °C. Exposure of desolvated MOF-5 to air for 2 h resulted in the appearance of a new XRD peak at around 8.4°, indicating commencement of decomposition. On subsequent exposure to air, peak relative intensity increased, indicating acceleration of decomposition. After 1 week of air exposure, decomposition was almost complete, as no MOF-5 crystal reflections were seen. However, even after 1 week in air, the reflections of MOFMC did not change. Thus, we believe that incorporation of MWCNTs into MOF-5 crystals protects the moisture-sensitive MOF-5 surface, now covered (at least partially) with rigid MWCNTs.

9.1.6
Composites of MOFs with Polymers

The large surface areas, low framework densities and high pore volumes of MOFs relative to other porous matrices have motivated a great deal of interest in these materials, which have significant potential for use in a variety of applications ranging from storage of gases to heterogeneous catalysis [56–58]. In particular, externally accessible nanosized cavities and channels allow for the incorporation of substrates inside the crystal to facilitate the heterogeneous catalytic action of these MOFs. Despite the vast number of MOF structures discovered (over 10 000), relatively few reports detail applications of MOFs functionalized by incorporation of metal ions, organic molecules incorporated via host–guest interactions (doping), or nanoparticles. The focus in this part has been on

applications of well-known MOF matrices that are rendered functional by doping with inorganic guest molecules with a known functionality tailored for catalytic functions. Chromium (III) terephthalate (MIL-101) because of its high thermal, chemical, and solvent stability, and large (~3.5 nm) cavities enable mass transport via pentagonal and hexagonal windows (~1.5 nm). In addition, the presence of chromium clusters not bound to the linkers provides coordinatively unsaturated sites (CUSs) with mild Lewis acid properties. The acidic CUS sites allow for the postsynthesis modification of MIL-101 with amines that transform MIL-101 into a basic catalyst functional in a Knoevenagel condensation. Due to its open-pore structure with large cavities, MIL-101 can be functionalized by Pd or Au nanoparticles and polyoxometalate (POM) anions, making the resulting composite materials effective in hydrogenation reactions and as oxidation catalysts. Among other POM materials that can be used to functionalize MIL-101 frameworks, phosphotungstic acid (PTA) is of interest, as it is the strongest heteropolyacid known, with a good thermal stability in the solid state. Following work by Férey *et al.*, there have been several reports on MIL-101 and PTA composites (MIL101/PTA) and their use in oxidation of alkenes using molecular oxygen and aqueous hydrogen peroxide as oxidants, H_2O_2-based alkene epoxidation, Knoevenagel condensation of benzaldehyde and ethyl cyanoacetate, liquid and gas-phase acid-catalyzed esterification (acetic acid with n-butanol, methanol dehydration) (110), and carbohydrate dehydration.

Here, synthesis of MIL-101 and MIL101/PTA composites in water without toxic and highly corrosive hydrofluoric acid (HF) has been studied. This approach makes the synthesis by solvothermal methods far less challenging. Further, the MIL/PTA composites were synthesized by either simple thermal treatment of aqueous mixtures of chromium (III) nitrate, terephthalic acid and PTA, or by impregnating already synthesized MIL-101 with PTA in aqueous media. It appeared that novel structures of the MIL101/PTA composites ensued, with Keggin ions of PTA being aligned within the MIL-101 pores and cavities. The acidic properties of the MIL-101 and MIL101/PTA to catalyze Baeyer condensation reactions has been exploited, wherein arylaldehydes react with phenols or *N*,*N*-dimethylaniline (Figure 9.4).

Heterogeneous acid catalysis of these industrially important reactions enhances product purity and greatly simplifies catalyst recovery and recycling, compared to the widely used homogeneous catalysis by strong acids such as hydrochloric or sulfuric acids and the like. Baeyer reactions have been chosen as they can be conducted solvent-free and therefore can attenuate the effect of the catalyst.

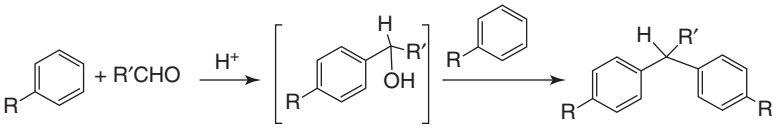

R: OH, OCH_3, $N(CH_3)_2$; R′: H, alcane, benzene

Figure 9.4 Schematic of the acid-catalyzed Baeyer condensation reaction.

Representative syntheses of bioactive drug intermediates, dibenzo (*a,j*) xanthenes and 1-amidoalkyl-2-naphthols, by condensation of 2-naphthol and benzaldehyde were conducted.

MIL101/PTA catalyst could be reused several times without extensive activity loss. The mild operating conditions and microwave-assisted heating did not cause any significant deterioration in the catalyst composition and structure, yet high yields were attained within minutes. Similarly, the MIL101/PTA composites appeared to catalyze epoxidation of caryophyllene by aqueous hydrogen peroxide. Caryophyllene oxide, an oxygenated terpenoid resulting from this reaction, is well known as a preservative in food, drugs, and cosmetics, and as an antimicrobial and antifungal agent. Caryophyllene epoxidation is analogous to reactions such as epoxidation of olefins, with epoxides being important intermediates that can be stereo- and regioselectively converted to a variety of oxygen-containing compounds. Due to the efficient heat supply by the microwaving, over 90% of the caryophyllene conversion has been obtained within minutes under mild conditions compared to hours required with conventional heat sources, and MIL101/PTA composites be recyclable.

9.1.6.1

Hybrids of MIL-101 and Phosphotungstic Acid (MIL101/PTA)

The large, 3.6-nm cages of MIL-101 are believed to accommodate the introduction of species such as PTA within the porous structure of the MOF, along with the possibility of the enhanced catalytic reactions favored by confinement effects in the cages. Férey *et al.* showed that each cage can accept five Keggin ions, that is, about 0.05 Keggin anions per chromium. Five Keggin ions take up 10.1 nm^3 volume, which is approximately 50% of the 20.6 nm^3 volume of a large cage. It was tested whether the MIL101/PTA hybrids resulting from the HF-free synthesis in water are different from those reported previously. TEM and SEM images of hybrid materials synthesized by the joint autoclaving of mixtures of the MIL-101 precursors and phosphotungstic acid (MIL101/PTAja) in water without pH adjustment are shown in Figure 9.5. Particles resulting from joint autoclaving of PTA and MIL-101 components were up to 10 μm in size, with a complex structure comprising rectangular pyramidal crystals on the surface and a spherical interior covered with rectangular crystalline assemblies.

Composites synthesized by impregnating MIL-101 crystals with PTA solutions, shown in Figure 9.6, maintained the overall octahedral shape of the autoclaved MIL-101 particles. The polydispersity of the MIL101/PTA imp particles was higher, and the shape slightly less well defined than the original autoclaved MIL-101 particles due to the prolonged exposure of the MIL-101 to water during the process of impregnation. EDX analysis of the TEM images of MIL101/PTA particles (found, Cr, 10.4 wt%; W, 40.3 wt%) showed large PTA content. Elemental analysis of the MIL101/PTA_{imp} material indicated heterogeneity of the samples, with the tungsten content varying 5–7% from batch to batch.

The quantity of gas absorbed during BET nitrogen absorption isothermal analysis indicated that the pore volumes of the MIL101/PTA materials were 4–5.5

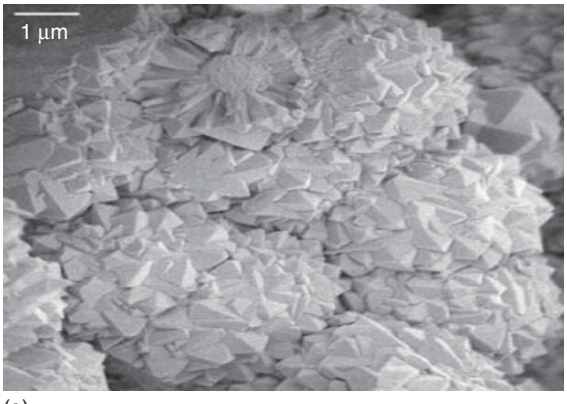

(a)

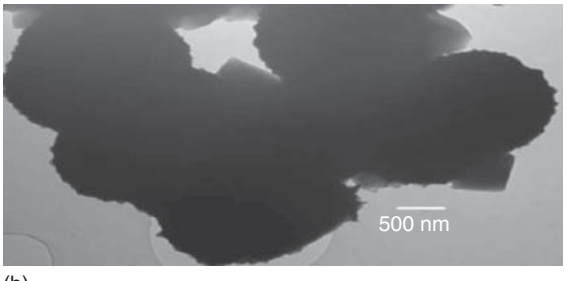

(b)

Figure 9.5 (a) SEM and (b) TEM images of the MIL/PTAja hybrid material obtained by the joint autoclaving of mixtures of MIL-101 components and PTA in deionized water, without pH adjustment.

times smaller than those of the original MIL-101 due to the loading of the MIL-101 pores with PTA in the composites. The smaller average pore size (2.3 nm) in the MIL101/PTA compared to that in the unmodified MIL-101 (3.5 nm) also provides evidence that the pores were partially occupied by the Keggin ions of PTA.

9.1.6.2

Reaction Catalysis by MIL-101 and MIL101/PTA Composites

The catalytic performance of the MIL101/PTA composites was assessed in the Baeyer condensation of benzaldehyde and 2-naphthol, in the three-component condensation of benzaldehyde, 2-naphthol and acetamide, and in the epoxidation of caryophyllene by aqueous hydrogen peroxide. In all experiments, no detectable product formation was observed without the catalysts. With PTA present, all experiments showed almost complete conversion of the reactants, demonstrating the effectiveness of PTA as a catalyst.

Notably, PTA dissolved in either benzaldehyde or water in these reactions, which then proceeded at given temperatures in the homogeneous catalysis regime. Upon equilibration at room temperature, precipitation of PTA was observed only in one reaction – the benzaldehyde, 2-naphthol, and acetamide

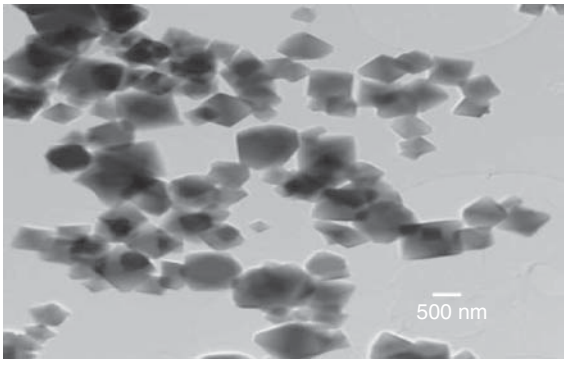

(a)

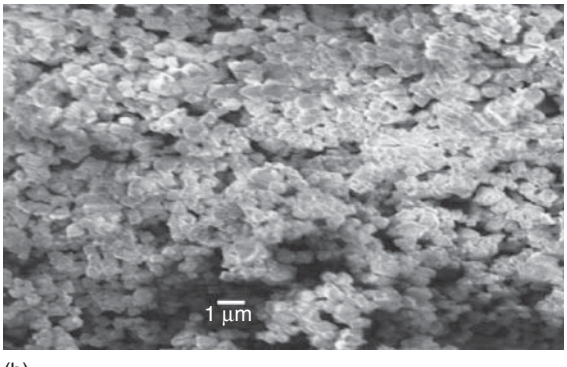

(b)

Figure 9.6 (a) TEM and (b) SEM images of the MIL/PTA_{imp} hybrid material obtained by impregnating MIL-101 particles by an aqueous solution of PTA.

condensation. However, the catalyst recovery by filtering was low (<30 wt% of initial loading).

Proton conductivity has attracted long-lasting research interests owing not only to its theoretical significance in biological systems, but also its potential applications in fuel cells, electrochemical sensors, and reactors. Currently, the fabrication of solid-state proton conductors is a highly sought-after area particularly for fuel-cell application. In this regard, intensive research efforts have been devoted to introduce proton conductivity into polymers [59]. Polymer-based electrolyte membranes use acidic groups as proton carriers, and hydrogen-bonding networks as proton-conducting pathways to accomplish proton transport or transfer. However, little evidence sheds light on conduction mechanisms and relationships between microstructure and conducting property due to the lack of long-range order. Dupont's commercially well-established Nafion, a perfluorosulfonic acid membrane, is widely used in fuel cells to date. However, Nafion membranes are prone to rapid dehydration at elevated temperatures and/or low humidity, which results in a loss of conductivity and irreversible changes of membrane microstructure in some cases. Nafion is expensive as well, and must

undergo hazardous manufacturing processes. Subsequently, proton-conductive membranes based on inorganic or composite solids have been explored to tackle the limitation of polymer membranes. Nevertheless, some inadequacies including high cost and low efficiency/performance cannot fully support these materials for commercialization. Therefore, it is necessary to exploit an alternative proton conductor to solve the difficult problem in realizing clean-energy systems.

In the past decade, MOFs have received much attention due to potentially useful properties. As a new type of functional materials, the exceptionally high crystallinity and designability of MOFs can also open the door to investigate the mechanism and functional regulation of proton conductivity. In general, some specific physicochemical properties of MOFs are controlled and modified by the judicious selection of organic ligands and metal centers. Similarly, proton-conducting MOFs have recently been obtained, and tuned by introducing acidic and hydrophilic units. This includes carboxylate, phosphonate, and sulfonate groups due to the presence of hydrophilic oxygen atoms to act as hydrogen-bonding acceptors. Furthermore, the hydrophilic amine moiety is also used by either accepting or donating protons to serve as a proton carrier and hydrogen-bonding donor. A few proton-conductive MOFs have successfully been synthesized by using the above-mentioned synthetic strategies. However, most proton-conductive MOFs are limited to being used under high-humidity conditions (~100% relative humidity), or at high temperatures (>100 °C). Only a small number of studies on the proton conductivity of MOFs under ambient conditions (i.e., low-humidity conditions and low temperatures) have been reported. It is imperative to develop a straightforward and universal strategy for practical proton conductors to maintain high proton conductivity under ambient conditions. Hence, we integrate MOF crystals as fillers into the polymer matrix to make composite (mixed-matrix) membranes for enhanced proton conductivity under ambient conditions. The approach employed in this study is based on the following considerations. Fabrication of MOF or composite membranes is considered as a crucial step for successful utilization of MOF materials in fuel-cell application. Also, the composite membrane combines the advantages of both inorganic fillers and polymer membranes, such as good reproducibility, high chemical and thermal resistance, and relatively economical processing. Moreover, the hygroscopic polymer as a matrix is an effective approach to enhance proton conductivity of the membranes depending on water concentration. The exploration of MOF-based composite membranes as novel proton conductors has not been documented and remains a significant challenge.

Here, a chiral two-dimensional MOF, $\{(Ca(D\text{-}Hpmpc)(H_2O)_2)\cdot 2HO_{0.5}\}_n$ (1, D-H_3pmpc = D-1-(phosphonomethyl) piperidine-3-carboxylic acid), and its composite membrane fabricated from polymer PVP and MOF 1 submicrorods with intrinsic proton conductivity have been studied. More interestingly, the composite membrane containing 50 wt% MOF 1 submicrorods exhibit a relatively higher proton conductivity under ~53% RH at 298 K. High conductivity is most likely to be benefited from the humidification of the highly hygroscopic PVP. It

is suggested that MOF 1–PVP composite membrane is very promising for the enhancement of proton conductivity under low-humidity conditions.

It has been found that the available proton carriers in the MOF structure provide a basis for the conductivity, and the large humidification effect of PVP with adsorbed water molecules greatly contributes to the proton transport in the composite membrane. Moreover, the proton transport mechanism shows that the proton conduction in composite membranes mainly follows the vehicle mechanism coupled with the Grotthuss mechanism.

9.1.7
Composites of MOFs with Mesoporous Silica and Alumina

Although many unique properties of MOFs have been reported, the MOFs are mostly microporous that gives rise to diffusion problems. Because micropores often impose diffusion limits in the rate of adsorption and reaction, introduction of mesopores has been attempted as a means to solve the diffusion problems. Ligand extension is an apparent strategy to enlarge pore size. However, an MOF constructed from a large ligand is often accompanied by framework interpenetration and, furthermore, the MOFs with large pore of mesosize tend to collapse upon guest removal and lose the nature of microporous materials. Another way to produce mesopores is the reduction of particle size that leads to voids between small particles. Recently, Kitagawa *et al.* prepared nano MOFs with averaged crystal size of 20 nm by adapting microwave-assisted solvothermal conditions with the coordination modulation method [60]. However, the sample did not show type IV adsorption isotherm with hysteresis loop and, furthermore, filtration of nanomaterials is difficult due to their colloidal properties. If micro/mesoporous materials are accomplished, the resulting bimodal pore-structured materials would further extend the applications of MOFs, since this would combine the benefits of both pore-size regimes. Micropores in MOFs provide size- and/or shape-selectivity for guest molecules, while mesopores provide easier access to the adsorption sites in micropores. Here, have been used from mesoporous silica as a support of MOF, because mesoporous silica has high thermal stability and well-established methods to realize high surface area, and high porosity can be adopted. CuBTC (HKUST-1) has been chosen [51], because this MOF has high adsorption ability and specific adsorption sites known as open metal sites. Under the coexistence of mesoporous silica, aggregated nanosized MOF crystals were formed around mesoporous silica, although large bipyramidal-shaped crystals were obtained in a reported synthetic procedure [49] without mesoporous silica. The composites showed high adsorption capacities with a hysteresis loop in nitrogen adsorption isotherms at 77 K and higher adsorption rate of ethanol at 303 K than a bulk CuBTC, indicating micropore/mesopore integration.

Amounts of reaction compositions for MOF-mesoporous silica composites have been shown in Table 9.1.

Ratios of weight percentage in composites 1–4 and yield of CuBTC have been shown in Table 9.2.

Table 9.1 Amounts of reaction compositions for MOF-mesoporous silica composites.

Sample name	1	2	3	4
$Cu(NO_3)_2 \cdot 3H_2O$ (mmol)	1.5	0.75	0.25	0.75
BTC (mmol)	1.0	0.5	0.17	0.25
Mesoporous silica (mg)	50	50	50	50

Table 9.2 Ratios of weight percentage in composites 1–4 and yield of CuBTC.

Sample	CuBTC/mesoporous silica	Yield of CuBTC[a)](%)
1	2.1	11
2	2.0	15
3	0.80	18
4	1.6	40

a) The yield of CuBTC was calculated based on the amount of BTC used.

Nitrogen adsorption isotherms at 77 K on 1–4 are shown in Figure 9.7. All samples show steep uptake at low relative pressure and hysteresis loop at around $P/P_o = 0.7$ derived from mesopores. Pore volumes and isosteric heat of adsorption, q_{st}, are summarized in Table 9.3. Micropore volume of 2 was the highest among 1–4. On the other hand, mesopore volume and total pore volume increased in

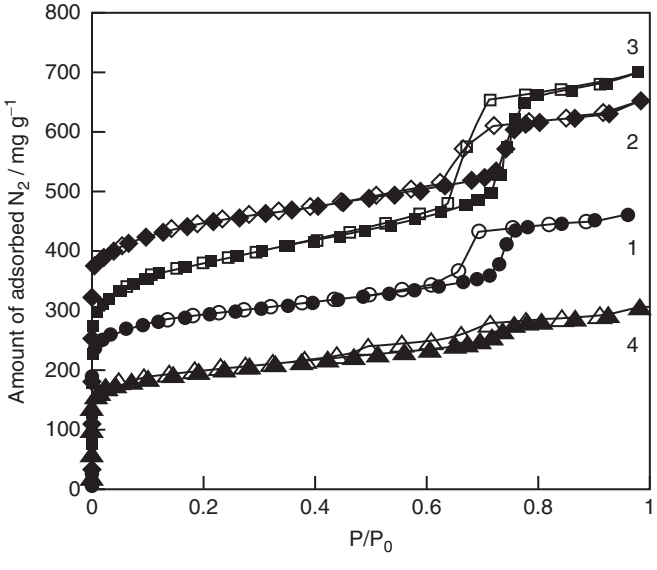

Figure 9.7 N_2 adsorption isotherms at 77 K on 1 (circle), 2 (diamond), 3 (square), and 4 (triangle). Solid and open symbols represent adsorption and desorption, respectively.

Table 9.3 Pore volumes and isosteric heat of adsorption q_{st} of samples 1–4.

Sample	Micropore volume[a] (ml g^{-1})	Mesopore volume (ml g^{-1})	Total pore volume (ml g^{-1})	Isosteric heat of adsorption, q_{st}[a] (kJ mol^{-1})
1	0.34	0.23	0.57	14.7
2	0.51	0.30	0.81	16.5
3	0.42	0.45	0.87	14.4
4	0.23	0.15	0.38	13.7

a) Estimated by using DR analysis.

the order from 1 to 3, corresponding to the inverse order of the concentration of CuBTC solution. Sample 4 showed the lowest adsorption capacity in micro-, meso-, and total pore volumes, and the shape of the hysteresis loop was different from those of the other samples, indicating the presence of CuBTC crystals in mesopores of mesoporous silica. According to BJH analysis of the desorption branches, mesopore diameter of 1–4 are 5.5–6.2 nm, indicating that most part of mesopores is preserved. The q_{st} value of 2 was the highest among 1–4 and all of the q_{st} values of 1–4 were higher than that of the mesoporous silica used (10.2 kJ mol^{-1}).

In conclusion, micropore- and mesopore-integrated materials have been synthesized by using mesoporous silica and MOF. The composites were composed of nano CuBTC crystals and mesoporous silica, and the ratio of micropore/mesopore volume can be tuned by controlling the initial concentration of the reaction solution of CuBTC. Under synthesis in low-concentration solution of CuBTC, the obtained composites showed higher adsorption uptake than the estimated uptake of MOF-mesoporous silica mixture showing the retention nature of micro- and mesoporous materials and formation of additional pore spaces that should be from the void that exists between nano CuBTC crystals.

On the other hand, the homochirality of MOFs has attracted considerable attention because of their applications in enantioselective separation and catalysis. Microporous MOFs with good solvent stability are attractive stationary phases for high-performance liquid chromatography, and some achiral MOFs, such as MOF-5, have been successfully used as stationary phases for HPLC separation of small achiral molecules. However, examples of chromatographic separations of enantiomers using homochiral MOFs are rare and only one example has been reported to date. Chiral sulfoxides constitute a class of highly valuable chiral auxiliaries for asymmetric synthesis and ligands for enantioselective catalysis. Moreover, a number of pharmaceutically important drugs such as omeprazole contain chiral sulfinyl groups. Although a number of publications have described the successful resolution of chiral sulfoxides on different types of chiral stationary phases such as amylose and cellulose derivatives, stationary phases showing complementary enantioselectivity and resolution for a wide range of chiral sulfoxides are rare. Here, the investigation of a new homochiral MOF–silica

composite as a new stationary phase for HPLC enantiomeric separation of various chiral sulfoxides with excellent selectivity has been reported.

(R)-MOF–silica composite 1 was synthesized from a mixture of (R)-H_2BDA [61], $Cu(NO_3)_2$, and monodisperse spherical silicagel (Daisogel SP-120-7P; particle size, 7 mm) in DMF under solvothermal conditions. The successful preparation of (R)-MOF–silica composite 1 has been shown in Figure 9.8, which was confirmed by SEM and PXRD.

In another work, modulated formations of MOFs by oriented growth over mesoporous silica has been studied and have successfully used different concentrations of SBA-15 mesoporous silica for directed growth of the archetypal MOF-5 microcrystals along preferred crystallographic orientations, resulting in the production of interesting flower-like and nanorod frameworks instead of the conventional cubic structure. The results point to the possibility of using mesoporous silicas for designation of a wide range of MOF structural motifs with expedient performance and applications via selective interactions of MOF crystal building blocks with active functionalities on mesoporous surfaces, allowing heterogeneous seeding and controlled expansion of the framework along a preferred direction. The modifications in the MOF structure have proven to improve the catalytic performance of MOF–silica nanocomposites up to 50% for Friedel–Crafts alkylation, compared to pure MOF-5. By discussing the effect of MOF texture on catalytic performance, this research aims to take MOF-5 beyond its bulk applications and opens up a new paradigm to design highly active and selective green heterogeneous catalysts based on MOFs.

XRD and SEM are applied to closely monitor the effect of different concentrations of SBA-15 mesoporous silica (1–10 wt%) on growth, phase, and structure of the resulting MS composites. The composites are referred to as MS/n with $n = 1$, 2, 3, and 4 for the different SBA contents (1, 3, 5, and 10 wt%, respectively). Comparing the results acquired for the parent MOF and the hybrid materials, the indispensible directing role of SBA moieties becomes evident (Figures 9.9 and 9.10). In fact, the product of homogeneous nucleation differs dramatically from the product of nucleation in the presence of mesoporous silica impurities. This dramatic effect may be attributed to additional constraints in the degrees of freedom during the synthesis in the presence of SBA-15 and the emergence of new

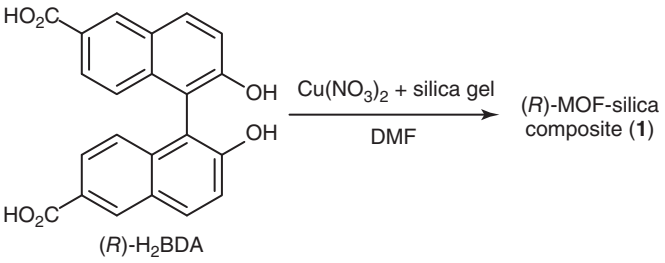

Figure 9.8 Preparation of (*R*)-MOF–silica composite (1).

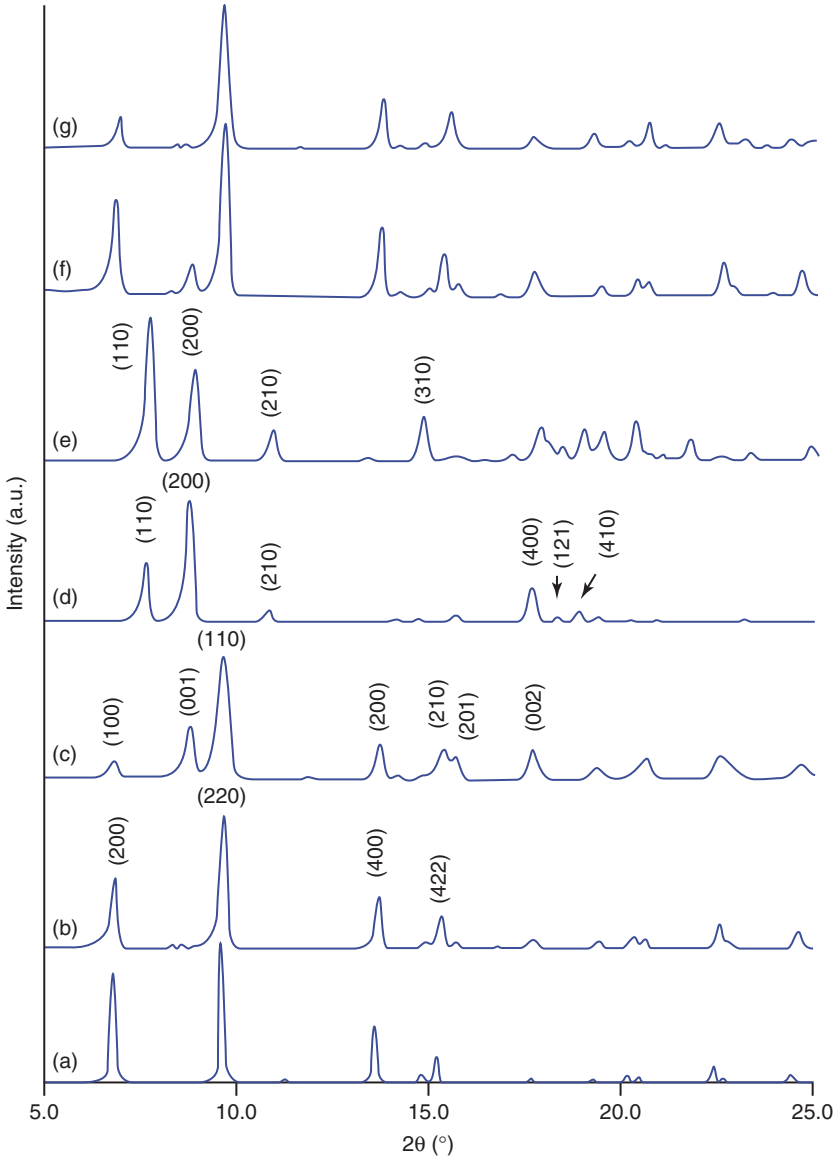

Figure 9.9 Powder XRD patterns of (a) MOF-5 single crystal simulated from X-ray data, (b) MOF-5, (c) MS/1, (d) MS/2, (e) MS/3, (f) MS/4, and (g) MS/C.

chemical interactions in the composite system, which will be discussed in more detail [62].

A schematic view of the proposed mechanism of homogeneous and heterogeneous MOF nucleation and the structure-directing role of mesoporous silica have been shown in Figure 9.11.

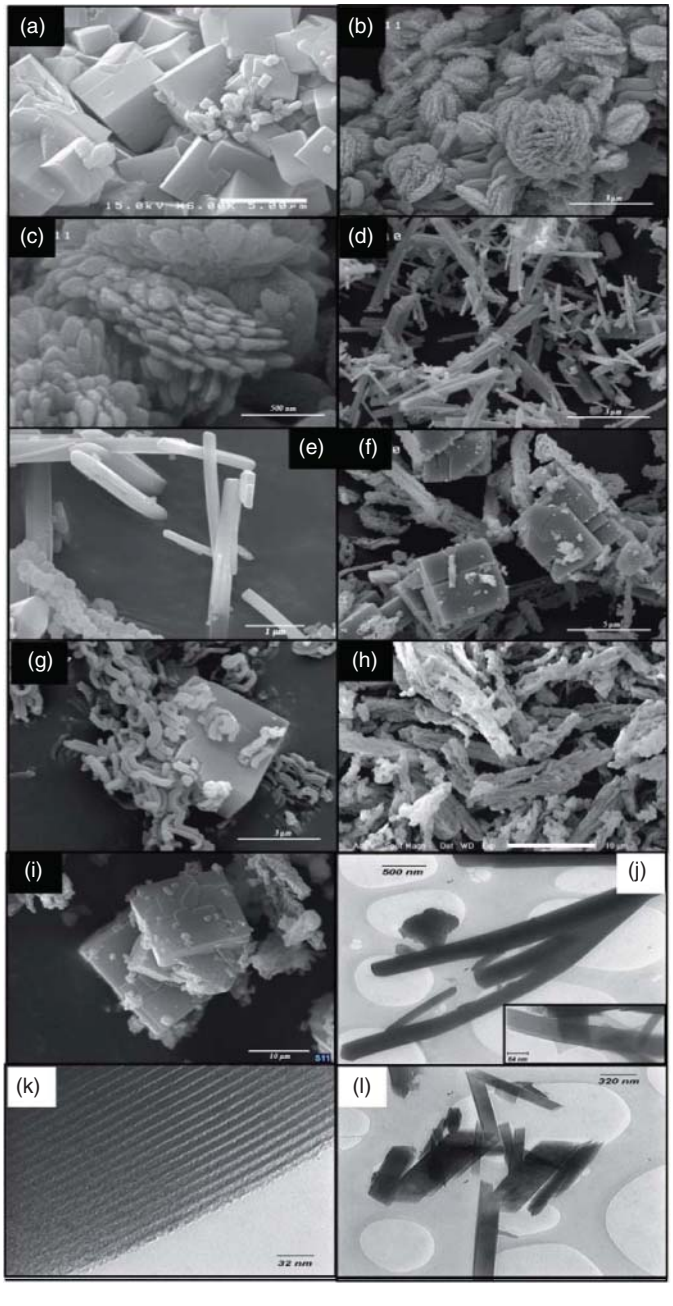

Figure 9.10 SEM images of (a) MOF-5, (b, c) MS/1, (d) MS/2, (e) MS/3, (f, g) MS/4, (h) SBA-C, (i) MS/C and TEM images of (j) MS/2, (k) SBA-15 moiety in MS/2 composite, and (l) MS/3.

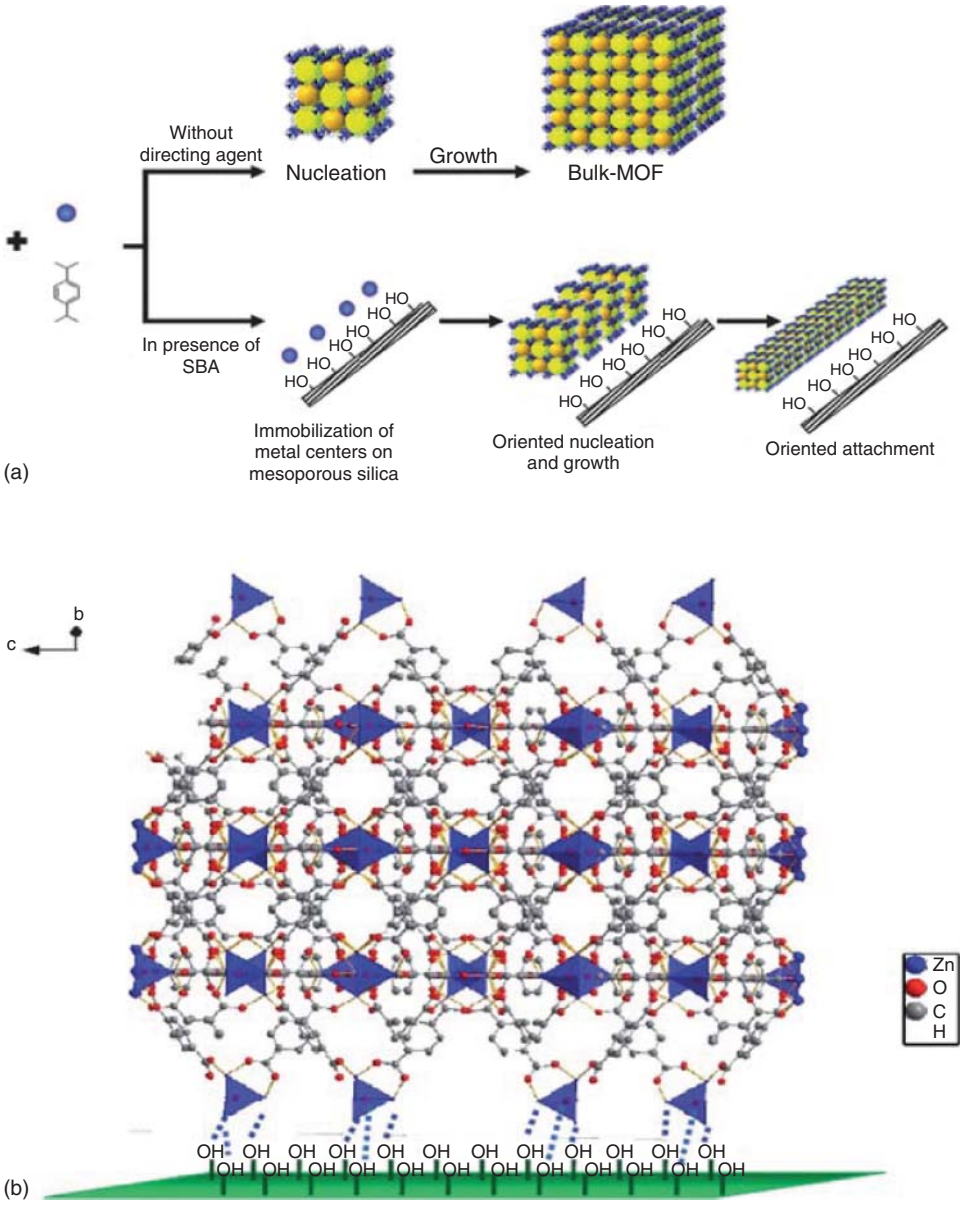

Figure 9.11 A schematic view of (a) the proposed mechanism of homogeneous and heterogeneous MOF nucleation and the structure-directing role of mesoporous silica and (b) proposed model for interaction between surface silanols of mesoporous silica and MOF.

Catalytic activity of the designed composite systems is assessed in Friedel–Crafts alkylation by studying the reaction of toluene with benzyl bromide to form p-benzyl toluene as the main product and o-benzyltoluene as the byproduct. Alkylation is carried out under atmospheric pressure at 100 °C with toluene (18.66 mmol), benzyl bromide (6.22 mmol), catalyst (0.012 g), and n-dodecane (0.74 ml) as an internal standard. Comparison of catalytic activity of the newly designed MOF-based composites has been shown in Figure 9.12 [62].

This study clearly unveils the tight connection of framework structure with its performance and opens a route to control the structure and orientation of MOF-based structures.

9.1.8
Composites of MOFs with Metal Nanoparticles

The combination of the long-range order of a solid-state template material with the tunable dimensionality and chemical tailoring of the inner surface of the channels and cavities makes MOFs a promising new class of templates for hosting nanoparticles. It has been shown that the embedding of functional nanoparticles inside the cavities of MOFs is relevant for a number of applications, including heterogeneous catalysis and better adsorbents. During the past 5 years, a number of examples for incorporation of a range of metals like Cu, Ru, Pd, Au, Ag, and Pt into MOF cavities have been reported [63]. On the other hand, supported metal catalysts, especially for noble metals, exhibit good catalytic activities for various reactions such as CO oxidation, hydrogenation, olefin epoxidation, and water-gas shift.

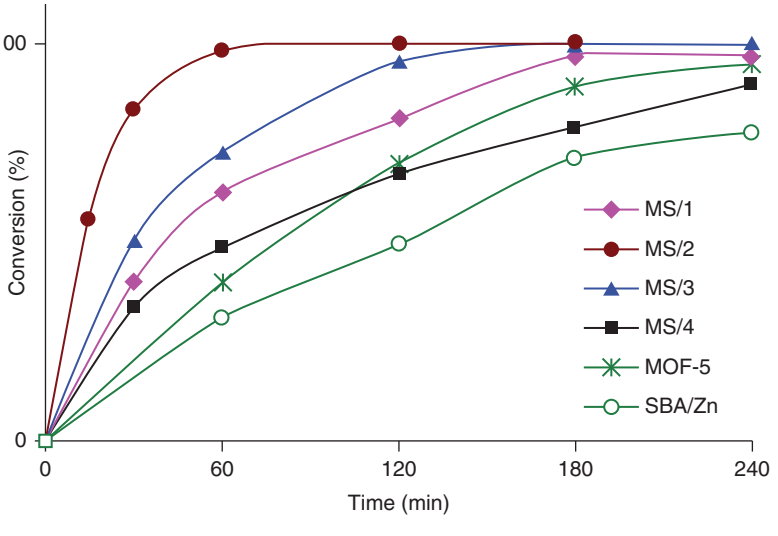

Figure 9.12 Comparison of catalytic activity of the newly designed MOF-based composites for heterogeneous alkylation of toluene with benzyl bromide.

One of these reports is on the assembly of a 3D porous coordination polymer, $[Pb(4bpdh)(NO_3)(H_2O)]_n$ (TMU-1) (4-bpdh = 2,5-bis(4-pyridyl)-3,4-diaza-2,4-hexadiene), supported by silver nanoparticles [64]. A three-dimensional porous coordination polymer, $[Pb(4\text{-}bpdh)(NO_3)(H_2O)]_n$ (TMU-1), has been synthesized with reaction of lead(II) nitrate and 4-bpdh. When solid TMU-1 was immersed in the ethanol solution of $AgNO_3$ for 5, 15, or 60 min and 20 h at room temperature, solids including Ag nanoparticles are formed (Ag@ TMU-1), as evidenced by HRTEM images and EDX spectrum (Figures 9.13 and 9.14).

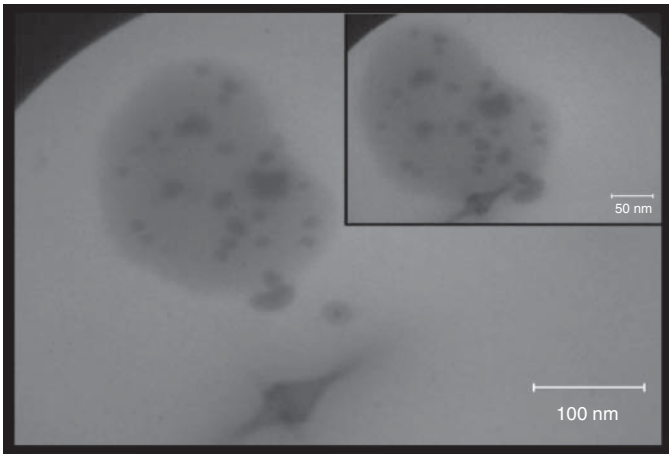

Figure 9.13 HRTEM images of Ag nanoparticles formed by immersion of solid TMU-1 in the ethanol solution of $AgNO_3$ (1.3×10^{-1} M) at room temperature for 5 min.

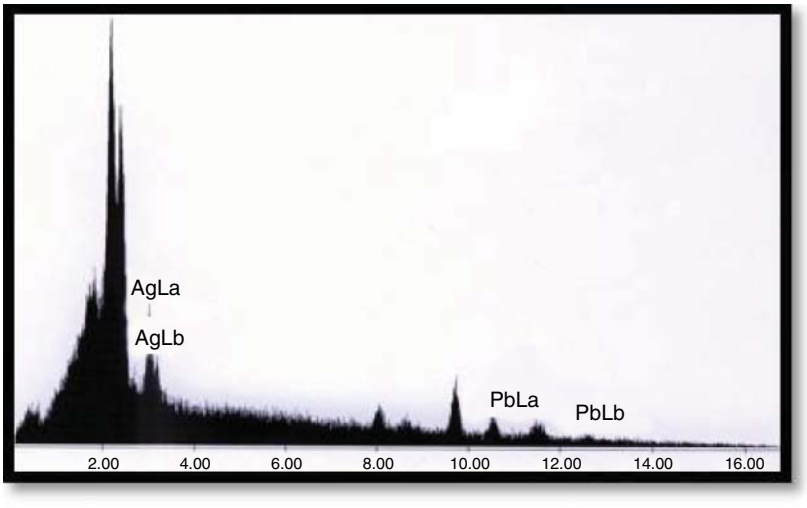

Figure 9.14 Energy dispersive X-ray spectrum (EDS) for the solid isolated after immersion in the ethanol solution of $AgNO_3$ (1.3×10^{-1} M) for 5 min. Measured at room temperature.

In this work, a new simple method was introduced for the synthesis of nanostructures Ag_2O/PbO and Ag/PbO in one-step process, which are direct calcinations of the MOF as precursor at 600 °C under air and Ar atmosphere. These processes build a direct link between MOF crystals and metal nanostructures and also supply new potential application for MOFs [64].

9.1.9 Composites of MOFs with Silk

An increasing population leads to environmental pollutions, which is one of the most important problems. There have been many efforts to eliminate polluting materials from the environment. The dyes and pigments using industries such as rubber, paper, textile, plastics, and cosmetics so visible and toxic even at very minimum concentrations. The MOFs are a class of nanoporous materials. MOFs are most attractive for their high capacity for hydrogen absorption and storage, capture and separation of gases, and for applications in catalysis.

This work is concerned with the possibility for uniform growth of MOF-5 coated on silk membrane filtration in the direct-mixing method as well as by ultrasound (US) irradiation from layer-by-layer (LBL) growth from molecular precursors. The adsorptive removal of hazardous anionic dye "Congo red" using MOF-5 on silk surface is discussed. MOF-5 that deposited on silk shows high adsorption capacity and rapid uptake for the Congo red. The silk fibers containing MOF-5 open a wide field of possible applications, such as protection layers or membranes in pollution remediation wastewater.

For preparation of silk the fabric was first immersed in a solution containing sodium hydroxide for 30 min which was followed by some rinses in pure water for 15 min. The pH of the solution was adjusted to pH = 10. In alkaline pH, the surface of silk fiber becomes negatively charged due to the deprotonation of the carboxylic group of the glutamic and aspartic acid present in the silk fiber. LBL deposition of MOF-5 on silk fiber in direct mixing synthesis has been shown in Figure 9.15 [65].

Ultrasonic synthesis of Zn-BDC-MOF onto silk surface was carried out under ultrasonic irradiation at ambient temperature and atmospheric pressure (Figure 9.16). Similarly to direct mixing synthesis, the synthesis solution containing zinc acetate in DMF, H_2BDC, and triethylamine in DMF were placed in ultrasonic bath. Zn-BDC-MOF particles on silk fibers were prepared by sequential dipping steps with sonicating. SEM images of BDC-MOF-coated silk yarns have been shown in Figure 9.17 too [56].

In another work, the LBL growth of nanoporous lead (II) coordination polymer on natural silk fibers and its application in the removal and recovery of iodide has been studied. The growth of a three-dimensional (3D) porous coordination polymer, [Pb(4-bpdh)(NO_3)(H_2O)] (TMU-1) on silk fibers were achieved by the stepwise LBL growth technique in alternating bath of lead (II) nitrate and 4-bpdh solutions. The silk fibers containing TMU-1 MOF similar to nanopowders of

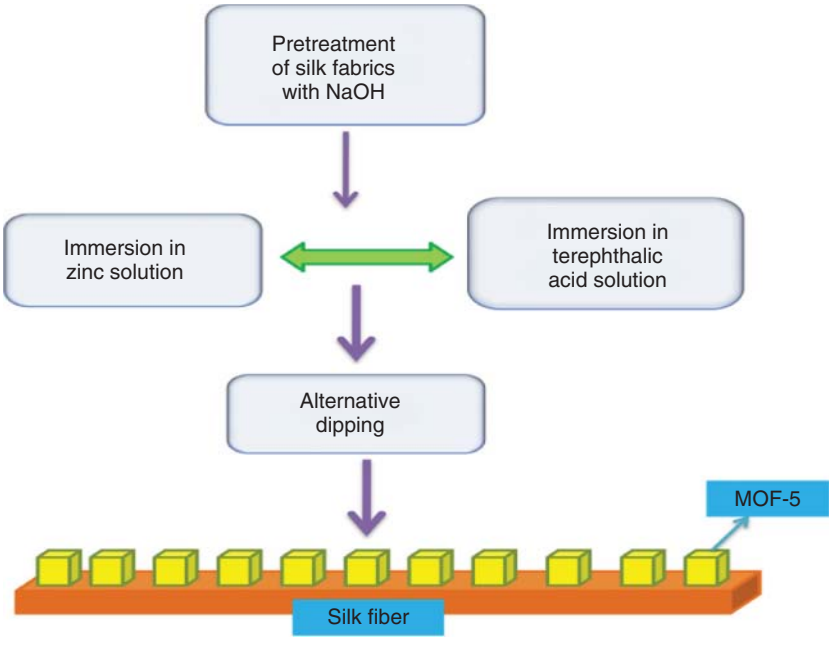

Figure 9.15 Layer-by-layer deposition of MOF-5 on silk fiber.

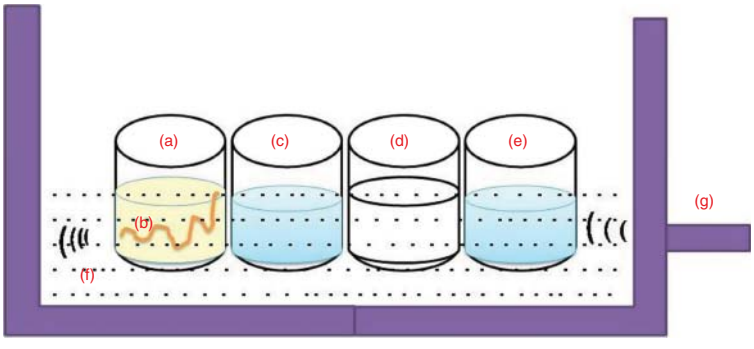

Figure 9.16 Schematic of the experimental setup used for the sonochemical reactions: (a) beaker of $Zn(OAc)_2$ solution; (b) silk fiber; (c) DMF for washing; (d) beaker of terephthalic acid (H_2BDC) solution; (e) DMF for washing; (f) ultrasound bath; and (g) water circulation.

TMU-1 synthesized by microwaving have superior adsorption capacity and recovery of I_2 under ambient condition [66].

Schematic of the LBL growth of the MOF on the silk surface by repeated immersion cycles, first in a solution of metal precursor and subsequently in a solution of organic ligand has been shown in Figure 9.18.

When silk containing 0.008 g TMU-1 in a sufficient amount of a cyclohexane solution of I_2 (about 0.012 g I_2 in 3 ml cyclohexane)was placed in a small sealed

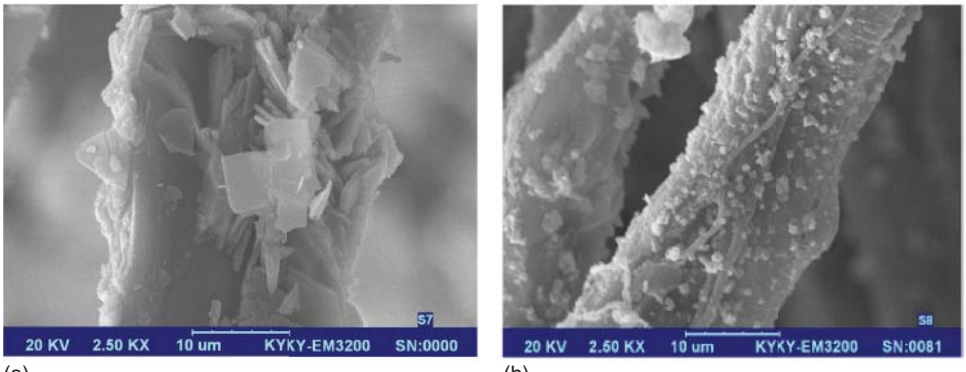

(a) (b)

Figure 9.17 SEM images of BDC-MOF-coated silk yarns synthesized by direct mixing (a), SEM images of BDC-MOF-coated silk yarns synthesized by ultrasound irradiation (b).

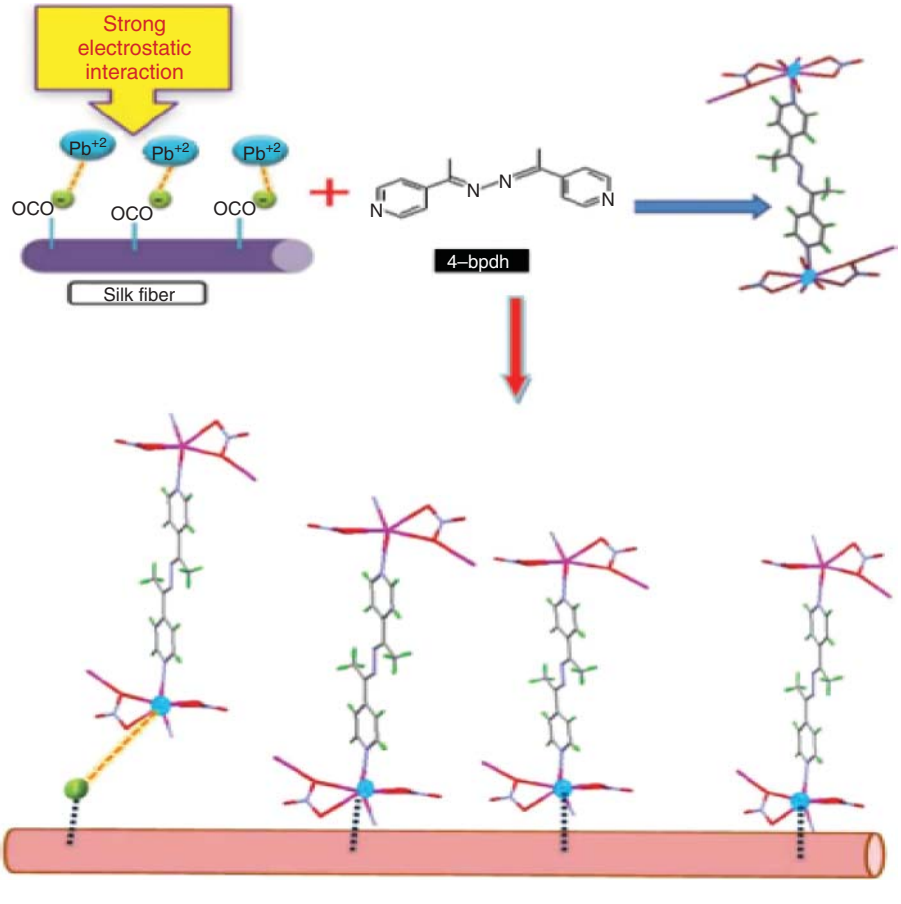

Figure 9.18 LBL growth of the MOF on the silk.

flask at room temperature, it was observed that the deep purple solutions of I_2 fade slowly to very pale red (Figure 9.19), and within 2 h became colorless. The final mass of silk fibers after being immersed in the cyclohexane solution of I_2 increased to 0.02 g, which could be associated with a maximum of $3I_2$ being adsorbed per formula unit of TMU-1 [66].

In another work, dense coating of surface-mounted CuBTC MOF nanostructures on silk fibers, prepared by the LBL method under ultrasound irradiation with antibacterial activity has been performed.

The growth of $Cu_3(BTC)_2$ (BTC = 1,3,5-benzenetricarboxylate), also known as CuBTC and HKUST-1, MOF nanostructures on silk fibers were achieved by the LBL technique in alternating bath of $Cu(OAc)_2 \cdot 2H_2O$ and H3BTC solutions under ultrasound irradiation. The effects of pH, reaction time, ultrasound irradiation, and sequential dipping steps in the growth of the CuBTC MOF nanostructures have been studied. These systems depicted a decrease in the size, which is likely to accompany a decrease in the sequential dipping steps. In addition, dense coating of silk fibers with CuBTC MOF results in decreasing the emission intensity of silk fibers. The silk fibers containing CuBTC MOF exhibited high antibacterial activity against *Escherichia coli* and *Staphylococcus aureus*. Schematic representation of the formation mechanism of CuBTC nanoparticles upon silk yarn has been shown in Figure 9.20 [67].

The growth of CuBTC on silk yarn was achieved by sequential dipping in alternating baths of aqueous $Cu(OAc)_2 \cdot 2H_2O$ and H3BTC in a mixed solution of DMF and EtOH under various conditions. Pristine silk fibers were dipped in alkaline solution. In alkaline pH, the surface of the silk fiber becomes negatively charged due to the deprotonation of the carboxylic group present at the fiber's surface. When negative silk was immersed in aqueous $Cu(OAc)_2 \cdot 2H_2O$, copper ions were readily impregnated into the silk yarn through the surface. Most of the incorporated Cu^{2+} ions were bound to silk yarn probably via electrostatic interactions, because the electron-rich oxygen atoms of polar carboxylic group of silk yarn are

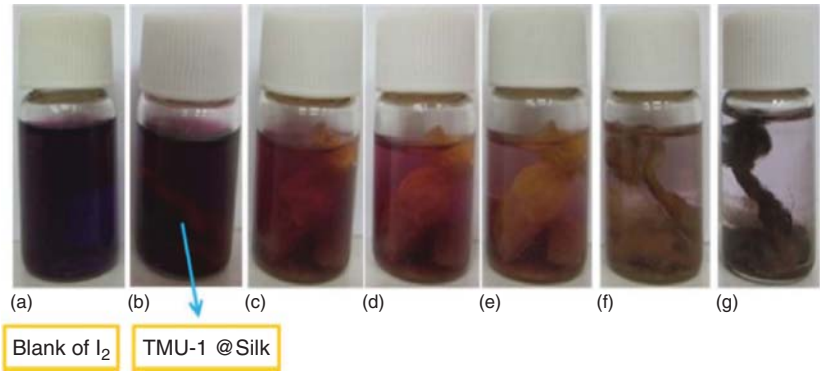

Figure 9.19 I_2 enrichment progress in (a) blank, (b) immediately, (c) 3 min, (d) 5 min, (e) 30 min, (f) 1 h, and (g) 2 h.

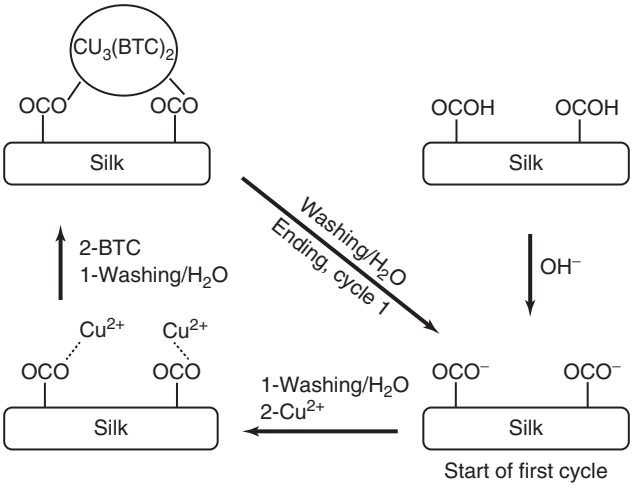

Figure 9.20 Representation of the formation mechanism of CuBTC nanoparticles upon silk yarn.

expected to interact with electropositive transition metal cations (Figure 9.20). Rinsing by double-distilled water effectively removed those Cu^{2+} ions that were not attached to the silk yarn. The dipping step in the H3BTC solution will allow the formation of the CuBTC MOF and initiate the formation of new CuBTC particles, as illustrated in Figure 9.20. The repeated alternating dipping steps lead to the growth of CuBTC particles [67].

SEM photographs and wavelength-dispersive X-ray (WDX) analysis of samples in four cycles have been shown in Figure 9.21 [67].

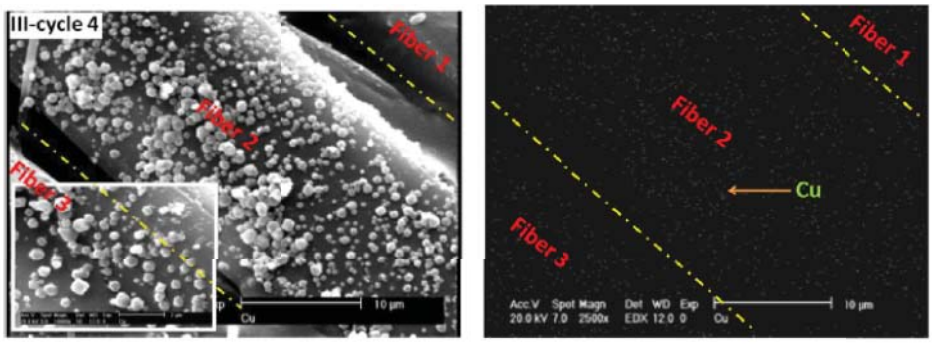

Figure 9.21 SEM photographs and wavelength-dispersive X-ray (WDX) analysis of samples in four cycles.

References

1. Work, W.J., Horie, K., Hes, M., and Stepto, R.F.T. (2004) *Pure Appl. Chem.*, **76**, 1985.
2. Hermes, S., Schrhoter, M.-K., Schmid, R., Khodeir, L., Muhler, M., Tissler, A., Fischer, R.W., and Fisher, R.A. (2005) *Angew. Chem. Int. Ed.*, **44**, 6237.
3. Lohe, M.R., Gedrich, K., Freudenberg, T., Kockrick, E., Dellmann, T., and Kaskel, S. (2011) *Chem. Commun.*, **47**, 3075.
4. Yang, S.J., Choi, J.Y., Chae, H.K., Cho, J.H., Nahm, K.S., and Park, C.R. (2009) *Chem. Mater.*, **21**, 1893.
5. Uemura, T., Yanai, N., and Kitagawa, S. (2009) *Chem. Soc. Rev.*, **38**, 1228.
6. Batten, S.R., Neville, S.M., and Turner, D.R. (2009) *Coordination Polymers: Design, Analysis and Application*, The Royal Society of Chemistry.
7. Blake, A.J., Champness, N.R., Hubberstey, P., Li, W.-S., Withersby, M.A., and Schröder, M. (1999) *Coord. Chem. Rev.*, **183**, 117–138.
8. Morsali, A. and Masoomi, M.Y. (2012) *Coord. Chem. Rev.*, **256**, 2921–2943.
9. Barnett, S.A. and Champness, N.R. (2003) *Coord. Chem. Rev.*, **246**, 145–168.
10. Roesky, H.W. and Andruh, M. (2003) *Coord. Chem. Rev.*, **236**, 91–119.
11. James, S.L. (2003) *Chem. Soc. Rev.*, **32**, 276–288.
12. Yaghi, O.M., Li, H., Davis, C., Richardson, D., and Groy, T.L. (1998) *Acc. Chem. Res.*, **31**, 474–484.
13. Kitagawa, S. and Noro, S. (2003) in *Comprehensive Coordination Chemistry II* (eds J.A. McCleverty and T.J. Meyer), Pergamon, Oxford, pp. 231–261.
14. Robin, A.Y. and Fromm, K.M. (2006) *Coord. Chem. Rev.*, **250**, 2127–2157.
15. Hu, M.-L., Morsali, A., and Aboutorabi, L. (2011) *Coord. Chem. Rev.*, **255**, 2821–2859.
16. Schwab, M.G., Senkovska, I., Rose, M., Koch, M., Pahnke, J., Jonschker, G., and Kaskel, S. (2008) *Adv. Eng. Mater.*, **10**, 1151.
17. Küsgens, P., Zgaverdea, A., Fritz, H.-G., Siegle, S., and Kaskel, S. (2010) *J. Am. Ceram. Soc.*, **93**, 2476.
18. Perez, E.V., Balkus, K.J. Jr., Ferraris, J.P., and Musselman, I.H. (2009) *J. Membr. Sci.*, **328**, 165.
19. Ordonez, M.J.C., Balkus, K.J. Jr., Ferraris, J.P., and Musselman, I.H. (2010) *J. Membr. Sci.*, **361**, 165.
20. Basu, S., Cano-Odena, A., and Vankelecom, I.F.J. (2010) *J. Membr. Sci.*, **362**, 478.
21. Basu, S., Maes, M., Cano-Odena, A., Alaerts, L., De Vos, D.E., and Vankelecom, I.F.J. (2009) *J. Membr. Sci.*, **344**, 190.
22. Díaz, K., Garrido, L., López-González, M., Castillo, L.F., and del Riande, E. (2010) *Macromolecules*, **43**, 316.
23. Ostermann, R., Cravillon, J., Weidmann, C., Wiebcke, M., and Smarsly, B.M. (2011) *Chem. Commun.*, **47**, 442.
24. Rose, M., Bohringer, B., Jolly, M., Fischer, R., and Kaskel, S. (2011) *Adv. Eng. Mater.*, **13**, 356.
25. Küsgens, P., Siegle, S., and Kaskel, S. (2009) *Adv. Eng. Mater.*, **11**, 93.
26. Ramos-Fernandez, E.V., Garcia-Domingos, M., Juan-Alcaniz, J., Gascon, J., and Kapteijn, F. (2011) *Appl. Catal., A*, **391**, 261.
27. Petit, C. and Bandosz, T. (2009) *J. Adv. Mater.*, **21**, 4753.
28. Petit, C., Burress, J., and Bandosz, T.J. (2011) *Carbon*, **49**, 563.
29. Petit, C. and Bandosz, T.J. (2011) *Adv. Funct. Mater.*, **21**, 2108.
30. Gorka, J., Fulvio, P.F., Pikus, S., and Jaroniec, M. (2010) *Chem. Commun.*, 6798.
31. Ameloot, R., Liekens, A., Alaerts, L., Maes, M., Galarneau, A., Coq, B., Desmet, G., Sels, B.F., Denayer, J.F.M., and De Vos, D.E. (2010) *Eur. J. Inorg. Chem.*, 3735.
32. O'Neill, L.D., Zhang, H., and Bradshaw, D. (2010) *J. Mater. Chem.*, **20**, 5720.
33. Stankovich, S., Dikin, D.A., Dommett, G.H.B., Kohlhaas, K.M., Zimney, E.J., Stach, E.A. *et al.* (2006) *Nature*, **442**, 282.
34. Brodie, B.C. (1860) *Ann. Chim. Phys.*, **59**, 466.
35. Liu, Z.-H., Wang, Z.-M., Yang, X., and Ooi, K. (2002) *Langmuir*, **18**, 4926.

36. Buchsteiner, A., Lerf, A., and Pieper, J. (2006) *J. Phys. Chem. B*, **110**, 22328.
37. Szabo, T., Tombacz, E., Illes, E., and Dekany, I. (2006) *Carbon*, **44**, 537.
38. Li, J.L., Kudin, K.N., McAllister, M.J., Prud'homme, R.K., Aksay, I.A., and Car, R. (2006) *Phys. Rev. Lett.*, **96**, 176101.
39. Hirata, M., Gotou, T., Horiuchi, S., Fujiwara, M., and Ohba, M. (2004) *Carbon*, **42**, 2929.
40. Rowsell, J.L.C. and Yaghi, O.M. (2004) *Microporous Mesoporous Mater.*, **73**, 3.
41. Yaghi, O.M. and Li, H. (1995) *J. Am. Chem. Soc.*, **117**, 10401.
42. Eddaoudi, M., Kim, J., Rosi, N., Vodak, D., Wachter, J., O'Keeffe, M., and Yaghi, O.M. (2002) *Science*, **295**, 469.
43. Kim, J., Chen, B., Reineke, T.M., Li, H., Eddaoudi, M., Moler, D.B., O'Keeffe, M., and Yaghi, O.M. (2001) *J. Am. Chem. Soc.*, **123**, 8239.
44. Hafizovic, J., Krivokapic, A., Szeto, K.C., Jakobsen, S., Lillerud, K.P., Olsbye, U., and Tilset, M. (2007) *Cryst. Growth Des.*, **7**, 2302.
45. Li, H., Eddaoudi, M., O'Keeffe, M., and Yaghi, O.M. (1999) *Nature*, **402**, 276.
46. Son, W., Kim, J., and Ahn, W. (2008) *Chem. Commun.*, **47**, 6336.
47. Huang, L.M., Wang, H.T., Chen, J.X., Wang, Z.B., Sun, J.Y., Zhao, D.Y., and Yan, Y.S. (2003) *Microporous Mesoporous Mater.*, **58**, 105.
48. Kaye, S.S., Dailly, A., Yaghi, O.M., and Long, J.R. (2007) *J. Am. Chem. Soc.*, **129**, 14176.
49. Chui, S.S.-Y., Lo, S.M.-F., Charmant, J.P.H., Orpen, A.G., and Williams, I.D. (1999) *Science*, **283**, 1148.
50. Petit, C., Mendoza, B., and Bandosz, T.J. (2010) *Langmuir*, **26**, 15302.
51. Figueroa, J.D., Fout, T., Plasynski, S., Mcilvried, H., and Srivastava, R.D. (2008) *Int. J. Greenhouse Gas Control*, **2**, 9.
52. (a) Rowsell, J.L.C., Millward, A.R., Park, K.S., and Yaghi, O.M. (2004) *J. Am. Chem. Soc.*, **126**, 5666; (b) Pan, L., Sander, M.B., Huang, X., Li, J., Smith, M., Bitter, E., Bockrath, B., and Johnson, J.K. (2004) *J. Am. Chem. Soc.*, **126**, 1308.
53. (a) Sun, D., Ma, S., Ke, Y., Collins, D.J., and Zhou, H.C. (2006) *J. Am. Chem. Soc.*, **128**, 3896; (b) Chen, B., Ma, S., Zapata, F., Lobkovsky, E.B., and Yang, J. (2006) *Inorg. Chem.*, **45**, 5718.
54. (a) Chen, B., Ockwig, N.W., Millward, A.R., Contreras, D.S., and Yaghi, O.M. (2005) *Angew. Chem. Int. Ed.*, **44**, 4745; (b) Dinca, M., Dailly, A., Liu, Y., Brown, C.M., Neumann, D.A., and Long, J.R. (2006) *J. Am. Chem. Soc.*, **128**, 16876; (c) Dietzel, P.D.C., Panella, B., Hirscher, M., Blom, R., and Fjellvag, H. (2006) *Chem. Commun.*, 959.
55. (a) Han, J.T., Kim, S.Y., Woo, J.S., and Lee, G.-W. (2008) *Adv. Mater.*, **20**, 3724; (b) Berson, S., De Bettignies, R., Bailly, S., Guillerez, S., and Jousselme, B. (2007) *Adv. Funct. Mater.*, **17**, 3363; (c) Coleman, J.N., Cadek, M., Blake, R., Nicolosi, V., Ryan, K.P., Belton, C., Fonseca, A., Nagy, J.B., Gun'ko, Y., and Blau, W.J. (2004) *Adv. Funct. Mater.*, **14**, 791.
56. Long, J.R. and Yaghi, O.M. (2009) *Chem. Soc. Rev.*, **38**, 1213.
57. Perry, J.J., Perman, J.A., and Zaworotko, M.J. (2009) *Chem. Soc. Rev.*, **38**, 1400.
58. Shimizu, G.K.H., Vaidhyanathan, R., and Taylor, J.M. (2009) *Chem. Soc. Rev.*, **38**, 1430.
59. Rikukawa, M. and Sanui, K. (2000) *Prog. Polym. Sci.*, **25**, 1463.
60. Diring, S., Furukawa, S., Takashima, Y., Tsuruoka, T., and Kitagawa, S. (2010) *Chem. Mater.*, **22**, 4531.
61. Tanaka, K., Oda, S., Nishihote, S., Hirayama, D., and Urbanczyk-Lipkowska, Z. (2009) *Tetrahedron: Asymmetry*, **20**, 2612.
62. Karimi, Z. and Morsali, A. (2013) *J. Mater. Chem. A*, **1**, 3047.
63. Meilikhov, M., Yusenko, K., Esken, D., Turner, S., Tendeloo, G.V., and Fischer, R.A. (2010) *Eur. J. Inorg. Chem.*, 3701.
64. Cheng, B., Hashemi, L., Hu, M.-L., and Morsali, A. (2014) *Chem. Eng. J.*, **249**, 210.
65. Khanjani, S. and Morsali, A. (2014) *Ultrason. sonochem*, **21** (4), 1424.
66. Khanjani, S. and Morsali, A. (2012) *CrystEngComm*, **14**, 8137.
67. Abbasi, A.R., Akhbari, K., and Morsali, A. (2012) *Ultrason. Sonochem.*, **19**, 846.

10
Modeling Methods for Modulus of Polymer/Carbon nanotube (CNT) Nanocomposites

Yasser Zare and Hamid Garmabi

10.1
Introduction

Carbon nanotubes(CNTs) with high mechanical, thermal, chemical, and electrical properties together with nanoscale dimension, high aspect ratio, and low density are good candidates for polymer reinforcement [1–3]. The CNT-reinforced nanocomposites are applied in a wide range of aerospace structures, automotive components, sporting goods, conducting plastics, electro-magnetic interference shielding, optical barriers, biomaterial devices, and different sensors [4].

The large contact area between nanotubes and rather strong inter-tube attraction by van der Waals forces harden the dispersion of CNTs in polymer matrices. As a result, the CNT dispersion is a challenging work, which can be improved by several methods such as ball milling, surface functionalization, and application of surfactants and ultrasonic vibration [5]. Additionally, the waviness and the random orientation of CNTs beside the poor polymer/CNT interfacial adhesion are other challenges that decrease the efficiency of CNTs in polymer nanocomposites [6, 7].

The mechanical properties of polymer nanocomposites depend on many parameters such as aspect ratio (α), alignment, waviness, dispersion, and agglomeration of nanoparticles as well as the interaction between polymers and nanofillers [8–12]. The mechanical properties can be predicted by various computer modeling methods at large scales of length and time from molecular, microscale to macroscale, and their combination as multiscale techniques (Figure 10.1a) [13, 14].

In the smallest length and time scale, computational chemistry is mostly used to predict the atomic structure by first-principles theory which assumes the presence of a separate molecular structure of material. Also, in the largest scale, computational mechanics are applied assuming a continuous structure in material. However, the multiscale methods are used in the middle scales. Figure 10.1b shows a diagram of modeling methods for mechanical properties in which the bold ones

Nanomaterials and Nanocomposites: Zero- to Three-Dimensional Materials and Their Composites,
First Edition. Edited by Visakh P.M. and Maria José Martínez Morlanes.

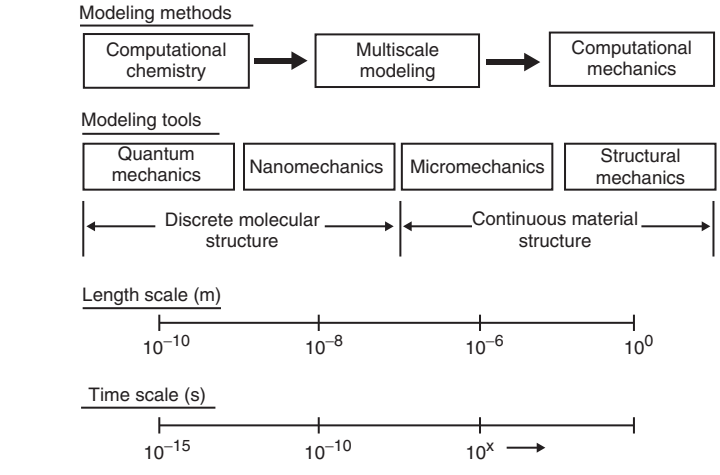

(a)

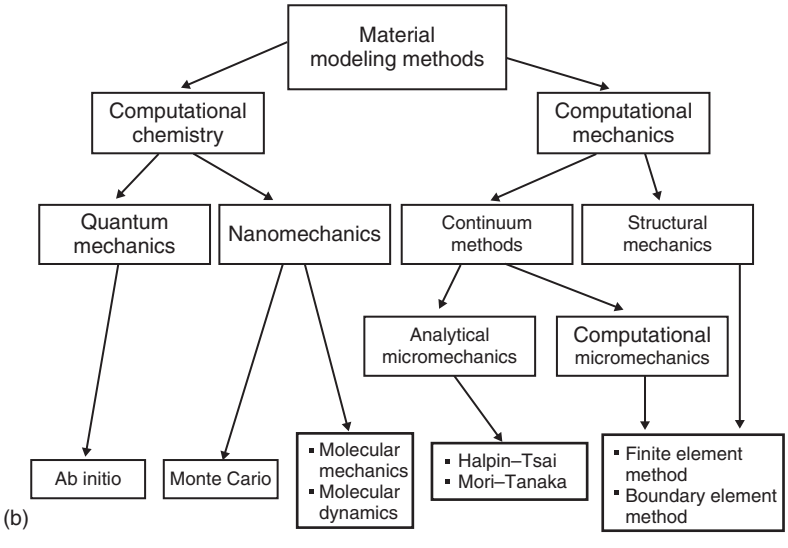

(b)

Figure 10.1 (a) The range of length and time scales for modeling of mechanical properties and (b) the techniques for material modeling. The methods indicated in bold are widely used for mechanical properties of polymer/CNT nanocomposites. (Reproduced from Ref. [13] with permission.)

have been widely used for modeling of modulus in polymer/CNT nanocomposites. This chapter focuses on the modeling of modulus in reinforced polymer/CNT nanocomposites. All modeling methods from molecular to macroscale and multiscale scales are extensively evaluated and the effective factors on the stiffening of polymer/CNT nanocomposites are studied.

10.2
Results and Discussion

10.2.1
Molecular Modeling

Molecular modeling is a powerful instrument to study the atomic structure and interaction at the nanometer scale [15]. This approach assumes a noncontinuous organization of material where its discrete nature often limits the length and time scales. The commonly used techniques of molecular modeling for mechanical properties of polymer/CNT nanocomposites are molecular dynamics (MD) and molecular mechanics (MM) [13].

10.2.1.1
Molecular Dynamics (MD)

MD is the most widely used modeling technique that allows the accurate prediction of interaction between constituent phases at the atomic size [16]. The time evolution of a set of interacting atoms is determined, followed by the integration of the motion equations given by Newton's second law ($F_i = m_i a_i$) in which F_i is the force on atom i and m_i and a_i are the mass and acceleration of atom i in a system. The MD simulation has revealed that a long CNT can greatly improve the elastic modulus of epoxy nanocomposites, by about 10 times, while an enhancement of about 20% is obtained by a short CNT [16, 17]. Griebel and Hamaekers [18] have shown an excellent agreement between MD results with rule of mixtures and extended rule of mixtures models for extremely long and short CNTs, respectively. The MD results demonstrated the significant enhancement of elastic properties by reduction of filler size. The MD simulation of polystyrene (PS)/CNT nanocomposites exhibited that the ion beam deposition modification produces many cross-links between CNTs and polymer chains, which reinforce the nanocomposites [19]. The optimum condition for this sample was observed in high ion energy and compact structure.

10.2.1.2
Molecular Mechanics (MM)

Using MM simulation, Mokashi *et al.* [20] found that the length of the CNT and the configuration of polyethylene (PE) play an important role in the tensile properties of nanocomposites. The crystalline PE caused a moderate improvement by a long CNT, while the short CNT caused a significant reduction in the modulus of amorphous PE that resulted from a poor load transfer at the interface.

10.2.2
Continuum Methods

The continuum models usually assume a simple geometry for each phase and a perfect load transfer between the constituents. They often evaluate the properties of nanocomposites by some important factors such as the volume fraction,

geometry, and orientation of nanofillers. The continuum techniques can overcome some problems such as expensive cost and configuration explanation of molecular simulations. The continuum modeling includes computational continuum and micromechanics methods.

10.2.2.1

Computational Continuum Modeling

The computational continuum modeling comprises finite element method (FEM) and boundary element method (BEM). The computational continuum techniques can provide very precise approximations for modulus of polymer/CNT nanocomposites.

Finite Element Method (FEM) FEM can be used for numerical computation of properties by geometries, properties, and volume fractions of components [13]. FEM involves the discretization of a material representative volume element (RVE) in elements in which the stress and strain fields are determined by elastic solutions. Figure 10.2 shows three possible RVE as circular, square, and hexagonal.

The main findings obtained from simulation of CNT-reinforced nanocomposites by FEM are explained as:

- Short CNT is not as effective as long CNT in the reinforcing of nanocomposites [22, 23].
- The interphase thickness should be at least of the order of the CNT thickness and the interphase modulus may show an exponential behavior [24].
- The CNT waviness enhances the modulus at poor interface bonding [25].
- The rubber incorporated with a single sinusoidal wavy CNT and perfect interfacial bonding shows linear and hyper-elastic behavior in low and large strains, respectively [26].
- The FEM, taking into account the CNT random distribution, agglomeration, waviness, and alignment together with the interphase properties, illustrates a good agreement with the experimental data [4, 27]. The model assuming the

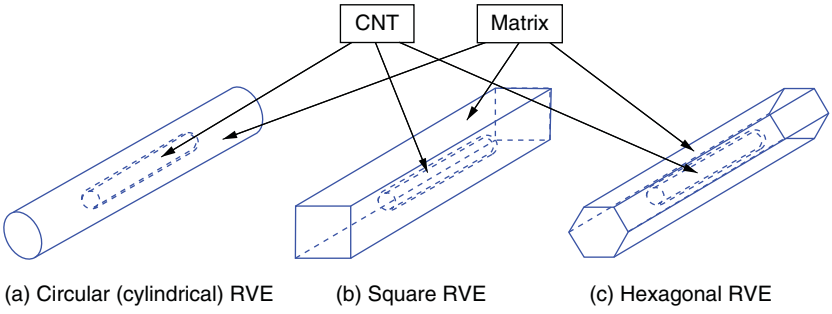

Figure 10.2 Three possible representative volume elements (RVEs) for the analysis of polymer/CNT nanocomposites: (a) Circular (cylindrical), (b) Square, and (c) Hexagonal. (Reproduced from Ref. [21] with permission.)

perfect interfacial adhesion in polypropylene (PP)/5 wt% CNT overpredicts the modulus by 85%.
- The cylindrical RVE overpredict the elastic modulus, due to overestimating the CNT loading. But, the predictions show good conformity with the experimental data using square RVE [28].

Some researchers have developed FEM for polymer/CNT nanocomposites. Huang *et al.* [29] considered the 3D end effects of single-walled carbon nanotubes (SWCNTs) by introduction of a length factor. Their model can be applied for CNT loading between 0 and 5 vol%, while the FEM model is suitable for a CNT content about 5 vol% [22]. Song and Youn [30] also used the asymptotic expansion homogenization method to perform both localization and homogenization for a heterogeneous system. They found a good agreement between the numerically and the analytically calculated elastic moduli.

The visco-elastic behavior of CNT-reinforced nanocomposites was investigated using the three-phase concentric cylindrical shell and the shear-lag models [31, 32]. It was found that the effective modulus of nanocomposites depends on seven parameters: CNT α, the cross-sectional area ratio of CNTs, the matrix to filler modulus ratio, the interphase to filler modulus ratio, the filler volume fraction, the interphase volume fraction, and the RVE to fiber length ratio. The obtained results revealed that α is a significantly effective parameter and a large CNT introduces a better reinforcement [32]. Although FEM represents good findings for polymer/CNT nanocomposites, high complexity, expensive software, and time-consuming simulation limit the utility of FEM.

Boundary Element Method (BEM) Unlike FEM, BEM uses elements along the boundary involving elements throughout the volume. BEM solves the boundary integral equations for evaluation of stress and strain fields [13]. As a result, BEM is less computationally complete compared to FEM. A fast multiple BEM was employed to evaluate the effective modulus of nanocomposites in which CNTs were assumed as rigid fibers in the elastic matrix [33]. As shown in Figure 10.3, the BEM results for aligned random and uniform cases are much nearer to the experimental data, MD simulation, and a multiscale method reported by Odegard *et al.* [34]. In general, the BEM presents some advantages over the FEM, such as fewer surface elements [21]. It is concluded the computational continuum methods can provide suitable predictions assuming the real structure and morphology of nanocomposites together with the properties of interphase.

10.2.2.2 Micromechanics Models

The micromechanics models can predict the modulus by the characteristics of each phase. They frequently consider a good dispersion of the CNT in the matrix and a great interfacial adhesion between the phases. Therefore, they show more

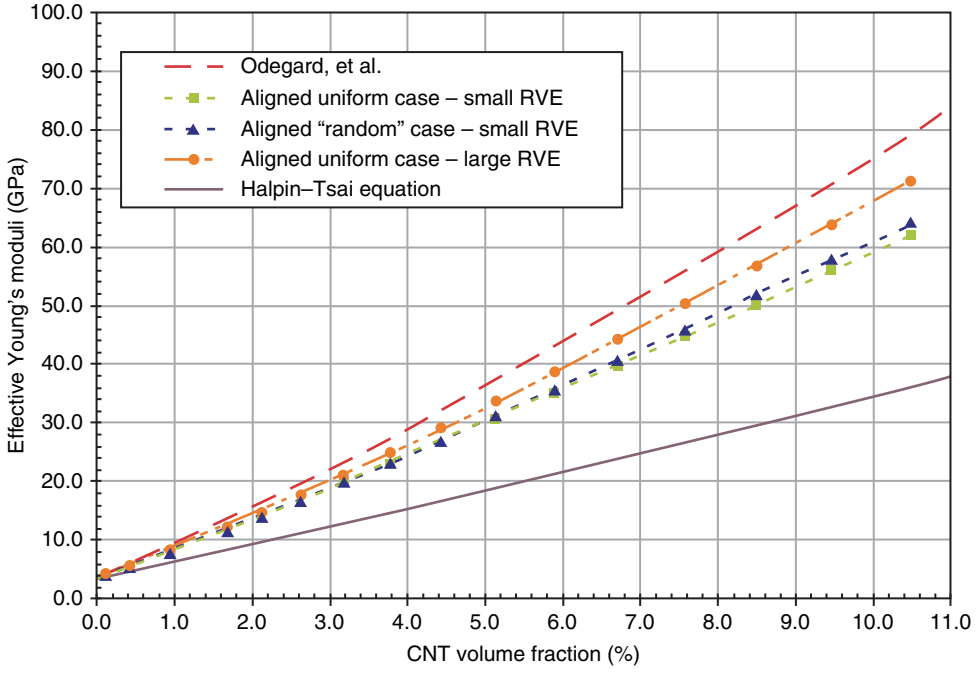

Figure 10.3 The BEM results for aligned random and uniform cases and comparison with the experimental results, MD simulation, and a multiscale method reported by Odegard. (Reproduced from Ref. [33] with permission.)

ease and speed for the calculation of modulus when compared to all other modeling techniques.

Krenchel Model The modulus of nanocomposites with randomly and homogeneously distributed CNT can be predicted by the modified rule of mixtures model proposed by Krenchel [35] as:

$$E_c = \eta_o \eta_L \varphi_f E_f + \varphi_m E_m \tag{10.1}$$

where E_c, E_f, and E_m are the Young's moduli of nanocomposite, CNT, and matrix, respectively. φ_f and φ_m are the volume fractions of CNT and matrix. η_o is an orientation factor, equally to 1 for fully aligned fillers, 3/8 for randomly in-plane two-dimensional (2D) orientation and 1/5 for randomly 3D arrangement. Similarly, η_L is a length efficiency parameter varying between 0 and 1. Some researchers have used the Thostenson and Chou approach [36] to take into account the diameter dependency of CNT density (ρ_f) as:

$$\rho_f = \frac{\rho_g (d_o^{\,2} - d_i^{\,2})}{d_o^{\,2}} \tag{10.2}$$

where d_i and d_o are the inner and outer diameters of the CNT. Also, the density of graphite (ρ_g) is assumed as 2.25 g cm^{-3}. Many studies neglected the diameter dependency of CNTs due to the extremely small diameter distribution. It was found that the Krenchel model cannot predict the modulus of polyurethane (PU)/MWCNT [37], PP/MWCNT [38], and epoxy/SWCNT [39] nanocomposites.

Cox and Developed Cox Models Cox modified the η_L factor in the Krenchel model (Eq. (10.1)) [35] as:

$$\eta_L = 1 - \frac{\tanh(a\alpha)}{a\alpha} \tag{10.3}$$

$$a = \sqrt{\frac{-3E_m}{2E_f Ln(\varphi_f)}} \tag{10.4}$$

where the aspect ratio of a CNT (α) is defined as $\alpha = l/d$ in which l and d are the length and diameter of the CNT, respectively. Various studies have indicated that the Cox model cannot be sufficiently fitted to the experimental results of polymer/CNT nanocomposites [35, 40, 41].

Omidi *et al.* [42] developed the Cox model for epoxy/MWCNT nanocomposites as:

$$E_c = \eta_o \eta_L \eta_w \varphi_f e^{z\varphi_f} E_f + E_m(1 - \varphi_f e^{z\varphi_f}) \tag{10.5}$$

$$\eta_w = 1 - \frac{a}{h} \tag{10.6}$$

$$z = \frac{Ln(\beta)}{\widehat{\varphi}_f} \tag{10.7}$$

$$\beta = \frac{\widehat{E}_c - E_m}{(\eta_0 \widehat{\eta}_L \eta_w - E_m)\widehat{\varphi}_f} \tag{10.8}$$

where a and h are the amplitude and half-wavelength of a curved CNT in a bow-like waviness. The parameters with a hat sign are determined by curve fitting. This model was also fitted to modulus of PS/MWCNT [43], epoxy/MWCNT [44], and phenolic/MWCNT [45] nanocomposites. Furthermore, Martone *et al.* [46] examined the bending modulus in epoxy/MWCNT nanocomposites by adjusting the α term in the Cox model. The effective α supposing more contacts between nanotubes was stated as:

$$\alpha_{\text{eff}} = \frac{\alpha}{1 + c} \tag{10.9}$$

where c is the average number of contacts per particle. c is 0 for isolated CNT with an average number of contacts with other nanotubes. The c parameter for nanotubes was studied by Philipse [47] as:

$$c = w\varphi_f \left(4 + \frac{3\alpha^2}{3\alpha + 2}\right) \tag{10.10}$$

$$w = \frac{V_{\text{ex}}^{\text{eff}}}{V_{\text{ex}}} \tag{10.11}$$

where the waviness parameter (w) is the ratio of the efficiently average excluded volume for a waved rod ($V_{\text{ex}}^{\text{eff}}$) and that for a straight one (V_{ex}). The appropriate values of w and c were chosen by fitting to the modulus.

As a result, the Krenchel and Cox models cannot calculate the modulus of CNT-reinforced nanocomposites. The reported studies have randomly chosen different parameters such as w and c without any appropriate characterization of parameters.

Halpin–Tsai Model (H–T) The most known H–T model [48] is given as:

$$E_c = E_m \left(\frac{1 + \eta\xi\varphi_f}{1 - \eta\varphi_f}\right) \tag{10.12}$$

$$\eta = (E_f/E_m - 1)/(E_f/E_m + \xi) \tag{10.13}$$

$$\xi = 2\alpha \tag{10.14}$$

Table 10.1 shows the calculated results by H–T and the fitted level for different nanocomposites. m_f is the weight percentage of the CNT in the nanocomposite. The H–T model can calculate the tensile modulus of some samples such as poly(methyl methacrylate) (PMMA)/functionalized MWCNT (f-MWCNT) [49] and poly(*p*-phenylenebenzobisoxazole) (PBO)/grafted-functionalized MWCNT (g-f-MWCNT) [50] fibers.

However, the Young's modulus of CNT is not accurate for the PMMA/f-MWCNT sample. The Young's modulus of CNT changes from 320 to 1470 GPa [54, 55], possibly due to the variation of defect density in the CNT. Also, the α of pristine CNT was used for some samples that cannot be correct, because CNT particles undergo high scission or bundling during the treatment and fabrication actions. In addition, the H–T model overestimates the modulus of some samples, mostly due to the poor dispersion of CNT in polymer matrix, weak interface properties, and the wavy CNT decreasing the modulus. The H–T model assumes the good dispersion of CNT as well as the perfect bonding between polymer and CNT.

Table 10.1 Calculation of modulus by Halpin–Tsai model [56].

Samples	m_f (wt%)	E_f (TPa)	α	Fitting	References
PET/SWCNT	0.1–0.3	1	1000 (r)	Good	[41]
PMMA/f-MWCNT	5	0.45	52 (TEM)	Good	[49]
PBO/g-f-MWCNT	0.18–0.54	1	33.3 (p)	Good	[50]
PP/MWCNT	1	0.9	140 (p-SEM)	Good	[51]
Epoxy/MWCNT	0.25–10	0.9	20–300 (p)	Overpredict	[42]
PAN/g-f-SWCNT	0.5–3	0.45	55 (r)	Overpredict	[52]
PE/SWCNT	1–20	1	100–1000	Overpredict	[53]

PET: poly(ethylene terephthalate); PMMA: poly(methyl methacrylate); PBO: poly(*p*-phenylenebenzobisoxazole); g-f-MWCNT: grafted-functionalized MWCNT; PP: polypropylene, PAN: polyacrylonitrile; PE: polyethylene; and p: determination of α from pristine CNT.

Halpin–Tsai Model for 2D In-Plane Random Arrangement of Filler (H–T2D) The extensively used micromechanics model for prediction of tensile modulus in polymer/CNT nanocomposites is H–T2D [57, 58] as:

$$E_c = \frac{3}{8}E_L + \frac{5}{8}E_T \tag{10.15}$$

$$E_L = E_m\left(\frac{1+\zeta\eta_L\varphi_f}{1-\eta_L\varphi_f}\right) \tag{10.16}$$

$$E_T = E_m\left(\frac{1+2\eta_T\varphi_f}{1-\eta_T\varphi_f}\right) \tag{10.17}$$

$$\eta_L = (E_f/E_m - 1)/(E_f/E_m + \zeta) \tag{10.18}$$

$$\eta_T = (E_f/E_m - 1)/(E_f/E_m + 2) \tag{10.19}$$

where E_L and E_T are longitudinal and transverse moduli, respectively. Table 10.2 shows the fitting of experimental modulus of many samples to H–T2D model.

First of all, it should be said that a good fitting was obtained at small contents of CNT and a deviation from predictions were found at higher CNT content. However, an incorrect α of pristine CNT was applied for many samples. Additionally, some samples were fitted by a low level of CNT modulus.

Moreover, this model overestimates the modulus of polymer/CNT nanocomposites in some cases [57, 69–71], due to the poor dispersion of CNT in the

Table 10.2 The modeling of modulus by H–T2D model [56].

Samples	m_f (wt%)	E_f (TPa)	α	References
PS/MWCNT	1–5	0.45	1500 (p)	[59]
PDCPD/f-MWCNT	0.05–0.4	0.4	100 (r)	[60]
PVA/MWCNT	0.1–1	1	800 (r)	[61]
PVA/SWCNT	5	0.64	32 (r)	[62]
PVA/m-SWCNT	1–2.5	0.0003	536 (p)	[63]
PVA/MWCNT	2–3	0.7	200 (p-TEM)	[64]
SBM/MWCNT	1–6	0.35	41 (TEM)	[65]
Epoxy/f-DWCNT	0.1–1	1	3571 (p)	[66]
Epoxy/f-MWCNT	0.34	1	800 (p)	[67]
Epoxy/MWCNT	0.34	1	400 (p)	[67]
Epoxy/MWCNT	0.2–10	1	100 (p)	[68]

PS: polystyrene; PDCPD: poly(dicyclopentadiene); PVA: poly(vinyl alcohol); SBM: poly(styrene-*block*-butadiene-*block*-methyl methacrylate) copolymer; and v%: volume fraction.

polymer matrix and little interfacial adhesion between matrix and CNT particles. As a result, in spite of the most application of the H–T2D model, it cannot give an acceptable calculation. Since the H–T and H–T2D often overpredict the Young's modulus of CNT-reinforced nanocomposites, many researchers modified these models to obtain a good predictability.

Modified H–T Models Thostenson and Chou [36] offered an efficient modulus for CNT (E_{eff}) as:

$$E_{\text{eff}} = \frac{4t}{d} E_f \tag{10.20}$$

where t and d are the thickness and diameter of CNT, respectively. They took into account the distribution and the tubular construction of CNT diameter. Their assumptions were successfully applied for modulus of PS/MWCNT nanocomposites [36].

Also, the degree of CNT aggregation (p) was assumed [72] as:

$$E_c = E_m \left(\frac{1 + p\eta\varphi_f}{1 - \eta\varphi_f} \right) \tag{10.21}$$

$$\eta = (E_f/E_m - 1)/(E_f/E_m + p) \tag{10.22}$$

$$m = 2\alpha p \tag{10.23}$$

The best-fitted modulus was obtained at $p \sim 18$ and $p \sim 67$ for functionalized and unfunctionalized SWCNT, respectively. The p values were proved by scanning

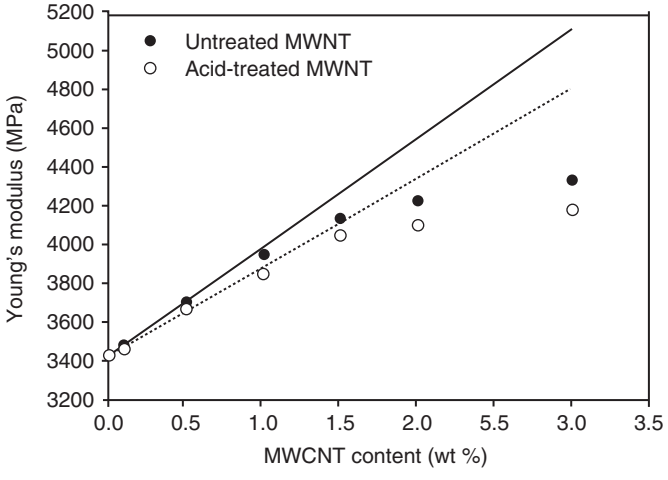

Figure 10.4 The Young's modulus of epoxy/MWCNT nanocomposite. (Reproduced from Ref. [73] with permission.)

electron microscopy (SEM) images. Also, the fitting for MWCNT nanocomposites was obtained with $p \sim 10$, which indicated the reduced agglomeration. The MWCNT with smaller α of 30 is probably responsible for decreased p, while higher bundling can cause greater mutual van der Waals forces in SWCNT.

The experimental modulus of polymer/CNT nanocomposites usually shows nonlinear improvement at high content of CNT loading (Figure 10.4), attributed to the aggregation of CNT at higher contents. Therefore, the a shape factor was added to H–T model [74] as:

$$\zeta = 2\alpha e^{-a\varphi_f - b} \tag{10.24}$$

where a and b constants demonstrate the degree of CNT aggregation. The greater values of a and b show the larger aggregation of CNT. It was found that the elastic modulus of epoxy/MWCNT nanocomposites [73] was fitted to higher a and b constants for untreated MWCNT compared to a treated one. The H–T2D model was also modified to increase its accurateness. Ayatollahi *et al.* [75] modified the α term as:

$$\alpha_m = a(l/d)^b \tag{10.25}$$

where a and b parameters show nonperfect interface, agglomeration, and other flaws in the nanocomposites. The best values of a and b were calculated as $a = 0.0488$ and $b = 1.141$ for epoxy/MWCNT nanocomposites [75] and other nanocomposites [45, 73, 76].

It is concluded that the modified models assumed the effective parameters such as aggregation, waviness, and so on, only by the fitting procedure. Undeniably, it is not a valid method for the calculation of modulus in polymer/CNT nanocomposites.

Mori–Tanaka Model (M–T) Mori–Tanaka (M–T) model is derived from the principles of Eshelby's inclusion model to calculate an elastic stress field in and around ellipsoidal filler in an infinite matrix. The M–T model for an isotropic matrix filled with spherical filler is expressed as [77]:

$$\frac{E_L}{E_m} = \frac{A_0}{A_0 + \varphi_f(A_1 + 2\nu A_2)} \tag{10.26}$$

$$\frac{E_T}{E_m} = \frac{2A_0}{2A_0 + \varphi_f(-2A_3 + (1-\nu)A_4 + (1+\nu)A_0A_5)} \tag{10.27}$$

where ν is the Poisson ratio of the matrix and A_0,A_1, … ,A_5 parameters are connected to Eshelby's tensor and filler and matrix properties such as Young's modulus, Poisson ratio, φ_f and α. The calculated modulus by M–T for PET (poly(ethylene terephthalate)/SWCNT nanocomposites [41] have been higher than the experimental results. Ogasawara *et al.* [78] also studied the effect of 3D random orientation and entangled distribution of CNT in polyimide/MWCNT nanocomposites, conducted based on the Eshelby–Mori–Tanaka theory. They obtained E_f as 38 GPa. The M–T method was developed to estimate the effective elastic moduli of nanocomposites containing straight and curved CNT with aligned or random orientation [79]. Finally, the influence of CNT agglomeration was considered using an Eshelby's inclusion model.

Furthermore, four homogenization arrangements, a sequential and various extensions of the M–T homogenization: two-level (M–T/M–T), two-step (M–T/M–T), and two-step (M–T/Voigt) were used to model the modulus [80]. For all morphologies, the two-level (M–T/M–T) model provided the best predictions. Also, the sequential and the two-level (M–T/M–T) models could give good calculations for fully aligned long CNT nanocomposites. The M–T approach was also modified to study the imperfect interfacial adhesion between polymers and fillers [81]. In this analysis, CNT was considered to be either an infinite long cylinder or ellipsoidal and the perfect alignment or randomly oriented fillers were evaluated. The results demonstrated that a perfect bonding is practical for low φ_f.

Developed Micromechanics Models Cadek *et al.* [82] empirically suggested the dependence of modulus on the total CNT surface area per unit volume of the nanocomposite (SA/V_c) as:

$$E_c/E_m = m\varphi_f + 1 \tag{10.28}$$

where m is a function of CNT diameter as $m = 1862\,\text{day}^{-1}$. Also, a linear dependence of the normalized tensile modulus (E_c/E_m) to (SA/V_c) was found for all

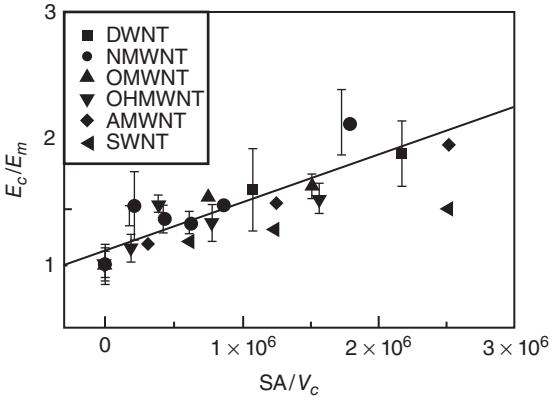

Figure 10.5 The effect of total surface area per volume (SA/V_c) on the normalized tensile modulus (E_c/E_m) for PVA/CNT samples. (Reproduced from Ref. [82] with permission.)

samples (Figure 10.5). A same interface was shown in all samples and the slope of the universal curve (k) was calculated by interfacial stress transfer as 457 ± 35 nm.

The relation between k and m was expressed as:

$$k = \frac{md}{4} \tag{10.29}$$

This equation demonstrated the vital role of interfacial stress transfer and the efficiency of low-diameter CNT for reinforcement of polymer.

Moreover, Coleman *et al.* [83] stated that the substantial increment of modulus in polymer/CNT nanocomposites is attributed to the formation of an ordered polymer layer around the CNT. The nucleation of this layer increases the crystallinity of the polymer, which improves the stiffness of the nanocomposite. Accordingly, a simple model based on the rule of mixtures was proposed as:

$$E_c = \varphi_f \eta_o E_{\text{eff}} + \varphi_m E_a + \varphi_f \left(\frac{b^2 + 2Rb}{R^2} \right) (E_x - E_a) \tag{10.30}$$

where E_{eff}, E_a, and E_x are the effective moduli of CNT, amorphous, and crystalline phases, respectively. b is the average thickness of the ordered polymer coating, R is the CNT radius, and $\eta_o = 3/8$.

Also, an analytically micromechanics model was developed for elastic properties of nanocomposite RVEs as a function of CNT waviness, length, and 3D random orientation [84]. This model showed good predictions when compared with experimental and FEM results. De Villoria and Miravete [85] also introduced a new micromechanics model called *dilute suspension of clusters* taking into account the influence of inhomogeneous dispersion of nanofillers in nanocomposites. The proposed model significantly improved the theoretical–experimental relationship for epoxy/clustered CNT nanocomposites.

10.2.3 Multiscale Techniques

The continuum models typically assume that each phase has identical properties as if the other phases do not exist. Also, many concepts in conventional composites cannot be applied in polymer nanocomposites, due to the hierarchical morphology of nanofillers and surrounding polymers at nanometer scale. Moreover, the polymer–filler interactions are extremely dependent on the local molecular structure and interfacial bonding. As a result, the structure of nanofillers and polymer chains cannot be assumed as a continuous phase at the small scales, and the mechanical properties cannot be successfully determined by traditional micromechanics models.

The equivalent-continuum method (ECM) is applied as a multiscale model to simulate the mechanical properties of nanocomposites. Figure 10.6 displays the simulating process of a CNT-reinforced nanocomposite by ECM [86]. At first, the molecular structure of CNT and neighboring polymer chains is modeled by MD in which all interactions are assumed. Then, an equivalent-truss model is developed. In the next step, considering the force constants that illustrate the bonded and nonbonded interactions of the atoms in the molecular model, the mechanical properties of truss elements are calculated. Finally, an ECM is given to evaluate the effective fiber [87].

The multiscale simulation can correlate the simulation methods in a wide range of length and time. Generally, two types of multiscale methods including sequential and concurrent are applied (Figure 10.7) [15]. In the sequential approach as a widely used model, a series of computational methods are related in which the calculated parameters at one scale are used to characterize the parameters of the model in the next larger scale. In the concurrent technique, several computational methods are connected together in a model where different scales are parallel and communicative by various types of procedures.

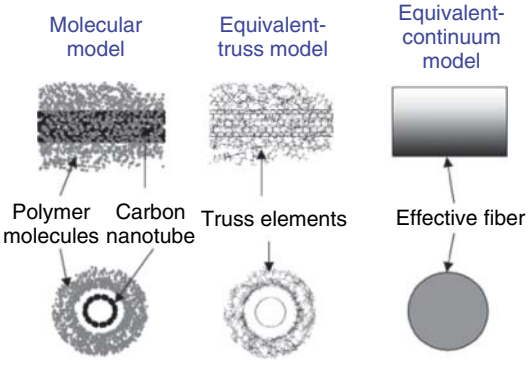

Figure 10.6 The equivalent-continuum modeling for polymer/CNT nanocomposites. (Reproduced from Ref. [86] with permission.)

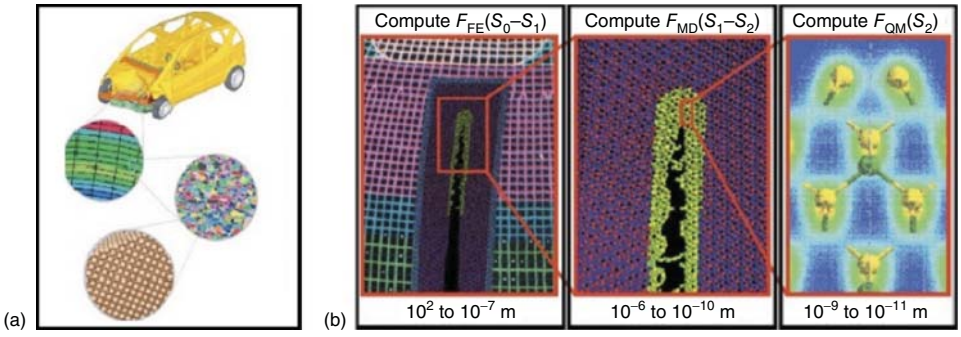

Figure 10.7 Two multiscale modeling and simulation strategies: (a) sequential (reproduced with permission) and (b) concurrent approaches. (Reproduced from Ref. [15] with permission.)

Another multiscale method proposed by Pipes and Hubert [88] is a self-similar approach, which includes three main steps. First, a helical array of CNT is assembled as a CNT nano-array containing 91 CNT in its cross-section. Then, nanoarrays are surrounded by a polymer matrix and collected in a second twisted array as CNT nano-wire. Lastly, CNT nanowires are further accumulated with a polymer matrix and form the concluding helical CNT microfiber. Odegard *et al.* [86] used both ECM and self-similar approaches to predict the elastic properties of polymer/SWCNT nanocomposites, which revealed that both methods can predict the elastic properties in a wide range of φ_f.

Several researchers have applied the multiscale method based on FEM (Table 10.3). In this approach, the CNT and the effective interaction between the polymer and CNT is simulated by computational chemistry techniques such as MD and then, the calculated parameters are employed by FEM to predict the modulus of nanocomposites. Also, some combined the molecular simulations

Table 10.3 The multiscale modeling of modulus by molecular techniques and continuum-based models [56].

Modeling subjects	References
Interfacial condition	[89–95]
CNT and RVE length	[89, 96]
Atomistic structure of CNT	[90]
CNT agglomeration, dispersion, and waviness	[96]
Atomic interface interactions	[97]
Imperfect interfacial condition	[98, 99]
Alignment, φ_f, α, and twist angle	[100]
Interphase, CNT length, φ_f, and orientations	[34, 101]
CNT size and weak interface	[102]
Homogeneous distribution and local/interface properties	[103]

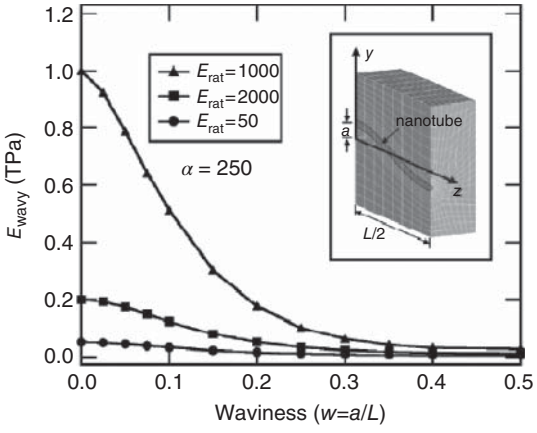

Figure 10.8 The effective modulus of a considerably long wavy CNT (E_{wavy}) embedded in a matrix at different waviness ratio ($w = a/L$) and $E_{rat} = E_f/E_m$ by multiscale modeling. (Reproduced from Ref. [105] with permission.)

with other continuum-based models such as M–T, multi-particle effective field (MEFM) and BEM to simulate the modulus (Table 10.3). It should be indicated that the multiscale methods have been successfully confirmed by the experimental data and/or other simulation procedures.

The multiscale models based on FEM and M–T have been applied to estimate the waviness of CNT. The CNT curvature is a dominant factor, which reduces the effective modulus of CNT nanocomposites [104]. Fisher *et al.* [105] demonstrated that the waviness ratio ($w = a/L$) and the ratio of phase moduli ($E_{rat} = E_f/E_m$) affect the effective modulus of a curved CNT (E_{wavy}) (Figure 10.8). It was presented that sufficiently large α has minimal influence on E_{wavy}. The calculated modulus for epoxy/MWCNT nanocomposites [104] with $E_f/E_m = 100$ shows good agreement with the experimental modulus.

Fisher *et al.* [106] also studied the effect of wavelength ratio of CNT on the modulus assuming the minimal CNT waviness distribution ($0 < w < 1$) and the more moderate waviness ($0 < w < 1$). Bradshaw *et al.* [107] also predicted the effective modulus of nanocomposites containing aligned or randomly oriented CNT. Furthermore, Shao *et al.* [108] proposed a model to calculate the effect of CNT curvature and interfacial bonding on the effective modulus of nanocomposites. They found that the modulus is very sensitive to waviness and this sensitivity decreases with the enhancement of waviness.

Lagoudas *et al.* [109, 110] also evaluated the effects of CNT clustering and polymer–CNT interphase. They found that the cylinder method provides acceptable results for a continuous range of φ_f below a critical value. Moreover, near and above the critical φ_f, FEM was much useful to consider the complex polymer–filler interactions. However, many multiscale models should be suggested to study the whole effective characteristics in polymer/CNT nanocomposites.

10.3 Conclusions and Future Challenges

Many simulation techniques for modulus in polymer/CNT reinforced nanocomposites including molecular simulations, computational continuum methods, micromechanics, and multiscale models are studied. The molecular simulations can be used to evaluate the molecular interaction and structure in the range of 0.1–10 nm. Although the obtained results are very useful for understanding the interaction between polymer and nanoparticles as well as the molecular origin of modulus, molecular-based methods are computationally very difficult. On the other hand, the application of macroscale techniques such as FEM and BEM involve high complexity, expensive software, and much time. Moreover, the micromechanics techniques employed for modulus of polymer/CNT nanocomposites show different strengths and weaknesses. The H–T, M–T, and so on, do not consider the crucial parameters such as interfacial interaction and the morphology of nanocomposites for the estimation of modulus. In addition, poor dispersion of CNT in the polymer matrix, weak interfacial adhesion, and CNT waviness significantly decrease the predictability of micromechanics models.

Therefore, it is essential to develop proper techniques at a wide range of time and length, from quantum structure (a few atoms) to molecular domain (many atoms), mesoscopic structure (many monomers or chains), and macroscopic structure to present a useful tool for calculation of modulus. The development of multiscale methods is very interesting and represents the certain future for simulation methods in polymer nanocomposites.

In future studies, the efficient characteristics of CNT in a polymer matrix should be taken into account. A large number of CNTs in different sizes and forms (curved or twisted), which is randomly distributed in the matrix should be developed in future researches. Also, the interphase between polymer and CNT and the exact characterization of CNT such as modulus, α, and the volume fraction are necessary for accurate modeling. Additionally, the final validation of simulation results should be carried out with enough experimental results and much appropriate modeling methods.

Researchers should know the structure of polymer chains, CNTs, and the interactions at the interface to correctly simulate the properties of nanocomposites. Therefore, a combination of polymer, mechanics, and mathematics sciences will be more useful in this area. The development of modeling methods will help to design and optimize the advanced nanocomposites.

References

1. Spitalsky, Z., Tasis, D., Papagelis, K., and Galiotis, C. (2010) Carbon nanotube–polymer composites: chemistry, processing, mechanical and electrical properties. *Prog. Polym. Sci.*, **35** (3), 357–401.
2. Moniruzzaman, M. and Winey, K.I. (2006) Polymer nanocomposites containing carbon nanotubes. *Macromolecules*, **39** (16), 5194–5205.
3. Pandey, G. and Thostenson, E.T. (2012) Carbon nanotube-based multifunctional

polymer nanocomposites. *Polym. Rev.*, **52** (3-4), 355–416.

4. Bhuiyan, M.A., Pucha, R.V., Worthy, J., Karevan, M., and Kalaitzidou, K. (2013) Defining the lower and upper limit of the effective modulus of CNT/polypropylene composites through integration of modeling and experiments. *Compos. Struct.*, **95**, 80–87.
5. Kessler, M.R. (2012) Polymer matrix composites: a perspective for a special issue of polymer reviews. *Polym. Rev.*, **52** (3-4), 229–233.
6. Zaminpayma, E. and Mirabbaszadeh, K. (2012) Interaction between single-walled carbon nanotubes and polymers: a molecular dynamics simulation study with reactive force field. *Comput. Mater. Sci.*, **58**, 7–11.
7. MatinGhahfarokhi, Z. and Golestanian, H. (2011) Effects of nanotube helical angle on mechanical properties of carbon nanotube reinforced polymer composites. *Comput. Mater. Sci.*, **50** (11), 3171–3177.
8. Zare, Y. (2014) Determination of polymer-nanoparticles interfacial adhesion and its role in shape memory behavior of shape memory polymer nanocomposites. *Int. J. Adhes. Adhes.*, **54**, 67–71.
9. Zare, Y. and Garmabi, H. (2014) Modeling of interfacial bonding between two nanofillers (montmorillonite and $CaCO_3$) and a polymer matrix (PP) in a ternary polymer nanocomposite. *Appl. Surf. Sci.*, **321**, 219–225.
10. Zare, Y. and Garmabi, H. (2011) Optimization of mechanical properties of PP/Nanoclay/$CaCO_3$ ternary nanocomposite using response surface methodology. *J. Appl. Polym. Sci.*, **122**, 3188–3200.
11. Zare, Y. (2013) Recent progress on preparation and properties of nanocomposites from recycled polymers: a review. *Waste Manage. (Oxford)*, **33**, 598–604.
12. Zare, Y. and Garmabi, H. (2012) Non-isothermal crystallization and melting behavior of PP/nanoclay/$CaCO_3$ ternary nanocomposite. *J. Appl. Polym. Sci.*, **124**, 1225–1233.
13. Valavala, P. and Odegard, G. (2005) Modeling techniques for determination of mechanical properties of polymer nanocomposites. *Rev. Adv. Mater. Sci.*, **9**, 34–44.
14. Zare, Y., Daraei, A., Vatani, M., and Aghasafari, P. (2014) An analysis of interfacial adhesion in nanocomposites from recycled polymers. *Comput. Mater. Sci.*, **81**, 612–616.
15. Zeng, Q., Yu, A., and Lu, G. (2008) Multiscale modeling and simulation of polymer nanocomposites. *Prog. Polym. Sci.*, **33** (2), 191–269.
16. Zhu, R., Pan, E., and Roy, A. (2007) Molecular dynamics study of the stress–strain behavior of carbon-nanotube reinforced Epon 862 composites. *Mater. Sci. Eng., A*, **447** (1), 51–57.
17. Frankland, S., Harik, V., Odegard, G., Brenner, D., and Gates, T. (2003) The stress–strain behavior of polymer–nanotube composites from molecular dynamics simulation. *Compos. Sci. Technol.*, **63** (11), 1655–1661.
18. Griebel, M. and Hamaekers, J. (2004) Molecular dynamics simulations of the elastic moduli of polymer–carbon nanotube composites. *Comput. Meth. Appl. Mech. Eng.*, **193** (17), 1773–1788.
19. Hu, Y. and Sinnott, S.B. (2004) Molecular dynamics simulations of polyatomic-ion beam deposition-induced chemical modification of carbon nanotube/polymer composites. *J. Mater. Chem.*, **14** (4), 719–729.
20. Mokashi, V.V., Qian, D., and Liu, Y. (2007) A study on the tensile response and fracture in carbon nanotube-based composites using molecular mechanics. *Compos. Sci. Technol.*, **67**, 530–540.
21. Liu, Y. and Chen, X. (2003) Continuum models of carbon nanotube-based composites using the boundary element method. *Electron. J. Boundary Elem.*, **1** (2), 316–335.
22. Liu, Y. and Chen, X. (2003) Evaluations of the effective material properties of carbon nanotube-based composites using a nanoscale representative volume element. *Mech. Mater.*, **35** (1), 69–81.

23. Joshi, U.A., Joshi, P., Harsha, S., and Sharma, S.C. (2010) Evaluation of the mechanical properties of carbon nanotube based composites by finite element analysis. *Int. J. Eng. Sci. Technol.*, **2** (5), 1098–1107.
24. Hernández-Pérez, A. and Avilés, F. (2010) Modeling the influence of interphase on the elastic properties of carbon nanotube composites. *Comput. Mater. Sci.*, **47**, 926–933.
25. Pantano, A. and Cappello, F. (2008) Numerical model for composite material with polymer matrix reinforced by carbon nanotubes. *Meccanica*, **43** (2), 263–270.
26. Motamedi, M., Eskandari, M., and Yeganeh, M. (2012) Effect of straight and wavy carbon nanotubeon the reinforcement modulus in nonlinear elastic matrix nanocomposites. *Mater. Des.*, **34**, 603–608.
27. Bhuiyan, M.A., Pucha, R.V., Karevan, M., and Kalaitzidou, K. (2011) Tensile modulus of carbon nanotube/polypropylene composites–A computational study based on experimental characterization. *Comput. Mater. Sci.*, **50** (8), 2347–2353.
28. Chen, X. and Liu, Y. (2004) Square representative volume elements for evaluating the effective material properties of carbon nanotube-based composites. *Comput. Mater. Sci.*, **29**, 1–11.
29. Huang, G., Mamedov, A., Gupta, S., Wang, B., and Lu, H. (2006) Material characterization and modeling of single-wall carbon nanotube/polyelectrolyte multilayer nanocomposites. *J. Appl. Mech.*, **73** (5), 737–744.
30. Song, Y.S. and Youn, J.R. (2006) Modeling of effective elastic properties for polymer based carbon nanotube composites. *Polymer*, **47** (5), 1741–1748.
31. Zhang, J. and He, C. (2008) A three-phase cylindrical shear-lag model for carbon nanotube composites. *Acta Mech.*, **196** (1-2), 33–54.
32. Gao, X.-L. and Li, K. (2005) A shear-lag model for carbon nanotube-reinforced polymer composites. *Int. J. Solids Struct.*, **42** (5), 1649–1667.
33. Liu, Y., Nishimura, N., and Otani, Y. (2005) Large-scale modeling of carbon-nanotube composites by a fast multipole boundaryelement method. *Comput. Mater. Sci.*, **34** (2), 173–187.
34. Odegard, G., Gates, T., Wise, K., Park, C., and Siochi, E. (2003) Constitutive modeling of nanotube–reinforced polymer composites. *Compos. Sci. Technol.*, **63** (11), 1671–1687.
35. Coleman, J.N., Cadek, M., Blake, R., Nicolosi, V., Ryan, K.P., Belton, C. *et al* (2004) High performance nanotube-reinforced plastics: understanding the mechanism of strength increase. *Adv. Funct. Mater.*, **14** (8), 791–798.
36. Thostenson, E.T. and Chou, T.-W. (2003) On the elastic properties of carbon nanotube-based composites: modelling and characterization. *J. Phys. D: Appl. Phys.*, **36** (5), 573.
37. McClory, C., McNally, T., Brennan, G.P., and Erskine, J. (2007) Thermosetting polyurethane multiwalled carbon nanotube composites. *J. Appl. Polym. Sci.*, **105** (3), 1003–1011.
38. Ma, J., Deng, H., and Peijs, T. (2010) Processing of poly(propylene)/carbon nanotube composites using $scCO_2$-assisted mixing. *Macromol. Mater. Eng.*, **295** (6), 566–574.
39. Fidelus, J., Wiesel, E., Gojny, F., Schulte, K., and Wagner, H. (2005) Thermo-mechanical properties of randomly oriented carbon/epoxy nanocomposites. *Composites Part A*, **36** (11), 1555–1561.
40. Kanagaraj, S., Varanda, F.R., Zhil'tsova, T.V., Oliveira, M.S., and Simões, J.A. (2007) Mechanical properties of high density polyethylene/carbon nanotube composites. *Compos. Sci. Technol.*, **67** (15), 3071–3077.
41. Gomez-del Rio, T., Poza, P., Rodriguez, J., García-Gutiérrez, M., Hernandez, J., and Ezquerra, T. (2010) Influence of single-walled carbon nanotubes on the effective elastic constants of poly(ethylene terephthalate). *Compos. Sci. Technol.*, **70** (2), 284–290.
42. Omidi, M., Rokni, D.T.H., Milani, A.S., Seethaler, R.J., and Arasteh, R. (2010) Prediction of the mechanical characteristics of multi-walled carbon nanotube/epoxy composites using

a new form of the rule of mixtures. *Carbon*, **48** (11), 3218–3228.

43. Andrews, R., Jacques, D., Minot, M., and Rantell, T. (2002) Fabrication of carbon multiwall nanotube/polymer composites by shear mixing. *Macromol. Mater. Eng.*, **287** (6), 395–403.
44. Yeh, M.-K., Hsieh, T.-H., and Tai, N.-H. (2008) Fabrication and mechanical properties of multi-walled carbon nanotubes/epoxy nanocomposites. *Mater. Sci. Eng., A*, **483**, 289–292.
45. Yeh, M.-K., Tai, N.-H., and Liu, J.-H. (2006) Mechanical behavior of phenolic-based composites reinforced with multi-walled carbon nanotubes. *Carbon*, **44** (1), 1–9.
46. Martone, A., Faiella, G., Antonucci, V., Giordano, M., and Zarrelli, M. (2011) The effect of the aspect ratio of carbon nanotubes on their effective reinforcement modulus in an epoxy matrix. *Compos. Sci. Technol.*, **71** (8), 1117–1123.
47. Philipse, A.P. (1996) The random contact equation and its implications for (colloidal) rods in packings, suspensions, and anisotropic powders. *Langmuir*, **12**, 1127–1133.
48. Zare, Y. and Garmabi, H. (2012) Analysis of tensile modulus of PP/nanoclay/$CaCO_3$ ternary nanocomposite using composite theories. *J. Appl. Polym. Sci.*, **123** (4), 2309–2319.
49. Liu, L.Q., Tasis, D., Prato, M., and Wagner, H.D. (2007) Tensile mechanics of electrospun multiwalled nanotube/poly(methyl methacrylate) nanofibers. *Adv. Mater.*, **19** (9), 1228–1233.
50. Zhou, C., Wang, S., Zhang, Y., Zhuang, Q., and Han, Z. (2008) In situ preparation and continuous fiber spinning of poly(p-phenylenebenzobisoxazole) composites with oligo-hydroxyamide-functionalized multi-walled carbon nanotubes. *Polymer*, **49** (10), 2520–2530.
51. Ji, M. and Torkelson, J.M. (2008) Dispersion and major property enhancements in polymer/multiwall carbon nanotube nanocomposites via solid-state shear pulverization followed by melt mixing. *Macromolecules*, **41** (16), 5974–5977.
52. Ji, J., Sui, G., Yu, Y., Liu, Y., Lin, Y., Du, Z. *et al* (2009) Significant improvement of mechanical properties observed in highly aligned carbon-nanotube-reinforced nanofibers. *J. Phys. Chem. C*, **113** (12), 4779–4785.
53. Haggenmueller, R., Zhou, W., Fischer, J., and Winey, K. (2003) Production and characterization of polymer nanocomposites with highly aligned single-walled carbon nanotubes. *J. Nanosci. Nanotechnol.*, **3** (1–2), 1–2.
54. Yu, M.-F., Files, B.S., Arepalli, S., and Ruoff, R.S. (2000) Tensile loading of ropes of single wall carbon nanotubes and their mechanical properties. *Phys. Rev. Lett.*, **84** (24), 5552.
55. Cai, J., Wang, C., Yu, T., and Yu, S. (2009) Wall thickness of single-walled carbon nanotubes and its Young's modulus. *Phys. Scr.*, **79** (2), 025702.
56. Zare, Y. and Garmabi, H. (2014) Attempts to simulate the modulus of polymer/carbon nanotube nanocomposites and future trends. *Polym. Rev.*, **54** (3), 377–400.
57. Seyhan, A.T., Tanoğlu, M., and Schulte, K. (2009) Tensile mechanical behavior and fracture toughness of MWCNT and DWCNT modified vinylester/polyester hybrid nanocomposites produced by 3-roll milling. *Mater. Sci. Eng., A*, **523** (1), 85–92.
58. Chen, G.-X., Kim, H.-S., Park, B.H., and Yoon, J.-S. (2006) Multi-walled carbon nanotubes reinforced nylon 6 composites. *Polymer*, **47** (13), 4760–4767.
59. Safadi, B., Andrews, R., and Grulke, E. (2002) Multi walled carbon nanotube polymer composites: synthesis and characterization of thin films. *J. Appl. Polym. Sci.*, **84**, 2660–2669.
60. Jeong, W. and Kessler, M. (2008) Toughness enhancement in ROMP functionalized carbon nanotube/polydicyclopentadiene composites. *Chem. Mater.*, **20** (22), 7060–7068.
61. Cadek, M., Coleman, J., Barron, V., Hedicke, K., and Blau, W. (2002) Morphological and mechanical properties of carbon-nanotube-reinforced semicrystalline and amorphous polymer

composites. *Appl. Phys. Lett.*, **81** (27), 5123–5125.
62. Zhang, X., Liu, T., Sreekumar, T., Kumar, S., Moore, V.C., Hauge, R.H. *et al* (2003) Poly(vinyl alcohol)/SWNT composite film. *Nano Lett.*, **3** (9), 1285–1288.
63. Konidari, M., Soulas, D., Papadokostaki, K., and Sanopoulou, M. (2012) Study of the effect of modified and pristine carbon nanotubes on the properties of poly(vinyl alcohol) nanocomposite films. *J. Appl. Polym. Sci.*, **125** (S1), 471–477.
64. Shaffer, M.S. and Windle, A.H. (1999) Fabrication and characterization of carbon nanotube/poly(vinyl alcohol) composites. *Adv. Mater.*, **11** (11), 937–941.
65. Périé, T., Brosse, A.-C., Tencé-Girault, S., and Leibler, L. (2012) Mechanical and electrical properties of multi walled carbon nanotube/ABC block terpolymer composites. *Carbon*, **50** (8), 2918–2928.
66. Gojny, F., Wichmann, M., Köpke, U., Fiedler, B., and Schulte, K. (2004) Carbon nanotube-reinforced epoxy-composites: enhanced stiffness and fracture toughness at low nanotube content. *Compos. Sci. Technol.*, **64** (15), 2363–2371.
67. Lachman, N. and Daniel, W.H. (2010) Correlation between interfacial molecular structure and mechanics in CNT/epoxy nano-composites. *Composites Part A*, **41** (9), 1093–1098.
68. Balakrishnan, A. and Saha, M.C. (2011) Tensile fracture and thermal conductivity characterization of toughened epoxy/CNT nanocomposites. *Mater. Sci. Eng., A*, **528** (3), 906–913.
69. Morcom, M., Atkinson, K., and Simon, G.P. (2010) The effect of carbon nanotube properties on the degree of dispersion and reinforcement of high density polyethylene. *Polymer*, **51** (15), 3540–3550.
70. Kim, J.Y., Han, S.I., and Kim, S.H. (2007) Crystallization behaviors and mechanical properties of poly(ethylene 2, 6-naphthalate)/multiwall carbon nanotube nanocomposites. *Polym. Eng. Sci.*, **47** (11), 1715–1723.
71. Kim, J.Y., Park, H.S., and Kim, S.H. (2007) Multiwall-carbon-nanotube-reinforced poly(ethylene terephthalate) nanocomposites by melt compounding. *J. Appl. Polym. Sci.*, **103** (3), 1450–1457.
72. Park, S. and Bandaru, P. (2010) Improved mechanical properties of carbon nanotube/polymer composites through the use of carboxyl-epoxide functional group linkages. *Polymer*, **51** (22), 5071–5077.
73. Montazeri, A., Javadpour, J., Khavandi, A., Tcharkhtchi, A., and Mohajeri, A. (2010) Mechanical properties of multi-walled carbon nanotube/epoxy composites. *Mater. Des.*, **31** (9), 4202–4208.
74. Yeh, M.-K., Tai, N.-H., and Lin, Y.-J. (2008) Mechanical properties of phenolic-based nanocomposites reinforced by multi-walled carbon nanotubes and carbon fibers. *Composites Part A*, **39** (4), 677–684.
75. Ayatollahi, M., Shadlou, S., Shokrieh, M., and Chitsazzadeh, M. (2011) Effect of multi-walled carbon nanotube aspect ratio on mechanical and electrical properties of epoxy-based nanocomposites. *Polym. Test.*, **30** (5), 548–556.
76. Kim, A., Seong, D.G., Kang, T.J., and Youn, J.R. (2006) Effects of surface modification on rheological and mechanical properties of CNT/epoxy composites. *Carbon*, **44** (10), 1898–1905.
77. Mori, T. and Tanaka, K. (1973) Average stress in matrix and average elastic energy of materials with misfitting inclusions. *Acta Metall.*, **21** (5), 571–574.
78. Ogasawara, T., Ishida, Y., Ishikawa, T., and Yokota, R. (2004) Characterization of multi-walled carbon nanotube/phenylethynyl terminated polyimide composites. *Composites Part A*, **35** (1), 67–74.
79. Huang, Y.Y., Hwang, K.-C., and Gao, H. (2004) The effect of nanotube waviness and agglomeration on the elastic property of carbon nanotube-reinforced composites. *Urbana*, **51**, 61801.
80. Selmi, A., Friebel, C., Doghri, I., and Hassis, H. (2007) Prediction of the

elastic properties of single walled carbon nanotube reinforced polymers: a comparative study of several micromechanical models. *Compos. Sci. Technol.*, **67** (10), 2071–2084.

81. Esteva, M. and Spanos, P.D. (2009) Effective elastic properties of nanotube reinforced composites with slightly weakened interfaces. *J. Mech. Mater. Struct.*, **4** (5), 887–900.
82. Cadek, M., Coleman, J., Ryan, K., Nicolosi, V., Bister, G., Fonseca, A. *et al* (2004) Reinforcement of polymers with carbon nanotubes: the role of nanotube surface area. *Nano Lett.*, **4** (2), 353–356.
83. Coleman, J.N., Cadek, M., Ryan, K.P., Fonseca, A., Nagy, J.B., Blau, W.J. *et al* (2006) Reinforcement of polymers with carbon nanotubes. The role of an ordered polymer interfacial region. Experiment and modeling. *Polymer*, **47** (26), 8556–8561.
84. Anumandla, V. and Gibson, R.F. (2006) A comprehensive closed form micromechanics model for estimating the elastic modulus of nanotube-reinforced composites. *Composites Part A*, **37** (12), 2178–2218.
85. Guzman de Villoria, R. and Miravete, A. (2007) Mechanical model to evaluate the effect of the dispersion in nanocomposites. *Acta Mater.*, **55** (9), 3025–3031.
86. Odegard, G., Pipes, R., and Hubert, P. (2004) Comparison of two models of SWCN polymer composites. *Compos. Sci. Technol.*, **64** (7), 1011–1020.
87. Ebrahimi, S., Ghafoori-Tabrizi, K., and Rafii-Tabar, H. (2012) Multi-scale computational modelling of the mechanical behaviour of the chitosan biological polymer embedded with graphene and carbon nanotube. *Comput. Mater. Sci.*, **53** (1), 347–353.
88. Pipes, R.B. and Hubert, P. (2003) Scale effects in carbon nanostructures: self-similar analysis. *Nano Lett.*, **3** (2), 239–243.
89. Ayatollahi, M., Shadlou, S., and Shokrieh, M. (2011) Multiscale modeling for mechanical properties of carbon nanotube reinforced nanocomposites subjected to different types of loading. *Compos. Struct.*, **93** (9), 2250–2259.
90. Giannopoulos, G., Georgantzinos, S., and Anifantis, N. (2010) A semi-continuum finite element approach to evaluate the Young's modulus of single-walled carbon nanotube reinforced composites. *Composites Part B*, **41** (8), 594–601.
91. Otero, F., Martínez, X., Oller, S., and Salomón, O. (2012) Study and prediction of the mechanical performance of a nanotube-reinforced composite. *Compos. Struct.*, **94** (9), 2920–2930.
92. Hu, N., Fukunaga, H., Lu, C., Kameyama, M., and Yan, B. (2005) Prediction of elastic properties of carbon nanotube reinforced composites. *Proc. R. Soc. A: Math., Phys. Eng. Sci.*, **461** (2058), 1685–1710.
93. Montazeri, A. and Naghdabadi, R. (2010) Investigation of the interphase effects on the mechanical behavior of carbon nanotube polymer composites by multiscale modeling. *J. Appl. Polym. Sci.*, **117** (1), 361–367.
94. Takeda, T., Shindo, Y., Narita, F., and Mito, Y. (2009) Tensile characterization of carbon nanotube-reinforced polymer composites at cryogenic temperatures: experiments and multiscale simulations. *Mater. Trans.*, **50** (3), 436–445.
95. Tserpes, K., Papanikos, P., Labeas, G., and Pantelakis, S.G. (2008) Multi-scale modeling of tensile behavior of carbon nanotube-reinforced composites. *Theor. Appl. Fract. Mech.*, **49** (1), 51–60.
96. Rafiee, R. (2013) Influence of carbon nanotube waviness on the stiffness reduction of CNT/polymer composites. *Compos. Struct.*, **97**, 304–309.
97. Tsai, J.-L., Tzeng, S.-H., and Chiu, Y.-T. (2010) Characterizing elastic properties of carbon nanotubes/polyimide nanocomposites using multi-scale simulation. *Composites Part B*, **41** (1), 106–115.
98. Yang, S., Yu, S., Ryu, J., Cho, J.-M., Kyoung, W., Han, D.-S. *et al* (2013) Nonlinear multiscale modeling approach to characterize elastoplastic behavior of CNT/polymer nanocomposites considering the interphase and

interfacial imperfection. *Int. J. Plast.*, **41**, 124–146.

99. Liu, Y., Nishimura, N., Qian, D., Adachi, N., Otani, Y., and Mokashi, V. (2008) A boundary element method for the analysis of CNT/polymer composites with a cohesive interface model based on molecular dynamics. *Eng. Anal. Boundary Elem.*, **32** (4), 299–308.

100. Ashrafi, B. and Hubert, P. (2006) Modeling the elastic properties of carbon nanotube array/polymer composites. *Compos. Sci. Technol.*, **66**, 387–396.

101. Odegard, G. and Gates, T. (2003) Constitutive modeling of nanotube/polymer composites with various nanotube orientations. Proceedings Annual Conference on Experimental and Applied Mechanical, vol. 63, pp. 1671–1687.

102. Yang, S., Yu, S., Kyoung, W., Han, D.-S., and Cho, M. (2012) Multiscale modeling of size-dependent elastic properties of carbon nanotube/polymer nanocomposites with interfacial imperfections. *Polymer*, **53** (2), 623–633.

103. Buryachenko, V., Roy, A., Lafdi, K., Anderson, K., and Chellapilla, S. (2005) Multi-scale mechanics of nanocomposites including interface: experimental and numerical investigation. *Compos. Sci. Technol.*, **65** (15), 2435–2465.

104. Cebeci, H., de Villoria, R.G., Hart, A.J., and Wardle, B.L. (2009) Multifunctional properties of high volume fraction aligned carbon nanotube polymer composites with controlled morphology. *Compos. Sci. Technol.*, **69** (15), 2649–2656.

105. Fisher, F., Bradshaw, R., and Brinson, L. (2002) Effects of nanotube waviness on the modulus of nanotube-reinforced polymers. *Appl. Phys. Lett.*, **80** (24), 4647–4649.

106. Fisher, F., Bradshaw, R., and Brinson, L. (2003) Fiber waviness in nanotube-reinforced polymer composites—I: modulus predictions using effective nanotube properties. *Compos. Sci. Technol.*, **63** (11), 1689–1703.

107. Bradshaw, R., Fisher, F., and Brinson, L. (2003) Fiber waviness in nanotube-reinforced polymer composites—II: modeling via numerical approximation of the dilute strain concentration tensor. *Compos. Sci. Technol.*, **63** (11), 1705–1722.

108. Shao, L., Luo, R., Bai, S., and Wang, J. (2009) Prediction of effective moduli of carbon nanotube–reinforced composites with waviness and debonding. *Compos. Struct.*, **87** (3), 274–281.

109. Seidel, G.D. and Lagoudas, D.C. (2006) Micromechanical analysis of the effective elastic properties of carbon nanotube reinforced composites. *Mech. Mater.*, **38** (8), 884–907.

110. Hammerand, D.C., Seidel, G.D., and Lagoudas, D.C. (2007) Computational micromechanics of clustering and interphase effects in carbon nanotube composites. *Mech. Adv. Mater. Struct.*, **14** (4), 277–294.

11
Nanocomposites Based on Cellulose, Hemicelluloses, and Lignin

Diana Elena Ciolacu and Raluca Nicoleta Darie

11.1
Introduction

In recent years, increased attention has been paid to the materials that are sustainable, green, and environmentally friendly. Moreover, nonrenewable materials can be substituted by new ones from renewable sources that can even surpass them in performance, cost, or added utility. In this regard, the use of biomaterials from lignocellulosic sources plays an important role in obtaining sustainable materials due to their reinforcement capacity, biodegradability, and biocompatibility.

The differences between nanomaterials and bulk materials are controlled by two main factors, as the increased relative surface area, so an enhanced reactivity and the quantum effects offered by the changes on mechanical, optical, thermal, and electrical properties. In addition, the combination of nanoparticles with polymers provides a route to a wide variety of established as well as new applications.

The ability to control the material features at the nanoscale level brings new and promising properties, such as high mechanical characteristics and low density, which provides the opportunity to develop new nanocomposite systems. Thus, with added properties, the nanocomposites can be used as active and intelligent materials for packaging, self-cleaning smart nanocoating, as nanoscale freshness indicators and nanosensors, as well as in tissue engineering and regenerative medicine, as drug-delivery carriers and wound-dressing systems.

The use of cellulose, hemicellulose, and lignin as components of nanocomposite materials are further described, with special focus on nanosized reinforcements. The incorporation of cellulose nanoparticles (CNs) into different polymeric matrices has already proven to be an important strategy for obtaining new green nanocomposites. The unique properties such as excellent biocompatibility, high strength and stiffness, surface reactivity, and the small dimensions of cellulose nanoparticles may well impart useful properties to nanocomposite materials. Hemicelluloses are the second most abundant renewable plant polymers after cellulose and are widely available feed stock. Due to their superior properties such as renewability, biodegradability, biocompatibility, and biological activity, their

Nanomaterials and Nanocomposites: Zero- to Three-Dimensional Materials and Their Composites,
First Edition. Edited by Visakh P.M. and Maria José Martínez Morlanes.

application area includes a broad range of fields, including electronics, optics, and pharmaceuticals. Lignin is the main aromatic component in vegetal biomass, and is a renewable and abundant resource having antioxidant capacity, antimicrobial activity, and strong antiviral activity against human immunodeficiency virus. However, in contrast to cellulose-based materials, lignin has not yet been significantly exploited in the biomedical field. Many results refer to lignin use as a stabilizer for plastic materials and rubbers, as an antioxidant, and a modifier of mechanical properties and rigidity. Lignin nanoparticles have found widespread applications as foam and emulsion stabilizers, as matrices for environmental remediation systems, as drug delivery vehicles, and as stabilizers of cosmetic and pharmaceutical formulations.

This chapter provides an overview on the production and characterization of the nanoparticles obtained from cellulose, lignin, and hemicellulose, as well as on the current and potential applications of their nanocomposites. In addition, the chapter refers to some aspects about the risk assessment of nanoparticles and nanomaterials.

11.2 Cellulose

11.2.1 Morphology and Structural Aspects of Cellulose

Cellulose is considered to be the most ubiquitous and abundant biopolymer on the planet, which has been used for many centuries as construction material, in forest products, as natural textile fibers, as paper and boards, and so on. In addition, cellulose is a versatile starting material for chemical conversion, aiming at the production of artificial, cellulose-based threads and films, as well as a variety of cellulose derivatives used in many areas of industry and domestic life [1]. The most commercially exploited resource of cellulose is wood, but there is another major source that contains a large amount of cellulose, namely, plant fibers (cotton, linen, hemp, jute, flax, etc.). In addition to these, there are forms produced by bacteria (bacterial cellulose), algae and by marine animals (tunicate cellulose).

Cellulose is defined as a linear β-1,4-linked homopolymer of anhydroglucose or, more recently as a homopolymer of anhydrocellobiose [2]. The cellulose chain consists at one end of a D-glucopyranose unit in which the anomeric carbon atom is involved in a glycosidic linkage (the nonreducing end), whereas the other end has a D-glucopyranose unit in which the anomeric carbon atom is free and is in an equilibrium with an aldehyde structure (the reducing end). Thus, the cellulose chain has a chemical polarity.

The spatial arrangement, or stereochemistry, of the acetal linkages is very important. The pyranose rings of the cellulose molecule have all the groups larger than hydrogen sticking out from the periphery of the rings (equatorial

positions). As a consequence, the hydroxyl groups are positioned in the ring plane (equatorial), while the hydrogen atoms are in the vertical position (axial). Because of the equatorial positions of the hydroxyls on the cellulose chain, they protrude laterally along the extended molecule [3]. Thus, the configuration of the cellulose chain results in intrachain hydrogen bonding between the hydroxyl groups and the oxygen of the ring from adjacent molecules. The two intramolecular hydrogen bonds from the cellulose structure are formed between the hydroxyl group form C3 of one anhydroglucopyranose unit (AGU) and the pyranose ring oxygen (O5′) of an adjacent unit, and between the hydroxyl group from C2 of 1 AGU and the OH group from C6 of the adjacent AGU, and are presented on both sides of the chain [4]. In addition, it was reported that the bond length of the OH-3 … O5′ was 0.275 nm and for the second intramolecular hydrogen bond OH-2′ … O6 the length was 0.287 nm [5]. The intramolecular hydrogen bonds are responsible for the stiffness of the chain and stabilize the twofold helix conformation of crystalline cellulose [6]. The intermolecular hydrogen-bonding in cellulose is responsible for the sheet-like nature of native cellulose. The possibility of two intermolecular linkages, one between C6 and the C3 hydroxyl groups of an adjacent 020 plane cellulose molecules was proposed. The second intermolecular hydrogen bond is with glucosidic oxygen (O4′) of a second neighboring 020-plane. However, by determination of two intramolecular hydrogen bonds, only an intermolecular bonding between C6 and C3′ was reported, as also positions of cellulose molecules adjacently located in the same lattice plane and with a bond length estimated to be 0.279 nm [7].

The intra- and intermolecular hydrogen bonds cause parallel arrangement of multiple cellulose chains, forming elementary fibrils, which aggregate into the lowest well-defined morphological entity, namely microfibrils. Within cellulose microfibrils there are regions where the chains are highly ordered (crystalline) and disordered region (amorphous) and the chains get through several different crystalline regions, with areas of disorder between them. The orientation and disposition of microfibrils in the walls are important because this more or less controls the capacity of the wall to deform and also influences the direction in which the deformation can occur [8].

Cellulose exists in several crystal modifications, differing in unit cell dimensions and possibly in chain polarity. The detailed crystal structure of these cellulose allomorphs have been reported since the mid 1970s from X-ray diffraction patterns, and this method has played and continues to play a major role in the structural characterization of cellulose [9]. There are four different polymorphs of cellulose: cellulose I, II, III, and IV and the relationships between them are shown schematically in Figure 11.1.

The most important and abundant crystalline form of cellulose is cellulose I, which can be found in the major structural component of all plant cell walls and represents the largest biomass on the earth. It exists as a highly crystalline microfibril in all higher plants, some bacteria, fungi, and algae. Further, native cellulose was found to be a composite of cellulose Iα and Iβ crystalline forms, and either form is predominant, depending on the source of cellulose [10]. Cellulose

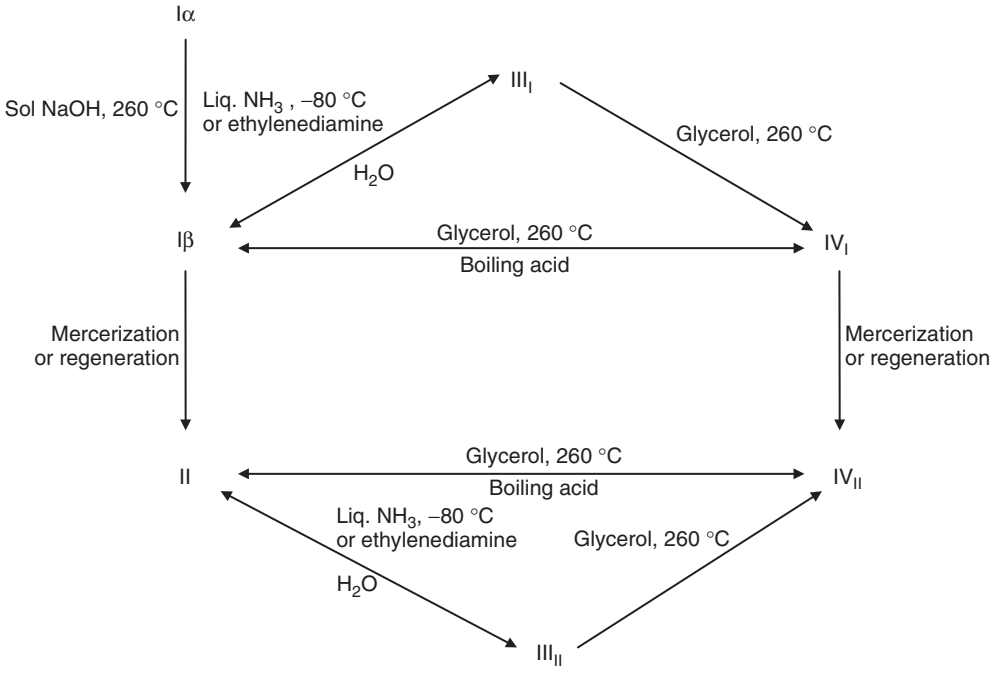

Figure 11.1 The relationship between the various cellulose allomorphs [2].

Iβ is the more common form that dominates the cotton, wood, and ramie fibers and cellulose Iα is enriched in some algae and bacterial cellulose. A notable exception is tunicin that is almost pure cellulose Iβ. In general, samples that are rich in cellulose Iα are biosynthesized by linear terminal complexes, while those rich in Iβ are organized in a rosette fashion [11].

The cellulose I form can be converted easily to the second crystalline form of cellulose II, by regeneration or mercerization processes, and the transition is not reversible. The major difference between these two forms of cellulose is the configuration of the atoms: cellulose II has antiparallel packing, whereas the chains in cellulose I have a parallel direction [12]. The other crystalline forms known as *cellulose III* and *cellulose IV* are also derived from both cellulose I and II by using different treatments. Cellulose III can be prepared by soaking cellulose samples in anhydrous liquid ammonia, at −80 °C or organic amine followed by removal of the reagent, while cellulose IV can be obtained from either cellulose I, II, or III by thermal treatments in glycerol, at about 260 °C [2].

The evolution in the understanding of cellulose structure has continued during recent decades and will be ongoing in the future.

11.2.2 Preparation and Characterization of Cellulose Nanoparticles (CNs)

The term *cellulose nanoparticles* generally refers to cellulosic particles having at least one dimension in the nanometer range [13]. On the basis of the cellulosic source and the processing conditions, CNs may be classified into three main subcategories, as nanofibrillated cellulose (NFC), cellulose nanocrystals (CNCs), and bacterial nanocellulose (BNC).

CNs can be extracted from a wide variety of vegetal resources, as wood fiber (bleached Kraft pulp [14, 15], bleached sulfite pulp [16, 17]) and plant fiber (cotton [18, 19], flax [20, 21], ramie [22, 23], wheat straw [24, 25], hemp [26], etc.); from marine animals such as tunicate [27]; from various species of green algae (*Valonia* [28], *Micrasterias denticulata* [29]); and can also be synthesized from some bacterial species (*Acetobacter xylinum* [30], *Gluconacetobacter xylinus* [31]). The variation of the lignocellulosic source and the influence of the type and severity of the extraction process, are responsible for differences in the particle size and shape, crystal structure, morphology, crystallinity, and properties of the CNs. For example, CNC extracted from tunicates and green algae have crystal lengths in the range of a few micrometers, while the crystallites from wood and cotton have lengths of the order of a few hundred nanometers [32].

Generally, the main extraction processes in the preparation of cellulose nanoparticles are mechanical treatment and acid hydrolysis. Mechanical processes can be divided into high-pressure homogenization and refining [33–35], microfluidization [36, 37], grinding [38], cryocrushing [24, 39], and high intensity ultrasonication [21, 40, 41]. These methods can be used independently or in combination with other pretreatments, like enzymatic or chemical pretreatments, in order to reduce the size of the fibers before homogenization and to help lower energy consumption [42]. Regarding acid hydrolysis, this process is strictly controlled by the concentration of cellulose, the acid type and concentration, the temperature, the hydrolysis time, agitation, or ultrasonic treatment time.

11.2.2.1 Nanofibrillated Cellulose (NFC)

NFC consists of a bundle of stretched cellulose chain molecules with long, flexible, and entangled cellulose nanofibers and are generally produced by delamination of wood pulp through mechanical pressure before and/or after chemical or enzymatic treatment [13, 31]. The difference between NFC and microfibrillated cellulose (MFC) is the fibrillation process that produces the finer particle diameters. Generally, MFC is produced when cellulose fibers are submitted to high mechanical shearing forces and are considered to contain multiple elementary fibrils, with a crystal length of 0.5–10 μm and a wide of 10–100 nm. On the other hand, NFC is reminiscent of elementary fibrils in the wood and plant cellulose biosynthesis process and is considered to consist of 36 cellulose chains arranged in Iβ crystal structure, with a length of 500–2000 nm, and a wide of 4–20 nm [43]. However,

there may appear some confusion between MFC and NFC terminology in the literature, which are sometimes used interchangeably.

The main raw material for NFC production is wood, followed by agriculture crops and their by-products, which demand less energy for the fibrillation process. NFC can be viewed as a cellulosic material, composed of expanded high-volume cellulose, moderately degraded, and greatly expanded in surface area, consisting of alternating crystalline and amorphous domains and obtained by a homogenization process [44]. The mechanical treatments applied for the disintegration of cellulosic materials in order to obtain NFC are: high-pressure homogenizers, microfluidizers or grinders (Figure 11.2), cryocrushing, high-intensity ultrasonic treatments or by the combinations of mechanical treatments with pretreatments or posttreatments with enzymatic or chemical treatments to either remove amorphous material or chemically functionalize the particle surface to endow it with new properties [35].

The first mechanical treatment was *high-pressure homogenization*, which was applied by Herrick *et al.* [45] and Turbak *et al.* [46] by using a Gaulin homogenizer. In this process cellulose slurries were pumped at high pressure and fed through a spring-loaded valve assembly. The valve opens and closes in rapid succession, so the fibers are subjected to a large pressure drop under high shearing forces. This procedure results in a high degree of cellulose fiber fibrillation [44].

An alternative to the Gaulin homogenizer is the *microfluidizer* (Microfluidics Inc., USA), in which wood pulp passes through thin z-shaped chambers (with channel dimensions that are usually 200–400 μm) under high pressure [47]. The obtained nanoparticles are more uniform, but there are two disadvantages, such as the needs of chambers with different sizes in order to increase the degree of fibrillation and the number of passes, from 10 to 30, which has a negative impact regarding the high energy consumption.

The *grinding* process requires fewer passes and the breakdown of the cell wall structure is realized by applying shearing forces between a static and a rotating grind stone (~1500 rpm). A comparison between high shear grinder and homogenizer revealed the fact that refining was the main process for isolation of NFC,

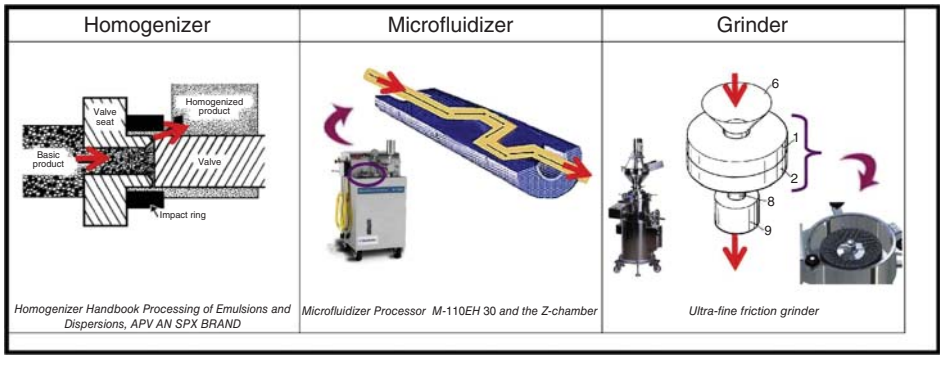

Figure 11.2 Basic design of a homogenizer, a microfluidizer, and a grinder [35].

while high-pressure homogenization led to the formation of nanofibers of smaller and uniform size [48]. However, by using only high shear grinder the fibrillation process in high-pressure homogenization was not complete. On the other hand, the extent of fibrillation is dependent on the distance between the discs, the morphology of the disc channels, and the number of passes through the grinder. Thus, the increasing of the number of passes through high-pressure homogenization, leads to a decrease in the polymerization degree and crystallinity of the NFC [49].

Cryocrushing process consists of crushing by mortar and pestle of the water-swollen cellulosic fibers immersed in liquid nitrogen [41]. Application of high-impact forces to the frozen cellulosic fibers leads to rupture of the cell wall due to the exertion of pressure by ice crystals and thus, liberating nanofibers [34]. Cryocrushing is apparently often used to manufacture NFC from agricultural crops and byproducts, as flax, hemp, and rutabaga fibers or soybean stock [35].

High-intensity ultrasonication is a process that uses the oscillating power to isolate NFC from cellulosic sources, by hydrodynamic forces of ultrasound [41, 50, 51]. During the process, cavitation leads to a powerful mechanical oscillating power and therefore, high-intensive waves, which consists of formation, expansion, and implosion of microscopic gas bubbles when molecules absorb ultrasonic energy [52].

All these mechanical methods involve high consumption of energy, which can cause dramatic decreases in both the yield and fibril length. Thus, current research has been focused on finding environmental conservation, high efficiency, and low-cost methods to isolate CNs [13]. Pretreatment of cellulose or combination of two or more methods have brought some positive results in this regard. Combination of refining and microfluidization processes led to the production of uniform NFC with high fibrillation whereas individual methods could not bring good results [53].

Several strategies have been proposed in order to obtain fibers that are less stiff and cohesive, thus decreasing the energy needed for fibrillation:

- *Enzyme pretreatment*, an environmentally friendly alternative to chemical pretreatment, was reported to reduce the processing cost by lowering the number of passes through the homogenizer. The most widely used enzyme is the commercial cellulose and in its presence the cell walls become softened by the enzymatic breakages of the cellulose networks prior to the mechanical disintegration, thus promoting cell wall delamination and the release of NFC [54]. A mild enzymatic hydrolysis has been combined with refining and homogenization in order to produce NFC from bleached softwood pulp and it was observed that using a monocomponent endoglucanase enzyme allowed a greater aspect ratio and was less aggressive compared to acid hydrolysis [16].
- *Steam explosion* process is based on short-time vapor phase cooking at temperatures in the range of 180–210 °C, followed by explosive decompression, and sudden release of pressure, during which the flash evaporation of water exerts a thermo-mechanical force causing the rupture of material. This effect results in a substantial breakdown of lignocellulosic structure, hydrolysis of

the hemicellulose fraction, depolymerization of the lignin components, and defibrillization [55]. The advantages of steam explosion include a significantly lower environmental impact, low energy consumption, lower capital investment, and use of less hazardous chemicals. Process should be repeated several times until efficient release of the cellulose microfibrils takes place [56].

- *TEMPO-mediated oxidation*, involves the addition of negatively charged entities at the microfibrils surface. Thus, 2,2,6,6-tetramethylpiperidine-1-oxyl (TEMPO) oxidation is a pretreatment that facilitates the isolation of nanofibers by selective introduction of carboxyl groups at the C6 of glucose unit [57, 58]. The study on the influence of carboxyl content on homogenization of TEMPO-oxidized eucalyptus reveals that the TEMPO-oxidation reduced passing cycles to obtain gel facilitates defibrillation and prevents the blockage of the homogenizer [59]. Compared to the energy consumption using high-pressure homogenizer, TEMPO-mediated oxidation pretreatment was shown to dramatically decrease the consumption by a factor more than 100 [60].
- *Alkaline-acid pretreatment* is used before mechanical isolation of NFC in order to solubilize the lignin, hemicelluloses, and pectins. This pretreatment included three steps [13, 61]: (i) soaking fibers in 12–17.5 wt% NaOH solution for 2 h in order to raise the surface area of cellulosic fibers, and to make it more susceptible to hydrolysis, (ii) hydrolysis of the fibers with HCl solution for 1 M at 60–80 °C to solubilize the hemicelluloses, and (iii) treating the fibers with 2 wt% NaOH solution for 2 h at 60–80 °C, which would disrupt the lignin structure, and would also breakdown the linkages between carbohydrate and lignin. Alemdar and Sain [24] obtained NFC from wheat straw and soy hull with a diameter around 10–80 nm and 20–120 nm, respectively. To individualize the nanofibers from the cell walls a mechanical treatment (cryocrushing, disintegration, and defibrillation steps) was applied to the chemically pretreated fibers (alkaline-acid pretreatment).
- *Carboxymethylation* process makes the surfaces negatively charged, promotes formation of stable suspension from carboxymethylated fibers and increases the breakup of lignocellulosic fibers to nanosize [42]. Wågberg *et al*. [62] reported that cylindrical cross-section NFC with diameter of 5–15 nm could be produced by passing carboxymethylated fibers through a homogenizer [62]. It was found that the pH and the concentration of salt were two important factors for this procedure, because a very high concentration of the salt or too low pH could cause a rapid agglomeration of the fibers. In addition, it has been observed that the nature of the resultant materials was extremely dependent on the initial materials. When native cellulose is used, even under harsh condition, oxidation happens only at the surface, and it would become negatively charged, whereas using mercerized and regenerated cellulose, water-soluble salt can be obtained as the oxidized product [34].
- *Acetylation* of cellulosic fibers is a method to make the surface of NFC more hydrophobic [63]. The principle of acetylation is the reaction of OH groups of cellulose with acetyl groups, which causes plasticization of lignocellulosic fibers [64]. Bulota *et al.* [65] studied the acetylation of the mechanically isolated NFC

in the presence of ethanol, toluene, and acetic anhydride, at 105 °C and they observed that after 30 min the maximum degree of substitution (DS) (0.43) was achieved [65]. At the end they demonstrated that the NFC with greater DS has a great influence on the properties of polylactic acid–acetylated NFC composite.

- *Silylation* – silane-based surface modification is a popular way to change the surface of fibers from hydrophilic to hydrophobic. In the absence of water, even at elevated temperatures, no reaction occurs between Si–OR and OH groups of cellulose, whereas Si–OR reacts with lignin's phenolic OH [13]. Addition of moisture initiates a reaction between silanol groups and OH groups of cellulose at high temperature [42]. The effect of three different pretreatments including acidic, alkaline, and silane in combination with high-pressure homogenizers on flax fibers was studied [21]. Toward alkaline and acid pretreatments, the silane pretreatment inhibited agglomeration and produced finer fibers. For alkaline and acid pretreatments, the thermal stability of NFC went up on increasing the number of cycles through high-pressure homogenizers, while for silane pretreatment the thermal stability of NFC showed major enhancement without high-pressure homogenizers. It was suggested that a combination of alkali and acid pretreatment would be more effective for flax fibers, which contains higher amount of pectin and hemicelluloses.

NFCs display two main drawbacks, which are associated with their intrinsic physical properties. The first one is the high number of hydroxyl groups, which lead to strong hydrogen interactions between two nanofibrils and to the gel-like structure once produced. The second drawback is the high hydrophilicity of this material, which limits their uses in several applications such as in paper coating (increase of dewatering effect) or composites (tendency to form agglomerates in petro-chemical polymers). The most feasible solution to this is chemical surface modification to reduce the number of hydroxyl interactions and also to increase the compatibility with several matrices [32, 54, 66–68].

11.2.2.2 Cellulose Nanocrystals (CNCs)

The preparation of cellulose whiskers or CNCs by acid hydrolysis is now an established laboratory process and has been applied to a wide variety of materials [44]. Compared to cellulose fibers, CNCs possess many advantages, such as nanoscale dimension, high specific strength and modulus, high surface area, unique optical properties, and so on, and therefore have a wide possibility of applications, a fact which has attracted significant interest from both research scientists and industrialists [32].

Ideally, CNCs are reminiscent of the crystalline regions within the elementary fibrils of the wood and plant cellulose biosynthesis processes and are considered to consist of 36 cellulose chains arranged in Iβ crystal structure [27, 43]. Actually, the structural dimensions of CNCs were found to have a wide variation because particle shape, length, and width depend on the source of cellulosic material and conditions under which the hydrolysis is performed.

The factors that govern the products of the acid hydrolysis are the concentration of the cellulose (the starting material), the acid type and concentration, the hydrolysis time and temperature, and the ultrasonic treatment time [69].

Cellulose sources are variable, and their degree of crystallinity strongly influences the dimensions of the liberated crystals: cotton, wood, and Avicel yield a narrow distribution of highly crystalline (90% crystallinity) nanorods (width: 5–10 nm, length: 100–300 nm), whereas other sources, such as tunicin, bacteria, and algae, generate crystals with larger polydispersities and dimensions comparable to those of MFC (width: 5–60 nm, length: 100 nm to several micrometers) [31]. CNC crystals may also show different geometries, depending on their biological source; for example, algal cellulose membrane displays a rectangular structural arrangement, whereas both bacterial and tunicate cellulose chains have twisted-ribbon geometry [27].

During the acid hydrolysis process, the hydronium ions penetrate the cellulose chains in the amorphous regions promoting the hydrolytic cleavage of the glycosidic bonds and releasing individual crystallites after mechanical treatment (sonication) [70]. Different strong acids have been shown to successfully degrade cellulose fibers, but hydrochloric (HCl) and sulfuric acids (H_2SO_4) have been extensively used. The surface of the CNC prepared in the presence of HCl is weakly negatively charged, while the preparation with H_2SO_4 leads to a more negatively charged surface, in which case approximately one tenth of the glucose units are functionalized with sulfate ester groups [71] Owing to their highly repulsive character, CNC suspensions prepared with H_2SO_4 exhibit higher colloidal stabilities in comparison with CNC suspensions prepared with HCl. The content of the introduced sulfate group increases with the acid concentration and hydrolysis time. It was shown that even at low levels, the sulfate groups caused a significant decrease in degradation temperature and increase in chair fraction, confirming that the sulfate groups act as flame retardants [69]. Furthermore, other acids such as phosphoric [72], hydrobromic [73, 74], and nitric acids [75] were studied for the preparation of crystalline CNCs. The dimensions of crystals were also found to depend on the duration of the hydrolysis, wherein a longer reaction time produced shorter crystals [27]. Beck-Candanedo *et al.* [76] established that the reaction time is one of the most important parameters in acid hydrolysis and they reported that very long reaction times result in the production of sugar molecules via the complete digestion of cellulose, while shorter reaction times yield large indispensable fibers and aggregates.

CNCs show some dispersibility in aqueous-based mixtures and in organic solvents with high dielectric constants, such as dimethyl sulfoxide (DMSO) and ethylene glycol, but tend to aggregate in highly hydrophobic solutions [31]. Stable CNs dispersions in apolar or low polarity solvent can be obtained by physically coating the surface with a surfactant [77] or by chemically grafting apolar moieties onto the surface [70]. Several surface chemical modifications have been applied to CNCs in order to improve their stability in organic media or to make them compatible with hydrophobic matrices. These can be classified into three distinctive groups (Figure 11.3), as (i) substitution of hydroxyl groups with small molecules

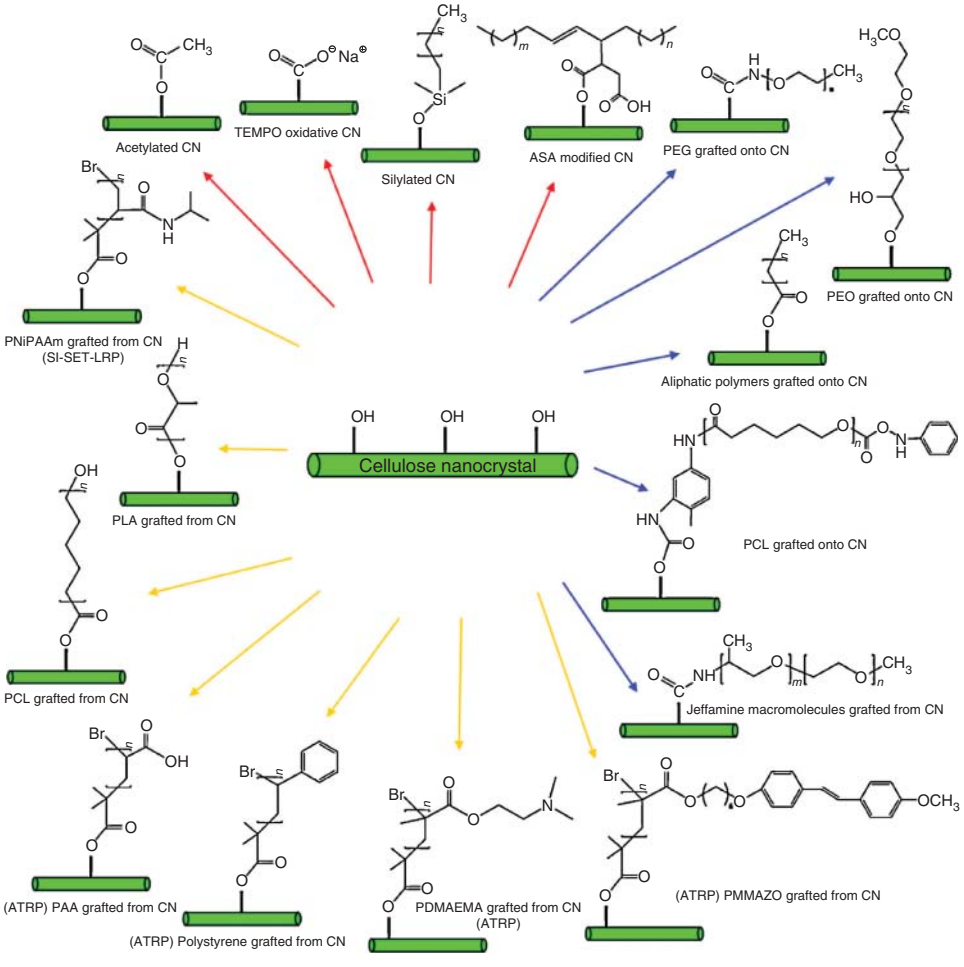

Figure 11.3 Common chemical modifications of CNCs; PEG: poly(ethylene glycol); PEO: poly(ethylene oxide); PLA: poly(lactic acid); PAA: poly(acrylic acid); PNiPAAm: poly(*N*-isopropylacrylamide); and PDMAEMA: poly(*N*,*N*-dimethylaminoethyl methacrylate) [70].

(indicated with red arrows), (ii) polymer grafting based on the "grafting onto" strategy with different coupling agents (indicated with blue arrows), and (iii) polymer grafting based on the "grafting from" approach with a radical polymerization involving ring opening polymerization (ROP), atom transfer radical polymerization (ATRP), and single-electron transfer living radical polymerization (SET-LRP) (indicated with yellow arrows) [70].

The main challenge with chemical modification is to choose a reagent and reaction medium that enable modification of the nanocrystal surface without the nanocrystal dissolving in the reaction medium and without undesired bulk changes. An alternative to chemical surface modification is the adsorption of

surfactants at the colloid surface to improve nanoparticle stability in organic solvents [31].

11.2.2.3 Bacterial Nanocellulose (BNC)

Highly crystalline cellulose could be secreted by various bacteria, such as *Gluconacetobacter xylinus* which are able to produce a layer of BNC in the liquid/air interface. This highly hydrated pellicle consists of a random assembly of ribbon-shaped fibrils, less than 100 nm wide, which are composed of a bundle of nanofibrils [78]. BNC shows a finer web-like network structure, higher water-holding capacity, and higher crystallinity. After simple purification, BNC contains no impurities and no functional groups other than hydroxyl groups. BNC is formed in yields up to 40% (in relation to the glucose substrate): a high efficiency for a biotechnological process [31]. The nanometer dimension of the BNC fibers causes a large fiber surface, which facilitates strong interactions with the surroundings like water, other low-molecular-weight and polymer compounds with functional groups active in hydrogen-bond formation, and different types of nanoparticles, including particles of various metals [31]. During the biosynthesis of BNC, well-defined cellulose network structures are formed. This direct formation of cellulose bodies is quite different from plant-cellulose processing. Such bodies are of high transparency and form pore systems. The incorporated water plays an important role as a spacer element and as a stabilizing agent with respect to the network and pore structure.

BNC is characterized by a high degree of polymerization (DP) in the range of 4000–10 000 anhydroglucose units, high crystallinity of 80–90%, and high stability of the single cellulose fibers similar to that of steel or Kevlar [79, 80]. After isolation of the never-dried BNC, bacteria and residues from the culture medium can be removed, for example, by heating in 0.1 m aqueous sodium hydroxide under reflux for 10–120 min, depending on the thickness of the cellulose body [31]. Under these conditions, no detectable damage to the polymer occurs.

The important features of BNC are showing great potential for biological applications, a fact which makes the biofabrication of cellulose materials a challenge for the future.

11.2.3 Cellulose Nanocomposites

Generally, nanocomposites are multiphase products in which at least one phase has a dimension of 1–100 nm [81]. Improved properties of nanocomposites can be attained if one takes into account the following parameters: size, aspect ratio, orientation and intrinsic properties of CNs, interfacial characteristics, structure and properties of polymeric matrix, and the end-use properties. Composites with nanoscale reinforcements have larger surface area and lower defects in reinforcing part compared to microsize-reinforced composites [82].

The use of CNs as the reinforcing agent in nanocomposites presents great advantages such as renewable nature, biodegradability, high specific surface area, low density, wide availability of sources, low energy consumption, relatively good reactive surface, and relatively easy processability due to their nanoabrasive nature, which allow high filling levels; it also has some major disadvantages, such as difficult compatibilization of highly hydrophilic CNs with most of polymeric matrices, high moisture absorption, and limitation of processing temperature [47, 78].

Favier *et al*. [83] was the first to report the preparation of CNC-based nanocomposites with uniform dispersion and high mechanical properties at very low nanofillers' grade. Since then, numerous nanocomposite materials were developed by incorporating CNs into a wide range of polymeric matrices. However, the main challenge is still related to their homogeneous dispersion within the polymeric matrix, in order to avoid the aggregation during the preparation process, which can lead to the loss of the nanoscale and thus, to limit the mechanical reinforcement.

Dufresne [84] summarized different strategies that have been reported in the literature to homogeneously mix CNs with a polymeric matrix (Figure 11.3). It was established that the most suitable processing medium is water, where water-soluble polymers and polymer aqueous dispersions can be used in combination with different CNs, in order to obtain nanocomposite film by simple casting or water evaporation. The strategies for improving the stability of cellulose nanoparticle dispersions in apolar or low polarity solvents are (i) physically coating the surface with a surfactant or (ii) chemically grafting apolar moieties onto the surface. The chemical modification of CNs improves its dispersibility in organic solvents and thus greatly enlarges its potential applications in different areas. Both methods allow the tuning of the surface and a decrease of the surface energy of the nanoparticle. The methods used to improve the compatibility between CNs and the host matrix, were previously discussed.

The cellulose nanocomposites can be produced via four general processing techniques: casting-evaporation [42, 85, 86], electrospinning [87–90], melt compounding [85, 86, 91], and impregnation [86].

Casting-evaporation is one of the most common techniques used to produce nanocomposites based on CNs. In order to obtain various nanocomposite materials, a wide range of polymeric matrices were used to incorporate nanocelluloses, such as poly(lactic acid) (PLA), polyvinyl alcohol (PVA), polyethylene, polypropylene, starch, polyaniline (PANI), polyhydroxybutyrate, poly(methyl methacrylate), and so on [54, 92–96]. The techniques used for their production consist in the dispersion of CNs in water or an organic solvent and then the mixture processing by casting on a suitable surface followed by evaporation, or freeze-drying and compression molding, or freeze-drying, extruding, and then compression molding of the mixture. An important issue is the incorporation of CNs in the solvent and in the polymeric matrix, water being the most proper solvent, due to their hydrophilic character. However, the chemical modifications of the CNs represent a new and promising way for the processing of nanocomposite materials.

Electrospinning is a simple and efficient technique to produce polymer nanocomposite fibers. The used polymeric matrices are polyethylene oxide (PEO) [97], PVA [98], PLA [54], or polystyrene [87]. The nanocomposite fibers are obtained by dispersing CNs in a proper solvent, then adding the polymer solutions and at the end, evaporating the solvent during the moves of the fibers between the source and the collector, forming a composite fiber. The electrospun obtained nanofibers can be dried or additionally treated for improved properties. The effect of various parameters, including electric field strength, tip-to-collector distance, and solution feed rate and composition are generally used for modeling and anticipating some of the morphological features of the electrospun nanofibers [99].

Extrusion is a technique that involves the incorporation of CNs into thermoplastic polymers by using thermal-mechanical mixing, extrusion of the melt mixture, and optional compression molding into specific test specimen geometries and configurations [99]. Due to the fact that the CNs have poor dispersion and thus present the tendency to agglomerate within the polymeric matrix, there are only a few studies concerning the processing of nanocellulose-reinforced nanocomposites by extrusion [100, 101]. A solution for this problem is the modification of the surface functional groups on CNs prior to extrusion, by grafting of organic aliphatic acid chains [102].

Impregnation is another technique used for obtaining the CNs-based nanocomposites. A cellulose thin film can be prepared via membrane filtration of CNs solution or by pressing the dried CNs, then is impregnated at low pressure, in a thermosetting resin, and cured to produce nanocomposites [103, 104]. This method is used for sample preparation in order to evaluate the mechanical [105], thermal [106], and optical [107] properties of CNs-filled nanocomposites.

11.2.4 Applications of Nanocellulose

The current trend to develop new materials from renewable sources is focused on the use of CNs as nanofillers in bionanocomposites, due to their physical and mechanical properties and to a wide possibility of applications, from technology to medical fields.

In recent years, CNs-based nanocomposites have been extensively used in different areas such as food packaging materials [34, 86, 91], printing and paper industry [3, 91], optical, light-responsive composites and other electronic devices [3, 34, 108, 109], advanced composites manufacturing [86, 110], and pharmaceutical and medical applications [3, 31, 108]. In biomedical applications, the CNs-based nanocomposites were used as scaffolds in artificial ligaments or tendon substitutes, because of their excellent cytocompatibility [111]. Moreover, due to the specific structure and properties (purity, high water retention capacity, shapability during biosynthesis and biocompatibility), BNC opens up the important and strongly expanding fields of personal care, medicine, and life sciences for the polysaccharide cellulose [112–114]. In the medical field, the

main applications are wound dressings and novel types of bioactive implants. The development of implants ranges from the design of materials for bone and cartilage repair to the development of tubular prototypes as grafts for vascular surgery. Hydrogels based on BNC mimic basic living processes and are of growing importance as bioactive scaffolds. In all cases, BNC is active as a 3D template for *in vitro* and *in vivo* tissue growth [31]. The formulations of CNs and silver nanoparticles can be used as microbial medicaments, antibacterial agents in wound dressing, bandages, implants, skins replacements for burnings, face masks, artificial blood vessels, cuffs for nerve surgery, drug delivery, cell carriers and support matrices for enzyme immobilization, cosmetic tissues, and so on [99]. In drug delivery, the development of "smart" responsive CNs-based bionanocomposites that can respond to changes in their surrounding environments will provide for new and improved methods of delivering molecules for therapeutic applications [115].

Chemical modification of cellulose surfaces is also a promising strategy to improve the mechanical and thermal properties of different polymers, for technical applications [31, 34]. As a consequence, surface-modified CNs can be used for many applications such as coating, adhesives, filters, membranes, packing and cosmetics, aerospace industry, optically transparent flexible devices such as flat displays, digital cameras, cellular telephones, and integrated circuits, paper or board for printing and recording information liquid crystals for transparent windows, lamps, or dials of clocks and watches, and so on [99].

There has been increasing interest in designing new nanocellulosic materials, based on NFC, CNC, or BNC, and to demonstrate their potential applications. Nowadays, CNC-based products are under advanced development at FP Innovations and CelluForce (Canada), while NFC-based products are under development at Innventia (Sweden) and StoraEnso (Finland). However, the data are still not so clear in some potential products areas and more work and studies are required to develop a strong business case.

11.3 Hemicellulose

Even if hemicelluloses represent an important renewable resource of biopolymers, their use for the achievement of new materials is rather limited. Moreover, the availability of hemicelluloses in their pure form is still challenging. These constitute about 20–30% of the total mass of annual and perennial plants and have a heterogeneous composition of various sugar units classified as, xylans (β-1,4-linked D-xylose units), mannans (β-1,4-linked D-mannose units), arabinans (α-1,5-linked L-arabinose units), and galactans (β-1,3-linked D-galactose units) [116]. Wide variations in hemicelluloses content and chemical structure can occur depending on the biomass type, that is, maize stems (28.0%), barley straw (34.9%), wheat straw (38.8%), and rye straw (36.9%) [117] or on the components of an individual plant, that is, stem, branches, roots, and bark [118].

Considerable interest has been directed to hemicelluloses-based biomaterials due to their nontoxicity, bio-based origin, bioactive, biocompatible, and oxygen barrier properties, which give them the potential in numerous applications, such as drug delivery, tissue engineering, and food packaging. Among these research activities, hemicellulose-based films have received ever-increasing interest as oxygen barrier films, but suffer from low film-forming ability and mechanical performance. Plasticizers or hydrophobization is usually required to make hemicelluloses suitable for packaging applications. Most of the hemicelluloses usage in biorefineries is focused on degradation of the polymer into sugars, not materials-oriented research.

Hemicelluloses can be easily hydrolyzed into pentose (xylose and arabinose) and hexose (glucose, galactose, and mannose), and can be transformed into fuel ethanol and other value-added chemicals, such as 5-hydroxymethylfurfural (HMF), furfural, levulinic acid, and xylitol (Figure 11.4) [118].

Xylans represent the main hemicelluloses in hardwood, but they are also predominant in annual plants and cereals such as straw, sugarcane, corn stalks and cobs, hulls and husks from starch. Xylans complexity and structural diversity strongly depend on the botanical source. Glucuronoxylan, arabinoglucuronoxylan, and arabinoxylan represent structural types of xylan that can be prepared from certain plant sources with similar chemical and physical properties.

11.3.1
Methods for the Isolation of Hemicellulose

Different isolation procedures for hemicellulose with both high purity and yield, obtained from various plant sources, have been described in scientific literature. Hemicelluloses are divided into two fractions: water-soluble and water-insoluble. Their solubility is a major factor for hemicelluloses extraction from cell walls that can be carried out in neutral or alkaline solutions [119]. Because hemicelluloses are bound to lignin or cellulose through ferulic acid bridges and also because hydrogen bondings exist between the nonsubstituted xylose residues and the cellulose chains, water extraction of cereal bran xylans is difficult [120].

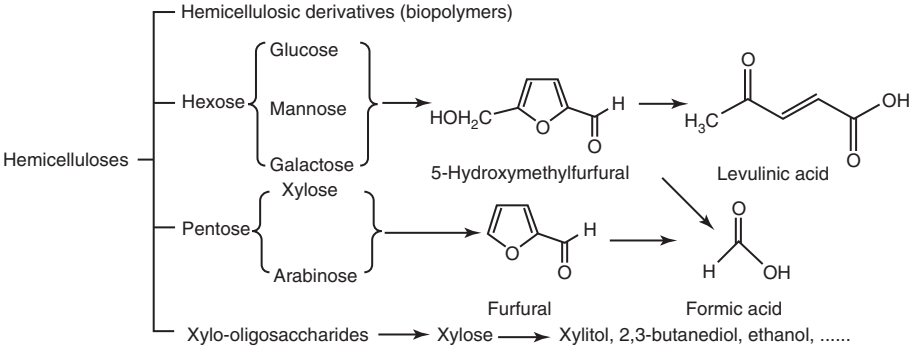

Figure 11.4 The potential products from hemicelluloses [118].

Current isolation and purification strategies are summarized by Peng *et al*. [118] and refer to alkali peroxide extraction, organic solvent extraction, steam explosion, ultrasound-assisted extraction, microwave-assisted extraction, column chromatography, and membrane separation. Isolation of hemicelluloses from grain crops and from cereal brands, involving water and alkali extraction, as well as combinations such as alkali and hydrogen peroxide, alkali and chlorite solutions, or DMSO have been developed [121]. Scaling up to an industrial level is feasible as pilot-scale isolation of cereal xylans has been demonstrated [122, 123].

Alkali treatment has been proven to be an efficient method for extracting the most available hemicelluloses from the cell wall of biomass, but the alkali extractions have the disadvantage of deacetylating the hemicelluloses. Alkali extraction of hemicelluloses from one-month-old bamboo (*Phyllostachys pubescens* Mazel) has been proposed by Luo *et al*. [124]. The bamboo powder was extracted with toluene–ethanol solution, and then the dewaxed sample was treated with sodium chlorite ($NaClO_2$) in an acidic solution. The obtained holocelluloses was subsequently extracted with hot distilled water and 2% sodium hydroxide (NaOH) solution, as presented in Figure 11.5. Finally, two alkali-soluble hemicellulosic fractions, HA and HB, were obtained with a total yield of 26.2%. Xylose was the main neutral sugar in the two hemicellulosic portions; in the fraction HA, arabinose came next, while for HB hemicelluloses, it was galactose.

Neutral sugar compositions measurements, Fourier transform infrared spectroscopy (FTIR) and nuclear magnetic resonance spectroscopy (NMR) indicated that arabinoxylans linked via (1 → 4)-β-glycosidic bonds with branches of arabinose and 4-*O*-methyl-D-glucuronic acid were the major polysaccharides in the young bamboo hemicelluloses. The HA hemicelluloses exhibited more branches than the HB hemicelluloses, according to neutral sugar analysis.

Hemicelluloses maintained their structural integrity when extracting with DMSO, which is the most common neutral solvent for extracting hemicelluloses. Methods for the acceleration of hemicellulose extraction and reduction of the consumption of chemicals involve steam explosion, microwave, and

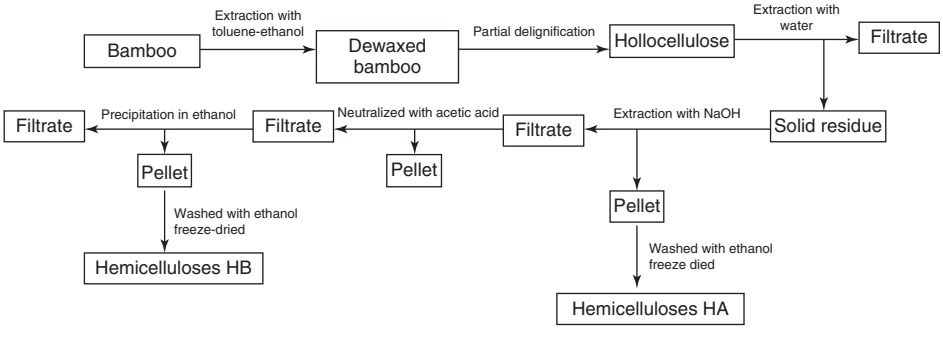

Figure 11.5 Scheme for alkali extraction of hemicelluloses from one-month-old bamboo.

ultrasound-assisted extraction. Membrane technologies such as microfiltration, ultrafiltration, nanofiltration, and reverse osmosis have drawn great attention in green biorefinery for separation and purification of lignocellulosic products, which provide relatively cost-competitive separation steps, and offer a commercial alternative to chromatographic methods for purification of hemicelluloses. Hemicellulosic polymers with high purity rates could be produced by the combination of twin-screw extrusion, ultrafiltration, and anion-exchange chromatography [118].

11.3.2 Preparation of Nanoparticles from Hemicelluloses

Micro- and nanoparticles of hemicellulose could be obtained by several methods, depending on the isolation procedure of the polymer. One method would be solubilization under alkaline conditions, where supersaturation and precipitation of hemicellulose result upon neutralization and alcohol addition.

Nanoscale particles of corncob xylan ranging from 120 to 1790 nm were obtained by Garcia *et al*. [125]. They prepared particles by a coacervation method based on neutralization of an alkaline solution with an acid solution. Neutralization of the xylan solution with HCl or acetic acid was able to generate micro- and nanoparticles while surfactant concentration influenced both the particle size stability and morphology. The authors established that the optimal concentration of surfactant was 1.5% (v/v).

Xylan may be extremely useful in the pharmaceutical field, especially for the production of colon-specific drug carriers, such as micro- and nanoparticles, and film coatings. Nano xylan is used as well in food applications; xylan nanoparticles raise food smell and taste and also change food texture and color. Particle size is influenced by several factors, namely, hemicellulose and neutralizing agent concentration, presence of additives, pH reached, lignin monomers, and polymerization enzymes [116].

Nanoxylan with particle size of 30–90 nm, xylose content of 90% and average molecular weight of 18 000 g mol^{-1} were prepared by a special method that comprise the following steps: isolation of xylan from wheat straw powder, addition of xylan into a NaOH solution, precipitating in ethanol (three times by volume), filtering to obtain a filter cake, dispersing the filter cake in ethanol according to the filter cake/ethanol mass ratio of 1 : 20–1 : 100, freezing, and drying. The proposed method has the advantages of simple technique, easily controlled conditions, low cost, and high purity of the obtained nanoxylan [126].

Other methods for obtaining nanohemicelluloses were developed, namely: dissolution of xyloglucans in DMSO, *N*,*N*-dimethylacetamide (DMAc) or acetone; dialysis; supercritical antisolvent precipitation (SAS), particles from gas saturated solutions (PGSSs), emulsion [116].

SAS, a relatively recent technology, was used by Haimer *et al*. [116] to obtain spherical xylan or mannan particles with a narrow particle size distribution precipitated from hemicellulose solutions in DMSO or DMSO/H_2O mixtures

by carbon dioxide (CO_2) as an antisolvent. The rate of supersaturation, type of hemicellulose, the DMSO/H_2O ratio, and the precipitation conditions such as pressure and temperature adjust the precipitate particle size and morphology. The resultant nano- and microstructured native xylans and mannans can be used in applications, such as encapsulation of active compounds, slow release agents, or chromatographic separation materials.

11.3.3 Hemicellulose Nanocomposites

An effective and simple method to produce hemicelluloses-based nanocomposite film of high quality was proposed by Peng *et al.* [127] who incorporated cellulose nanofibers (CNFs) into xylan (XH) films in the presence of plasticizers. The sugar composition (relative weight percent) by the sugar analysis is 89.38% xylose, 5.75% arabinose, 1.87% glucose, 0.66% galactose, 1.78% glucuronic acid, and 0.55% galacturonic acid. Morphological studies showed that the surface of the XH film and the nanocomposite film reinforced with CNF were primarily composed of nodules that had a diameter of 10–70 nm, and CNFs were embedded in the XH matrix. Aggregates began to form in an interval of the arabinose/xylose ratio between 0.23 and 0.31 in an aqueous solution, so the removal of arabinose substituents resulted in a gradual association of unsubstituted xylan chains. These results indicate that the intermolecular interaction can be tailored by controlling the substituted groups or by incorporating a secondary component that would interact with the molecular chains of hemicelluloses. High aspect ratio and strong interactions between CNF and the XH matrix resulted in better film formation and a significant improvement in the tensile strength.

The freeze–thaw technique was used by Guan *et al.* [128] to prepare a novel hybrid hydrogel from hemicelluloses extracted from bamboo (*Phyllostachys pubescens*) holocellulose, PVA, and chitin nanowhiskers. The FTIR and NMR results indicated that physical crosslinking rather than chemical reaction occurred during the gelation process. PVA played the role of a hydrogel scaffold, whereas the hemicelluloses exhibited a strong hydrophilic and hydrogen-bonding character with chitin nanowhiskers, as a cross-linker. Atomic force microscopy (AFM) images of chitin showed that the size of whiskers reached a nanometer level with an average length of about 200 nm and width of 40 nm. The mechanical properties of the hydrogels were significantly improved with increasing proportion of chitin nanowhiskers; these hydrogels were considered as potential candidates for use in tissue engineering applications.

Laminated films consisting of one layer of a thermoplastic film (polyester) and the other made of carbon nanotubes and hemicellulose have been patented in Japan [129]. Hemicellulose was extracted from *Abelmoschus manihot* or *Hydrangea paniculata* obtaining polymers with DP of 100–10 000. The carbon nanotubes were uniformly dispersed in the hemicellulose films giving conducting and mechanically strong films.

11.4 Lignin

11.4.1 Procedures for Lignin Isolation and Their Properties

Lignin, the main aromatic component of vegetable biomass, presents a special interest due to its vast reserves that are still less valorized, as well as due to its active part in the complex process of organic material of formation and conversion in biosphere.

Several studies revealed that similar functional groups are found in all types of lignin [130, 131]. Thus, softwood lignin contains guaiacyl propane units, which include a methoxy group bonded to the third carbon atom of the aromatic ring, while hardwood lignin has guaiacyl propane units and syringyl propane units. The proportion of the main functional groups found in natural lignin, namely, phenolic hydroxyl, primary and secondary aliphatic hydroxyl, methoxyl, ketone, and aldehyde groups depends on the method used to isolate the lignin and the plant species containing it.

The source of the lignin and the method of extraction significantly influence the composition and properties of lignin. Most of the lignin extraction and delignification processes occur by either acid or base-catalyzed mechanisms [132].

Organosolv and kraft pulping processes are particularly relevant when referring to the different available processes for extracting lignin from vegetal sources. In the organosolv process, lignin is extracted with an organic solvent and water, usually in the presence of an acid catalyst. Such lignin has a low molecular weight and contains many reactive sites available for functionalization, these aspects being advantageous when compared with lignin obtained from other processes. Nevertheless, kraft pulping is the most used delignification process in the paper and cellulose industries [133]. Kraft lignin is a polydispersed, branched biopolymer with high molecular weight. Hydrolytic lignin maintains an acidic character, unlike the two other types of lignin, being a heterogeneous product of acidic wood processing, composed of lignin (up to 88%), poly and monosaccharide residues, organic acids, resins, waxes, nitrogenous compounds, ashes, and mineral acids that were not washed out after wood hydrolysis [134].

Lignin is a biopolymer whose reactivity is induced by its particular structure described function of its double nature, namely:

- lignin – unitary macromolecular compound;
- lignin – assembly of structural units which differ by their behavior in various chemical reactions.

Lignin's use in polymeric systems is limited due to its poor compatibility and absence of thermoplasticity. This could be explained by structural polydispersity and molecular weight as well as the presence of strong intermolecular interactions in polymeric complex. Although, there are many studies on nanomaterials containing lignin or its derivatives with enhanced mechanical, thermal, dielectric, and

biodegradable properties. The results referring to lignin useas stabilizer for plastic materials – for example, polyethylene (PE), polypropylene (PP), poly(vinyl chloride) (PVC), polyamide (PA), polyurethane (PU), and rubbers have been reported in literature, lignin acting also as antioxidant, modifier of mechanical properties, and rigidity, its efficiency for bio-degradation capacity improvement being well known [135, 136]. The reactivity of lignin can be increased using different reactions such as hydroxymethylation, epoxidation, carboxymethylation, esterification, oxidation and sulfonation, and so on.

Products obtained from lignin are very attractive research topics, but it is a very complex issue due to its complicated structure which depends on the separation method and plant species.

11.4.2 Lignin-based Nanomaterials and Nanocomposites

Nanotechnology allows using chemical, physical, and biological effects that do not occur outside the nanoscale world. The main advantage of the hydroxymethylated lignin is its high content of hydroxyl groups, which allows using it as a phenol substitute in phenol formaldehyde resin synthesis [137], composites, biocides systems, and bioremediation [138]. By using the hydroxymethylation reaction of lignin, Gilca *et al*. [139] obtained lignin nanoparticles and by mathematical modeling established the optimum reaction conditions as being temperature of 72 °C, pH of 9.8, lignin/formaldehyde ratio = 1. The nanoparticles were characterized from a dimensional aspect. The modifications determined by hydroxymethylation reaction were confirmed by FTIR spectroscopy, gel permeation chromatography (GPS), and ^{31}P-NMR spectroscopy techniques, showing that use of the proposed chemical method leads to hydroxymethylated lignin nanoparticles.

Nevárez *et al*. [140] prepared biopolymer nanocomposite films by vapor-induced phase separation at controlled temperature (35–55 °C) and relative humidity, RH (10–70%) using lignin as a filler and cellulose triacetate (CTA) as a polymer matrix. Three types of lignin were used in the form of nanoparticles incorporated at 1 wt% in CTA: organosolv, hydrolytic, and kraft, with or without acetylation. The efficiency of acetylation of each type of lignin as well as its effects on film structure, homogeneity, and mechanical properties was studied and discussed. The obtained results are explained in terms of intermolecular filler–matrix interaction at the nanometer scale, for which the highest mechanical resistance was reached using hydrolytic lignin in the nanocomposite. The low molecular weight of the lignin is crucial for membrane performance, regardless of the RH or temperature during casting, and a higher temperature and RH improve the material homogeneity. The mechanical properties were considerably improved through the incorporation of 1 wt% lignin. The highest Young's moduli were obtained with hydrolytic lignin, which had the smallest particles among the studied lignins.

Enzyme-hydrolyzed lignin (EHL) (up to 30 wt%) was used as a dispersant to optimize the structure and properties of the PANI–lignin nanocomposites

prepared via an *in situ* polymerization from aniline [141]. Lignin nanoparticles with an average diameter of 70 nm were observed by field emission scanning electron microscopy (FE-SEM) and transmission electron microscopy (TEM) and the images revealed that the composites contained 10 wt% EHL. The silver ions adsorbability of the PANI–lignin nanocomposites was examined by a static sorption technique, the results showing that the maximal adsorption capacity was up to 565.4 mg g^{-1} for the PANI–lignin nanocomposite with the EHL content of 10 wt% and the initial silver ions concentration of 0.05 mol l^{-1}. TEM and wide angle X-ray diffraction (WAXD) results showed that silver nanobelts with length up to 1 cm, width of 0.220–4.38 μm and thickness of 219–311 nm were achieved after adsorption of silver ions onto the PANI–lignin nanocomposite with 10 wt% EHL.

A new strategy to partially replace carbon black with lignin was proposed by Jiang *et al*. [142], which obtained natural rubber/lignin nanocomposites by coprecipitation of colloidal lignin–cationic polyelectrolyte complexes (LPC) and rubber latex. The LPCs resulted by dropwise the various mass of sulfate lignin solution into the poly(diallyldimethylammonium chloride) (PDADMAC) solution. A schematic process to obtain natural rubber/lignin nanocomposites was presented by authors in Figure 11.6. They found out that up to the stoichiometric point of mass ratio of lignin to PDADMAC, the formed LPC complexes were positively charged and water-soluble. A homogeneous distribution of lignin in natural rubber matrix was observed as the natively charged natural rubber latex was subsequently adsorbed onto the positively charged LPCs via electrostatic self-assembly. The degree of dissociation of carboxylic groups decreases with

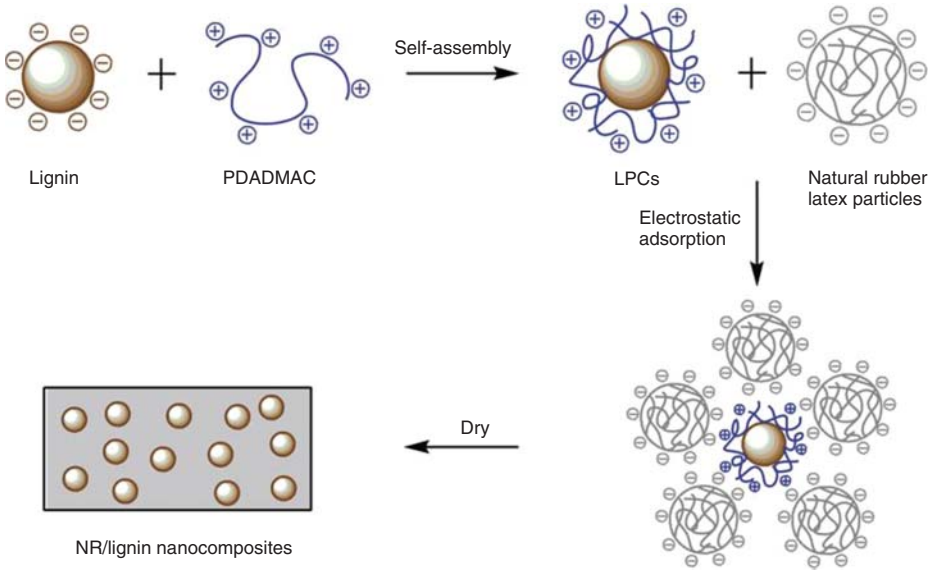

Figure 11.6 Schematic illustration of process for natural rubber/lignin nanocomposites [142].

decreasing pH, so the pH of the solution affects the particle size of lignin. Authors observed a decrease of lignin macromolecules from about 380 to about 110 nm at the pH range of 6 to 4. They concluded that PDADMAC intensively interacted with lignin by cation–π and π–π interactions confirmed by UV–Vis and FTIR spectroscopy, and lignin particles were stable in aqueous solution with an average particle size less than 100 nm.

Hilburg *et al*. [143] obtained nanocomposites using ATRP of nanolignin particles (5 nm) with styrene or methyl methacrylate, which provided a 10-fold increase in toughness over a lignin/polymer blend equivalent due to strong polymer–lignin interactions. The results illustrate the potential for using nanolignin in composites whose structures are engineered on the molecular scale.

Nanocomposites containing organosolv lignin obtained by alcohol pulping (Alcell™) and organoclays were obtained by mechanical mixing and subsequent melt intercalation at 130 and 150 °C depending on the hybrid composition [144]. Varying amounts (from 1 to 10 wt%) of two organically modified montmorillonite (MMT) clays with different ammonium cations were used. Thermal results revealed an increase in T_g for the nanocomposites as compared with the original organosolv lignin. X-ray diffraction (XRD) proved lignin intercalation into the silicate layers for both organoclays and the possibility of complete exfoliation at 1 wt% organoclay Cloisite 30B. A substantial increase in the tensile strength of the nanocomposites was observed when incorporating intercalated hybrids. Thus, by adding 5 wt% of Cloisite 20A, the tensile strength increased by 54%, while the same amount of Cloisite 30B enhanced the tensile strength by 70%.

11.4.3
Applications of Nanomaterials Containing Lignin

The nanocomposite membranes studied by Nevárez *et al.* [140] whose properties were discussed above could be applied in continuous water purification processes, where lignin incorporation improved the resistance of the material to bacteria-induced fouling.

Lin *et al.* [141] showed that the EHL content affected the structure and properties of the PANI–lignin nanocomposites. The adsorption capacity of silver ions onto the PANI–lignin nanocomposites with the EHL content of 0–30 wt% increased first and then decreased. The obtained results indicated that the PANI–lignin nanocomposites possess a strongly reactive adsorbability of silver ions. The successful preparation of the PANI–lignin nanocomposites can provide an effective method to remove and recover silver ions from wastewater.

The improvement of some fabric UV barrier properties and washing resistance was observed by treating linen fabric with a solution of nanolignin obtained from kraft lignin by ultrasonic treatment [145]. Nanolignin application for the finishing process of linen fabrics could result in obtaining multifunctional textile products with UV protection, antibacterial properties (against *Corynebacterium xerosis, Bacillus licheniformis, Micrococcus flavus, Staphylococcus haemolyticus, Staphylococcus aureus, Klebsiella pneumoniae, Escherichia coli, Pseudomonas*

aeruginosa) and antistatic properties guaranteeing a positive effect on human physiology. The linen fabric was covered 10 times with nanolignin by padding, while silicone emulsion (5%, 25%, and 50%) was applied for better fixation of the nanolignin particles on linen fabric. The highest UV protection factor (UPF) had a value of 25 and was obtained after eight covering passages. Other textiles like hemp or flax coated by nanolignin have excellent UV protection.

The application of nanosuspensions resulting from Protobind lignin epoxidation reaction with epichlorohydrin in alkaline medium on oak and poplar veneer confers biostability and increased capacity for liquid adsorption on the surface [146]. Particle size distribution data of micro- and nanoparticles resulting from epoxidation of commercial lignins (Pb1000, Pb2000, and Pb3000) recorded average sizes between 70 and 200 nm. The authors reported that samples of oak and poplar veneer were immersed for 30 min in the nanosuspensions of epoxidated lignin, were then dried at room temperature and weighed to assess the retention degree. The biostability was investigated by determining the weight loss and contact angle variation in time for the samples buried in cultivated soils for 6 months (garden soil sown with wheat to combine the effects of micro-organisms with those of rhizospheres). The efficiency of the treatment depends on the type of product used and also on the species of treated wood. Reduced mass loss was observed for the treated poplar veneer samples buried in cultivated soil for 6 months, this being more stable in soil, compared to oak veneer.

Active sensor membranes were obtained by combining high-performance nanolignin recovered from paper pulp waste with proteins and nanomaterials [147]. Authors used a combination of self-assembled monolayer chemistry and electrodeposition to obtain catalytic nanomaterial platforms, these methods being used to develop electrochemical biosensors for studying physiological transport in biomedical, agricultural, and environmental applications.

11.5 Risk Assessment of Nanoparticles and Nanomaterials

Since 2001, the Environmental Protection Agency (EPA) is involved in setting research directions to develop the environmental applications of nanotechnology and to understand and address the potential risks to human health from exposure to nanoscale materials and products containing nanoscale materials. USEPA (2014) defines "risk" as "a measure of the probability that damage to life, health, property, and/or the environment will occur as a result of a given hazard" [148].

When establishing risk assessment, beside other valuable properties, properties such as particle size distribution, surface area/volume, shape, electronic properties, surface characteristics, state of dispersion/agglomeration, and conductivity need to be studied; however, the high complexity and great diversity of nanoparticles make their characterization very difficult.

A number of experimental studies were performed *in vivo* and *in vitro* in order to demonstrate the degree of hazardous effects and toxicity of some types of nanoparticles or nanomaterials on the tested organisms. Unfortunately, most of them were not meant to facilitate risk assessment as they used nonstandardized tests, differing greatly from each other in regard to endpoints, tested species, methods of administration, dose ranges, and exposure periods [149].

In order to fully assess the potential risks and environmental impacts of nanoparticles and nanomaterials, protocols and practical methodologies for toxicology studies, transport studies, and scaling approaches are needed. As the environmental impacts of nanoproducts can occur in any life-cycle stage (use, reuse, recycling and/or final treatment, and disposal of products containing nanomaterials), a life-cycle assessment (LCA) study is necessary, but the lack of data and understanding in certain areas represent the main problem with LCA in case of nanomaterials.

New researches are under study, but they advance at low speed because risk assessment tools are urgently needed to trigger adequate regulatory response. This would enable current regulation to adequately reflect the risks of nanoparticles and nanomaterials and protect the environment and the community.

11.6
Future Perspectives and Conclusions

Due to the current social, political, economic, and environmental status, there is a pressing need for innovative, sustainable, and recyclable materials. Toward this, the nanocomposites containing nanoparticles of cellulose, hemicellulose, or lignin are of great interest. Owing to the great abundance and source diversity in nature, it is expected that there will be growing interest in the development of nanocomposite structures based on these biopolymers. Generally, nanocomposites are transparent and exhibit improved properties compared with traditional ones, such as increased modulus or strength, heat resistance, excellent barrier properties, lower flammability, improved solvency, and ductility. However, three requirements were identified that could have the greatest potential for significant contribution: compatibilization, control, and cost. In addition, a significant challenge is to match the properties of the nanoparticles from renewable resources with the ones required for specific applications. A possibility to increase the applications area of nanocomposites is the surface chemical modification of nanoparticles, which has been extensively studied.

Despite the constant growing scientific production in the field of nanocomposites, the practical transition from the laboratory scale to the industrial scale is not so simple and requires the development of technology in the field of chemical engineering to reduce the production costs of such nanoparticles. Although many potential applications of materials based on nanoparticles from renewable resources were identified and demonstrated in the laboratory scale, the products can successfully provide many technical benefits, so the market value for potential

end-users must be considered. In order to succeed in a valuable product, these materials must fulfill some criteria: they must provide a cost advantage when replacing products and provide a clear environmental advantage, and improved product performance should be quantifiable.

References

1. Klemm, D., Schmauder, H.P., and Heinze, T. (2005) in *Biopolymers, Polysaccharides II: Polysaccharides from Eukaryotes*, vol. 6 (eds E.J. Vandamme, S. De Baets, and A. Steinbüchel), Wiley-VCH Berlag GmbH & Co. KGaA, pp. 275–278.
2. Ciolacu, D. and Popa, V.I. (2011) *Cellulose Allomorphs: Structure, Accessibility and Reactivity*, Chapter 1, Nova Science Publisher, New York, pp. 1–3.
3. Kalia, S., Dufresne, A., Cherian, B.M., Kaith, B.S., Avérous, L., Njuguna, J., and Nassiopoulos, E. (2011) Cellulose-based Bio- and nanocomposites: a review. *Int. J. Polym. Sci.*, **2011**, 1–35.
4. Blackwell, J., Kolpak, F.J., and Gardener, K.H. (1977) in *Cellulose Chemistry and Technology*, ACS Symposium, Series, vol. 48 (ed. J.C. Arthur), American Chemical Society, Washington, DC, pp. 42–55.
5. Salmén, L., Åkerholm, M., and Hinterstoisser, B. (2004) in *Polysaccharides: Structural Diversity and Functional Versatility* (ed S. Dumitriu), Marcel Dekker, Inc., New York, pp. 159–188.
6. Klemm, D., Philipp, B., Heize, T., Heinze, U., and Wagwnknecht, W. (1998) *Comprehensive Cellulose Chemistry: Fundamentals and Analytical Methods*, vol. 1, WILEY-VCH Verlag GmbH, Weiheimem, pp. 167–223.
7. Ciolacu, D. and Popa, V.I. (2010) in *Cellulose: Structure and Property, Derivatives and Industrial Uses* (eds A. Lejeune and T. Deprez), Nova Science Publishers, New York, pp. 1–38.
8. Pérez, S. and Mazeau, K. (2005) in *Polysaccharides: Structural Diversity and Functional Versatility* (ed S. Dumitriu), Marcel Dekker, Inc., New York, pp. 41–69.
9. Isogai, A. (1994) in *Cellulose Polymers, Blends and Composites* (ed R.D. Gilbert), Hansere Publishers, Munich, Vienna and New York, pp. 1–24.
10. Atalla, R.H. and VanderHart, D.L. (1984) Native cellulose: a composite of two distinct crystalline forms. *Science*, **223** (4633), 283–285.
11. Wada, M., Sugiyama, J., and Okano, T. (1993) Native celluloses on the basis of the two crystalline phase (Ia/Ib) system. *J. Appl. Polym. Sci.*, **49**, 1491–1496.
12. Credou, J. and Berthelot, T. (2014) Cellulose: from biocompatible to bioactive material. *J. Mater. Chem. B*, **2**, 4767–4788.
13. Khalil, H.P.S.A., Davoudpour, Y., Islam, M.N., Mustapha, A., Sudesh, K., Dungani, R., and Jawaid, M. (2014) Production and modification of nanofibrillated cellulose using various mechanical processes: a review. *Carbohydr. Polym.*, **99**, 649–665.
14. Spence, K.L., Venditti, R.A., Habibi, Y., Rojas, O.J., and Pawlak, J.J. (2010) The effect of chemical composition on microfibrillar cellulose films from wood pulps: mechanical processing and physical properties. *Bioresour. Technol.*, **101**, 5961–5968.
15. Taipale, T., Österberg, M., Nykänen, A., Ruokolainen, J., and Laine, J. (2010) Effect of microfibrillated cellulose and fines on the drainage of kraft pulp suspension and paper strength. *Cellulose*, **17**, 1005–1020.
16. Pääkkö, M., Ankerfors, M., Kosonen, H., Nykänen, A., Ahola, S., Österberg, M., Ruokolainen, J., Laine, J., Larsson, P.T., Ikkala, O., and Lindström, T. (2007) Enzymatic hydrolysis combined with mechanical shearing and high-pressure homogenization for nanoscale cellulose fibrils and strong gels. *Biomacromolecules*, **8**, 1934–1941.

17. Stenstad, P., Andresen, M., Tanem, B., and Stenius, P. (2008) Chemical surface modifications of microfibrillated cellulose. *Cellulose*, **15**, 35–45.
18. Braun, B., Dorgan, J.R., and Chandler, J.P. (2008) Cellulosic nanowhiskers. Theory and application of light scattering from polydisperse spheroids in the Rayleigh-Gans-Debye regime. *Biomacromolecules*, **9**, 1255–1263.
19. Karande, V.S., Bharimalla, A.K., Hadge, G.B., Mhaske, S.T., and Vigneshwaran, N. (2011) Nanofibrillation of cotton fibers by disc refiner and its characterization. *Fibers Polym.*, **2** (3), 399–404.
20. Cao, X.D., Dong, H., and Li, C.M. (2007) New nanocomposite materials reinforced with flax cellulose nanocrystals in waterborne polyurethane. *Biomacromolecules*, **8**, 899–904.
21. Qua, E.H., Hornsby, P.R., Sharma, H.S.S., and Lyons, G. (2011) Preparation and characterisation of cellulose nanofibres. *Mater. Sci.*, **46**, 6029–6045.
22. Habibi, Y., Goffin, A.L., Schiltz, N., Duquesne, E., Dubois, P., and Dufresne, A. (2008) Bionanocomposites based on poly(ε-caprolactone)-grafted cellulose nanocrystals by ring-opening polymerization. *J. Mater. Chem.*, **18**, 5002–5010.
23. Habibi, Y. and Dufresne, A. (2008) Highly filled bionanocomposites from functionalized polysaccharide nanocrystals. *Biomacromolecules*, **9**, 1974–1980.
24. Alemdar, A. and Sain, M. (2008) Isolation and characterization of nanofibers from agricultural residues—wheat straw and soy hulls. *Bioresour. Technol.*, **99**, 1664–1671.
25. Zimmermann, T., Bordeanu, N., and Strub, E. (2010) Properties of nanofibrillated cellulose from different raw materials and its reinforcement potential. *Carbohydr. Polym.*, **79**, 1086–1093.
26. Alila, S., Besbes, I., Vilar, M.R., Mutje, P., and Boufi, S. (2013) Non-woody plants as raw materials for production of microfibrillated cellulose (MFC): a comparative study. *Ind. Crops Prod.*, **41**, 250–259.
27. Elazzouzi-Hafraoui, S., Nishiyama, Y., Putaux, J.L., Heux, L., Dubreuil, F., and Rochas, C. (2008) The shape and size distribution of crystalline nanoparticles prepared by acid hydrolysis of native cellulose. *Biomacromolecules*, **9**, 57–65.
28. Revol, J.F. (1982) On the cross-sectional shape of cellulose crystallites in *Valonia ventricosa*. *Carbohydr. Polym.*, **2** (2), 123–124.
29. Hanley, S.J., Revol, J.F., Godbout, L., and Gray, D.G. (1997) Atomic force microscopy and transmission electron microscopy of cellulose from *Micrasterias denticulata*; evidence for a chiral helical microfibril twist. *Cellulose*, **4**, 209–220.
30. Tokoh, C., Takabe, K., Fujita, M., and Saiki, H. (1998) Cellulose synthesized by *Acetobacter xylinum* in the presence of acetyl glucomannan. *Cellulose*, **5** (4), 249–261.
31. Klemm, D., Kramer, F., Moritz, S., Lindström, T., Ankerfors, M., Gray, D., and Dorris, A. (2011) Nanocelluloses: a new family of nature-based materials. *Angew. Chem. Int. Ed.*, **50**, 5438–5466.
32. Peng, B.L., Dhar, N., Liu, H.L., and Tam, K.C. (2011) Chemistry and applications of nanocrystalline cellulose and its derivatives: a nanotechnology perspective. *Can. J. Chem. Eng.*, **89**, 1191–1206.
33. Malainine, M.E., Mahrouz, M., and Dufresne, A. (2005) Thermoplastic nanocomposites based on cellulose microfibrils from *Opuntia ficus-indica* parenchyma cell. *Compos. Sci. Technol.*, **65**, 1520–1526.
34. Siró, I. and Plackett, D. (2010) Microfibrillated cellulose and new nanocomposite materials: a review. *Cellulose*, **17**, 459–494.
35. Lavoine, N., Desloges, I., Dufresne, A., and Bras, J. (2012) Microfibrillated cellulose – its barrier properties and applications in cellulosic materials: a review. *Carbohydr. Polym.*, **90**, 735–764.
36. Lee, S.Y., Chun, S.J., Kang, I.A., and Park, J.Y.D. (2009a) Preparation of cellulose nanofibers by high-pressure homogenizer and cellulose-based composite films. *J. Indian Eng. Chem.*, **15**, 50–55.

37. Ferrer, A., Filpponen, I., Rodríguez, A., Laine, J., and Rojas, O.J. (2012) Valorization of residual Empty Palm Fruit Bunch Fibers (EPFBF) by microfluidization: production of nanofibrillated cellulose and EPFBF nanopaper. *Bioresour. Technol.*, **125**, 249–255.
38. Panthapulakkal, S. and Sain, M. (2012) Preparation and characterization of cellulose nanofibril films from wood fibre and their thermoplastic polycarbonate composites. *Int. J. Polym. Sci.*, 1–6.
39. Chakraborty, A., Sain, M., and Kortschot, M. (2005) Cellulose microfibrils: a novel method of preparation using high shear refining and cryocrushing. *Holzforschung*, **59**, 102–107.
40. Johnson, R.K., Zink-Sharp, A., Renneckar, S.H., and Glasser, W.G. (2009) A new bio-based nanocomposite: fibrillated TEMPO-oxidized celluloses in hydroxypropylcellulose matrix. *Cellulose*, **16**, 227–238.
41. Frone, A.N., Panaitescu, D.M., Donescu, D., Spataru, C.I., Radovici, C., Trusca, A., and Somoghi, R. (2011) Preparation and characterization of PVA composites with cellulose nanofibers obtained by ultrasonication. *BioResources*, **6** (1), 487–512.
42. Hubbe, M.A., Rojas, O.J., Lucia, L.A., and Sain, M. (2008) Cellulosic nanocomposites: a review. *BioResources*, **3** (3), 929–980.
43. Moon, R.J., Martini, A., Nairn, J., Simonsen, J., and Youngblood, J. (2011) Cellulose nanomaterials review: structure, properties and nanocomposites. *Chem. Soc. Rev.*, **40**, 3941–3994.
44. Plackett, D. and Iotti, M. (2013) in *Biopolymer Nanocomposites: Processing, Properties, and Applications*, Chapter 14 (eds A. Dufresne, S. Thomas, and L.A. Pothen), John Wiley & Sons, Inc., Hoboken, NJ, pp. 309–338.
45. Herrick, F.W., Casebier, R.L., Hamilton, J.K., and Sandberg, K.R. (1983) Microfibrillated cellulose: morphology and accessibility. *J. Appl. Polym. Sci.: Appl. Polym. Symp.*, **37**, 797–813.
46. Turbak, A.F., Snyder, F.W., and Sandberg, K.R. (1983) Microfibrillated cellulose, a new cellulose product: properties, uses, and commercial potential. *J. Appl. Polym. Sci.: Appl. Polym. Symp.*, **37**, 815–827.
47. Siqueira, G., Bras, J., and Dufresne, A. (2010) Cellulosic bionanocomposites: a review of preparation, properties and applications. *Polymer*, **2** (4), 728–765.
48. Hassan, M.L., Mathew, A.P., Hassan, E.A., El-Wakil, N.A., and Oksman, K. (2012) Nanofibers from bagasse and rice straw: process optimization and properties. *Wood Sci. Technol.*, **46**, 193–205.
49. Iwamoto, S., Nakagaito, A.N., and Yano, H. (2007) Nano-fibrillation of pulp fibers for the processing of transparent nanocomposites. *Appl. Phys. A*, **89**, 461–466.
50. Cheng, Q., Wang, S., and Rials, T.G. (2009) Poly(vinyl alcohol) nanocomposites reinforced with cellulose fibrils isolated by high intensity ultrasonication. *Composites Part A*, **40**, 218–224.
51. Wang, H., Li, D., and Zhang, R. (2013) Preparation of ultralong cellulose nanofibers and optically transparent nanopapers derived from waste corrugated paper pulp. *BioResources*, **8** (1), 1374–1384.
52. Chen, P., Yu, H., Liu, Y., Chen, W., Wang, X., and Ouyang, M. (2013) Concentration effects on the isolation and dynamic rheological behavior of cellulose nanofibers via ultrasonic processing. *Cellulose*, **20**, 149–157.
53. Qing, Y., Sabob, R., Zhub, J.Y., Cai, Z., and Wu, Y. (2013) Comparative study of cellulose nanofibrils: disintegrated from different approaches. *Bioresour. Technol.*, **130**, 783–788.
54. Kalia, S., Boufi, S., Celli, A., and Kango, S. (2014) Nanofibrillated cellulose: surface modification and potential applications. *Colloid. Polym. Sci.*, **292**, 5–31.
55. Cristobal, C., Encarnacion, R., Mercedes, B., Paloma, M., Jose, M.N., and Eulogio, C. (2008) Production of fuel ethanol from steam-explosion pretreated olive tree pruning. *Fuel*, **87**, 692–700.
56. Cherian, B.M., Leao, A.L., de Souza, S.F., Thomas, S., Pothan, L.A., and Kottaisamy, M. (2010) Isolation of

nanocellulose from pineapple leaf fibres by steam explosion. *Carbohydr. Polym.*, **81**, 720–725.

57. Iwamoto, S., Isogai, A., and Iwata, T. (2011) Structure and mechanical properties of wet-spun fibers made from natural cellulose nanofibers. *Biomacromolecules*, **12**, 831–836.

58. Xhanari, K., Syverud, K., Chinga-Carrasco, G., Paso, K., and Stenius, P. (2011) Reduction of water wettability of nanofibrillated cellulose by adsorption of cationic surfactants. *Cellulose*, **18**, 257–270.

59. Besbes, I., Alila, S., and Boufi, S. (2011) Nanofibrillated cellulose from TEMPO-oxidized eucalyptus fibres: effect of the carboxyl content. *Carbohydr. Polym.*, **84** (3), 975–983.

60. Isogai, T., Saito, T., and Isogai, A. (2011) Wood cellulose nanofibrils prepared by TEMPO electro-mediated oxidation. *Cellulose*, **18**, 421–431.

61. Wang, B., Sain, M., and Oksman, K. (2007) Study of structural morphology of hemp fiber from the micro to the nanoscale. *Appl. Compos. Mater.*, **14**, 89–103.

62. Wågberg, L., Decher, G., Norgren, M., Lindström, T., Ankerfors, M., and Axnas, K. (2008) The build-up of polyelectrolyte multilayers of microfibrillated cellulose and cationic polyelectrolytes. *Langmuir*, **24**, 784–795.

63. Ifuku, S., Nogi, M., Abe, K., Handa, K., Nakatsubo, F., and Yano, H. (2007) Surface modification of bacterial cellulose nanofibers for property enhancement of optically transparent composites: dependence on acetyl-group DS. *Biomacromolecules*, **8**, 1973–1978.

64. Bledzki, A.K., Mamun, A.A., Lucka-Gabor, M., and Gutowski, V.S. (2008) The effects of acetylation on properties of flax fibre and its polypropylene composites. *Express Polym. Lett.*, **2** (6), 413–422.

65. Bulota, M., Kreitsmann, K., Hughes, M., and Paltakari, J. (2012) Acetylated microfibrillated cellulose as a toughening agent in poly(lactic acid). *J. Appl. Polym. Sci.*, **126**, 448–457.

66. Missoum, K., Belgacem, M.N., and Bras, J. (2013) Nanofibrillated cellulose surface modification: a review. *Materials*, **6**, 1745–1766.

67. Hasani, M., Cranston, E.D., Westman, G., and Gray, D.G. (2008) Cationic surface functionalisation of cellulose nanocrystals. *Soft Matter*, **4**, 2238–2244.

68. Lin, N., Huang, J., and Dufresne, A. (2012) Preparation, properties and applications of polysaccharide nanocrystals in advanced functional nanomaterials: a review. *Nanoscale*, **4**, 3274–3294.

69. Pereda, M. and Dufresne, A. (2013) in *Biomass-Based Biocomposites*, Chapter 15 (eds V.K. Thakur and A.S. Singha), Smithers Rapra Technology, pp. 305–348.

70. Dufresne, A. (2013) Nanocellulose: a new ageless bionanomaterial. *Mater. Today*, **16** (6), 220–227.

71. Edgar, C.D. and Gray, D.G. (2003) Smooth model cellulose I surfaces from nano- crystal suspensions. *Cellulose*, **10**, 299–306.

72. Okano, T., Kuga, S., Wada, M., Araki, J., and Inata, J. (1999) Fine cellulose particle and its production. JP Patent 11343301, filed Jun. 01, 1998 and issued Dec. 14, 1999.

73. Lee, S.Y., Mohan, D.J., Kang, I.A., Doh, G.H., Lee, S., and Han, S.O. (2009b) Nanocellulose reinforced PVA composite films: effects of acid treatment and filler loading. *Fibers Polym.*, **10** (1), 77–82.

74. Filpponen, I. and Argyropoulos, D.S. (2010) Regular linking of cellulose nanocrystals via click chemistry: synthesis and formation of cellulose nanoplatelet gels. *Biomacromolecules*, **11** (4), 1060–1066.

75. Liu, D., Zhong, T., Chang, P.R., Li, K., and Wu, Q. (2010) Starch composites reinforced by bamboo cellulosic crystals. *Bioresour. Technol.*, **101** (7), 2529–2536.

76. Beck-Candanedo, S., Roman, M., and Gray, D.G. (2005) Effect of reaction conditions on the properties and behavior of wood cellulose nanocrystal

suspensions. *Biomacromolecules*, **6** (2), 1048–1054.

77. Kvien, I., Tanem, B.S., and Oksman, K. (2005) Characterization of cellulose whiskers and their nanocomposites by atomic force and electron microscopy. *Biomacromolecules*, **6** (6), 3160–3165.
78. Martínez–Sanz, M., López-Rubio, A., and Lagarón, J.M. (2013) in *Food Biopackaging Applications, in Ecosustainable Polymer Nanomaterials for Food Packaging: Innovative Solutions, Characterization Needs, Safety and Environmental Issues* (eds C. Silvestre and S. Cimmino), CRC Press, New York, pp. 195–220.
79. Guhados, G., Wan, W., and Hutter, J.L. (2005) Measurement of the elastic modulus of single bacterial cellulose fibers using atomic force microscopy. *Langmuir*, **21** (14), 6642–6646.
80. Yano, H., Sugiyama, J., Nakagaito, A.N., Nogi, M., Matsuura, T., Hikita, M., and Handa, K. (2005) Optically transparent composites reinforced with networks of bacterial nanofibers. *Adv. Mater.*, **17** (2), 153–155.
81. Manocha, L.M., Valand, J., Patel, N., Warrier, A., and Manocha, S. (2006) Nanocomposites for structural applications. *Indian J. Pure Appl. Phys.*, **44**, 135–142.
82. Seydibeyoglu, M.O. and Oksman, K. (2008) Novel nanocomposites based on polyurethane and microfibrillated cellulose. *Compos. Sci. Technol.*, **68**, 908–914.
83. Favier, V., Chanzy, H., and Cavaille, J.Y. (1995) Polymer nanocomposites reinforced by cellulose whiskers. *Macromolecules*, **28** (18), 6365–6367.
84. Dufresne, A. (2010) Processing of polymer nanocomposites reinforced with polysaccharide nanocrystals. *Molecules*, **15** (6), 4111–4128.
85. Habibi, Y., Lucia, L.A., and Rojas, O.J. (2010) Cellulose nanocrystals: chemistry, self-assembly, and applications. *Chem. Rev.*, **110** (6), 3479–3500.
86. Eichhorn, S.J., Dufresne, A., Aranguren, M., Marcovich, N.E., Capadona, J.R., Rowan, S.J., Weder, C., Thielemans, W., Roman, M., Renneckar, S., Gindl, W., Veigel, S., Keckes, J., Yano, H., Abe, K., Nogi, M., Nakagaito, A.N., Mangalam, A., Simonsen, J., Benight, A.S., Bismarck, A., Berglund, L.A., and Peijs, T. (2010) Review: current international research into cellulose nanofibres and nanocomposites. *J. Mater. Sci.*, **45** (1), 1–33.
87. Rojas, O.J., Montero, G.A., and Habibi, Y. (2009) Electrospun nanocomposites from polystyrene loaded with cellulose nanowhiskers. *J. Appl. Polym. Sci.*, **113** (2), 927–935.
88. Zoppe, J.O., Peresin, M.S., Habibi, Y., Venditti, R.A., and Rojas, O.J. (2009) Reinforcing poly(ε-caprolactone) nanofibers with cellulose nanocrystals. *ACS Appl. Mater. Interfaces*, **1** (9), 1996–2004.
89. Park, W.I., Kang, M., Kim, H.S., and Jin, H.J. (2007) Electrospinning of poly(ethylene oxide) with bacterial cellulose whiskers. *Macromol. Symp.*, **249-250** (1), 289–294.
90. Magalhães, W.L.E., Cao, X., and Lucia, L.A. (2009) Cellulose nanocrystals/cellulose core-in-shell nanocomposite assemblies. *Langmuir*, **25** (22), 13250–13257.
91. Kamel, S. (2007) Nanotechnology and its applications in lignocellulosic composites, a mini review. *eXPRESS Polym. Lett.*, **1** (9), 546–575.
92. Chinga-Carrascoa, G., Averianova, N., Gibadullin, M., Petrov, V., Leirseta, I., and Syverud, K. (2013) Microstructural characterization of homogeneous and layered MFC nanocomposites. *Micron*, **44**, 331–338.
93. Luong, N.D., Korhonen, J.T., Soininen, A.J., Ruokolainen, J., Johansson, L.S., and Seppala, J. (2013) Processable polyaniline suspensions through in situ polymerization onto nanocellulose. *Eur. Polym. J.*, **49**, 335–344.
94. Hietala, M., Mathew, A.P., and Oksman, K. (2013) Bionanocomposites of thermoplastic starch and cellulose nanofibers manufactured using twin-screw extrusion. *Eur. Polym. J.*, **49**, 950–956.
95. Littunen, K., Hippi, U., Saarinen, T., and Seppälä, J. (2013) Network formation of nanofibrillated cellulose in

solution blended poly(methyl methacrylate) composites. *Carbohydr. Polym.*, **91**, 183–190.

96. Liu, A. and Berglund, L.A. (2013) Fire-retardant and ductile clay nanopaper biocomposites based on montmorillonite in matrix of cellulose nanofibers and carboxymethyl cellulose. *Eur. Polym. J.*, **49**, 940–949.

97. Fortunato, G., Zimmermann, T., Lubben, J., Bordeanu, N., and Hufenus, R. (2012) Reinforcement of polymeric submicrometer sized fibers by microfibrillated cellulose. *Macromol. Mater. Eng.*, **297**, 576–584.

98. Medeiros, E.S., Mattoso, L.H.C., Ito, E.N., Gregorski, K.S., Robertson, G.H., Offeman, R.D., Wood, D.F., Orts, W.J., and Imam, S.H. (2008) Electrospun nanofibers of poly(vinyl alcohol) reinforced with cellulose nanofibrils. *J. Biobased Mater. Bioenergy*, **2**, 1–12.

99. Rebouillat, S. and Pla, F. (2013) State of the art manufacturing and engineering of nanocellulose: a review of available data and industrial applications. *J. Biomater. Nanobiotechnol.*, **4**, 165–188.

100. Oksman, K., Mathew, A.P., Bondeson, D., and Kvien, I. (2006) Manufacturing process of cellulose whiskers/polylactic acid nanocomposites. *Compos. Sci. Technol.*, **66** (15), 776–2784.

101. Bondeson, D. and Oksman, K. (2007) Polylactic acid/cellulose whisker nanocomposites modified by polyvinyl alcohol. *Compos. Sci. Technol.*, **38** (12), 2486–2492.

102. de Menezes, A. Jr., Siqueira, G., Curvelo, A.A.S., and Dufresne, A. (2009) Extrusion and characterisation of functionalised cellulose whiskers reinforced polyethylene nanocomposites. *Polymer*, **50** (19), 4552–4563.

103. Nakagaito, A. and Yano, H. (2008) Toughness enhancement of cellulose nanocomposites by alkali treatment of the reinforcing cellulose nanofibers. *Cellulose*, **15** (2), 323–331.

104. Özgür, S.M. and Oksman, K. (2008) Novel nano- composites based on polyurethane and micro fibrillated cellulose. *Compos. Sci. Technol.*, **68** (3-4), 908–914.

105. Iwamoto, S., Abe, K., and Yano, H. (2008) The effect of hemicelluloses on wood pulp nanofibrillation and nanofiber network characteristics. *Biomacromolecules*, **9**, 1022–1026.

106. Shimazaki, Y., Miyazaki, Y., Takezawa, Y., Nogi, M., Abe, K., Ifuku, S., and Yano, H. (2007) Excellent thermal conductivity of transparent cellulose nanofiber/epoxy resin nanocomposites. *Biomacromolecules*, **8**, 2976–2978.

107. Nogi, M., Handa, K., Nakagaito, A.N., and Yano, H. (2005) Optically transparent bionanofiber composites with low sensitivity to refractive index of the polymer matrix. *Appl. Phys. Lett.*, **87**, 243110–243112.

108. Zhang, J. and Zhang, J. (2010) Advanced functional materials based on cellulose. *Acta Polym. Sin.*, **0** (12), 1376–1398.

109. Khalil, H.P.S.A., Bhat, A.H., and Yusra, A.F.I. (2012) Green composites from sustainable cellulose nanofibrils: a review. *Carbohydr. Polym.*, **87**, 963–979.

110. Samir, M.A.S.A., Alloin, F., and Dufresne, A. (2005) Review of recent research into cellulosic whiskers, their properties and their application in nanocomposite field. *Biomacromolecules*, **6**, 612–626.

111. Mathew, A.P., Oksman, K., Pierron, D., and Harmand, M.F. (2012) Fibrous cellulose nanocomposite scaffolds prepared by partial dissolution for potential use as ligament or tendon substitutes. *Carbohydr. Polym.*, **87**, 2291–2298.

112. Klemm, D., Schumann, D., Udhardt, U., and Marsch, S. (2001) Bacterial synthesized cellulose – artificial blood vessels for microsurgery. *Prog. Polym. Sci.*, **26**, 1561–1603.

113. Nakayama, A., Kakugo, A., Gong, J.P., Osada, Y., Takai, M., Erata, T., and Kawano, S. (2004) High mechanical strength double-network hydrogel with bacterial cellulose. *Adv. Funct. Mater.*, **14**, 1124–1128.

114. Gatenholm, P. and Klemm, D. (2010) Bacterial nanocellulose as a renewable material for biomedical applications. *MRS Bull.*, **35**, 208–213.

115. Fernandes, E.M., Pires, R.A., Mano, J.F., and Reis, R.L. (2013) Bionanocomposites from lignocellulosic resources: properties, applications and future trends for their use in the biomedical field. *Prog. Polym. Sci.*, **38** (10–11), 1415–1441.
116. Haimer, E., Liebner, F., Potthast, A., and Rosenau, T. (2012) in *Polysaccharide Building Blocks: A Sustainable Approach to the Development of Renewable Biomaterials*, 1st edn (eds Y. Habibi and L.A. Lucia), John Wiley & Sons, Inc., Hoboken, NJ, pp. 367–386.
117. Fang, J.M., Sun, R.C., Tomkinson, J., and Fowler, O. (2000) Acetylation of wheat straw hemicellulose B in a new non-aqueous swelling system. *Carbohydr. Polym.*, **41**, 379–387.
118. Peng, F., Peng, P., Xu, F., and Sun, R.C. (2012) Fractional purification and bioconversion of hemicelluloses. *Biotechnol. Adv.*, **30**, 879–903.
119. Vuorinen, T. and Alen, R. (1999) in *Analytical Methods in Wood Chemistry, Pulping, and Papermaking*, 3rd Series (eds E. Sjostrom and R. Alen), Springer-Verlag, Berlin and Heidelberg, pp. 37–76.
120. Nilsson, M., Saulnier, L., Andersson, R., and Åman, P. (1996) Water unextractable polysaccharides from three milling fractions of rye grain. *Carbohydr. Polym.*, **30** (4), 229–237.
121. Ebringerova, A. and Heinze, T. (2000) Xylan and xylan derivatives – biopolymers with variable properties, 1 – naturally occurring xylan structures, procedures and properties. *Macromol. Rapid Commun.*, **21**, 542–556.
122. Bataillon, M., Mathaly, P., Nunes Cardinali, A.P., and Duchiron, F. (1998) Extraction and purification of arabinoxylan from destarched wheat bran in a pilot scale. *Ind. Crops Prod.*, **8** (1), 37–43.
123. Faurot, A., Saulnier, L., Berot, S., Popineau, Y., Petit, M., Rouau, X., and Thibault, J. (1995) Large scale isolation of water-soluble and water-insoluble pentosans from wheat flour. *Food Sci. Technol.*, **28** (4), 436–441.
124. Luo, Q., Peng, H., Zhou, M., Lin, D., Ruan, R., Wan, Y., Zhang, J., and Liu, Y. (2012) Alkali extraction and physico-chemical characterization of hemicelluloses from young bamboo (*Phyllostachys pubescens* Mazel). *BioResources*, **7** (4), 5817–5828.
125. Garcia, R.B., Nagashima, T. Jr., Praxedes, A.K.C., Raffin, F.N., Moura, T.F.A.L., and do Egito, E.S.T. (2001) Preparation of micro and nanoparticles from corn cobs xylan. *Polym. Bull.*, **46** (5), 371–379.
126. Li, Y., Zhang, L., and Sun, X. (2012) Nano xylan and preparation method thereof. CN Patent 102675481 A, filed Jun. 11, 2012 and issued Sept. 19, 2012.
127. Peng, X., Ren, J., Zhong, L., and Sun, R.C. (2011) Nanocomposite films based on xylan-rich hemicelluloses and cellulose nanofibers with enhanced mechanical properties. *Biomacromolecules*, **12**, 3321–3329.
128. Guan, Y., Zhang, B., Bian, J., Peng, F., and Sun, R.C. (2014) Nanoreinforced hemicellulose-based hydrogels prepared by freeze–thaw treatment. *Cellulose*, **21**, 1709–1721.
129. Tatsuro, T., Satoshi, K., and Takashi, M. (2003) Laminate and its manufacturing method. JP Patent 2005014332-A, filed Jun. 25, 2003 and issued Jan. 20, 2005.
130. El Mansouri, N.E. and Salvado, J. (2007) Analytical methods for determining functional groups in various technical lignins. *Ind. Crops Prod.*, **26** (2), 116–124.
131. Pua, F.L. and Sapuan, S.M. (2013) in *Biomass-Based Biocomposites* (eds V.K. Thakur and A.S. Singha), Smithers Rapra Technology Ltd, Shawbury, Shrewsbury, Shropshire, pp. 259–276.
132. Doherty, W.O.S., Mousaviouna, P.C., and Fellows, M. (2011) Value-adding to cellulosic ethanol: lignin polymers. *Ind. Crops Prod.*, **33**, 259–276.
133. Thielemans, W. and Wool, R.P. (2005) Lignin esters for use in unsaturated thermosets: lignin modification and solubility modeling. *Biomacromolecules*, **6** (4), 1895–1905.
134. Novikova, L.N., Medvedeva, S.A., Volchatova, I.V., and Bogatyreva, S.A. (2002) Changes in macromolecular

characteristics and biological activity of hydrolytic lignin in the course of composting. *Appl. Biochem. Microbiol.*, **38** (2), 181–185.

135. Darie, R.N., Constantinescu, G., Cazacu, G., and Vasile, C. (2010) in *Adezivi, materiale compozite şi alte aplicaţii pe bază de lignină* (Binders, Composites and Other Applications Based on Lignins) (eds M. Totolin and G. Cazacu), MPIM Publishing, Iasi, pp. 90–126.

136. Chiellini, E., Cinelli, P., Corti, A., Kenawy, E.R., Fernandes, E.G., and Solaro, R. (2000) Environmentally sound blends and composites based on water-soluble polymer matrices. *Macromol. Symp.*, **152**, 83–94.

137. Malutan, T., Nicu, R., and Popa, V.I. (2008) Contribution to the study of hydroxymethylation reaction of alkali lignin. *BioResources*, **3**, 13–20.

138. Popa, V.I., Capraru, A.M., Grama, S., and Malutan, T. (2011) Nanoparticles based on modified lignins with biocide properties. *Cellul. Chem. Technol.*, **45**, 221–226.

139. Gilca, I.A., Ghitescu, R.E., Puitel, A.C., and Popa, V.I. (2014) Preparation of lignin nanoparticles by chemical modification. *Iran. Polym. J.*, **23**, 355–363.

140. Nevárez, L.A.M., Casarrubias, L.B., Celzard, A., Fierro, V., Muñoz, V.T., Davila, A.C., Lubian, J.R.T., and Sánchez, G.G. (2011) Biopolymer-based nanocomposites: effect of lignin acetylation in cellulose triacetate films. *Sci. Technol. Adv. Mater.*, **12**, 1–16.

141. Lin, T.T., Wu, H.J., Lu, Q.F., Ling, Y.H., and He, L.H. (2013) Preparation of polyaniline-lignin nanocomposites and their reducing adsorption for silver ions. *Acta Polym. Sin.*, **0** (3), 320–326.

142. Jiang, C., He, H., Jiang, H., Ma, L., and Jia, D.M. (2013) Nano-lignin filled natural rubber composites: preparation and characterization. *eXPRESS Polym. Lett.*, **7** (5), 480–493.

143. Hilburg, S.L., Elder, A.N., Chung, H., Ferebee, R.L., Bockstaller, M.R., and Washburn, N.R. (2014) A universal route towards thermoplastic lignin composites with improved mechanical properties. *Polymer*, **55**, 995–1003.

144. Sevastyanova, O., Qin, W., and Kadla, J.F. (2010) Effect of nanofillers as reinforcement agents for lignin composite fibers. *J. Appl. Polym. Sci.*, **117** (5), 2877–2881.

145. Zimniewska, M., Kozłowski, R., and Batog, J. (2008) Nanolignin modified linen fabric as a multifunctional product. *Mol. Cryst. Liq. Cryst.*, **484**, 43/[409]–50/[416].

146. Gilca, I.A. and Popa, V.I. (2013) Study on biocidal properties of some nanoparticles based on epoxi lignin. *Cellul. Chem. Technol.*, **47** (3-4), 239–245.

147. Burrs, S.L., Jairam, S., Vanegas, D.C., Tong, Z., and McLamore, E.S. (2013) in *Lignin and Silicate Based Hydrogels for Biosensor Applications*, vol. 8719. Proceedings of the Smart Biomedical and Physiological Sensor Technology X, May 1-2, 2013 (eds B.M. Cullum and E.S. McLamore), United States, Baltimore, MD.

148. USEPA (2007) *Nanotechnology White Paper*, Science Policy Council, U.S. Environmental Protection Agency, Washington, DC, pp. 4–21.

149. Hristozov, D. and Malsch, I. (2009) Hazards and risks of engineered nanoparticles for the environment and human health. *Sustainability*, **1**, 1161–1194.

Index

Nanomaterials and Nanocomposites: Zero- to Three-Dimensional Materials and Their Composites,
First Edition. Edited by Visakh P.M. and Maria José Martínez Morlanes.

WILEY END USER LICENSE AGREEMENT

Go to www.wiley.com/go/eula to access Wiley’s ebook EULA.